THERMAL-HYDRAULIC ANALYSIS OF INNOVATIVE FUEL CONFIGURATIONS FOR THE SODIUM FAST REACTOR

By

Matthew J Memmott

V. 1

B.S., Chemical Engineering (2005)
Brigham Young University

M.S., Nuclear Engineering (2007)
Massachusetts Institute of Technology

SUBMITTED TO THE DEPARTMENT OF NUCLEAR SCIENCE
AND ENGINEERING
IN PARTIAL FULFILLMENT OF THE REQUIREMENTS FOR THE DEGREE OF

DOCTOR OF PHILOSOPHY IN NUCLEAR SCIENCE AND ENGINEERING
AT THE
MASSACHUSETTS INSTITUTE OF TECHNOLOGY
[JUNE]
MAY 2009

Signature of Author: ______________________________
Matthew J Memmott
Department of Nuclear Science and Engineering
May 22, 2009

Certified by ______________________________
Dr. Pavel Hejzlar
Reactor Design Lead
Thesis Co-Supervisor

Certified by ______________________________
Dr. Jacopo Buongiorno
Associate Professor of Nuclear Science and Engineering
Thesis Co-Supervisor

Accepted by: ______________________________
Jacquelyn C. Yanch
Professor of Nuclear Science and Engineering
Chair, Department Committee on Graduate Students

THERMAL-HYDRAULIC ANALYSIS OF INNOVATIVE FUEL CONFIGURATIONS FOR THE SODIUM FAST REACTOR

By

Matthew J Memmott

Submitted to the Department of Nuclear Science and Engineering on May 22, 2009 in partial
fulfillment of the requirements for the degree of Doctor of Philosophy in
Nuclear Science and Engineering

Abstract

The sodium fast reactor (SFR) is currently being reconsidered as an instrument for actinide management throughout the world, thanks in part to international programs such as the Generation-IV and especially the Global Nuclear Energy Partnership (GNEP). The success of these programs, in particular the GNEP, is dependent upon the ability of the SFR to manage actinide inventory while remaining economically competitive. In order to achieve these goals, the fuel must be able to operate reliably at high power densities. However, the power density of the fuel is limited by fuel-clad chemical interaction (FCCI) for metallic fuel, cladding thermal and irradiation strain, the fuel melting point, sodium boiling, and to a lesser extent the sodium pressure drop in the fuel channels.

Therefore, innovative fuel configurations that reduce clad stresses, sodium pressure drops, and fuel/clad temperatures could be applied to the SFR core to directly improve the performance and economics. Two particular designs of interest that could potentially improve the performance of the SFR core are the internally and externally cooled annular fuel and the bottle-shaped fuel.

In order to evaluate the thermal-hydraulic performance of these fuels, the capabilities of the RELAP5-3D code have been expanded to perform subchannel analysis in sodium-cooled fuel assemblies with non-conventional geometries. This expansion was enabled by the use of control variables in the code. When compared to the SUPERENERGY II code, the prediction of core outlet temperature agreed within 2%. In addition, the RELAP5-3D subchannel model was applied to the ORNL 19-pin test, and it was found that the code could predict the measured outlet temperature distribution with a maximum error of ~8%. As an application of this subchannel model, duct ribs were explored as a means of reducing core outlet temperature peaking within the fuel assemblies. The performance of the annular and bottle-shaped fuel was also investigated using this subchannel model.

The annular fuel configurations are best suited for low conversion ratio cores. The magnitude of the power uprate enabled by metal annular fuel in the CR = 0.25 cores is 20%, and is limited by the FCCI constraint during a hypothetical flow blockage of the inner-annular channel due to the small diameters of the inner-annular flow channel (3.6 mm). On the other hand, a complete blockage of the hottest inner-annular flow channel in the oxide fuel case results in sodium boiling, which renders the annular oxide fuel concept unacceptable for use in a SFR. The bottle-shaped fuel configurations are best suited for high conversion ratio cores. In the CR = 0.71 cores, the bottle-shaped fuel configuration reduces the overall core pressure drop in the fuel channels by up to 36.3%. The corresponding increase in core height with bottle-shaped fuel is between 15.6% and 18.3%.

A full-plant RELAP5-3D model was created to evaluate the transient performance of the base and innovative fuel configurations during station blackout and UTOP transients. The transient analysis confirmed the good thermal-hydraulic performance of the annular and bottle-shaped fuel designs with respect to their respective solid fuel pin cases.

Thesis Co-Supervisor: Jacopo Buongiorno
Title: Associate Professor of Nuclear Science and Engineering, MIT

Thesis Co-Supervisor: Pavel Hejzlar
Title: Reactor Design Lead, TerraPower, LLC

Acknowledgements

I would like to first thank my co-advisors, Professor Jacopo Buongiorno and Dr. Pavel Hejzlar for their continued guidance and direction with this work. Their knowledge of thermal-hydraulics, reactor systems, and fast reactor technology helped make this thesis possible. I have joined the ranks of students who have benefited from Jacopo's tutelage. I feel fortunate to have been one of Pavel's last students before he left MIT, and I am grateful for the time and effort he put into guiding me through this work. His careful scrutiny and vast knowledge of fast reactor systems provided the framework for the topics addressed in this thesis.

I would like to especially thank Cliff B. Davis (INL), who provided constant direction, guidance, and suggestions for using RELAP5-3D. His ideas provided the basis for the subchannel model. He patiently explained complex modeling concepts and thoroughly investigated many input decks. I could not have done this work without his generous help.

I would like to acknowledge the United States Department of Energy (DOE). The funding they provided through the nuclear engineering and health physics (NEHP) fellowship made this work and my education at MIT possible.

Matt Denman provided a great deal of neutronics analysis support through MCNP modeling. Alexander Rockwell "Sandy" Ludington provided the code, reference material, and even input and output files required to model the radial compressors in RELAP5-3D, and spent much time helping me, even when his own thesis was due. Thanks! Finally Dustin Langewisch developed the base metal fuel core model used for the SFR full plant model used in this thesis.

Special acknowledgement to the Nuclear Regulatory Commission (NRC) who provided funding for my final semester at MIT, and the Idaho National Laboratory (INL) who funded the innovative fuels configurations when the idea was first forming in our minds.

I'd like to thank my parents and siblings for the support and encouragement they gave when I was frustrated or stuck. If it wasn't for their good influence, I may have stayed a grad student for 15 more years.

Finally, I owe everything that I am to my wonderful wife, Renee. If it were it not for her great patience, her multitudinous sacrifices, and her willingness to help me when I needed it the most, I never would have made it. She is my better half, and she dedicated a good portion of her life to helping me finish despite having so much of her own work to do. I look forward to our continued adventures together!

Table of Contents

List of Figures

List of Tables

Chapter 1: Introduction

1.1 Motivation

The demand for clean, affordable energy is increasing throughout the world, and nuclear energy may play a substantial role in meeting this demand. As of January 5th, 2009, there are 436 plants world-wide, which produce a total of 372 GWe. This corresponds to about 15% of the world's electricity. Predictions for overall electricity consumption increases, combined with the growing concern over fossil fuel stores, indicate that nuclear power should play a larger role in electricity production through the coming years [1.1]. In response to the growing need for clean, safe and economical nuclear power, the Generation IV international forum selected six basic reactor design concepts for potential development and commercialization [1.2]. The Global Nuclear Energy partnership (GNEP), now the Advance Fuel Cycle Initiative (AFCI), with a focus on actinide management, has selected the sodium-cooled fast reactor (SFR) as the reactor of choice.

Sodium-cooled fast reactors have regained worldwide interest in recent years thanks to international programs such as Generation IV and especially the Global Nuclear Energy Partnership. The success of these reactors in accomplishing their mission of improved actinide management, while attaining competitive economics, will largely depend upon the ability of their fuel to operate reliably at high power density. Recent focus has been placed upon the improvement of the thermal performance of the SFR concept [1.3]. The purpose of this thesis is to propose and investigate two innovative fuel configurations that aim to improve the thermal-hydraulic performance of the SFR while maintaining both a similar neutronic performance and meeting the current safety margins. These innovative fuel configurations consist of both internally/externally cooled annular fuel and bottle-shaped fuel. The annular fuel configuration allows for an increase in the power density of the SFR low conversion ratio core by reducing the peak clad and fuel temperatures within the core. The bottle-shaped fuel configuration allows for a decrease in the pump size of the reactor by decreasing the hydraulic flow resistance in the plenum region of the core.

1.2 Objectives and Contributions

The objective of this thesis is to assess the thermal-hydraulic performance of both internally/externally cooled annular fuel configurations and bottle-shaped fuel configurations for both oxide and metal fuels at high and low conversion ratios. This includes an assembly design study for each fuel configuration, a subchannel analysis of each fuel configuration, and a safety analysis for each fuel configuration. The safety analysis includes investigation of various accident conditions, including the station blackout transient, using RELAP5-3D. It has been widely recognized that reactivity feedbacks play a major role in the safety performance of the SFR fuel. The parameters used in this thesis for safety analyses have been taken from previous SFR design reports. Design of the core configuration was performed with assistance from MIT graduate student Matthew Denman, who created annular and solid fuel models for neutronic analysis using MCNP and evaluated key aspects of the neutronic performance.

A key point of this thesis is the investigation of the benefits derived from utilizing a supercritical carbon dioxide (S-CO_2) cooled Brayton cycle for power conversion in the SFR. These benefits include higher efficiencies and heat withdrawal without the use of auxiliary feedwater system or steam dump to condenser system. A RELAP5-3D model of a S-CO_2 power conversion system (PCS) was created in collaboration with MIT graduate student Alexander Rockwell "Sandy" Ludington, who designed the 500 MW thermal S-CO_2 PCS using CYCLES III.

The elements of this thesis include:

1. The development of an assembly design with annular fuel pins capable of operating at 20% higher power density to be used in the low conversion ratio SFR.
2. Creation of a RELAP5-based subchannel analysis model that can be used to evaluate the steady state subchannel characteristics of annular and bottle-shaped fuel assemblies.
3. Investigation of "duct ribs" as a method to reduce the core outlet temperature nonuniformities seen in all standard hexagonal SFR fuel assemblies.
4. Development of an assembly design for bottle-shaped fuel configurations capable of reducing the pressure drop in the SFR core by ~33-36%.
5. Characterization of clad structural integrity at critical points of bottle-shaped and annular fuel configurations.
6. Development of a full plant SFR RELAP5-3D model based upon the ABR1000 design parameters for future contributors to use in both thermal-hydraulic and uncertainty propagation simulations.

7. Evaluation of the performance of the base, annular, and bottle-shaped fuel configurations during station blackout and unprotected transient overpower (UTOP) events.
8. Identification of neutronic, thermal-hydraulic, and structure aspects of the bottle-shaped and annular fuel configurations that require further analysis or improvement of the design.
9. Creation of an S-CO_2 PCS RELAP5-3D model which utilizes radial compressors rather than axial compressors for use with the SFR full plant RELAP5-3D model by future contributors.
10. Evaluation of the performance of the S-CO_2 PCS during an unprotected loss of flow (ULOF) accident in the SFR.

The key original contributions are items # 1, 2, and 4.

1.3 The Sodium-Cooled Fast Reactor

The Department of Energy's (DOE's) Global Nuclear Energy Partnership was announced February 6th, 2006 as part of the Advanced Energy Initiative [1.4]. One of the key goals of GNEP was the development and deployment of advanced nuclear recycling technology. Under the plan proposed by GNEP, a prototypical advanced burning reactor was to be demonstrated and the concept was to be commercialized [1.5]. Currently, reactor burner concept is under development within the framework of Advanced Fuel Cycle Initiative (AFCI). This "burner" reactor will be a sodium-type reactor and will be based upon the experience and knowledge derived from the S-PRISM reactor [1.6] and the EBR II reactor [1.7].

The Argonne National Laboratory (ANL) developed a pre-conceptual design for a burner reactor, known as the advanced burner test reactor (ABTR) [1.8], which is based upon the S-PRISM and EBR II designs. The ABTR is a 250MWth pool-type sodium-cooled fast reactor, which can be fitted with either a steam Rankine power conversion system, or a super-critical carbon dioxide cooled Brayton power conversion system. The size and parameters for this test reactor were selected to be representative of commercial scale reactors, but small enough to avoid cost enhancements based upon the complex designs and engineering required for larger reactors. The pool design was selected because of past experience with this design, the inherent safety, and the improved economics [1.8]. The ABTR, although too small for the current thesis analysis, paved the way for the development of a 1000 MWth configuration, known as the ABR1000. The ABR1000 is also a pool-type sodium reactor with four separate secondary loops, direct reactor auxiliary cooling systems (DRACS), and 4x25% Rankine PCS trains.

The full plant model developed in Section 5 is based upon a combination of engineering judgment and the current ABR1000 concepts. This reactor design is a scaled up version of the ABTR, and is thus also based upon the S-PRISM and EBR II design and operation experience. The success of commercially deployed SFRs depends upon the economic performance of these reactors [1.9, 1.10]. In an attempt to improve SFR economics, the capital cost can be reduced by minimizing the pump sizes and thus minimizing the reactor vessel size. Additionally, the power density of the core can be increased, resulting in a higher power output. The innovative fuel configurations analyzed in this thesis attempt to improve these two aspects of the economic performance of the ABR reactor.

1.4 SFR Safety

There is a large range of accidents that could occur within the SFR system. It is a recent practice in SFR design, however, to focus on three primary accident scenarios that encapsulate all the potential pathways to core damage. These accidents are the unprotected loss of flow accident, the unprotected transient overpower accident, and the unprotected loss of heat sink accident (ULOHS). These accidents are each unprotected, or they do not include the scram of the control rods. If a core is not damaged in the course of these events, it is considered suitable for use in the SFR system.

ULOF – In the unprotected loss of flow accident, the primary pumps stop, resulting in a loss of forced convection flow through the core and intermediate heat exchangers (IHX). The pumps can either coast down, based upon the inertia of a flywheel (if they are mechanical pumps) or an electrical capacitor (if they are electromagnetic pumps), or the pumps can seize, where the pump velocity instantaneously drops to zero. In each of these accidents, natural circulation becomes the only means of carrying heat away from the core. The heat is transferred through the IHX to the secondary system where it is then transferred to the still-operational PCS. The feedwater regulation in a Rankine PCS steam generator is accomplished using either condensers or some type of safety-grade auxiliary feedwater system. If a S-CO_2 PCS is used, the turbine is on the same shaft as the compressors, and thus can drive the compressors, which ensures a heat sink for the reactor decay heat. In order to prevent overcooling (which could lead to large positive reactivity injection), the flow rates through the turbine or steam generator must be carefully controlled.

UTOP – In the unprotected transient overpower accident, reactivity is inserted into the core, typically by the ejection or slow removal of one or more control rods. As a conservative estimate, it is generally considered that the rod with the highest worth in the core is the rod that is withdrawn. In both cases, the increase in reactivity is balanced by the negative core reactivity feedbacks; the power will peak and then attain a new steady state level at some point higher than the power level prior to the reactivity insertion.

ULOHS – In the unprotected loss of heat sink accident, the heat sink fails, either by a leak in the PCS coolant system or by a loss of pumps or feedwater. In each case, the temperature difference across the core collapses, the core gradually shuts down due to negative reactivity feedbacks, and the DRACS initiates. The coolant temperatures steadily rise until the DRACS modules can withdraw an amount of heat equivalent to the decay heat produced in the core, at which point temperatures in the core peak and begin to decrease.

Unprotected Station Blackout – A station blackout is considered the most severe of the SFR transients. This accident is a loss of all electrical power to the system and assumes that backup electrical power also fails. In addition, scram is assumed to fail. In essence, this transient is equivalent to a combined ULOHS and ULOF accident. In this transient, the flow stops and the DRACS valves open upon initiation. The temperatures increase, making the core subcritical, and then natural circulation becomes the primary mode of transferring heat away from the core. Typically, it is assumed that only two out of three DRACS valves open, while the third DRACS module remains inoperable (this is the so-called "single failure criterion"). This transient is performed in the current thesis as the design-basis accident and determines which fuel configurations are acceptable for utilization in the SFR design discussed in this work.

1.5 Previous Work at MIT

A large degree of progress and contributions have been made before the work described in the thesis was initiated. These works include several aspects of innovative fuel and PCS contributions in addition to the SFR concepts and designs described above. The major contributions at MIT that laid the groundwork for analyses performed in this thesis are given below:

- In previous studies, the S-CO_2 was identified as an ideal candidate for a PCS when the reactor system had an outlet temperature greater than ~500 °C. A RELAP5-3D model of a S-CO_2 PCS was developed by Pope for use with the S-CO_2 cooled GFR [1.11]. His work provided a RELAP5-3D template, including pumps, turbines pipes, and branches in the S-CO_2 system. Pope also developed RELAP5-3D models for the HEATRIC PCHE exchangers that provided the volumetric material property curves, heat length correlations, and multiplication factors utilized in this thesis.
- CYCLES III, a code that designs and sizes a S-CO_2 PCS loop given certain inlet parameters, was developed, improved, and simplified into a user friendly code [1.12, 1.13]. The results of a CYCLES III optimization run provides the sizes,

flow rates, and flow areas needed to modify the RELAP5-3D template created by Pope for use in the ABR1000 plant model.

- A MCNP model for the ABR1000 core was created and verified by Denman [1.14, 1.15]. This MCNP model could accommodate both annular and solid fuel configurations and provided power peaking profiles utilized in the current thesis.
- A sodium subchannel analysis code known as SUPERENERGY II was created by Todreas and Basehore [1.16]. This code can only perform analyses on hexagonal assemblies of 8 rings or less, and does not evaluate fuel rods. It has been verified against experimental EBR II data, however, and was used to verify the RELAP5-3D subchannel analysis code developed in this thesis.

1.6 Organization of this Thesis

Chapter 2 introduces the reference fuel assembly design and performance parameters of the SFR for both metal and oxide fuel configurations at high and low conversion ratios. The annular and bottle-shaped fuel configurations are introduced, and constraints and figures of merit in creating these configurations are presented. The relations used to optimize both of the innovative fuel configurations are described, and the most promising fuel configurations for high and low conversion ratios are discussed.

Chapter 3 describes the development of a subchannel analysis model using RELAP5-3D that is capable of evaluating the innovative fuel configurations. The assumptions and equations used to develop this model are found in this chapter as well.

As a first application of the subchannel model, the inclusion of duct ribs within the SFR assemblies is discussed.

Chapter 4 presents the results of the subchannel analyses of the innovative fuel configuration fuel assemblies. The fuel assembly geometries for annular fuel were optimized based upon the results of the subchannel analyses. This chapter describes the magnitude of the power uprate possible for annular fuel configurations. An analysis of an inner-annular subchannel flow blockage accident is presented in this chapter in which performance of an annular fuel assembly with the hottest channel blocked was modeled. The reduction in core pressure drop, which is made possible by using bottle-shaped fuel configurations, is presented, and a structural analysis for key aspects of the innovative fuel configurations concludes each fuel discussion.

Chapter 5 develops a full plant RELAP5-3D SFR model based on the ABR1000. This model includes the primary pool, the secondary system, the PCS boundary, the core, and the DRACS modules. Assumptions, material properties, geometric relations, thermal properties, and hydraulic properties are described, while details of each RELAP5-3D component are listed. Alternate core configurations for each of the valid innovative core configurations are developed. The steady-state performance of the full plant model with each core configuration is detailed.

Chapter 6 analyzes the performance of each core configuration during station blackout and UTOP transients. The key parameters and figures of merit for each transient are presented. Optimization of the full plant model performance is discussed as well as the safety limits and figures of merit for the transients. A comparison of each innovative fuel configuration against the corresponding base configuration is also provided as an assessment of the safety performance of the innovative fuel configurations.

Chapter 7 describes the S-CO_2 PCS developed at MIT and the creation of a RELAP5-3D plant model to simulate this system. The steady state performance of the RELAP5-3D plant model is presented. An evaluation of the performance of the SFR during an unprotected loss of flow (ULOF) accident with both a Rankine PCS boundary and an S-CO_2 PCS is included.

Chapter 8 includes a summary of the work performed in this thesis and a description of areas where future work is required.

Chapter 2: Preliminary Scoping Studies

The innovative fuel configurations studied in this thesis aim to reduce clad stresses, fuel and/or clad temperatures, and pumping requirements for the SFR core designs. In turn, these improvements will have a direct positive impact on the achievable power density in the sodium reactor core. To fully evaluate the performance of innovative fuel configurations, a detailed subchannel model is needed, which has the capacity to thermal-hydraulically investigate the temperature distributions, hot channels, and hot spots within the fuel. Additionally, pressure gradients, turbulent flow patterns, and coolant velocities should be assessed using this subchannel model.

In addition to subchannel analyses, safety analyses, which evaluate the performance of the entire plant, must be performed to ensure that the fuel does not negatively affect plant performance during key accident scenarios. As acceptance criteria for these nuclear safety analyses, the innovative fuel must perform at least as well as, if not better than, the standard fuel types currently used in the SFR designs. If the innovative fuel meets this standard, they will be considered acceptable from a safety point of view for use in the SFR.

Before the computationally and time intensive analyses described above are initiated, it is important to ensure that the fuel design in question has the potential to improve thermal hydraulic performance of the core in the SFR. Thus, a specific set of SFR fuel designs was selected as the base case. Using these designs, simple, one-dimensional, single rod and full assembly models were created using MathCAD [2.1] to determine the thermal hydraulic performance of the simplified base fuel assembly. Then, a similar model was created for each innovative fuel type, and the thermal hydraulic performance was again calculated. The results of these preliminary studies served as the basis for evaluating which designs merited further investigation using a subchannel and full plant model.

2.1 Base Fuel Designs

A comprehensive analysis of potential fuel designs has been undertaken by Hoffman et al. [2.2] in which several core and assembly designs are identified for both metal and oxide fuels. As a fair amount of uncertainty remains as to which conversion ratio (CR) will be utilized in the SFR, a wide range of conversion ratios are considered in these core designs. The base cases for the scoping study are the breakeven (CR=1.0) and low (CR=0.25) conversion ratio cores for both metal and oxide fuel. These fuel designs are considered bounding conditions, as the low conversion ratio core would serve as a burner reactor, while the high conversion ratio core would serve as a breakeven reactor. Breeder reactors, (CR>1.0) are not part of the current SFR programs in the US (e.g., GNEP), and thus are not considered in this thesis.

The Advanced Burner Reactor (ABR1000) is the reactor of choice for the GNEP burner reactor. Thus, it is the reactor upon which the core and plant dimensions and operating parameters are based. The ABR1000 reactor design is based upon the SUPERPRISM (S-PRISM) reactor, which is a 1000 MWth pool reactor with a modular design intended to operate at either breakeven or burning conditions [2.3].

2.1.1 High Conversion Ratio Cores

The breakeven core is the current core design of choice for the ABR1000. The core consists of driver (fuel) assemblies, primary and secondary control assemblies, reflector assemblies, and shield assemblies. The driver assemblies are divided into three regions. The inner driver assemblies, which have the lowest fuel enrichment, the middle driver assemblies, which have moderate enrichment, and the outer driver assemblies which have the highest fuel enrichment. The design details of the core configurations for each type of breakeven conversion ratio core can be found in Table 2.1, while an illustration of the core layout can be found in Fig. 2.1.

Table 2.1: Design configuration of breakeven (CR = 1.0) cores [2.2]

	Metal	Oxide
Driver assemblies	151	151
- Inner	19	19
-Middle	66	66
-Outer	66	66
Blanket assemblies	0	0
Primary control assemblies	9	9
Secondary control assemblies	3	3
Gas expansion modules	0	0
Reflector assemblies	90	138
Shield assemblies	60	60
Equivalent core diameter	2.18	2.18
Equivalent reactor diameter	3.02	3.24

Both oxide and metal fuel assemblies (FA) are wire-wrap spaced hexagonal FA based upon the S-PRISM assembly design, and the key dimensions are maintained so as to ensure interchangeability between different assembly designs in the core [2.2]. HT9 is used as the primary material for the duct walls, clad, and wire wrap due to its satisfactory performance in the high temperature, high flux environment of the fast reactor [2.4]. The duct gap provides sufficient space to allow for assembly withdrawal, swelling, and bending throughout the lifetime of the fuel. The key parameters of the assembly design are found in Table 2.2.

Table 2.2.: Base assembly design parameters for high and low conversion ratio cores based upon [2.2]

Assembly pitch (cm)	16.142
Inter-assembly gap (cm)	0.432
Duct outside flat-to-flat distance (cm)	15.71
Duct material	HT9
Duct thickness (cm)	0.394

The fuel pin designs for both the oxide and metal assembly designs are found in Table 2.3. The height of the fuel in the oxide fuel pins is 36 cm longer than in the metal fuel pins, while the gas plenum of the oxide fuel pins is ~20 cm shorter than the gas plenum in the metal fuel pins. This difference was based upon a similar difference in the S-PRISM design and was maintained for the reference designs. A potential challenge for these breakeven fuel pin designs is the wire-wrap spacer. In order to reach CR=1.0, a very tight lattice is required within the assembly. This is accomplished through reducing the pitch diameter ratio by decreasing the wire-wrap thickness. However, as seen in Table 2.3, this results in very small wire-wrap diameters, which would certainly pose fabrication challenges, as well as potential performance and structural issues. Thus, ameliorating this problem was a factor in designing the innovative fuel configurations considered in this thesis. The breakeven assembly and core designs, as described above, serve as the basis for the investigation of innovative fuel designs for breakeven cores.

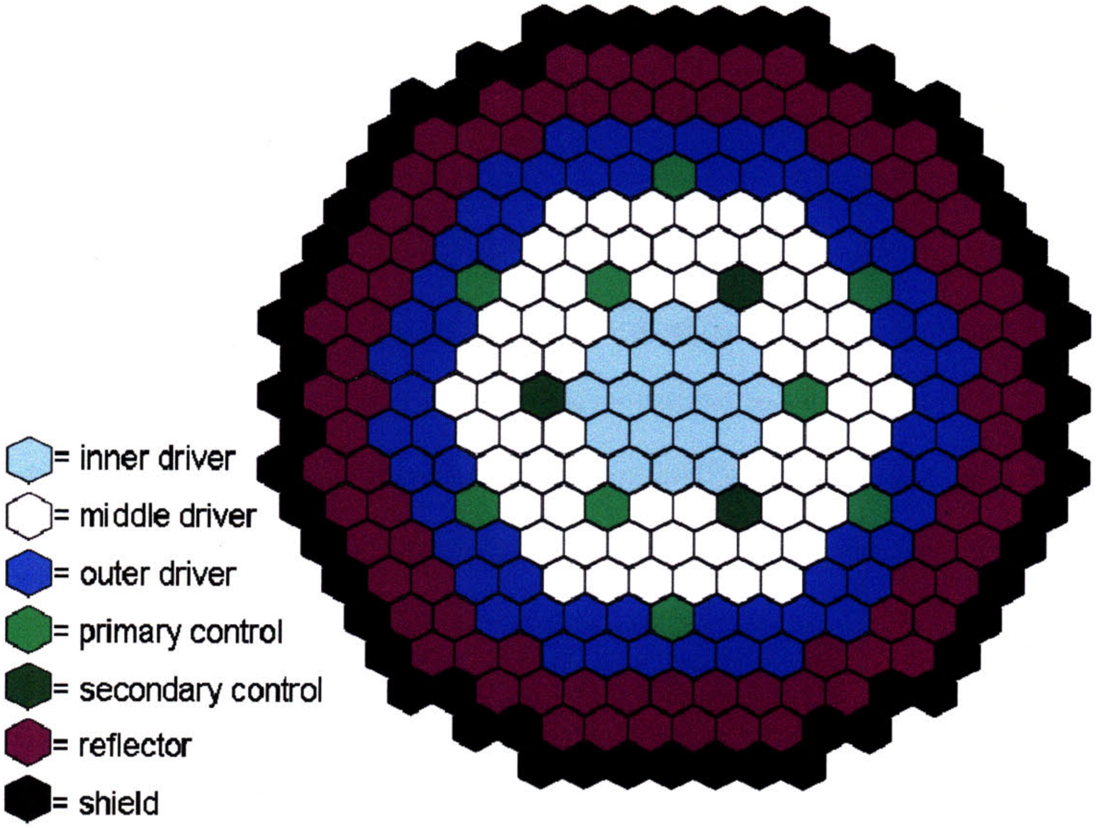

Figure 2.1: Breakeven core design (both metal and oxide)

Table 2.3: Fuel rod design parameters for high conversion ratio cores [2.2]

	Metal	Oxide
Fuel pins per assembly	271	271
Bond material	Na	He
Height (core), cm	101.60	137.16
Height (plenum), cm	191.14	170.82
Overall pin length	407.04	422.28
Fuel smeared density, %TD	75.00	85.00
Fabrication density, %TD	100.00	89.40
Pin diameter, cm	0.852	0.868
Pin pitch-to-diameter ratio	1.163	1.023
Cladding thickness, cm	0.0559	0.0635
Wire-wrap diameter, cm	0.0805	0.0195
volume fraction, %		
-fuel	31.02	49.29
-bond	10.34	2.55
-structure	24.16	28.58
-coolant	34.48	19.58

2.1.2 Low Conversion Ratio Cores

The low CR assembly designs, as described by Hoffman et al. [2.2], have the same assembly parameters, as found in Table 2.2. However, these assemblies contain fuel rods that are spaced by triangular grid spacers rather than wire-wrap spacers. The core layouts for both oxide and metal cores are quite different from the CR = 1.0 core designs as well. The burnup reactivity swing is greater in the burner core designs, which requires an increased number of control rods. Also, there is a greater number of inner driver assemblies in the burner cores, while the number of middle and outer driver assemblies is decreased in an attempt to flatten the power distribution. The design characteristics of the low conversion ratio metal and oxide cores are found in Table 2.4, while a layout of the metal and oxide burner cores are found in Figs. 2.2 and 2.3, respectively.

Table 2.4: Design configuration of burner (CR = 0.25) cores [2.2]

	Metal	Oxide
Driver assemblies	144	144
-Inner	48	72
-Middle	54	36
-Outer	42	36
Blanket	0	0
Primary control assemblies	22	16
Secondary control assemblies	3	3
Gas expansion modules	0	0
Reflector assemblies	84	102
Shield assemblies	60	60
Equivalent core diameter	2.22	2.18
Equivalent reactor diameter	3.02	3.07

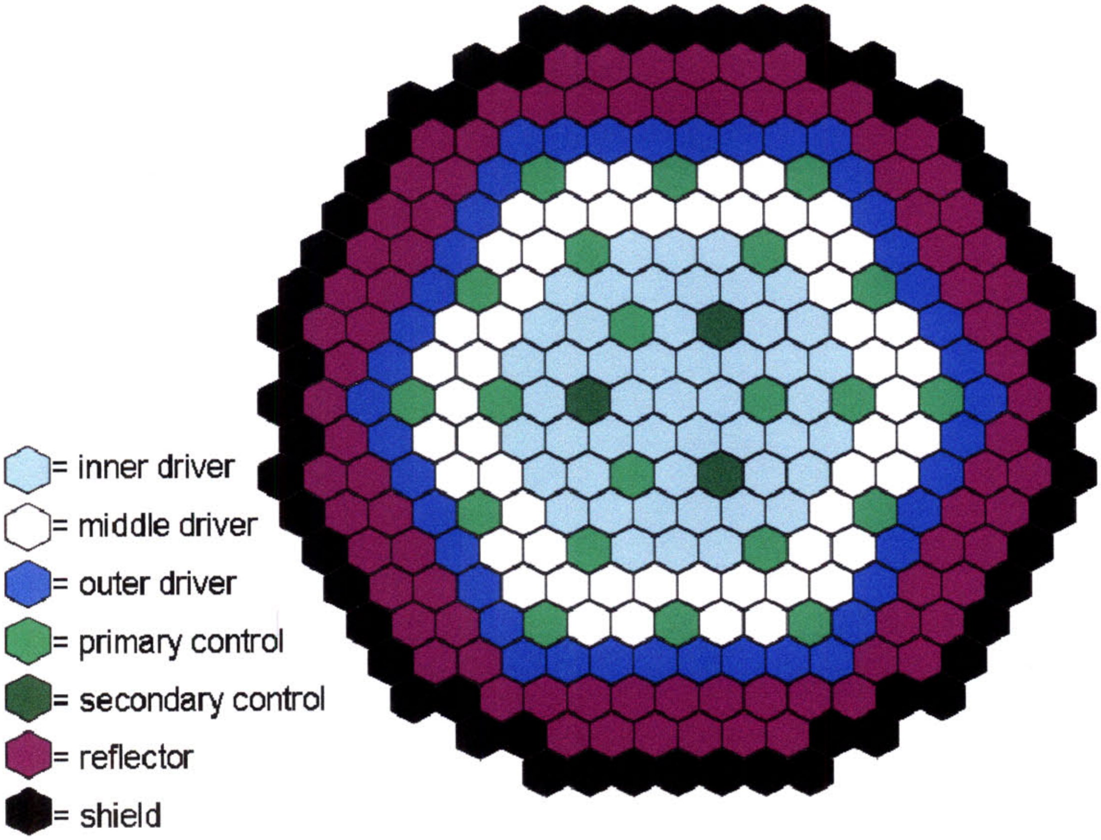

Figure 2.2: Burner core design for metal fuel [2.2]

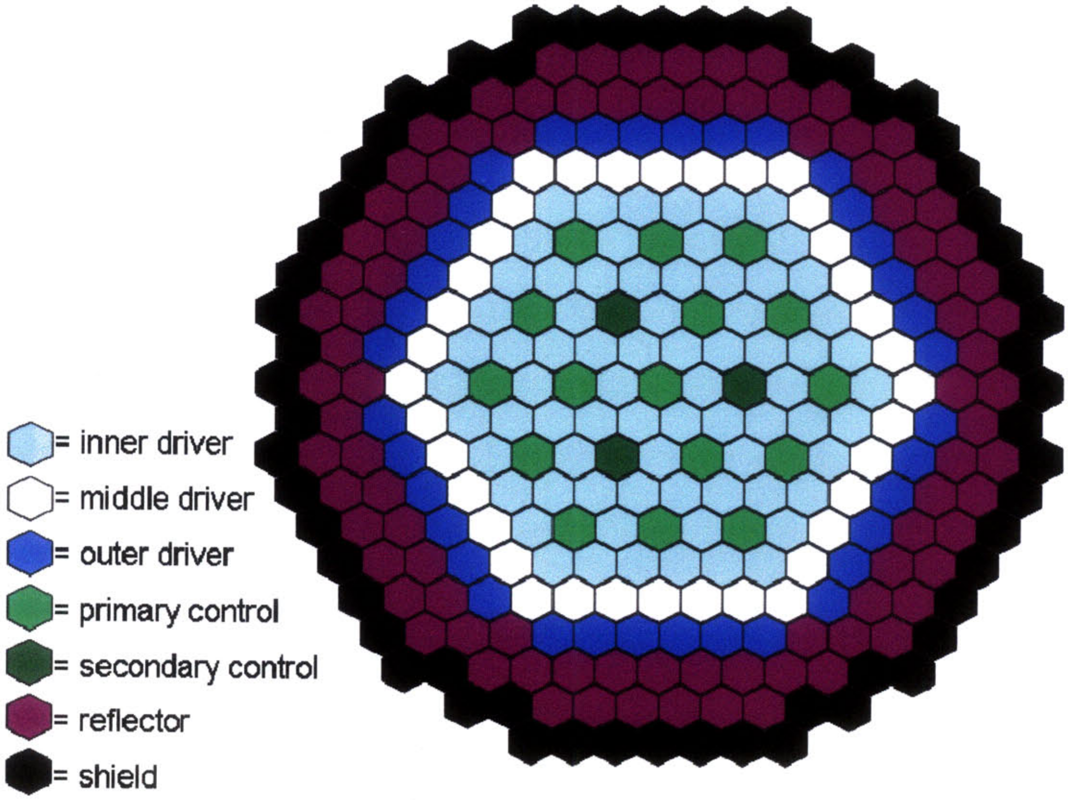

Figure 2.3: Burner core design for oxide fuel [2.2]

As with the breakeven fuel pin designs, an inspection of the fuel rod properties, as seen in Table 2.5, reveals that there is a major challenge in utilizing this low conversion ratio fuel: the diameter of the fuel rods is very small. The thermal conductivity of the fuel for the metal rods decreases as enrichment increases due to the increase in the amount of Zirconium contained in the metal fuel at lower conversion ratios. Thus, to maintain safety limits, decreased fuel rod diameters (with lower linear power) are necessary. For both metal and oxide fuels, the pin diameter is decreased because such a low CR requires that the fuel volume fraction and linear power be minimized. The resulting burner assemblies, therefore, contain a very large number of very small pins.

Table 2.5: Fuel rod design parameters for low conversion ratio cores [2.2]

	Metal	Oxide
Fuel pins per assembly	540	324
Bond material	Na	He
Height (core), cm	101.6	137.16
Height (plenum), cm	191.14	170.82
Overall pin length	407.04	422.28
Fuel smeared density, %TD	75	85
Fabrication density, %TD	100	89.4
Pin diameter, cm	0.464	0.556
Pin pitch-to-diameter ratio	1.357	1.448
Cladding thickness, cm	0.0559	0.0635
volume fraction, %		
-fuel	17.44	19.73
-bond	5.81	1.02
-structure	29.15	26.22
-coolant	47.60	53.02

These assemblies containing a large number of very small rods are challenging designs for several reasons: 1) the fabrication of small diameter pins could prove economically disadvantageous, 2) the structural integrity of the rod during operation would need to be confirmed, as such small rods are more susceptible to vibration-induced failure under operating coolant-flow conditions, and 3) this requires the inclusion of "structure rods" in the assembly, which are basically solid HT9 rods used to support the grid spacers. Inclusion of these rods reduces the number of fuel rod positions, and thus reduces the effectiveness of the fuel overall. Therefore, the design of innovative fuel configurations for the low conversion ratio fuel sought to eliminate the need for small fuel rods. These low CR assembly configurations serve the other basis for comparison with innovative fuel configuration rods.

2.1.3 Base Design MathCAD Model

Using the parameters of the CR = 0.25 FA and fuel rods, two simple, single-assembly models were created using MathCAD to evaluate the geometric and thermal hydraulic properties of the base FA. These calculated properties can then be used as a point of reference for comparison with the innovative FA. For geometric and hydraulic comparisons, a full assembly is modeled, and the area fractions for fuel, coolant, structures, and bond are evaluated. These values directly correspond to the volume fractions of the same materials, which is significant to note for neutronic purposes in the core. Additionally, the pressure drop across the core is calculated using this "full assembly" model.

Table 2.6: Fuel rod design parameters for low conversion ratio cores [2.2]

	Metal	Oxide
Core outlet temperature (°C)	510	510
Core inlet temperature (°C)	355	355
Rings	13	11
Assembly outer flat-to-flat length (cm)	15.71	15.71
Core height (cm)	101.6	137.16
Plenum height (cm)	191.14	170.82
Total Height (cm)	407.14	422.28
Fuel smear density (%)	75	85
Theoretical fabricated density (%)	100	89.4
Outer rod diameter (mm)	8.08	8.68
Clad thickness (mm)	0.559	0.635
Fuel assemblies	151	151
Total assemblies	163	163
Reactor power (MW)	1000	1000
Fuel thermal conductivity (W/m°C)	11	4
Number of grid spacers (CR = 0.25)	11	11
Grid spacer thickness (mm) (CR = 0.25)	0.5	0.5

The MathCAD model is based upon the parameters described in sections 2.1.1-2.1.2 and geometric relations found in [2.5]. A list of the parameters, which served as input to the MathCAD model, is found in Table 2.6. A description of the full assembly model for the base fuel is given below.

The number of rods per assembly (N) is calculated according to the equation:

$$N = 1 + 3 \cdot R + 3 \cdot R^2, \tag{2.1}$$

where R = the number of rings per assembly. The outer flat-to-flat diameter of the hexagonal assembly (D_{HO}) is an input parameter, and the inner flat-to-flat dimensions and flow cell (including the bypass) flat-to-flat dimensions are found according to the equations:

$$\begin{aligned} D_{HC} &= D_{HO} + g_{IA} \\ D_{HI} &= D_{HO} - 2 \cdot t_d \end{aligned}, \tag{2.2}$$

where:

D_{HI} = assembly flat-to-flat inner hexagonal distance (m)

D_{HC} = flow cell flat-to-flat hexagonal distance (m)

g_{IA} = inter-assembly gap (m)

t_d = thickness of the fuel assembly duct wall (m).

The inner assembly, outer assembly, and hexagonal flow cell areas were found using the basic geometric formula for the area of a hexagon with the inner flat-to-flat, outer flat-to-flat, and assembly pitch lengths (as seen in Figure 2.4), respectively:

$$A_H = \frac{\sqrt{3}}{2} D_H^2 \quad . \tag{2.3}$$

where:

A_H = hexagonal area of inner, outer, and flow cell areas (m^2)

D_H = hexagonal flat-to-flat distance of inner, outer, and flow cell areas (m^2).

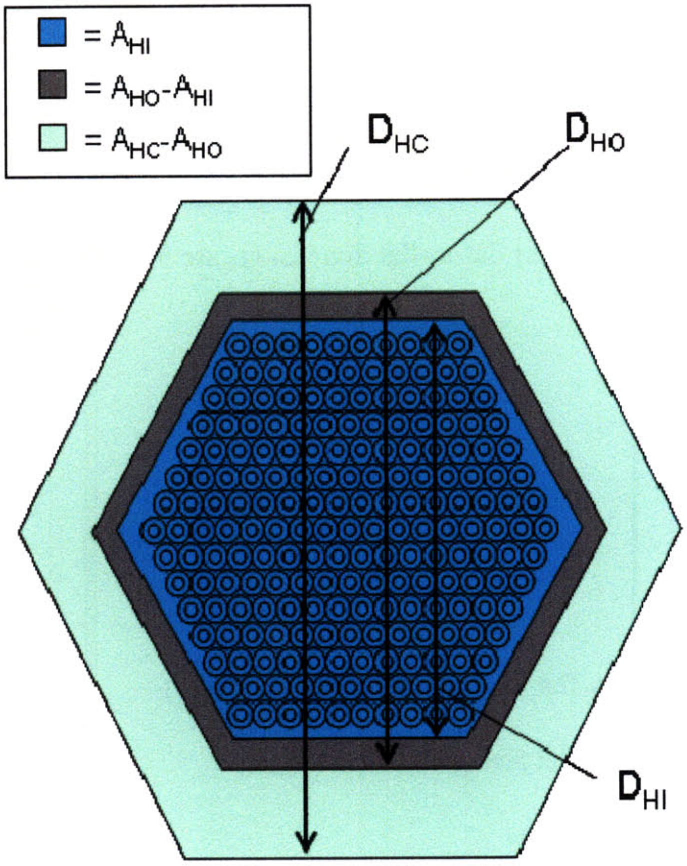

Figure 2.4: Hexagonal areas with their corresponding flat to flat distances (not to scale)

The radii of the cladding inner surface and the fuel surface (as depicted in Figure 2.5) were calculated from the following equations:

$$R_{ci} = \frac{D_o}{2} - \delta \tag{2.4}$$

$$R_{fo} = R_{ci} \cdot \sqrt{\frac{\rho_s}{\rho_f}} \tag{2.5}$$

where:

R_{ci} = radius at inner clad surface (m)

R_{fo} = radius at fuel outer surface (m)

ρ_s = fuel smeared density (%)

ρ_f = fuel theoretical fabricated density (%)

δ = clad thickness (m)

D_o = fuel rod outer diameter (m).

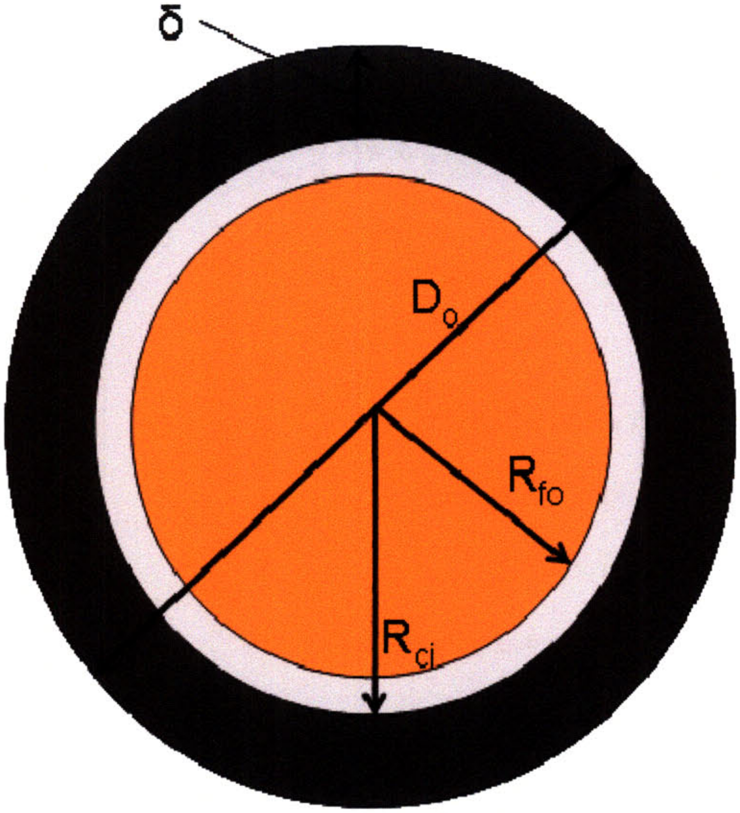

Figure 2.5: Cross section of solid fuel pin with corresponding nomenclature

The area of fuel, clad, and bond in each pin is determined as follows:

$$A_f = \pi \cdot R_{fo}^{\ 2}$$
$$A_b = \pi \cdot \left(R_{ci}^{\ 2} - R_{fo}^{\ 2}\right)$$
$$A_c = \pi \cdot \left(\frac{D_o^{\ 2}}{4} - R_{ci}^{\ 2}\right) \qquad (2.6)$$

where:

A_f = area of fuel per pin (m^2)

A_b = area of bond per pin (m^2)

A_c = area of clad per pin.

In the high conversion ratio cores, the fuel rods are separated by wire-wrap spacers. The total equivalent area of the wire-wrap in the assembly is the sum equivalent cross sectional areas of the wire-wraps around each pin. The cross-sectional equivalent area of each individual wire-wrap is determined from the following equation suggested by Chen & Todreas [2.6]:

$$A_w = \frac{\pi}{4}\cdot\left(\frac{D_w}{\cos(\phi)}\right)^2$$

$$\cos(\phi) = \frac{H_w}{\sqrt{H_w^{\,2} + \pi\cdot(D_o + D_w)^2}} \tag{2.7}$$

where:

A_w = area of wire wrap per pin (m^2)

D_w = diameter of wire wrap (m)

H_w = helical pitch of wire wrap (m)

$\cos(\phi)$ = correction factor accounting for the ellipticity of the wire cross section.

When the grid spacers were used instead of wire-wrap spacers in the ANL model, the area of grid spacers was simply assumed to be 2.5% of the total hexagonal cell area [2.2]. This method was maintained for clarity of comparison in the current study.

The volume fractions in the FA are determined for fuel, coolant, bond, and structure as follows:

$$F_{Fuel} = \frac{A_f \cdot N}{A_{HC}}, \tag{2.8}$$

$$F_{Coolant} = \frac{A_{HC} - (A_{HO} - A_{HI}) - (A_f + A_b + A_c + A_w)N}{A_{HC}}, \tag{2.9}$$

$$F_{Bond} = \frac{A_b \cdot N}{A_{HC}}, \tag{2.10}$$

$$F_{Structure} = \frac{(A_{HO} - A_{HI}) + (A_c + A_w)N}{A_{HC}}, \tag{2.11}$$

where:

A_{HC} = assembly hexagonal cell area (includes half of the inter-assembly gap) (m^2)

A_{HO} = outer area of hexagonal assembly (m^2)

A_{HI} = inner area of hexagonal assembly (m^2).

Finally, an important metric for each base fuel assembly is the fuel to coolant ratio. This ratio dictates to a large degree the neutronic performance in the core. Because the current thesis focuses on the thermal-hydraulic performance of innovative fuel designs, the fuel to coolant ratio was kept constant across the various innovative fuel configurations, so as to maintain, as much as possible, a similar neutronic performance as what was found in the base fuel configurations.

To verify the accuracy of these calculations, the volume fractions obtained from Eq. (2.8)-(2.11) were compared to the listed values from Hoffman et al. [2.2]. The agreement was very reasonable, as can be seen in Table 2.7.

Table 2.7: Comparison of calculated volume fractions for ANL and current models

	Metal CR=1.00		Metal CR = 0.25		Oxide CR = 1.00		Oxide CR = 0.25	
	ANL Paper	MathCAD Model	ANL Paper	MathCAD Model	ANL Paper	MathCAD Model	ANL Paper	MathCAD Model
Fuel Fraction (%)	34.26	34.29	17.44	17.49	49.29	49.24	19.73	19.73
Bond Fraction (%)	11.42	11.43	5.81	5.83	2.55	2.55	1.02	1.02
Structure Fraction (%)	25.73	25.74	29.15	28.55	28.58	28.58	26.22	25.51
Coolant Fraction (%)	28.59	28.54	47.6	48.14	19.58	19.63	53.02	53.74

Next, coolant flow rate through the core, the hydraulic resistance of the core, and the pressure drop across the core was calculated using the MathCAD full assembly model. The constant pressure heat capacity (C_p) of the sodium coolant was evaluated at the mean temperature through the core according to property data obtained from Fink and Leibowitz [2.7]. The coolant mass flow rate through the core was calculated according to the relation:

$$m_c = \frac{Q}{C_p \cdot (T_{out} - T_{in})}, \tag{2.12}$$

where:

m_c = coolant mass flow rate through the core (kg/s)

Q = total power generated in core (MW)

T_{out} = average coolant temperature at the core outlet (°C)

T_{in} = average coolant temperature at the core inlet (°C),

and the average mass flow through each assembly (m_a) is:

$$m_a = \frac{m_c}{N_{at}}, \tag{2.13}$$

where:

m_c = coolant mass flow rate through a single assembly (kg/s)

N_{at} = total number of assemblies in the core region.

The pressure drop through the assembly channels is influenced by the height and width of the wire-wrap, as well as the pitch and outer diameter of the fuel rods. The total pressure drop due to friction (dP) in the assembly can be calculated according to the equation:

$$dP = f \cdot \frac{L}{D_h} \cdot \left[\frac{\left(m_a / A_{flow} \right)^2}{2\rho} \right] \tag{2.14}$$

where

f = friction factor for turbulent flow

L = total length of axial flow through core (m)

D_h = hydraulic diameter of assembly (m)

A_{flow} = flow area of the hexagonal flow cell (m^2)

ρ = average coolant density through core (kg/m^3), and the hydraulic diameter is calculated using the following equation:

$$D_h = 4 \cdot \frac{A_{flow}}{P_w}, \tag{2.15}$$

where P_W is the wetted perimeter of hexagonal flow cell in meters.

The friction factor is dependent primarily upon the geometry and flow conditions through the assembly, and is calculated according to the equation:

$$f = \frac{C_{ft}}{\mathrm{Re}^{0.18}} \tag{2.16}$$

where C_{ft} is the turbulent drag coefficient, and Re is the Reynolds number:

$$\mathrm{Re} = \frac{{}^{m_a}\!\big/_{A_{flow}} \cdot D_h}{\mu}, \tag{2.17}$$

where μ is the dynamic viscosity of the coolant (Pa·s).

The turbulent drag coefficient is highly dependant upon the geometric configuration of the wire-wrap spacers and the fuel rods, and is determined using the relations developed by Chen and Todreas [2.6]:

$$C_{ft} = 0.8063 - 0.9022\log\left(\frac{H_w}{D_o}\right) + 0.3526\left(\log\left(\frac{H_w}{D_o}\right)\right)^2 \cdot \left(\frac{P}{D_o}\right)^{9.7}\left(\frac{H_w}{D_o}\right)^{1.78-2\left(P/D_o\right)} \tag{2.18}$$

where P is the fuel rod pitch in the assembly in meters.

For the burner core configurations, the hexagonal assemblies do not contain wire-wrap spacers. Rather, the fuel rods are spaced using triagonal grid spacers distributed evenly along the axial length of the assembly. The total pressure drop, therefore, for the axial assembly includes the frictional pressure drop and the pressure drop due to grid spacers. The frictional pressure drop is calculated similarly to the assemblies with wire-wrap grid spacers, save that the turbulent drag coefficient is calculated using the correlation for bare rods, rather than for wire-wrapped rods. This correlation is:

$$C_{fTp} = a + b_1\left(\frac{P}{D_o} - 1\right) + b_2\left(\frac{P}{D_o} - 1\right)^2 \tag{2.19}$$

where C_{fTp} is the bare rod plenum drag coefficient. The coefficients a, b_1, and b_2 are taken from the Cheng and Todreas correlation for pressure drop in bare rod bundles [2.5] and are:

$$\begin{aligned} a &= 0.09378 \\ b_1 &= 1.398 \\ b_2 &= -8.664 \end{aligned} \tag{2.20}$$

for a pitch-to-diameter ratio between 1.0 and 1.1, and

$$\begin{aligned} a &= 0.1458 \\ b_1 &= 0.03632 \\ b_2 &= -0.03333 \end{aligned} \tag{2.21}$$

for a pitch-to-diameter ratio greater than 1.1.

The pressure drop across the spacers (Δp_s) was calculated using the Rehme correlation for grid spacer pressure drops [2.5], which is:

$$\Delta p_s = Cv\left(\rho \cdot \frac{V_v^2}{2}\right)\left(\frac{A_s}{A_v}\right)^2, \tag{2.22}$$

where:

C_v = modified drag coefficient, read from data in [2.5]

V_v = average bundle fluid velocity (m/s)

A_s = projected frontal area of spacer (m^2)

A_v = unrestricted flow area away from the grid spacer (m^2).

In addition to the pressure drop due to friction and the grid spacers, entrance and exit effects will increase the pressure drop across the core. These effects are not considered in this simplified model, but in future models these effects should be included in the form of minor or form losses.

For thermal considerations, a single rod model was created in which the fuel rod was assumed to be bare (no clad or bond) with a single, uniform heat generation rate (average rod conditions). The thermal conductivity of the bare pellet was assumed to be constant, with approximate values. These assumptions were made to simplify the thermal analysis, as well as to provide a clear basis for comparison between standard and innovative fuel designs.

The power density of the core is calculated first. This will be used as a basis for comparison with the innovative fuel configurations to compensate for changes in the size of the assembly, however slight. The core power density (Q''') can be calculated using the equation:

$$Q''' = \frac{Q}{A_{HC} \cdot N_{at} \cdot H_c}, \tag{2.23}$$

where H_c is the height of the core in meters. The linear heat rate (q`) for the fuel rod can then be calculated using the following equation:

$$q' = \frac{Q''' \cdot N_{at} \cdot A_{HC}}{N_{af} \cdot N}. \tag{2.24}$$

Once the linear heat rate is known, the heat flux, fuel power density, and fuel radial temperature distribution can be calculated from the following equations:

$$q'' = \frac{q'}{\pi D_o} \tag{2.25}$$

$$q'''=\frac{q'}{\pi\left(\frac{D_o}{2}\right)^2} \qquad (2.26)$$

$$\Delta T_{\max}=\frac{q'}{4\pi k_f} \qquad (2.27)$$

where:

q'' = heat flux at fuel rod surface (W/m^2)

q''' = fuel power density (kW/L)

$\Delta T_{\max}$ = fuel radial maximum temperature difference (°C).

k_f = thermal conductivity of the fuel, oxide or metal (W/m°C).

The core-average thermal and hydraulic performance of all of the base FA can be found in Table 2.8. These parameters will serve as figures of merit for the comparison between innovative fuel designs and the standard solid pin fuel designs.

Table 2.8: Comparison of calculated thermal-hydraulic parameters for each type of base fuel assembly

	CR = 0.25		CR = 1.0	
	Metal	**Oxide**	**Metal**	**Oxide**
Fuel/coolant volume ratio	0.366	0.372	1.198	2.517
Power density (kW/L)	258.09	191.18	267.59	198.22
Linear heat rate (kW/m)	12.66	15.63	24.05	17.82
q" (kW/m^2)	868.33	894.62	947.54	653.37
$\Delta T_{\max}$ (°C)	91.57	310.88	174	354.45
q"' (W/cm^3)	1732	1137	842.44	434.53
Core ΔP (kPa)	141.54	99.1	797.73	2885.9

2.2 Innovative Fuel Designs

In fast reactor systems, the clad operates at relatively high temperature (~600°C), fast neutron flux (>10^{15} n/cm^2), and mechanical stresses (>100 MPa); therefore, clad thermal and irradiation creep limits the achievable burnup. On the other hand, the power density is limited by the fuel melting point and fuel clad chemical interactions (FCCI) (especially for metal fuel), fuel/clad mechanical interaction (especially for oxide fuel) and, to a lesser extent, by the sodium pressure drop in the fuel channels. Therefore, innovative fuel configurations that reduce clad stresses, fuel and/or clad temperatures will have a direct positive impact on the achievable burnup and power density in the sodium reactor core. The two innovative fuel designs studied in this work are internally and externally cooled annular shaped fuel and bottle-shaped fuel.

The large heat transfer surface of the annular fuel configuration, attainable with simultaneous internal and external cooling, reduces the fuel operating temperature and the surface heat flux dramatically. If oxide fuel is used in a fast reactor, the benefit of annular fuel would mainly be a reduction of the fission gas (FG) release and fuel swelling, which will lower stresses in the clad, allowing for higher burnup. If a metal fuel (with a thermal bond) is used, the main benefit would be an increase in the margin to fuel melting, which may allow for higher power density.

The benefit of bottle shaped fuel is primarily a reduction in the core pressure drop. In traditional fast-reactor cores, the FG plenum region above the active fuel accounts for about half of the total coolant pressure drop. For a given coolant mass flow rate, the pressure drop is directly proportional to the FG plenum length, but inversely proportional to the cube of the flow area. Therefore, if the diameter of the FG plenum is reduced, while increasing its length (thus maintaining the total FG plenum volume), a very significant reduction of the total coolant pressure drop can be obtained. The resulting fuel pin configuration has a "bottle" shape and will allow for higher sodium mass flow rates in the core, thus opening the possibility of a power density increase. Alternatively, for given mass flow rate, it will reduce the pumping power, thus cutting operating costs somewhat. Furthermore, a lower pressure drop in the core should aid natural circulation during transients and accidents.

2.3 Annular Fuel

Annular fuel is not a new concept. It has been suggested previously for use in a range of reactors, including both PWRs and BWRs [2.8, 2.9]. Annular UO_2 fuel with internal and external cooling has been studied at MIT for over 6 years and has been shown to enable power density increases of up to 50% in PWR cores [2.9]. The large heat transfer surface attainable with simultaneous internal and external cooling reduces the fuel operating temperature and the surface heat flux dramatically. This approach is expected to work for sodium reactors as well.

Annular fuel for the sodium fast reactor is made feasible by increasing the overall fuel rod diameter and including an inner channel in the center of the fuel rod, which is separated from the fuel by an additional clad and bond layer. A scale depiction of the annular fuel rod design compared to the traditional solid fuel pin design is seen in Fig. 2.6. The fuel rod outer diameter is significantly larger. In order to maintain a nearly constant assembly size, the number of fuel rods per assembly must be decreased. In Fig. 2.7, the transition from a solid fuel rod assembly to an annular fuel rod assembly is shown.

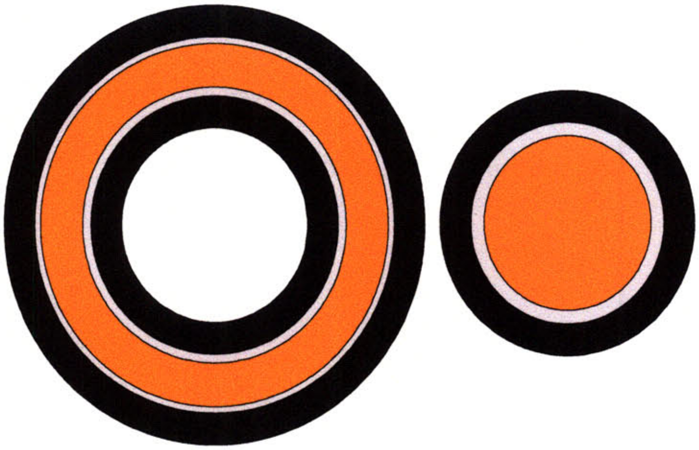

Figure 2.6: Annular fuel rod cross section (left) vs traditional solid fuel rod (right)

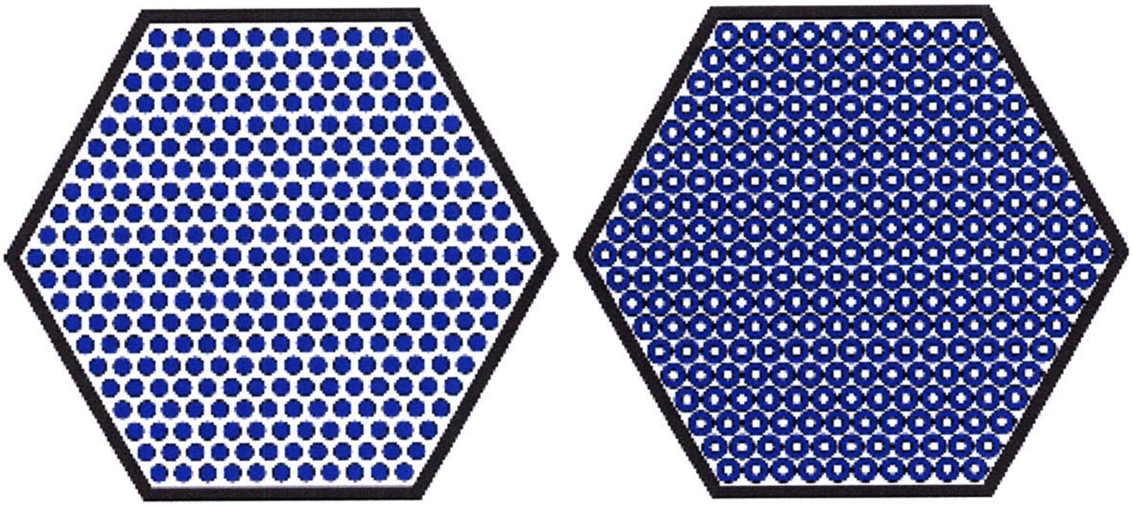

Figure 2.7: Annular fuel rod assembly (left) vs traditional solid fuel rod assembly (right).

2.3.1 Annular Fuel Constraints and Figures of Merit

For the purpose of the scoping study, certain variables remained unchanged between the base and annular fuel assembly designs. This allowed for clarity and simplicity in comparing the performance of the two fuel configurations. In the analysis of the annular fuel assembly (FA) designs, the following parameters are held equal to the corresponding ANL core designs:

- The fuel-to-coolant volume ratio and core height (101.6 cm for metal fuel, 137.2 cm for oxide fuel). This approximately preserves the overall neutronic characteristics of the core, e.g., spectrum, reactivity coefficients, reactivity letdown, etc.
- Smeared density (i.e., 75% for metal fuel, 85% for oxide fuel). This allows for adequate accommodation of fuel swelling under irradiation.
- Inter-assembly gap (0.432 cm) and FA duct thickness (0.394 cm). These parameters provide adequate FA clearance and mechanical robustness, respectively.
- Core power density. This ensures the fairness of the comparison between solid and annular FAs.

The gap between the FA duct and the adjacent fuel pins is set at a reasonable value of 0.3 mm to enable sliding of the fuel pin bundle into the duct during fabrication and to allow for swelling and thermal expansion. The wire helical pitch was held at

20.32 cm. Also, the inner diameter of the annular fuel pins is limited to ≥4 mm, as smaller channels are deemed susceptible to clogging.

In comparing the annular FA designs to the ANL designs, the following two figures of merit are adopted:

- Average heat flux at the clad surface, q''.
- Radial temperature rise in the fuel, ΔT, i.e., the difference between the maximum temperature in the fuel, T_{max}, and the temperature on the fuel surface, T_{fo}.

Everything else being the same (i.e., sodium inlet temperature and flow rate, power density), it is clear that FAs with lower q'' and ΔT than the ANL designs will also have lower clad and fuel temperatures. Therefore, it will be possible to uprate the core power density.

2.3.2 Annular Fuel MathCAD Model

The geometric parameters of the annular FA are calculated in much the same way as for the solid FA, as discussed in section 2.1.3. Equations (2.1) and (2.2) apply to the annular fuel FA unchanged. The radii for fuel and clad surfaces (as shown in Figure 2.8) are found by the following relations:

$$
\begin{aligned}
R_{cii} &= R_{coi} + \delta \\
R_{cio} &= R_{coo} - \delta \\
R_{fo} &= \sqrt{R_{cio}^{\;2} - \left(\frac{1-\rho_s/\rho_f}{2}\right)\cdot\left(R_{cio}^{\;2} - R_{cii}^{\;2}\right)} \\
R_{fi} &= \sqrt{R_{cii}^{\;2} + \left(\frac{1-\rho_s/\rho_f}{2}\right)\cdot\left(R_{cio}^{\;2} - R_{cii}^{\;2}\right)}
\end{aligned}
\tag{2.28}
$$

where:

R_{coi} = clad outer surface radius of inner channel

R_{cii} = clad inner surface radius of inner channel

R_{coo} = clad outer surface radius of outer channel

R_{cio} = clad inner surface radius of outer channel

R_{fo} = radius of fuel outer surface

R_{fi} = radius of fuel inner surface

δ = clad thickness (assumed equal for the inner and outer clad)

The fuel, bond, and clad areas for each pin are then calculated as follows:

$$
\begin{aligned}
A_f &= \pi\cdot\left(R_{fo}^{\;2} - R_{fi}^{\;2}\right) \\
A_b &= \pi\cdot\left(R_{cio}^{\;2} - R_{cii}^{\;2} - \left(R_{fo}^{\;2} - R_{fi}^{\;2}\right)\right) \\
A_c &= \pi\cdot\left(R_{coo}^{\;2} + R_{cii}^{\;2} - R_{cio}^{\;2} - R_{coi}^{\;2}\right)
\end{aligned}
\tag{2.29}
$$

The area of the wire can be calculated by means of Eq. (2.7). The volume fractions of the fuel, coolant, bond, and structures are calculated from Eqs. (2.8)-(2.11).

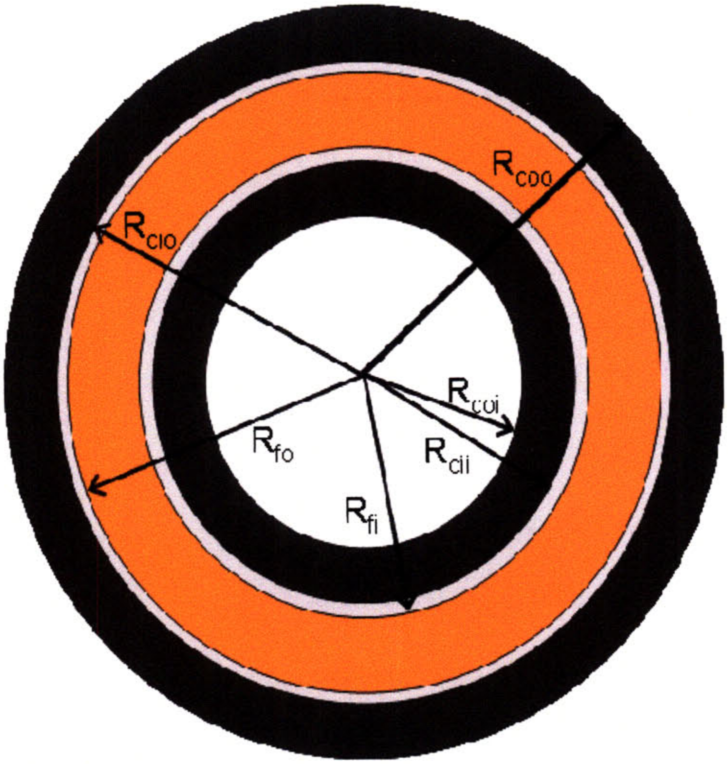

Figure 2.8: Cross section of annular fuel with corresponding nomenclature

The thermal parameters are calculated for annular fuel pin assemblies similarly to those calculated for solid fuel pin assemblies. The pin linear power is calculated for annular fuel using Eq. (2.24). However, unlike solid fuel pin assemblies, the average heat flux at the surface of the fuel rod is:

$$q''=\frac{q'}{2\pi(R_{coo}+R_{coi})} \tag{2.30}$$

The fuel power density, q‴ (W/cm^3), is of interest as it relates to the fuel cycle cost, and can be calculated as:

$$q''' = \frac{q'}{\pi(R_{fo}^2 - R_{fi}^2)} \tag{2.31}$$

To calculate ΔT, we make use of the heat conduction equation and its boundary conditions:

$$\begin{aligned} &\nabla \circ k_f \nabla T + q''' = 0 \\ &BC: T_{R_{fo}} = T_{R_{fi}} = T_o \end{aligned} \tag{2.32}$$

Note that for simplicity it is assumed that the fuel temperature at the inner and outer surface of the annular pins is the same. Solving Eq. (2.32) for both solid and annular fuel provides the following solutions:

$$T(r) = T_o + \frac{q'}{4\pi k_f}\left(1 - \frac{r^2}{R_{fo}^2}\right) \tag{2.33}$$

$$T(r) = T_o + \frac{q'}{4\pi k_f}\left[\frac{\left(R_{fi}^{\ 2} - r^2\right)}{\left(R_{fo}^{\ 2} - R_{fi}^{\ 2}\right)} + \frac{\ln\left(r/R_{fi}\right)}{\ln\left(R_{fo}/R_{fi}\right)}\right] \tag{2.34}$$

respectively, where:

T(r) = temperature of the fuel as a function of the radius

r = radius at which the temperature is being evaluated

k_f = thermal conductivity of the fuel (assumed independent of temperature for simplicity). For oxide fuels this is 4 W/m·K and for metal fuels it is 11 W/m·K.

With these solutions, finding the maximum temperature is then accomplished by taking the derivative of the temperature distribution and setting it equal to zero for the annular fuel. Then we have:

$$\Delta T = \frac{q'}{4\pi k_f}\left[\frac{\left(R_{fi}^{2}-R_{\max}^{2}\right)}{\left(R_{fo}^{2}-R_{fi}^{2}\right)}+\frac{\ln\left(R_{\max}/R_{fi}\right)}{\ln\left(R_{fo}/R_{fi}\right)}\right]$$
$$R_{\max} = \sqrt{\frac{\left(R_{fo}^{2}-R_{fi}^{2}\right)}{\ln\left[\left(R_{fo}/R_{fi}\right)^{2}\right]}} \tag{2.35}$$

where $R_{\max}$ is the radius at which the temperature is the maximum within the annular fuel. It can also be readily shown from Eq. (2.34) that the fraction of power going towards the inner channel of an annular fuel pin is equal to:

$$\frac{\dot{Q}_i}{\dot{Q}_i+\dot{Q}_o} = \frac{1}{\ln(R_{fo}/R_{fi})^2} - \frac{1}{(R_{fo}/R_{fi})^2-1} \tag{2.36}$$

where:

$\dot{Q}_i$ = power to inner channel (kW)

$\dot{Q}_o$ = power to outer channel (kW).

The flow split between the inner and outer channels is important because it controls the coolant temperature rise in those channels. The flow split is determined by the pressure drop (hydraulic resistance) in each channel. The pressure drop in the inner channel is determined using the approximate relations:

$$
\begin{aligned}
&m_r = \frac{m}{N} \\
&m_i = m_r \cdot x_i \\
&A_i = \pi R_{coi}{}^2 \\
&\mathrm{Re}_i = \frac{{m_i}\!\big/{A_i} \cdot 2R_{coi}}{\mu} \\
&f_i = 0.182\,\mathrm{Re}_i{}^{-0.2} \\
&dP_i = f_i \cdot \frac{L}{2R_{coi}} \cdot \left[\frac{\left({m_i}\!\big/{A_i} \right)^2}{2\rho_i} \right]
\end{aligned}
\qquad (2.37)
$$

where:

m_r = mass flow rate per rod

$m_{i/o}$ = mass flow rate of inner/outer channel

$x_{i/o}$ = fraction of flow in inner/outer channel

i/o = subscript denoting the inner/outer channel

A = flow area channel

Re = Reynolds number of fluid in channel

μ = viscosity of fluid in channel

f = friction factor of channel

dP = pressure drop of channel

ρ = density of fluid in channel

L = channel length.

Again, the pressure drop for the outer channels is influenced by the height and width of the wire-wrap, as well as the pitch and outer diameter of the fuel rods. The equation for the turbulent drag coefficient for the outer channel of the annular fuel rod is the same as Eq. (2.18). This pressure drop for the inner channel is determined using the following equations:

$$\begin{aligned}
m_o &= m_r \cdot (1 - x_i) \\
A_o &= A_{HI} - (A_f + A_c + A_b) \cdot N - \pi R_{coi}^{\ 2} \cdot N \\
\mathrm{Re}_o &= \frac{m_o / A_o \cdot D_{ho}}{\mu_o} \\
D_{ho} &= 4 \cdot \frac{A_o}{\mathrm{P}_w} \\
f_o &= \frac{C_{ft}}{\mathrm{Re}_o^{\ 0.18}} \\
dP_o &= f_o \cdot \frac{L}{D_{ho}} \cdot \left[\frac{\left(m_o / A_o \right)^2}{2\rho_o} \right]
\end{aligned} \qquad (2.38)$$

where:

D_{ho} = hydraulic diameter of outer channel

C_{ft} = coefficient of friction for turbulent flow.

The flow split is determined by finding the mass flow rate in the inner and outer channels at which the pressure drops for each channel are the same. Obviously, it is desirable that the inner channel flow fraction and the inner channel power fraction (Eq. 2.36) be as close as possible so that the coolant temperature rise in the inner and outer channels is equalized.

2.3.3 Annular Fuel Model Results

Several different assembly designs were created for the annular FA based upon the number of fuel rods, and hence the number of rings in each assembly. As discussed in section 2.2.1, the fuel to coolant ratio was maintained so as to preserve the neutronic properties of the assembly as much as possible. Also, it was desired to maintain the size of the assembly as closely as possible. With these two constraints, annular fuel rod assembly designs for the burner and breakeven core configurations were developed. For the burner core configurations, the original assembly was sufficiently open so that no additional adjustments to rod inner diameter (R_{coi}) were necessary. However, for the breakeven core configurations, the pitch was so tight, and the wire-wrap in the solid fuel configuration so thin, that optimizing of the annular fuel design by adjusting wire-wrap thickness and rod inner diameter was required in order to obtain a feasible annular fuel rod assembly configuration. Tables (2.9)-(2.12) list the resulting parameters for the annular fuel rod assembly configurations as well as the parameters for the solid fuel rod assemblies. The most promising configurations are highlighted in yellow.

Table 2.9: Results for the metal annular fuel rod configurations (CR = 0.25)

	Base Design	Annular Fuel Designs			
Rings	13	11	10	9	8
Pins	540	397	331	271	217
Flat to flat (cm)	15.71	21.32	19.57	17.83	16.23

Pin outer diameter (mm)	4.64	9.29	9.31	9.34	9.41
Pin inner diameter (mm)	-	5	5	5	5
P/D_o	1.357	1.087	1.087	1.087	1.086
Dwire (mm)	-	0.805	0.805	0.805	0.805
Clad thickness (mm)	0.559	0.559	0.559	0.559	0.559
Fuel volume fraction (%)	17.44	16.79	16.73	16.65	16.66
Bond volume fraction (%)	5.81	5.60	5.58	5.55	5.55
Structure volume fraction (%)	29.15	31.78	32.05	32.35	32.31
Coolant volume fraction (%)	47.6	45.83	45.65	45.45	45.48
Fuel/coolant volume ratio	0.366	0.366	0.366	0.366	0.366
Power density (kW/L)	258.09	258.09	258.09	258.09	258.09
Linear heat rate (kW/m)	12.66	31.27	31.72	32.27	33.54
q'' (kW/m^2)	868.33	696.31	705.41	716.52	740.92
ΔT (°C)	91.57	12.12	12.39	12.72	13.61
q''' (W/cm^3)	1732.00	1803.94	1810.89	1819.14	1817.93
Inner channel flow (%)	-	55.40	55.36	55.33	53.47
Inner channel power (%)	-	46.43	46.40	46.37	46.26
Core ΔP (kPa)	141.54	188.85	193.49	199.41	201.01

Table 2.10: Results for the oxide annular fuel rod configurations (CR = 0.25)

	Base Design	Annular Fuel Designs			
Rings	10	9	8	7	6
Pins	324	271	217	169	127
Flat to flat (cm)	15.71	17.66	15.93	14.20	12.47
Pin outer diameter (mm)	5.56	9.23	9.25	9.28	9.33
Pin inner diameter (mm)	-	5	5	5	5
P/D_o	1.45	1.09	1.09	1.09	1.09
Dwire (mm)	-	0.805	0.805	0.805	0.805
Clad thickness (mm)	0.635	0.635	0.635	0.635	0.635
Fuel volume fraction (%)	19.73	17.13	17.05	16.95	16.83
Bond volume fraction (%)	1.02	0.89	0.88	0.88	0.87
Structure volume fraction (%)	26.22	35.95	36.25	36.61	37.06
Coolant volume fraction (%)	53.02	46.04	45.82	45.56	45.24
Fuel/coolant volume ratio	0.372	0.372	0.372	0.372	0.372
Power density (kW/L)	191.18	198.22	198.22	198.22	198.22
Linear heat rate (kW/m)	15.63	23.46	23.96	24.61	25.47
q'' (kW/m^2)	894.62	524.93	535.25	548.45	565.98
ΔT (°C)	310.88	28.34	29.27	30.48	32.12
q''' (W/cm^3)	1137.00	1309.74	1315.89	1323.42	1332.84
Inner channel flow (%)	-	55.56	55.45	55.37	55.28
Inner channel power (%)	-	46.25	46.20	46.13	46.05
Core ΔP (kPa)	99.10	201.32	208.39	218.06	231.34

Table 2.11: Results for the metal annular fuel rod configurations (CR = 1.0)

	Base Design	Annular Fuel Designs							
		D_i = 5 mm			D_i = 5 mm		D_i = 4.5 mm		D_i = 4
Rings	9	8	7	6	7	6	7	6	7
Pins	271	217	169	127	169	127	169	127	169
Flat to flat (cm)	15.71	21.76	19.38	17.01	18.46	16.20	18.43	16.18	18.40
Pin outer diameter (mm)	8.08	13.57	13.65	13.75	13.13	13.24	12.91	13.01	12.70
Pin inner diameter (mm)	-	5	5	5	5	5	4.5	4.5	4
P/D_o	1.0996	1.062	1.062	1.062	1.008	1.008	1.008	1.008	1.008
Dwire (mm)	0.805	0.805	0.805	0.805	0.1	0.1	0.1	0.1	0.1
Clad thickness (mm)	0.559	0.559	0.559	0.559	0.559	0.559	0.559	0.559	0.559
Fuel volume fraction (%)	34.26	35.20	34.99	34.72	34.42	34.15	34.71	34.42	34.99
Bond volume fraction (%)	11.42	11.73	11.66	11.57	11.47	11.38	11.57	11.47	11.66
Structure volume fraction (%)	25.73	23.68	24.15	24.74	25.39	25.97	24.76	25.37	24.14
Coolant volume fraction (%)	28.59	29.38	29.20	28.97	28.72	28.50	28.96	28.73	29.20
F/C ratio	1.198	1.198	1.198	1.198	1.198	1.198	1.198	1.198	1.198
Power density (kW/L)	267.59	267.59	267.59	267.59	267.59	267.59	267.59	267.59	267.59
Linear heat rate (kW/m)	24.05	56.79	58.12	59.90	52.83	54.52	52.66	54.33	52.51
Q” (kW/m^2)	947.54	973.71	992.17	1016.68	927.53	951.64	963.03	987.45	1000.79
ΔT (°C)	174.00	50.16	51.71	53.82	44.69	46.63	48.18	50.18	51.93
q”’ (W/cm^3)	842.44	820.51	825.61	832.06	839.30	845.92	832.27	839.12	825.45
Inner channel flow (%)	-	51.68	52.23	52.88	56.36	47.15	42.85	43.76	30.75
Inner channel power (%)	-	41.88	41.82	41.74	42.22	42.14	41.59	41.51	40.92
Core pressure drop (kPa)	797.73	403.23	428.39	462.55	413.79	464.08	416.62	457.53	401.55

Table 2.12: Results for the oxide annular fuel rod configurations (CR = 1.0)

		Annular Fuel Designs					
	ANL Design	D_i = 5 mm			D_i = 4.5 mm		D_i = 4
Rings	9	7	6	5	7	6	7
Pins	271	169	127	91	169	127	169
Flat to flat (cm)	15.71	29.56	27.38	25.60	27.60	25.80	26.00
Pin outer diameter (mm)	8.68	21.16	22.48	24.64	19.73	21.14	18.54
Pin inner diameter (mm)	-	5	5	5	4.5	4.5	4
P/D_o	1.023	1.009	1.009	1.008	1.010	1.009	1.011
Dwire (mm)	0.198	0.198	0.198	0.198	0.198	0.198	0.198
Clad thickness (mm)	0.635	0.653	0.653	0.653	0.653	0.653	0.653
Fuel volume fraction (%)	49.29	57.44	57.84	58.46	56.72	57.26	56.11
Bond volume fraction (%)	2.55	2.97	2.99	3.03	2.94	2.96	2.90
Structure volume fraction (%)	28.58	16.76	16.19	15.30	17.81	17.04	18.70
Coolant volume fraction (%)	19.58	22.82	22.98	23.22	22.53	22.74	22.29
F/C ratio	2.517	2.517	2.517	2.517	2.517	2.517	2.517
Power density (kW/L)	198.22	198.22	198.22	198.22	198.22	198.22	198.22
Linear heat rate (kW/m)	17.82	98.62	112.87	138.01	86.16	100.41	76.60
q'' (kW/m^2)	653.37	1199.85	1307.42	1481.90	1131.70	1246.42	1081.60
ΔT (°C)	354.45	174.83	208.75	270.42	153.56	187.74	138.68
q''' (W/cm^3)	434.53	372.48	369.94	366.03	377.23	373.70	381.37
Inner channel flow (%)	-	25.49	21.67	17.09	23.25	16.29	20.22
Inner channel power (%)	-	33.84	33.16	32.19	33.76	32.98	33.51
Core pressure drop (kPa)	2885.90	656.56	624.90	585.39	723.70	767.77	801.66

The annular fuel approach seems very promising for the low-conversion cores (Tables 2.9 and 2.10), as their initially high P/D_o value allows for easy accommodation of the annular fuel pins. The most promising configurations are highlighted in the tables and show a significant decrease of the average heat flux (-19.8% in the metal fuel core, -

41.3% in the oxide core), an enormous decrease of the temperature rise in the fuel (-86.76% in the metal core, -90.9% in the oxide core), and also a good match between the fraction of power and flow into the inner channel of the annular fuel pins. The reduction in average heat flux and fuel temperature can be used to increase the core power density and/or operate with higher safety margins. Another attractive feature of the annular fuel FAs is their much higher mechanical robustness with respect to the very small pins of the ANL low conversion ratio designs.

Use of annular fuel in the high conversion ratio cores is more problematic. These cores are very tight to begin with, so there is little room for accommodation of the annular fuel pins. This results in a higher average heat flux than for the solid fuel base case (e.g., first three columns to the right of the "Base Design" in Tables 2.11 and 2.12). Tightening the P/D_0 to make room for more fuel pins does not seem to help much with the heat flux and actually results in unrealistically low values of P/D_0 and D_{wire} (fourth through eighth column to the right of the "Base Design" in Tables 2.11 and 2.12). In fact, for these configurations, one should probably think of ribs vs. wire as the method for spacing the pins. Finally, the match between flow and power in the inner channel of the annular fuel pins is not good for the high conversion cores.

In the high CR annular FAs, the pressure drop across the core is lower than in the solid FAs. The increased flow area in the annular FAs is the primary reason for this decrease. In the low CR annular FAs, however, the pressure drop increases, as can be seen in column two of Tables 2.9 and 2.10. This increased pressure drop is significantly lower than pressure drops for typical tight cores with a high CR, and is subsequently of little concern.

According to the results listed in this section, it was found that the low conversion cores could readily accommodate the annular fuel pins and would greatly benefit in terms of lower clad and fuel temperature, as well as enhanced mechanical robustness. On the other hand, use of annular fuel pins in the high conversion cores would be problematic due to the tightness of the fuel pin array, which does not allow for a good balance of flow between the inner and outer channels.

The next logical step is to conduct a more thorough analysis of the thermal-hydraulic performance of the promising FA configurations with annular fuel pins. This will entail use of a subchannel analysis model to study the distribution of the sodium flow within the FA and calculate the clad and fuel temperatures at the hot spot, as well as the use of a physics code (e.g., MCODE) to verify the acceptability of the power distribution, reactivity coefficients, and reactivity-limited burnup of the new FA designs. The development of the subchannel analysis model is discussed in Chapter 5, while the subchannel analysis itself is discussed in Chapter 6. For a brief discussion of the verification of this MathCAD model, see Appendix A.

2.4 Bottle-Shaped Fuel

The fuel rod plenum accounts for up to ~40% of the overall fuel rod length, yet its geometry is not subject to major neutronic restrictions. Bottle-shaped fuel refers to a fuel pin whose diameter is smaller in the plenum region than in the active region, which results in a significant decrease in the overall core pressure drop. To compensate for the decrease in radial area of the gas plenum region of the fuel rod, the length of the gas plenum region is increased, thus maintaining a constant gas plenum volume.

This reduction in fuel rod diameter in the plenum region opens up the core lattice, resulting in less hydraulic resistance via a larger hydraulic diameter. In order to implement this type of innovative fuel, there must be sufficient space to increase the length of the fuel rods by moderate amounts (~10% to 20%). Additionally, the increased gap width between fuel rods necessitates the use of a spacer other than wire-wrapped spacers, so grid spacers are used in the plenum region for the bottle-shaped core. A representation of such bottle-shaped fuel can be seen in Fig. 2.9.

The friction pressure drop in all axial regions (active core, shield, and plenum) can be determined from Eq. (2.14). This relation indicates that the flow area and the hydraulic diameter both contribute inversely to the pressure drop in the core. Therefore, by decreasing the radius of the fuel rod in the plenum region (and simultaneously increasing its length, thus maintaining the necessary plenum volume for fission gas collection), the pressure drop in the plenum region can be decreased. The fuel rod pitch remains constant in the fuel plenum region, so the gap between fuel rods is larger in the plenum region. In order to ensure the stability of the fuel rods in the plenum region, it was assumed that a grid spacer was needed for every 0.5 meters of plenum length, and that the grid spacers were triagonal honey-combed spacers with a thickness of 0.5 mm.

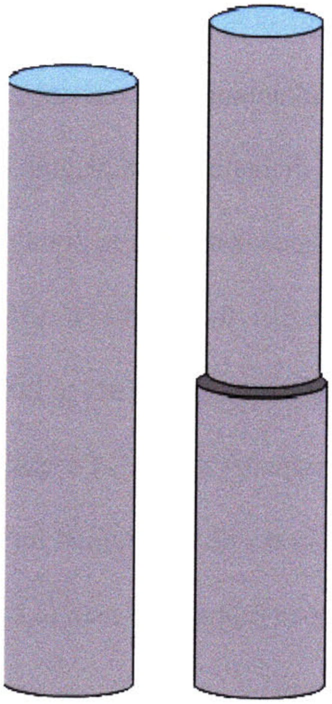

Figure 2.9: Segments of the base (left) and bottle-shaped fuel pins (right) (drawing to scale)

2.4.1 Bottle-Shaped Fuel Constraints and Figures of Merit

As with the annular fuel design, certain variables remains unchanged between the base and bottle-shaped fuel assembly designs. In fact, the general core region remains unchanged throughout the analysis of the bottle-shaped fuel, and only the plenum region parameters are adjusted while investigating the effect that these changes have on core pressure drop and overall core height. In the analysis of the bottle-shaped FA designs, the following parameters are held equal to the corresponding ANL core designs:

- The core region geometric parameters including core height, core pitch, rod diameters, core mass flow rate, wire-wrap dimensions, etc.

- Core thermal and neutronic properties, such as power profiles (uniform), power generation rate, and neutronic performance, e.g., spectrum, reactivity coefficients, reactivity letdown, etc.
- Fuel assembly pitch in both core and gas plenum regions
- Shielding thickness and assembly entrance/exit configurations.

In comparing the annular FA designs to the ANL designs, the following two figures of merit are adopted:

- Pressure drop across the core
- Total fuel rod length or core height.

Everything else being the same (i.e., sodium inlet temperature and flow rate, pitch), it is clear that FAs with lower pressure drop across the plenum will also have a lower pressure drop across the entire core and will thus allow for either lower pumping costs or potentially power uprates. In addition to adjusting the plenum radius, further investigations will center on the adjustment of the following parameters:

- Rate of change of rod radius, as a function of length (gradual or sudden expansion)
- Length between grid spacers
- Number of grid spacers.

The most promising configurations will be considered the assemblies in which large decreases in the overall core pressure drop are achieved (>15%) while the increase in core height is minimized (<25%). Additionally, mechanical robustness of the bottle-shaped fuel is a potential problem. Failure due to mechanical stresses induced at the core/plenum interface of the rod could be a potential problem. These challenges are investigated in Chapter 4.

2.4.2 Bottle-Shaped Fuel MathCAD Model

The total pressure drop for the bottle-shaped fuel rod, ΔP_b, is:

$$\Delta P_b = \Delta P_s + \Delta P_c + \Delta P_p + K\frac{v_c \rho}{2}, \tag{2.39}$$

where:

ΔP_s = pressure drop across the grid spacers

ΔP_c = pressure drop in the (wire-wrapped) active core region of the fuel rod

ΔP_p = pressure drop across the plenum region of the fuel rod

K = minor loss coefficient for the subchannel expansion at the plenum bottom

v_c = core average velocity.

The pressure drop across the core and shield regions is dominated by friction losses, while the pressure drop across the plenum is both due to friction losses, and form losses from the grid spacers. This is illustrated in the following equation:

$$\Delta P_p = \Delta P_{pf} + \Delta p_s\,, \tag{2.40}$$

where ΔP_{pf} represents the total pressure drop across the grid spacers and can be calculated using Eq. (2.22) The turbulent drag coefficient for all regions can be calculated using Eq. (2.18) in the core and lower shielding regions, and Eqs. (2.19) – (2.21) in the gas plenum region.

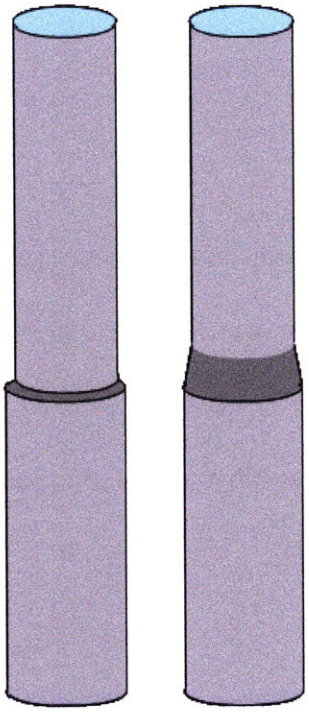

Figure 2.10: Bottle-shaped fuel with sudden and gradual flow area expansions

The pressure drop across the subchannel flow area expansion at the bottom of the plenum region depends on the 'rate' of expansion of the subchannel flow area. Two types of expansions were explored in this study: a sudden expansion of the subchannel area at the plenum base, and a gradual 30 degree expansion of the subchannel area at the plenum base. Both of these expansion methods are shown in Fig. 2.10. As a simple and conservative upper-bound estimate, the forward form loss coefficient, *K*, for the sudden expansion is assumed to be 1 (in reality this is only true for an expansion to a plenum), while the form loss coefficient for the gradual expansion of 30° is found by [2.10]:

$$\begin{aligned} K &= \left(1-\frac{1}{n}\right)^2 \\ n &= \frac{A_{fp}}{A_{fc}} \end{aligned}, \qquad (2.41)$$

where:

A_{fp} = flow area in the plenum subchannels (post-expansion)

A_{fc} = flow area in the core subchannels (pre-expansion).

If it is desired to investigate other angles of expansion than 30°, tables and correlations can be found in [4.10].

The pressure drop for bottle-shaped fuel over a wide range of plenum radii was modeled for each of the four separate base design assembly models from Hoffman et al. [2.2]: metal and oxide fuels for conversion ratios of 1.0 and 0.25 as found in Tables 2.3 and 2.5. Using the high conversion ratio metal fuel base assembly as an example, the effects of reducing the plenum rod diameter for an unsupported gas plenum region is investigated in Fig. 2.11. As grid spacers are added, the pressure drop increases proportionally to the number of grid spaces. In the MathCAD model, the number of grid spacers used was dependant upon the length of the gas plenum. It was assumed that for each 50cm segment of gas plenum length, 1 grid spacer would be necessary. The resulting plot of grid-spacer pressure drop as a function of gas plenum outer rod diameter is shown in Fig. 2.12. Additionally, in order to determine the influence of this "intra-spacer" length exerted on the grid-spacer pressure drop, plots of the pressure drop across the grid spacers are included for an intra-spacer length of 70cm, 20cm, and 10cm in Fig.

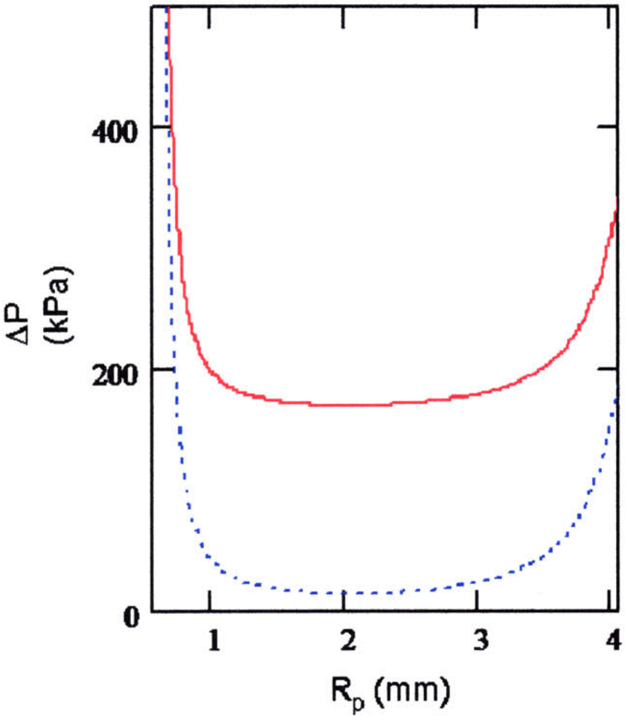

Figure 2.11: Plot of pressure drops both across bare plenum (blue) segment of assembly and the entire assembly (red) (no grid spacers) as a function of plenum outer radius

2.12. As can be seen in this plot, there are jagged discontinuities periodically seen in the pressure drop curves. These sudden increases in pressure drop correspond to the introduction of a new grid spacer (i.e. the plenum height has increased beyond the marginal 50 cm gap required per spacer. As the inter-spacer length requirement decreases, as expected, the discontinuities occur more frequently. For the inter-spacer length of 10 cm, the discontinuities are very frequent, but also barely discernable from the curve seen in Fig. 2.11. On the other hand, as the inter-spacer length increases, the benefit obtained from having fewer grid-spacers is reduced. This is seen as the shift from an inter-spacer length of 50 cm to 70cm produces a very small reduction in pressure drop, while the shifts from 10cm to 20cm, or even from 20cm to 50 cm each produce larger reductions in the total grid spacer pressure drop.

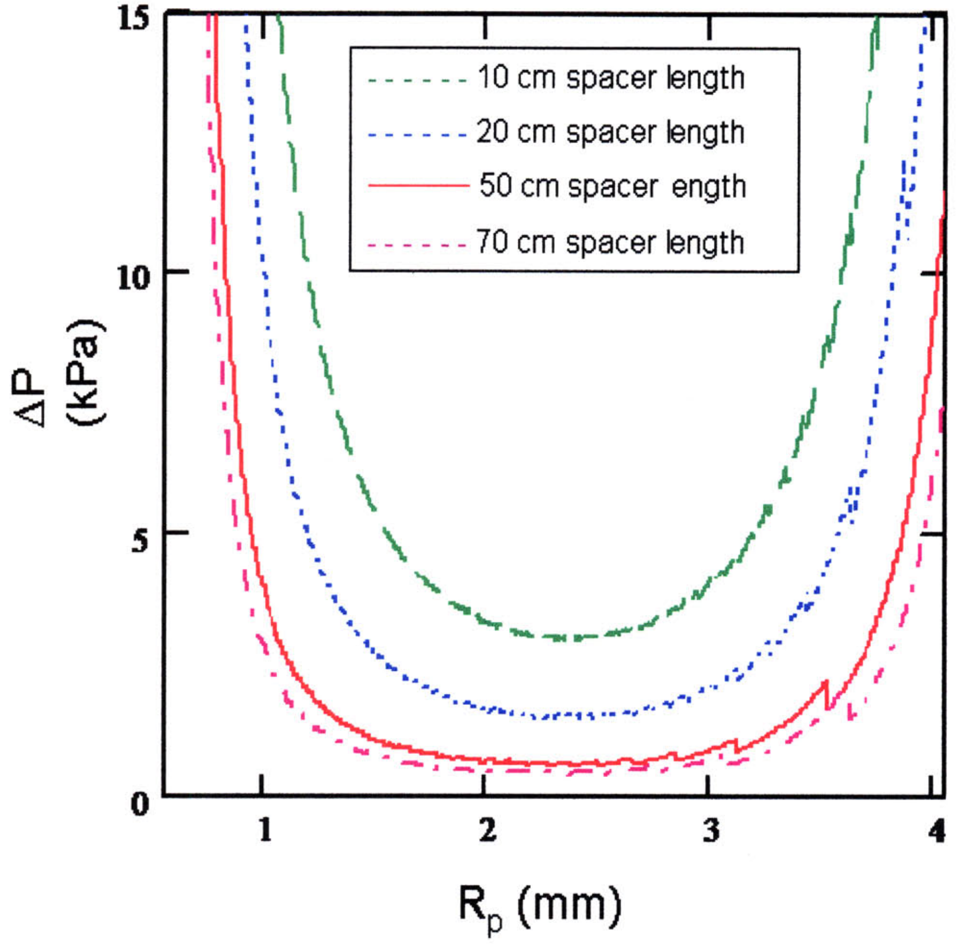

Figure 2.12: Plot of pressure drop across grid spacers for various inter-spacer lengths as a function of plenum outer radius

The overall influence that the grid spacers exert on core total pressure drop is seen in Fig. 2.13. All the inter-spacer lengths plotted in Fig. 2.12 are also plotted in Fig. 2.13. The additional pressure drop associated with the additional decreasing inter-spacer length is quite small, and the jagged pattern seen so acutely in the Fig. 2.12 is effectively too small to be seen in terms of the overall pressure drop. Thus, although the benefit of utilized bottle shaped fuel is reduced as the inter-spacer length decreases, this effect is small enough to be inconsequential. For the final results discussed in the next section, an inter-spacer length of 50 cm is assumed, and the number of grid spacers included changes accordingly. The patterns witnessed in the pressure drop vs. plenum rod radius plots (Figs. 2.11 – 2.13) are identical for all assemblies modeled, and thus the plots for other assembly types are not included.

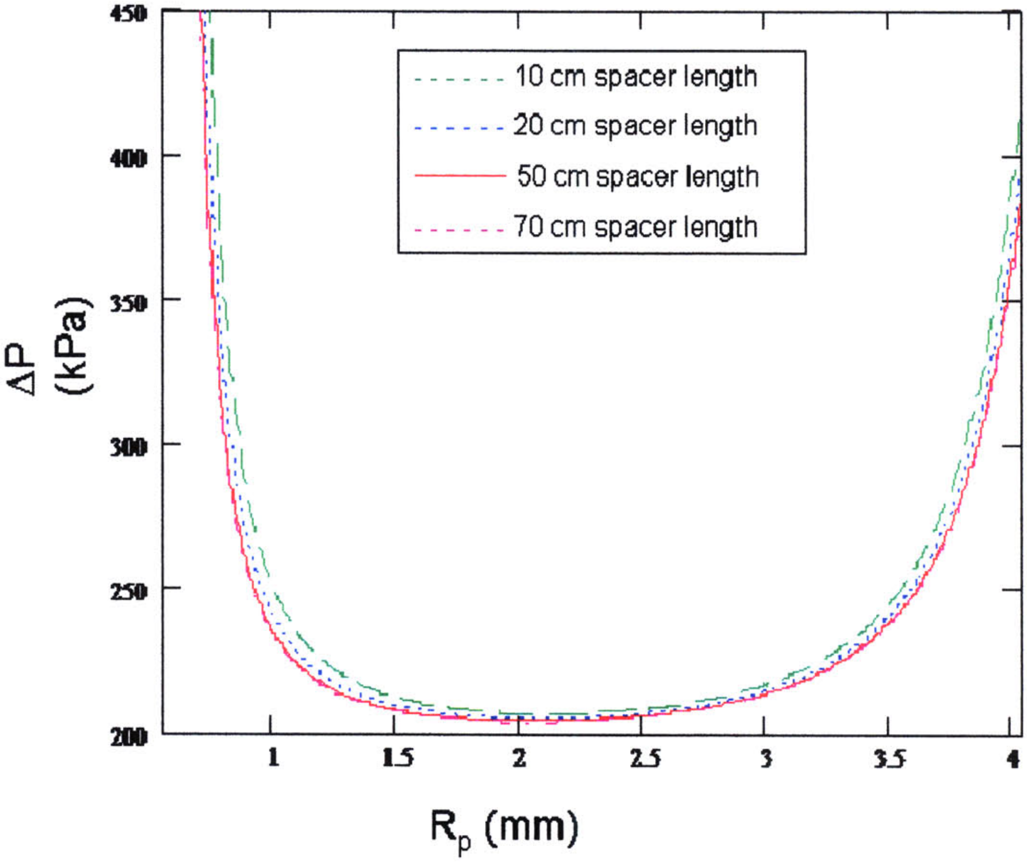

Figure 2.13: Plot of the total core pressure drop (with grid spacers) for various inter-spacer lengths as a function of plenum outer radius

2.4.3 Bottle-Shaped Fuel Results

A plot of the total core pressure drop, ΔP_b, as a function of the plenum radius for each assembly type is found in Figs. 2.14 – 2.17. The pressure drop decreases dramatically as the plenum radius is initially decreased for each model. The increase in the subchannel flow area in FG plenum is proportional to the square of the reduction in gas plenum radius. Therefore, as the radius of the fuel rod decreases, the increase in subchannel flow area becomes marginally smaller. Additionally, by decreasing the FG plenum area, the FG plenum height is increased to maintain a constant FG plenum volume. At very small radii, the pressure drop due to the FG plenum length increase begins to dominate, and an increased pressure drop is seen. Therefore, the ideal FG plenum radius would be found at the design point indicated in Figs. 2.14 – 2.17, where the increase in FG plenum height is small, but the resulting reduction in pressure drop is relatively high. Interestingly, the sharp and gradual expansion configurations seem to differ minimally in all cases. The optimal plenum radii for each model, as well as the resulting core pressure drop and plenum height, are found in Table 2.13.

Table 2.13: Specifications of "optimal radius" bottle-shaped fuel

	CR = 1.0		CR = 0.25	
	metal	**oxide**	**metal**	**Oxide**
Optimal plenum radius (mm)	3.5	3.6	2	2.5
Plenum height (m)	2.547	2.483	2.572	2.112
Bottle-shaped to base plenum height ratio	1.332	1.453	1.346	1.236
Bottle-shaped to base core height ratio	1.156	1.183	1.162	1.096
Plenum ΔP (kPa)	84.75	105.01	38.40	21.94
Core ΔP (kPa)	402.71	1299.28	138.94	95.21
Bottle-shaped to base core ΔP ratio	0.589	0.493	0.814	0.894

The breakeven cores (CR = 1.0) experience a large pressure drop reduction (40-50%), due to the tightness of the original core. The burner cores (CR = 0.25) experience much less benefit (10-20%) from the bottle-shaped fuel design, because the original core flow areas were already quite large. In conclusion, the bottle-shaped fuel appears to be most beneficial to high conversion (tight) ratio core designs, and less beneficial for low conversion ratio core designs.

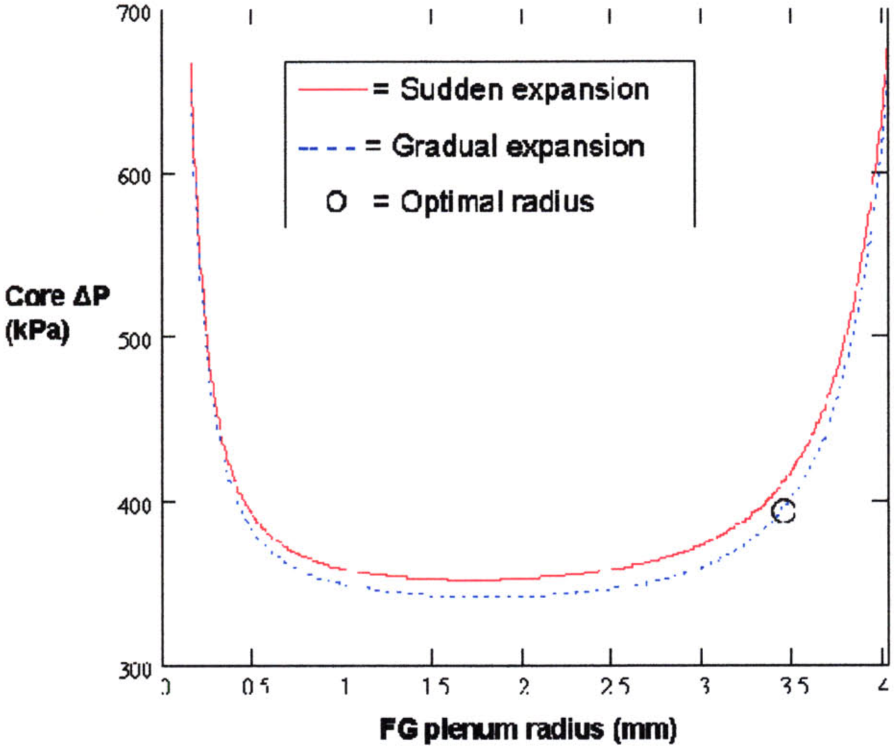

Figure 2.14: Core pressure drop as a function of FG plenum radius for metal fuel (CR = 1.0)

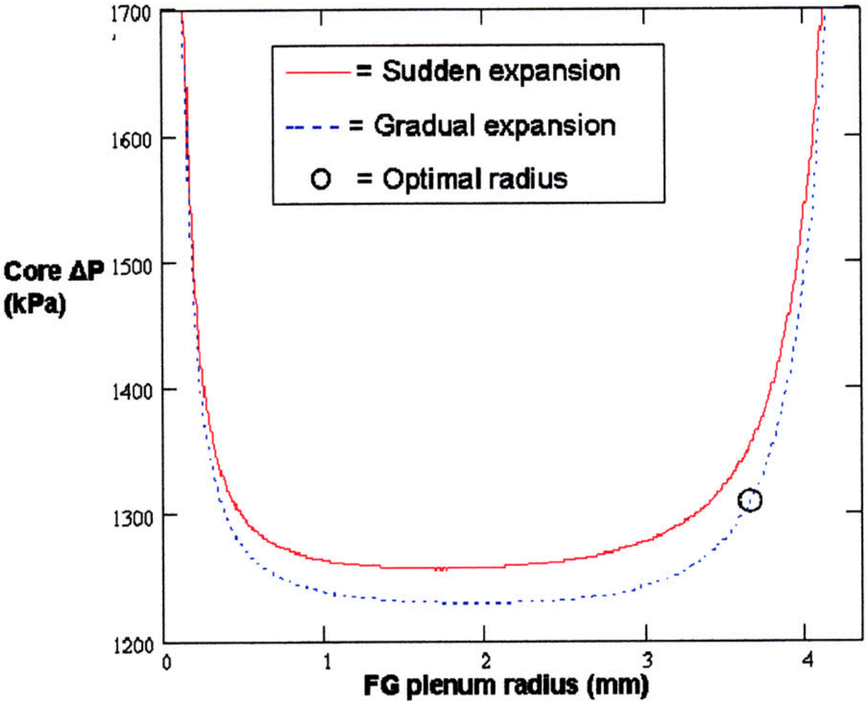

Figure 2.15: Core pressure drop as a function of FG plenum radius for metal fuel (CR = 1.0)

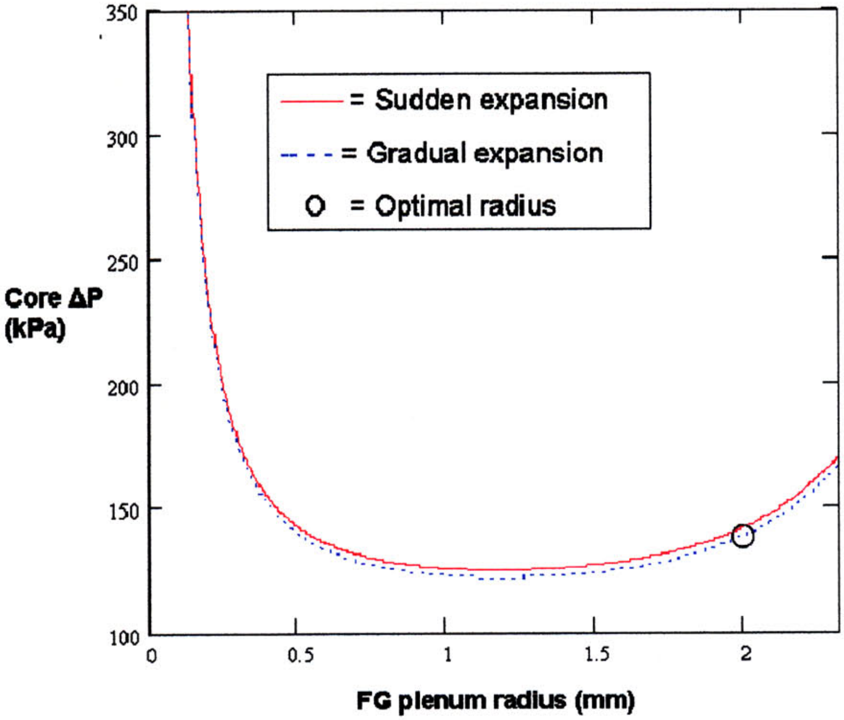

Figure 2.16: Core pressure drop as a function of FG plenum radius for metal fuel (CR = 0.25)

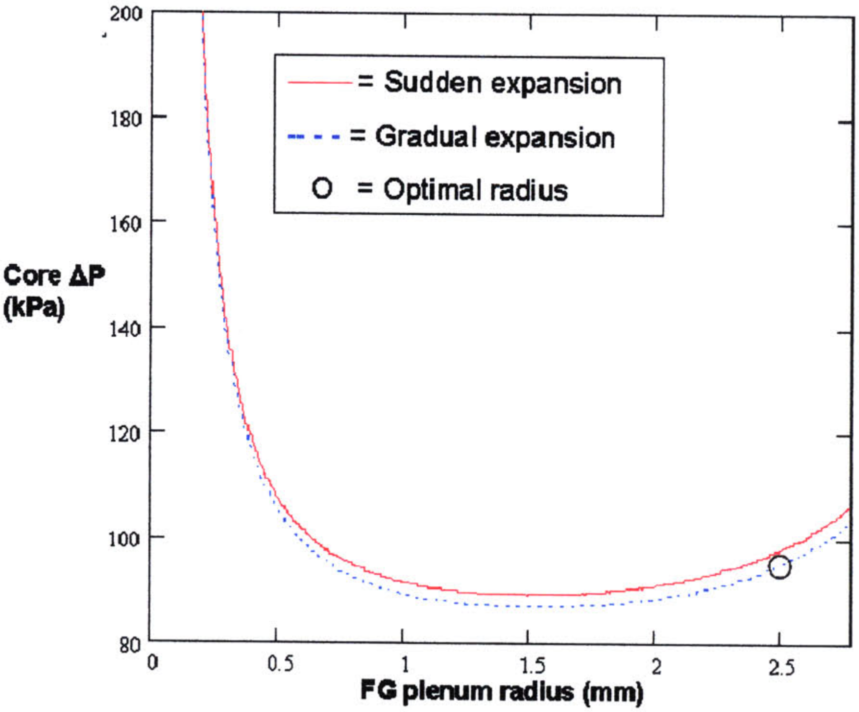

Figure 2.17: Core pressure drop as a function of FG plenum radius for oxide fuel (CR = 0.25)

2.5 Conclusions

Both bottle-shaped and oxide fuels were investigated using simplified, single rod fuel cell and single assembly MathCAD models. The results of these models indicate that the annular fuel configuration is best suited to low conversion ratio cores, while the bottle-shaped design is best suited for high conversion ratio cores. In order to quantify the benefits of utilizing these fuels, subchannel analyses must be performed for both the base and innovative fuel configurations.

Chapter 3: Subchannel Analysis Model

The investigation of the innovative fuel types described in Chapter 4 required adequate subchannel analysis codes to quantify the important thermal-hydraulic parameters in the core, such as peak cladding temperature, centerline fuel temperature and coolant velocities. However, traditional subchannel codes for sodium reactors, such as SUPERENERGY II [1.16], can only evaluate hexagonal assemblies with wire-wrapped fuel pins, but cannot be used for analysis of different fuel geometries or non-hexagonal assembly configurations. Meanwhile, subchannel codes for water-cooled reactors, such as VIPRE, are not suitable for analysis of liquid-metal systems. Therefore, in this thesis we have expanded the capabilities of the RELAP5-3D code to perform subchannel analysis in sodium-cooled fuel assemblies with non conventional geometries. This expansion was enabled by the use of control variables in the code. Since it is the first time that RELAP5 has been used for this type of analysis, extra care was taken in validating it. First, the code was compared with the SUPERENERGY II code for the case of solid fuel pins in a conventional hexagonal lattice. It was shown that the temperature predictions from the two codes agreed within 2%. Second, the RELAP5 subchannel model was applied to the ORNL 19-pin test, and it was found that the code could predict the measured outlet temperature distribution with a maximum error of ~8%.

Using this new RELAP5-3D model, the geometry of a traditional hexagonal assembly with wire-wrapped fuel was optimized first. This assembly exhibited large core outlet temperature distributions, even with a uniform local power peaking profile. The flow distribution was optimized through the utilization of semi-circular duct "ribs," which diverted flow from the edge subchannels and flattened the flow and temperature profiles within the assembly. This model was then used to analyze the innovative core designs described in Chapter 2. The details and results of this analysis are found in Chapter 6.

3.1 Selection of RELAP5-3D as the Code for Subchannel Analysis

Several subchannel analysis codes have been used for both water and sodium reactors over the past three decades [3.1, 3.2, 3.3, 3.4, 3.5, 3.6, 3.7, 3.8, 3.9, 3.10, 3.11, 3.12]. Traditional LWR subchannel analysis codes such as VIRPE [3.6] or COBRA IV [3.10] have been successfully demonstrated using water systems, but are not suitable for use with sodium, and in the case of VIPRE, cannot accurately or simply model the geometry associated with the hexagonal wire-wrapped fuel assembly used in the SFR.

There are other codes that have been used to analyze SFR core performance in the US, Korea, and the UK. These codes are based upon methods developed in the SUPERENERGY II code, with various adaptations and adjustments in capability. SUPERENERGY II, a simplified, steady-state subchannel code developed by Basehore and Todreas [1.16], has been used to model both single assembly and multi-assembly arrangements, however, the code does not include any type of fuel rod analysis. Rather, the energy is deposited directly into the coolant. Additionally, there are severe limitations to fuel configurations (only solid cylindrical pins with constant pitch and diameter axially) and assembly geometries (only standard hexagonal, wire-wrapped fuel assemblies) that can be modeled. Size limitations inherent in the code also prevent the analysis of an assembly with more than 8 rings. As each of these conditions would be breached in the application of innovative fuel types in subchannel modeling, SUPERENERGY II was considered unsuitable for the modeling of innovative fuels.

SLTHEN (Steady-state LMR core Thermal-Hydraulics analysis code based on ENERGY Model) [3.11] is based upon SUPERENERGY II code, but fuel and clad calculations are incorporated, as well as the capability to more accurately model inter-assembly convective flows. Despite these improvements, however, it is still unable to model alternate fuel and assembly geometries. Other US codes used for SFR core analysis, such as the SASSYS/SAS4 code, actually perform hot spot analyses, but not full-scale subchannel analyses, and thus are not suitable for the study of alternative fuel configurations, as described in this thesis.

Other codes are used for SFR subchannel analysis in the UK, France, and Japan, and these codes were assessed to determine the capability of using them for the analysis of innovative fuel types. SABRE4 [3.12] is capable of performing subchannel analyses for both steady-state and transient conditions, but cannot accommodate annular fuel pin designs. Subchannel analyses for SFR assemblies in JAPAN utilizes the ASFRE-III code. This code is the standard code for use in analyzing fast breeder reactor (FBR) thermal-hydraulics, but as with SABRE4, it is unable to accommodate innovative fuel configurations. In France, the CADET code has been used to perform subchannel analyses for SFR assemblies. This code can accommodate varying power profiles, boundary conditions, and the standard SFR fuel assembly geometry (hexagonal assembly with wire-wrapped fuel rods), but cannot accommodate innovative fuel configurations or natural circulation flow conditions.

Therefore, none of these traditional subchannel codes are suitable for performing subchannel analyses of sodium-cooled assemblies with annular or bottle-shaped fuel. The Trio-U code [3.13] used in France can model various innovative fuel rod configurations. However, this code is a full CFD code, the use of which is beyond the scope of the simple subchannel analysis codes investigated here. A list of the major subchannel analysis codes along with a summary of their capabilities and their limitations is given in Table 3.1. Many of these codes implement the pressure drop correlations developed by Basehore and Todreas. SUPERENERGY II [1.16] was utilized in SFR modeling at ANL [3.14] and is an example of such a code.

As mentioned above, SUPERENERGY II is not suitable for analysis of the fuel configurations explored in this project due to two primary limitations. The first limitation is on the assembly and fuel rod geometry. The only type of assemblies that can be analyzed utilizing SUPERENERGY II is hexagonal assemblies with wire-wrapped solid fuel pins. Additionally, there is no allowance for adjusting the area of the edge channels, nor is there the capacity to alter the type of spacer or to have differing pin diameters within the same assembly. This lack of flexibility prevents investigation of innovative design features into the assembly, such as the use of "ribs" in the edge subchannel to flatten the power profile, as discussed later in this chapter. Furthermore, the fuel rods must be solid pin-type fuel rods, with a single clad, fuel, and bond region for each rod. This prevents the analysis of annular fuel because the coolant flow in the inner-annular channel, as well as temperature distributions, heat splits, and even the distribution of flow between the inner and outer fuel channels, cannot be modeled by SUPERENERGY II.

Table 3.1: Major codes used in LWR and sodium fast reactors subchannel analysis

CODE	Country	Description	Limitations
Cobra IV	USA	Standard LWR subchannel analysis code in US	LWR only, no sodium
SuperEnergy2 (SE2)	USA	Based on Chen/Todreas correlations, steady state, does not evaluate fuel rod temperatures	Up to only 8 hexagonal rings in the assembly, only cylindrical fuel rods allowed
CADET	FRANCE	Used for all French sodium subchannel analyses, takes into account power distributions, boundary conditions, and helical wire-wrap, for forced and mixed convection	Only for nominal pin geometries, no natural circulation or mixed flow
TRIO_U	FRANCE	CFD Code that can be used in an unstructured mesh treatment	Complex, full CFD code
MATRA-LMR	KOREA	Based on Cobra and MATRA, benchmarked against SABRE4 and SLTHEN and found to be comparable, with slightly different prediction of pressure drop, implements Chen & Todreas pressure drop correlations	Only single assembly subchannel analysis + cannot model annular fuel
SLTHEN	US/KOREA	Based on SE2	Same as SE2
SABRE4	UK	Steady state or transient, 1 or 2 phase flow, blockage or bowed pins	Cannot analyze for annular fuel pins
SASSYS/SAS4	USA	System code, performs "hot channel" analysis, not actual subchannel analysis	Cannot model annular fuel, not full subchannel analysis
VIPRE	USA	US LWR subchannel analysis code, recently modified by MIT to analyze annular fuel	Water only, no correlations for sodium-cooled wire-wrapped assemblies
ASFRE-III	JAPAN	Japanese standard for fast breeder reactor (FBR) development thermal-hydraulics; can evaluate triangular pitched sodium cooled assemblies	Cannot model inner channel of annular fuel

The second limitation of SUPERENERGY II relates to assembly size. Only up to eight rings of fuel pins per assembly are allowed in the SUPERENERGY II subchannel analysis. Because the base ABR design contains nine rings of fuel in the fuel assemblies, SUPERENERGY II cannot be used to analyze even the base fuel designs for the ABR.

For these reasons, we decided to use RELAP5-3D to create a flexible subchannel model, which could perform subchannel analyses for the fuel assemblies with annular fuel pins and bottle shaped fuel pins, or any other assembly geometry that may be worth studying in the future (e.g., vented fuel, cross-shaped fuel, etc.). Since RELAP5-3D has not been used for subchannel analysis before, the development of these capabilities took a good fraction of the project focus for this thesis. The RELAP5-3D subchannel model combines several components, including sodium properties, wire-wrap correlations, and control variables. A detailed description of the RELAP5-3D subchannel model is reported in Section 3.2. The new RELAP5-3D model was verified by comparison with the SUPERENERGY II code for a simple geometry and experimental data from the ORNL 19 Pin test, as discussed in Section 3.3. Section 3.4 reports on the initial use of the RELAP5-3D model for optimization of the fuel assembly geometries with traditional solid fuel pins. The analysis and work for both bottle-shaped fuel and internally/externally cooled annular fuel are discussed in Chapter 6.

3.2 Development of the RELAP5-3D Subchannel Model

Subchannel analyses provide detailed information regarding coolant and fuel temperature, and coolant velocity and pressure distributions in the assembly of interest. In subchannel analysis the flow is assumed to occur primarily in the axial direction, while transverse flow is accounted for as a first order perturbation [3.15]. A coarse three-dimensional model of sorts is then created by joining several subchannels together into a single multi-ring assembly. If greater detail and accuracy is desired, this assumption can be lifted through the use of a computational fluid dynamics (CFD) model, but this approach is beyond the scope of the current study.

RELAP5-3D has the capacity to model 3-D geometries, but the computational cost is significantly larger than for 2-D or 1-D volumes. A "pseudo 3D" model can easily be created in RELAP5-3D by creating a pipe, or a group of volumes, connected in series through which the primary flow is in the axial direction. This pipe represents a single subchannel. Junctions can then be added to the sides of this pipe to connect it to an adjacent axial pipe, representing the cross-flow junctions. By connecting a series of pipes via transverse flow junctions, a three dimensional subchannel mesh is created in RELAP5-3D. Heat structures are created and joined to each pipe representing the fuel rod adjacent to the subchannel. Because heat structures can only be connected to two volumes (one on either side of the heat structure), each fuel rod is divided into six equal segments azimuthally and connected to their respective subchannels, as seen in Fig. 3.1. Finally, inlet and outlet plena are connected to the top and bottom of each subchannel, and in turn are connected to a time dependent volume via a time dependent junction and single junction, respectively. These allow for implementation of the assembly boundary conditions, such total inlet flow and exit pressure.

The transverse flow due to pressure gradients, or cross-flow, can be modeled for this subchannel geometry in RELAP5-3D utilizing form losses and junctions, but other physical phenomena such as turbulent mixing and coolant conduction can not be explicitly modeled by RELAP5-3D in the same way. Thus, a new approach must be undertaken to include these important phenomena. In this report, the method used to model these physical phenomena is outlined in detail. For each physical effect of assembly flow, RELAP5-3D control variables were used to numerically model this effect. Once an appropriate physical model was identified and the control variable scheme was selected, these control variable schemes were then applied to each volume within the subchannel geometry. This “brute force” method allows for RELAP5-3D to perform subchannel analyses for fuel assemblies of any conceivable geometry.

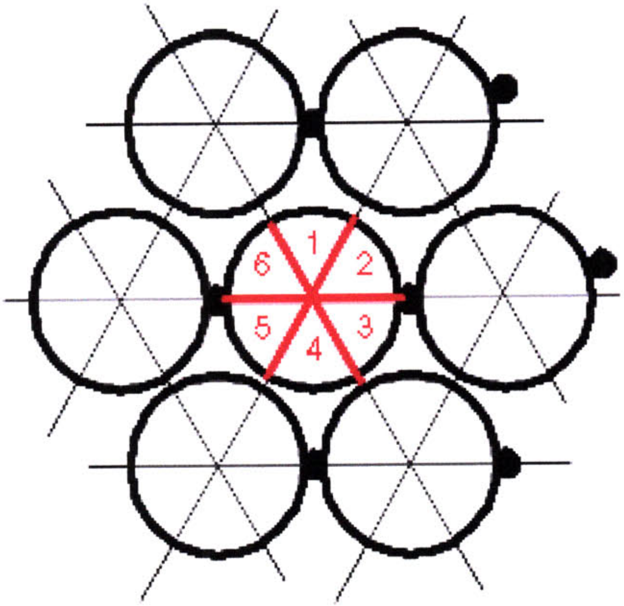

Figure 3.1: Heat structure “split” for fuel rod

3.2.1 Subchannel Model Components

The assembly type initially investigated was a hexagonal wire-wrapped triangular pitch fuel assembly, which can also be modeled by SUPERENERGY II. For the RELAP5-3D subchannel model there are four basic components:

1. The geometry, which consists of various subchannels and fuel rods

2. The cross-flow model, which takes into account flow between subchannels
3. The conduction model, which accounts for conduction axially and radially within the coolant
4. The turbulent mixing model, which accounts for coolant mixing and heat transfer due to flow currents induced by the helical wire-wrap.

A description of these four elements is provided in the following sections.

3.2.2 Reference Geometry Model

The basic geometry of the fuel assembly is a hexagonal wire-wrapped fuel assembly. The parameters used in the assembly model were adapted from an ANL report on core layouts for the Advanced Burner Reactor with conversion ratios (CR) [2.2]. In the ANL report, various cores are described for the ABR using a wide range of conversion ratios for both oxide and metal fuel. The details of these assemblies are discussed in Chapter 2, sections 2.1.1 and 2.1.2. The metal-fuel breakeven (CR=1) assembly was used as the base model. The investigation of the conduction effects (see Section 3.2.4 below) was completed using this model, which has nine rings. However, it was subsequently found that SUPERENERGY II cannot model more than eight rings. Therefore, the metal fuel breakeven assembly from [2.2] was scaled down directly to have only eight rings, so that a direct benchmark between RELAP5-3D and SUPENERGY II could be accomplished. The dimensions of both base assemblies are given in Table 3.2. The pitch between rods is the wire-wrap thickness, while a small gap between the wire-wrap at the outermost rods and the duct wall allows for thermal expansion of the assembly and bundle insertion during fabrication. A scale model of the eight ring assembly used for benchmarking is shown in Fig. 3.2.

Table 3.2: Dimensions of both 8 and 9 ring metal fuel assemblies

Parameter	Value	
	ANL original FA design	Scaled down FA design
Fuel type	Metal	Metal
CR	1.00	1.00
Rings	9	8
Fuel pins per assembly	271	217
Core inlet temperature (°C)	355	355
Linear heat rate (W/m)	33.71	33.71
Mass flow rate (kg/s)	37.44	30.04
Flat to flat distance (cm)	15.71	13.28
Inter-assembly gap (mm)	3.94	3.94
Pin data		
- Bond material	Na	Na
- Active core height, cm	101.6	101.6
- Height (plenum), cm	191.14	191.14
- Overall pin length, cm	407.04	407.04
- Fuel smeared density	0.75	0.75
- Fabrication density, % TD	100	100
- Pin diameter, cm	0.808	0.808
- Pin pitch-to-diameter ratio	1.10	1.10
- Cladding thickness, cm	0.0559	0.0559
Wire-wrap helical pitch (cm)	20.32	20.32

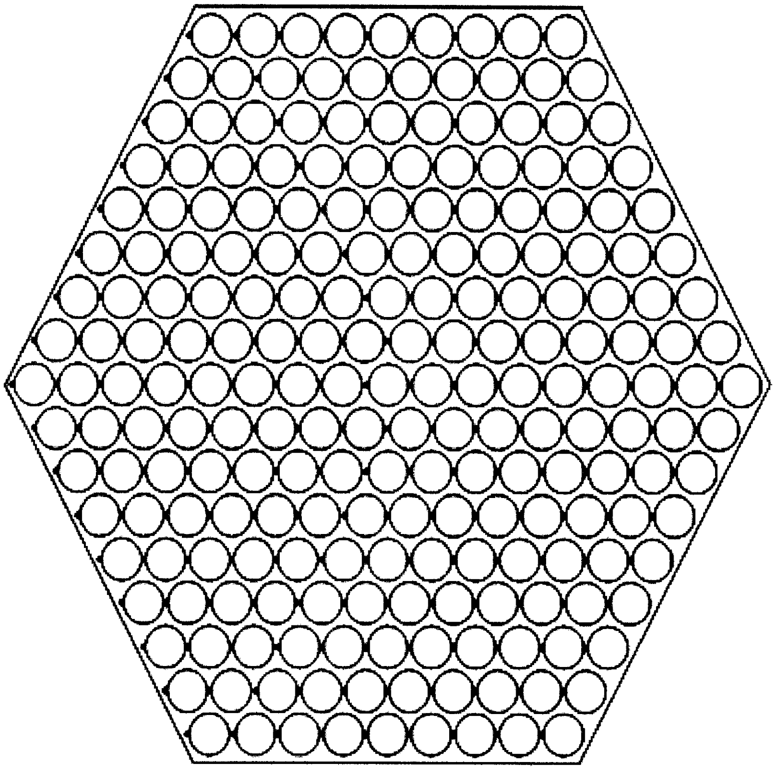

Figure 3.2: Scale representation of 8-ring wire-wrapped fuel assembly

Because of symmetry in the hexagonal fuel assembly, only 1/12 of the assembly needs to be explicitly modeled. A representative subchannel section indicative of an eight ring subchannel model geometry can be seen in Fig. 3.3.

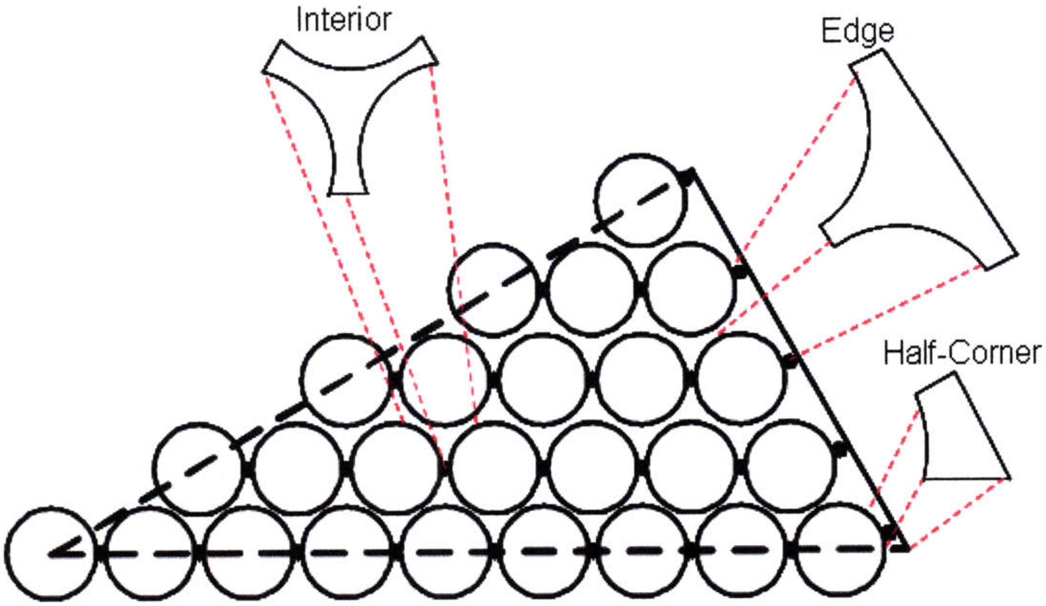

Figure 3.3: Portion of an 8-ring hexagonal assembly represented in a subchannel model

The subchannels in each fuel assembly can be divided into three different types: interior subchannels, edge subchannels, and corner subchannels (as shown in Fig. 3.3). The number of each subchannel in each assembly is found according to the following formulae:

$$\begin{aligned} N_i &= 6R^2 \\ N_e &= 6R \\ N_c &= 6 \end{aligned} \tag{3.1}$$

where:

N_i = number of interior channels

N_e = number of edge channels

N_c = number of corner channels

R = number of rings.

The respective areas of each of these subchannels in the hexagonal assembly are [3.16]:

$$\begin{aligned} A_i &= \frac{\sqrt{3}}{4}P^2 - \pi\frac{D_o^2}{8} - \pi\frac{D_w^2}{8} \\ A_e &= P\left(\frac{D_o}{2} + g\right) - \pi\frac{D_o^2}{8} - \pi\frac{D_w^2}{8} \\ A_c &= \frac{1}{\sqrt{3}}\left(\frac{D_o}{2} + g\right)^2 - \pi\frac{\left(D_o^2 + D_w^2\right)}{24} \end{aligned} \tag{3.2}$$

where:

A_i = area of interior channels

A_e = area of edge channels

A_c = area of corner channels

D_o = rod outer diameter

g = gap between rod bundle and duct wall

D_w = wire-wrap spacer diameter

P = fuel rod pitch.

The wetted perimeter for each type of subchannel is given by:

$$
\begin{aligned}
P_{wi} &= \pi \frac{D_o}{2} + \pi \frac{D_w}{2} \\
P_{we} &= \pi \frac{D_o}{2} + \pi \frac{D_w}{2} + P \\
P_{wc} &= \frac{\pi}{6}\left(D_o + D_w\right) + \frac{2}{\sqrt{3}}\left(\frac{D_o}{2} + g\right)
\end{aligned}
\tag{3.3}
$$

where:

P_{wi} = wetted perimeter of interior channels

P_{we} = wetted perimeter of edge channels

P_{wc} = wetted perimeter of corner channels.

The hydraulic diameter of each subchannel can then be calculated as:

$$D_h = 4\frac{A}{P_w}, \tag{3.4}$$

where D_h is the hydraulic diameter. The perimeter, area, and hydraulic diameter of each type of subchannel are shown in Table 3.3. With these parameters, the subchannels can then be adequately modeled as hydraulic components (pipes) in RELAP5-3D. Each subchannel was created in RELAP5-3D by creating a pipe and dividing it into a sufficient number of volumes in order to provide the required level of detail in the final model: one each for the entrance and exit regions, five for the gas plenum, and 22 for the heated core length. Each of these subchannel "pipes" is then connected to a heat structure representing a fuel rod, and an inlet and outlet plenum at each end is created to connect each of the subchannels. Fig. 3.4 is a side view of the basic subchannel geometry. Figs.

3.5 and 3.6 show top-down views of the subchannel model, including the RELAP5-3D numbering scheme for the volumes and heat structures, respectively.

Table 3.3: Parameters of each of the subchannel types in the base study

	Interior	Edge	Half-Corner
Area (mm^2)	8.29	21.70	3.97
Wetted perimeter (mm)	12.71	21.59	5.20
Hydraulic diameter (mm)	2.61	4.02	3.05

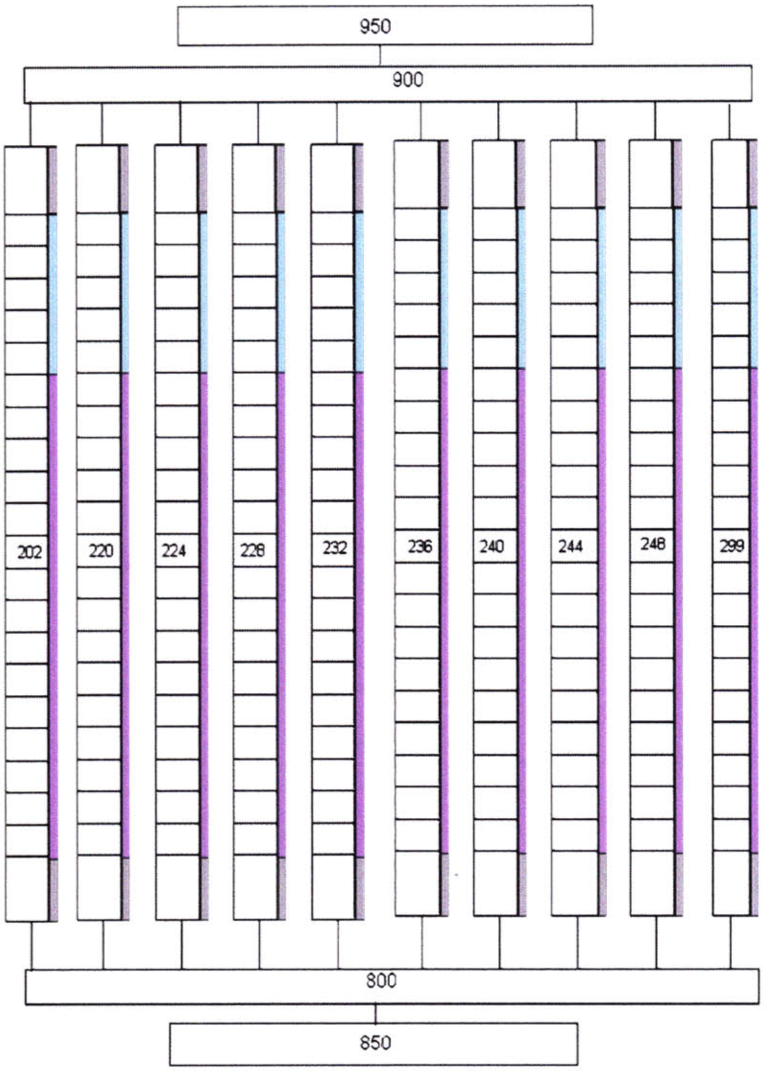

Figure 3.4: Side view of subchannel model depicting pipe, heat structure, and junction layouts for each subchannel

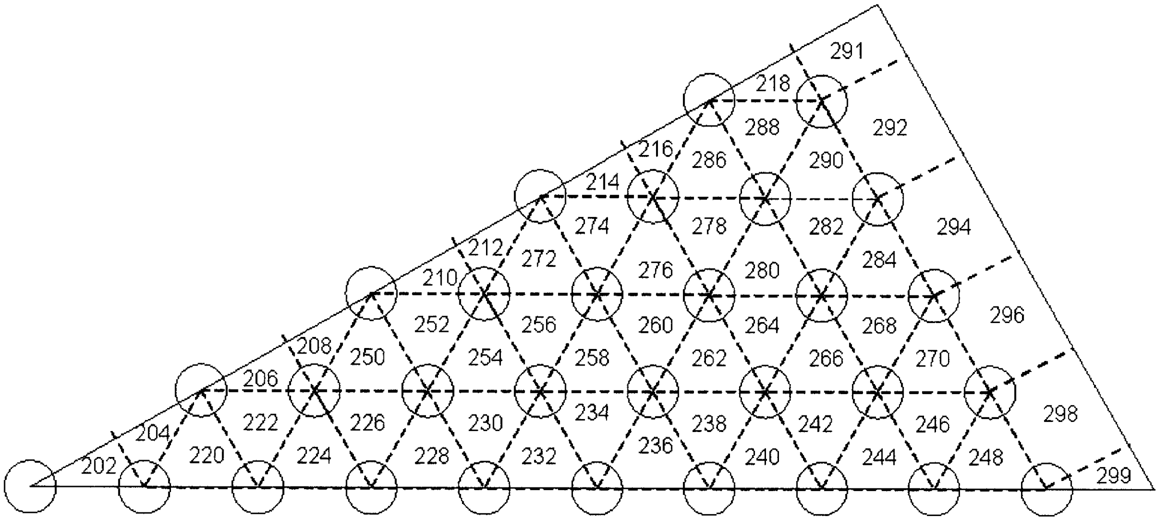

Figure 3.5: Cross-sectional view of RELAP5-3D subchannel geometry including volume numbering

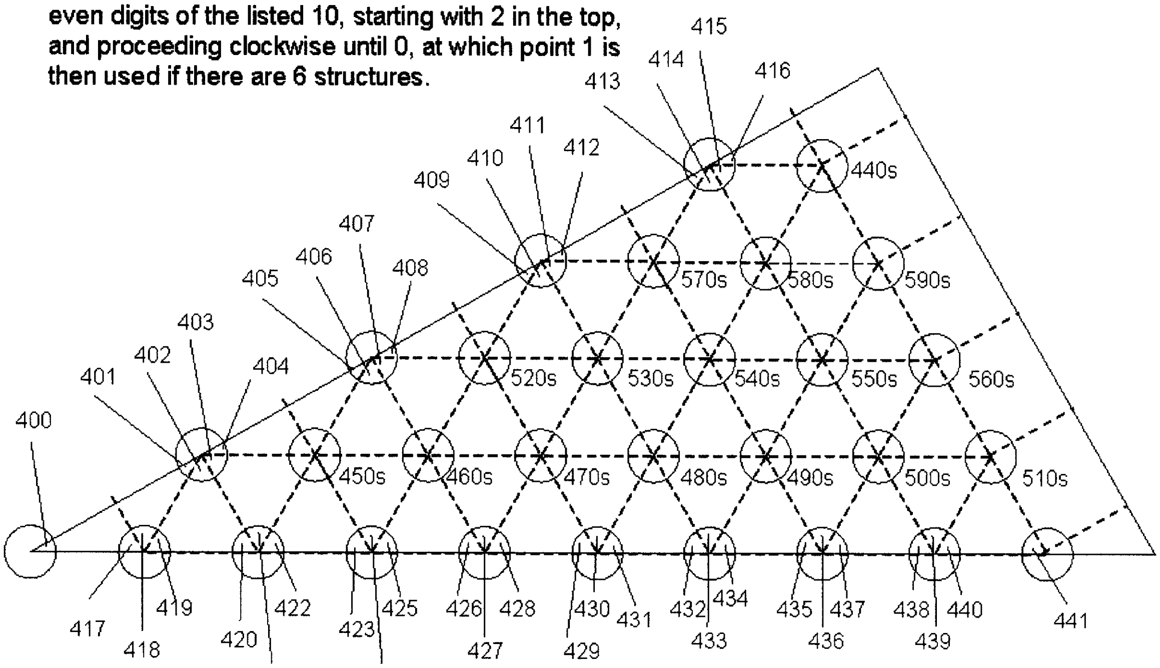

For the interior channels, the numbering follows the even digits of the listed 10, starting with 2 in the top, and proceeding clockwise until 0, at which point 1 is then used if there are 6 structures.

Figure 3.6: Cross-sectional view of RELAP5-3D subchannel geometry including heat structure numbering

The RELAP5-3D model described thus far constitutes the base geometry of a hexagonal assembly with triangular-pitch fuel rods spaced using wire-wrap. Further general additions to this model were needed, including localized (within the assembly) pressure drop correlations, axial power distributions, and radial power distributions. The pressure drop for each of the subchannels was calculated in RELAP5-3D by inputting the turbulent or laminar drag coefficient correlation for wire-wrapped triangular-pitch fuel subchannels developed by Chen and Todreas [3.17]:

$$\begin{aligned} C_{fT} &= \left(0.8063 - 0.90221 \cdot \log\left(\frac{H_w}{D_o}\right) + 0.35261 \cdot \log\left(\frac{H_w}{D_o}\right)^2\right) \cdot \left(\frac{P}{D_o}\right)^{9.7} \cdot \left(\frac{H_w}{D_o}\right)^{1.78-2\left(\frac{P}{D_o}\right)} \\ C_{fL} &= \left(974.6 + 1612 \cdot \left(\frac{P}{D_o}\right) - 598.5 \cdot \left(\frac{P}{D_o}\right)^2\right) \cdot \left(\frac{H_w}{D_o}\right)^{0.06-0.085\left(\frac{P}{D_o}\right)} \end{aligned} \quad , (3.5)$$

where:

H_w = the helical wire-wrap cycle height or axial lead of the wire-wrap

C_{fT} = the turbulent drag coefficient for flow through each subchannel.

The friction factor and pressure drops were then calculated in RELAP5-3D utilizing the relations:

$$f = \frac{C_{f(TorL)}}{\mathrm{Re}^{nf}}, \qquad (3.6)$$

$$\Delta P = f\frac{H}{D_h}\left(\frac{G^2}{2\rho}\right), \tag{3.7}$$

where:

f = wire-wrapped subchannel friction factor

H = axial height of the subchannel

G = the axial max flux of the subchannel in question

ΔP = pressure drop of the subchannel in question

nf = Reynolds exponent; 0.18 for turbulent or 1.0 for laminar flow

C_{fTorL} = turbulent or laminar drag coefficient.

By programming these correlations and factors directly into the input deck, the pressure drop for each subchannel is determined by RELAP5-3D. The axial and radial power distributions can also be input directly into the RELAP5-3D input deck.

The base model contains 36 interior channels, 9 half-interior channels, 4.5 edge channels, and 0.5 corner channels. The first set of calculations with RELAP5-3D did not include cross-flow, turbulent mixing, and conduction; therefore, each subchannel was effectively an isolated heated pipe. For simplicity, both the axial and radial power distributions were assumed to be perfectly flat, i.e., local and axial peaking factors equal to one. Under these assumptions, the outlet temperature for all subchannels with the same geometry is expected to be the same. This expectation was confirmed by the RELAP5-3D results, which are shown in Fig. 3.7.

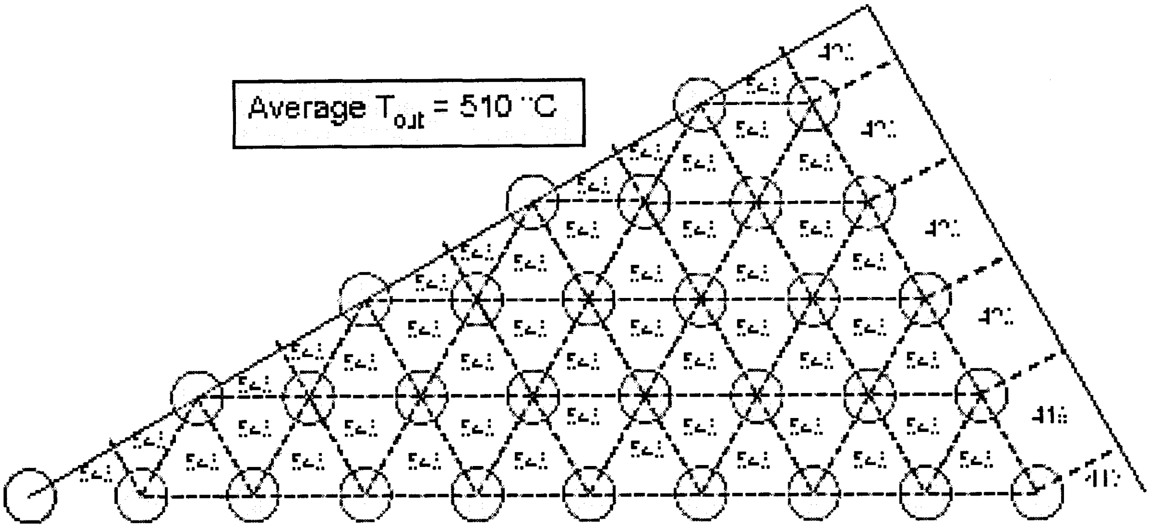

Figure 3.7: Outlet temperature distribution of RELAP5-3D basic model (no cross-flow)

The edge and corner subchannel outlet temperatures are significantly lower than the interior subchannel outlet temperatures, which was also expected because the edge channels have a significantly larger cross-sectional flow area than the interior channels (~2.1 time larger), and thus experience higher flow rates, but their heat rate is exactly the same as for the interior subchannels (1/2 fuel rod per subchannel). This means that the flow-to-power ratio (m/Q) is larger for the edge channels, resulting in a lower outlet temperature. The corner channel has a smaller cross-sectional flow area than the interior channels, but the power input is also 1/6 of the power input for the interior channels, resulting in the decreased corner subchannel outlet temperature.

3.2.3 Cross-Flow Model

Next, the cross-flow model was added. In addition to axial flow in the subchannel, each subchannel communicates via cross-flow due to pressure gradients between subchannels, which drive fluid flow from one subchannel to another in the transverse direction. The degree of communication depends upon the magnitude of the pressure gradients between subchannels, as well as the resistance to transverse flow. The pressure gradients are calculated automatically within RELAP5-3D, while the resistances to transverse flow were modeled explicitly as part of the cross-flow junctions.

These cross-flow junctions were modeled in RELAP5-3D by creating several "multiple junction" components. These are simply single objects that consist of many junctions. Each "multiple junction" component contains 22 junctions; these junctions connect to the sides of the axial subchannel pipes at each of the corresponding 22 segments. These junctions have an area equal to the flow area of the respective volume in the transverse direction (y and z), which represents the area between the closest point between fuel rods, as seen in Fig. 3.8. These transverse junctions, as shown in Fig. 3.9, allow fluid to flow from one subchannel to another. The magnitude of the flow between subchannels also depends on the resistance to flow. This resistance to flow can be modeled as a form loss, K_t, and this constant can be input directly into the junction definition in RELAP5-3D. According to literature [3.18], an appropriate value for transverse flow across staggered rod bundles can be found using the equations:

$$K_t = Z_r \cdot A \cdot \Psi \cdot \mathrm{Re}^{-0.27}, \tag{3.8}$$

$$A = 3.2 + 0.66a_1 + \left(13.1 - 9.1\left(\frac{P}{D_o}\right)\right) \cdot (0.8 + 0.2a_1), \tag{3.9}$$

$$a_1 = 1.7 \cdot \left(\frac{S_2}{S_1}\right)^{1.5}, \tag{3.10}$$

Where:

Z_r = number of rows of tubes plus 1 divided by number of transverse junctions

Ψ = Factor relating to bundle to flow angle (for 90° flow/rod angle, $\Psi = 1$)

S_2/S_1 = bundle pattern factor (for a triangular bundle, $S_2/S_1 = 1$)

For the assembly configurations described in Chapter 2, Kt ranges from 0.21 to 0.67, and these values were used in the respective assembly models.

The transverse area of the subchannel is related to the wire-wrap diameter, which is small (0.805mm in the base case). The transverse flow area for each volume in the subchannel, and thus for each cross-flow junction is then:

$$A_t = g \cdot L_i, \tag{3.11}$$

where:

A_t = transverse flow area

L = volume axial length

g = gap between rods

i = volume type: c – core, e – entrance/exit, p – plenum.

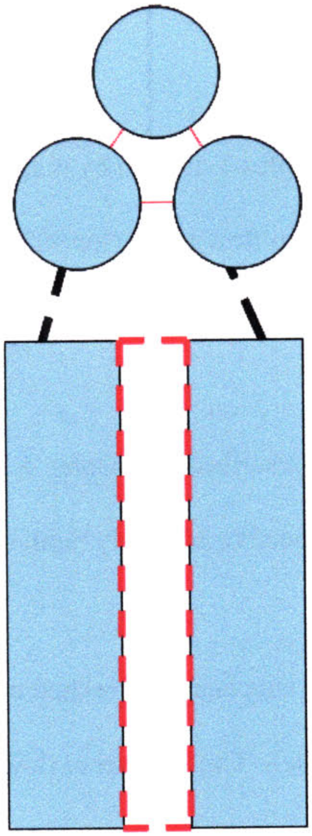

Figure 3.8: Cross-sectional and lateral views of the transverse (cross-flow) area for a subchannel

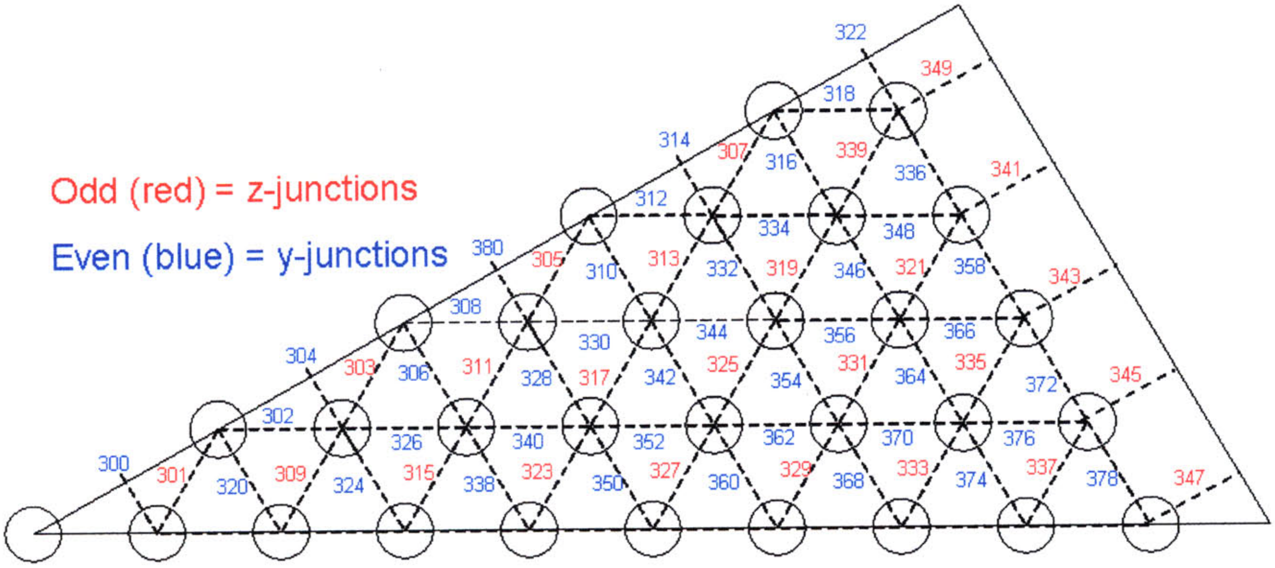

Figure 3.9: Top-down view of RELAP5-3D subchannel geometry including junction numbering

Incorporating the above junction system and the cross-flow resistance, one obtains the coolant temperature distribution (at the end of the heated length) seen in Fig. 3.10. In this figure, it appears that there is no difference in temperatures upon addition of cross-flow. There is indeed a slight change in the temperature profile, but the scale of this change is on the order of 1/10°C, which is too small to identify upon comparison between Figs. 3.8 and 3.10. This indicates that there is indeed communication between subchannels due to cross- flow, but that it is almost imperceptible. This lower-than-expected influence of cross-flow communication between subchannels is due to the very small transverse flow area, as well as the small pressure gradients between subchannels through the heated length of the core. To verify that these were the causes for the low transverse flow effect, several cases were run in which the cross-flow resistance was adjusted from $K_t = 0$ to 1.0. Each of these cases produced similarly small changes in the temperature distribution at the core outlet for the subchannels, indicating that indeed the small amount of communication between subchannels is due to small transverse areas and pressure gradients, rather than an erroneously high transverse flow resistance.

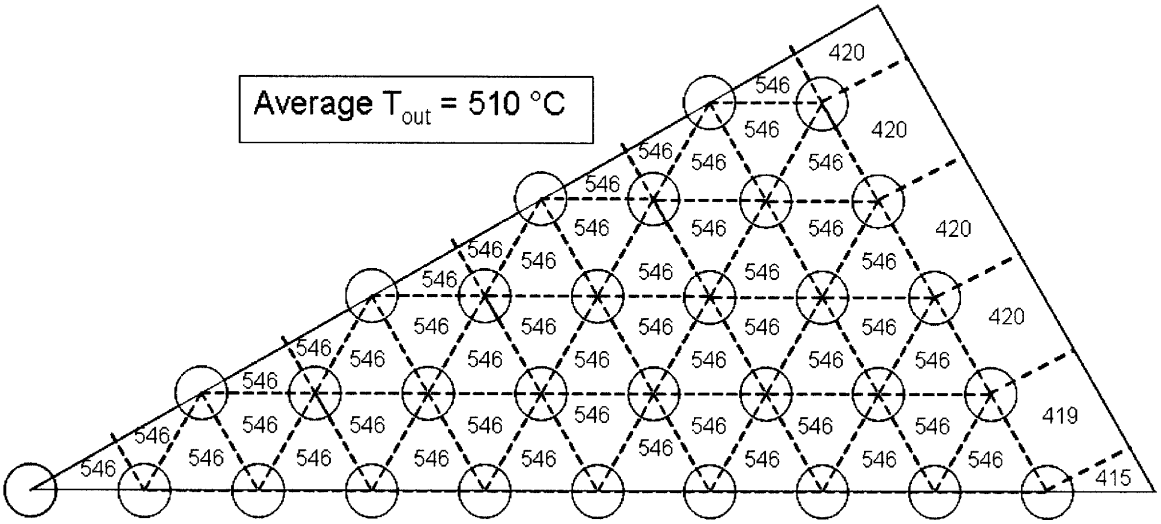

Figure 3.10: Core outlet temperatures for model containing cross-flow junctions

3.2.4 Fluid Conduction Model

Next, heat conduction in the sodium coolant was introduced in the subchannel model. Conduction can occur within the assembly coolant in both the axial and radial directions. Axial conduction increases the amount of energy transferred in the direction of the flow, while radial conduction tends to flatten the core temperature non-uniformities. RELAP5-3D does not account for conduction within the fluid, due to its primary development for use with light water reactors (LWRs). However, the thermal conductivity of sodium is nearly 100 times larger than that of water, and thus may in principle affect heat transfer within the assembly. This influence is dependent upon flow regime, flow rate, and the physical properties of the fluid. Methods for modeling the effects of conduction within the coolant in RELAP5-3D have been previously investigated [3.19] and a similar approach is used in this subchannel model. Yoo et. al.

[3.20] state that as a simple rule, fluid conduction becomes important when the modified Peclet number (Pe^*) is less than 100. Their modified Peclet number is defined as:

$$Pe^* = \mathrm{Re}\,\mathrm{Pr}\frac{L}{D_h}, \tag{3.12}$$

where:

Pr = Prandtl number

L = length of the component,

D_h = hydraulic diameter of the component.

The modified Peclet number for the steady-state full-power model is much greater than 100, indicating that axial conduction should be negligible, but at lower flow rates, the Reynolds number decreases, and this effect may become significant. Thus, the model utilizing axial conduction was constructed as described below.

Control variables can be used to calculate the heat transfer due to conduction and to add them to the fluid via "pseudo" heat structures. These pseudo heat structures are small structures (less than 1% of the actual heat structure volume, so as to have negligible thermal capacity), which are connected at the right side (as pertaining to the RELAP metric for right and left sides of heat structures) to the appropriate volume, while the left side of the heat structures remain adiabatic. These structures are then linked to the control variables, which calculate heat due to conduction so that the conducted heat is added directly to the fluid in the appropriate volume. Fourier's Law was used to calculate the heat transfer due to conduction in the fluid:

$$q = -kA\frac{dT}{dz},\tag{3.13}$$

where:

q = heat rate transferred due to conduction

k = thermal conductivity of fluid

T = temperature of fluid

z = physical distance over which temperature gradient is measured.

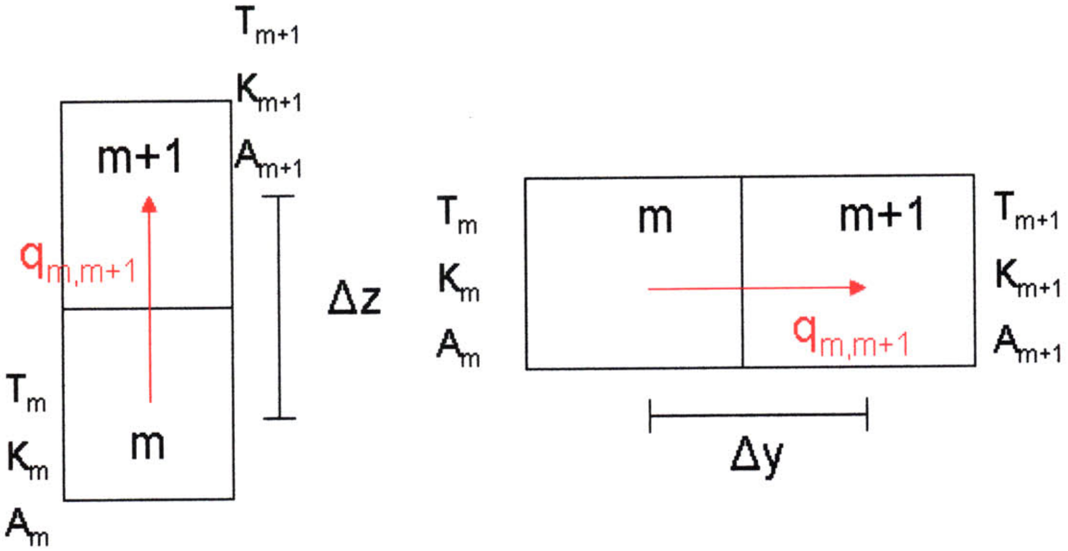

Figure 3.11: Schematic of volume connections axially (left) and radially (right)

Control variables were created, which calculate conduction via Fourier's Law. Fig. 3.11 illustrates the schematics for volume connections both axially and radially. Utilizing the nomenclature of Fig. 3.11, the axial heat conduction in the coolant from one volume, volume m, to the next volume, volume m+1, can be calculated as:

$$q_{m,m+1} = -k_{m-\frac{1}{2}} A_{m-\frac{1}{2}} \frac{T_{m+1} - T_m}{\Delta z}, \tag{3.14}$$

where:

$q_{m,m+1}$ = heat transferred from volume m to volume m+1

$k_{m1/2}$ = linear average of thermal conductivity of fluid in volumes m and m+1

$A_{m1/2}$ = area of the junction connecting volumes m and m+1

T_{m+1} = temperature in volume m+1

T_m = temperature in volume m

Δz = distance between the midpoints of volumes m and m+1.

For simplicity, the physical constants of the model are lumped into a single term, B_m:

$$B_m = -\frac{k_{m-\frac{1}{2}} A_{m-\frac{1}{2}}}{\Delta z}. \tag{3.15}$$

Thus, the equation used to calculate the heat transfer axially is:

$$q_{m,m+1} = B_m (T_{m+1} - T_m). \tag{3.16}$$

This same logic can be used to calculate the heat transfer due to conduction radially in the fluid, merely by substituting Δz for Δy, and by utilizing the appropriate volume properties and conditions.

Fig. 3.12 shows the core outlet temperatures for the subchannel model, which contains cross-flow and axial conduction. As can be seen in this figure, the axial conduction effects are extremely small (no difference up to two significant figures), and can be considered negligible. To demonstrate the effect of conduction at reduced flow conditions (where the modified Peclet number is significantly less than 100), a RELAP5-3D conduction model was created, which has a flow and power level reduced to 4% of the power/flow at steady state. Fig. 3.13 shows the axial temperature profile of the hot channel for both the steady state conditions model and the reduced flow/power model, both including conduction and cross-flow. At the end of the heated length of the channel, and through the plenum, the temperature difference between the steady state model and the reduced flow model is approximately 8°C. Though small, this number indicates that at low flow, such as during transient conditions or conditions that would favor natural circulation, conduction would indeed become significant. Perhaps more revealing is Fig. 3.14, which shows the comparison of temperatures at low flow/power conditions (4% steady state flow and 4% power) with and without axial conduction. This demonstrates the effect of decreasing the Reynolds number throughout the assembly coolant subchannels. As the Reynolds number decreases, the modified Peclet number also decreases, and the effect of conduction becomes increasingly significant.

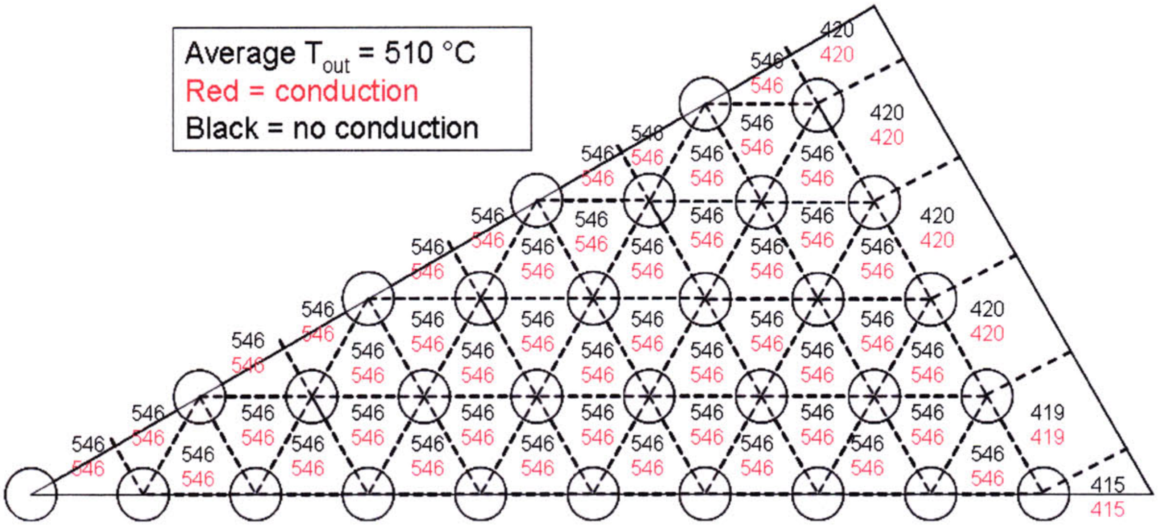

Figure 3.12: Comparison of core outlet temperatures for the basic cross-flow subchannel model with and without axial conduction at full flow/power

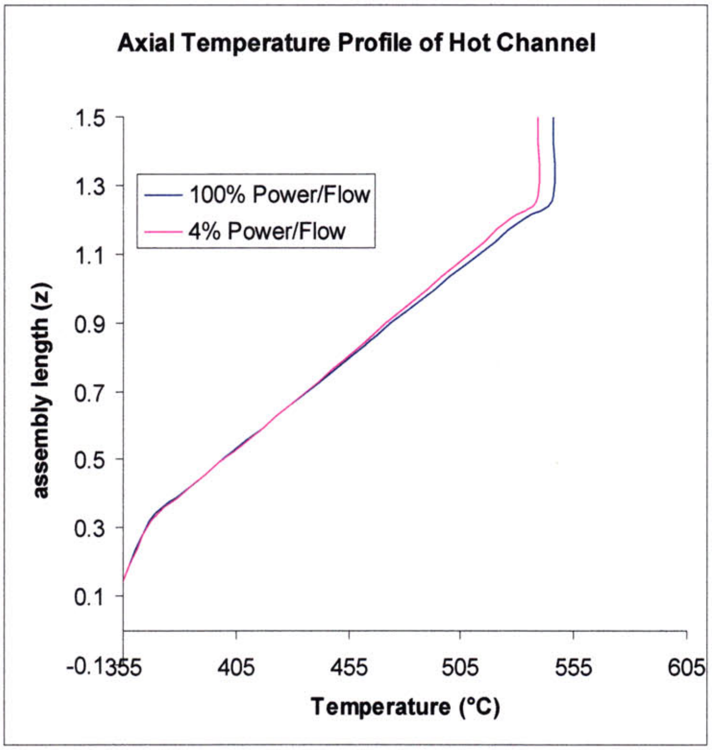

Figure 3.13: Comparison of the hot channel axial temperature profile for a steady state and low flow/power model, both with conduction effects

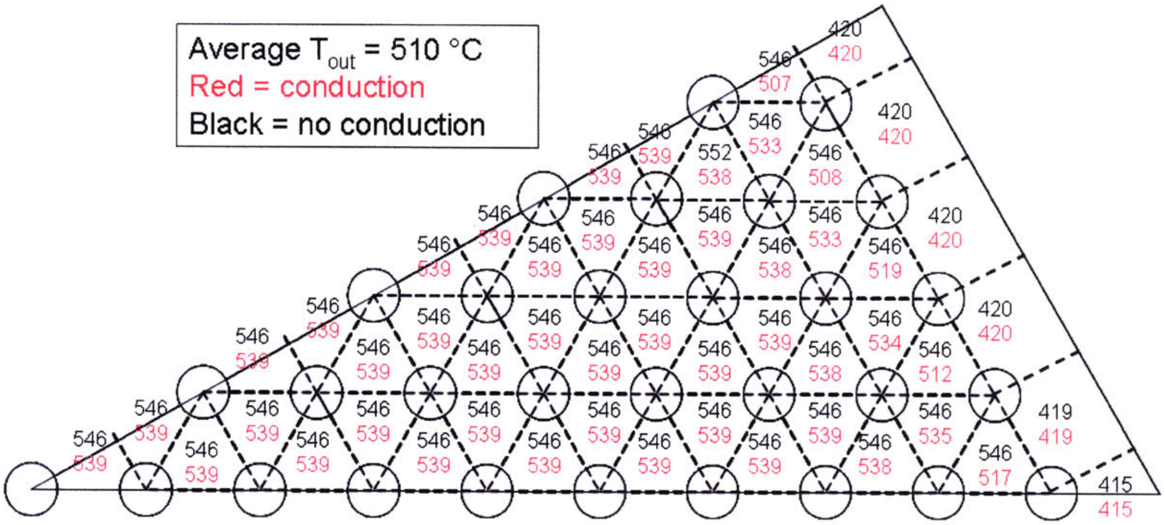

Figure 3.14: Comparison of core outlet temperatures for the basic cross-flow subchannel model with and without axial conduction at 4% flow and power[1]

In addition to axial conduction, radial conduction can become significant through the assembly at low flow conditions. Radial conduction effects were incorporated into the RELAP5-3D input deck instead of axial conduction effects (including both effects is quite expensive computationally, and for little benefit at this point), and the model was run at both full power/flow conditions and 4% power/flow conditions. The resulting core outlet temperature profiles for the full power/flow and 4% power/flow conditions as compared to the basic cross-flow model can be seen in Figs. 3.15 and Fig. 3.16, respectively. As seen in Fig. 3.15, radial conduction has no discernable influence on the outlet temperatures for the inner subchannels, where temperature differences between subchannels are quite small. Near the assembly edge, however, where the temperature differences are quite large (~126°C), radial conduction influences the outlet temperature profile. The temperatures in the interior channels immediately adjacent to the edge

---

[1] Due to rounding the edge subchannels appear to have the same temperature with and without conduction. In reality these subchannels have 0.1-0.3°C higher temperature when conduction is accounted for, which is sufficient to compensate for the lower temperature in the other subchannels. Therefore, the average outlet temperature is indeed 510°C in both cases.

channels are decreased, due to heat transfer via fluid conduction to the edge subchannels while the temperatures of the edge subchannels are increased. Though the effects of radial conduction at full power seem to be significant in this model, this is only for very large temperature differences between subchannels. When turbulent mixing (as described in the next section) is included, the largest temperature difference seen between subchannels is about 21°C. This is nearly seven times less than in the model which does not include turbulent mixing. Thus, the influence of radial conduction at high flow can be neglected when turbulent mixing is included.

Fig. 3.16 shows the effects of radial conduction for a decreased modified Peclet number. In this figure, the flow rate and power were decreased to 4% of the full power levels and the radial conduction effects were again modeled. At these decreased flow conditions, radial conduction begins to have a very large influence on the core outlet temperatures. Due to the increased communication via fluid conduction, a temperature distribution is created, which is quite similar to the distribution created when turbulent mixing is included, as discussed later in this report. Therefore, for transients and other low-flow (and thus low modified Peclet number) scenarios, both radial and axial conduction should be included to maintain accuracy.

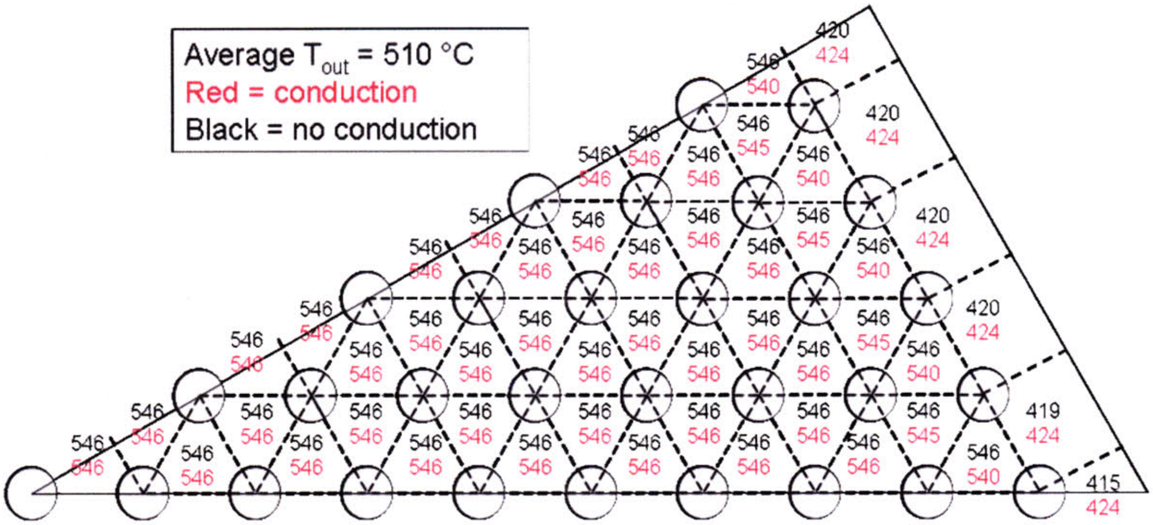

Figure 3.15: Comparison of core outlet temperatures for the basic cross-flow subchannel model with and without radial conduction at full power/flow

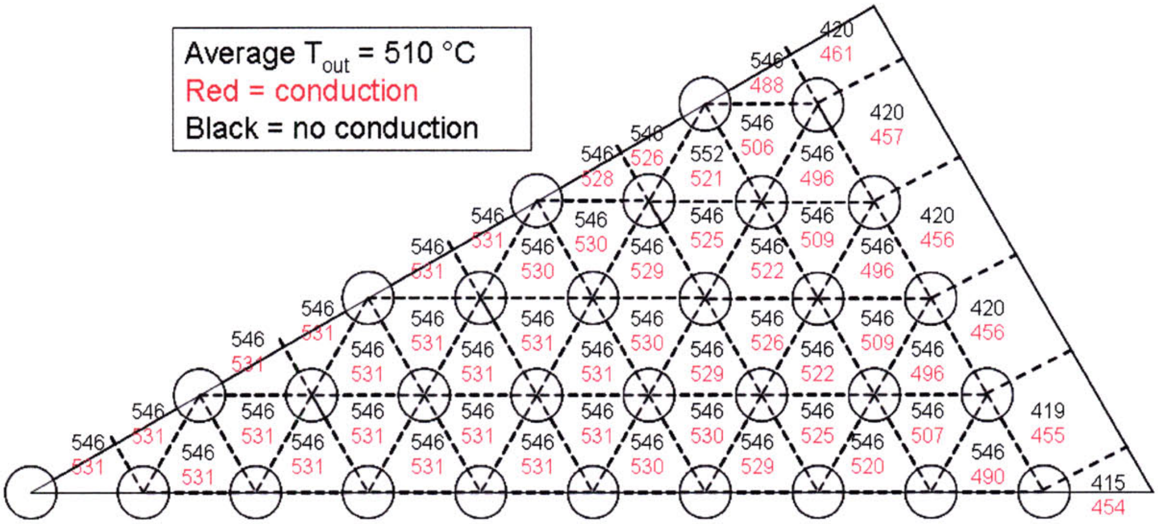

Figure 3.16: Comparison of core outlet temperatures for the basic cross-flow subchannel model with and without radial conduction at 4% power/flow

3.2.5 Turbulent Mixing Model

Significant mixing occurs between subchannels due to the random turbulence and coherent swirl flow generated by the wire-wrap spacers around each rod. The helical shape of the wire-wrap induces radial and azimuthal flow components in the coolant as it flows upward through the core. There are two primary physical effects of having wire-wrap spacers in the assembly. The first effect is experienced only in the interior subchannels of the assembly. The axial flow hits the wire-wrap and begins to "swirl" around the rod as it follows along the wire-wrap's helical shape. This phenomenon is illustrated in Fig. 3.17. For the interior channels of the assembly, each subchannel's transverse boundary experiences mass inflow and outflow. This transverse mass flow is directly proportional to the axial mass flux in each of the adjacent channels. Thus, for the interior channels where the mass flux is about the same for each channel, the net transverse mass flux is zero. However, the edge subchannel axial mass flow rate is substantially different from the interior triangular subchannels. Therefore, there is a small amount of transverse mass flow between the triangular and the edge subchannels. Because the net mass flow between interior channels is zero, mass flux between adjacent subchannels is important only in determining the amount of energy transferred due to mixing that occurs in this region. For the boundary between the edge and interior subchannels, there is a net mass flux, but this mass flux cannot be modeled with RELAP5-3D. This is because the only way to set a mass flow through a junction in RELAP5-3D is to use time-dependent junction components, but these components cannot dictate mass flow based upon control variable calculations in-situ. The mass flow can only be set at a predetermined amount (as a function of time) that is input prior to the initiation of the run; this flow can vary with time, but only according to constant values given in the input deck. Therefore, this introduces an error, estimated to be of ~3% to 4.5%, in the axial mass flow rates of the edge channels.

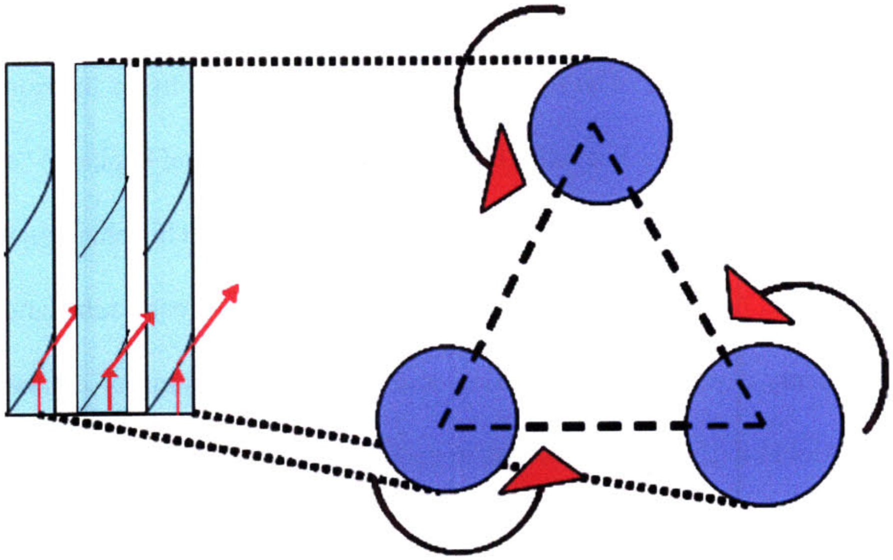

Figure 3.17: Swirl mixing in interior subchannels

The effects of this phenomenon have been investigated in depth by Chen and Todreas [3.17]. The dimensionless effective eddy diffusivity, ε*, is a measure of the transverse mass flux induced by this physical mixing effect. The effective eddy diffusivity is defined by the parameters of the fuel rod and wire-wrap only, and is found by the following relation:

$$\varepsilon^* = .14\left(\frac{P-D_o}{D_o}\right)^{-0.5}\left[\frac{\left(\frac{\pi}{6}\right)\left(P-\frac{D_o}{2}\right)^2-\left(\frac{\pi D_o^{\,2}}{24}\right)}{\left(\frac{\sqrt{3}}{4}\right)P^2-\frac{\pi D_o^{\,2}}{8}}\right]^{0.5}\tan\theta \tag{3.17}$$

where θ is defined by:

$$\cos\theta = \frac{H_w}{\sqrt{H_w^{\,2}+\left(\pi\left(D_o+D_w\right)\right)^2}}. \tag{3.18}$$

Once ε* has been determined, the transverse mass flow rate can be calculated as a function of the axial mass flow and the transverse area, which is simply equal to the junction area, as defined above. This relation is:

$$m_T = \varepsilon^* G A_T \tag{3.19}$$

where:

m_T = transverse mass flow rate through each interior subchannel face.

The transverse mass flow rate due to the turbulence and swirl mixing is not specifically input in the mass balance of the RELAP5-3D model. This is due to the fact that sodium is, to a very good approximation, an incompressible fluid; therefore, a turbulent eddy entering the subchannel displaces a volume of sodium equal to its own, thus resulting in a zero net change of mass within the subchannel volume. However, the energy balance is affected by mixing, and this effect was included in the RELAP5-3D model, as follows. When the transverse mass flow rate has been determined, the energy transfer due to the turbulent and swirl mixing in from volume m to volume m+1 can be determined from the equation:

$$q_T = m_T C_p \left(T_{m+1} - T_m\right) \tag{3.20}$$

where:

q_T = the transverse energy transfer due to turbulent and swirl mixing

C_p = heat capacity of the coolant.

The second effect that is derived from utilizing wire-wrap spacers is the flow phenomenon that occurs in the edge subchannels of the assembly. All the wire-wrap spacers in the assembly are wound in the same direction around the rods. When there are only two rods per subchannel, there is an absence of countercurrent rotational flow. This effect, when summed up over the edge rods, results in the production of a "swirl" flow around each of the edge channels of the assembly. There is a net mass flux, which flows in a single direction around the periphery of the assembly. This physical effect is illustrated in Fig. 3.18. The swirl flow, measured by the dimensionless swirl ratio, C_{1L}, flattens the core outlet temperature distribution along the assembly duct (which would otherwise be somewhat large due to the small heat input to mass flow ratio in the corner channels with respect to the edge channels). The swirl ratio, C_{1L}, is the ratio of the transverse to axial flow velocities in the edge channels. It is also dependent only on fuel rod and wire-wrap properties, and is defined as:

$$\frac{v_T}{v} = C_{1L} = 0.75\left(\frac{H_w}{D_w}\right)^{0.3}\left(\frac{\left(\frac{\pi}{4}\right)\left(\frac{D_o}{2}+D_w\right)^2 - \frac{\pi D_o^{\,2}}{16}}{P\left(\frac{D_o}{2}+D_w\right) - \frac{\pi D_o^{\,2}}{8}}\right)^{0.5} \tan\theta\,, \tag{3.21}$$

where:

v_T = transverse velocity

v = axial velocity.

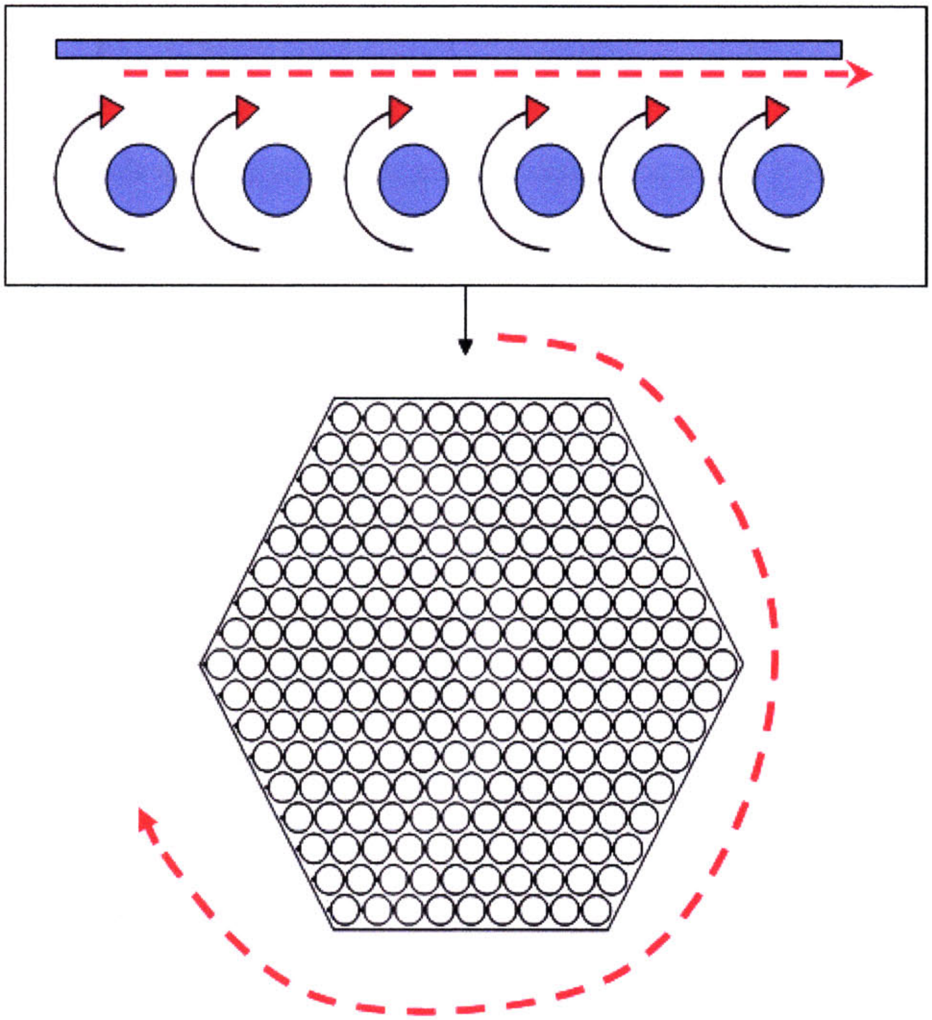

Figure 3.18: Swirl mixing in edge and corner subchannels

The energy transfer due to transverse flow induced in the edge channels can then be determined from (3.17) where m_T is:

$$m_T = v_T \rho A_T , \tag{3.22}$$

where ρ is the coolant density in the edge junction connecting the two volumes.

Once the control variables have been programmed into RELAP5-3D, the energy must be added or subtracted to the control volume of relevance. This is done by creating a “pseudo” heat structure, as described by Davis [3.19]. Again, this pseudo heat structure is small (less than 1% of the actual heat structure volume, so as to not absorb significant amounts of heat) and is connected to the appropriate volume. Therefore, as the model is converging to steady state, there are actually 2 distinct “heat” sources/sinks connected to each volume. The first heat source is fission in the fuel rods themselves. The second source/sink is the pseudo heat structure which either adds or subtracts heat from the volume based upon the dynamically determined turbulent and swirl mixing heat transfer, as calculated by the control variable relations described above.

When both mixing flow phenomena are included in the subchannel model, the overall effect is to flatten the core outlet temperature distribution. Fig. 3.19 shows the subchannel model core outlet temperatures both with and without the turbulent mixing system included. As can be seen in this figure, there is dramatic improvement in the core outlet temperature profile when turbulent and swirl mixing (no conduction) is included.

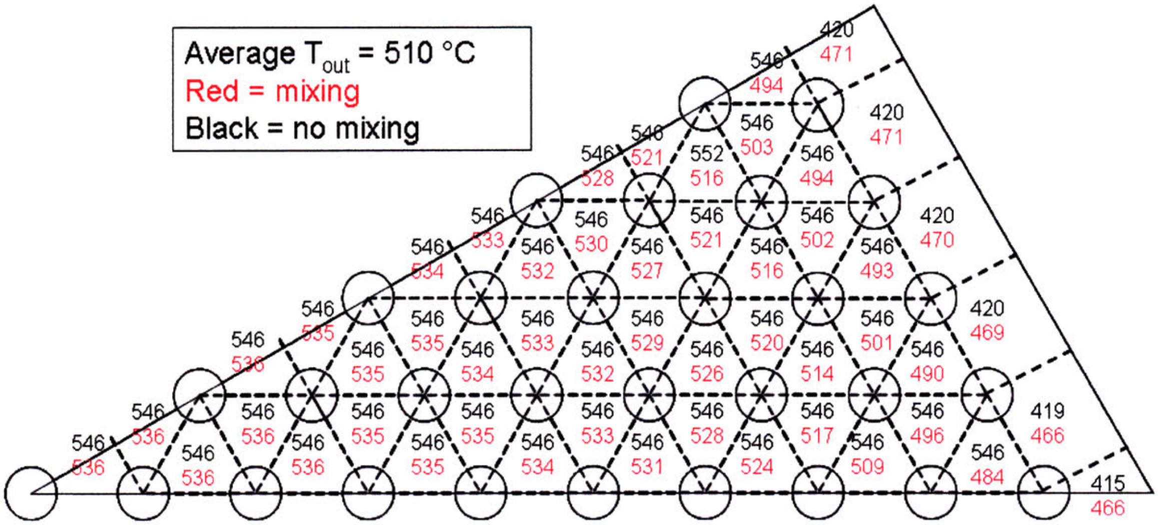

Figure 3.19: Comparison of core outlet temperatures for the basic cross-flow subchannel model with and without turbulent and swirl mixing

3.2.6 Some Limitations of the RELAP5-3D Model

There are four limitations to using this model. These limitations pertain to the use of the control variable scheme, scratch space availability, input deck creation time, and heat transfer approximations. The first limitation is the amount of control variables allowed in each input deck. The "brute force" method described above requires approximately 5 to 7 control variables for each volume to model mixing and 4 to 6 variables to model coolant conduction. Therefore, using control variables to model physical phenomena within the assembly is suitable for moderate-sized assemblies (up to 13 rings), but it cannot be done for larger assemblies. This is primarily due to the fact that RELAP5-3D only allows 10,000 control variables, and the total number of control variables utilized for the mixing model alone for a 13 ring model is around 9,600. Hence, the subchannel model described in this report is limited to 1/12 assembly models of 13 rings or less (with turbulent mixing but without conduction).

An additional limitation is the amount of scratch space allotted for RELAP5-3D calculations. This space is limited, and a subchannel model of 10 or more rings cannot be run using the RELAP5-3D executable 3.4.1.1.d., which is the current executable used at MIT. The subchannel model is a massive model with 22 volumes per subchannel, and in a 10 ring, 1/12 assembly model, there are 60 pipes, which means that there are over 1,320 volumes with corresponding heat structures and junctions. Therefore, the space required to perform a RELAP5-3D run exceeds the scratch space in the 3.4.1.1.d. executable. To overcome this limitation, a special version of the RELAP5-3D executable 3.4.2 was created specifically with a larger scratch space [3.21]. This larger scratch space allows for the modeling of larger assemblies, but the tradeoff is that a massive amount of data will be dumped in the event of run failure, resulting in a computer freeze for a significant time while the data is printed to a file.

The third limitation is the time investment required to create the subchannel model. The basic geometry, while large, is not restrictive in scope. Creation of a subchannel model that does not include any control variable schemes would require approximately 15-30 hours from scratch, depending upon user experience and the size of the model. However, the time required to create control variable schemes for each volume is quite large. Because errors in control variables can be difficult to detect after the completion of the subchannel model, careful attention must be given to each control scheme to ensure that the physical effects are modeled correctly. Additionally, it is difficult to create a macro which would adequately produce a control variable scheme for differing volumes, as unique volume identifiers must be included in each and every control variable. Therefore, the time required to create a subchannel model that includes control schemes and pseudo-heat structures is increased by a factor of around 3-5 times. This is a substantial increase in required resources, and is the largest drawback of utilizing RELAP5-3D as a subchannel modeling tool. This drawback has to be weighed against the flexibility afforded by the RELAP5-3D approach.

The final limitation is the evaluation of azimuthal conduction within the fuel rods. While the rods are divided into different segments azimuthally, our model does not account for conduction of heat from one subchannel to another via fuel rods. This effect is also neglected in SUPERENERGY II, which does not even evaluate the temperature of the fuel rods.

3.3 Verification of the RELAP5-3D Subchannel Model

To gain confidence in the accuracy of RELAP5-3D as a subchannel analysis code, we compared its performance to that of SUPERENERGY II, a traditional sodium-cooled reactor subchannel code.

3.3.1 The SUPERENERGY II Code

SUPERENERGY II is a steady-state subchannel analysis code originally created by Todreas et al. [1.16]. This code is specifically designed to accommodate sodium-cooled, wire-wrapped, hexagonal fuel assemblies, and has been used extensively by Argonne National Lab (ANL). In essence, the SUPERENERGY II code was adapted so that flow data could be read from the EBRFLOLW code (an ANL internal code which determines the flow splits between the various assemblies of the EBR II reactor) and neutronic data could be read from DIF3D. When incorporated with these codes, it provided very accurate subchannel analysis (within 10% of the inlet-to-outlet coolant temperature increase) for EBR II cores [3.22]. This result essentially verified SUPERENERGY II as a code capable of producing accurate results for subchannel analyses using wire-wrapped, triangular-pitch sodium-cooled assemblies.

An 8-ring 217-pin assembly was modeled in SUPERENERGY II with identical dimensions to the 8-ring 217-pin RELAP5-3D model described in Section 3.2.2. Unfortunately, SUPERENERGY II does not provide a map of the fluid velocities in the channels. Rather, only the average velocity for each of the subchannel types is printed at the given axial position. These velocities, as well as the average Reynolds number in the subchannels, are found in Table 3.4. The agreement with RELAP5-3D is very reasonable. The SUPERENERGY II core outlet temperatures are shown in Fig. 3.20. This figure shows the subchannel coolant temperatures at the core exit (heated length) for the entire assembly (although significant symmetry is present). The numbers shown each indicate a subchannel coolant temperature, while the asterisks represent the duct wall. The numbers immediately to the outside edge of the asterisks represent the duct wall temperatures.

Table 3.4: SUPERENERGY II and RELAP5-3D single assembly parameters

	Average Velocities (m/s)			
	Interior	**Edge**	**Corner**	**Channel Re**
SUPERENERGY	9.648	10.342	10.342	70810
RELAP5-3D	9.6	11.2	10.6	71093

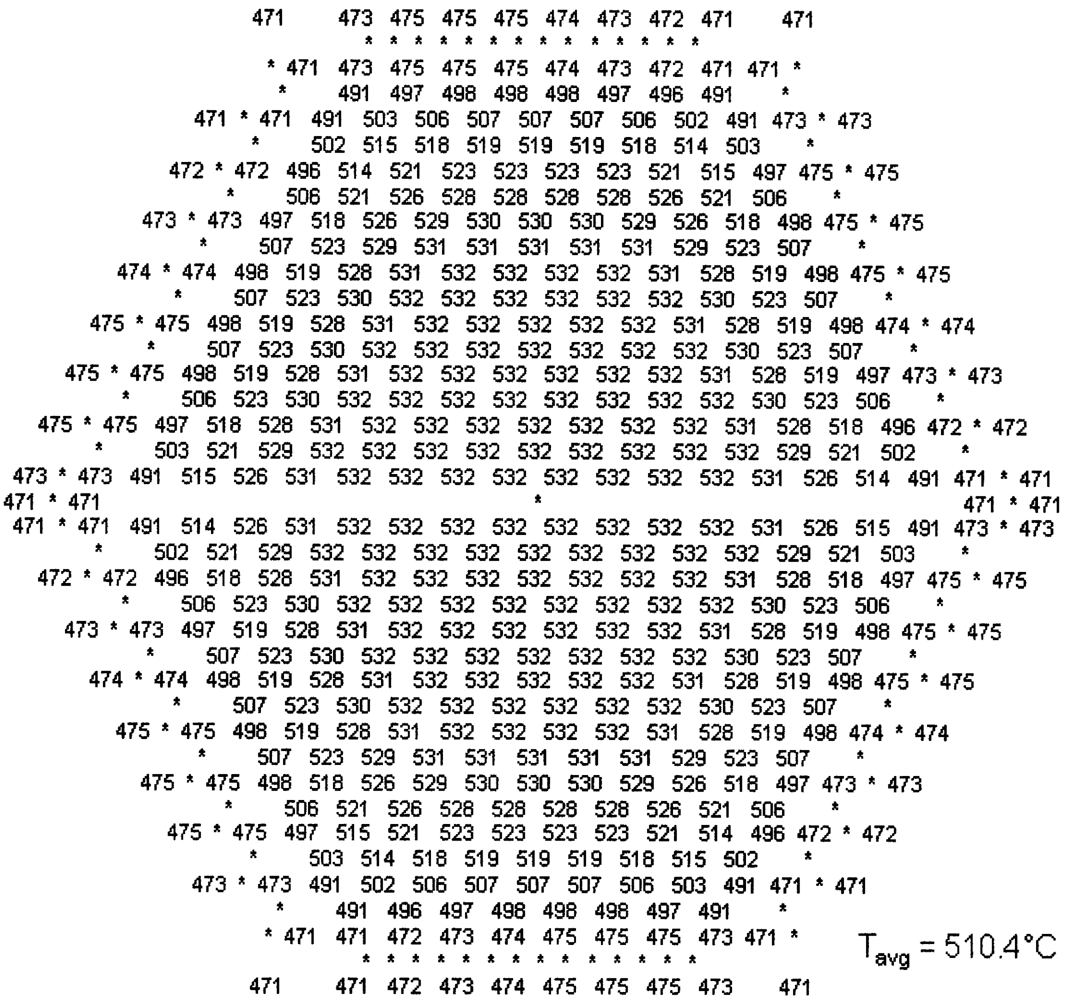

```
                    471    473  475  475  475  474  473  472  471     471
                            *  *  *  *  *  *  *  *  *  *  *  *  *  *
                   * 471  473  475  475  475  474  473  472  471  471 *
                    *     491  497  498  498  498  497  496  491     *
               471 * 471  491  503  506  507  507  507  506  502  491  473 * 473
                  *     502  515  518  519  519  519  518  514  503     *
             472 * 472  496  514  521  523  523  523  523  521  515  497  475 * 475
                *     506  521  526  528  528  528  528  526  521  506     *
           473 * 473  497  518  526  529  530  530  530  529  526  518  498  475 * 475
              *     507  523  529  531  531  531  531  531  529  523  507     *
         474 * 474  498  519  528  531  532  532  532  532  531  528  519  498  475 * 475
            *     507  523  530  532  532  532  532  532  532  530  523  507     *
       475 * 475  498  519  528  531  532  532  532  532  532  531  528  519  498  474 * 474
          *     507  523  530  532  532  532  532  532  532  532  530  523  507     *
     475 * 475  498  519  528  531  532  532  532  532  532  532  531  528  519  497  473 * 473
        *     506  523  530  532  532  532  532  532  532  532  532  530  523  506     *
   475 * 475  497  518  528  531  532  532  532  532  532  532  532  531  528  518  496  472 * 472
      *     503  521  529  532  532  532  532  532  532  532  532  532  529  521  502     *
 473 * 473  491  515  526  531  532  532  532  532  532  532  532  532  531  526  514  491  471 * 471
471 * 471                                      *                                         471 * 471
 471 * 471  491  514  526  531  532  532  532  532  532  532  532  532  531  526  515  491  473 * 473
      *     502  521  529  532  532  532  532  532  532  532  532  532  529  521  503     *
   472 * 472  496  518  528  531  532  532  532  532  532  532  532  531  528  518  497  475 * 475
        *     506  523  530  532  532  532  532  532  532  532  532  530  523  506     *
     473 * 473  497  519  528  531  532  532  532  532  532  532  531  528  519  498  475 * 475
          *     507  523  530  532  532  532  532  532  532  532  530  523  507     *
       474 * 474  498  519  528  531  532  532  532  532  532  531  528  519  498  475 * 475
            *     507  523  530  532  532  532  532  532  532  530  523  507     *
         475 * 475  498  519  528  531  532  532  532  532  531  528  519  498  474 * 474
              *     507  523  529  531  531  531  531  531  529  523  507     *
           475 * 475  498  518  526  529  530  530  530  529  526  518  497  473 * 473
                *     506  521  526  528  528  528  528  526  521  506     *
             475 * 475  497  515  521  523  523  523  523  521  514  496  472 * 472
                  *     503  514  518  519  519  519  518  515  502     *
               473 * 473  491  502  506  507  507  507  506  503  491  471 * 471
                    *     491  496  497  498  498  498  497  491     *
                   * 471  471  472  473  474  475  475  475  473  471 *
                            *  *  *  *  *  *  *  *  *  *  *  *  *  *
                    471    471  472  473  474  475  475  475  473     471
```

T_{avg} = 510.4°C

Figure 3.20: Core outlet temperatures for subchannel analysis using SUPERNERGY II at the heated length outlet

3.3.2 SUPERENERGY II Results Comparison

For a more direct comparison of the SUPERENERGY II and the RELAP5-3D models, Fig. 3.21 shows the core outlet temperatures predicted by both codes. The agreement is rather good. Fig. 3.22 displays a one dimensional radial profile comparison of the two models, so that trends and differences can be noted and identified.

This plot indicates that the two codes predict a very similar distribution. Upon closer inspection of the RELAP5-3D data, it can be seen that the innermost subchannel coolant temperatures are slightly higher (~3°C) than the SUPERENERGY II innermost subchannel coolant temperatures. At the same time, the edge subchannels and the outermost interior channel coolant temperatures are slightly lower (~1-2°C) in the RELAP5-3D model than the same channels in the SUPERENERGY II model. This trend indicates that the wire-wrap induced turbulent mixing is over-predicted in the edge channels of the RELAP5-3D model. This over-prediction indicates that the mixing parameters at the edge have a smaller effect in the SUPERENERGY II model than in the RELAP5-3D model. However, the maximum difference of 3.5°C is quite small and easily falls within the uncertainty band allowed for code verification. Additionally, it is smaller than the 10% (coolant temperature increase) error experienced in the validation of SUPERENERGY II using the EBR II reactor. Also, the temperature prediction in RELAP5-3D is higher in the hot channels than for SUPERENERGY II. This difference, therefore, errs on the side of conservatism, and is acceptable for the scope intended in utilizing the RELAP5-3D model. An additional difference between the SUPERENERGY II model and the RELAP5-3D model is the coolant properties. SUPERENERGY II calculates the coolant properties at a single temperature input by the user with which it performs the necessary heat balances. RELAP5-3D, however, utilizes temperature-dependent coolant properties, improving the accuracy of the heat balances performed by the code a small amount.

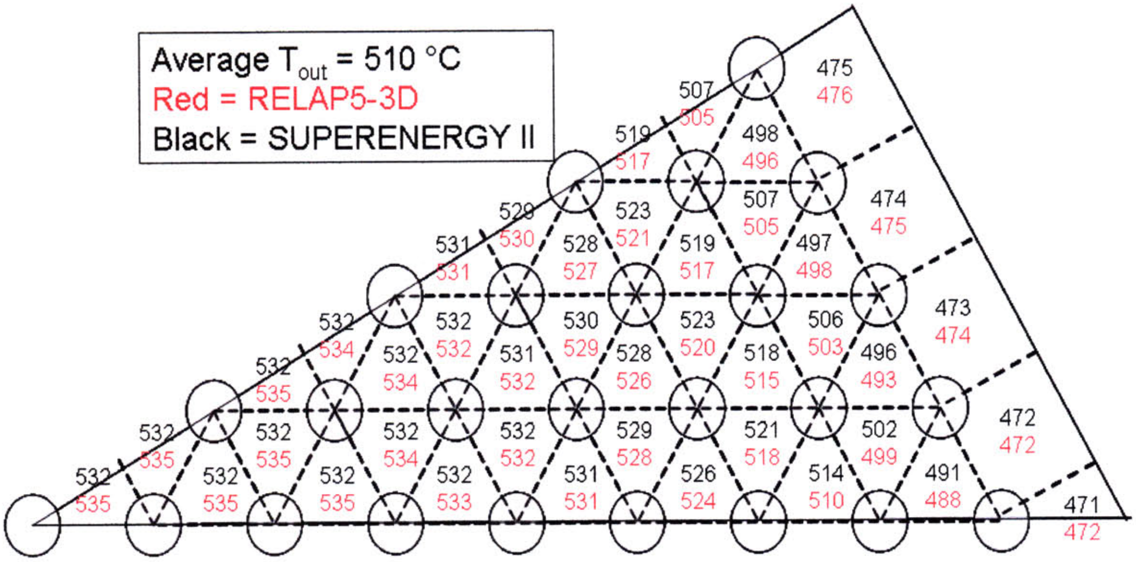

Figure 3.21: RELAP5-3D and SUPERENERGY subchannel model core outlet temperatures (1/12 assembly)

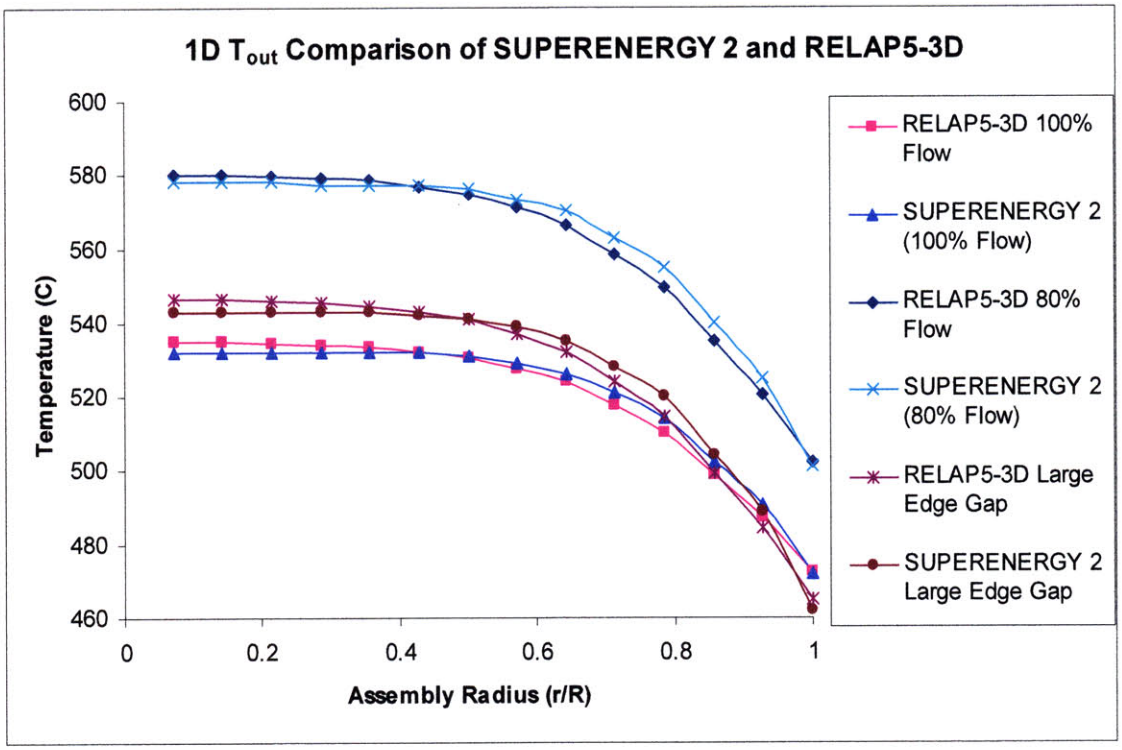

Figure 3.22: 1-D Radial temperature distribution comparison for SUPERENERGY II and RELAP5-3D

Table 3.5 shows the change in the specific heat as a function of temperature for sodium. The error for C_p (which is related to outlet T by $Q=C_p*m*dT$) for a change in temperature of 100 °C is approximately 1.2%. Therefore, a coolant temperature rise of 155 °C (which is the distribution in the core) yields a change in temperature of ~2% due to the differences in specific heat. This is consistent with RELAP5-3D predictions, which show higher outlet temperatures in hotter inner channels, where the C_p is the lowest.

Table 3.5: Change in sodium properties for a 100°C in temperature

T (°C)	C_p (J/kg*K)
513.12	1261.275
413.12	1276.448
ΔT=100°C	1.189%

To ensure that the agreement between SUPERENERGY II and the RELAP5-3D subchannel model holds for a reasonably broad range of conditions, comparisons between the results of two codes were made for different flow/power conditions and for a modified geometry. A 1-D temperature radial distribution for both models is plotted in Fig. 3.22 for reduced flow conditions (80% flow) at full power and for a different geometry (a larger edge gap) at full flow and power. As can be seen, the agreement between the two subchannel models is maintained under each of these conditions. Therefore, it is concluded that the RELAP5-3D model can be used for subchannel analysis of sodium-cooled reactors.

3.3.3 Benchmark: The ORNL 19-Pin Test

As a more robust benchmark, the RELAP5-3D subchannel analysis model was compared to experimental data from the 19-pin heated rod experiment performed at Oak Ridge National Laboratory (ORNL) [3.23]. The 19-pin ORNL experiment was conducted in the fuel failure mockup (FFM), a large sodium high temperature facility built specifically for testing liquid metal fast breeder reactor (LMFBR) fuel rod bundles. Multiple runs were conducted at various flow and power conditions. Two of these runs are of interest in the following benchmark: one at high flow and one at low flow conditions (for which the effect of conduction is expected to be important). The parameters of the test assembly are found in Table 3.6.

Table 3.6: Parameters for the ORNL 19-pin test assembly

Rod diameter (mm)	5.84
Rod pitch (mm)	7.26
Wire-wrap diameter (mm)	1.42
Rod pitch/rod diameter	1.24
Duct inside flat-to-flat distance (cm)	3.41
Total length (m)	1.02
Pressure (MPa)	0.101
Inlet temperature (°C)	315
Inlet mass flow (kg/s) (high/low)	3.0378 / 0.004087
Modified Peclet Number	57.236 / 4019.66
Average rod power (W) (high/low)	16975 / 263
Axial power distribution	uniform
Radial power distribution	uniform

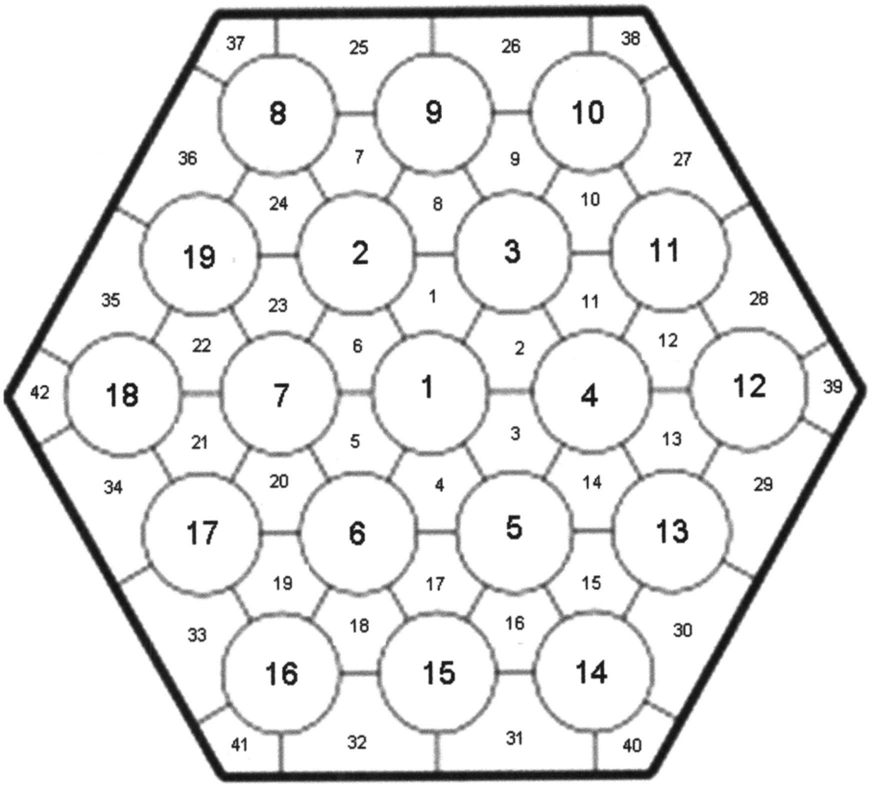

Figure 3.23: Normalized outlet temperatures for ORNL 19-pin test [3.2]

The subchannel numbering scheme for the ORNL 19-pin test assembly is shown in Fig. 3.23. Thermocouples were placed at the outlets of subchannels 41, 32, 18, 17, 4, 1, 9, and 38, which form a diagonal "corner-to-corner" line across the hexagonal assembly. The outlet temperatures from each of these subchannels were monitored and used to form a steady-state 1D core outlet temperature profile for the test assembly. The 1D outlet temperature distribution for the high flow test is plotted in Fig. 3.24, along with temperature predictions from subchannel codes MATRA-LMR, SABRE4, and SLTHEN.

It is interesting to note that SLTHEN is a slightly modified version of SUPERENERGY II and thus the temperature predictions made by SLITHEN closely resemble those that would have been made by SE2. As can be seen, there is reasonable agreement between SLTHEN and the test data, although the code over-predicts the temperature in the center of the assembly. This indicates that SLTHEN (and thus SUPERENERGY II) have good agreement with experimental data.

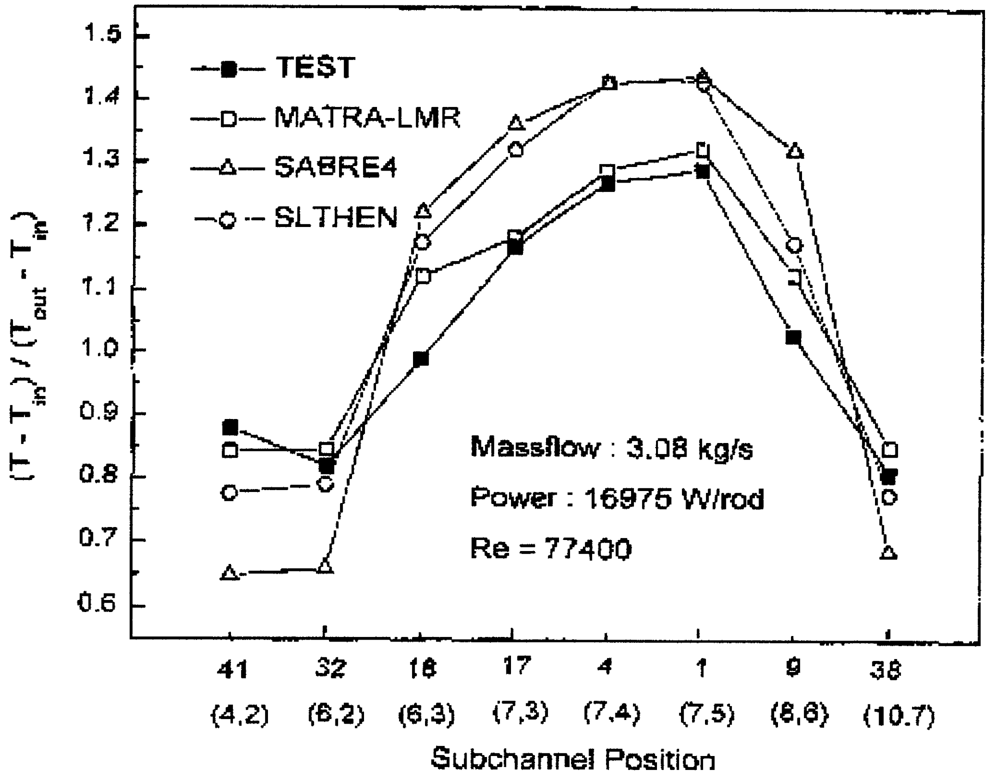

Figure 3.24: Normalized outlet temperatures for ORNL 19-pin test [3.2]

The ORNL 19-pin test assembly was modeled using RELAP5-3D during high flow conditions with a subchannel numbering scheme outlined in Fig. 3.25.

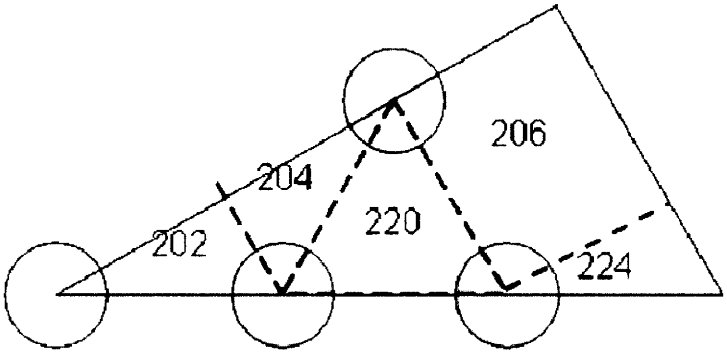

Figure 3.25: RELAP5-3D subchannel numbering for ORNL 19-pin test model

The core normalized outlet temperature profile for this model is plotted in Fig. 3.26 along with the actual test data from the ORNL 19-pin test. Here, the normalized outlet temperature (T_{norm}) is represented by the equation:

$$T_{norm} = \frac{(T - T_{in})}{(T_{out} - T_{in})}, \qquad (5.23)$$

where:

T_{norm} = normalized outlet temperature

T = core outlet temperature of the individual subchannel in question

T_{in} = assembly temperature

T_{out} = outlet bulk temperature as measure by a thermocouple, (not calculated as the average of all the subchannels)

Additionally, error bands at the 95% confidence interval based on 6 runs are included in Fig. 3.26. As can be seen in this figure, RELAP5-3D can accurately predict the outlet temperature distribution within the test assembly with a maximum error of ~8%. Additionally, the temperature distribution predicted by RELAP5-3D is in good agreement with, and well within the bounds of the predictions made by the other accepted sodium subchannel analysis codes. Moreover, the RELAP5-3D provides conservative results. Nevertheless, a critical assessment of the advantages and disadvantages of RELAP5-3D with respect to other accepted sodium subchannel analysis codes is of interest, and is discussed in the following section.

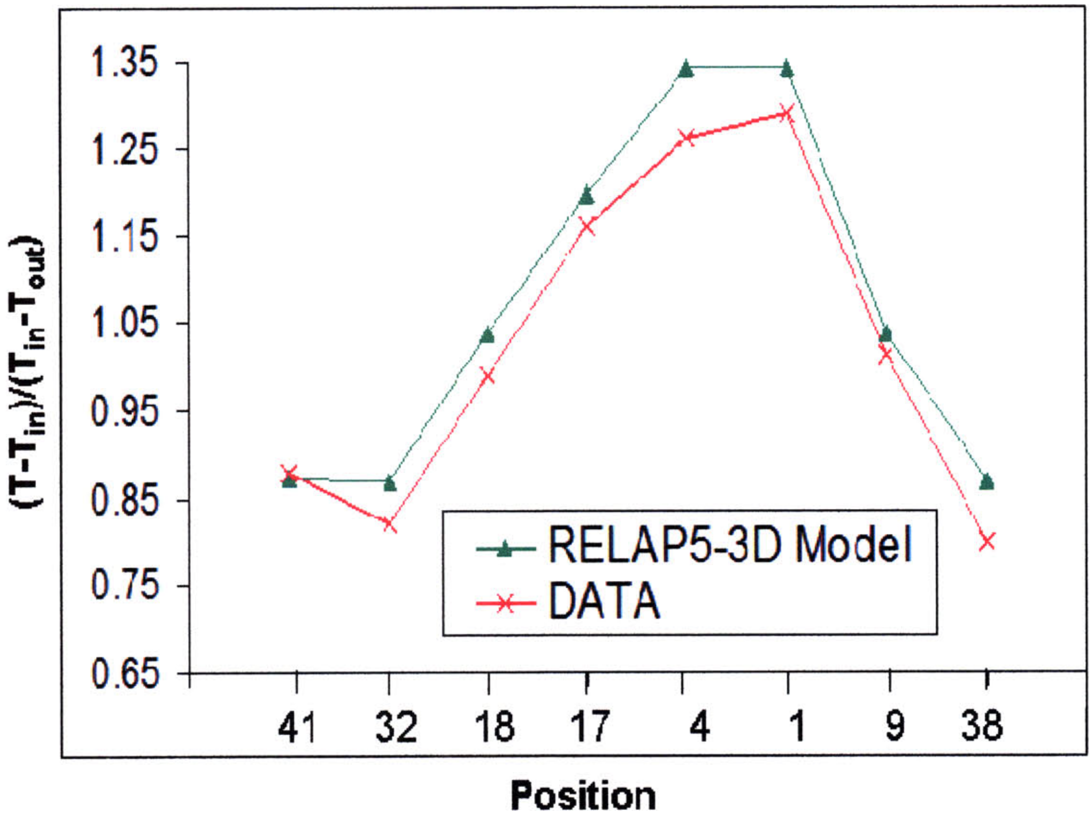

Figure 3.26: Normalized outlet temperatures for ORNL 19-pin test [3.23] and RELAP5-3D subchannel model

The low flow ORNL 19 pin test was also modeled using RELAP5-3D, and is of particular interest. Fig. 3.27 shows the core outlet temperature distribution across key subchannels for the low flow case, in comparison with standard subchannel code predictions [3.2]. Unlike the high flow case, the difference is significant; the actual test results provide a line that is for all intents and purposes flat, while the subchannel models still predict a peaked profile. This difference is due to fluid conduction, which is not explicitly modeled in some of the other subchannel analysis codes.

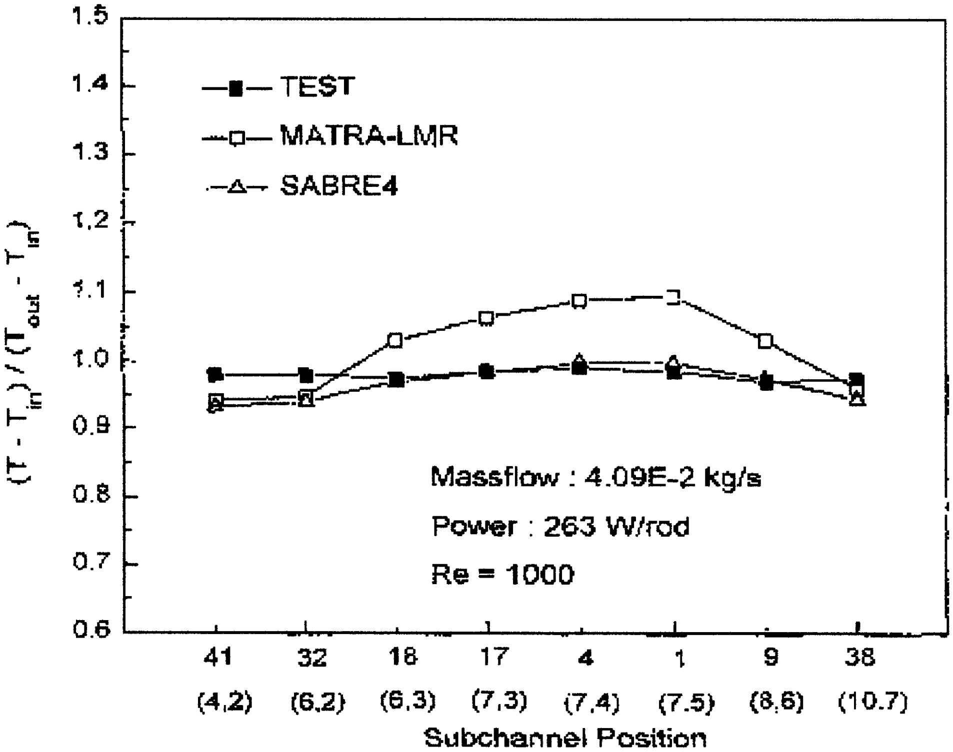

Figure 3.27: Normalized outlet temperatures for ORNL 19-pin test [3.2]

As discussed in section 3.2.4, the coolant conduction becomes significant when the modified Prandtl number, as calculated in Eq. 3.12, is less than 100. The Reynolds number in the ORNL 19 pin test configuration subchannels at low flow is ~1100 while the Prandtl number is ~0.005417. With the length and hydraulic diameter of each core volume calculated from the data given in Table 3.6 (3.554 cm and 3.7 mm, respectively) the modified Peclet number is ~54.6. Thus, fluid conduction is significant at the low flow conditions of the 19 pin FFM experiments, and should be incorporated. Fig. 3.28 shows the REALP5-3D 19-pin model core outlet temperatures for the low flow and power conditions listed in Table 3.6. This figure includes both a model with axial only conduction, axial and radial conduction, and the actual experimental data. Essentially, the RELAP5-3D model that includes axial and radial conduction with turbulent mixing effects underestimates the effects of conduction, but can still predict the outlet temperature of the test assembly with a maximum error of only 6%. Thus, the performance of the RELAP5-3D model is considered acceptable with respect to predicting the outlet temperatures of the ORNL 19 pin test assembly at high and low flow/power conditions.

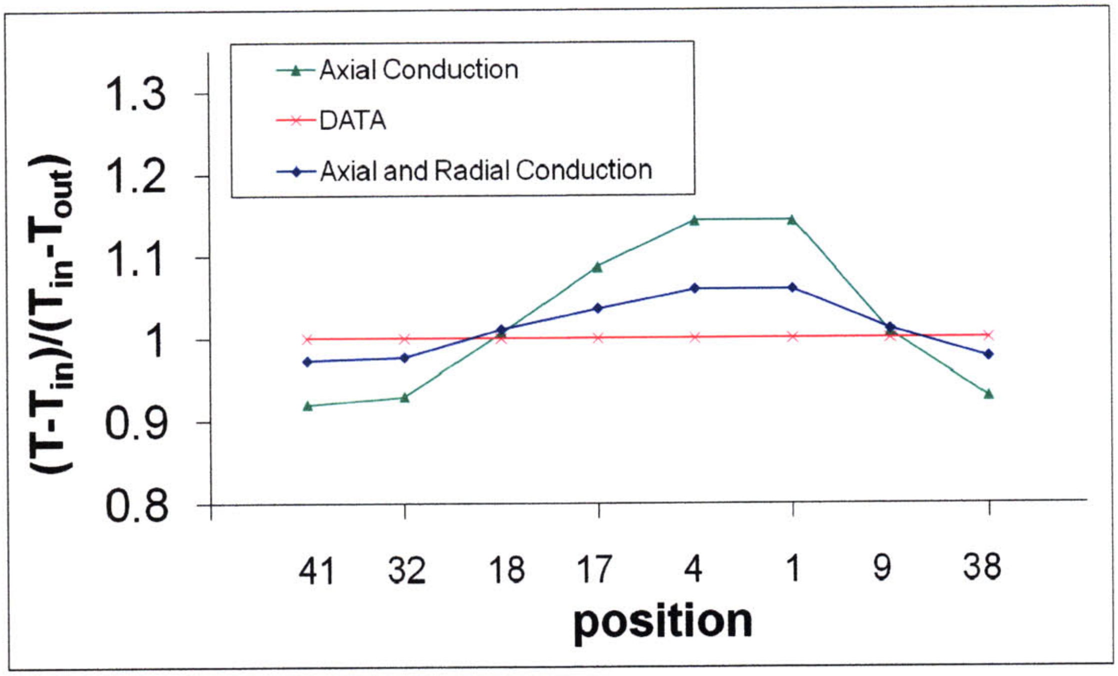

Figure 3.28: Normalized outlet temperatures for ORNL 19-pin test [3.23] and RELAP5-3D subchannel model at low flow/power conditions

3.4 Critical assessment of the advantages and disadvantages of RELAP5-3D as a subchannel analysis code with respect to SUPERENERGY II

Though RELAP5-3D is not typically used for subchannel analysis, this study determines the feasibility of utilizing RELAP5-3D for such an analysis. The subchannel model clearly produces reasonable results, as explained in Sections 3.3.3 and 3.3.4. In the creation of the subchannel model, each of the individual and significant components of single-assembly flow and heat transfer was included via control variables. Upon comparison with SUPERENERGY II results for an identical assembly, it was determined that the RELAP5-3D subchannel analysis model has been verified, with a conservative difference between core outlet coolant temperatures of no greater than 3.5°C. Thus, RELAP5-3D can be considered a suitable platform with which to perform subchannel analyses with accuracy comparable to SUPERENERGY II. In considering the appropriate code to utilize for modeling subchannel analyses in SFR applications, the following points are significant:

1. SUPERENERGY II is restricted to hexagonal fuel assemblies with wire-wrapped fuel pins, while RELAP5-3D can model any lattice geometries, with any spacers desired, or even a combination of grid spacers within an assembly, provided that the right correlations are available.
2. RELAP5-3D has the capacity to model innovative fuel pin types such as annular fuel, bottle-shaped fuel, and cross-shaped fuel, as well as other geometric variations, such as the assembly duct ribs described in this report, if correlations for turbulent mixing are available. SUPERENERGY II can only model cylindrical fuel, without significant modification of the source code.
3. SUPERENERGY II requires a constant geometry throughout the axial length of the assembly, while RELAP5-3D has the capacity to model an assembly of varying dimensions (e.g. to model thermal expansion or blockage or bottle-shaped fuel pins).
4. SUPERENERGY II does not have temperature dependent properties, while RELAP5-3D calculates thermal properties of the fluid as a function of temperature.
5. RELAP5-3D includes clad, fuel, and gap temperatures, while SUPERENERGY II only calculates the temperature distribution in the coolant.

6. The time required to create and debug a subchannel model from scratch using RELAP5-3D ranges from 1-3 weeks, depending on the complexity of the fuel assembly, while the model construction time for SUPERENERGY II ranges from several hours to up to 3 days, depending on the complexity.
7. The runtime for RELAP5-3D subchannel models ranges from 1 to 24 hours, while the SUPERENRGY II models require only a few minutes to complete.
8. SUPERENERGY II is a steady-state only code, while RELAP5-3D has the capacity to perform both steady-state and transient analyses.

Thus, as listed above, the primary disadvantages of RELAP5-3D rest with the time required to create a model and the runtime of the model itself. SUPERENERGY II requires a 30-545 line input file for a single assembly requiring from two hours to three days to create, depending on the size and complexity. RELAP5-3D, on the other hand, requires an input file of about 31,000 lines of code, which requires from 1 to 3 weeks to create and debug. This is not an insignificant time commitment, which gives RELAP5-3D a distinct disadvantage. However, being able to perform subchannel analyses for LMFR cores is a significant step towards making RELAP5-3D a more versatile, comprehensive, and flexible program. The incorporation of the turbulent and swirl mixing model capabilities directly into RELAP5-3D source code options would reduce the time requirement of the input preparation by a factor of 10 or more. By including mixing models for hexagonal wire-wrapped fuels, RELAP5-3D could become a code that has the potential to perform subchannel analyses, with reasonable accuracy, for various reactor types, which would further increase the scope and utility of the code at large in terms of LMFR modeling. Having confirmed the capability of RELAP5-3D to model rod bundle flow in sodium-cooled assemblies and predict the coolant temperature distribution with good accuracy in comparison with the validated SUPERENERGY II code, the innovative rod geometries are analyzed next.

3.5 APPLICATION OF THE RELAP5-3D SUBCHANNEL MODEL

3.5.1 Optimization of the traditional fuel assembly configuration using flow-diverting ribs in edge subchannels

It is of interest to note that for the base fuel assembly design, the temperature distribution is in not flat, even when cross-flow, turbulent and swirl mixing effects are included (see Fig. 3.22). Rather, there is a 60°C temperature difference between the inner and edge channels (30°C if hot dimensions are used). This large temperature difference within a fuel assembly (particularly the hot fuel assembly) is undesirable because for a given margin to the postulated thermal limits (i.e., maximum allowable fuel and clad temperatures), it results in a lower core-average outlet temperature, which in turn correlates to a lower thermal efficiency of the plant. Upon examination, it was found that this large temperature non-uniformity at the core outlet was due to the magnitude of the coolant flow in the edge subchannels. This coolant flow was significantly larger than the coolant flow for the interior and corner subchannels, by a factor greater than 3 to 4, thus resulting in lower temperature in the edge subchannels. This increased coolant flow in the edge channels is a direct result of the hexagonal geometry; in order to accommodate the hexagonal rod bundle, and also have sufficient room to include the wire-wrap spacers, the area of the edge subchannel must be quite large. This problem is greatly exacerbated if the "cold" assembly dimensions are utilized, as was the case for the model whose results are shown in Fig. 3.21. This is because there is an additional gap between the wire-wrap spacers of the outer rods and the assembly duct wall. This increased gap is included for two separate reasons; first, to accommodate the thermal expansion of the rods during reactor heat up from cold conditions, and, second, to allow for easy insertion of the fuel bundle into the assembly duct. Because the "hot" dimensions for the assembly are not given, the conditions at operation are approximated for this model; in essence, the rod bundle-wall gap was reduced to the size of the wire-wrap thickness. This assumes that at normal operating conditions the rod bundle comes in contact with the duct wall due to thermal expansion.

This approximation in the subchannel model design did indeed reduce the flow area of the edge channels, but even with this adjustment corresponding to steady-state operation, the edge channel flow area was larger than the interior channel area by a factor of over two. Therefore, some investigations were made to determine the feasibility of flattening the core outlet temperature distribution by reducing the edge channel flow area. A model was created in which the assembly duct included "ribs", or long, semicircular protrusions along the axial length of the assembly, which reduced the flow area in the, edge channels, as shown in Fig. 3.29. This is similar to the approach used in the BOR-60 reactor [3.24, 3.25, 3.26], but instead of using cylinders (which would be limited by the small size of the edge subchannels in the ABR1000 design) the semi-circular ribs used. The resulting 1-D radial temperature profile, as given in Fig. 3.30, indicates that the rib-based strategy can be very effective at flattening the outlet temperature profile of the base assembly.

What is not seen in Fig. 3.30, however, is the impact that adding duct ribs has upon the corner subchannels in the assembly. In adding these ribs, the corner subchannel temperatures actually are *lower* than without the duct ribs. This is due primarily to two effects: 1) there are no ribs to reduce the flow area in the corners. This results in a similar mass flow through the corner channels whether or not duct ribs are included. 2) The swirl flow heat transfer correlation was not included. This is because it is unclear what effect the ribs would have on the swirl flow. As a conservative estimate, this parameter was neglected and swirl flow was eliminated from the duct rib models. This resulted in a lack of mixing in the edge and corner channels, which in turn caused a decrease core outlet temperature for the corner channels. However, the mass flow through the corner channels is small, and thus there is little effect on the temperatures in the other subchannels; the profile is quite flat except for the corner channels for each assembly design, as can be seen in the Figs. 4.17 – 4.18 in chapter 4. Therefore the use of ribs should be seriously considered in the design of fuel assemblies in advanced sodium-cooled reactors.

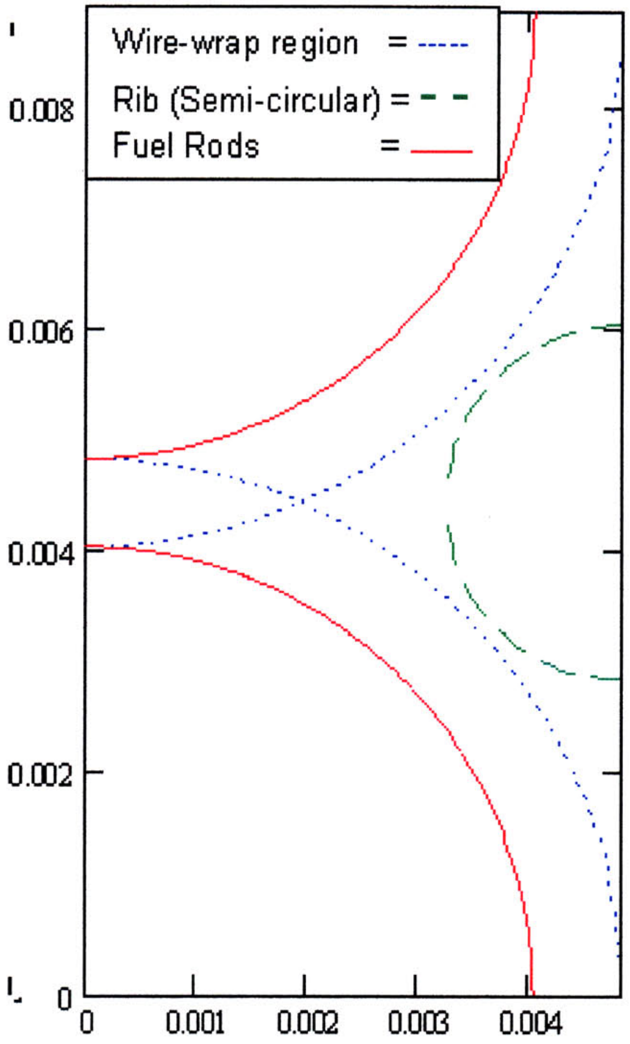

Figure 3.29: Cross-sectional view of a "rib" (green semi-circle) along the duct wall

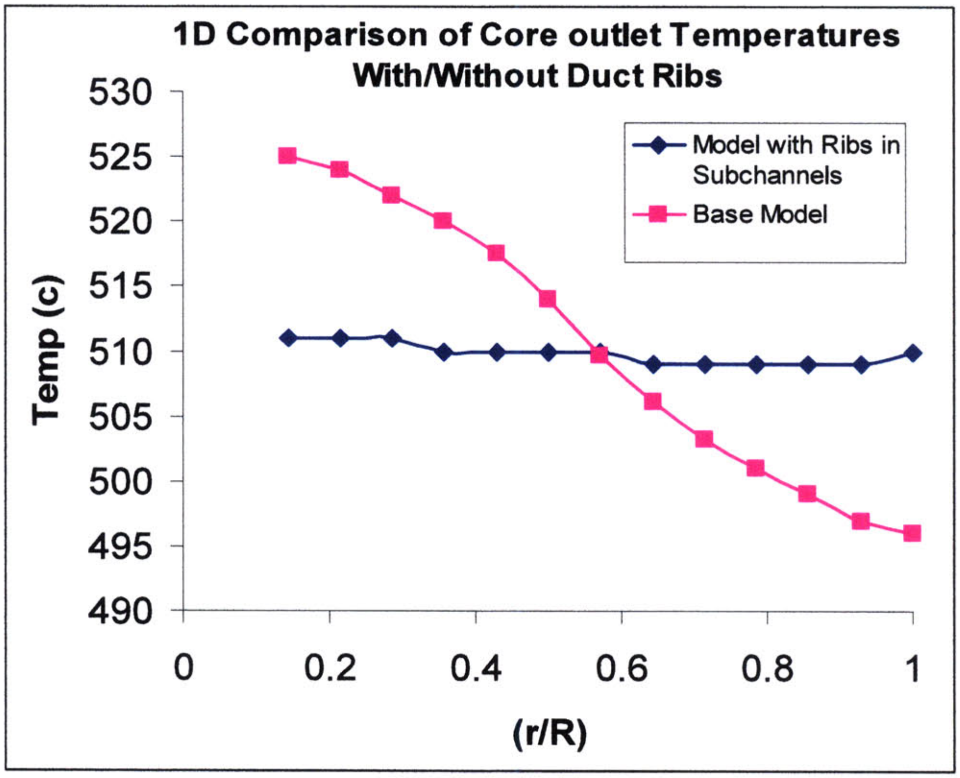

Figure 3.30: 1-D radial temperature distribution within the assembly with and without duct wall ribs

3.6. RELAP5-3D Subchannel Model Conclusions

The study of innovative fuel configurations for the SFR required that a subchannel analysis code capable of modeling novel fuel and assembly geometries be developed. RELAP5-3D was adapted through the utilization of control variables to accomplish subchannel analyses for sodium-cooled assemblies. This model was verified through comparison with the SUPERENERGY II subchannel code. A basic eight ring assembly with metal fuel was modeled in both SUPERENERGY II and RELAP5-3D, and the comparison of the results revealed that the temperature distributions at the core outlet according to RELAP5-3D and SUPERENERGY II are in agreement within about 3.5°C.

The benefits of using RELAP5-3D rather than SUPERENERGY II to model subchannel analyses include:

1. flexibility in fuel geometry (annular, vented, spiral cross, etc.)
2. temperature dependant coolant, duct, and clad property calculations
3. full fuel rod analyses (clad, bond, and fuel meat), as opposed to a coolant-only approach
4. flexibility in assembly parameters and geometry (spacers other than wire-wrap, duct ribs, axially varying geometries due to design and/or differential thermal expansion, etc).

The primary disadvantages of using RELAP5-3D as a subchannel analysis code rather than SUPERENERGY II are the model creation time and the model run time. To create a RELAP5-3D subchannel model from scratch requires 1 to 3 weeks, while the same model in SUPERENERGY II requires only a few hours to three days. Additionally, a RELAP5-3D subchannel analysis run requires between 1 and 24 hours, while the same run with SUPERENERGY II requires only a few minutes.

The RELAP5-3D subchannel analysis model was applied to a conventional design of SFR hexagonal assemblies with wire-wrapped fuel pins. The model was used to optimize the flow and temperature distributions by the addition of duct wall "ribs" which divert flow from the edge subchannels to the interior subchannels. The resulting assembly design exhibited coolant temperature radial variations of 1°C -2°C at most. In the following chapter, Chapter 6, this subchannel model will be applied to both annular and bottle neck fuel designs, as described in Chapter 4, to determine the performance of these fuels in steady-state, standard reactor operating conditions.

Chapter 4: Subchannel Analysis of Innovative Fuel Configurations

Chapter 4 discussed in detail the innovative fuel configurations considered in this thesis. The basic assembly and fuel rod designs for these configurations were established through the utilization of simplified MathCAD single pin/single assembly models. For convenience, the parameters of these fuel configurations, found in Sections 2.4.2 and 2.4.3, are displayed along with the base designs and adjusted annular designs in Table 4.2.

The internally and externally cooled annular fuel configuration is most effective for low conversion ratio burner core designs due to the open assembly design and small rod sizes. The bottle-shaped fuel configuration, on the other hand, is most suitable for high conversion ratio core designs due to the very tight pitch and large pressure drops associated with such a design. This chapter is devoted to detailed subchannel analyses of both the annular and bottle-shaped fuel configurations.

4.1 Annular Fuel

As presented previously [4.1], annular fuel has the potential to increase power density, decrease fuel costs, and provide structural robustness for the fuel of a SFR burner. It is crucial that these claims be tested using subchannel analyses. The two most promising annular fuel designs investigated were the burner reactor designs: one for metal fuel, and one for oxide fuel, as explained in [4.2]. At first, the annular fuel assemblies were assumed to have the same core average power density as the solid fuel assembly design, to facilitate the comparison of their thermal-hydraulic behavior. Also, both flat power distributions within the assembly as well as the effects of realistic power peaking factors were investigated for both solid and annular designs.

4.2 Annular Fuel Subchannel Model Development

The subchannel model described in Chapter 5 was adapted to accommodate annular fuel. This was done by creating a series of 22 volume pipes that represent the coolant channels enclosed by the fuel rods, or the inner-annular (IA) volumes. Next, the heat structures were adjusted to accommodate a left boundary connection (as related to RELAP5-3D definition of right and left heat structure boundaries) to the IA volumes. It is important to realize that in annular flow the fraction of fission heat that goes to the IA subchannels vs. the fraction that goes to the external subchannels (i.e., the so-called "heat split") depends on the geometry of the fuel rod, but also on the coolant temperature and heat transfer coefficient in the IA and external subchannels. In other words, the heat split is not specified by the user, but is calculated by the code, based on the local coolant conditions and fuel rod geometry.

Fig. 4.1 provides the volume numbering for the oxide fuel subchannel model, while Fig. 4.2 shows the volume numbering for the metal fuel subchannel model. Note that for each of these figures, the numbers within the circular rod are for the IA channels, not for the fuel rod itself.

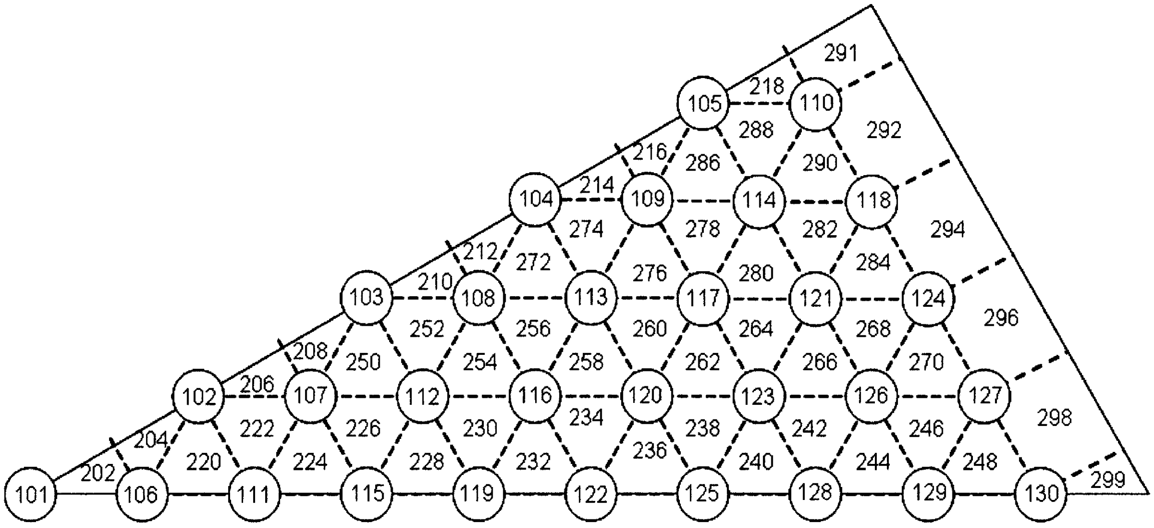

Figure 4.1: Volume numbering for oxide annular fuel subchannel model

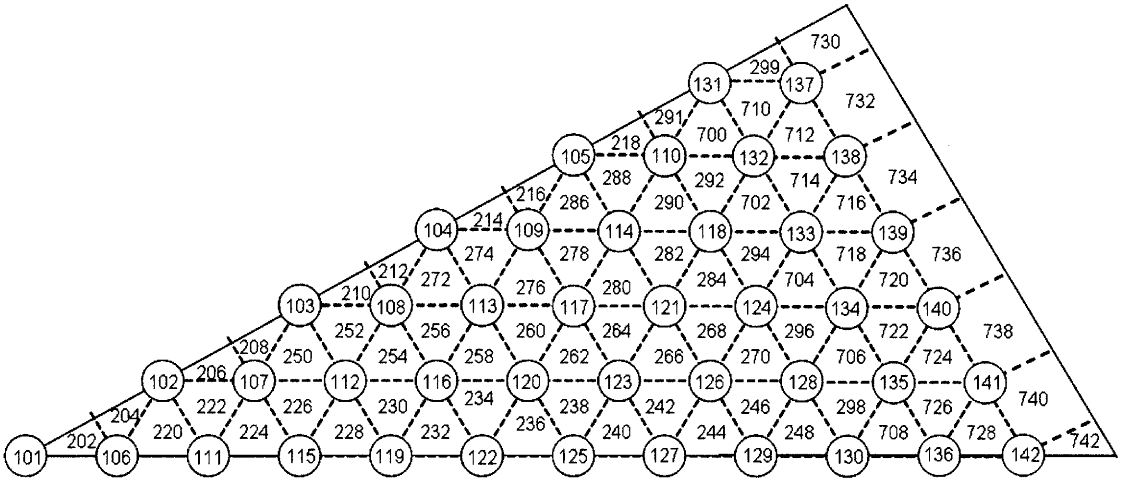

Figure 4.2: Volume numbering for metal annular fuel subchannel model

A significant aspect of the annular fuel models is the flow split between the inner and outer annular subchannels. The fraction of flow that enters the internal annular subchannels is such that the pressure drops of the internal and external regions of the annular fuel are equalized. The pressure drop for the external channels is calculated using Eq. (2.38), with a friction factor calculated from Eq. (2.18). The friction factor for the inner channels is calculated using the Blasius correlation,

$$f = \frac{0.316}{\mathrm{Re}^{0.25}}, \tag{4.1}$$

which applies if the Reynolds number is less than 30,000. If the Reynolds number is greater than 30,000, then the McAdams correlation is utilized:

$$f = \frac{0.184}{\mathrm{Re}^{0.2}}. \tag{4.2}$$

This friction factor is then used with Eq. (2.14) to determine the overall pressure drop in the IA subchannels. Because RELAP5-3D calculates pressure drops internally once the above correlations are programmed into the input deck, the flow split is calculated automatically by the code.

Conduction models within the fuel meat are also incorporated into these analyses. For both metal and oxide fuels, the heat conduction equation is used to determine the temperature distribution within the fuel rods. For oxide fuel, the default fuel and gap properties included within the RELAP5-3D code are used, while the thermophysical properties of stainless steel (SS316) were input to model the cladding. For metal fuel, the gap is filled with a purely-conductive sodium bond with properties from [2.7], while the U-Pu-Zr thermophysical properties from [4.3] are used for the fuel meat. The values used for the metal fuel, as well as the other material properties used in the subchannel and full plant models, are tabulated in Appendix B.

Initially, the subchannel model consisted of vertical pipes with 22 nodes representing each subchannel: 1 for the entrance and lower shield regions, 15 for the core region, 5 for the gas plenum region, and 1 for the duct standoff/outlet regions. However, with 15 core volumes, the number of control variables was excessively large, and the model required large amounts of time (~12 hours) to reach steady state. In order to ameliorate this, the number of volumes in the core was reduced to five volumes, and the runs were repeated. With 5 core volumes, the results were exactly the same as with 15 core volumes. Thus, for all future subchannel analyses, the subchannel pipes contained only 5 core volumes, bringing the total axial subchannel flow volumes to 12, rather than 22.

4.2.1 Annular Fuel Model Design Results – Oxide

The oxide fuel subchannel model was first run according to the parameters in Table 2.10. The resulting core outlet temperature profile, for both inner and outer channels, is found in Fig. 4.3. Note that the temperature at the outlet of all IA channels is basically the same, as expected, since these are parallel identical channels connected only at the inlet and outlet plena.

One major concern with the results of this run is the difference between the regular subchannel outlet temperatures (inner, edge, and corner) and the IA subchannels outlet temperatures. As can be seen in Fig. 4.3, this difference is as large as 60°C at the hot channel outlet. This indicates that the IA channels, which have the lower temperatures, are allowing for an excessively large fraction of the total coolant flow.

Large radial temperature gradients are unacceptable for two reasons. First, large temperature gradients reduce the margins to failure specified by the design limits, thus forcing the reactor to operate at lower power levels than is technically achievable. Second, the recombination of two separate coolant flows with large temperature differences produces thermal striping, i.e., the development of a cyclic thermal stresses that can result in thermal fatigue failure [4.4]. This phenomenon is highly undesirable and can be avoided by ensuring that the outlet temperatures in all channels are relatively the same.

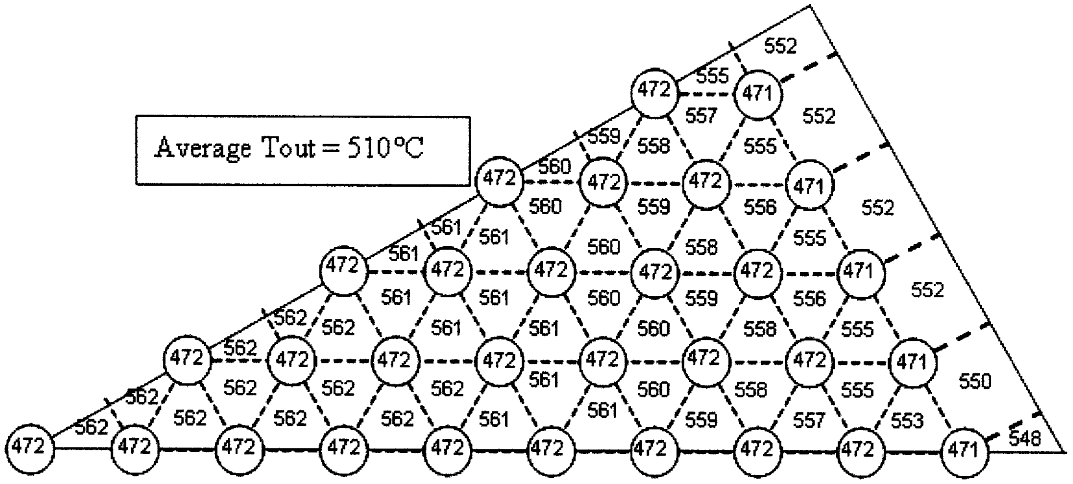

Figure 4.3: Core outlet temperatures for initial configuration of annular oxide fuel assembly

The mismatch in flow between the inner and outer channels was not predicted in the simple (average-channel) analyses performed in Chapter 2. This is primarily due to the mismatch flow distribution between the edge and inner flow channels. The edge subchannels have a flow area of nearly twice the inner subchannel flow area. In the single average-channel model performed previously, the entire flow area was distributed evenly among the fuel pins. This artificially increases the flow area of the inner channels, since the edge channels are nearly twice the area of the interior channels. This increase in area caused the flow splitting between the IA and inner channels to match the heat flow split. This phenomenon is common to both metal and oxide fuels, since it is caused primarily by the geometry of the hexagonal assembly design.

In an attempt to flatten the radial temperature distribution across the fuel assembly, several changes were implemented in the design. Briefly, the assembly duct-rib feature, described in Chapter 3, was added, which forced more flow from the outer subchannels to the inner subchannels. The wire-wrap diameter was increased, allowing for more flow to the through the inner subchannels, with the added benefit of more realistic fabrication dimensions. Because too much flow was still entering the inner channels, the inner diameter, D_i, of the annular fuel rod was decreased until the flow distribution was more even. This means that additional fuel was included in the annular fuel pin in order to reduce D_i. However, the P/D_o ratio was kept constant. Fig. 4.4 shows how this additional fuel was added in order to reduce the inner fuel diameter. This additional fuel resulted in a higher fuel-to-coolant ratio in the core, which would decrease the necessary TRU wt% for the fuel in a burner reactor, a neutronic (and thus economic) advantage of this new design. The subchannel temperature distribution at the core outlet of the oxide annular fuel for the optimized assembly design is shown in Fig. 4.5. The 1D core outlet temperature profile for both the initial configuration and optimized oxide annular fuel assemblies can be found in Fig. 4.6. It can be seen that a very flat temperature profile is possible for annular fuel assemblies. The significant flow rates for the subchannels of the oxide (and metal) models are found in Table 4.1.

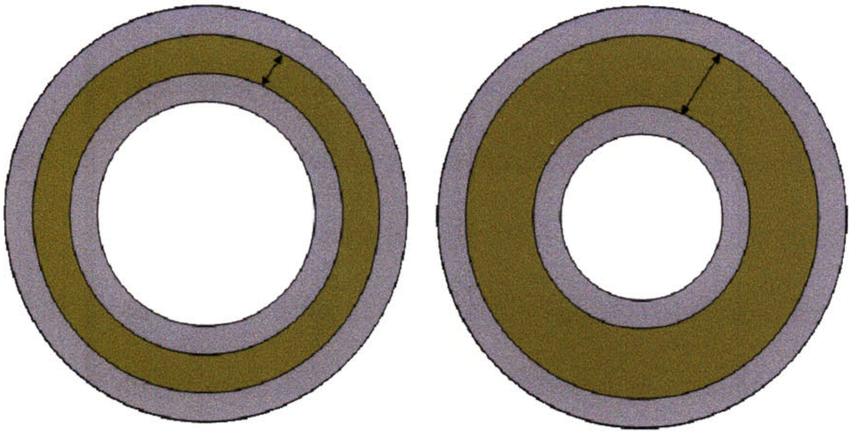

Figure 4.4: Annular fuel rod (oxide) with large D_i (5 mm) and with decreased Di (3.7 mm). D_i is decreased by increasing the fuel meat. (drawing not to scale)

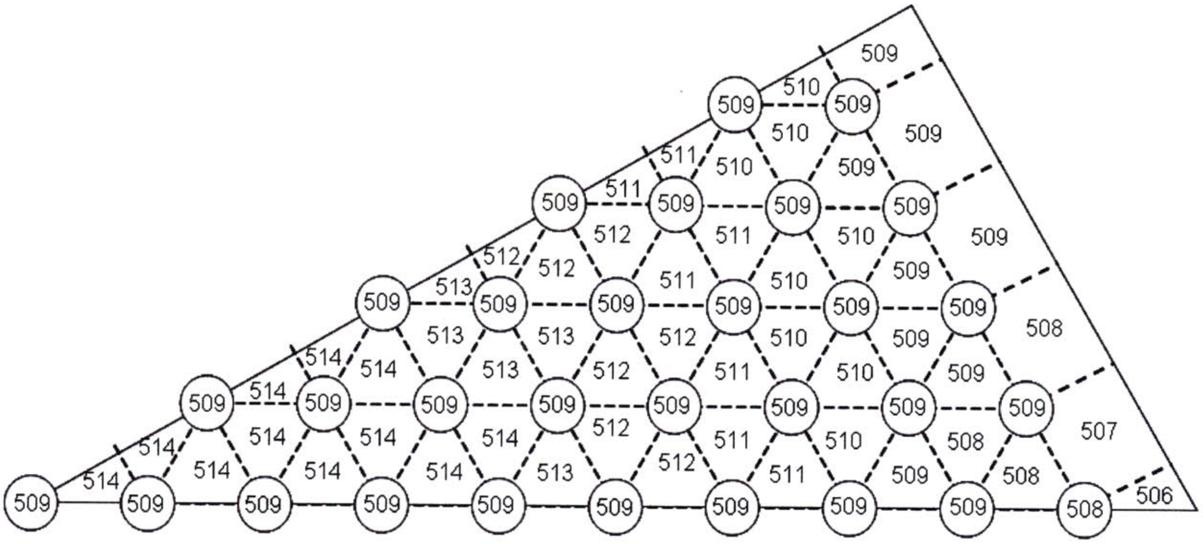

Figure 4.5: Core outlet temperatures for the optimized annular oxide fuel assembly

Table 4.1: Coolant flow rates for metal and oxide annular fuel subchannels

	Metal Fuel		Oxide Fuel	
	D_i = 5 mm	D_i = 3.4 mm	D_i = 5 mm	D_i = 3.7 mm
Average Velocities (m/s)				
IA	6.64	8.21	6.00	5.94
Inner	1.97	3.77	3.91	5.49
Edge	3.72	5.33	4.56	4.35
Corner	3.33	6.35	3.29	4.41
Average Mass Flow (g/s)				

IA	110.7	64.12	90.73	53.89
Inner	16.36	40.49	31.90	58.34
Edge	53.02	67.75	77.85	71.42
Corner	7.82	21.34	15.14	26.74

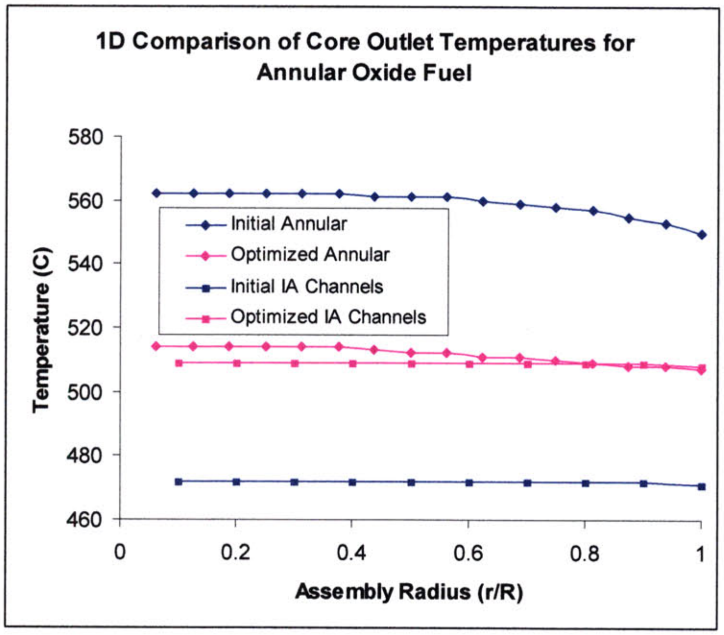

Figure 4.6: 1D outlet temperature distribution for initial configuration and optimized configuration of oxide annular fuel

4.2.2 Annular Fuel Model Design Results – Metal

Subchannel analyses were completed also for a metal annular fuel assembly. Figure 4.7 shows the coolant outlet temperature distribution for the initial annular metal fuel assembly design; note the large temperature gradient across the fuel assembly. Figure 4.8 shows the temperature distribution for the optimized design, including the use of ribs on the duct wall. The parameters for the optimized annular metal fuel design are found in Table 4.4, while the coolant flow rates are found in Table 4.1. The 1D core outlet temperature profile for both the initial configuration and optimized metal annular fuel assemblies can be found in Fig. 4.9. Note that even in the "optimized" design, the temperature distribution could not be made as flat as in the optimized oxide fuel case discussed in Section 3.2.1. This is due primarily to differences in the base models of the oxide and metal fuel assemblies, and constraints in decreasing the fuel inner diameter, as described in the previous section.

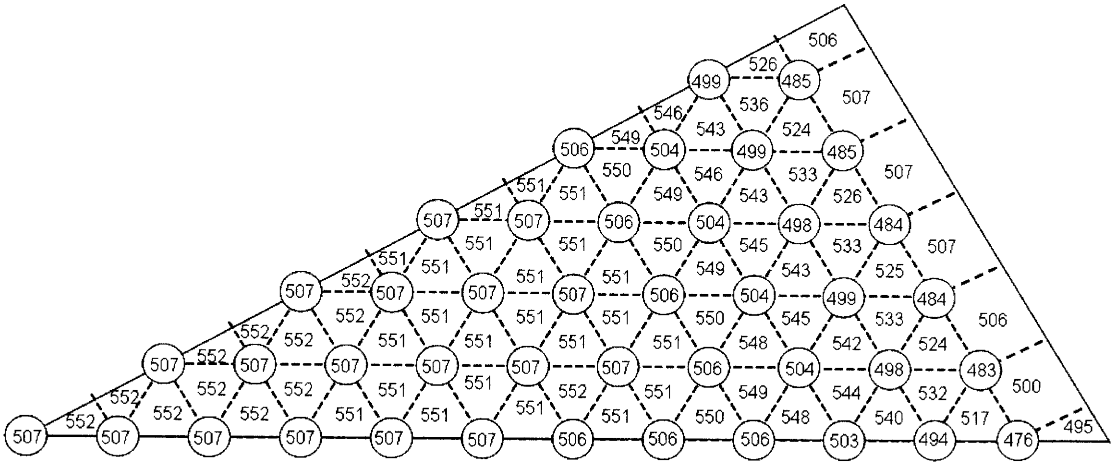

Figure 4.7: Core outlet temperatures for initial annular metal fuel assembly configuration

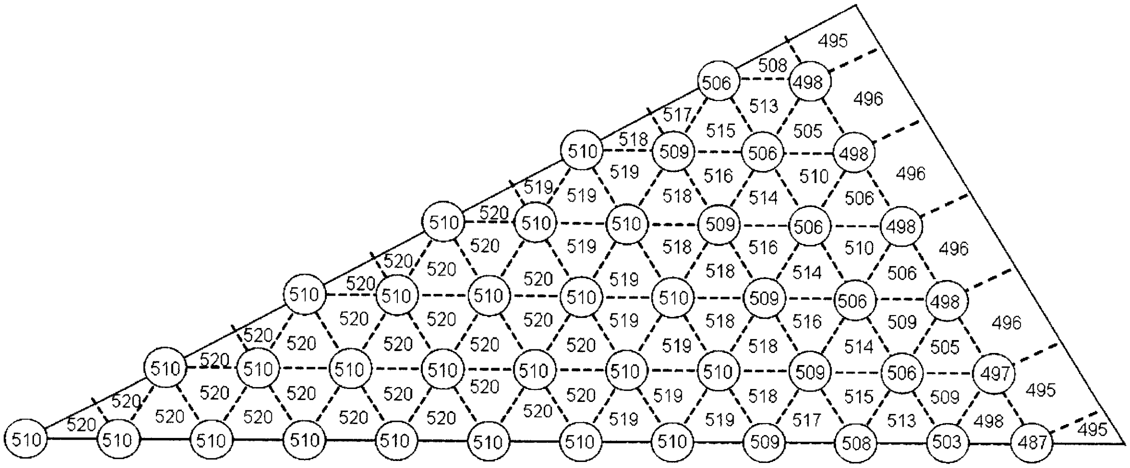

Figure 4.8: Core outlet temperatures for optimized annular metal fuel assembly

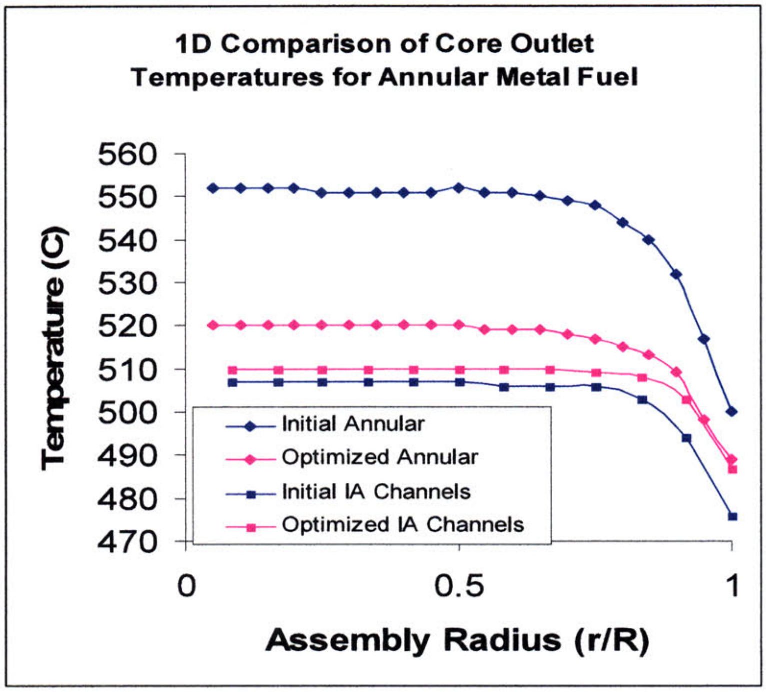

Figure 4.9: 1D Core outlet temperature distribution for initial configuration and optimized configuration of metal annular fuel

Upon further inspection of the "optimized" annular fuel configuration, however, one reveals some unacceptable qualities for this method of moderating the flow split between IA and inner subchannels. In the oxide fuel (and to a lesser degree, the metal fuel), the decrease of fuel rod diameter by increasing fuel meat alters the neutronic performance of the fuel assembly. As can be seen in Table 4.2, the fuel-to-coolant ratio is nearly double the base ratio for the oxide annular fuel configuration. This change significantly alters the neutronic performance of the core, which effects the conversion ratio which would require significant neutronic analyses an possible changes of heavy metal to diluent ratio. Because the focus of this thesis is on the thermal-hydraulic performance of the fuel, such neutronic analyses were not made. It should be noted, however, that it may be possible to develop an improved and optimal model should thermal-hydraulic and neutronic analyses be performed in tandem for the annular fuel assemblies.

The metal fuel annular configuration also has a significantly increased fuel-to-coolant ratio, but to a lesser degree than the oxide fuel design. This is due to the primary geometric differences between the oxide and metal fuels. The annular fuel configuration for oxide fuel has an outer diameter of 9.36 mm, as compared to the metal fuel outer diameter of 8.71 mm. As the inner diameter is reduced, the amount of fuel added varies with the square of the radius, so larger amounts of fuel are added relatively for larger initial diameters. Additionally, the larger wire wrap in the metal annular optimized configuration leads to a larger pitch, and subsequently larger inner flow area, and thus larger coolant fraction, which helps to compensate for loss of coolant flow area in the IA subchannels.

Table 4.2: Comparison of original and optimized annular fuel models

	Metal CR = 0.25		**Oxide CR = 0.25**		**Optimized Annular Fuel Assemblies**	
	Solid (ANL)	**Annular (MIT)**	**Solid (ANL)**	**Annular (MIT)**	**Metal (MIT)**	**Oxide (MIT)**
Rings	13	11	10	9	11	9
Pins	540	397	324	271	397	271
Flat to flat (cm)	15.71	20.96	15.71	17.41	18.29	15.74
Pin outer diameter (mm)	4.64	9.21	5.56	9.17	7.67	7.85
Pin inner diameter (mm)	-	5.00	-	5.00	3.6	3.6
P/Do	1.357	1.087	1.45	1.09	1.11	1.14
Dwire (mm)	-	0.805	-	0.805	1.0	1.1
Clad thickness (mm)	0.559	0.559	0.635	0.635	0.559	0.635
Fuel volume fraction (%)	17.44	16.59	19.73	16.93	16.03	17.48
Bond volume fraction (%)	5.81	5.53	1.02	0.88	5.33	0.22
Structure volume fraction (%)	29.15	32.61	26.22	36.70	34.98	37.71
Coolant volume fraction (%)	47.6	45.28	53.02	45.49	43.68	43.91
Fuel/coolant volume ratio	0.366	0.366	0.372	0.372	0.366	0.398
Power density (kW/L)	258.09	258.09	198.22	198.22	258.09	198.22
Linear heat rate (kW/m)	12.66	29.16	15.63	22.83	26.80	18.76
q" (kW/m2)	868.33	653.01	894.62	521.94	756.50	521.55

q''' (W/cm3)	1732	1761.13	1137	1325.38	2191	1284
ΔT within fuel (°C)	91.57	10.93	310.88	24.82	20.32	20.32
Rib diameter (mm)	-	-	-	-	1.2	1.2
Wire-wrap helical pitch (cm)	-	20.32	-	20.32	1.10	1.16

Another difficulty concerning metal fuel in particular is thermal constraints on the annular design. As described in section 2.3, the number of rods is decreased by removing one or more rings. The loss of rings is then compensated by the increase of fuel rod diameter. Recall that the metric for the development of the annular fuel assembly is maintenance of a constant power density. For a large number of rings, as is found in the metal base fuel assembly, the removal of a single ring in order to fit the annular fuel within the assembly results in a large number of pins being removed. In order to compensate for this loss of a large number of rings, the linear heat rate must be increased. This can be seen in Table 4.2, where the optimal annular fuel configuration (2nd column) has a linear heat rate of 29.16 kW/m, up from 12.66 kW/m, or an increase of 130.3%. Thus, in order to reduce the size of the annular fuel configuration assembly to match the assembly size of the base metal fuel assembly (15.71cm), 8-9 rings must be used. However, at this number of rings, the linear heat rate is so high that all benefit derived from using annular fuel is eliminated. This challenge does not prohibit the use of annular fuel, but it merits the relaxation of the constraint that the fuel assembly for the annular fuel configuration matches the size of the fuel assembly for the base fuel configuration. The consequences of relaxing this constraint are significant, and are discussed in Chapter 7 of this thesis.

4.2.3 Final Annular Assembly Designs

Attempting to optimize the flow split between IA and inner subchannels by adding fuel meat to the annular fuel rods has challenges that cannot be overcome, as described in the previous section. As a result, a new optimized annular fuel assembly configuration was designed for both metal and oxide fuel. This design was created by relaxing the minimum fuel rod inner diameter constraint of 5 mm. In essence, the inner diameter was reduced, as previously attempted, but without the addition of fuel. Thus, the fuel-to-coolant ratio was maintained constant, which eliminates the problem of altered neutronic performance for the fuel. The geometric parameters of the final annular fuel configurations are found in Table 4.3.

Table 4.3: Comparison of original solid and optimized annular fuel models

	Metal CR = 0.25		Oxide CR = 0.25	
	Solid (ANL)*	Annular (MIT)	Solid (ANL)*	Annular (MIT)
Rings	13	11	10	9
Pins	540	397	324	271
Flat to flat (cm)	15.71	18.29	15.71	15.74
Pin outer diameter (mm)	4.64	7.67	5.56	7.85
Pin inner diameter (mm)	-	3.6	-	3.6
P/Do	1.357	1.11	1.45	1.14
Dwire (mm)	-	1.0	-	1.1
Clad thickness (mm)	0.559	0.559	0.635	0.635
Fuel volume fraction (%)	17.48	16.03	19.73	17.48
Bond volume fraction (%)	5.83	5.33	1.02	0.22
Structure volume fraction (%)	28.55	34.98	26.22	37.71
Coolant volume fraction (%)	48.13	43.68	53.02	43.91
Fuel/coolant volume ratio	0.366	0.366	0.372	0.398
Power density (kW/L)	258.09	258.09	198.22	198.22
Linear heat rate (kW/m)	15.19	26.80	15.63	18.76
q" (kW/m^2)	1041.99	756.50	894.62	521.55

Fuel q''' (W/cm^3)	2078	2191	1137	1284
Wire-wrap helical pitch (cm)	-	20.32	-	20.32
Radial Power Peaking	1.2	1.2	1.2	1.2
Axial Power Peaking	1.10	1.10	1.16	1.16

4.2.3.1 Neutronic Parameters

The assumption of flat power profiles was relaxed at this point, and a rigorous neutronic evaluation of the oxide fuel was performed by Matthew Denman using MCNP [4.5]. For the oxide fuel, a two region core was used with inner and outer driver assemblies, as with the ABR1000 base fuel. The beginning-of-cycle (BOC) and end-of-first-cycle (EOFC) burnups are 0MWD/kgU and 22.64 MWD/kgU, respectively. Figure 4.10 shows the nominal power distribution within the core at BOC, while Fig. 4.11 shows the nominal power distribution within the core at EOC. The hot assembly occurs at EOC, and has a power peaking of 1.22 +/- 1%. As an estimate, a radial power peaking factor of 1.2 was used. The resulting axial and local (within a single assembly) power peaking factors are listed in Table 4.4.

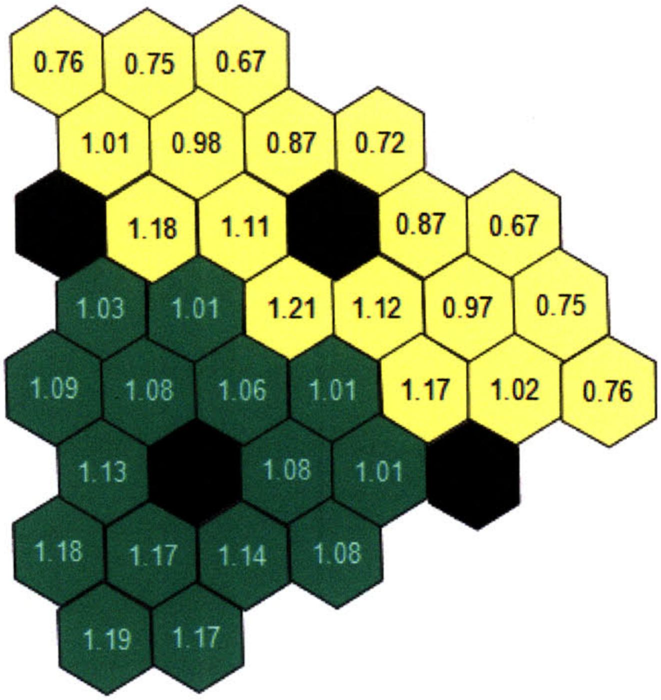

Figure 4.10: BOC power distribution in oxide annular fuel core

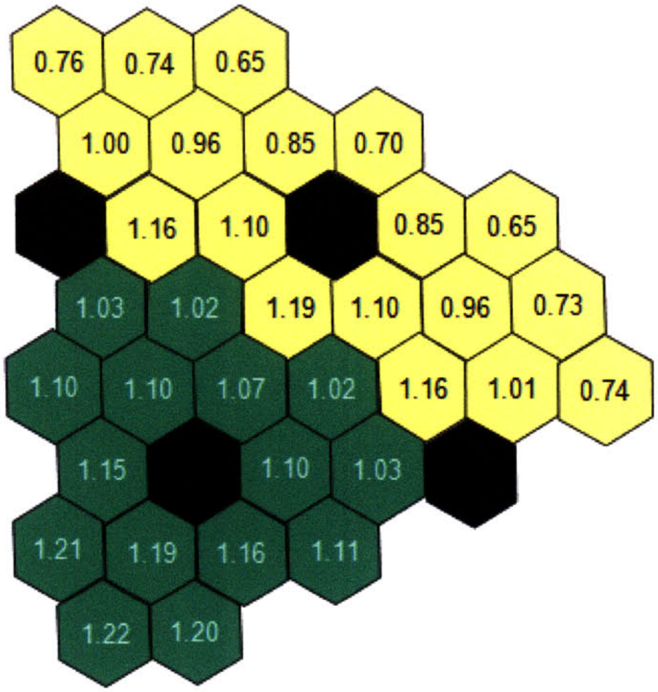

Figure 4.11: EOFC power distribution in oxide annular fuel core

Table 4.4: Axial and local power peaking factors for EOFC hot channel

Axial Zone	Axial Power Peaking Power	Local Peaking (per zone)
1	0.73	1.02
2	1.03	1.02
3	1.16	1.02
4	1.13	1.04
5	0.94	1.02

The local power peaking is quite small (<3% maximum) and thus is neglected for simplicity in modeling the assembly. These power distributions were included in the RELAP5-3D input deck, and used as the basis for the detailed power uprate analysis.

The axial and radial power peaking profiles for metal fuel were determined using an MCNP model created by MIT student Matt Denman [1.15]. For the metal fuel core, the enrichments and zoning described in [2.2] were used to evaluate an MCNP model of the metal fuels. The axial peaking for both solid and annular metal fuel configurations can be seen in Table 4.5. The axial peaking factors are similar for both solid and annular fuel, with the annular fuel configuration having a slightly higher power at the bottom of the core and the solid fuel having a slightly higher power at the top of the core.

Table 4.5: Axial peaking factors for CR = 0.25 solid metal fuel core configurations (with a maximum error of ±0.5%)

Volume Number	Solid	Annular
1	0.92	1.00
2	1.19	1.20
3	1.23	1.23
4	1.03	1.02
5	0.64	0.56

The radial power peaking profile for the metal solid fuel is depicted in Fig. 4.12 with an error of ±0.4%. The numbers on this plot represent the BOC power for each assembly. The blackened assemblies with the word "out" on them represent the control assemblies, while the green-blue, teal, and light green assemblies represent the inner, middle, and outer driver regions. For the subchannel analysis considered in this chapter, the hot assembly peaking is the most significant parameter derived from these studies.

The specific core layout for the annular fuel configuration requires special consideration, since the fuel assemblies are not the size as in the base case. The details of developing the annular fuel assembly layout are not given here, but can be found in Section 5.3.3. The radial power profile for the metal annular fuel is depicted in Fig. 4.13 with an error of ±1%. Note that the radial power peaking for the annular fuel core configuration is ~4% less than the radial power peaking for the solid fuel core configuration. For both metal fuel CR = 0.25 core configurations, a radial power peaking of 1.2 is utilized, not only to provide some margin and to account for engineering and modeling uncertainties, but to provide clarity of comparison between the annular and solid fuel designs.

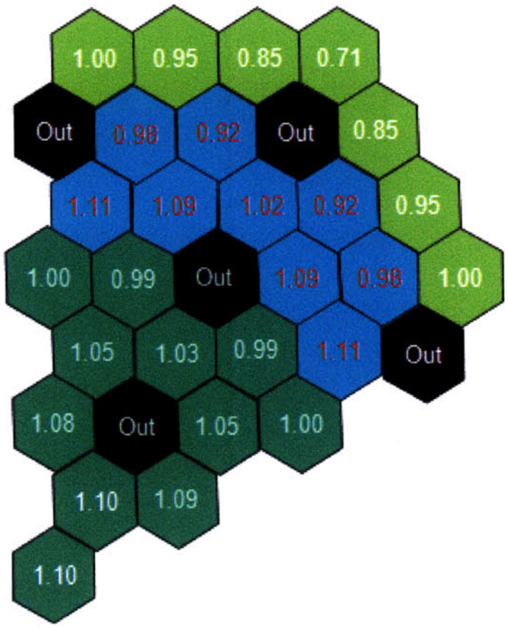

Figure 4.12: Core-wide radial assembly power profile of the CR = 0.25 solid metal fuel pin core configuration (±0.4%) [5.15]

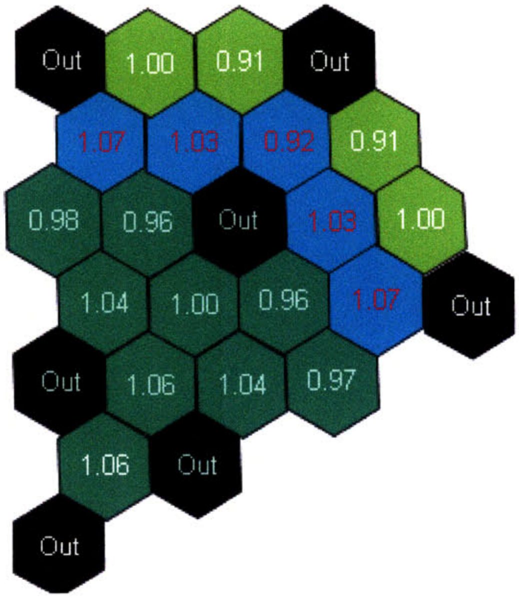

Figure 4.13: Core-wide radial assembly power profile of the CR = 0.25 annular metal fuel pin core configuration (±1%)

4.2.3.2 Final Annular Fuel Assembly Configuration Results

Subchannel models were created for the hottest fuel assemblies both with and without duct ribs. These ribs divert the coolant flow from the edge to the inner subchannels, thus flattening the core outlet distribution, as described in Section 3.5. The steady state, full power temperature profiles of the oxide and annular fuel assemblies without duct ribs are found in Figs. 4.14 and 4.15, respectively. The steady state, full power temperature profiles of the oxide and annular fuel assemblies with duct ribs included are found in Figs. 4.16 and 4.17, respectively. The maximum clad and fuel temperatures for each of these annular fuel configurations are found in Table 4.6.

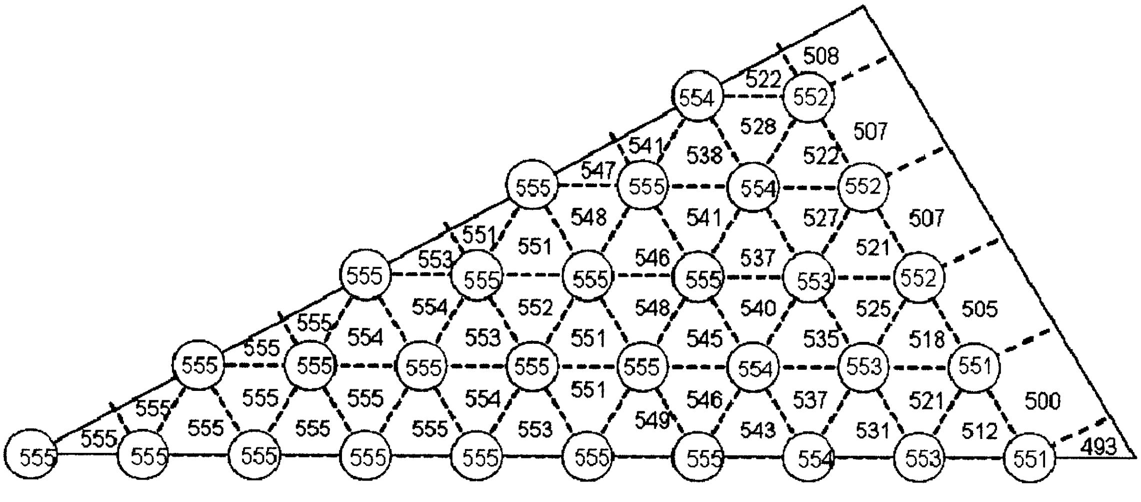

Figure 4.14: Core outlet temperatures for annular oxide fuel assembly model. (The #s within each circle represent the outlet coolant temperature of the corresponding annular fuel rod inner channels)

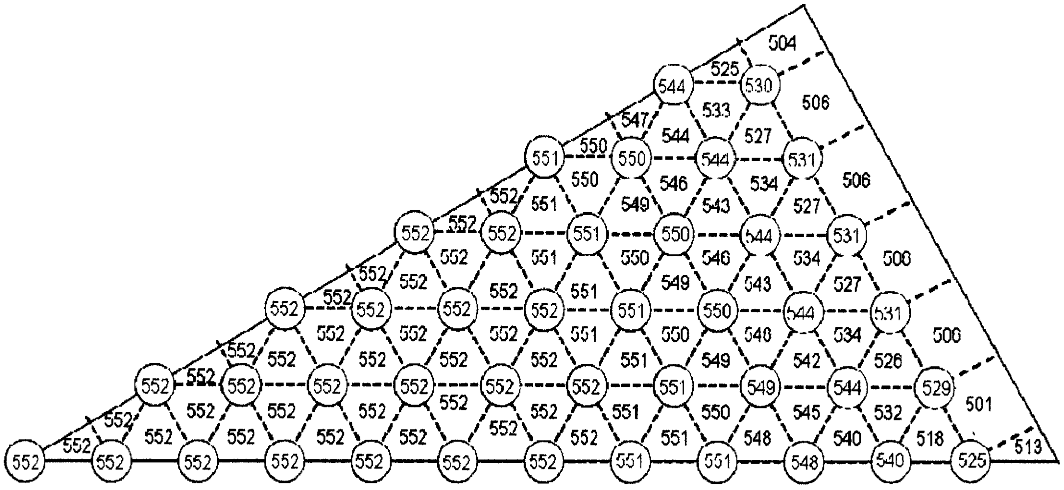

Figure 4.15: Core outlet temperatures for metal annular fuel assembly model. (The #s within each circle represent the outlet coolant temperature of the corresponding annular fuel rod inner channels)

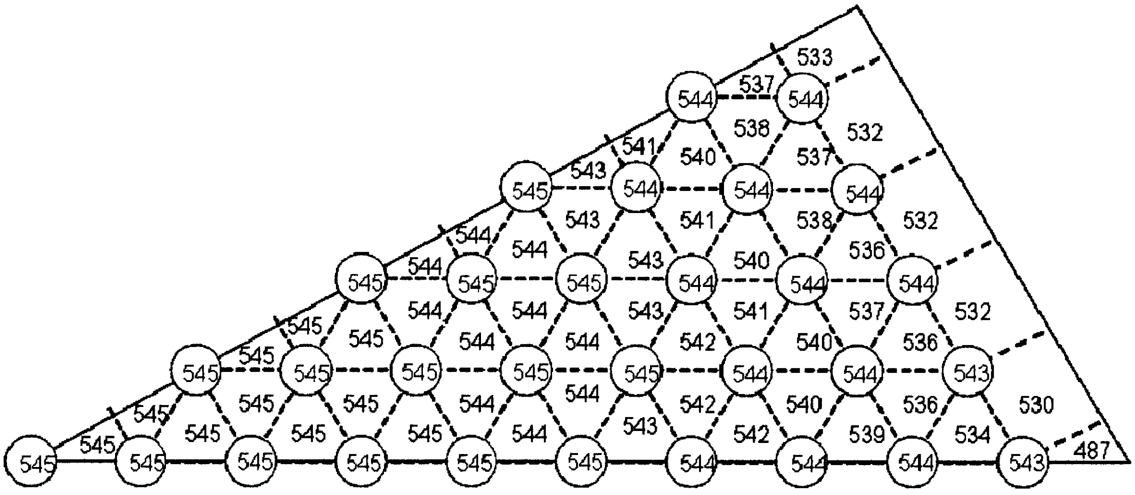

Figure 4.16: Core outlet temperatures for annular oxide fuel assembly model with duct ribs included. (The #s within each circle represent the outlet coolant temperature of the corresponding annular fuel rod inner channels)

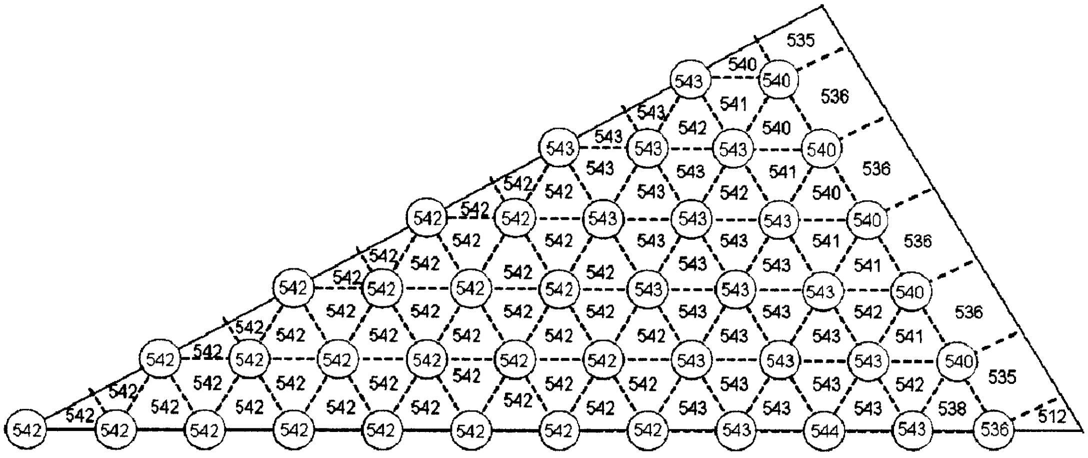

Figure 4.17: Core outlet temperatures for metal annular fuel assembly model with duct ribs included. (The #s within each circle represent the outlet coolant temperature of the corresponding annular fuel rod inner channels)

Table 4.6: Key parameters of annular fuel configurations

	Oxide		Metal	
	Ribs	**No Ribs**	**Ribs**	**No Ribs**
Core ΔP (MPa)	0.2735	0.248	0.209	0.191
Max Clad Temperature (°C)	560.28	570.57	560.96	569.28
Max Fuel Temperature (°C)	688.22	698.3	578.02	584.45

Both metal and oxide fuel assembly designs demonstrate good balance of heat and coolant flow: there is no longer a large difference between IA and inner subchannel core outlet temperatures. However, for the assemblies with no duct ribs, the difference in temperature between inner subchannels is rather large, and thus less acceptable. This results in large (~30 °C to 50 °C) differences between the IA and inner/edge subchannels at the outer edge of the assembly. However, when the duct ribs are included, the temperature profile of the inner channels is much more flat, resulting in a very desirable core outlet temperature profile. This allows for increased efficiency by increasing the core-average outlet temperature, while keeping the same hot spot margins.

Note that as mentioned in Chapter 4, the corner channels of the assembly model have lower temperatures when duct ribs are incorporated, due to the elimination of the swirl flow in the assembly. Relatively small amounts of coolant flow through these channels however, and thus these low temperatures do not generator temperature peaking, as do the edge channels without duct ribs.

4.2.4 Power Uprates

The fuel rods for a given core configuration must perform within an envelope of acceptable conditions to avoid breaching safety limits. For the sodium fast reactors, fuel must be designed so as to prevent excessive pellet-clad mechanical interaction, fuel clad chemical interaction (FCCI) and over-pressure of the fuel rod due to excessive fission gas release. Most of these phenomena are dependent, to varying degrees, on the temperature of the cladding and fuel. Thus, the cladding and coolant temperature are the primary figures of merit to consider when investigating the safety of fast reactor fuel. The base fuel configurations were modeled using the RELAP5-3D subchannel analyses model, and used as the standard for steady-state operating limits.

The core outlet temperature distributions for the metal and oxide fuel assemblies are seen in Figs. 4.18 and 4.19. Although the base assemblies do not call for duct ribs, a comparison of designs with duct ribs to those without would be inaccurate. Therefore, base fuel assemblies which incorporate duct ribs were also modeled, for comparison against the annular fuel assemblies with duct ribs. The core outlet temperatures for these assemblies are shown in Figs. 4.20 and 4.21. Recall that these assemblies have very thin fuel rods with grid spacers, and require structural rods (solid steel rods) to support the grid spacers. These structural rods are depicted by red circles in Figs. 4.18 – 4.21. The maximum clad and fuel temperatures, as well as pressure drops for the base designs as predicted by the RELAP5-3D subchannel model are shown in Table 4.7. The duct rib radii and flow area ratio for edge to inner channels are shown in Table 4.8.

It is important to note that the inclusion of structural rods results in a large temperature distribution in the assembly. The channels immediately surrounding the structural rod have a lower heat-to-flow ratio, resulting in a significantly lower temperature. As with the corner channels, however, this is a local depression of temperature, rather than an assembly wide temperature peaking.

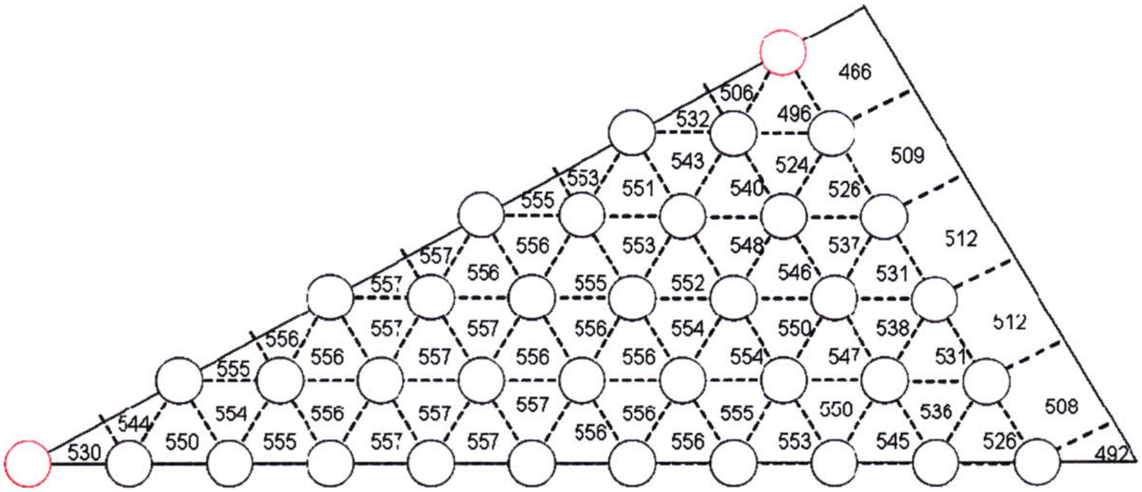

Figure 4.18: Core outlet temperatures for base oxide fuel assembly model (with structural rods depicted in red)

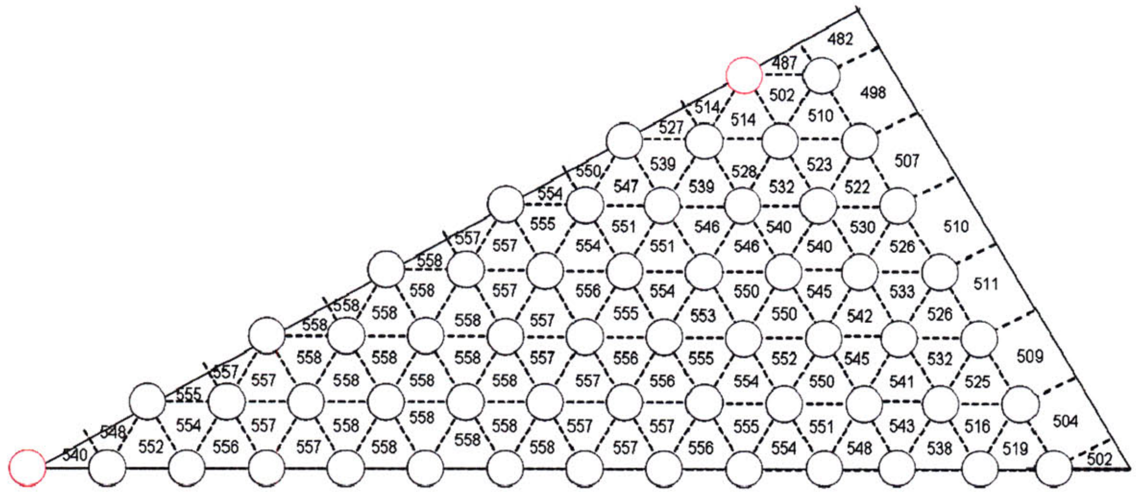

Figure 4.19: Core outlet temperatures for base metal fuel assembly model (with structural rods depicted in red)

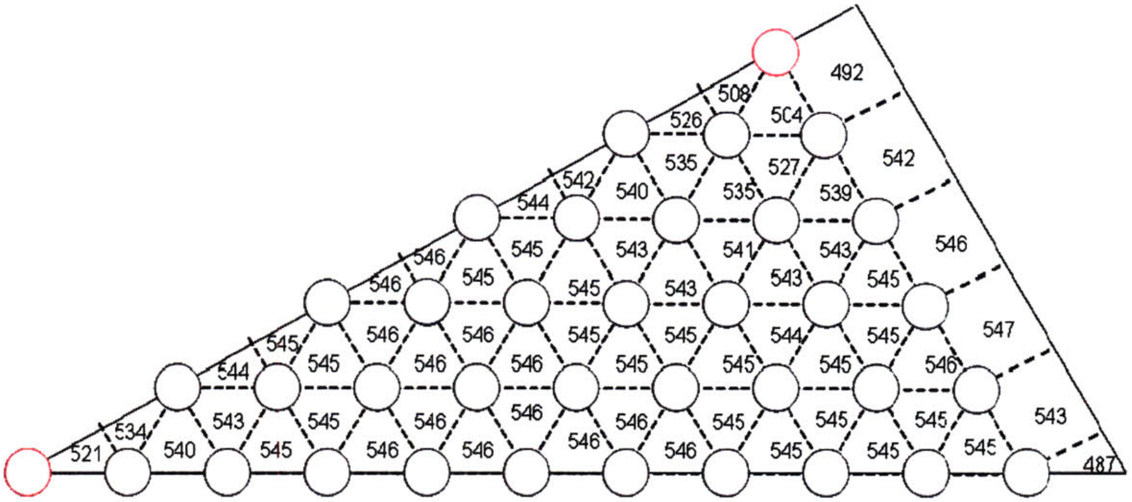

Figure 4.20: Core outlet temperatures for base oxide fuel assembly model with duct ribs included

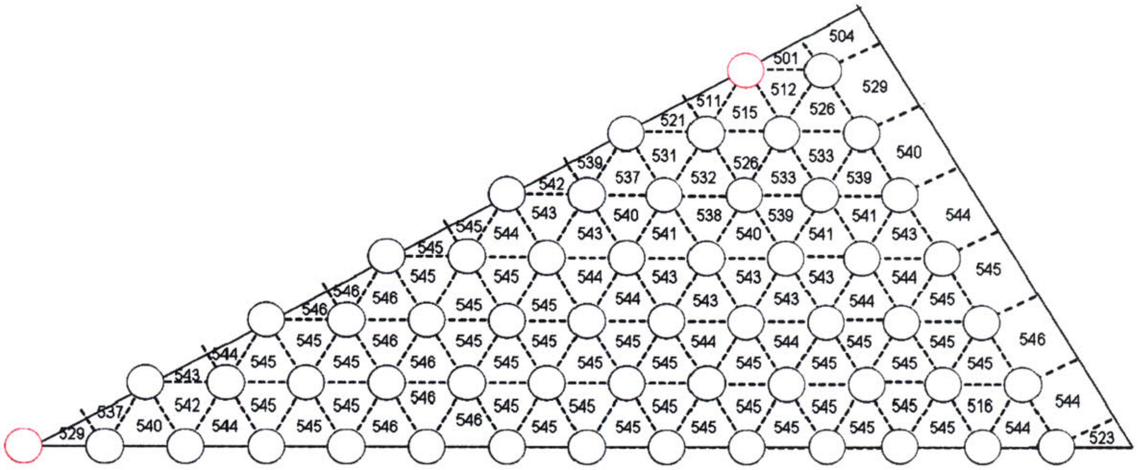

Figure 4.21: Core outlet temperatures for base metal fuel assembly model with duct ribs included

Table 4.7: Key parameters of the base (solid) fuel configurations

	Oxide		Metal	
	Ribs	**No Ribs**	**Ribs**	**No Ribs**
Core ΔP (MPa)	0.078	0.072	0.108	0.0942
Max Clad Temperature (°C)	579.63	622.6	578.73	590.99
Max Fuel Temperature (°C)	1821.25	1828.45	694.36	705.72

Table 4.8: Duct Rib Properties for annular and base fuel assembly designs (oxide and metal)

	Base		Annular	
	Oxide	Metal	Oxide	Metal
Rib Radius (mm)	2.10	1.85	1.69	1.65
Edge to Inner Subchannel Area Ratio (no ribs)	1.708	1.903	2.028	2.035
Edge to Inner Area Ratio With Duct Ribs	1.273	1.286	1.579	1.563

A comparison of the maximum cladding and fuel temperatures dictates the magnitude of the potential power uprate possible with each type of configuration. The reduction of the maximum fuel temperatures realized in utilizing the annular fuel concept is ~1-2 orders of magnitude larger than the reduction of the maximum clad temperatures, thus suggesting that clad temperatures (not fuel temperatures) are the dominant thermal limit, as the annular fuel concept is considered as a means to increase the power density in the core. Such increase was quantified by increasing the rod linear power (and proportionally the coolant flow rate, to maintain the same outlet temperature) until the maximum clad temperature in the annular fuel assembly matches the maximum clad temperature in the base fuel assembly. Another constraint to the magnitude of the power uprate is imposed by the core pressure drop increase. In this analysis we have imposed that core pressure drop increase for both metal and oxide fuels can at most double with respect to the base case. Table 4.9 lists the resulting maximum cladding temperatures, max fuel temperatures, potential magnitude of power uprate possible, and average coolant velocities for the solid fuel (base) design and the annular design.

Table 4.9: Results of subchannel analyses for solid, nominal annular, and uprated annular fuel designs (oxide and metal)

	Oxide					
	Solid		**Nominal Annular**		**Uprated Annular**	
	Ribs	**No Ribs**	**Ribs**	**No Ribs**	**Ribs**	**No Ribs**
Core ΔP (MPa)	0.078	0.072	0.2735	0.248	0.547	0.496
Max Clad Temperature (°C)	579.63	622.60	560.28	570.57	564.67	577.19
Max Fuel Temperature (°C)	1821.25	1828.45	688.22	698.30	750.95	765.35
Power Uprate (%)	-	-	-	-	40	44
Average Coolant Velocities (m/s)						
Inner	-	-	5.17	5.20	7.72	7.55
Inner	3.93	3.72	4.54	4.56	6.70	6.52
Edge	2.98	3.49	4.75	4.77	5.26	6.84
Corner	3.07	2.92	3.60	3.60	5.31	5.17
	Metal					

	Solid		**Nominal Annular**		**Uprated Annular**	
	Ribs	**No Ribs**	**Ribs**	**No Ribs**	**Ribs**	**No Ribs**
Core ΔP (MPa)	0.108	0.0942	0.209	0.191	.414	0.379
Max Clad Temperature (°C)	578.73	590.99	560.96	569.28	568.04	575.93
Max Fuel Temperature (°C)	694.36	705.72	578.02	586.45	592.89	600.85
Power Uprate (%)	-	-	-	-	45	45
	Average Coolant Velocities (m/s)					
Inner	-	-	5.35	5.10	7.83	7.47
Inner	4.31	4.05	4.52	4.27	6.52	6.17
Edge	3.27	4.07	3.44	4.84	4.95	5.86
Corner	3.67	3.45	3.49	3.29	5.02	4.74

As can be seen in Table 4.9, the potential power uprate for both oxide and metal fuels is substantial. In both the metal and oxide fuel cases, the power uprates are limited not by the clad temperature, but by the core pressure drop limitation. This limit is exceeded far before the annular design max clad temperature matches the max clad temperature of the solid fuel design.

The difference in magnitude of the decrease in core temperature for the oxide and metal fuels is primarily due to the geometric differences between the two fuel designs, as reflected in Table 4.3. The metal fuel has a lower fuel fraction and fuel/coolant ratio, plus the fuel to flow area ratio is smaller for the metal fuel assembly. Thus, a decrease in clad surface temperature will allow for a greater power uprate than in the oxide fuel assemblies. Though a power uprate is possible for designs with and without the duct ribs, the significantly non-uniform coolant temperature distribution in assemblies without duct ribs for both fuel types is problematic. This large temperature difference within a fuel assembly (particularly the hot fuel assembly) is undesirable, because, for a given margin to the postulated thermal limits (i.e., maximum allowable fuel and clad temperatures), it results in a lower core-average outlet temperature. Also, it can cause structural problems due to bending and thermal fatigue (thermal striping). Thus, the assemblies which include the duct ribs provide the potential to uprate the core power, while at the same time reducing the core outlet temperature distribution of the base assembly designs.

The max clad temperatures for both the solid fuel and the annular fuel assemblies are decreased with the addition of the duct ribs. This is primarily due to the reduction of the radial temperature gradients at the core outlet. This effect is very pronounced for the base case assemblies, but somewhat less dramatic for the annular fuel, because of restrictions on duct rib size directly resulting from the wire-wrap spacers in the edge channels. The potential power uprate from using annular fuel however, is driven by the pressure drop and velocity of the core, rather than the clad temperature.

Another interesting benefit from using the ribs is the potential for an increase in the thermal efficiency of the SFR. As the outlet temperature distribution for all assembly designs is flattened, a higher core average outlet temperature is possible at steady state reactor operation. By maintaining a higher reactor outlet temperature while maintaining a constant core inlet temperature, the thermal efficiency for the SFR can be increased, though this effect has not been quantified

4.2.5 Annular Fuel IA Channel Blockage Analyses

Finally, it is significant to note the small inner diameter required to eliminate the large temperature differences between inner and external subchannels. Having an inner diameter of only 3.4 or 3.7 mm introduces the concern of flow blockage. Debris filters will be important for this design in order to ensure that complete blockage of a subchannel is avoided. The potential for a complete blockage of an IA subchannel is a major concern with the annular fuel assembly concept. Because the inner diameter of the interior coolant channel is small (3.6 mm), the potential for blockage of the coolant channels is significant. To determine whether the complete blockage of the flow through the hot interior-annular coolant channel would be a limiting condition for annular fuel, the hot fuel assembly for the metal and oxide uprated annular fuel was analyzed assuming that no coolant would enter the inner channel of the hot pin in the assembly.

4.2.5.1 Max Temperatures During Complete IA Channel Blockage

The major concern for metal fuel annular design is that the blocked fuel rod would fail because of excessive fuel-clad chemical interaction (FCCI). FCCI occurs primarily at higher temperatures [4.6], and an upper temperature limit has been defined for steady state or long term operation. This limit applies to the max temperature of the clad at the inner surface, which cannot exceed a temperature of 650 °C (for steady-state) and 725 °C (for transients) for safe operation of the fuel.

Therefore, in order to be a feasible design, the cladding temperature at the inner surface of the inner-annular blocked channel must not exceed 650 °C for a prolonged time period and 725 °C for a short duration. Fuel temperature limits are higher than this, but are not discussed here, because the maximum temperature for the blocked channel fuel rod occurs in the inner clad of the rod.

The core-outlet temperature distributions for the blocked channel annular fuel models are very similar to those seen in Figs. 4.15 and 4.16, except that the maximum coolant temperature in the blocked channel is significantly higher, the adjacent inner channels are at a slightly higher temperature (due to the additional heat conducted out of the blocked channel rod) and the remaining channel are slightly lower in temperature (due to higher coolant flows in the remaining channels, compensating for the loss of flow in the blocked channel). This is shown in Fig. 4.22 which illustrates the blocked hot channel for the metal annular fuel design.

The maximum coolant temperature for the uprated metal fuel in the blocked channel is 674 °C (an increase of ~129 °C). This is a relatively small increase, primarily because all of the heat is efficiently conducted by the metal fuel to the outer surface of the rod when the inner channel is blocked.

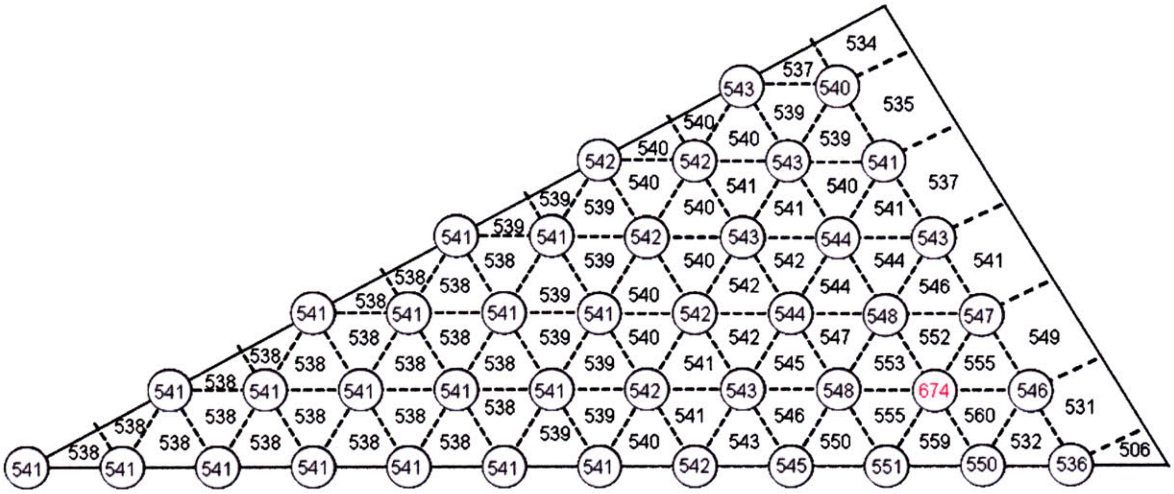

Figure 4.22: Core Outlet Temperatures for Metal Annular Fuel Assembly Model (duct ribs) with blocked hot channel (red). (The #s within each circle represent the outlet coolant temperature of the corresponding annular fuel rod inner channels)

The coolant temperature profile for the blocked channel rod, as seen in Fig. 4.23, is thus similar to the standard parabolic temperature profile seen in a solid fuel rod. The clad inner surface temperature for the metal fuel and the max fuel temperatures are both around 674 °C. This temperature is above the limit, and is thus undesirable. In order to maintain a blocked channel temperature that is below the long term clad temperature limits, the potential uprate found in Table 4.8 was reduced until the max clad temperature of the blocked channel was below the steady-state temperature limit. This new uprate potential is ~20% for the metal annular fuel design with duct ribs. However, the analysis presented here does not include all the engineering uncertainty factors in either the base case or the annular fuel case; therefore, the actual power uprate enabled by annular fuel may be somewhat different from, possibly lower than 20%. For instance, a power uprate of 10% would result in a maximum clad temperature of 640 °C should a complete blockage of the hot inner channel occur. However, because of the high uncertainties associated with the fuel thermal conductivities, and due to the lack of a margin for a 20% power uprate, more detailed fuel property data should be used before a final uprate magnitude can be decided upon. A plot of the axial temperature profile for the inner coolant, inner clad, peak fuel, outer clad, and outer coolant regions as a function of core height can be found in Fig. 4.21, while the radial temperature profile is found in Fig. 4.23.

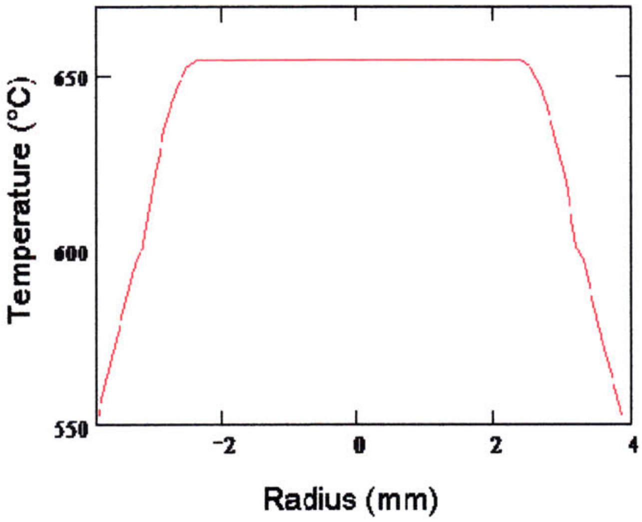

Figure 4.23: Radial temperature profile for hot blocked-flow channel at the core outlet (includes coolant and fuel regions)

Figure 4.24 illustrates that throughout the clad, fuel, and inner coolant channel, during a complete blockage at a 20% power uprate, the long term limit of 650 °C is not exceeded. This indicates that even should a worst-case blockage of the inner channel in a hot pin occur, there will not be damage to the fuel or cladding of the metal assembly during steady state operation. It should be noted in this discussion that the fuel properties for the metal CR = 0.25 fuel was taken from [2.2]. However, the thermal conductivity presented there is only a single value, 9.1 W/m·C, and it significantly underpredicts the thermal-conductivity. In addition, no volumetric heat capacity data was presented, and thus the volumetric heat capacity was assumed to be the same as for the metal CR = 0.71 fuel. It is important to note that the lack of margin for the 20% uprate, and the high uncertainties require that a more accurate thermal conductivity data be obtained before a final uprate decision is made.

The maximum coolant temperature in the blocked inner channel of the oxide fuel, however, is well over 1250 °C. This indicates that the sodium would completely boil in the hot channel, but also the clad would be severely damaged. The RELAP5-3D subchannel model failed prior to completing the blocked channel analysis, due to that the coolant boiling and the cladding failing. The fuel itself would not melt, but the clad barrier would be lost and sodium boiling would increase reactivity, potentially resulting in further damage. As such, the annular fuel concept is not feasible for oxide fuels.

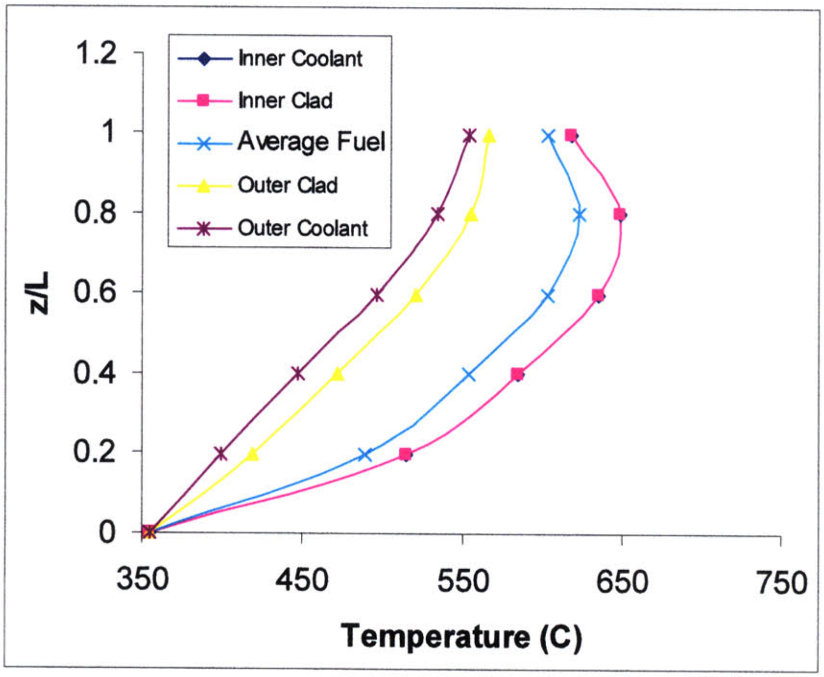

Figure 4.24: Axial temperature profiles for hot rod with blocked flow channel. (the inner coolant and inner clad curves perfectly overlap, as expected in the case of blockage)

4.2.5.2 Fuel Rod Structural Integrity During Complete IA Channel Blockage

During steady state operation of the annular fuel core, the inner and outer clad is at roughly the same temperature. This results in very little thermal stresses induced by the annular fuel design. However, during a coolant channel blockage, the temperature differential between the inner and outer clad of the blocked channel could pose structural problems. The inner clad, where the coolant channel is blocked, would expand more than the outer channel, as depicted in Fig. 4.25. However, the end-cap restricts the differential expansion, thus resulting in the development of axial compressive and tensile stresses in the inner and outer clad, respectively. Additionally, shear stresses develop in the end-cap. Thus, there are two potential mechanical failures introduced by the blockage of the hot channel in annular fuel: buckling of the inner clad due to the increased axial stresses on the clad surfaces, and end-cap failure due to the increased bending shear-stresses.

Buckling failure is fairly straightforward to evaluate. The average axial thermal expansion is calculated for each volume according to the equation:

$$\varepsilon_{avg} = \frac{\alpha \cdot (\Delta T_i + \Delta T_o)}{2} \tag{4.3}$$

where:

ε_{avg} = average thermal strain of the annular tube per volume

$\Delta T_i / \Delta T_o$ = the inner and outer clad temperatures minus the reference temperature (coolant inlet temperature) in the volume

α = linear thermal expansion coefficient (this is equal to 1.1E-5 for HT9) (1/K)

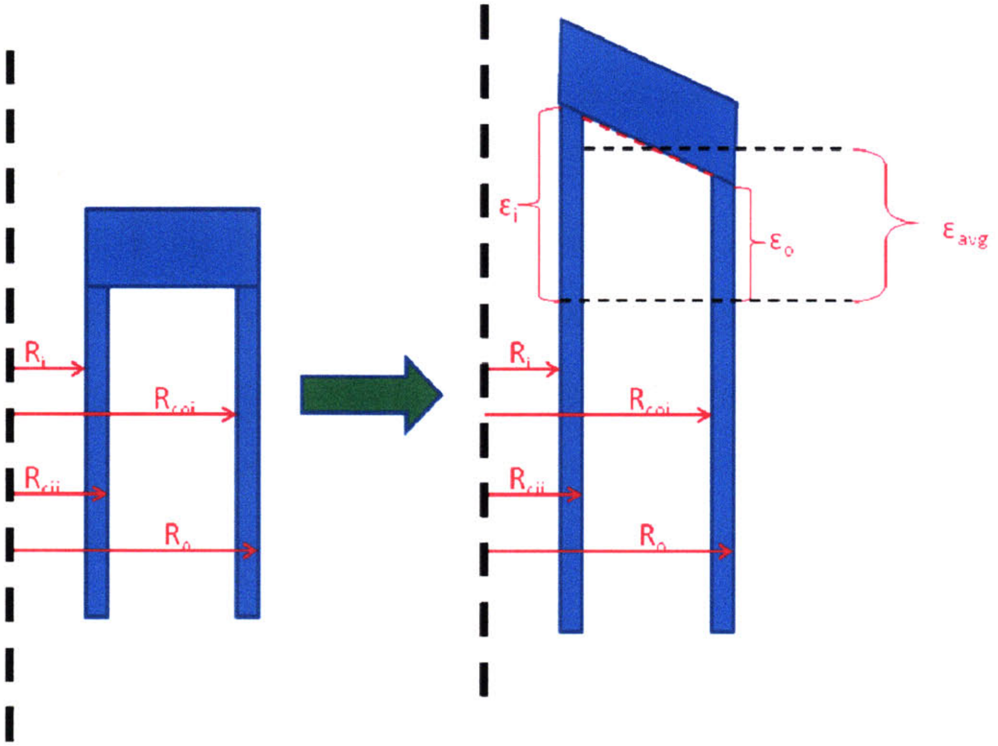

Figure 4.25: Illustration of differential expansion of annular fuel cladding and stresses induced upon cladding and end-cap

Therefore, the tube expands by the linear average of the inner and outer cladding structures. The stress in the inner and outer clad can be then calculated from Hooke's law as:

$$E(\alpha \Delta T_{i/o} - \varepsilon_{avg}) = \sigma_{i/o} . \tag{4.4}$$

where $\sigma_{i/o}$ = axial stress in the inner/outer clad structures.

Buckling is a form of elastic instability which can occur when the axial loading exceeds a given buckling limit, which is based upon the material and the beam geometry. According to literature [4.7], the buckling limit for a long thin circular tube is calculated using the equation:

$$P' = \frac{\pi^2 E \cdot I}{l^2}, \tag{4.6}$$

where l is the clad length, and I is the secondary moment of inertia for the tubular beam, found by:

$$I = \frac{\pi}{4}\left(R_{cii}^4 - R_i^4\right), \tag{4.7}$$

and R_{cii} and R_i are the outer and inner radii of the inner cladding, respectively. Using the properties for HT9 (E=160GPa) and the annular fuel inner clad dimensions, axial strains during an inner subchannel blockage accident are found in Table 4.10. The buckling forces derived from Eq. (4.6) are divided by the cross sectional area of the tube:

$$A_{cs} = \pi\left(R_{cii}^2 - R_i^2\right), \tag{4.8}$$

in order to determine the stresses associated with these force limits. These buckling stress limits are found in Table 4.10.

Note the very small limit for buckling in the inner clad structures of the annular fuel. These very small limits are due to the fact that the clad structures are very long and thin with no support on the inner cladding, and only the wire-wrap as support for the outer cladding. It is apparent from Table 4.10 that in the case of a subchannel blockage, the inner cladding axial stresses far exceed the buckling limit, and thus buckling is possible. This is primarily due to the large length of the inner clad without any support structures throughout. Initially, the bond is large enough that fuel pellets cannot be considered a structural support to prevent buckling, but after 1-2% when fuel swells and contact the cladding, the fuel can support cladding against buckling. Nevertheless, buckling would still be an issue in plenum region. The wire-wrap may be considered a structural support to prevent major rod buckling, but this possibility hasn't been considered in detail. In addition, bucking may occur due to axial stresses induced by coolant flow through the inner channel [4.9]. This potential for buckling instabilities could be more severe than the thermal stresses during an IA blockage, since these axial stresses are present throughout steady-state operation, while the thermal stresses are only present during the rare case of a complete IA blockage. Thus, it is recommended that for future work, buckling instabilities due to fluid flow forces and potential solutions should be investigated, and that potential solutions to the annular fuel IA subchannel blockage also be developed and investigated. If no feasible solutions are found, the issues of buckling under either inner channel blockage conditions or buckling due to flow forces could prevent the utilization of annular fuel.

Table 4.10: Key Parameters of annular fuel blockage structural analysis

	Inner Clad
Inner Radius, R_i (mm)	1.8
Outer Radius, R_{cli} (mm)	2.359
E (GPa)	160
Length (m)	4.071
Moment of Inertia (m^4)	1.61E-11
Axial Stress (MPa)	8.78
Buckling Limit	0.21
End-cap Shear-Stress (MPa)	0.17
ASME secondary local membrane stress limit (MPa)	~630.0

The differential expansion of the inner and outer clad structures during an IA subchannel blockage accident, as shown in Fig. 4.25, results in the addition of shear stresses in the fuel end-cap. A simplified method for evaluating the magnitude of these stresses is performing a force balance on a control volume surrounding a section of the end-cap, as seen in Fig. 4.26. The axial force exerted by the expanding inner clad is balanced by the shear stress at a given point within the clad:

$$F_z = F_s, \tag{4.9}$$

where F_s is the applied force due to shear stress in the end-cap. The applied force is the shear stress times the cross sectional area:

$$F_s(r) = 2\pi \cdot r \cdot t_e \cdot \tau , \tag{4.10}$$

where τ is the shear stress in the end-cap and r is the radius at which the stress force is evaluated. This shear stress is a function of radius, and is calculated using the equation:

$$\tau(r) = \frac{F_z}{2\pi \cdot r \cdot t_e}, \tag{4.11}$$

where:

F_Z = axial force due to thermal expansion

t_e = end cap thickness.

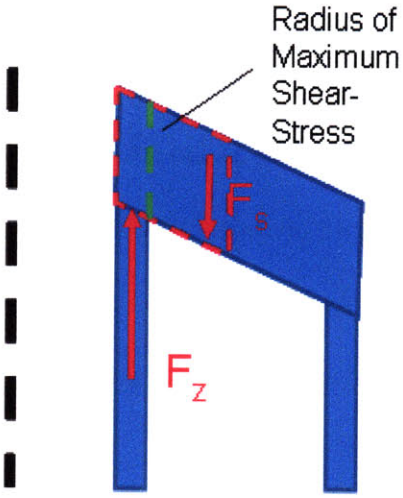

Figure 4.26: Force balance for control volume surrounding a segment of the end-cap of the annular fuel rod with a completely blocked IA channel

The axial thermal expansion force is calculated from Eq. 4.4 using the inner cladding parameters. The radially-dependent axial force due to shear-stress is plotted in Fig. 4.27. The radius of maximum shear stress is clearly at the outer edge of the inner clad, with a magnitude of 0.172 MPa. According to ASME code, this stress is considered a secondary local membrane stress. This stress cannot exceed the design limit (S_m) times a factor of 3.0. The design stress as a function of temperature for HT9 can be found in Fig. 4.28 [4.10], and the overall secondary moment stress limit can be found along with the maximum end-cap stress in Table 4.10.

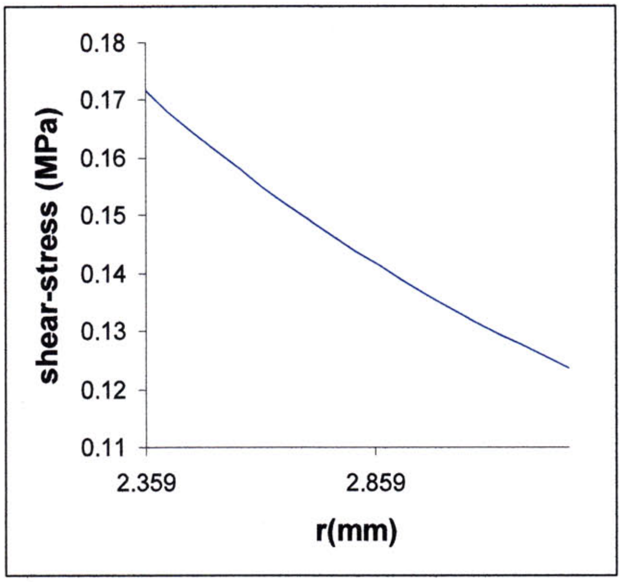

Figure 4.27: Shear-stresses in end cap as a function of radius during a blocked IA channel accident for metal annular CR = 0.25 fuel

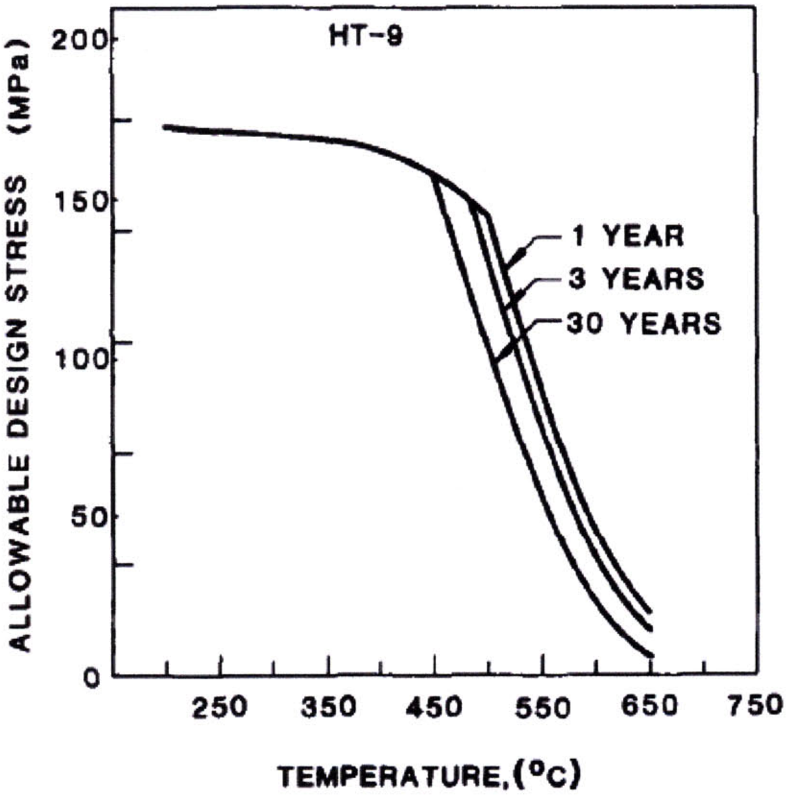

Figure 4.28: HT9 design stress based upon the ASME code [4.9]

4.3 Bottle-Shaped Fuel

The preliminary studies performed in Chapter 4 reveal that bottle-shaped fuel designs have the potential to reduce the total pressure drop across the core, while maintaining similar neutronic performances. Although these scoping studies indicated that large decreases in the plenum region is possible, it is worthwhile to determine the detailed performance of the bottle shape fuel configuration via subchannel analysis of the fuel assemblies. These analyses are described in the following sections.

4.3.1 Bottle-Shaped Fuel Subchannel Configuration

Chapter 4 includes scoping analyses of the bottle-shaped fuel configurations. These preliminary calculations revealed that a high conversion ratio core is best suited for the use of bottle-shaped fuel, due to the tight fuel rod pitch in the assembly designs for high CR cores. Previously a breakeven core (CR = 1.0) was used as the base design. However, because the innovative fuel configurations described in this thesis are intended for use in the ABR1000, it is worthwhile to utilize the core design and fuel configurations utilized in the ABR1000 as the base fuel configuration. Because there is no very low conversion ratio fuel design for the ABR 1000, the configuration described in Chapter 4 has been maintained as the base fuel configuration [2.2]. The ABR1000 standard fuel configuration for both metal and oxide fuels however, is a higher CR fuel, with CR =

0.71. This higher CR fuel configuration is therefore used as the base configuration for comparison with bottle shaped fuels throughout the bottle-shaped subchannel analyses. Table 4.11 lists the design parameters of the high conversion ratio fuel, while Table 4.12 lists the optimum plenum radii and other parameters based on calculations similar to those described in section 2.4.2. An axial power profile similar to that found in the low conversion ratio cores is employed. Additionally, there are four grid spacers supporting the plenum region of the core. The details and assumptions for these grid spacers as described in 2.4.2.

Table 4.11: Design Parameters of the ABR1000 Base Fuel Assemblies (CR = 0.71)

	Metal	Oxide
Rings	9	9
Pins	271	271
Flat to flat (cm)	15.71	15.71
Pin outer diameter (mm)	7.55	7.55
Pin inner diameter (mm)	-	-
P/Do	1.18	1.18
Dwire (mm)	1.31	1.31
Clad thickness (mm)	0.56	0.56
Fuel volume fraction (%)	29.2	37.0
Bond volume fraction (%)	9.8	2.0
Structure volume fraction (%)	25.7	25.7
Coolant volume fraction (%)	35.3	35.3
Fuel/coolant volume ratio	0.827	1.048
Power density (kW/L)	303	231
Linear heat rate (kW/m)	23.3	18.8
Heated Length (cm)	81.29	106.68
Plenum Height (cm)	124.40	160.02
Total Core Height (cm)	477.52	477.52

Table 4.12: Design Parameters of the Optimized Bottle-Shaped Fuel Assemblies (CR = 0.71)

	CR = 1.0

	metal	oxide
Optimal plenum radius (mm)	3.5	3.5
Plenum height (m)	2.547	2.483
Bottle-shaped to base plenum height ratio	1.332	1.453
Bottle-shaped to base core height ratio	1.156	1.183

4.3.2 Bottle-Shaped Fuel Subchannel Results

Because the core dimensions are identical for the bottle-shape and base fuel assemblies, the temperature distribution is also identical, and thus a core outlet temperature profile is no included here. The most significant performance metric is the pressure drop across the core for each fuel type in both base and bottle-shaped fuel assemblies. These values are shown in Table 4.13. The cumulative core pressure drops as a function of axial assembly length for both the base and bottle-shaped fuel assemblies are plotted for both oxide and metal fuel types in Figs. 4.29 and 4.30, respectively. As can be seen in these figures, the pressure drop through the core region of the assembly is identical for both oxide and metal fuels. However, in the plenum region of the assembly the pressure drop is significantly less through the bottle-shaped plenum than for the base fuel plenum. Significant pressure drop reductions can be realized with relatively small increases in overall core length.

Though this large reduction in pressure drop is a worthwhile benefit for a SFR, there are other aspects to consider for the bottle shaped fuel. The first has been briefly mentioned, and that is considering the design and manufacturing feasibility for increasing the core height by 5%-18% for the bottle-shaped fuel. If this proves to be too costly, or if it cannot be included without adjusting the pool design (in particular increase of vessel height), this configuration may prove unacceptable. Significant vessel height increase would most certainly cancel any benefit gained from decreasing the core pressure drop. The fabrication complexity is also increased by the need to include both wire-wrap spacers and grid spacers in the bottle-shaped fuel assembly. The wire-wrap spacers are needed in the lower shield/core regions of the fuel rods, while grid spacers are required in the plenum region of the fuel rods. This increase in fabrication complexity should also be considered when evaluating bottle-shaped fuel.

In addition to the fabrication and manufacturing considerations, there is an additional safety consideration for the bottle-shaped fuel that needs further analysis. The core radial expansion reactivity coefficient is a key reactivity feedback making possible core shutdown in events without scram. The impact of bottle-shape fuel on the value of this coefficient needs to be investigated, but it is expected that the effect will be small since this coefficient is primarily determined by the design of above the core load pads that are placed on the duct walls. These additional considerations are not considered in this thesis, since the primary focus is thermal-hydraulic performance, but they should be evaluated carefully in future work.

Table 4.13: Core Pressure Drop for Bottle-Shaped and Base Fuel Assemblies for both Metal and Oxide Fuels

Pressure Drop	Oxide	Metal
Pressure Drop in Base Assembly (kPa)	227.85	209.55
Pressure Drop in Bottle-Shaped Assembly (kPa)	156.31	133.45
Reduction (%)	31.4	36.3

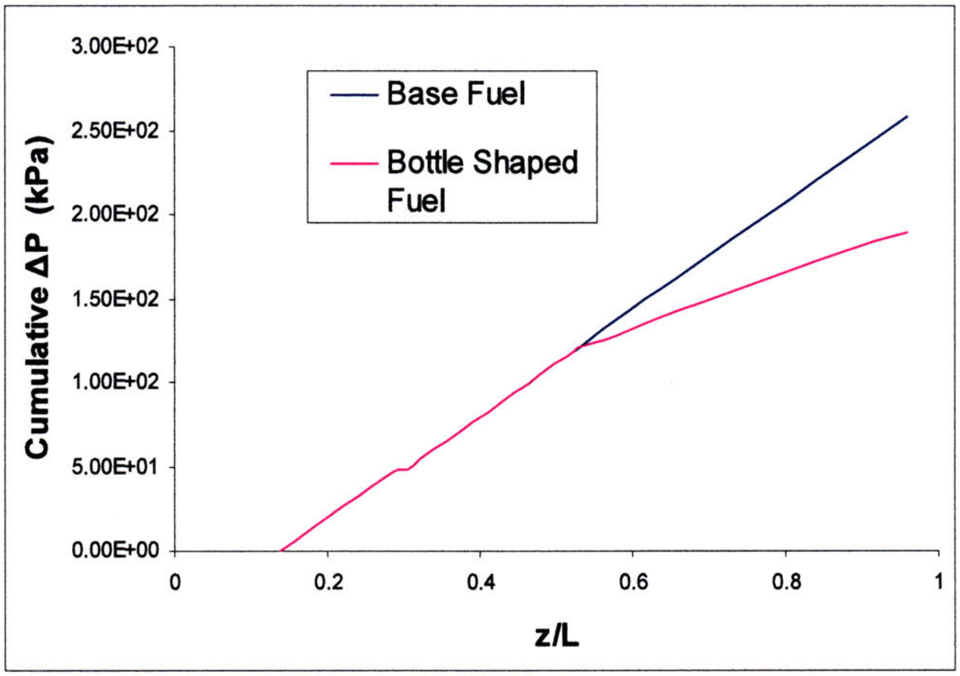

Figure 4.29: Cumulative pressure drop across the core as a function of nominal assembly length for both the base and bottle-shape oxide assembly designs

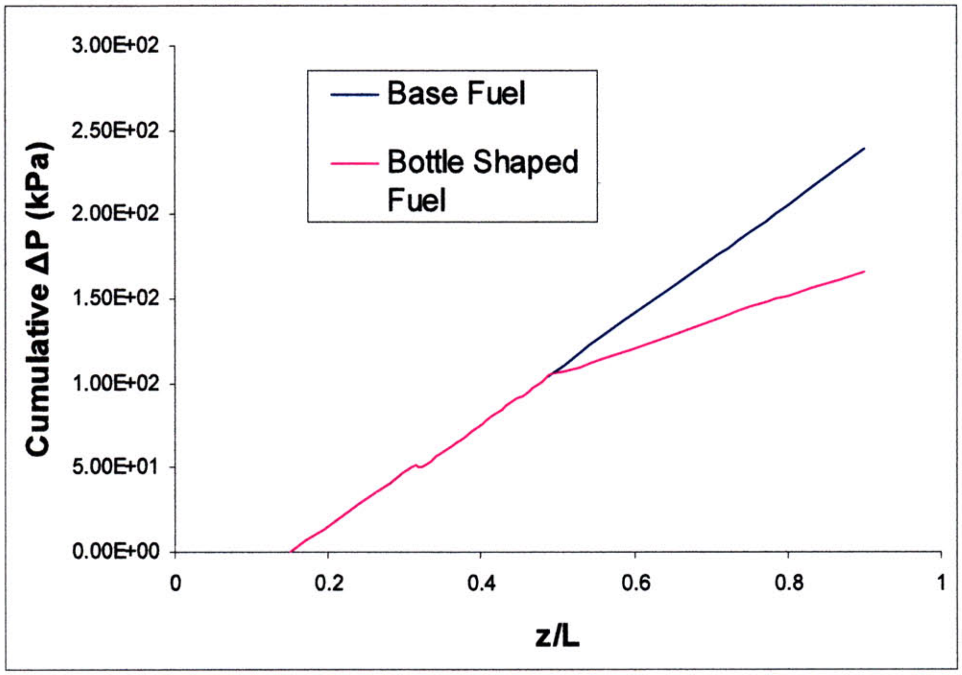

Figure 4.30: Cumulative pressure drop across the core as a function of nominal assembly length for both the base and bottle-shape metal assembly designs

4.3.3 Mechanical Stresses on Cladding at Plenum/Core Interface

As with annular fuel, the structural integrity of the clad for the bottle-shaped fuel must be verified. The bottle-shaped fuel configuration has a gradual reduction in the fuel rod radius at the onset of the gas plenum in order to minimize the pressure drop across the core. However, the original design was an abrupt area change, and this design is more conservative, as the bending moments will be larger across a sudden change in cross-sectional area. As with the annular fuel end-cap, the maximum shear-stress in the bottle shaped fuel can be estimated using a simplified force balance calculation.

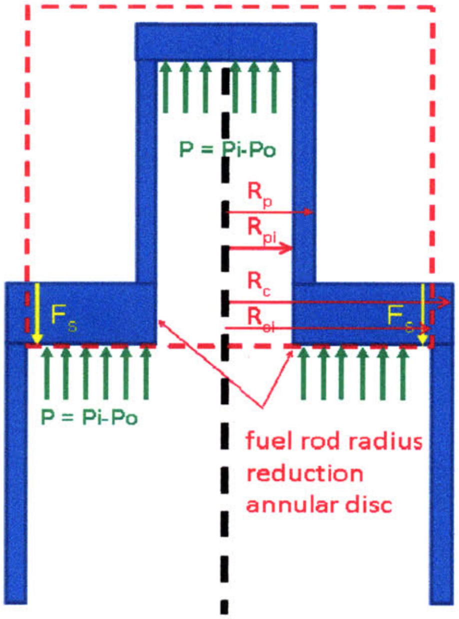

Figure 4.31: Illustration of bottle-shaped fuel rod radius reduction annular disc and balance of forces due to internal pressure and shear-stress

Fig. 4.31 illustrates the "radius reduction annular disc" or the annular disc that connects the plenum and core portions of the fuel rod. It is in this disc that the control volume for the force balance is located. Unlike the annular fuel end-cap, the axial force is not due to thermal expansion, but is due to the internal pressure, and thus the shear stress is a primary local membrane stress. This stress can be evaluated according to the equation:

$$\tau(r) = \frac{P \cdot r}{2t_e}, \tag{4.12}$$

where P = net pressure on the annular disc, or inner pressure (P_i) minus outer pressure (P_o).

The internal pressure of the fuel rod in a sodium fast reactor depends on many factors, but a reasonable range for metal and oxide fuels is between 5 MPa and 15 MPa. Fig. 4.32 plots the shear-stress of the annular radius-reduction disc for both these bounding cases. According to ASME limits, the primary local membrane stresses are not so exceed 1.5 Sm, which is ~315 MPa for HT9.

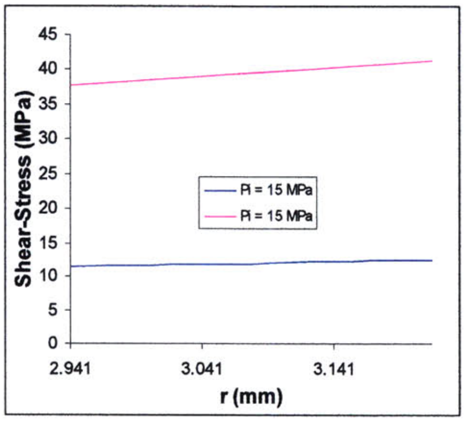

Figure 4.32: Shear-stress as a function of radius within the bottle-shaped fuel annular disc during steady state-operation

Table 4.14 lists the parameters of the bottle-shaped fuel annular disc, as well as the maximum shear stress in the annular disc. This value is significantly less than the ASME secondary bending stress limit also listed in Table 4.13. Because the sudden contraction of the bottle-shaped fuel is the most conservative case with the largest bending stresses, the more conservative bottle-shaped fuel configuration with a gradual reduction in rod radius at the bottom of the gas plenum will also be structurally stable.

Table 4.14: Key Parameters of bottle-shaped fuel rod reduction point annular disc

	Metal
Inner radius (mm)	2.941
Outer radius (mm)	3.775
Modulus of elasticity (GPa)	160
Disc Thickness (same as clad) (mm)	0.559
Bottle-shape restriction bending stress (MPa)	12.46 – 41.22
ASME primary local membrane stress limit (MPa)	~315.0

4.4 Conclusions

The innovative fuel configurations were analyzed with a RELAP5-3D based subchannel model to evaluate their potential to improve the thermal-hydraulic performance of the SFR. The use of internally and externally-cooled annular fuel in a low CR core with oxide fuel reduces the clad temperature of oxide fuel by up to 62 °C. This leads to a possible power uprate of 44%. Annular fuel could reduce the clad temperature of the metal fuel by about 18 °C, and this results in a 43% power uprate.

If a complete blockage of the hot interior-annular subchannel were to occur in the hot assembly, clad failure would occur in the oxide fuel annular assembly, while for the metal fuel annular assembly, complete blockage of an interior-annular subchannel should not result in significant clad or fuel damage so long as the power uprate remains below 20%. This does not provide for much margin to clad failure. However, this uprate potential was determined base upon fuel properties from [2.2], which are estimated, and have a high degree of uncertainty. These properties may be inaccurate, and future work should be done in which more accurate fuel properties be utilized to determine the amount of margin possible during a blockage accident. Annular fuel is not a feasible design for oxide fuel due to the potential for cladding damage should complete blockage of the hot channel occur.

Additionally, if a complete blockage of the hottest inner-annular subchannel were to occur, buckling of the inner clad would be a potential problem, although the subsequent shear stresses in the end-cap would not result in mechanical failure. Future work for annular fuel should focus on the investigation of this potential buckling problem.

The bottle-neck fuel configurations allow for a reduction in core pressure drop. For oxide fuel configurations at CR = 0.71, the pressure drop is reduced by 31%, while for metal fuel configurations, the core pressure drop is reduced by 36% with core height increases of 16% and 18%, respectively. The thermal expansion of the clad in the core region results in bending moment stresses upon the annular disc located at the fuel rod reduction area, but these additional secondary stresses are far below the ASME limit for such stresses. As such, the bottle-shaped fuel is structurally sound during standard operating conditions. Potential future work should include a detailed investigation of the structural integrity of bottle-shaped fuel through various accident scenarios.

Chapter 5: SFR Full-plant Model

As discussed in Chapter 4, the annular fuel configurations allowed for sizable power uprates in CR = 0.25 cores with both metal and oxide fuel, while the bottle-shaped fuel configurations provided a ~31% – 36% decrease in pressure drop across the core for CR=0.71 cores. These innovative fuel configurations cannot be utilized, however, if their performance during postulated SFR transients is worse than the standard base fuel. Therefore, a SFR full-plant model was created using RELAP5-3D in order to evaluate the performance of the base, annular, and bottle-shaped fuel configurations during steady state operation and key transients. This chapter describes the creation of this full-plant model, along with the assumptions associated with the material properties, kinetic parameters, and geometric relations.

Initially, the steady-state solution runtime was on the order of 72 hours, due to the very small volume lengths in the direct reactor auxiliary cooling system (DRACS) models, as well as the explicit modeling of all four secondary loops. The time step limits were increased through secondary loop and IHX lumping and Courant limit manipulation via the adjusting of volume lengths in the core and DRACS systems. The completed full-plant model operation conditions were obtained after ~15,000 seconds of runtime; a comparison of these parameters (obtained with a metal CR = 0.71 core) against the ABR1000 steady-state operating parameters (based on the configuration described in [5.1]) is included in Section 5.3. Finally, the innovative core configurations along with their respective base fuel configurations were incorporated into the RELAP5-3D model through direct adjustment of the core component in the RELAP5-3D model. A description of the various core models for the CR = 0.25 solid fuel and annular fuel and the CR = 0.71 base fuel is included in section 5.4 of this chapter.

5.1 Full-plant RELAP5-3D Model

The full-plant design parameters for the SFR* model are based upon a concept for the ABR1000 described in [5.1]. The full-plant model was constructed using RELAP5-3D, based upon a previous RELAP5-3D input deck created by the author for the Advanced Burner Test Reactor (ABTR) concept in Spring 2007. This model consists of 5 separate components that were created individually and then combined to create the full-plant model. These components are:

1. The Core
2. The Primary System
3. The Secondary Loop
4. The Power Conversion System (PCS) Boundary
5. The DRACS

A description of each of these systems, along with the assumptions and calculations required for each system are provided in the following sections.

---

* The sodium reactor primarily addressed in this report is the advanced burner reactor (ABR), though for simplicity, the term SFR will be continue to be used to reference this reactor

5.1.1 SFR Core Model

There are two major components that need to be included in the SFR full-plant model in order to accurately portray the physics involved in the steady state operation of the full-plant. The first component is the geometry and thermal-hydraulic characteristics. This broad category includes the assembly parameters, the core layout, the drag coefficients for both laminar and turbulent regimes (which are used by RELAP5-3D to evaluate the friction factors), and the bypass flow characteristics. The heat transfer coefficients are calculated by the RELAP5-3D code based upon geometric and hydraulic characteristics of the model. The RELAP5-3D model of the SFR core was created by Dustin Langewisch [5.2] by scaling up the RELAP5-3D core model developed by the author for the ABTR. The second component of complete SFR core design is the neutronic characteristics. This includes both axial and core-wide power profiles, reactivity feedback mechanisms, and neutronic properties. The design parameters for both components of the SFR core model were inspired by the ABR1000 concept described in [5.1], and these parameters are detailed in the following sections.

5.1.1.1 SFR Core Geometric Parameters [5.2]

The SFR core inspired by the ABR1000 concept described in [5.1] consists of 180 driver assemblies divided into two primary segments. The inner driver assemblies (78), which have a lower enrichment, are located in the center of the core, and the outer driver assemblies (102), which have a higher enrichment, are located around the inner driver assemblies in the core. The outer drivers are surrounded by 114 reflector assemblies in order to reduce neutron leakage, and the outermost ring of the core consists of 66 shield assemblies. The control mechanism for this SFR core consists of 15 primary control rods throughout the inner and outer core with four secondary control rods, which are located primarily in the inner core region. A top down view of the core (both metal and oxide, as they are identical) that illustrates the placement of these assemblies is found in Fig. 5.1. Each of these assemblies is similar to the assembly design described in Chapter 4: a hexagonal duct with a flat-to-flat diameter of 15.71 cm with cylindrical rods arranged in a triangular pitch. The rods in the driver assemblies and control assemblies are all wire wrapped.

In addition, the assemblies are separated by a 0.432 cm gap to allow for assembly expansion during irradiation as well as to allow assembly insertion and withdrawal during fuel reloading. This gap or “bypass flow” provides an additional flow path allowing some sodium coolant to bypass the core. Table 5.1 summarizes typical design parameters for the SFR core assemblies, including the assembly and pin geometry and composition, while Fig. 5.2 illustrates the typical axial profiles for an assembly and pin in a SFR metal fuel assembly (the pin and assembly layouts are similar for oxide fuel assemblies, though with different lengths). The fuel pins are composed of three axial zones: a shield region at the bottom of the pin composed entirely of HT9, the active core region (which includes the U-TRU-Zr or MOX fuel pellets and sodium bond or He gap), and the gas plenum to capture released fission gases.

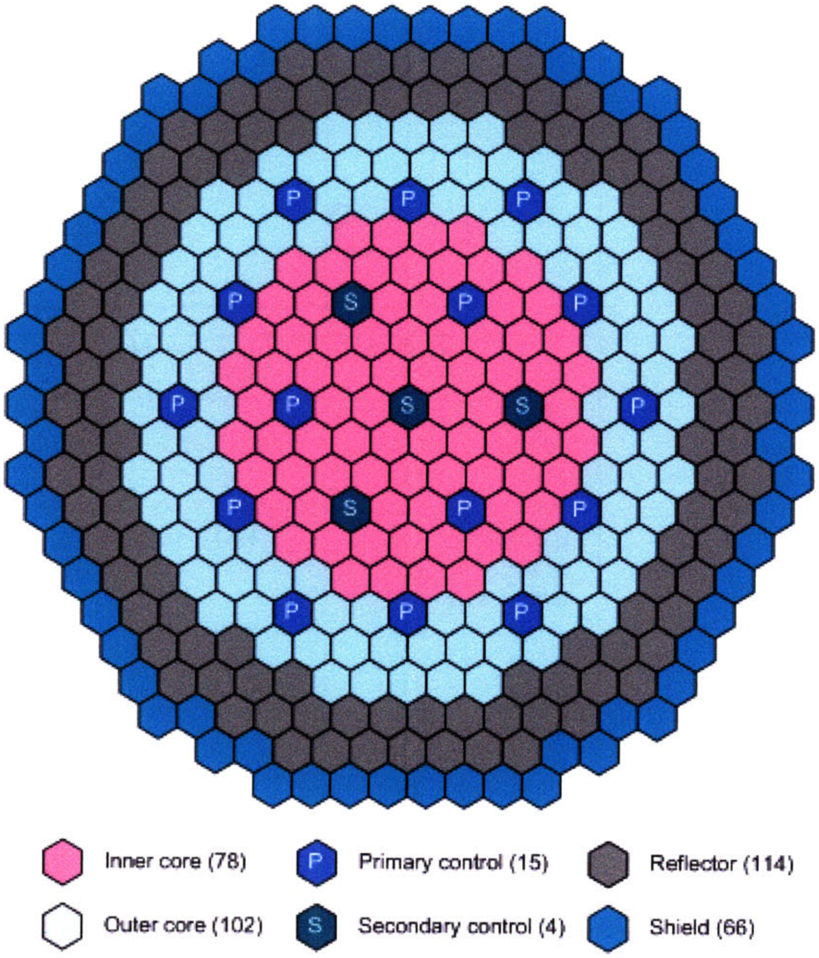

Figure 5.1: Core assembly layout for typical SFR core (metal or oxide) as described in [5.1]

Table 5.1: Assembly design parameters for a typical SFR core

	Fuel assembly		Reflector	Shield	Control
	Oxide	Metal			
Assembly data					
- Number of pins	271	271	91	19	7
- Assembly pitch, cm	16.142	16.142	16.142	16.142	16.142
- Inter-assembly gap, cm	0.432	0.432	0.432	0.432	0.432
- Duct outside flat-to flat Distance, cm	15.710	15.710	15.710	15.710	15.710
- Duct thickness, cm	0.394	0.394	0.394	0.394	0.394
- Gap between duct and interior Duct, cm	-	-	-	-	0.400
- Interior duct thickness, cm	-	-	-	-	0.394
- Interior duct inside flat-to-flat Distance, cm	-	-	-	-	13.334

- Overall duct height, cm	477.52	477.52	477.52	477.52	477.52
Pin data					
- Pin material and type	MOX	U-TRU-Zr	HT9	[a] B_4C	[b] B_4C
- Bond/gap material	He	Na	-	He	He
- Overall pin length, cm	400.1	332.7	[c] 400.1/332.7	400.1/332.7	119.3/86.3
- Active core height, cm	114.3	81.3	-	-	-
- Pellet smeared density, % TD	85.0	75.0	-	81.0	85.0
- Pellet diameter, cm	0.625	0.557	1.541	2.553	4.193
- Cladding material	HT9	HT9	-	HT9	HT9
- Clad outer diameter, cm	0.745	0.755	-	3.337	4.688
- Pin pitch-to-diameter ratio	1.190	1.180	1.001	1.001	1.029
- Cladding thickness, cm	0.060	0.056	-	0.250	0.070
- Wire wrap diameter, cm	0.140	0.131	-	-	0.133
Volume fraction at fabrication, %					
- Fuel or absorber	35.0	29.2	-	43.1	42.8
- Bond	1.9	9.8	-	10.1	7.6
- Structure	26.6	25.7	84.5	29.7	20.8
- Coolant	36.5	35.3	15.5	17.1	28.8

a) Natural boron was used.

b) Natural and 60% enriched boron was used for 4th and 7th row primary control assemblies, respectively.

c) Data for oxide and metal core

The power rating of the SFR is 1000MWth with a coolant inlet temperature of 355°C. The sodium coolant flow rate is chosen such that the average temperature rise across the core is 155°C, thus having a core outlet average temperature of 510°C; the corresponding flow rate has been determined to be approximately 5024 kg/s. This flow is maintained by electromagnetic (EM) pumps in the primary system cold pool. In order to ensure that an adequate amount of coolant flows through each assembly, the assemblies are orificed; this provides a measure of control by which the core designers can equalize the outlet temperature across assemblies. The maximum allowable coolant temperature difference across the assembly outlets was taken as 44°C. Through careful orificing, the actual difference between the coolant outlet temperatures for the various assemblies is ~15 °C for the metal fuel core, and ~30°C for the oxide core (the larger oxide core temperature difference is due primarily to a larger power peaking, as described in the following section).

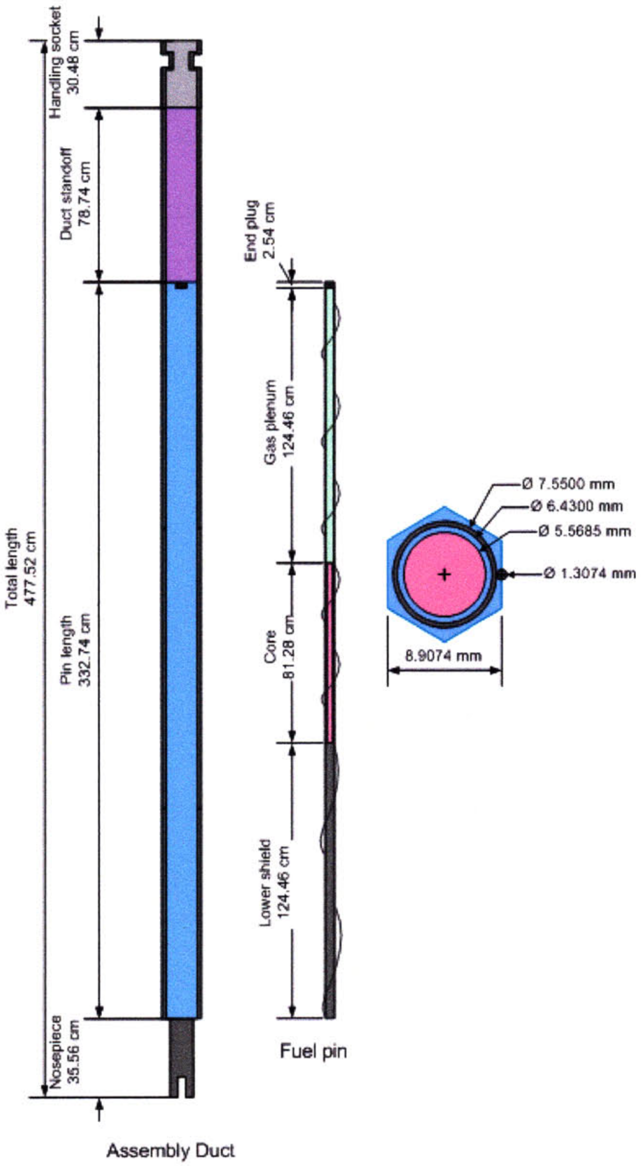

Figure 5.2: Axial profile for assembly duct and fuel pin in typical metal SFR core as shown in ABTR design report [5.3]

5.1.1.2 ABR1000 Neutronic Parameters

The neutronic parameters of the metal and oxide core fuel assemblies used in the full-plant model were also inspired by the ABR1000 configuration referenced by Chikazawa and Grandy [5.1]. The power generation per assembly is dependant upon the neutronic characteristics of the fuel and changes throughout the life of the core. As a conservative estimate, the beginning of equilibrium cycle (BOEC) power profile is used for both the metal and oxide fuels. The BOEC power profiles for typical SFR (both oxide fuel and metal fuel) were derived by scaling up the power profiles for the ABTR core [5.3] and are shown in Figs. 5.3 and 5.4, respectively. The axial power profiles for the SFR fuel were assumed to be chopped cosine profiles, with peaking factors matching the peaking profiles described in Section 4.2.3.1.

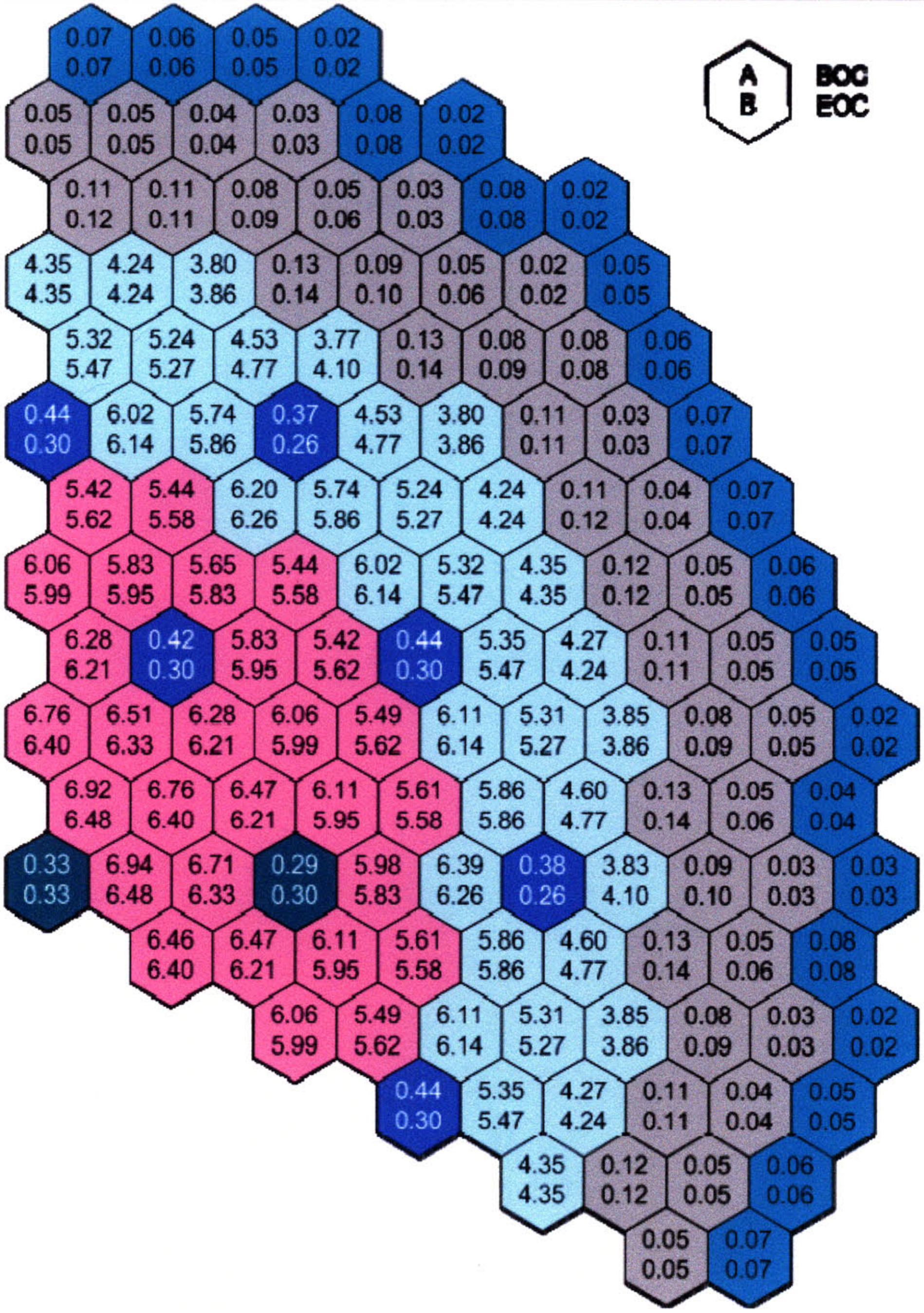

Figure 5.3: Metal fuel startup core power pofile at BOC and EOC, where the numbers are the assembly power in MW, as scaled up from [5.3]

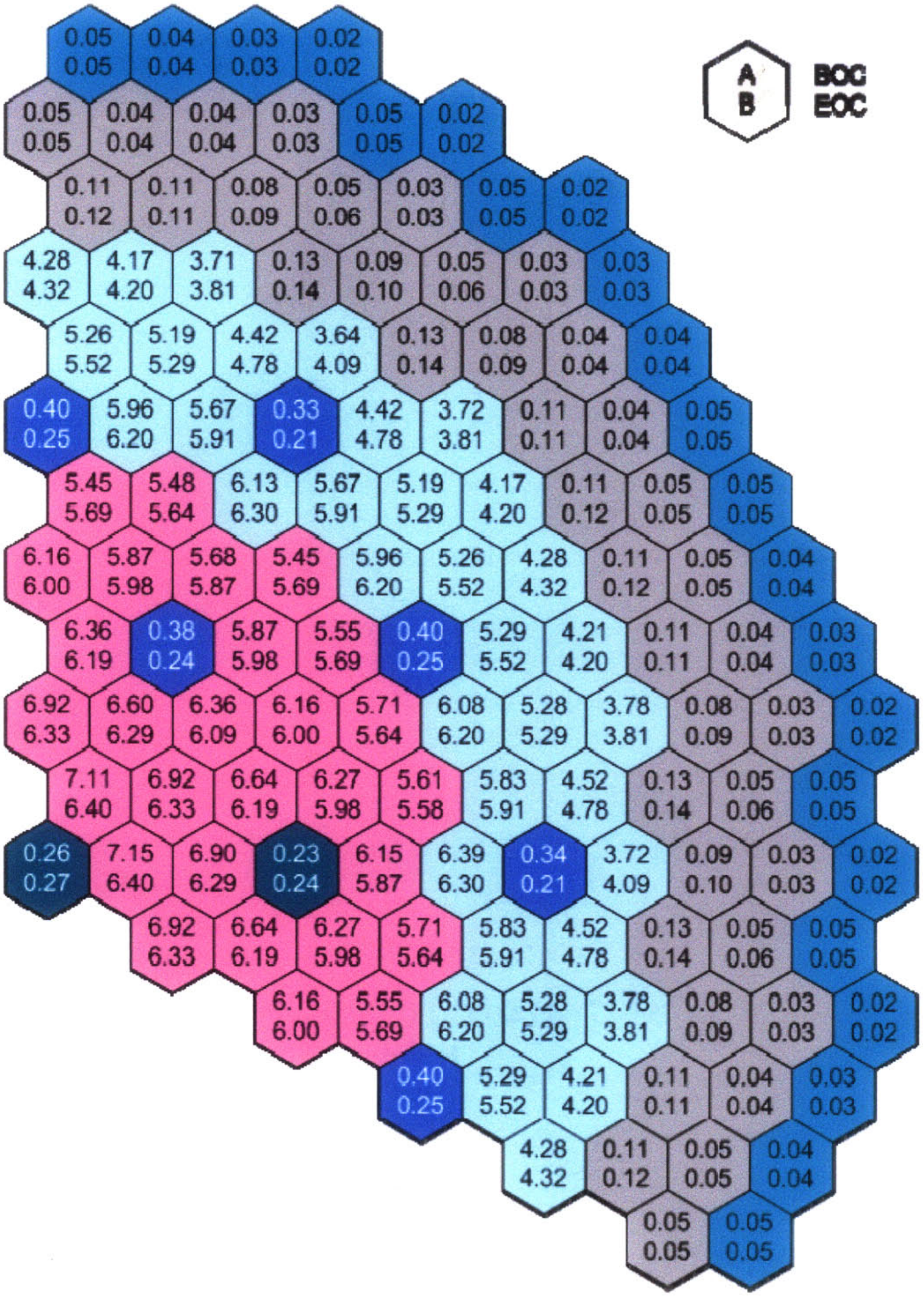

Figure 5.4: Oxide fuel startup core power pofile at BOC and EOC, where the numbers are the power in MW as scaled up from [5.3]

In addition to the power profiles, typical fast reactor reactivity feedbacks were incorporated into the full-plant core model. These included the fuel expansion coefficient, the Doppler coefficient, sodium density coefficient, the axial expansion coefficient, the radial core-expansion coefficient, the vessel expansion coefficient, and the control rod drive-line expansion (CRDLE) coefficient.

The Doppler coefficient and the fuel density coefficients reflect the change in reactivity due to, respectively, temperature-induced fuel resonance broadening and axial and radial leakage from thermal expansion (axial and radial) of the fuel. These are combined into a single fuel/temperature coefficient for the purposes of this model. The sodium temperature coefficient takes into account the reactivity effect of the varying sodium temperature (and thus density) as a temperature changes in the core.

The radial expansion coefficient refers to the "core flowering" effect, which is seen during reactor operation. As the coolant temperature increases as it axially flows through the assembly, the temperature of the structural components of the assemblies also increases, particularly at the core outlet. Because the temperatures of the core structural components are higher at the core outlet than the core entrance, the thermal expansion of the two regions is quite different. The expansion at the core outlet is considerably higher, resulting in an "opening" of the coolant channels at the top of the core, which increases neutron leakage.

The axial expansion coefficient reflects the changes in the fuel rod dimensions (axially and radially) due to thermal expansion. At higher burnups, the fuel contacts the clad, and the thermal expansion of the fuel is limited by the thermal expansion of the clad. Thus the axial expansion coefficient is determined using the average clad temperatures.

The CRDLE coefficient describes the negative reactivity insertion associated with an expanding control rod drive shaft. As the core effluent sodium temperature increases, the control rod drive-line temperature also increases. This induces expansion of the control rod drive-lines, which pushes the control rods further into the core. This introduces a large negative reactivity as every control rod in the core is subsequently partially inserted in the core, reducing reactivity. The CRDLE coefficient is given in terms of $/cm instead of $/°C as are the other reactivity coefficients due to its derivation. This will be described in more detail in Chapter 6. Table 5.2 describes the reactivity feedback coefficients used in the reference core configuration.

The vessel expansion coefficient is a positive coefficient, relating to the effect of thermal expansion on the reactor vessel. As the reactor vessel (which supports the core and internals) expands downward, the core is lowered relative to its original position. The length of rod in-core for all the control rods in the core is thus decreased. This reduces control rod worth, and injects positive reactivity into the core.

Table 5.2: Kinetic and reactivity parameters for a typical SFR core

	Metal Startup Core (BOEC)	Oxide Startup Core (BOEC)
Effective delayed neutron fraction	0.00335	0.00316
Prompt neutron lifetime (μs)	0.36	0.48
Radial expansion coefficient (¢/°C)	-0.39	-0.32
Axial expansion coefficient (¢/°C)	-0.05	-0.05
Fuel density coefficient (¢/°C)	-0.71	-0.46
Vessel expansion coefficient (¢/°C)	0.06	0.07
Sodium temperature coefficient (¢/°C)	0.11	0.10
Doppler coefficient (¢/°C)	-0.13	-0.16

5.1.1.3 RELAP5-3D Full Core Model

A simplified RELAP5-3D model has been developed to evaluate the thermal-hydraulic performance of a typical SFR core, as described in 5.1.1.1 and 5.1.1.2. For simplicity, the various assembly types were "lumped" into a single flow geometry for each assembly type. Thus, the core model has seven separate channels, with a single channel representing each of the six assembly types: inner driver, outer driver, control, reflector, shield, plus a bypass flow channel and the "hottest" fuel assembly flow channel. This core layout is illustrated in Fig. 5.5 (not to scale), which is a side-view of the core channels. The seven channels illustrated in Fig. 5.5 represent, respectively, the 19 control assemblies (primary and secondary) and the thimble bypass region, the 66 shield assemblies, the 114 reflector assemblies, the 102 outer driver assemblies, 77 inner driver assemblies (excluding the hottest channel), the single hottest driver assembly, and the core bypass discussed previously. The colored segments to the right of each flow channel represent a heat structure that was created to model the core (pink), plenum (teal), and shield (gray) regions. The colored segment to the left of each channel represents the assembly duct walls attached to the flow channels on one side and the bypass flow on the other. Note that a partial flow channel has been created to represent the "thimble" or outer flow region of the control assemblies. This segment is attached to the main assembly flow, as illustrated in Fig. 5.5.

A description of the volumes and their labeling scheme is given in Table 5.3. Because of the large computational cost of modeling cross-flow and mixing within a single subchannel, the subchannel model is not included in the full-plant RELAP5-3D model. Thus, the hot assembly is included as a flow channel in the current full-plant core model, and this flow channel is where the maximum clad, coolant, and core temperatures are found throughout both steady state and transient operation of the SFR. Each of the assemblies modeled in the SFR full plant model are assumed to include the duct ribs described in Chapter 4, which results in a nearly flat (~±3°C) radial temperature distribution within each assembly. Thus no hot channel factor is required to model the temperature peaking within the hot assembly.

Each of the seven channels has been axially divided into 26 axial segments of varying length and type. The first two segments represent the flow volume through the nosepiece region, the second two represent the flow volume through lower shielding regions, the next 15 segments represent the flow volume through the core region, the next represent the flow volume through the gas plenum region, and the final two segments represent the flow volume through the duct standoff and handling socket regions.

Table 5.3: Channel description and labeling for the RELAP5-3D core model

Volume Number	Description
001	Flow source
002	Inlet plenum
201	Outlet plenum
202	Flow sink
110	Control assemblies (15 primary / 4 secondary)
190	Thimble bypass (one per control assembly)
132	Shield assemblies (66 assemblies)
131	Reflector assemblies (114 assemblies)
123	Outer driver assemblies (102 assemblies)
111	Inner driver assemblies (77 assemblies)
150	Single hottest assembly
180	Core bypass

Each segment of the fuel channel is linked to appropriate heat structures that represent the assembly duct walls and fuel/absorber/reflector pins.

The RELAP5-3D reactor point kinetics model was employed for the full-core model. A separable point kinetics block was input, and the reference core power of 1000MWth was input as the power generation rate. The heat generation rates for each heat structure were evaluated based on the power distributions depicted in Figs. 5.3 and 5.4 by adding the heat generated by each individual assembly. This summed power generation rate was then divided by the total power of the core and inserted into each individual heat structure input. This fractional value was then used to reference how much of the total power generated in the core (according to the kinetics/power model) is generated within each heat structure. Based on MCNP calculations, the assembly peaking factor (or radial peaking factor) was taken to be 1.28 and 1.31 for metal and oxide core configurations, respectively. The local peaking factor within each assembly was approximated at 1.03 for both metal and oxide fuels. Thus, the power generation in the hottest assembly was conservatively taken to be 1.308 ($=1.28\times1.03$) times the average power generated in the other driver assemblies. This approximation was made to guarantee that the cladding temperature calculated in the hot channel would correspond to the hottest rod. In addition, a chopped cosine axial power profile was assumed with a peaking factor of 1.19. The power generation rates used for each channel are summarized in Table 5.4.

The axial expansion, radial expansion, CRDLE and vessel expansion reactivity feedbacks were insert directly into the RELAP5-3D reactor kinetics block. For the radial expansion, control variables were used to evaluate the average core outlet coolant temperature, and this multiplied by the radial expansion coefficient to determine the reactivity insertion due to radial expansion. The time delay for heat transfer from coolant to above core load pads was neglected. This same procedure was used for axial and vessel expansions, but the temperatures used were the core average clad and the average vessel wall temperatures, respectively. The CRDLE feedback coefficient is based upon the thermal expansion of the control rod drive shaft, and is discussed in more detail in Section 6.2.3. The temperature used to evaluate the thermal expansion was the average temperature along the affected region of the drive shaft, and was determined using control variables within the code.

The Doppler coefficient is required by the code if the reactor kinetics block is used. Both the Doppler coefficient and the fuel density coefficient were summed, and then input in the form of a temperature table. A reference temperature was selected (26.85°C) at which the Doppler and fuel density coefficient combination was 0.0 ¢/°C. The change in Doppler and fuel density reactivity insertions are then entered for each change in temperature. These reactivity insertions are then applied to each individual fuel rod structure segment based upon heat structure weighting factors, which are essentially the fraction of power generated in the relevant heat structure. The sodium temperature coefficient is also required by the RELAP5-3D code, and is evaluated by multiplying the feedback coefficient by the power fraction weight in each volume

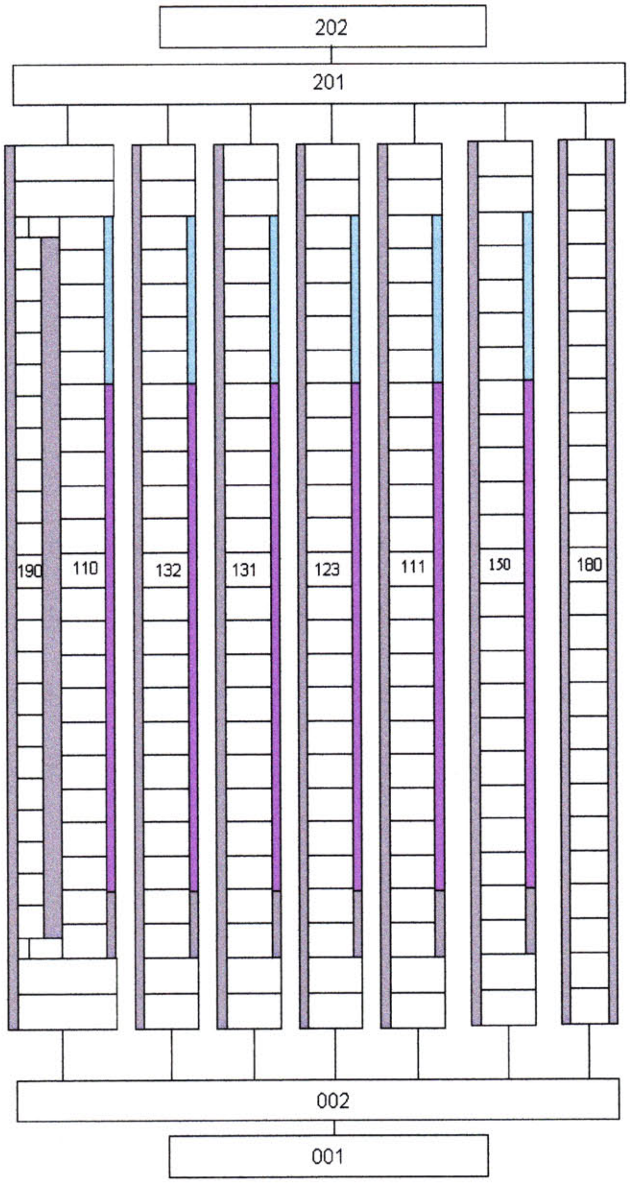

Figure 5.5: RELAP5-3D nodalization diagram for the reference core

Table 5.4: Heat generation rates in the reference metal fuel SFR core

Assembly	Power (MW)
Control	7.35
Inner driver	481.16
Outer driver	492.27
Hot channel	7.18
Reflector	8.37
Shield	3.39
Total:	**999.69**

Orificing of the channels was accomplished by introducing restricted junctions between the inlet plenum and the individual channels. The flow area for each junction was iteratively determined such that the outlet coolant temperature difference was as small as possible. For the metal fueled CR=0.71 core, the difference was ~15 °C, while in the oxide fueled core, this difference was ~33 °C. Both of these temperature gradients are within the generally accepted limit of 44°C [5.4]. The orifice junction was assumed to represent a sudden area contraction with a rounded edge, and was hence modeled as a form loss coefficient applied to the appropriate junction, with a value of K_L=0.2. The type of restriction was unchanged from orifice to orifice; only the area of each orifice was adjusted. Table 5.5 lists the orifice areas required to produce the core outlet distributions listed above.

Table 5.5: Orificing areas required to minimize the assembly outlet temperature distributions in both metal and oxide core designs

	Area (m^2)	
Orifice Area (m2)	**Metal Fuel**	**Oxide Fuel**
Hot assembly	-	-
Inner driver	0.0900	-
Outer driver	0.2200	0.2000
Control	0.0022	0.0073
Reflector	0.0016	0.0012
Shield	0.0007	0.0006
Bypass	0.0025	0.001

The clad properties were based upon ss-316, which was used as a surrogate from HT9. The sodium properties in the full-plant model were the same as those used for the subchannel analysis model [2.2], while the fuel model was taken from property tables calculated by Billone et al. [5.6] (where the unirradiated material thermal conductivities are multiplied by 0.7 to account for the long term effects of radiation. The bond properties (conductance, etc) for the metal fuel are the same as the sodium properties, while the gap properties for the oxide fuel were evaluated in RELAP5-3D base upon the code's internal gap properties model [5.5]. Finally, the decay power curve was estimated by assuming that the fission decay power was generated by only Pu-239, according to the ANSI standard [5.7]. In the analysis of fast reactors, this assumption produces a more appropriate decay power curve than the standard LWR model included in RELAP5-3D. The reasoning for selecting this decay power curve rather than calculating a decay power curve specific to each core is discussed in Section 6.2.2.

The hydraulic resistance of the flow channels for turbulent flow conditions is calculated using the same methodology as was described in Section 2.1.3, only the hydraulic diameter and flow areas correspond to the entire assembly, rather than a single subchannel. For laminar flow, however, a different friction factor must be used. The laminar shape factor, Φ, defined as [5.8]:

$$\Phi = \frac{64}{C_{fL}}, \tag{5.4}$$

where C_{fL} is defined as the laminar drag coefficient, defined as:

$$C_{fL} = \left[-974.6 + 1612 \cdot \frac{P}{D_o} - 598.5 \cdot \left(\frac{P}{D_o} \right)^2 \right] \cdot \frac{H_w}{D_o}^{\left(0.06 - 0.085 \cdot P/D_o \right)}. \tag{5.5}$$

The laminar shape factor, f_L is then calculated by the equation:

$$f_L = \frac{64}{\Phi \cdot \mathrm{Re}}. \tag{5.6}$$

Both the laminar shape factor and the turbulent friction factor were used in the RELAP5-3D full-plant core model to evaluate the hydraulic resistances, and thus pressure drop across the core.

Steady-state calculations of the standalone core model described in this section were run to verify that the model was working as expected. Fig. 5.6 illustrates the axial temperature profile for the sodium coolant in each channel of the model. As should be expected, the sodium temperature rises steadily along the length of the active core (nodes 4-19). Once the sodium enters the gas plenum region, the temperature profile largely levels off. A notable exception is seen for the reflector assemblies and the bypass channel; the sodium in these channels continues to heat up as heat is transferred from the hotter channels to these cooler channels by conduction. As expected, the highest outlet temperature is found in the hot assembly. For this assembly, the outlet temperature is computed to be 636.35 °C. The peak cladding temperature in the hot assembly is computed to be 546.9°C, well below the assumed safety limit of 650°C. In addition, the peak centerline temperature in the fuel rod is 758.4°C. The pressure drop across the core has been computed as 0.376 MPa, and the maximum outlet temperature difference is 37.7°C, which is below the design limit of 44°C.

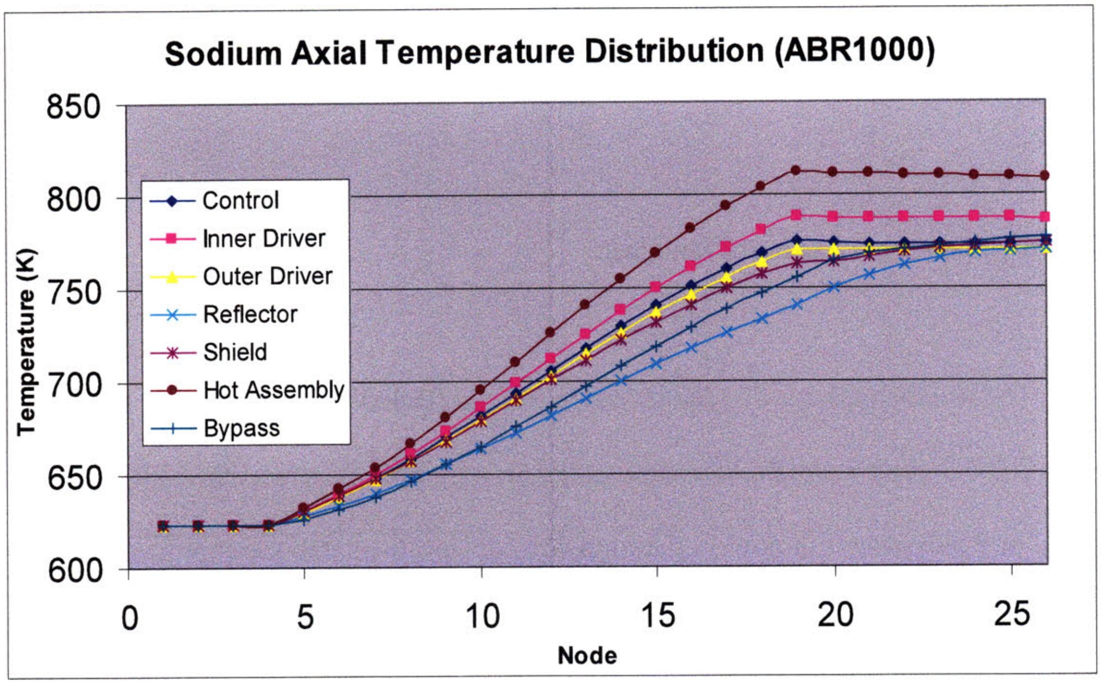

Figure 5.6: RELAP5-3D nodalization diagram for a typical SFR core

Having verified the general performance of the standalone core model against basic engineering judgment (using the metal fuel core), this complete core model was then utilized in combination with the other four components described later in this chapter to create the full-plant model.

5.1.2 Primary Pool System

The SFR full-plant design is a pool-type, 1000MWth plant with minimal piping in the primary system. This design minimizes potential sodium leakage through extensive sodium piping networks. The primary pool is several meters below the secondary loop, so as to maintain a large enough head that any break in the IHX tubing will result in secondary sodium draining into the primary pool, rather than primary sodium draining into the secondary system. The details of the primary pool utilized in the modeling are described below.

5.1.2.1 Primary Pool Sodium Flow Path

The reactor vessel is divided by a steel shroud (called the redan) into hot and cold pools. Fig. 5.7 gives a simple schematic of the primary pool system of the SFR full-plant model. In steady-state full power operation, the coolant flows into the core from the inlet plenum (depicted as a blue rounded rectangle at the bottom of the core barrel in Fig. 5.7), where it is heated by the fuel rods in the core. The hot sodium leaves the core with a temperature of 510 °C, and flows up through the Upper Internals System (UIS). The distance between the core outlet and the UIS is ~7.62 cm.

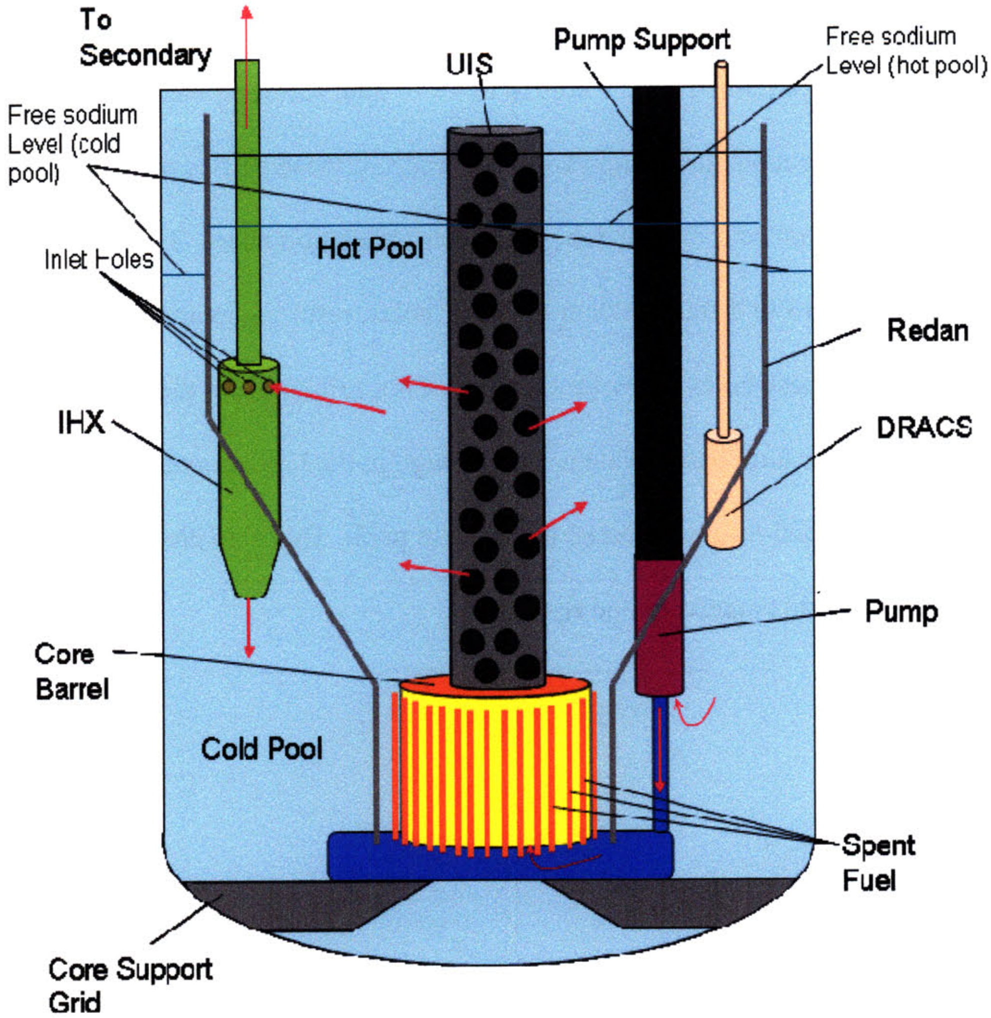

Figure 5.7: Schematic of the key components of the SFR pool-type primary system, including DRACS emergency systems

The UIS is a large, 2.2 meter diameter cylinder with a total length of ~6.467 m and is composed of 1cm thick ss-316 steel surrounding the primary and secondary control rod drivelines, along with the instrumentation needed to maintain steady-state core operation. The UIS also serves as a location for the core effluent sodium to mix thoroughly so as to prevent thermal striping or other mixing induced effects further downstream, particularly in the intermediate heat exchangers (IHX's). The coolant flows upward through the UIS, past a series of three perforated baffles (surface porosity of 75%, where the surface porosity is the area of holes to total surface area), at which point a solid baffle plate prevents further upward flow. Each of these baffles contain perforations for the control rod guide tubes and instrumentation tubes. The UIS shroud is perforated with over 1370 different 20cm diameter holes, resulting in an overall surface porosity of ~50%. These holes allow for the flow of hot sodium from the UIS into the sodium hot pool. The solid baffle plate is located high in the UIS structure, at which point all of the hot sodium flow is forced into the hot pool. This is to ensure that the surface of the hot pool is quiescent and ripple free.

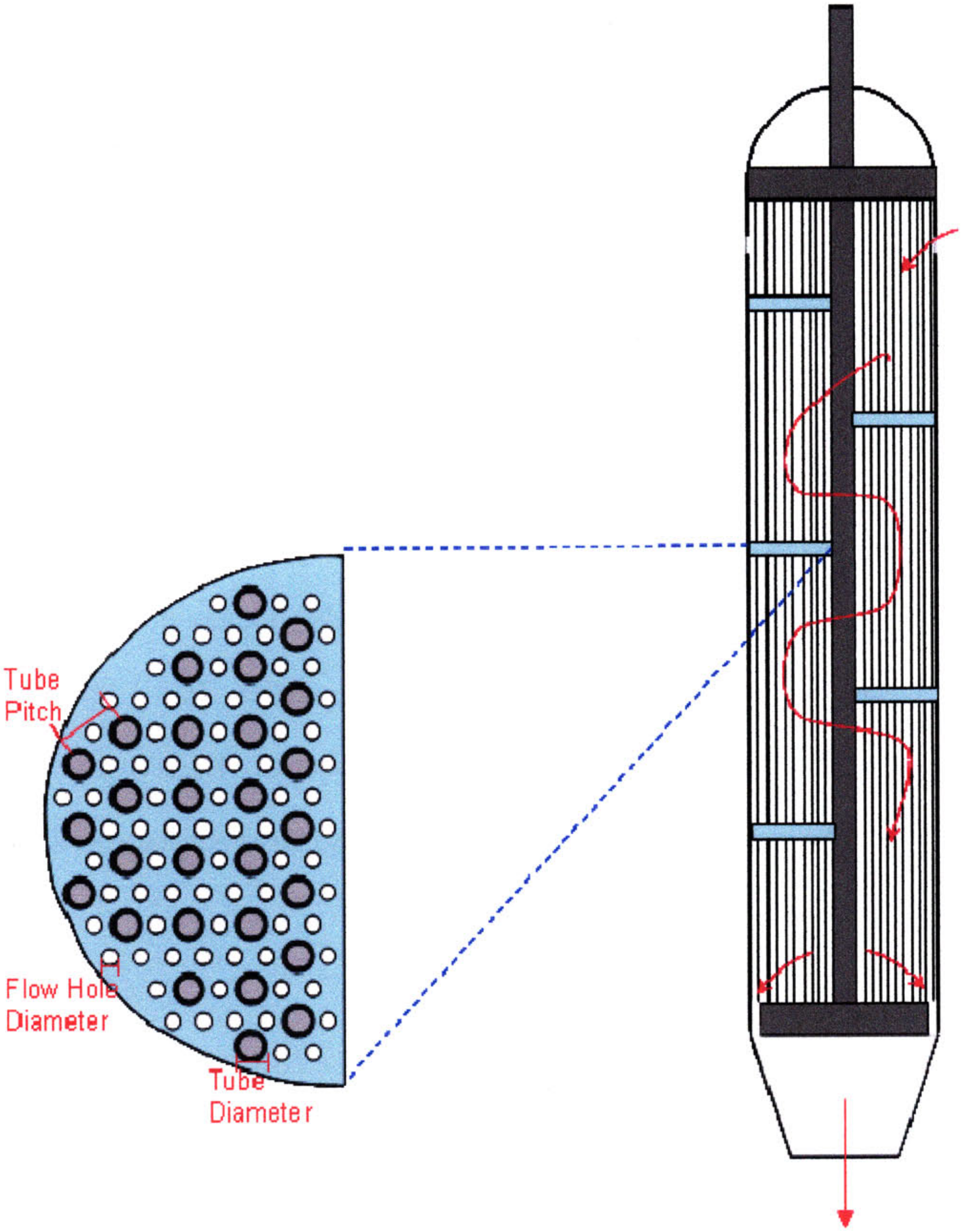

Figure 5.8: Schematic of primary pool IHX including baffle plate detail

The hot sodium in the hot pool then flows into one of the four IHX's via a series of eight different 20 cm diameter inlet holes surrounding the top outer wall of the IHX. The hot sodium then flows through the shell side of the tube and shell IHX, heating the tube-side secondary sodium. There are five perforated baffles spaced evenly throughout the IHX shell, which partially divert the sodium flow, enhancing heat transfer in the shell side. A perforated baffle profile, along with other aspects of the IHX design, are shown in Fig. 5.8, while key design parameters of the IHX are found in Table 5.6. The primary sodium then exits the IHX by flowing downward through the 61 cm diameter IHX outlet nozzle into the primary cold pool. The temperature of the IHX effluent entering the cold pool is ~355 °C.

The secondary side sodium flows through a downcomer and enters the IHX at a temperature of 333 °C, where it flows (still in the downcomer) through the entire length of the IHX. At the bottom of the IHX, the secondary sodium flow enters a plenum where it turns 180° and flows upwards through a series of tubes. This is where the primary heat transfer takes place in the IHX to the secondary sodium. The secondary sodium enters a plenum above the upper tube sheet where it flows into an annular pipe surrounding the downcomer with an outlet temperature of 488 °C.

Table 5.6: Key design parameters of the IHX's in the primary system

Parameter	Value
Heat transfer capacity (MWt)	250
Heat exchanger design	Straight tube, counter-flow
Heat transfer area (m^2)	1074
Primary sodium temperature inlet (°C)	510
Primary sodium temperature outlet (°C)	355
Primary sodium mass flowrate (kg/s)	1256
Secondary sodium temperature outlet (°C)	488
Secondary sodium temperature inlet (°C)	333
Secondary side sodium mass flowrate (kg/s)	1256
Tube outer diameter (cm)	1.59
Tube wall thickness (mm)	0.889
Tube pitch (cm)	2.23
Active tube length (m)	4.78
Number of tubes	4500
Upper tube sheet - area (m^2)	2.25
Upper tube sheet - thickness (cm)	10

Lower tube sheet - area (m^2)	2.25
Lower tube sheet - thickness (cm)	10
Downcomer piping - OD (cm)	61
Downcomer piping - thickness (mm)	12.7
Downcomer piping - length (m)	10.8
Outlet piping - OD (cm)	86.4
Outlet piping - thickness (mm)	12.7
Outlet piping - length (m)	6.6
Shell baffle plates - thickness (mm)	6.4
Shell baffle plates - number (spacing - cm)	5 (91)
Baffle plate cut (transverse dist. across IHX not occluded by plates) (%)	50
Baffle plat perforation (open flow area/ total axial flow area) (%)	45
Perforation hole diameter (mm)	8.12
Number of perforation holes per IHX tube	2
Shell (primary) side pressure drop (kPa)	18.2
Tube (secondary) side pressure drop (kPa)	14.8
Shell height (m)	5.88
Shell outside circumference (m)	5.4
Shell thickness (cm)	1.3
Shell cross-sectional area (m^2)	2.32
Tube material	9Cr-1Mo

Within the cold pool, just below the conical portion of the redan, there are three protrusions into the redan into which are inserted the DRACS exchangers. In the middle portion of the cold pool, below the IHX outlet, are four electro-magnetic (EM) double stator annular linear induction pumps (ALIP). These pumps by necessity have entrance and exit in the bottom side of the pump. These pumps have been designed for use in the advanced burner test reactor (ABTR) and further details of their operation can be found in the design report for the ABTR [5.3]. The EM ALIP pumps used in the full-plant model described here are a scaled up version of the EM ALIP pumps designed for the ABTR. A schematic of these pumps can be seen in Fig. 5.9. Key parameters of the EM ALIP pumps can be found in Table 5.7. These pumps are suspended by a shaft connected to the rotating plug at the reactor vessel head. The cold pool liquid sodium is drawn in to the pump inlet where it flows the length of the pump through the return duct, at which point it turns 180 degrees and flows through the central duct of the EM ALIP pump. The pump effluent is piped directly into the core inlet plenum, where it enters the core.

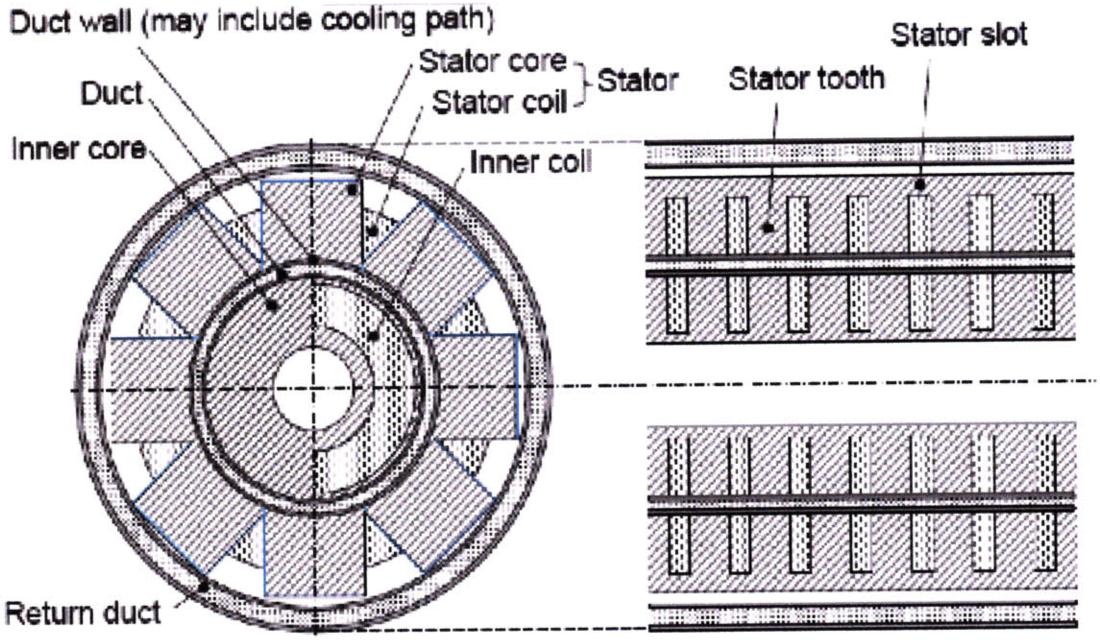

Figure 5.9: Schematic of a double stator ALIP EM pump[5.3]

Table 5.7: Key design parameters of the EM double stator ALIP pumps

EM Pump Parameters	
Power (kW)	2315
Efficiency (%)	48.6
Mass (kg)	6176
Number of poles	8
Number of coils	24
Temperature (°C)	355
Flow rate, (m^3/s)	1.51
Discharge pressure (kPa)	758.423
Length (m)	1.6
Pump diameter (m)	1.18

5.1.2.2 Primary Pool RELAP5-3D Model

The sodium pool RELAP5-3D model is composed of several pipes and branches representing the cold and hot pools with separate components representing the IHX and pump components. A complete nodalization of the primary system RELAP5-3D model is shown in Fig. 5.10. Table 5.8 lists descriptions of each of the components in the primary model, along with their labeling scheme. The hot pool is composed of three pipe components and two branch components. The branch components represent the core outlet and IHX inlets, while the pipe components represent the lower, middle, and upper hot pool segments. These segments represent the spent fuel storage region, the hot pool below the IHX inlet, and the hot pool above the IHX, respectively.

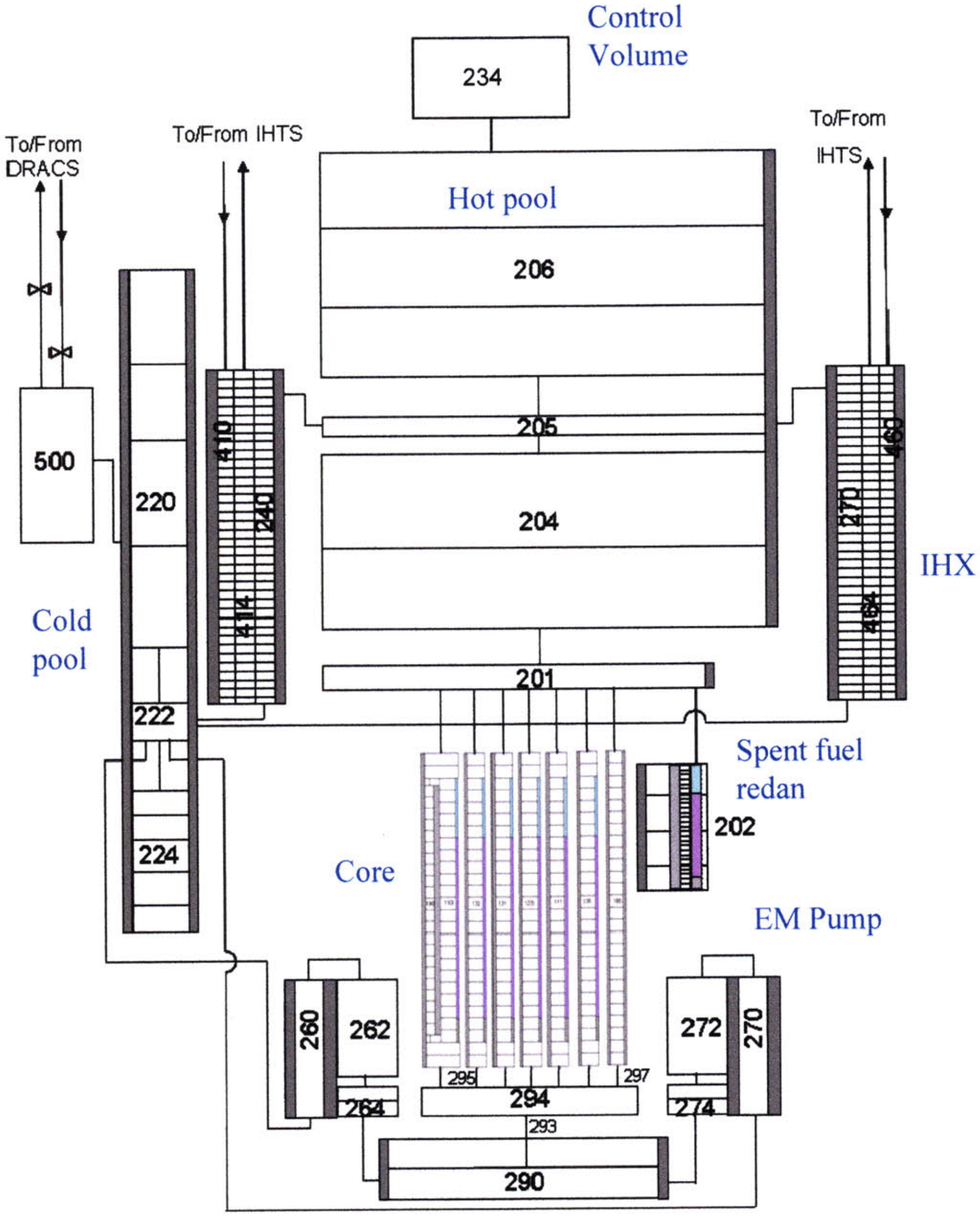

Figure 5.10: Nodalization diagram of primary system (cold and hot pools) RELAP5-3D model

The IHX model consists of a pipe component representing the primary shell side of the exchanger and two pipe components representing the downcomer and exchanger tubes on the secondary side. The IHX baffles were modeled in RELAP5-3D using junction restrictions. In essence, the baffle occludes 50% of the shell side flow area, while the baffle surface perforation is 45%. Thus, the total flow area at each baffle (represented by a junction between the relevant pipe modules) is reduced to 72.5% of the flow area of the shell side. The RELAP5-3D abrupt area option is used in tandem with this area change to approximate the effect of the baffles, as depicted in Fig. 5.11. In this figure, the red lines represent either the IHX inlet junction, or the flow area at each baffle. The volume segments are numbered sequentially from top to bottom. At the bottom of the exchanger, a thin duct allows flow past the lower tube sheet, and this is reflected in the decrease flow area in segments 58-51 of the IHX nodalization. Finally, after entering the lower plenum segment (segment 52), the sodium exits the IHX via the outlet nozzles, represented by segments 53-54. The pressure drop correlation in the first 47 segments is based upon the pressure drop across a bare rod bundle, with abrupt constrictions at the key junctions representing a baffle. The pressure drop in the lower segments is calculated by RELAP5-3D as open geometries with abrupt area change models where needed. This approach is a simplifying approximation of the effect of the baffles and duct flow in the IHX; a detailed depiction of the flow path through and around the baffles approach would require a CFD model, and is beyond the scope of this thesis. The heat transfer coefficient in this region was calculated by the code based upon the vertical bundle boundary condition option for the geometry described in Section 5.1.2.1.

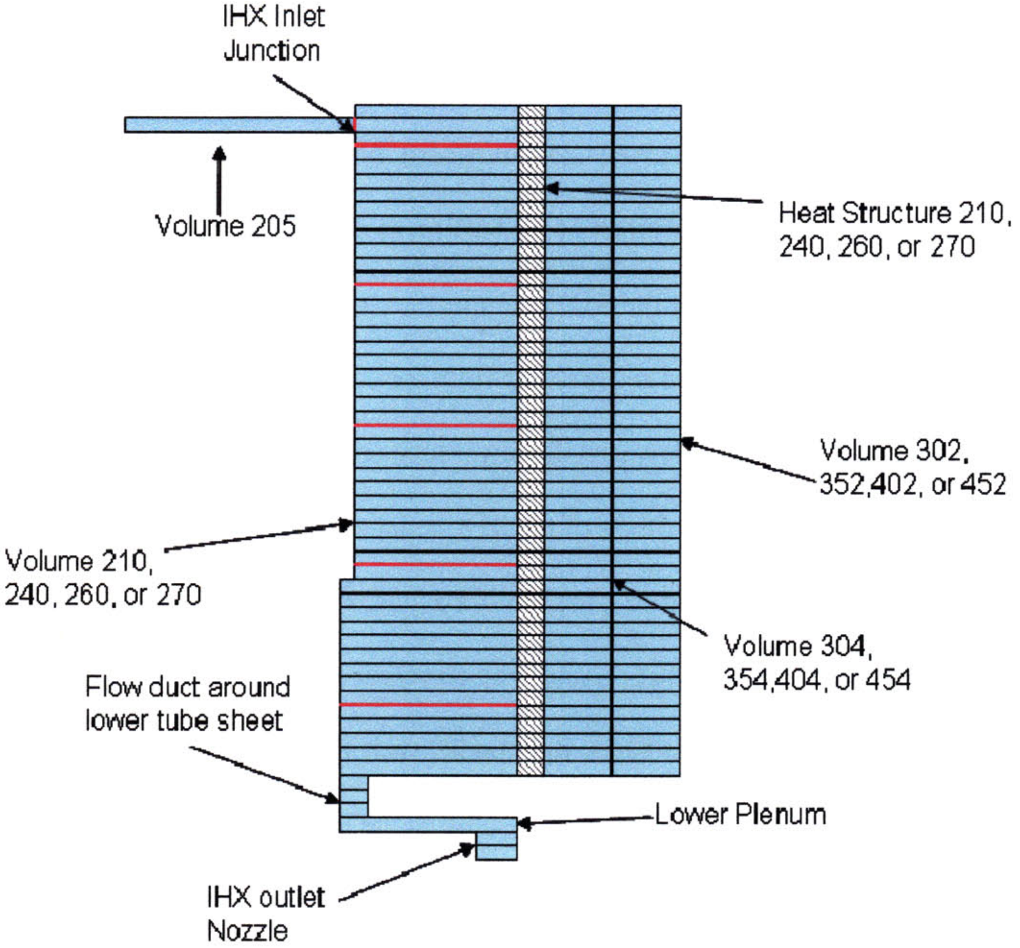

Figure 5.11: Detailed nodalization diagram of IHX model including baffle and inlet junctions (depicted as red lines), lower tube sheet bypass flow, lower plenum, and IHX outlet nozzles

Note that a single junction leads serves as the IHX inlet. This junction is a lumped representation of each of the inlet holes described in section 5.1.2.1, with a cross sectional flow area equal to the combined area of the inlet holes. The junction height is 20 cm, and since the inlet holes are all at the same vertical height along the IHX tube, this accurately represents the vertical height of each inlet hole.

The upper cold pool and lower cold pools are each represented by a pipe component, while a single branch serves as the IHX outlet and pump inlets. The pumps are composed of a pipe representing the return duct, with a mechanical pump component as the pump itself. A pipe component represents the piping into the core inlet plenum, while the inlet plenum itself is modeled using a branch. Flow is then directed from the inlet plenum into either the core bypass channel or one of the seven flow channels described in section 5.1.1. The flow through each channel is determined by the flow rate that equalizes the pressure drop across all the channels.

Table 5.8: Channel description and labeling for the RELAP5-3D primary system model (cold and hot pools)

Component Number	Type	Description
201	Branch	Core outlet branch
202	Pipe	Lower hot pool/spent fuel storage
204	Pipe	Middle hot pool
205	Branch	IHX inlet branch
206	Pipe	Upper hot pool
240,250,260,270	Pipe	Shell side of IHX 1, 2, 3, and 4
220	Pipe	Upper cold pool
222	Branch	IHX outlet and EM pump inlet branch
224	Pipe	Lower cold pool
260, 270	Pipe	Pump inlet return duct
262, 272	Pump	EM pump
264, 274	Pipe	Pump outlet piping
290	Pipe	Inlet plenum
293	Junction	Junction to core inlet
294	Branch	Core inlet path
295	Multiple Junction	Connection to 7 flow paths in core
297	Junction	Connection to core bypass flow path
410, 460, 510, 560	Pipe	IHX secondary side downcomer
414, 464, 514, 564	Pipe	IHX secondary side flow tubes

The sodium free surfaces for the hot and cold pool were not modeled explicitly in this RELAP5-3D model. The sodium pool surface elevations do play a role in natural circulation flows, however, and future work should develop a model to evaluate the levels of these pools. In order to prevent artificial pressure increases due to thermal expansion of sodium coolant in primary system, an inventory control volume was modeled above the hot sodium pool. This volume is a time dependent volume connected to the upper surface of the hot pool (volume 206, segment 3) via a standard junction. This allows for free flow of sodium in order to maintain a constant pressure at the surface of the sodium hot pool. Even though the free level changes were not explicitly modeled for the hot and cold pools, they can be approximated using the code output by measuring the mass flow through this junction. A negative flow through the junction corresponds to a decrease in the elevation of the free level, and the change in the elevation of the sodium pool surface can be calculated based upon the total amount of sodium that flowed through the junction and the hot pool cross sectional area positive flow through the junction corresponds to an increase in the elevation of the free level, and the net change can again be calculated based upon the total volume of sodium that has flowed through the junction and the hot pool cross sectional area. For simplicity, the control volume was connected only to the hot pool. This is acceptable for the current investigation, since the primary purpose is to provide a comparison of innovative fuels to standard fuels, not to provide a detailed evaluation of the ABR1000 reference design. However, future work should focus on incorporating an in code system for evaluating the sodium surface level for both hot and cold pools.

Heat structures representing the redan, vessel wall, core barrel, pump walls, and inlet plenum walls were connected to the corresponding volumes. The heat transfer between primary and secondary sodium flows is calculated using RELAP5-3D heat structure models. The primary inputs to the heat structure models include the material properties and the heated lengths. It is assumed that each structure in the primary pool is composed of SS-316. The heated length (L_H) for each component is calculated using the equation:

$$L_H = L \cdot N, \tag{5.7}$$

where L is the heat structure segment length and N is the number of structures associated with each segment. The dimensions of the heat structure input into RELAP5-3D correspond to the dimensions of the individual structures within the segment. For example, in the IHX, the heated length is calculated by multiplying the segment length by the number of secondary tubes in the heat structure. The inner and outer radii of the heat structure then correspond to the inner and outer radii of the individual heat exchanger tubes. This procedure is then repeated for every heat structure in the full-plant model. Table 5.9 summarizes the key parameters of each heat structure in the primary pool of the full-plant model.

Table 5.9: Key parameters of the RELAP5-3D heat structures in the primary pool portion of the full-plant model

Heat Structure	Description	Segments	Inner Radius (m)	Outer Radius (m)	Heated Length (m)
12011	Middle redan	1	2.213	2.233	0.861
-		2	2.213	2.233	1.627
12021	Lower redan	1	2.503	2.603	1.723
12041	Upper redan	2	6.599	6.699	1.123
12051	Upper redan	1	6.599	6.699	0.200
12061	Upper redan	1	6.599	6.699	0.850
-		2	6.599	6.699	0.763
12021	Spent fuel rods - shield	2	0.000	0.004	65.100
12031	Spent fuel rods - plenum	5	0.348	0.004	52.080
12041	Spent fuel rods - core	15	0.000	0.004	11.573
12101	IHX tubes	1	0.493	0.495	0.300
-		1	0.493	0.495	0.200

-		1	0.493	0.495	0.540
-		45	0.493	0.495	0.092
-		1	0.493	0.495	0.100
-		1	0.493	0.495	0.190
-		1	0.493	0.495	0.130
-		1	0.493	0.495	0.100
-		2.000	0.493	0.495	0.315
12501	Reactor vessel	2.000	7.030	7.081	0.100
-		1.000	7.030	7.081	1.123
-		1.000	7.030	7.081	2.584
-		1.000	7.030	7.081	0.630
-		1.000	7.030	7.081	0.297
-		1.000	7.030	7.081	0.969
-		1.000	7.030	7.081	0.321
-		1.000	7.030	7.081	0.963
-		1.000	7.030	7.081	0.963
-		1.000	7.030	7.081	1.605
12601, 12701	EM pump outer wall	1.000	0.588	0.590	0.297
-		1.000	0.588	0.590	0.630
-		1.000	0.588	0.590	0.673
12621, 12721	EM pump duct wall	1.000	0.215	0.488	1.600
12641, 12741	EM pump inner core	1.000	0.314	0.331	0.969
-		1.000	0.588	0.590	0.321
-		1.000	0.588	0.590	0.963
-		1.000	0.588	0.590	0.563
12901	Core inlet plenum wall	1.000	2.368	2.408	0.100
-		1.000	2.368	2.408	0.790
-		1.000	2.368	2.408	0.200
11804	Core barrel wall	2.000	1.776	1.801	0.178
-		2.000	1.776	1.801	0.622
-		15.000	1.776	1.801	0.054
-		2.000	1.776	1.801	0.302
-		2.000	1.776	1.801	0.546

Each pipe segment requires a set of inputs that includes, but is not limited to: the number of volumes, the length of each volume, the hydraulic diameter of each volume, and the flow area of each volume. The length and number of volumes is adjusted arbitrarily to accurately represent the overall length of the pipe while optimizing the steady state and transient runtimes of the model. This will be discussed further in Section 5.2. The flow area and hydraulic diameter of each volume are dictated by the flow properties of each individual component. The hydraulic diameter for each pipe is calculated using Eq. (4.15), while the flow area for each component is calculated using simple geometric relations. For example, the total actual volume of sodium (V_{ST}) in the conical section of the hot pool, which accounts for sodium displaced by the DRACS, IHX, UIS, and Instrumentation and controls, is calculated using the equation:

$$V_{ST} = V_{CR} - V_{PS} - V_{DRACS} - V_{IHX} - V_{UIS} - V_I , \tag{5.8}$$

where:

V_{CR} = total volume within the conical segment of the hot pool

V_{PS} = total volume occupied by the pump shafts within the cone region

V_{DRACS} = total volume occupied by the DRACS protrusions within the cone region

V_{IHX} = total volume occupied by the IHX within the cone region

V_{UIS} = total volume occupied by the UIS within the cone region

V_I = total volume occupied by the instrumentation/controls within the cone region.

Once the total volume for the conical section of the hot pool is calculated, a pipe segment is created to represent this portion of the hot pool in the RELAP5-3D full-plant model. The height of the pipe segment (H_{CR}) is equivalent to the height of the conical segment of the hot pool, while the flow area (A_{flow}) of this pipe segment is calculated by the equation:

$$A_{Flow} = \frac{V_{ST}}{H_{CR}}. \qquad (5.9)$$

This process is repeated for every pipe in the RELAP5-3D full-plant model. Table 5.10 summarizes the key parameters of each pipe in the primary pool of the full-plant model.

Table 5.10: Key parameters of the RELAP5-3D pipe segments included in the primary pool portion of the full-plant model

Component	Volumes	Flow Area (m^2)	Length (m)	Hydraulic Diameter (m)
201	1	84.499	1.405	4.764
202	2	3.747	1.627	0.483
-	1	8.967	0.861	0.483
-	1	84.499	0.242	4.766
204	2	132.031	1.123	6.483
205	1	132.216	0.200	1.322
206	1	132.761	0.820	6.647
-	2	132.761	0.763	6.647
210, 260, 410, 440	1	4.537	0.300	0.195
-	1	4.537	0.200	0.195
-	1	4.537	0.054	0.195
-	31	4.537	0.917	0.195
-	14	6.822	0.917	0.029
-	1	2.285	0.100	0.200
-	1	2.285	0.190	0.200
-	1	2.285	0.130	0.379
-	1	9.280	0.100	1.540
-	2	4.676	0.315	0.610
220	1	13.859	0.100	0.642
-	2	13.859	1.123	0.642
-	1	81.347	2.584	3.916
-	1	132.537	0.630	6.257
224	1	138.219	0.969	7.338
-	1	138.219	0.321	7.338
-	1	138.219	0.963	7.338

-	1	82.385	0.963	4.442
-	1	50.458	1.605	0.992
222	1	134.910	0.297	7.338
260, 270	1	0.676	1.600	0.200
262, 272	1	0.405	1.600	-
264, 274	1	0.618	0.969	0.627
-	1	0.618	0.321	0.627
-	1	0.618	0.963	0.627
-	1	0.618	0.963	0.627
290	1	70.466	0.079	-
-	1	70.466	0.100	-

The EM ALIP pump is modeled in RELAP5-3D using the standard mechanical pump model. Though this model is not typically utilized for EM pumps, the RELAP5-3D mechanical pump model can adequately model the performance of an EM ALIP pump, so long as appropriate EM characteristic curves (pressure head vs. flow rate) and parameters are input into the model [5.9]. The parameters and characteristic curves of the EM pump found in the ABTR report [5.3] were scaled up to create pumps for the SFR full-plant model. For the primary pool model, there are four EM ALIP pumps, but for simplicity in modeling, these were lumped into two separate pumps. Lumping the pumps is similar to lumping volumes using RELAP5-3D, except that the rated torque and flow rates are doubled. The characteristic curves for the primary EM pumps are found in Fig. 5.12. For standard pump modeling, several empirically derived performance curves known as homologous curves are created using dimensionless parameters defined by pump operation. The formulation of these homologous pump curves requires a description of the efficiency of the pump and the head generated at various flow rates. There are eight separate homologous curves, each curve corresponding to the pump performance for given condition of operation. There are two homologous pump curves for each of four conditions of pump operation, defined by the pump head and shaft speed:

two curves representing normal pump operation (positive pump head and positive pump speed), two curves representing pump dissipation (negative pump head and positive pump speed), two curves representing turbine operation (negative pump head and negative pump speed), and two curves representing reverse pump operation (positive pump head and negative pump speed) [5.10]. In each region, the two curves are differentiated by dependence on either flow or speed. Table 5.11 summarizes each of the variables associated with the eight homologous pump curves. Each of these curves for all regions of pump operation except for the turbine operation region must be input into RELAP5-3D in order to ensure appropriate operation of the EM ALIP pumps. Thus, using the data from the EM pump curves in Fig. 5.12 and the rated conditions described in Table 5.7, homologous curves were generated to describe the performance of the EM pumps in various regimes [5.9].

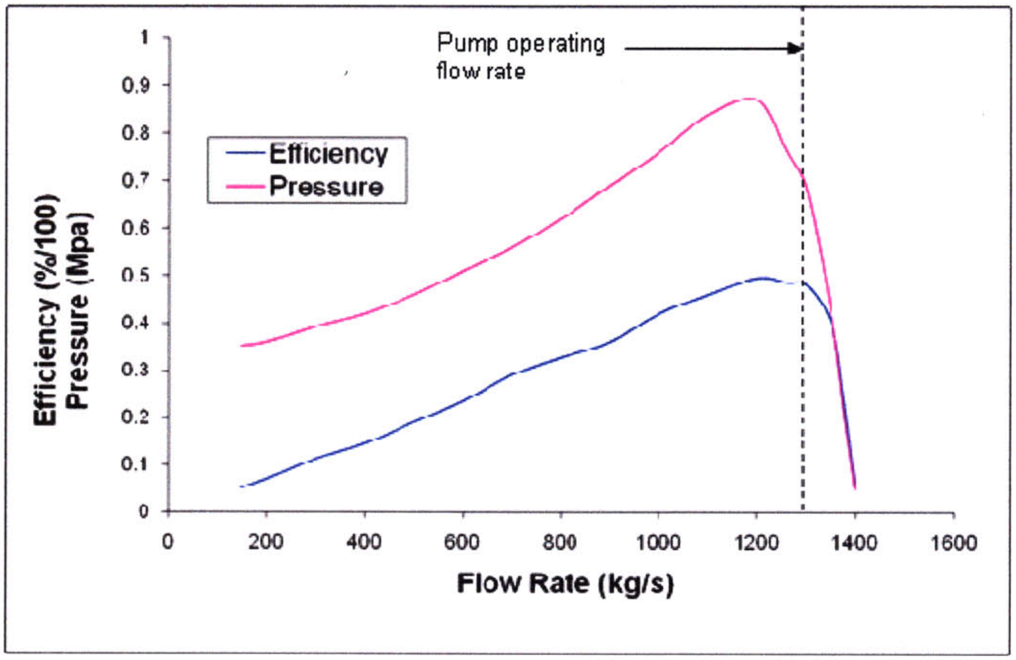

Figure 5.12: Empirical pump and efficiency curves based upon EM ALIP pumps as a function of mass flow rate through the pump

The homologous pump curves are based upon four primary dimensionless parameters: rotational ratio (α), flow ratio (v), head ratio (h), and torque ratio (β). These dimensionless parameters are calculated using the equations:

$$\alpha = \frac{N}{N_R}, \tag{5.10}$$

$$v = \frac{Q}{Q_R}, \tag{5.11}$$

$$h = \frac{H}{H_R}, \tag{5.12}$$

$$\beta = \frac{\tau}{\tau_R}, \tag{5.13}$$

where:

N = pump shaft speed (rad/s)

N_R = rated pump shaft speed (rad/s)

Q = flow rate (m^3/s)

Q_R = rated flow rate (m^3/s)

H = pump head (m)

H_R = rated pump head (m)

τ = pump torque (N-m)

τ_R = rated pump torque (N-m).

Table 5.11: Summary of homologous pump curves describing various regions of pump performance [5.10]

Regime number	Regime mode ID name	α	v	v/α	Independent variable[a]	Dependent[a] variable head	Dependent[a] variable torque
1	HAN BAN Normal pump	> 0	≥ 0	≤ 1	v/α	h/α^2	β/α^2
2	HVN BVN Normal pump	≥ 0	≥ 0	> 1	α/v	h/v^2	β/v^2
3	HAD BAD Energy dissipation	> 0	< 0	≥ -1	v/α	h/α^2	β/α^2
4	HVD BVD Energy dissipation	≥ 0	< 0	< -1	α/v	h/v^2	β/v^2
5	HAT BAT Normal turbine	< 0	≤ 0	≤ 1	v/α	h/α^2	β/α^2
6	HVT BVT Normal turbine	< 0	≤ 0	> 1	α/v	h/v^2	β/v^2
7	HAR BAR Reverse pump	< 0	> 0	≥ -1	v/α	h/α^2	β/α^2
8	HVR BVR Reverse pump	< 0	> 0	< -1	α/v	h/v^2	β/v^2

---

a. α = rotational ratio; v = volumetric flow ratio; h = head ratio; and β = torque ratio. Note: For the case $\alpha = 0$ and $v = 0$ in regime 2, $h = 0$ and $\beta = 0$.

The pump flow rates and corresponding pump heads and pump efficiencies (η) are taken directly from pump performance curves. The pump head and torque are calculated using the equations:

$$H = \frac{\Delta P}{\rho g}, \tag{5.14}$$

$$\tau = \frac{\rho_R Q g H}{N\eta}, \tag{5.15}$$

where g is the gravitational constant, ρ is the density of fluid in the pump, and ρ_R is the rated density of fluid in the pump. The head and torque homologous pump curves representing normal pump operation of the primary EM pumps are found in Fig. 5.13. Each of the four bounding homologous pump curves (curves 3, 4, 7, and 8) must be input, however, in order for RELAP5-3D to correctly initialize the pumps. Therefore, simple curves consisting of constant values taken from the boundaries of curves 1 and 2 have extrapolated constant values. These curves are thus not accurate depictions of pump operation in the various regions. Only the pump curves that represent normal operation (regions 1 & 2) are utilized in the actual operation of the full-plant SFR model, however, and thus this approximation is sufficient for the current thesis. These curves are included in the full-plant SFR model only as placeholders required by RELAP5-3D, and should be calculated if pump performance in dissipation or reverse regions is to be investigated.

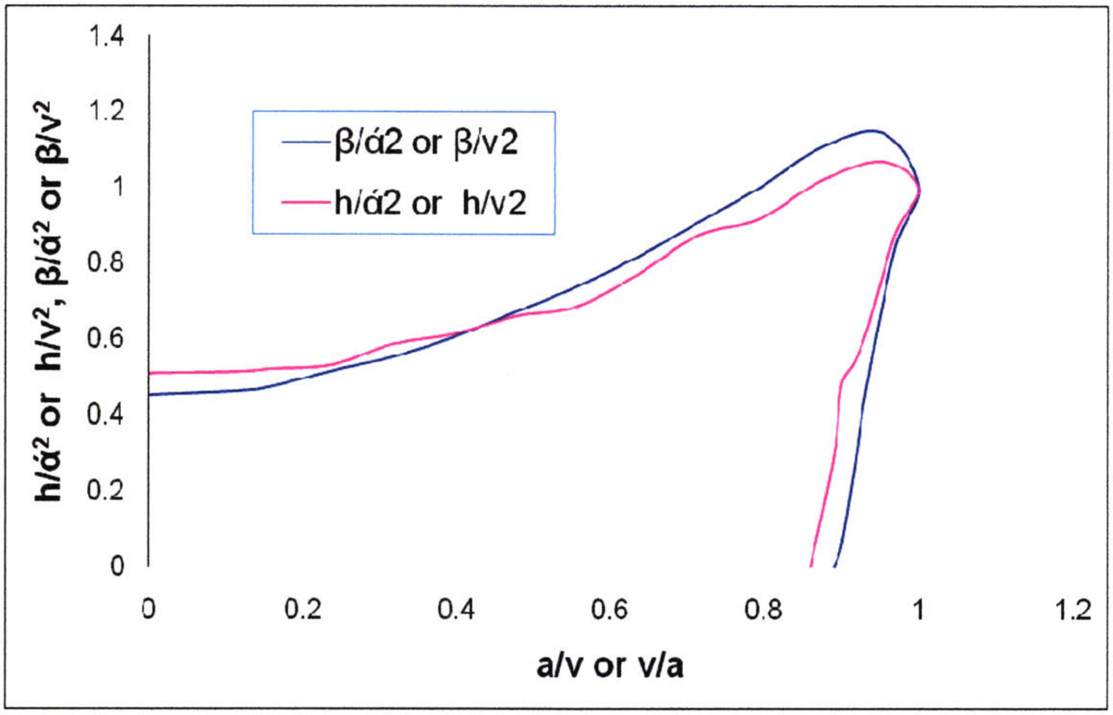

Figure 5.13: Head and torque homologous pump curves for normal pump operation of the EM ALIP primary pumps

Each of these basic component models were created and input into RELAP5-3D, then were combined to create the full-plant primary pool model. The performance and capabilities of the primary pool component of the full-plant model are described as part of the full-plant model in Section 5.2.

5.1.3 Secondary Loop

The secondary system consists of four separate loops, which thermally connect the primary system to the steam generator and serve as buffers between the radioactive sodium in the primary system and the water in the PCS. The secondary loop is significantly elevated above the reactor vessel and primary system to provide a head in the secondary side of the IHX sufficient that any crack in the IHX tubing would result in leakage from the secondary system (tubes) into the primary system (shell) rather than leakage from the primary system into the secondary system. The secondary loops also contain additional sodium inventory, pump tanks, and sodium purification systems, though these components are not explicitly included in the RELAP5-3D model.

5.1.3.1 Secondary Loop Flow Path

The secondary sodium heated to a IHX outlet temperature of 488 °C by the primary sodium exits the IHX via an annular riser pipe surrounding the downcomer pipe. This piping extends upward for ~6.6 m. The sodium then flows through circular piping to the top of the steam generator. The steam generator is an ~11.6 m high shell and tube helical coil heat exchanger. The design parameters of the steam generator are found in Table 5.12. Note the very high pressure drop on the water side of the steam generator; this large pressure drop is due to the introduction of a flow orifice in the SG. The purpose of this orifice is to prevent density wave oscillation instabilities since the exit steam is superheated. The secondary sodium flows down through the shell side of the steam generator, and out into the cold leg of the secondary loop.

Table 5.12: Key design parameters of the four helical coil steam generators for a standard SFR design

Heat transfer capacity (MWt)	250
Number of tubes	184
Tube OD (cm)	3.18
Tube ID (cm)	2
Overall tube length (m)	98.5
Overall tube heat transfer surface (m^2)	1806
Heat transfer surface area margin (%)	20

Tube bundle transverse pitch (cm)	5.72
Tube bundle longitudinal pitch (cm)	4.76
Tube pitch angle (°)	7.55
Number of tube coil rows	6
Helical coil bundle height (m)	11.6
Vessel outside diameter (cm)	281
Inner shroud outside diameter (cm)	137
Steam generator height (m)	20.72
Water side tube pressure drop (MPa)	1.172
Inlet restrictor pressure drop (MPa)	0.655
Sodium side pressure drop (MPa)	0.019
Shell thickness (cm)	3.81
Elliptical head thickness (cm)	4.45
Tube sheet thickness (cm)	8.89

The cold leg piping flows from the bottom of the steam generator horizontally to the location of the pump tanks and purification systems, where the flow enters into the secondary EM ALIP pumps. These pumps are similar to the pumps found in the primary system, but are slightly smaller. The design parameters of the four secondary EM ALIP pumps are found in Table 5.13. Primary sodium then flows through the cold leg piping until it is directly above the IHX inlet, where it then flows downward through the 10.8m downcomer pipe into the IHX.

Table 5.13: Key design parameters of the four secondary system EM ALIP pumps for a standard SFR design

Pump diameter (m)	0.585
Power (kW)	609
Efficiency (%)	46
Mass, kg	2271
# of poles	14
# of coils	42
Temp (°C)	355
Vol. flow rate (m^3/s)	0.369
Discharge pressure (psig)	110
Length (m)	2.4
Rated efficiency (%)	48.59
Rated power (kW)	2315
Rated pressure (MPa)	0.23

Rated density (kg/m^3)	873.984
Rated flow rate (kg/s)	1290
Rated flow rate (m^3/s)	1.476
Rated torque (N-m)	2779.889
Rated head (m)	26.834

5.1.3.2 Secondary Loop RELAP5-3D Model

The secondary loop RELAP5-3D model consists of pipe and pump components, composed similarly to those contained in the primary pool model. Additionally, heat exchangers representing the tubes of the steam generator are also included. A summary of the key parameters for the flow components in the secondary loop is found in Table 5.14, while a similar summary for the heat structures is found in Table 5.15. A nodalization diagram of the secondary loop is seen in Fig. 5.14.

Table 5.14: Key parameters of the RELAP5-3D pipe segments included in the secondary loop of the full-plant model

Component	Description	Volumes	Flow Area (m^2)	Length (m)	Hydraulic Diameter (m)
302, 352, 402, 452	IHX downcomer (depicted in Fig. 5.11)	1	1.074	1.104	0.585
		1	1.074	2.292	0.585
		1	1.074	1.934	0.585
		1	9.280	0.190	1.719
304, 354, 404, 454	IHX tubes (depicted in Fig. 5.11)	1	2.819	0.100	0.247
		15	2.819	0.092	0.012
		31	2.819	0.092	0.020
		1	2.819	0.300	0.020
		1	8.111	0.550	1.172
318, 368, 418, 468	Riser	6	1.040	1.219	0.485
		8	1.039	0.750	0.575
320, 370, 420, 470	Hot leg piping	10	1.039	1.565	0.575

		3	1.039	1.333	0.575
		1	1.039	1.000	0.575
322, 372, 422, 472	Steam generator head	3	1.039	1.017	0.575
340, 390, 440, 490	Steam generator (shell side)	50	12.619	0.232	0.090
326, 376, 426, 476	Cold leg piping	3	1.039	1.017	0.575
		1	1.039	1.000	0.575
		4	1.039	1.250	0.575
		3	1.039	1.184	0.575
328, 378, 428, 478	Pump inlet piping	2	1.039	0.800	0.575
334, 384, 434, 484	Secondary pump	1	1.621	1.600	-
338, 388, 438, 488	Cold leg piping/downcomer	3	1.039	1.717	0.575
		7	1.039	1.250	0.575
		17	1.039	1.197	0.575

Table 5.15: Key parameters of the RELAP5-3D heat structures included in the secondary loop of the full-plant model

Heat Structure	Description	Segments	Inner Radius (m)	Outer Radius(m)	Heated Length(m)
13021	IHX downcomer	1	0.290	0.310	0.520
		1	0.290	0.310	1.680
		1	0.290	0.310	1.2
		1	0.290	0.310	0.8
		1	0.290	0.310	2.160
		25	0.290	0.310	0.367
		20	0.290	0.310	0.367
		1	0.290	0.310	0.4
		1	0.290	0.310	0.760
13041	IHX tubes	1	0.007	0.008	1800.0
		45	0.007	0.008	1650.4
		1	0.007	0.008	972.0
		1	0.007	0.008	3600.0
		1	0.007	0.008	5024.0
13181	Hot leg piping	6	0.288	0.305	4.877
		8	0.288	0.305	3.00
13201	Steam generator inlet	10	0.288	0.305	6.260
		3	0.288	0.305	5.320
		1	0.288	0.305	4.0
13221	Steam generator head	3	0.288	0.305	4.067
13401	Steam generator tubes	50	0.010	0.016	344.000
13261	Cold leg piping	3	0.190	0.203	4.067
		1	0.190	0.203	4.0
		4	0.190	0.203	5.0
		3	0.190	0.203	4.737

13281	Secondary pump inlet piping	2	0.190	0.203	3.2
13441	Secondary pump structures	1	0.290	0.293	6.4
13381	Cold leg piping	3	0.190	0.203	4.737
		4	0.190	0.203	5.0
		10	0.190	0.203	4.788

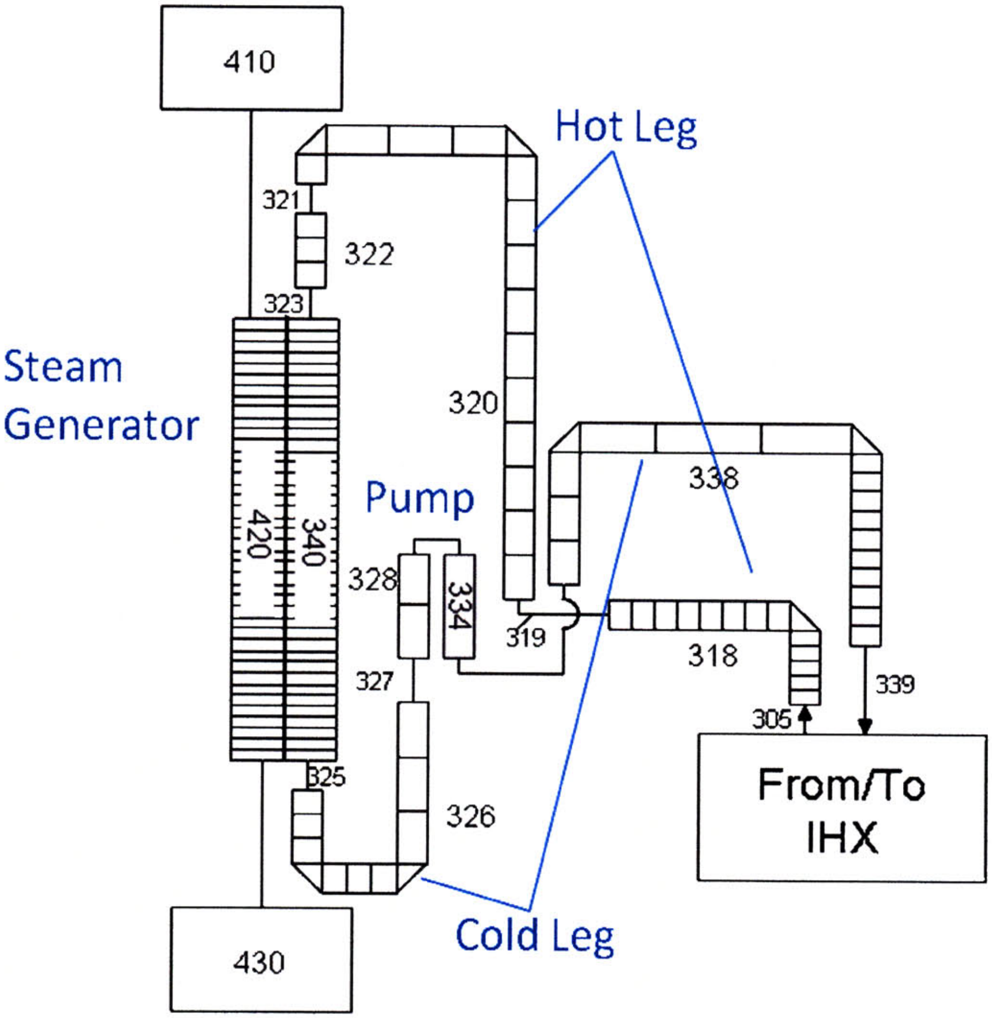

Figure 5.14: Nodalization diagram of secondary loop system

5.1.4 Power Conversion System Boundary

The power conversion system for a typical SFRs consists of a steam Rankine cycle with generator connected to the electrical grid. The Rankine cycle utilized in the current full-plant design is a scaled-up version of the steam PCS described in the ABTR report [5.3]. Including a complete Rankine cycle as part of the full-plant RELAP5-3D model, however, dramatically increases runtime and reduces the maximum time step limit (as dictated by mass errors) on the time-step size. The entire PCS system is not necessary, as the transient scenarios of interest do not include detailed behavior of the turbine, condenser and feedwater system. Thus, a simple steam generator boundary with adjustable conditions matching the conditions of the PCS is sufficient for investigating the suitability of innovative fuel configurations in fast reactor applications.

The steam generator is not explicitly modeled, as are the other components in the full plant model. This is primarily due to a lack of design parameters for the stem generator design. However, modeling the steam generator details is not necessary; it is only necessary for the purposes of this thesis for certain critical parameters, the total heat transferred, the mass flow rates, and the inlet/outlet fluid conditions (particular the temperature and pressure) to match the critical parameters of the reference reactor. Therefore, the steam generator was modeled as a "black box" where the heat transfer and hydraulic parameters were adjusted until the critical parameters as described above matched those of the reference reactor.

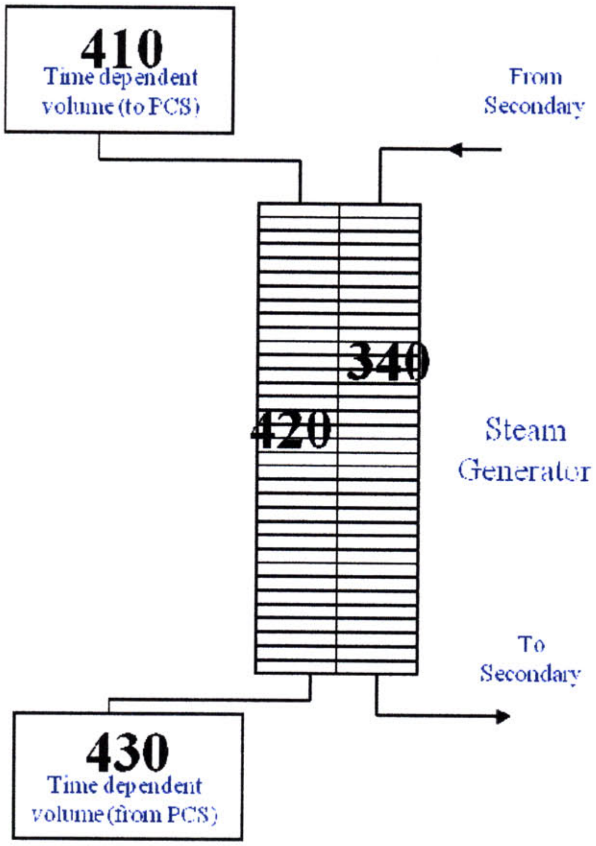

Figure 5.15: Nodalization diagram of the PCS boundary condition

A nodalization diagram of the PCS boundary is shown in Fig. 5.15. The inlet flow conditions are defined by a time-dependent inlet volume. This component of RELAP5-3D allows for the definition of the feedwater temperature and pressure as a function of time, and thus can be used to model in detail the boundary of steady state and transient conditions in the PCS. The flow rate is controlled by a time-dependent junction, which allows a set mass flow rate as a function of time. By careful manipulation of these two volumes, the behavior of the PCS during any transient scenario can be modeled.

During steady state operation of the SFR, water at 216 °C and 167 bars enter the steam generator through the bottom at a rate of 111.8 kg/s per generator and flows upward through a series of tubes that spiral circumferentially through the length of the steam generator shell. Hot secondary sodium at 488 °C flows through the shell side of the steam generator and is cooled to 333 °C. The steam flows upward out of the steam generator at 454 °C and 155 bars. The outlet steam is super-heated, with a saturation temperature of 345 °C at the exit pressure. The thermal efficiency of the PCS Rankine cycle with these steam parameters is estimated to be 38%.

For the three most limiting transients or accidents investigated in this thesis (UTOP, ULOF, and station blackout), the only accident that does not require the manipulation of the time-dependent boundaries (i.e. the pressure temperature and mass flow rate) is the UTOP transient. In the station blackout accident, the transfer of heat from the secondary system to the PCS via the steam generator is conservatively assumed to be instantaneously lost. This is modeled in the RELAP5-3D model by deleting the heat structure representing the heat steam generator tubes, effectively making the steam generator an insulated flow path. In the ULOF transient, the PCS flow must be adjusted to prevent overcooling. The details of this transient, including the magnitude of the PCS steam flow rates as a function of time, are discussed in Chapter 7.

5.1.5 DRACS Operation

The direct reactor auxiliary cooling system (DRACS) serves as the emergency safety-grade cooling system for the SFR. A DRACS has been selected as the emergency cooling system rather than reactor vessel auxiliary cooling (RVACS) due to potential limitations on reactor vessel size, and thus reactor power rating [5.11], lower vessel temperatures during anticipated transients without scram (ATWS), and new NRC regulations against aircraft impact against the reactor containment. In particular, as the reactor vessel size increases, less fractional heat can be removed by RVACS systems, which imposes a limit on the power rating of the reactor. In order to prevent this limitation, and to allow for potential increases in the SFR size beyond 1000MWth, DRACS are included in the SFR full-plant model.

5.1.5.1. Physical Description of DRACS

A schematic of the DRACS, as designed for the ABTR, can be seen in Fig. 5.16. There are three heat exchangers and three separate flow loops. The first loop is the loop created by the primary sodium coolant flowing from the cold pool into the primary DRACS heat exchanger and then back into the cold pool. There are three vertical protrusions in the redan structure from the cold pool into which the DRACS exchangers are placed, as seen in Fig. 5.17. Sodium from the cold pool can then flow upward through the gap between the redan wall and the DRACS outer surface. At the top of the redan-DRACS exchanger gap, the sodium flows into the DRACS exchanger through a series of holes designed to minimize the hydraulic resistance, and then flows downward as it is cooled through the shell side of the primary DRACS exchanger. Heat flows through tubes to cold sodium-potassium eutectic coolant (NaK) in an intermediate loop of the primary DRACS heat exchanger. The cold sodium then flows downward through an exit hole into the cold pool. The driving mechanism for this flow is buoyancy due to the temperature difference between the rising and sinking sodium. The design parameters of the three DRACS primary exchangers can be found in Table 5.16.

The second flow loop is a liquid NaK flow loop, which is heated by the primary system sodium in the primary DRACS exchanger. This hot NaK then rises via buoyant forces and at the top of the DRACS secondary piping loop is cooled by air in a shell and tube multiple pass heat exchanger, the NDHX. The NaK flows through horizontal tube bundles cooled by air flowing cross-wise across the tube bundles. This cooled NaK then flows downward to the primary DRACS exchanger, completing the secondary flow loop. The key parameters of the secondary NaK/air heat exchanger are listed in Table 5.17.

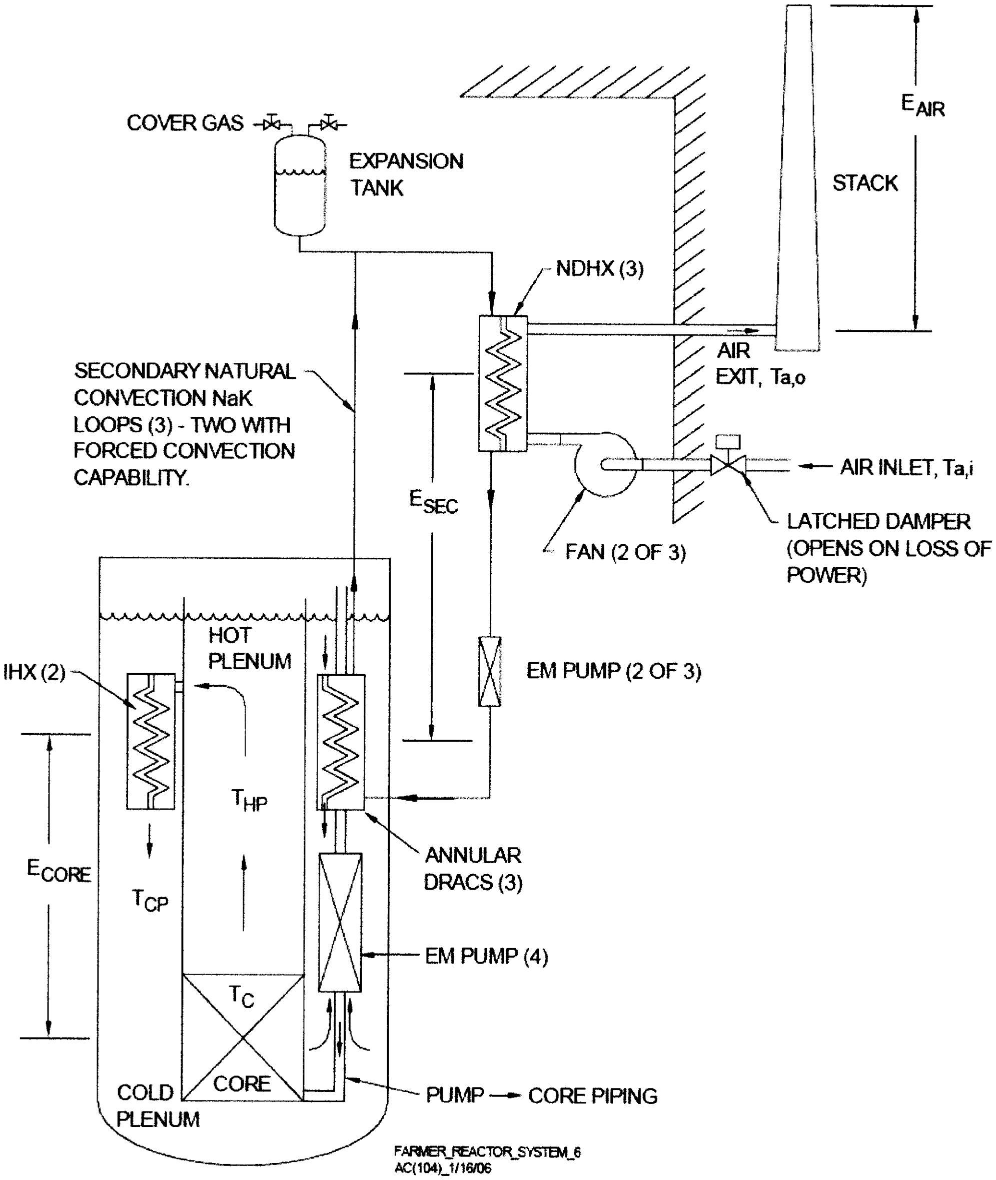

Figure 5.16: Schematic of DRACS found in the ABTR, which is scaled up for use in the SFR full-plant model [5.3]

Table 5.16: Key design parameters of DRACS primary heat exchanger (NaK/Na)

Heat transfer capacity (MW)	2.5
Heat transfer area (m^2)	17.4
Primary sodium inlet temperature (°C)	355
Primary sodium outlet temperature (°C)	510
Primary sodium flow rate (kg/s)	12.6
Secondary NaK inlet temperature (°C)	328
Secondary NaK outlet temperature (°C)	484
Secondary NaK flowrate (kg/s)	17.5

Tube outer diameter (cm)	2.22
Tube wall thickness (mm)	0.9
Tube pitch (cm)	3.79
Active tube length (m)	2.5
Number of tubes	100
Upper tube sheet area (m^2)	0.125
Lower tube sheet area (m^2)	0.125
Annular width of gap (riser) between redan and DRACS exchanger (cm)	6.9
OD of unit including riser (cm)	46.9
Shell thickness (mm)	6.4
Material	9Cr-1Mo
Height between Na/NaK and NaK/air exchangers (m)	5.92

The final flow loop consists of outside air, which is drawn through the DRACS valves via natural circulation. This air flows upward across the horizontal NaK tubes, then upward through an air stack, where it is vented to the atmosphere. The width and height of the stacks control the air flow rate and are sized so as to provide 2.5MW of heat removal (0.25% of the total reactor power) per DRACS loop. The air flow rate corresponding to full DRACS operation is ~402kg/s air, which can be derived when the air stack is designed with a height of 5m and a cross sectional area of 8.25m^2.

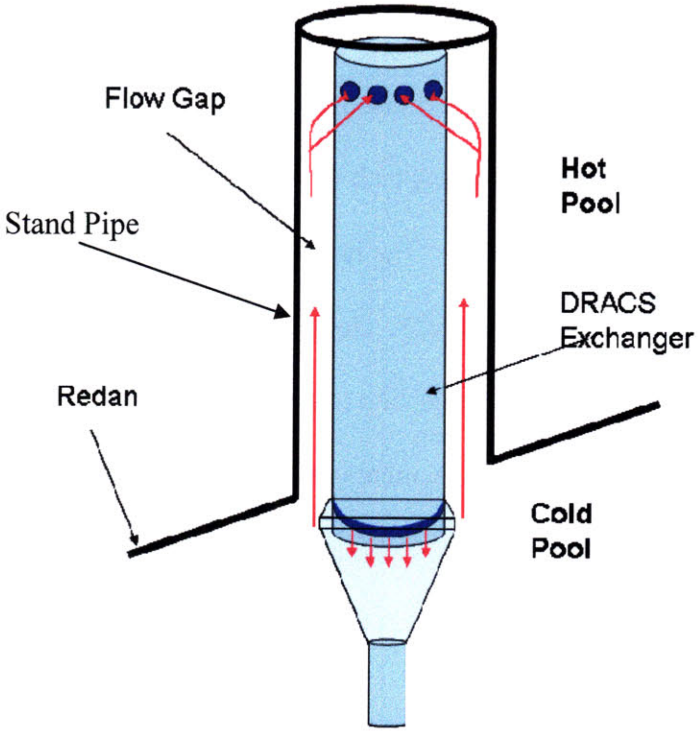

Figure 5.17: Schematic of DRACS primary exchanger inlet and outlet from the cold pool (not-adjusted)

The DRACS system is initiated upon loss of electrical power when the magnetic DRACS valves fail open, initiating the full circulation of outside air. When the DRACS valves are closed, approximately 4.02kg/s, or 1% of the nominal DRACS air flow passes through the secondary air/NaK heat exchanger. This flow helps to ensure that the correct direction of flow for natural circulation is established upon initiation of the system, as well as to prevent localized freezing of the NaK loop. This small air flow results in minor parasitic losses of heat from the SFR system during steady-state, full power operation (~0.31MW per module). Additionally, in case of the need for increased heat removal, two of the three DRACS loops have blowers and pumps installed within the air and NaK loops, respectively, so that forced circulation is possible. This allows the DRACS systems to operate as completely passive or active safety systems. However, in this study the blowers and pumps were assumed not to be safety-grade, so no credit was taken for forced circulation in the DRACS during accidents.

It is of interest to note that the flow path of the DRACS is quite complex with several reversals in the direction of flow. The hot sodium must still flow through the core, IHX, and then up through the DRACS. However, the flow areas along each segment of the coolant flow path are large, and hydraulic resistances are low with the exception of the IHX and core. These segments have relatively high hydraulic resistances and serve as the flow limiting components during transient natural circulation flow. The general design of the DRACS was taken from [5.3]. Design of an optimized DRACS is beyond the scope of this thesis.

Table 5.17: Key design parameters of DRACS primary heat exchanger (NaK/Na)

Heat transfer capacity (MW)	2.5
Design	Finned tube cross-flow, four pass
Active tube length (m)	9.55
Material	ss-304
HX tube OD (without fins) (cm)	4.22
Tube wall thickness (mm)	3.55
Fin height (mm)	3.2
Fin spacing (mm)	3.2
Fin thickness (mm)	1
Number of tubes	72
Tube horizontal center-to-center spacing (cm)	7.62
Tube vertical center-to-center spacing (between passes) (cm)	10.2
Stack riser cross-sectional area (m^2)	8.25
Stack height (m)	5

5.1.5.2 DRACS Loops RELAP5-3D Model

The piping and heat exchangers of the DRACS were modeled in RELAP5-3D using the same procedures as for the other systems: a series of pipes and heat structures with appropriate parameters were joined to create an accurate thermal-hydraulic model of the DRACS. Table 5.18 lists the key modeling parameters of each hydraulic component in the DRACS model, while Table 5.19 lists the key modeling parameters for each heat structure in the DRACS model. Perfect insulation was assumed in order to simplify the DRACS models. Thus, heat structures for the piping between the Na/NaK and the NaK/air exchangers were not included in this model. However, the parasitic losses in these pipes may prove significant; these structures should be included in future models so that these losses can be quantified. Two of the three loops have the capacity to run via forced circulation, and these loops were lumped into a single large loop for modeling purposes. This lumping is accomplished by doubling the area, the heated lengths, and the flow rates, while maintaining the hydraulic diameters of each pipe. For transient scenarios where two out of three DRACS are operational, the lumped loop is used to represent the two operational loops, while the third loop remains inoperable. Recall that although two of the three loops have the capacity to operate using forced convection, neither pumps nor blowers are used in these analyses; all DRACS modules operate only via natural circulation flow. A full nodalization diagram of the DRACS loops can be found in Fig. 5.18.

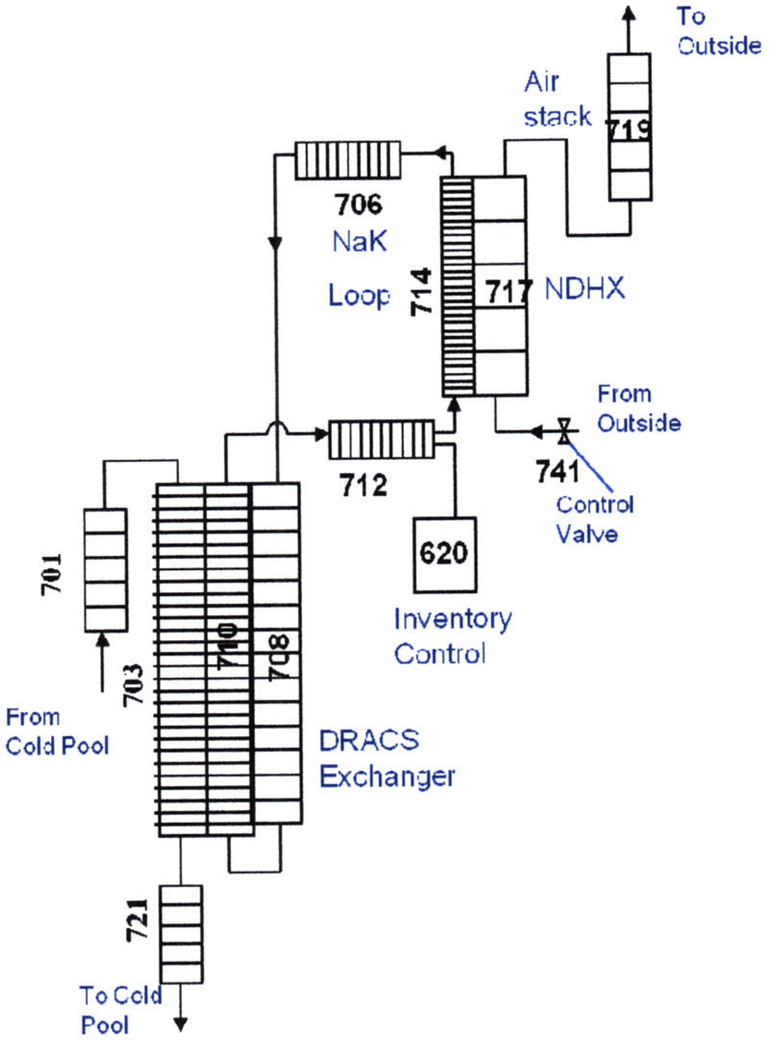

Figure 5.18: Nodalization diagram of the DRACS loop used in the SFR

It is of interest to note the additional volume, volume 721, found in both Table 5.18 and Fig. 5.18. Originally, the DRACS model was created to match explicitly the DRACS primary exchanger design shown in Fig. 5.17. However, in this design, the inlet and outlet of the DRACS exchanger connect to the same hydrodynamic model. This would prevent the use of natural circulation, as each volume within the RELAP5-3D model has a single volume-average temperature. In order to prevent this difficulty, an extension to the DRACS exchanger was created, which is simply a pipe that surrounds the annular outlet hole of the DRACS exchanger as indicated by the translucent volumes in Fig. 5.17. The pipe below the DRACS has similar geometric parameters as the DRACS primary exchanger shell side (and is thus effectively a simply extension of the DRACS), while the outlet ring was modeled as a junction with the appropriate cross-sectional flow area and an abrupt area change. This pipe extends downward for an additional ~3.2 m. This eliminated the modeling difficulty of having a single volume represent the inlet and outlet of the DRACS exchanger, while maintaining a viable flow path of the naturally circulating sodium coolant. The length of this extender does not alter the properties of the DRACS system, so long as its discharge elevation is not below the core inlet plenum. The difficulty encountered with the DRACS outlet is not a modeling complication; rather this difficulty is a direct result of the current DRACS design: the close proximity of the inlet and outlet regions would inhibit successful operation of the DRACS modules in reality, and thus future work should focus on improving and optimizing the DRACS inlet/outlet flow design, so that this difficulty can be avoided.

Table 5.18: Key design parameters of the RELAP5-3D DRACS model volumes

Component	Description	Volumes	Flow Area (m^2)	Length (m)	Hydraulic Diameter (m)
701, 751*	Riser	5	0.0867	0.5000	0.1380
703, 753	DRACS primary exchanger (hot side)	40	0.2314	0.0625	0.0110
721, 771	DRACS outlet extension	5	0.0231	0.6428	0.0110
706, 767	NaK cold leg	9	0.0898	0.5800	0.0853
620, 670	NaK inventory control	1	0.9416	1.0000	-
708, 758	Primary exchanger downcomer (NaK)	10	0.0167	0.2500	0.1460
710, 760	DRACS primary exchanger (cold side)	40	0.0327	0.0625	0.0204
712, 762	NaK hot leg	9	0.0898	0.5800	0.0853

		1	0.0898	0.7000	0.0853
714, 764	NDHX tube (hot) side	10	0.0697	0.2388	0.0351
		1	0.0697	0.1750	0.0351
		10	0.0697	0.2388	0.0351
		1	0.0697	0.1750	0.0351
		10	0.0697	0.2388	0.0351
		1	0.0697	0.1750	0.0351
		10	0.0697	0.2388	0.0351
		1	0.0697	0.1750	0.0351
704, 754	Air inlet volume	1	1.0000	1.0000	-
717, 767	NDHX shell (cold) side	4	4.4769	2.0000	1.1938
719, 769	Air stack	5	8.2500	1.0000	0.2000
749, 799	Air outlet volume	1	2.7500	0.3000	-

*the second component number indicates the lumped 2nd and 3rd DRACS loops; the length, volume number, and hydraulic diameter are the same, but the flow area is double the listed value

It is also of interest to discuss the ratings of the DRACS systems. The rated power of each DRACS loop is 2.5MW. This rating is the power that the DRACS withdraws when the DRACS power matches the reactor decay power at the long-term peak during the station blackout transient. Because the power withdrawn by the DRACS is driven by the sodium temperature in the cold pool, the power actually withdrawn by the DRACS loops at any given time varies for each transient type.

Table 5.19: Key design parameters of the RELAP5-3D DRACS model heat structures

Heat Structure	Description	Segments	Inner Radius	Outer Radius	Heated Length
17011	DRACS primary exchanger outer wall	40	0.1591	0.1655	0.0625
17031	DRACS tubes	40	0.0102	0.0111	6.25
17141	NDHX tubes	40	0.01755	0.0211	18.145

5.2 Full-plant Model Performance

This section outlines the performance of the full-plant SFR RELAP5-3D model. The performance of this model is verified against previous SFR concepts to ensure accurate performance of the RELAP5-3D model. The results of the RELAP5-3D full-plant model were tabulated and compared to the design specifications of a standard SFR model, as described by Grandy et al. [5.12].

5.2.1 RELAP5-3D SFR vs. ABR1000

The standard operating parameters of the SFR design described by Grandy et al. are for the ABR1000, which is a scaled up version of the ABTR [5.3]. The operating parameters of the ABR1000 are fairly standard for most pool-type moderate sized (1000 MW) SFR concepts and are based upon a combination of detailed modeling and engineering judgment. A comparison of these parameters with those derived from the RELAP5-3D full-plant model is found in Table 5.20. The numbers that represent the DRACS performance in this table were calculated assuming that the cold pool temperature was 510°C, as this is the condition used in the ABR1000 design to estimate DRACS performance.

Table 5.20: Results of the RELAP5-3D full-plant model compared to the same operating parameters for the ABR1000

	Model	ABR1000		Model	ABR1000
Primary inventory (MT)	1445	1309	DRACS		
Secondary inventory (MT)	533	-	Na T_{in} (°C)	510	510

Primary Side			Na T_{out} (°C)	355.85	355
IHX T_{in} (°C)	520.09	510	NaK T_{in} (°C)	489.62	484
IHX T_{out} (°C)	365.18	355	NaK T_{out} (°C)	314.87	328
IHX ΔP primary (kPa)	9.58	18.2	NaK H (m)	5.22	-
Core T_{in} (°C)	365.18	355	Air T_{in} (°C)	30	-
Core T_{out} (°C)	520.09	510	Air T_{out} (°C)	48.36	-
Core ΔP (MPa)	0.323384	0.314	Stack A (m^2)	8.25	8.25
m_{dot} (kg/s)	1269.1	1256	Stack H (m)	5	5
Secondary Side			Na m_{dot} (kg/s)	12.6	12.6
IHX T_{in} (°C)	335.85	333	Nak m_{dot} (kg/s)	17.5	17.5
IHX T_{out} (°C)	491.81	488	air m_{dot} (kg/s)	110	-
IHX ΔP secondary (kPa)	22.1975	14.8	PCS System		
m_{dot} (kg/s)	1253.5	1256	H2O T_{in} (°C)	216	216
SG T_{in} (°C)	488.837	477	H2O T_{out} (°C)	453.987	454
SG T_{out} (°C)	330.955	326	PCS Pressure (MPa)	2.26	1.17

The numbers that represent the DRACS segment of this model were taken assuming that the cold pool temperature is 510°C, as this is the condition used in the ABR1000 design to estimate DRACS performance. As can be seen, there is good agreement between most parameters, but the core outlet and inlet temperatures are ~10 °C higher for the RELAP5-3D model than for the ABR1000. However, the overall change in temperature across the core and intermediate heat exchangers is the same as for the ABR1000 design. In addition, the temperatures across the secondary loop for the RELAP5-3D model are nearly identical to those found in the ABR1000 design. These comparisons indicate that the correct flow and heat sources are present, but that the heat transfer resistance between the primary and secondary systems is high resulting in a 10 °C higher temperature drop across the IHX boundary at the operational temperatures indicated in the ABR1000 description.

The discrepancy is due to RELAP5 underestimating the heat transfer coefficient on the primary side of the IHX. As can be seen in Fig. 5.8, the baffle design of the IHX instigates additional transverse flow and mixing, which enhances heat transfer, an effect that was not modeled with RELAP5-3D. It is possible to couple RELAP5-3D with computational fluid dynamics (CFD) codes to investigate complex mixing effects [5.13, 14], but this was beyond the scope of the current thesis.

An additional option in the RELAP5-3D heat structures is to add a "fouling factor," or a multiplier, to the heat transfer coefficient of the heat structure right or left boundary. By implementing a factor of less than one, the heat transfer through the heat structure is mitigated, while implementing a factor of greater than one provides for enhanced heat transfer. Therefore, to mimic the additional heat transfer effects for the IHXs, the fouling factor for the full-plant model was increased until the temperatures of the primary system matched those of the ABR1000 design concept. This occurred for a fouling factor of ~3.45.

The new comparison between the RELAP5-3D model and the ABR1000 design is found in Table 5.21. The temperature rise across the core is slightly lower in the RELAP5-3D model (< 0.5°C), which corresponds to the parasitic losses of the DRACS system during steady-state operation. The primary sodium inventory of the RELAP5-3D model is approximately 10% higher than the ABR1000 primary sodium inventory due primarily to assumptions and simplifications for the RELAP5-3D model, but the difference is small enough that the RELAP5-3D model can be considered sufficient. The secondary sodium inventory was not clearly given by Grandy et al., but this inventory is only important for transients in which the thermal inertia of the secondary coolant is important, such as an accident that involves loss of flow in the secondary system and retention of the PCS as a heat sink.

A significant different in temperature is witnessed between the IHX and the SG entrance of the ABR1000 design. There is nothing between the IHX and the SG that would remove such a significant amount of heat from this system, and thus the cause for difference between these state points in the ABR1000 is unknown. The RELAP5-3D model does not reflect this difference, and because the reason remains unknown, no attempt was made to match this drop in pressure with the RELAP5-3D model

Finally, the pressure drop in the IHX of the RELAP5-3D model is 50% that of the pressure drop estimated for the ABR1000, again primarily due to modeling simplifications. The pressure drop across the core, however, is larger in the RELAP5-3D model by the same amount that the IHX is deficient, thus producing the same overall pressure drop for the loop. This provides a nearly equivalent mass flow rate through the primary pool and is considered acceptable for model verification purposes. Now that a full-plant SFR model has been created and loosely verified using RELAP5-3D, the various core models need to be constructed. The core models utilized thus far are the metal fuel and oxide fuel CR = 0.71 cores described in section 5.1.1.1. The following section describes the adaptations made to the SFR RELAP5-3D full-plant core model to incorporate also the bottle-shaped fuel assembly configurations (both oxide and metal) and the annular fuel configurations (only metal).

Table 5.21: Final comparison of the RELAP5-3D full-plant model results and the same operating parameters for the ABR1000

	Model	Report		Model	Report
Primary inventory (MT)	1445	1309	DRACS		

Secondary inventory (MT)	533	-	Na T_{in} (°C)	510	510
Primary Side			Na tout (°C)	355.85	Na T_{out} (°C)
IHX T_{in} (°C)	508.189	510	NaK T_{in} (°C)	489.62	484
IHX T_{out} (°C)	353.848	355	NaK T_{out} (°C)	314.87	328
IHX ΔP primary (kPa)	9.58	18.2	NaK H (m)	5.22	-
Core T_{in} (°C)	353.006	355	Air T_{in} (°C)	30	-
Core T_{out} (°C)	508.35	510	Air T_{out} (°C)	48.36	-
Core ΔP (MPa)	0.323384	0.314	Stack A (m^2)	8.25	8.25
m_{dot} (kg/s)	1267.7	1256	Stack H (m)	5	5
Secondary Side			Na mdot (kg/s)	12.6	Na m_{dot} (kg/s)
IHX T_{in} (°C)	333.014	333	Nak m_{dot} (kg/s)	17.5	17.5
IHX T_{out} (°C)	488.871	488	air m_{dot} (kg/s)	110	-
IHX ΔP secondary (kPa)	22.1975	14.8	PCS System		
m_{dot} (kg/s)	1253.5	1256	H2O T_{in} (°C)	216	216
SG T_{in} (°C)	488.837	477	H2O T_{out} (°C)	453.987	454
SG T_{out} (°C)	330.955	326	PCS Pressure (MPa)	2.31	1.17

5.3 Full-Plant Alternate Core Configuration Models

This section describes the RELAP5-3D core models created for the bottle-shaped and internally/externally cooled annular fuel assemblies. For the bottle-shaped configurations, both metal and oxide fuel cores are described, while for the annular fuel, only the metal fuel core is included. This is because the oxide fuel has already been considered unacceptable for use in the SFR due to the potential for fuel and clad damage during an IA subchannel blockage accident. In the following core models, only the fuel assembly models have been altered for the CR = 0.71 core models and the base CR = 0.71; the assembly design parameters for control, shield, and reflector assemblies are the same. The assembly sizes are similar for the CR = 0.71 cases and base CR = 0.25 cores, but not for the CR = 0.25 annular core, as described in section 5.1.1.1. For the annular CR = 0.25 metal fuel core, the assemblies flat-to-flat distance is larger than for other core configurations, so this required an adjustment of the core and assembly parameters, as described in Section 5.3.3.

5.3.1 Bottle-Shaped Fuel Core Models

The full-plant core model remains nearly unchanged for bottle-shaped fuel configurations. The core segments (volumes 4-9) for each pipe in the core remain unchanged. In the plenum region (volumes 10-14), the lengths, flow areas, and hydraulic diameters for the flow channel pipes are altered to reflect the reduced fuel rod plenum diameters. In order to compensate for the increased fuel rod lengths, the height of the core and core barrel heights were increased by the same amount as the fuel rods. The core outlet branch component was shortened by the same amount to compensate for the increased core length. The lower plenum volume was manipulated by adding an additional volume with the same properties as the core outlet branch, which represents the additional hot pool volume adjacent to the taller core barrel. Table 5.22 lists the changes implemented in the RELAP5-3D model for both oxide and metal core configurations.

Table 5.22: Adjustments to components of RELAP5-3D model from base and bottle-shaped fuel cores

	Oxide		Metal	
	Base Fuel	**Bottle-Shaped**	**Base Fuel**	**Bottle-Shaped**
Plenum rod volume lengths (m)	0.32004	0.38891	0.254	0.30234
Core outlet volume length (m)	1.64658	1.30223	1.64658	1.40488

Lower hot pool number of volumes	3	4	3	4
Plenum flow area per assembly (m^2)	0.00678	0.008854	0.00678	0.008854
Plenum hydraulic diameter (m)	0.003361	0.005468	0.003361	0.005468
Plenum turbulent drag coefficient	0.175	0.1531	0.175	0.1531
Plenum laminar drag coefficient	0.7757	0.59716	0.7757	0.59716

The orificing at the core entrance was the same for the bottle-shaped and base fuel configurations so as to maintain clarity in the comparison; any adjustments to the orifice sizes could offset the gains from utilizing a reduced plenum rod diameter. The bottle-shaped design has a slightly higher mass flow rate, which results in a small decrease in the core average outlet temperature (~0.5°C – 1°C). Because this decrease is so small, no effort was made to correct it by adjusting the pumping power. The pressure drops across the core for steady state operation in the full-plant model for both bottle-shaped configurations and base configurations can be found in Table 5.23.

Table 5.23: Core pressure drop for bottle-shaped and solid cores for both metal and oxide fuel configurations

	Metal Fuel	Oxide Fuel
Solid fuel core ΔP (kPa)	294.4788	399.6515
Bottle-shaped fuel core ΔP (kPa)	223.6985	336.2784
Reduction of core ΔP (%)	24.04%	15.86%

The final bottle-shaped fuel configurations have a reduced pressure drop across the core during steady state operation, but this reduction in pressure drop is not as large as predicted according to the preliminary and subchannel analyses. This is because of the addition of several non-fuel assemblies, which, like the bottle-shaped fuel, have increased assembly lengths (in order to have a uniform height across the core at the core outlet). The flow area in these assemblies, however, is not adjusted in the plenum region. This results in a slight increase in pressure drop across the core for these assemblies. The net result is a reduction in pressure drop across the core, but a more moderate drop than for fuel assemblies alone. Future work should include resolving this problem by increasing the plenum region flow area and thus reduce the hydraulic resistance in the reflector, control, and shield assemblies.

5.3.2 CR = 0.25 Base Metal Fuel Core Model

A new full-plant core model was adjusted to accommodate the low CR metal fuel, as described in Section 2.1.2. Because the CR = 0.25 core is divided into three different regions, a seven channel core model is used. These channels represent the inner driver, middle driver, outer driver, hottest assembly, shield, reflector, and control assemblies, as depicted in the nodalization diagram found in Fig. 5.19. The fuel is still a U-Pu-Zr fuel, but the enrichment (TRU/HM) of the inner, middle, and outer driver zones is 46.2%, 57.8%, and 69.3%, respectively. This enrichment is maintained for all CR = 0.25 metal fuel core configurations as well.

Initially, core radial and axial power profiles based upon the high conversion ratio (CR = 0.71) SFR cores were used, as described in section 4.2.3.1. However, these profiles are not accurate, considering the highly different configuration of the fuel at low conversion ratios. The reactivity feedback coefficients provided by Hoffman et al. were used in the low CR = 0.25 cores, while the axial and radial power peaking profiles were calculated using MCNP. This neutronic analysis was performed by Matt Denman [1.14, 1.15] for the solid and annular fuel cores in order to provide the power peaking profiles.

The feedback coefficients therefore utilized for the low CR metal core were provided by Hoffman et al. [2.2] and are listed in Table 5.24. These reactivity feedback coefficients are assumed to be valid for the annular fuel core as well, as the fuel-to-coolant ratio and core height were maintained from the solid to the annular fuel configurations.

Table 5.24: Reactivity coefficients for the metal CR 0.25 core [2.2]

	Metal (BOEC)	Metal (EOEC)
Effective delayed neutron fraction	0.0027	0.0027
Prompt neutron lifetime (μs)	0.44	0.44
Radial expansion coefficient (¢/°C)	-0.48	-0.48
Axial expansion coefficient (¢/°C)	-0.63	-0.63
Fuel density coefficient (¢/°C)	-0.93	-0.93
Vessel expansion coefficient (¢/°C)	0.10	0.10
Sodium density coefficient (¢/°C)	0.18	0.18
Doppler coefficient (¢/°C)	-0.06	-0.06

The axial peaking for both solid were taken from Table 4.5, while the radial peaking was assumed to be 1.2, as with the other core radial peaking. Though this is higher than the predicted radial peaking, this provides a small margin to account for various uncertainties.

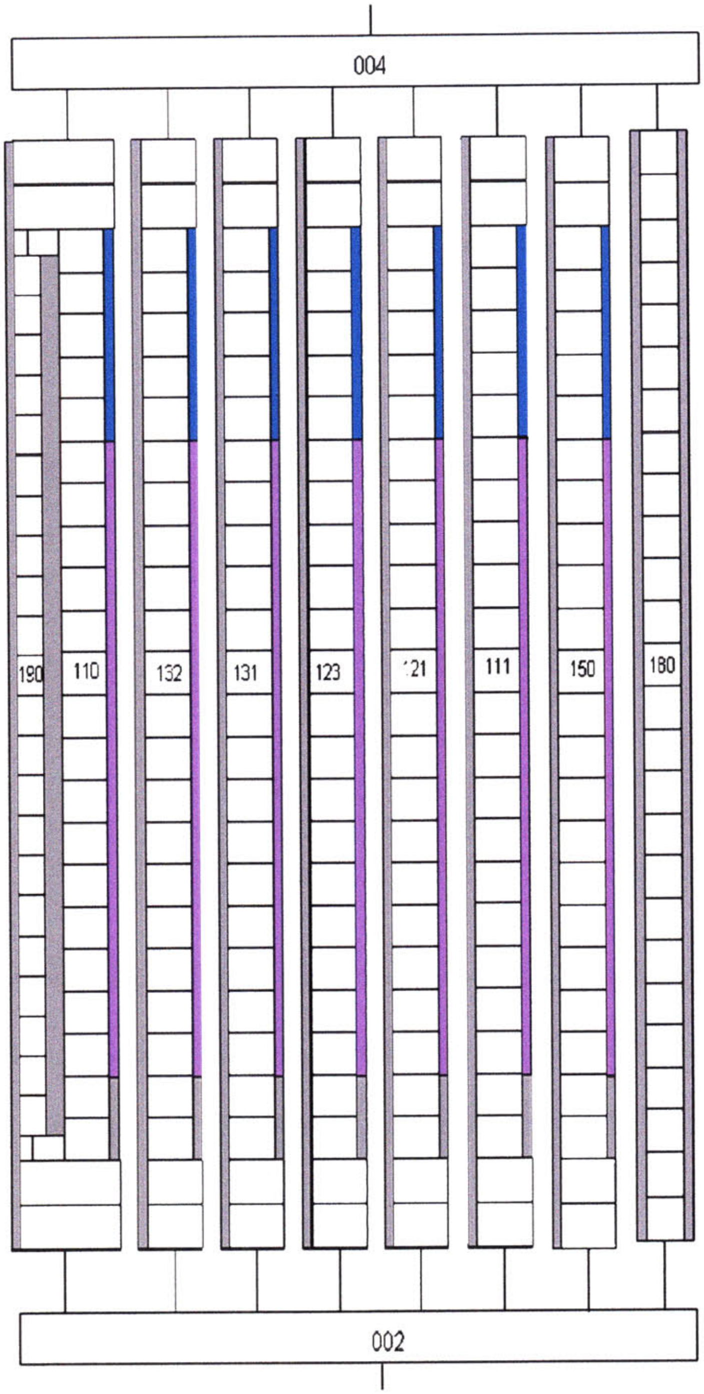

Figure 5.19: Nodalization diagram of the metal CR = 0.25 core RELAP5-3D model

The hydraulic resistance across the fuel assemblies in the CR = 0.25 core layout is considerably less than the CR = 0.71 core due to the larger pitch and hydraulic diameters.

This would result in a larger flow rate through the fuel assemblies and lower core outlet temperatures in general. Therefore, the primary pump rated volumetric flow rate and rated head were slightly reduced to 2.92 m^3/s and 90.06 m, respectively, in order to maintain a similar coolant temperature increase across the core as was seen in the higher conversion ratio core configurations.

The fuel rod and assembly lengths were adjusted so that the metal fuel assemblies would fit inside the current SFR full-plant model. The new fuel lengths and the old fuel lengths are listed together for comparison in Table 5.25. The CRDLE reactivity feedback is not included in [2.2], but as a simplifying assumption, the feedback coefficients are assumed to be the same as for the CR=0.71 metal core. A complete listing of the RELAP5-3D hydraulic component parameters for the CR = 0.25 metal fuel core can be found in Table 5.26, while a complete listing of the heat structure parameters can be found in Table 5.27.

The hydraulic resistance of the CR = 0.25 metal fuel core configuration is lower than CR = 0.71 metal fuel core configuration. Thus, the pumping power was decreased while maintaining pump performance, as dictated by the homologous pumping curves, until the flow rate matched the flow rate of the higher CR core configurations. At this point, the parameters for the CR = 0.25 metal fuel core full-plant model matched those of the base model described in this chapter. The orificing required to minimize the core outlet temperature distribution, while at the same time minimizing additional hydraulic resistance, is found in Table 5.28

The CR = 0.25 solid metal fuel core model was combined with the balance of the full-plant RELAP5-3D model and together was the basis against which the annular fuel core performance was compared. The next section focuses on the RELAP5-3D core model for the metal annular fuel core.

Table 5.25: Pin and assembly lengths for the metal CR = 0.25 and CR = 0.71 cores

Lengths (m)	CR = 0.71	CR = 0.25
Nosepiece	0.3556	0.3556
Lower Shield	1.2446	1.07
Core	0.8128	1.016
Gas plenum	1.2446	1.9114
End cap and duct standoff	0.8128	0.11745
Handling socket	0.30485	0.3048
Total	4.77525	4.77525

Table 5.26: Hydraulic components of the CR = 0.25 solid fuel pins core RELAP5-3D model

Component	Description	Volumes	Flow Area (m^2)	Hydraulic Diameter (mm)
110	Control	12	0.083	8.677
111	Inner driver	12	0.46719	4.552
121	Middle driver	12	0.52559	4.552
123	Outer driver	12	0.40879	4.552
131	Reflector	12	0.19415	1.878
132	Shield	12	0.15998	4.251
150	Hottest assembly	12	0.00973	4.552

Table 5.27: Heat structure components of the CR = 0.25 solid fuel pins core RELAP5-3D model

Heat Structure	Description	Segments	Inner Radius	Outer Radius (mm)	Heated Length (Core Segment)
11102	Control core	5	0.00	20.965	35.560
11112	Inner driver core	5	0.00	2.32	5925.312
11212	Middle driver core	5	0.00	2.32	5925.312
11232	Outer driver core	5	0.00	2.32	4608.576
11312	Reflector core	5	0.00	7.705	1553.261
11322	Shield core	5	0.00	16.685	231.648
11502	Hottest assembly core	5	0.00	2.32	109.728

Table 5.28: Orifice diameters required to flatten the outlet temperature profile and minimize the core pressure drop

	CR=0.25 orifice area (m^2)
110	0.0025
111	-
121	0.035
123	0.05
131	0.0021
132	0.0009
150	-

5.3.3 Annular Metal Fuel CR = 0.25 Core Model

The internally and externally cooled annular fuel assemblies for metal fuel do not translate as easily to the SFR full-plant model as does the annular oxide fuel configuration. Because of the larger assembly size required for metal annular fuel (18.29 cm vs. 15.71 cm), it is not possible to preserve the same core layout without a large increase in the effective core diameter. Therefore, a new core layout was created to approximately preserve the core effective diameter, allowing direct application of the annular fuel core into the SFR full-plant model. Because the metal annular fuel assemblies are larger in size, fewer of them are needed to constitute a 1000 MW core, but including fewer, higher power assemblies also alters the neutronic performance of the core. The constraints for developing an annular fuel CR = 0.25 core layout are that the core must:

1. Produce 1000 MWth

2. Maintain a similar control worth as the base core layout
3. Have a core effective diameter that approximately matches the effective diameter of the solid fuel core effective diameter (2.22m).

The average assembly parameters described in Chapter 2 for the metal annular fuel assembly were used to determine the number of fuel assemblies required in order to match the core power of the solid fuel core layout. Approximately 111 fuel assemblies are needed to provide a power of 1000 MWth in the annular fuel core. However, it is impossible to have 111 fuel assemblies while keeping all 25 control rod assemblies and maintaining a similar neutronic behavior in the core. Thus, without performing detailed neutronic evaluations on possible annular fuel core configurations, two options were possible for proceeding with the annular fuel configuration: 1) the number of control assemblies could be reduced, and 2) the number of fuel assemblies could be reduced. Neither of these options is a perfect alternative, but rather each would provide a way to thermal-hydraulically evaluate an acceptable core design without diverting to thorough neutronic analyses of various core configurations, which is beyond the scope of this thesis.

The first option indicates a decrease in core control worth, while the second option indicates a decrease in power, and thus a decrease in the benefit of utilizing annular fuel. It is not desirable to adjust the control rod worth, particularly to decrease the worth of control rod assemblies, without a detailed neutronic analysis. For the purposes of this study, the power was decreased, and nine fuel assemblies were removed from the core layout in order to keep all 25 control assemblies.

Because this core configuration is not ideal, future work should focus on a careful analysis of core design in order to determine a layout and control rod assembly design that does not require a loss of control or power. For the current study, the decision was made to maintain the number of control assemblies in the core. This could potentially provide too much control rod worth to the more compact core. If future studies reveal that this is the case, the control rod worth in the core could be adjusted by decreasing the B_4C concentration in the control rods.

The potential power uprate achievable by utilizing annular fuel was decreased because of the loss of nine fuel assemblies, but was still sizable enough to be considered worthwhile at ~14.3%. The final core layout consisted of 102 fuel assemblies, 86 reflector assemblies, 54 shield assemblies, and 25 fuel assemblies. Fig. 5.20 shows the final core layout of the annular fuel core.

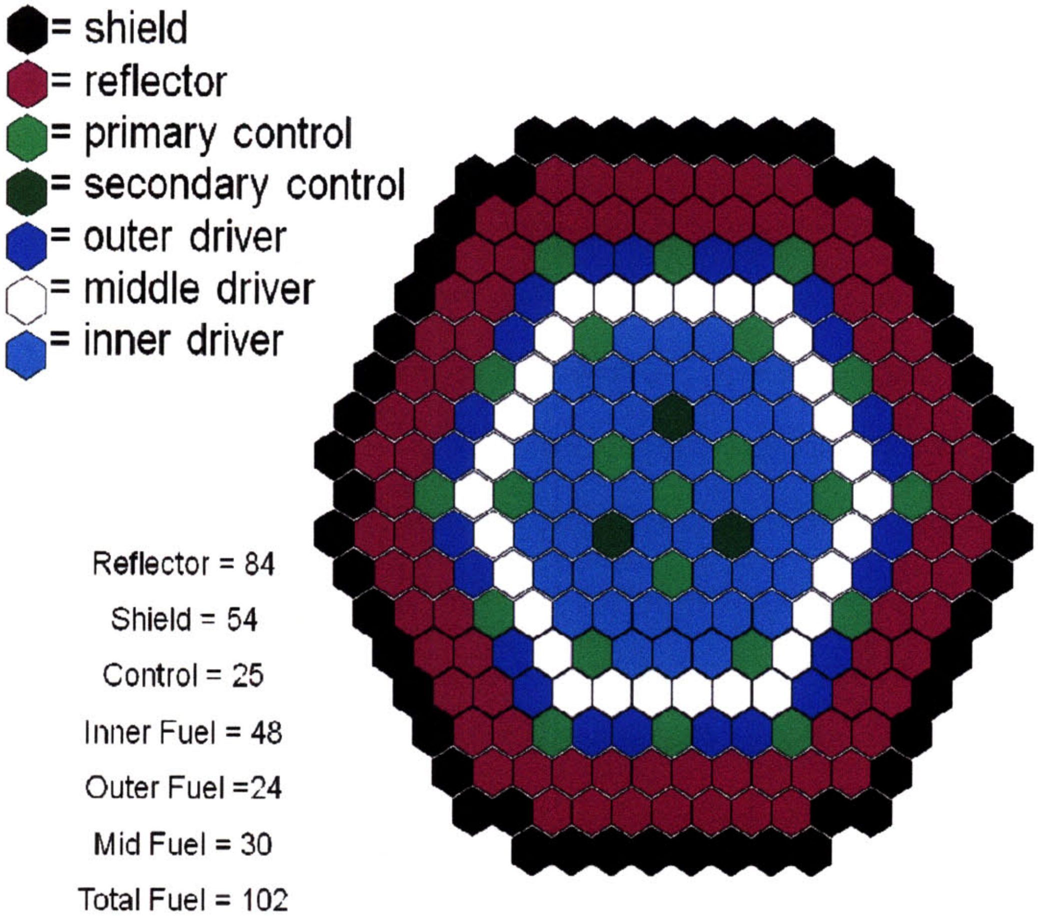

Figure 5.20: Core layout for annular fuel metal CR = 0.25 core

With only 102 fuel assemblies, the power generated by this core is only 952.7 MWth. Considering a power uprate of ~20%, as discussed in Chapter 6, the power generated in the annular fuel core is 1143.32MWth. Thus, the overall power uprate of an annular fuel core when considering core layout limitations is ~11.4%. Should a more desirable and accurate core configuration be developed, the size of the net uprate could be increased. For transparency of comparison with the solid metal fuel core, the core coolant temperature increase was maintained at ~155 °C. The required flow rate to maintain the core average outlet temperature of 510 °C is ~5744 kg/s, and the primary pumps rated flow and head were increased to provide this flow rate through the core. The flow rates through the secondary and PCS systems were also increased by 11.4%, so that similar temperatures are seen for the uprated annular fuel full-plant model. Finally, the DRACS modules were resized so that the heat withdrawn was also increased by 11.4%. A nodalization diagram of the SFR annular metal fuel core is found in Fig. 5.21.

The axial peaking for the metal annular fuel is taken from Table 4.5, while the radial peaking was assumed to be 1.2. Again, this is larger than the peaking of 1.07 predicted by Fig. 4.13, but as with the solid fuel, this elevated peaking not only provides some margin to account for engineering and modeling uncertainties, but it helps to provide clarity of comparison between the annular and solid fuel designs.

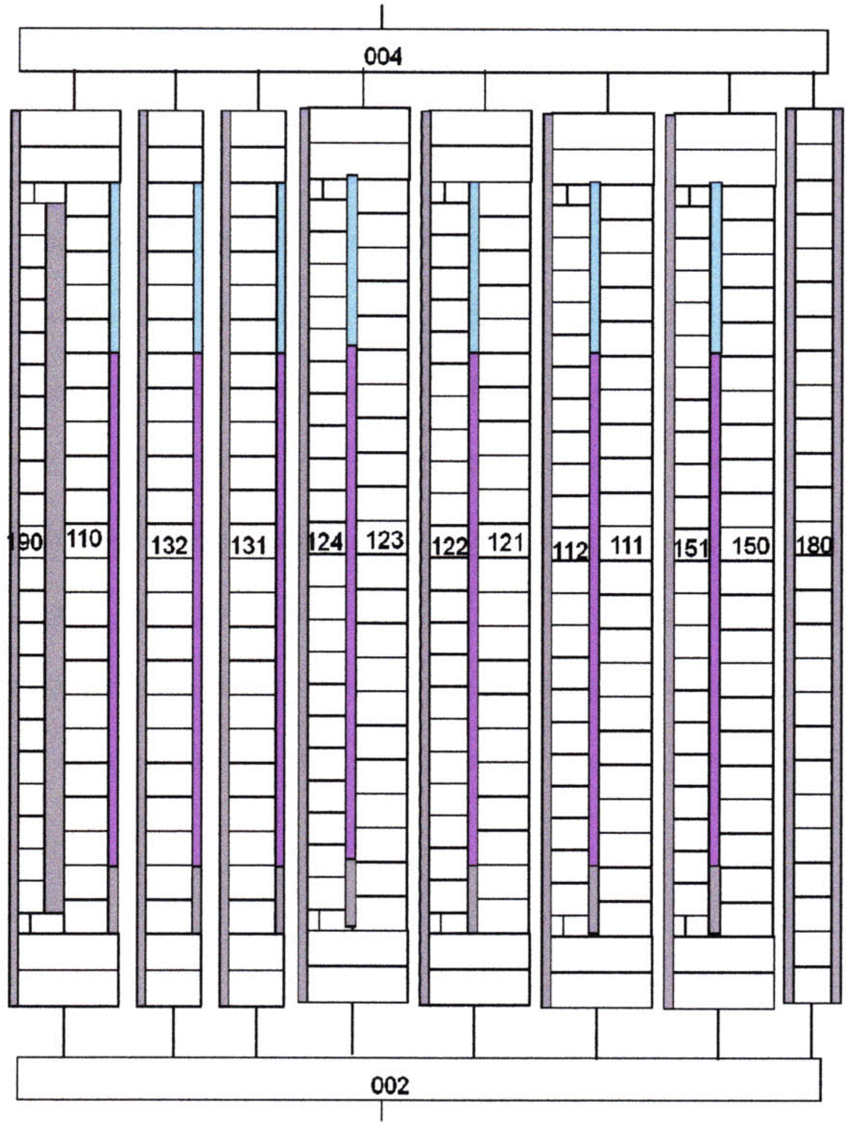

Figure 5.21: Nodalization diagram for annular fuel CR = 0.25 core RELAP5-3D model

The fuel assemblies in the annular fuel core are based upon the design developed in Chapter 4, and include both internally/externally cooled fuel rods and assembly duct ribs. Table 5.29 contains a complete listing of the RELAP5-3D hydraulic component parameters for the CR = 0.25 metal fuel annular core, while the corresponding heat structure parameters can be seen in Table 5.30. These parameters were derived similarly to the core parameters in section 5.1.1.1.

Table 5.29: Hydraulic components of the CR = 0.25 annular fuel pins core RELAP5-3D model

Component	Description	Volumes	Flow Area (m^2)	Hydraulic Diameter (mm)
110	Control	12	0.0826	8.677
111	Inner driver	12	0.3490	2.600
112	Inner driver IA	12	0.1967	3.625
121	Middle driver	12	0.2182	2.600
122	Middle driver IA	12	0.1229	3.625
123	Outer driver	12	0.1821	2.600
124	Outer driver IA	12	0.0983	3.625
131	Reflector	12	0.1942	1.878
132	Shield	12	0.1600	4.251
150	Hottest assembly	12	0.0073	2.600
151	Hottest assembly IA	12	0.0043	3.625

Table 5.30: Heat structure components of the CR = 0.25 annular fuel pins core RELAP5-3D model

Heat Structure	Description	Segments	Inner Radius (mm)	Outer Radius (mm)	Heated Length (Core Segment)
11102	Control core	5	0.00	20.965	35.560
11112	Inner driver core	5	1.80	3.835	3872.179
11212	Middle driver core	5	1.80	3.835	2420.112
11232	Outer driver core	5	1.80	3.835	1936.09
11312	Reflector core	5	0.00	7.705	1553.261
11322	Shield core	5	0.00	16.685	231.648
11502	Hottest assembly core	5	1.80	3.835	80.6704

The steady state operation of the annular fuel core is similar to the steady state operation of the solid fuel core, with one primary difference: the hydraulic resistance for the annular fuel design is higher than for the solid fuel design. This requires a larger pump, and results in a larger pressure drop across the core. This increased hydraulic resistance across the core results in a slightly worse performance during a long term station blackout transient, as the natural circulation flow rate will be less. This will be discussed in more detail in Chapter 6. In order to maintain the steady state performance, the pumping power was increased (while maintaining the same homologous curves) until the temperature rise across the core matched that of the solid fuel core model. At this point, both core power and flow rate were increased by 20.0% (a net increase of power density of 11.4%) to simulate an uprated metal annular fuel core. The temperatures at key points for this steady state model match that of the base model within ~1%.

5.4 Conclusions

A RELAP5-3D model representing the entire SFR plant was created, using scaled up ABTR parameters and best engineering judgment. Certain comparisons were made against the ABR1000 concept described by Grandy et al., and the final performance of the RELAP5-3D model was found to be acceptable. This RELAP5-3D model includes the primary pool (including hot and cold regions, the core, the primary IHXs, and the primary pumps), the secondary loops (including the secondary pumps, secondary IHXs and the steam generators), and a PCS boundary representing water flow through a steam generator. Also included is the DRACS safety system, which actuates upon either operator action or loss of electrical power to the DRACS control valves. The steady state performance of this model matches the expected performance of a typical SFR.

Three additional core models were created to represent the bottle-shaped, low conversion ratio, and annular fuel cores. These cores were included in the full-plant model. With minor adjustments to the pumping power of the CR = 0.25 full-plant models, all steady state runs with these cores matched the expected steady state operating parameters. These full-plant models were then used to model the three transients of interest: the station blackout transient, the ULOF transient, and the UTOP transient. A description and analysis of each of the transients with respect to the relevant core configurations can be found in Chapter 6.

Chapter 6: Transient Analyses

The innovative fuel configurations described in Chapter 4 must perform as well as or better than the base fuel configurations during the three postulated SFR transient scenarios if they are to be feasible fuel designs. These "design basis" SFR transient scenarios are the loss of heat sink transient, the loss of flow transient, and the transient overpower. Because it is more conservative, the loss of heat sink and the loss of flow accidents were combined into the more severe station blackout transient. As a conservative assumption, each of these transients are considered unprotected, or in other words, the control rods do not scram at any time during the accident, so as to verify that the SFR is potentially walk-away safe.

Also, unique benefits of utilizing supercritical carbon dioxide (S-CO_2) during a loss of flow accident merit further investigation. Therefore, a loss of flow transient without scram, also known as an unprotected loss of flow (ULOF) transient, was simulated for the full plant model utilizing metal CR = 0.71 solid fuel and a Rankine PCS for use as a comparison against the same transient using a S-CO_2 PCS. This is discussed in detail in Chapter 7.

Throughout the station blackout and transient overpower accidents, certain thermal limits must not be exceeded. For metal fuel, the primary figures of merit are the peak clad and maximum fuel temperatures. Fuel-clad chemical interaction (FCCI) is the primary clad failure mechanism, and thus should be avoided. Many factors affect the clad-fuel eutectic attack rate and depth, such as time at the given temperature, fuel composition, and rate of clad-fuel eutectic attack [4.6]. A current standard for FCCI avoidance is that the clad temperature must remain below a generally accepted limit of 725°C for very short time-frames (minutes) and under 650 °C for the long time-frames consistent with normal operation.

For oxide fuel, the fuel and clad must avoid melting temperatures. The first constraint is that of the clad temperature. HT9 is not a very creep resistance material above around 630 °C. This severely limits the use of HT9 with oxide fuel, as PCMI at the top of the fuel results in potential creep failure due to large straining [6.1] in both steady state and transient operation. Thus, it is recommended that oxide dispersed steels (ODS) be used when they become available [6.2], but at this point, these materials are not yet ready for use as cladding in the SFR. Thus, HT9 is used as cladding in the model as described in Chapter 5. As an additional limitation, sodium coolant boiling must be avoided due to the positive void coefficient; if coolant in the hot channel boils at any time throughout the transients, super-criticality could be achieved, which is considered unacceptable. However, the boiling point of sodium is significantly higher than the clad limit of 630°C, and thus this limit will be used as the limiting temperature for the oxide fuel cladding, and oxide fuel transients where the clad temperatures exceed this value will be considered unacceptable.

The first transient modeled with the RELAP5-3D full plant model was an unprotected loss of heat sink (ULOHS) transient. This transient aided in identifying two potential complications, which limited the ability of the model to perform the station blackout transient completely; these issues were the model size and the maximum time-step limitations.

6.1. Full Plant Model Runtime and Time Step Optimization

Prior to the running of a station blackout transient, an unprotected loss of heat sink (ULOHS) transient was initiated in order to evaluate the transient performance of the SFR full plant model. The full plant model described in Chapter 5 included four explicitly modeled secondary loops and PCS trains. This resulted in a larger than necessary model, which required large amounts of time in order to run a transient scenario. Additionally, the core volume to coolant velocity ratio in certain hydrodynamic volumes was so small that the Courant limit prevented the use of time steps greater than 0.0007 seconds. The courant limit is a stability limit, which dictates that a time step cannot be larger than the time it takes the coolant to cross one volume length. Thus, short volumes that sustain high coolant velocities often limit the time step size of the model. The initial LOHS run provided results that indicated reasonable performance of the full plant model. However, these results were only short term, (~1000 seconds) and required ~1.5 days of runtime. Because some of the station blackout transients required nearly 60,000 seconds of runtime, this limitation prevented the complete analysis of the station blackout transient.

Because none of the three standard SFR transients relate to a secondary loop failure, it was not necessary to include 4 separate trains. Thus, each of the 4 secondary loops was lumped into a single loop with areas and flow rates increased appropriately. In addition, the number of core nodes was reduced similarly to the reduction made in the subchannel model, as described in Section 4.2. With these adjustments, the courant limit was increased to 0.03 seconds, allowing for a time step of ~0.007 seconds. The overall model runtime was therefore decreased by a factor of 40 and was determined suitable for the evaluation of station blackout transients.

6.2 Station Blackout Transient

The station blackout transient is a loss of electrical power accident. It is assumed that all electrical power to the plant is lost and that emergency backup power fails. Under these conditions, the heat sink (PCS) is lost, the pumps stop working, and the fail-open valves of the DRACS open. For the station blackout transients performed here, the PCS is lost instantly upon accident initiation, while the pumps continue to operate at progressively decreasing speeds for a period of time. This gradual decrease in pump speed after accident initiation is called the pump "coast-down." The core continues to produce decay heat at a larger rate than natural circulation can remove the heat via DRACS, therefore it is important to consider the long term, as well as the short term, results of the station blackout. The RELAP5-3D station blackout transients, therefore, are run for ~60,000 seconds to ensure that decay heat has indeed fallen below the power removal capabilities of the safety systems.

There are four separate phases of an unprotected station blackout transient. The first phase of the station blackout transient consists of sharply increasing core temperatures, as the pumps trip and begin to slow down. The reactor power is reduced due to the net negative reactivity coefficients, but it remains higher than the heat removed by the flow through the core, causing an increase in coolant temperature. The coolant temperature increases until the core power drops below the heat removed by the coolant flow. The second phase of the station blackout accident is a decrease in core temperatures (clad, fuel, and coolant) as the reactor power continues to decrease. The third phase of the station blackout transient begins as the pump completely stops and natural circulation flow is established. The natural circulation flow rate carries heat from the core to the DRACS exchanger, where the heat is rejected, and then returns to the core inlet. The heat removed from the DRACS is less than the decay heat produced by the core, so the coolant and clad and fuel temperatures slowly increase. A second peak is seen after a large time has elapsed from the initiation of the transient. This occurs when the decay heat from the core matches the decay heat removed by the DRACS systems. The fourth and final phase is where the DRACS systems effectively cool the pool by removing more heat than is generated in the core.

The length, magnitude, and location of these phases on the accident timescale are dependent upon several parameters, as well as the fuel configuration of the core itself. Since both oxide and metal fuels will be investigated separately, it is useful to first identify and investigate the primary universal parameters that define the length and severity of each phase of the unprotected station blackout accident. These parameters are the pump coast-down curves, the control rod drive-line expansion feedback, the DRACS performance, and the decay heat curve. A parametric study of these factors with respect to a solid metal fuel CR = 0.71 core configuration is found in the following sections.

6.2.1 Pump Coast-down Model

The location and height of the first temperature peak depends primarily upon the fuel type and the rate at which the pump coasts down. Typically, pump coast-down is driven by the momentum of an external flywheel, but the pumps contained in the SFR described in this thesis are EM pumps, and thus do not have flywheels. However, in order to utilize EM pumps, a major requirement is that they must perform similarly to mechanical pumps in term of sufficient coast-down time. Thus, it is assumed that the EM pumps in the SFR model operate after having been tripped via a capacitor, whose discharge would allow an EM pump coast-down similar to a mechanical pump in the same application. The pump mass flow rate coast-down is an exponential decay curve, typically with a "halving time" of between 5 and 20 seconds for SFR applications. In RELAP5-3D, the option is available to either specify the velocity of the pump, or to evaluate the pump velocity due to both pump inertia and the frictional torque within the pump, utilize the torque and inertia equations during coast-down. The frictional torque and inertia equations can be defined as [6.3]:

$$\tau_{fr} = \pm\left(\tau_{fr0} + \tau_{fr1}\left|\frac{\varpi}{\varpi_R}\right|^{x1} + \tau_{fr2}\left|\frac{\varpi}{\varpi_R}\right|^{x2} + \tau_{fr3}\left|\frac{\varpi}{\varpi_R}\right|^{x3}\right)\tau_{frn} \qquad \text{for } \left|\frac{\varpi}{\varpi_R}\right| \geq S_{PF} \tag{6.1}$$

$$\tau_p = I_p \frac{d\varpi}{dt}, \tag{6.2}$$

respectively, where:

τ_p = pump torque

I_p = pump inertia

ω = pump speed

ω_R = pump rated speed

τ_{fr} = pump frictional torque

τ_{fr0} = constant frictional torque coefficient

τ_{fr1} = first frictional torque coefficient

τ_{fr2} = second frictional torque coefficient

τ_{fr3} = third frictional torque coefficient

x_1 = first frictional torque exponent

x_2 = first frictional torque exponent

x_3 = first frictional torque exponent

S_{PF} = pump critical speed ratio.

Table 6.1: Pump frictional coefficient/exponent values for ABTR pumps [5.3]

Pump inertia (kg/m^2)	160.0
Second frictional coefficient	0.1
Constant frictional coefficient	21.5
First frictional coefficient	21.5
Third frictional coefficient	-
First frictional exponent	1.0
Second frictional exponent	2.0
Third frictional exponent	-

A scoping analysis of the influence of pump coast-down on the first temperature peak for the metal CR = 0.71 base configuration was performed in which four separate pump coast-down curves were modeled: an exponential coast-down with halving time of 5 seconds, an exponential coast-down with halving time of 20 seconds, a logarithmic coast-down, and a coast-down utilizing the inertia and frictional relations, with values derived from the ABTR EM pumps [5.3], as seen in Table 6.1. The logarithmic coast-down curve is simply the pump velocity fitted to a logarithmic curve with similar starting and 150 second finishing flows, to explore the validity of this type of flow coast-down. The resulting temperatures and fractional mass flow rates can be seen in Figs. 6.1 and 6.2, respectively.

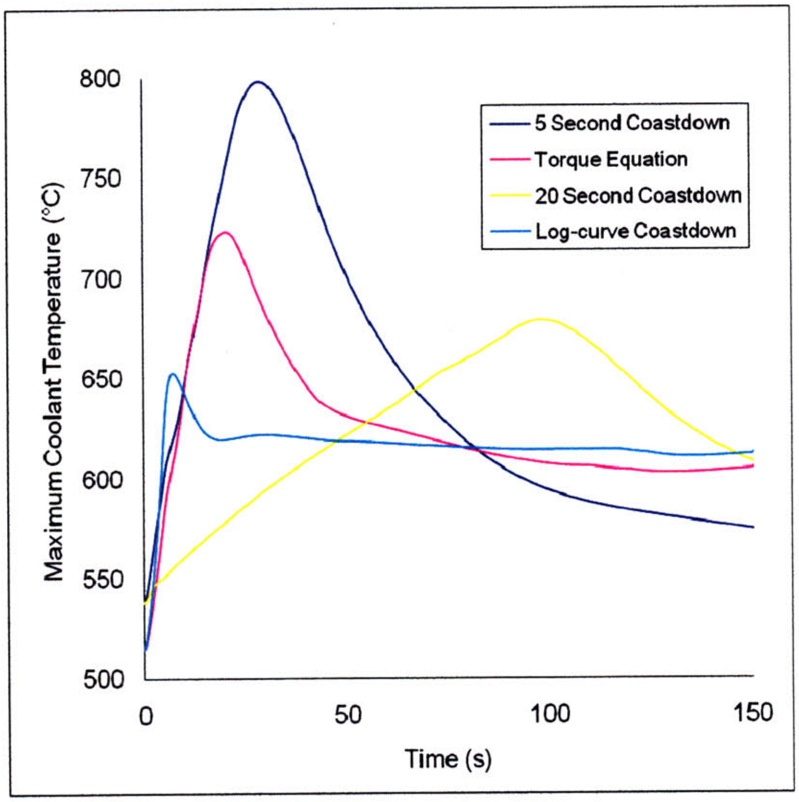

Figure 6.1: Maximum coolant temperature for various pump coast-down curves

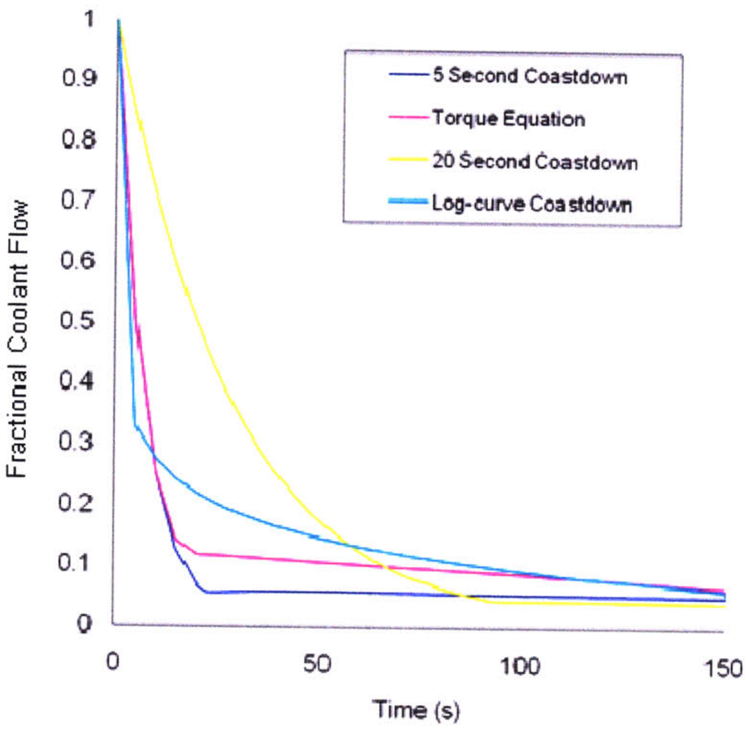

Figure 6.2: Fractional core coolant flow for various pump coast-down curves

For the slower pump coast-down curves, the initial temperature peaks are smaller, and they occur later on in the transient because the pump fractional flow decreases at a lower rate and takes longer to drop below the fractional power curve. The fractional core power curves for all cases can be seen in Fig. 6.3.

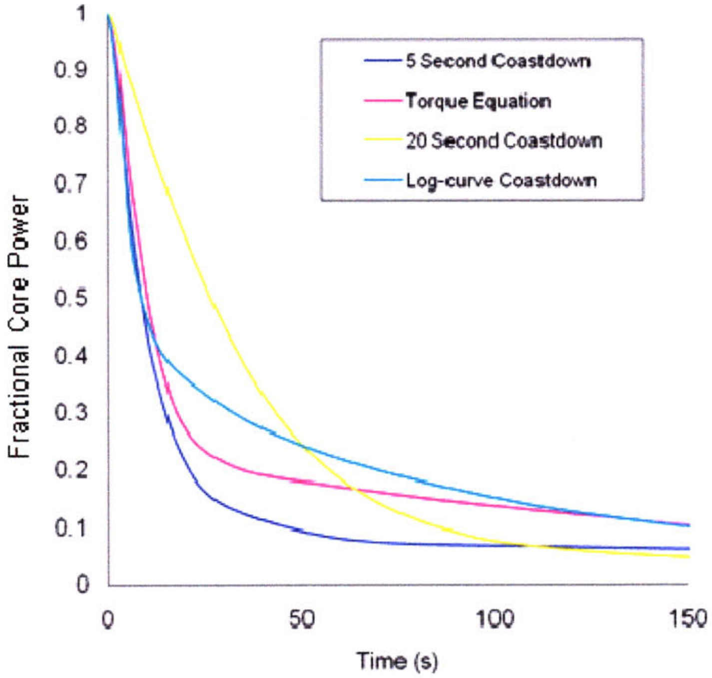

Figure 6.3: Fractional core power for various pump coast-down curves

Based upon these findings, engineering judgment was enforced to select a conservative pump coast-down standard halving time of 5 seconds for the station blackout transient runs. It was found that in some cases, 5 second halving times resulted in initial peak cladding temperatures that were above the short term FCCI and PCMI limits. However, in each of these cases, the halving time was increased to an upper bound of 20 seconds to determine if a longer pump coast-down would prevent the breach of the transient temperature limits.

6.2.3 Control Rod Drive-Line Expansion (CRDLE) Model

The core kinetic reactivity feedback coefficients play a large role in determining the height and location of the first peak, along with the pump coast-down curve. The feedbacks utilized for the full plant model, as described in Section 5.1.1.2 are used for all of the transient analyses performed in this thesis. However, the CRDLE feedback was not clearly defined in this section because of the uncertainties associated with this feedback. The CRDLE feedback was calculated explicitly from known design parameters of the SFR model. The CRDLE reactivity insertion ($\Delta\rho_{CRDLE}$) in ¢/°C was calculated according to the following equation:

$$\Delta\rho_{CRDLE} = \alpha \cdot \Delta T_{CRDL} \cdot L_o \cdot \alpha_{CR}, \tag{6.3}$$

where:

α = thermal expansion coefficient of the control rod drive-line
ΔT_{CRDL} = change in temperature of the control rod drive-line
L_o = initial control rod drive-line length submerged in sodium
α_{CR} = control rod worth in ¢/cm.

The control rod drive-line was assumed to be made of stainless steel (ss-316), and thus a thermal expansion coefficient of $1.9\text{x}10^{-5}$ was used. The change in temperature of the control rod drive-line is calculated directly by the RELAP5-3D model, and is thus not an input to the model. This temperature represents the average temperature of the sodium in the hot pool region adjacent to where the control rod drive-line would be. The CRDL is not explicitly modeled as a heat structure in RELAP5-3D due to lack of a concrete design in the reference plant model. Thus, as a simplifying assumption, the temperature of the core outlet was used instead of the actual CRDL temperature. It should be noted that such an assumption neglects the time required to heat the driveline, and thus the CRDLE is encountered earlier than in reality. The third parameter, the control rod drive-line length submerged in sodium pool, is assumed to be 6.0 m, according to engineering judgment. This leaves only the control rod worth as an uncertainty.

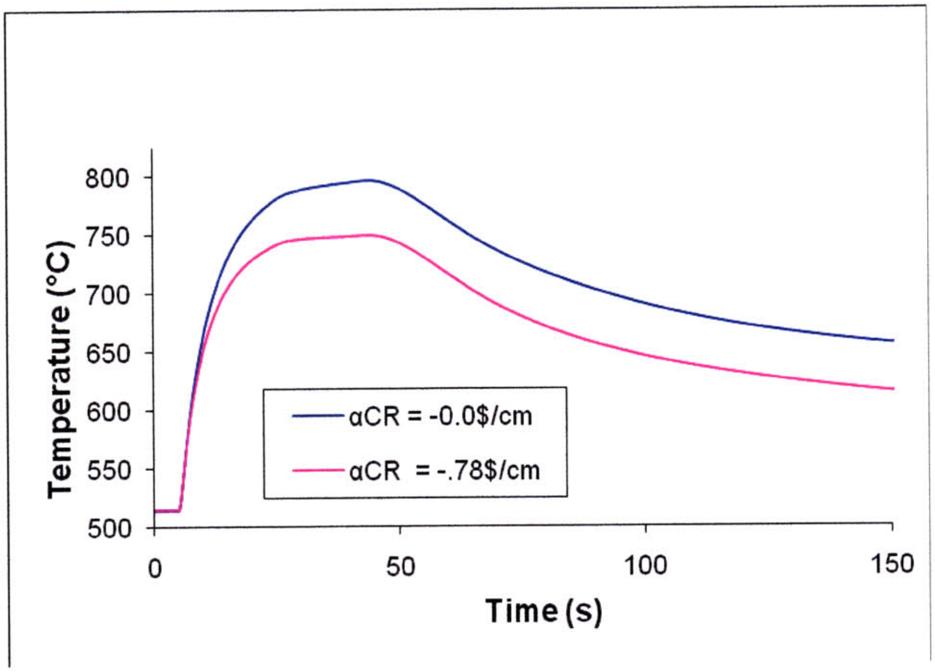

Figure 6.4: Maximum coolant temperature for given values of control rod worth in the CRDLE model (assuming BOL conditions)

For a single rod, the worth associated with control rod drive-line expansion is negligible, but it is quite significant for all the control rods being withdrawn together. Thus, a sensitivity analysis of the CRDLE feedback in the full plant CR = 0.71 metal fuel core model was conducted in order to evaluate the influence of control rod worth on the max coolant temperature during the first 150 seconds of the station blackout transient.

Figure 6.4 shows the short term influence of the CRDLE. The temperature peak is smaller for a larger CRDLE because the added worth shuts down the reactor more quickly. However, there is a potential problem if too much rod worth is claimed, as large reactivity swings as a function of temperature are possible.

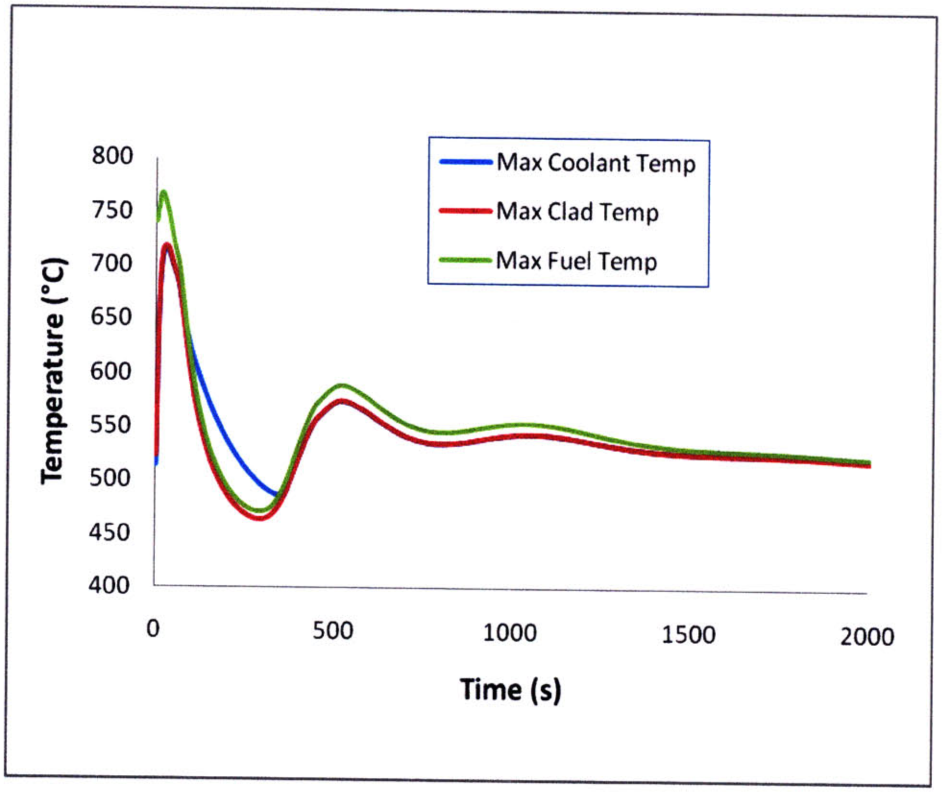

Figure 6.5: Maximum coolant, clad, and fuel temperatures for a high value of control rod worth in the CRDLE model (assuming BOL conditions)

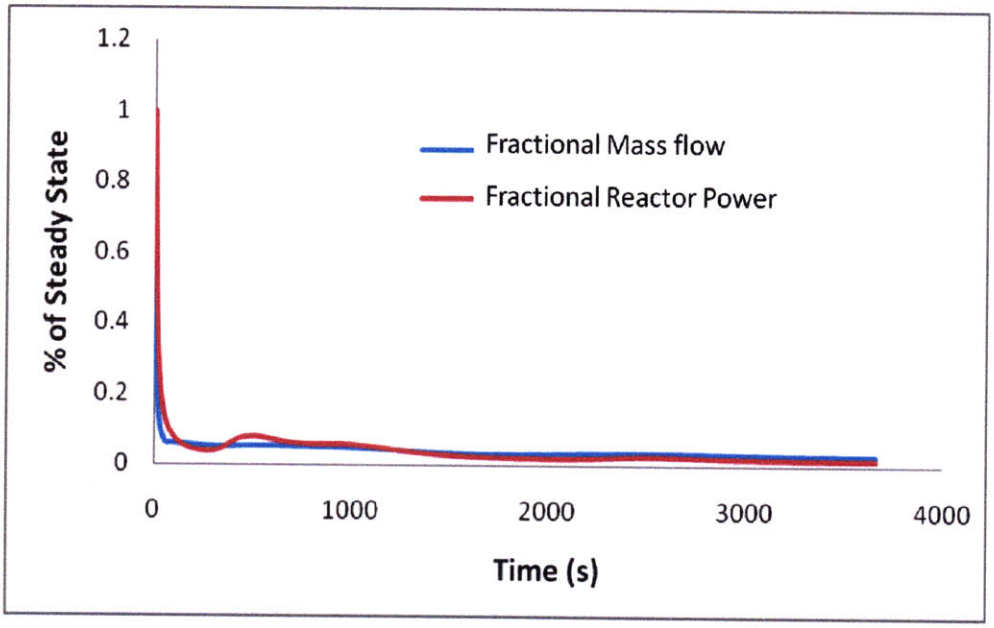

Figure 6.6: Fractional power and mass flow curves for a high value of control rod worth in the CRDLE model (assuming BOL conditions)

A plot of maximum coolant temperature for very high CRDLE feedback is shown in Fig. 6.5, while the fractional power and flow curves are plotted in Fig. 6.6. The corresponding reactivity is shown in Fig. 6.7. Note that at very high values of the control rod worth, the temperature begins to oscillate during the second phase of the transient. This is primarily due to reactivity oscillations resulting in periodic re-criticality of the core. This occurs as the control rod drive-line cools and positive reactivity is essentially inserted as the rods withdraw relative to the core. The core then increases in temperature, which in turn heats the CRDL, which expands and re-inserts the rods. This then reduces the reactor power again, causing a decrease in power and temperature. These oscillations become more severe as the control rod worth increases. Thus, to mitigate such severe responses, a reasonable control rod worth of 49¢/cm for the metal fueled cores, and 35¢/cm for the oxide fueled cores was assumed.

It is of importance to note that the CRDLE influence described in this section is only valid at BOL. At EOL, the CRDLE feedback will be significantly smaller, and could lead to clad failure in the case of a station blackout transient with a 5 second halving time pump coast-down. One possible solution to this is to impose a condition that the control rods always be inserted, which requires a higher initial k_{eff} and higher enrichment, which leads to decreased economic performance. A different solution is to incorporate a passive scram device that inserts negativity if an increase in power or temperature is detected [6.4]. These devices could potentially be used to provide additional negative reactivity at EOL.

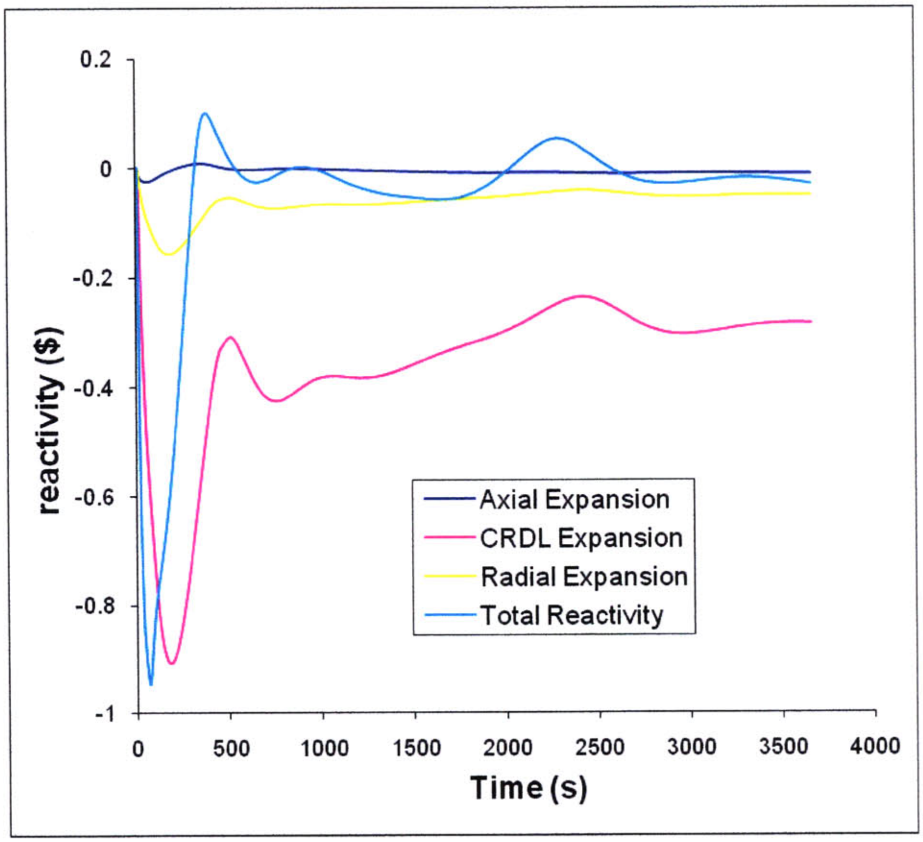

Figure 6.7: Selected reactivity feedbacksas a function of time for a high α_{CR} case

6.2.4 DRACS System

The DRACS system is one of two components that determines the time and height of the second temperature peak. Each DRACS loop, as described in Section 5.1.5.2, is capable of removing 2.5MW, or 0.25%, of steady-state power. All three DRACS are thus capable of removing 0.75% of steady-state full power. For all three transient scenarios investigated in this thesis, however, only two of the three DRACS are assumed to operate, according to the so-called "single-failure criterion". Thus, in the RELAP5-3D model, the DRACS valve is only opened for 2 of the DRACS loops, resulting in 5 MW total power removal. Note that the rated DRACS power is the power removed at the second peak, or in other words, the power removed by the DRACS system when the DRACS power equals the reactor decay power.

The DRACS size remains constant for all the transients except for the uprated annular fuel transients. The models in these transients have a core power uprated by 11.4%, and thus the DRACS system is uprated by 14.3% as well so that a constant heat withdrawal of 0.25% of steady-state full power can be removed.

6.2.5 Decay Power Curve

The second parameter that determines the height and time at which the second temperature peak occurs is the decay power of the core. The decay power for fast reactors is quite different from the decay power for light water reactors. In previous fast reactor applications [5.2, 5.3], a decay curve was assumed to be 100% of the ANSI 5.1

standard [6.5] for Pu-239. Although this is more acceptable than assuming the same decay curve as light water reactor cores, it is still not entirely accurate. A rigorous calculation of the decay heat for a lead-bismuth eutectic reactor was performed previously [6.6] for a CR = 1.0 core. A comparison of this decay curve with the 100% Pu-239 decay curve and the LWR decay heat curve is found in Fig. 6.8.

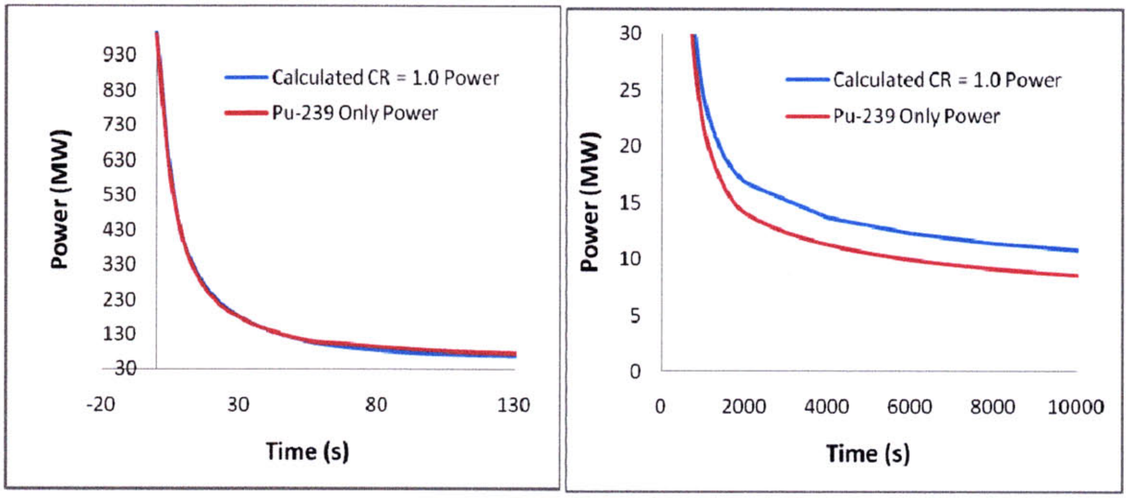

Figure 6.8: Comparison of CR = 1.0 lead-bismuth and 100% Pu-239 decay curves

A decay heat curve for CR = 0.71 fuel has not been calculated to date, but the CR = 1.0 curve serves as a conservative approximation. However, this curve is not utilized in this thesis, primarily so that a clear comparison can be made between the current station blackout runs, and those modeled in the reference design [5.12], as the decay heat curve utilized in those studies is 100% of the ANSI 5.1 standard for Pu-239. A more accurate curve should be used in future work to determine actual performance of the reactor, however. The CR = 1.0 decay heat curve was included in initial runs (not shown here) but the SFR DRACS systems were not appropriately sized to remove the heat generated with the CR =1.0. It is beyond the scope of this thesis to design a new DRACS systems that can remove the additional heat generated by the CR = 1.0 decay heat curve, however. For these reasons, therefore, the convention of utilizing the decay heat curve for 100% of the ANSI 5.1 standard for Pu-239 was followed for all of the transients modeled in this study.

Since the purpose of this thesis is to compare the innovative fuel designs to the traditional fuel design, not to verify the feasibility of the DRACS design, it is acceptable to use a reasonable, albeit not conservative, curve, such as that for Pu-239. However, future work should focus on resizing the DRACS systems to successfully remove the decay heat generated in the CR = 1.0 curve.

6.3 Station Blackout Results

There are six different core configurations for which the station blackout transient was run: the CR = 0.71 base fuel configurations (both metal and oxide), the CR = 0.71 bottle-shaped fuel configurations (both metal and oxide), the CR = 0.25 metal base fuel configuration, and the CR = 0.25 metal annular fuel configuration. The results of each of these transients are presented and discussed in the following sections.

6.3.1 Base Fuel Configurations (CR = 0.71)

The base fuel configurations of the higher conversion ratio core serve as the standard by which the innovative fuel designs are to be compared. The metal and oxide fuels both undergo similar blackout transients, with 2/3 DRACS systems operable, a 100% Pu-239 decay curve, and a pump curve defined by a 5 second halving time. Both short and long term results are plotted for each fuel configuration, as significant trends are present in each. The results for the metal fuel CR = 0.71 base fuel configuration station blackout transient are found in Figs. 6.9 - 6.13.

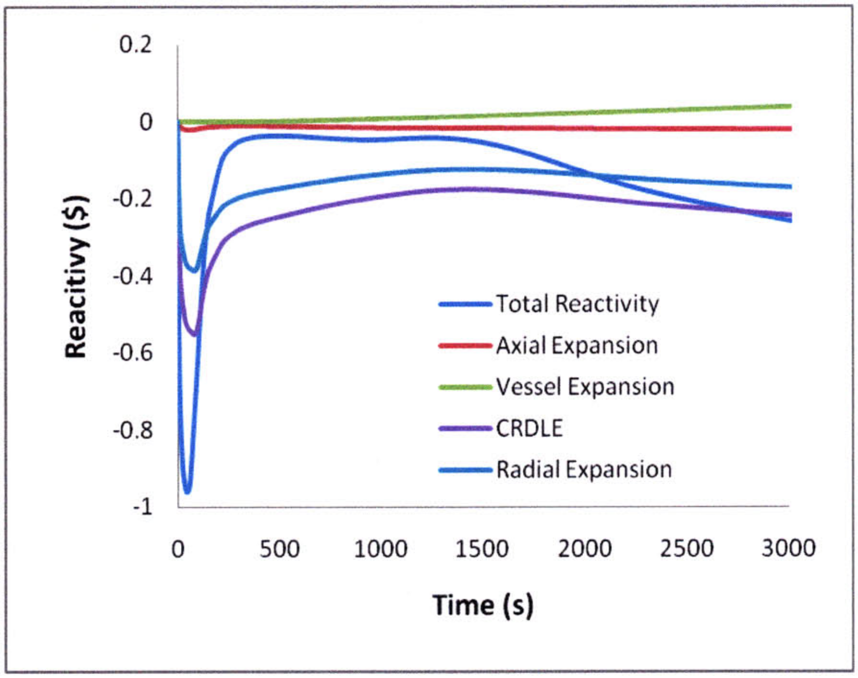

Figure 6.9: Selected reactivity feedbacks for metal CR = 0.71 base fuel configuration during the station blackout

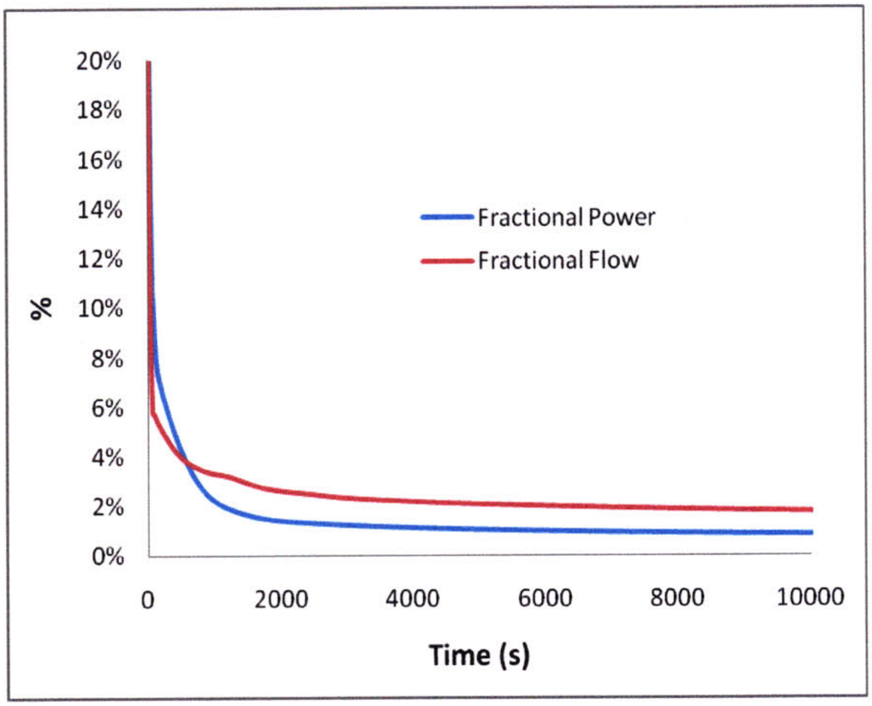

Figure 6.10: Fractional core power and coolant flow rate for the metal CR = 0.71 base fuel configuration during the station blackout

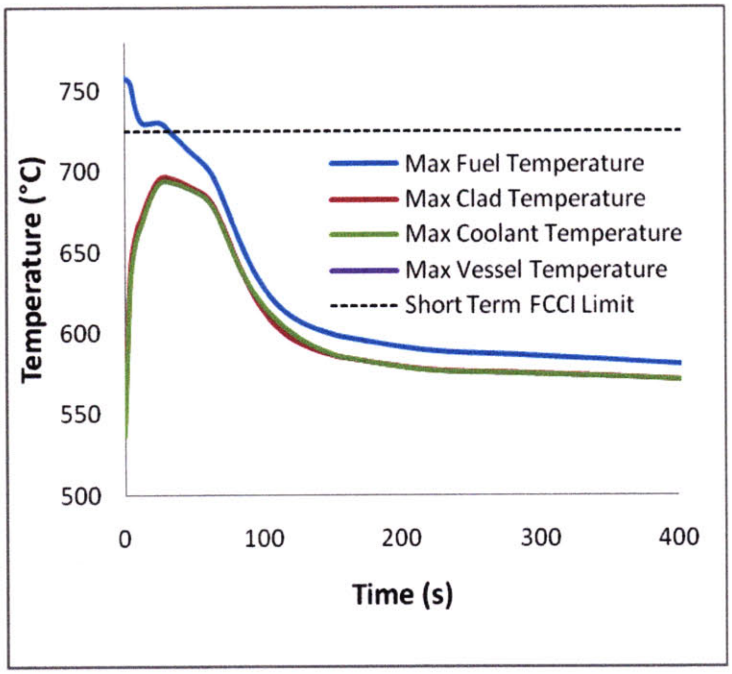

Figure 6.11: Short term key temperatures for the metal CR = 0.71 base fuel configuration during the station blackout

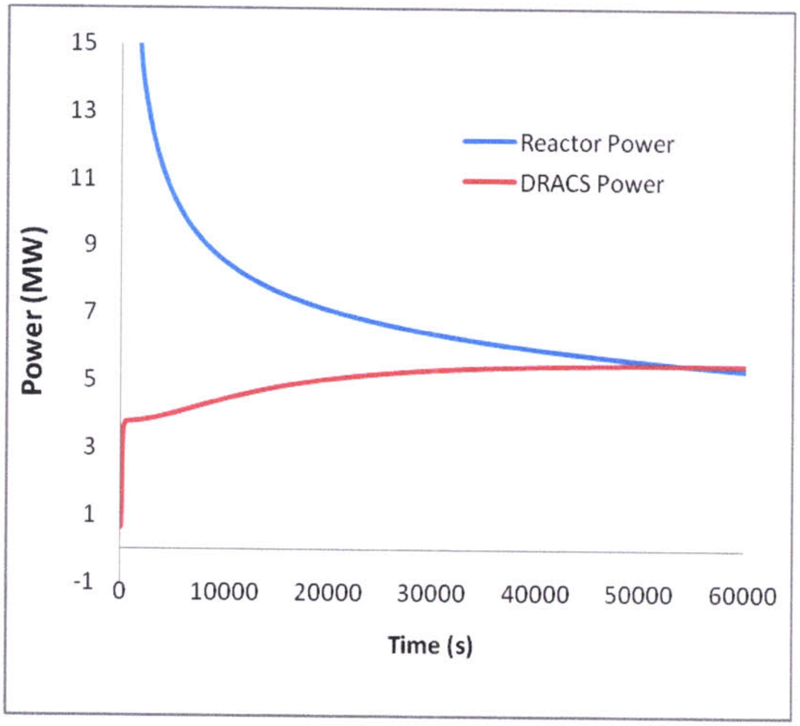

Figure 6.12: Long term DRACS and core power withdrawn for the metal CR = 0.71 base fuel configuration during the station blackout

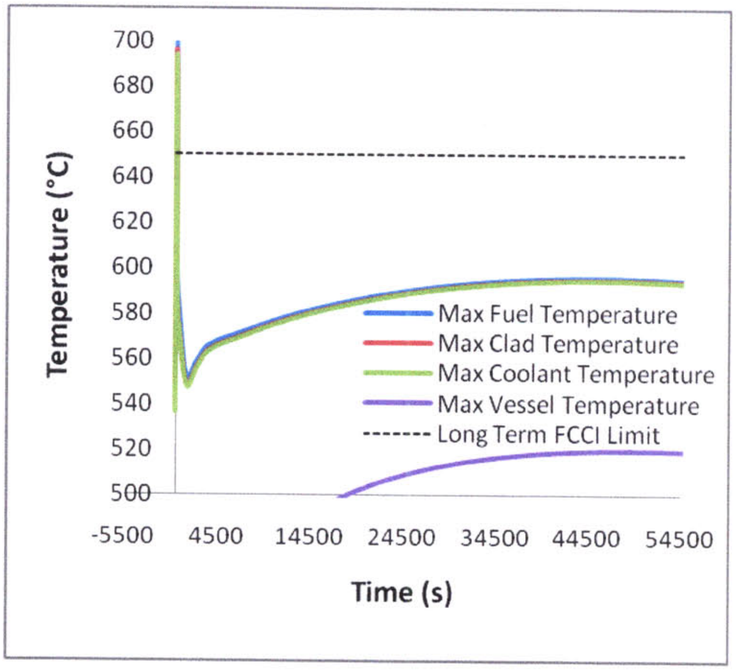

Figure 6.13: Long term key temperatures for the metal CR = 0.71 base fuel configuration during the station blackout

The radial, Doppler, and CRDLE feedback mechanism all drop with the initial increase in temperature resulting in the power reduction of the reactor. As the temperatures begin to drop off, so do these negative feedbacks. It should be noticed that the positive reactivity resulting from vessel expansion gradually begins to increase as the vessel temperature increases, but this is more than compensated for by the CRDL expansion, and thus re-criticality is never achieved.

The maximum clad temperature occurs at the hottest assembly core outlet, and is 695 °C at ~25.2 seconds. The fuel temperature decreases as the reactor power decreases below the power removable by the coolant flow, and through the second temperature peak it never reaches the operating temperature, and thus is not a safety concern during a station blackout transient. Neither the clad nor fuel temperatures exceed the safety limits in the second peak, further bolstering the performance of the metal CR = 0.71 base fuel configuration during a station blackout transient. Note that our analysis does not include all the engineering uncertainty factors required in a rigorous quantitative core analysis, so the feasibility of the reference core design is yet to be proven. However, since the purpose of this thesis is simply to compare the innovative fuel designs to the reference design, this simpler approach is deemed acceptable.

The fractional coolant flow drops proportionally with the pump velocity during the early time periods of the station blackout. After ~90 seconds, however, natural circulation velocity is established, and the fractional flow (~6% at this point) begins to decay much more slowly, eventually leveling off at ~2%. This fractional flow is driven by the difference in the hot and cold pool temperatures, and these changes in natural circulation reflect the changes in these temperatures.

The oxide CR = 0.71 base fuel configuration station blackout transient results are plotted in Figs. 6.14-6.18. Unlike the metal fuel configuration, the clad temperature increases dramatically, such that the clad temperature limit of 630°C is breached not only for the initial peak, but for the entirety of the transient. The max temperature of the cladding in the initial peak is 1063 °C and occurs at ~37 seconds, while the max clad temperature of the second peak was not ascertained, as the code failed due to instabilities introduced from sodium boiling before the end of the transient, as the current model is not capable of modeling the core during coolant boiling.

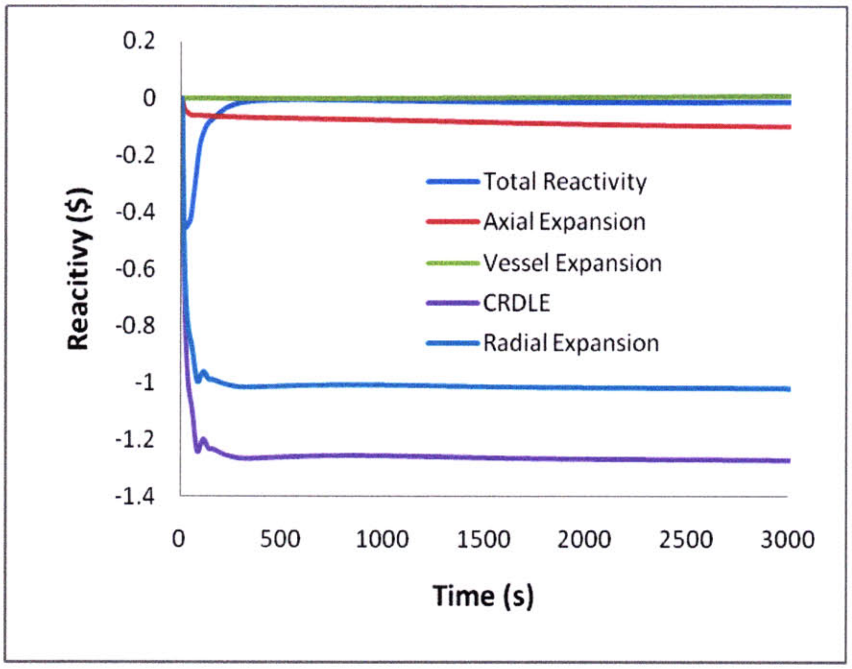

Figure 6.14: Selected reactivity feedbacks for oxide CR = 0.71 base fuel configuration during the station blackout

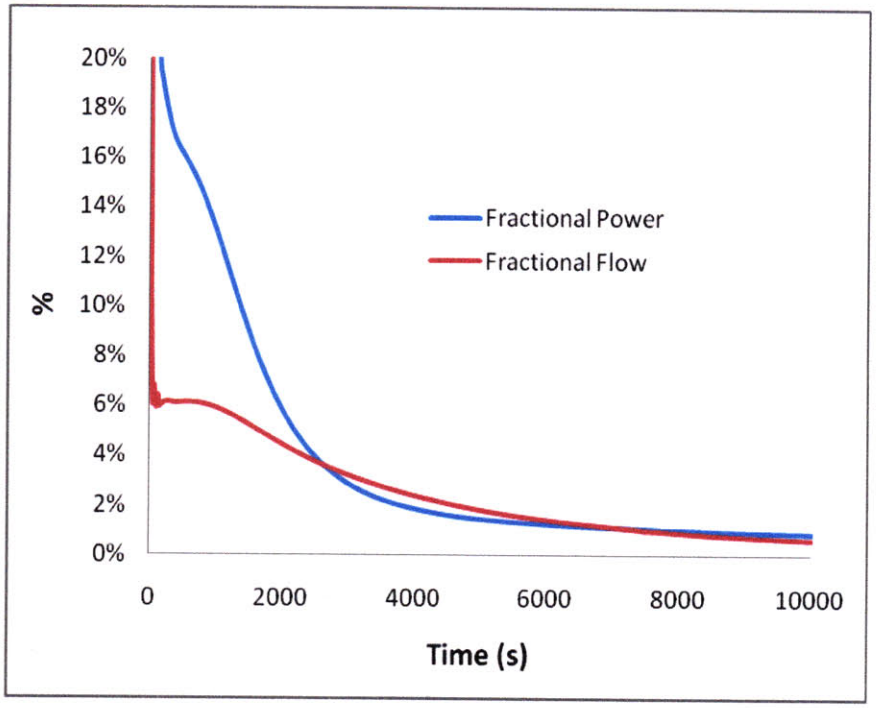

Figure 6.15: Fractional core power and coolant flow rate for the oxide CR = 0.71 base fuel configuration during the station blackout

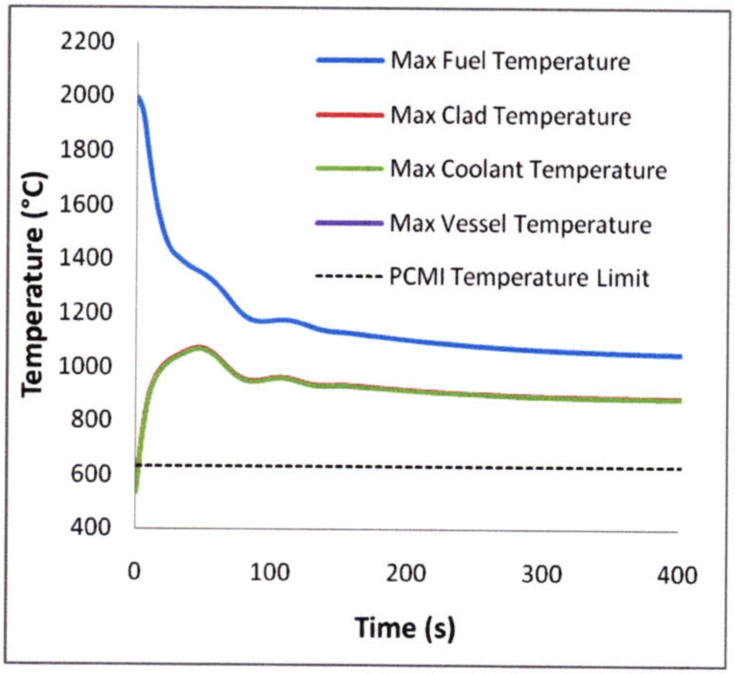

Figure 6.16: Short term key temperatures for the oxide CR = 0.71 base fuel configuration during the station blackout

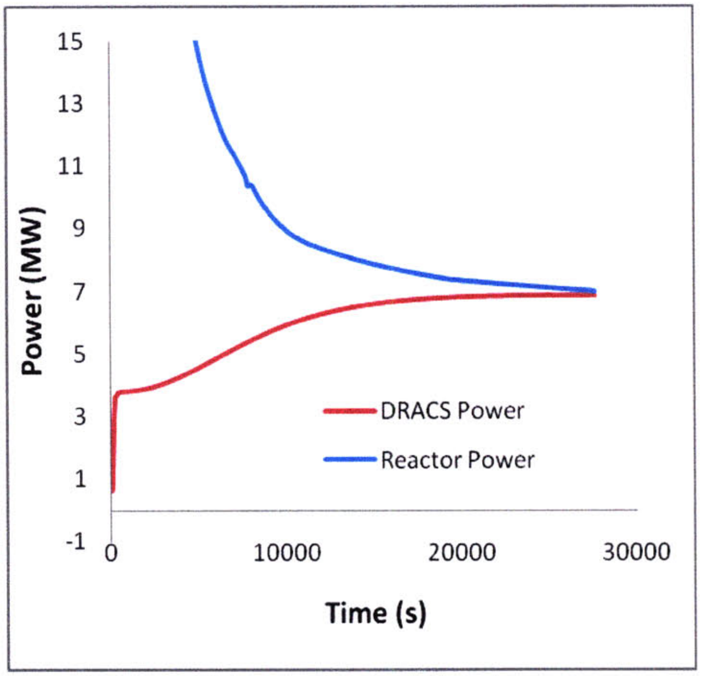

Figure 6.17: Long term DRACS and core power withdrawn for the oxide CR = 0.71 base fuel configuration during the station blackout

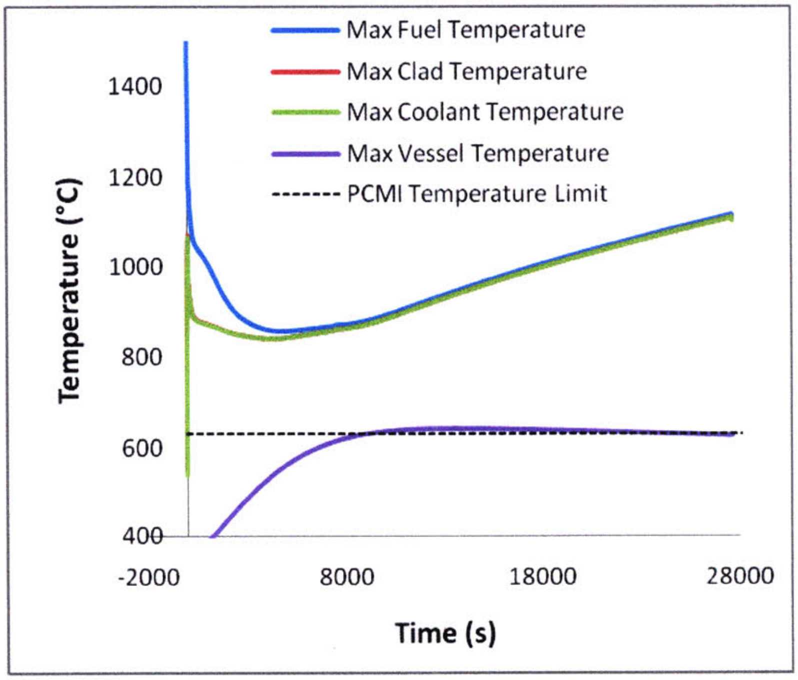

Figure 6.18: Long term key temperatures for the oxide CR = 0.71 base fuel configuration during the station blackout

It can be seen from these figures that the oxide fuel PCMI clad creep temperature limit of ~630°C is exceeded in the early seconds of the station blackout accident, as well as in the long term transients. The power coast-down is slower than in the metal CR = 0.71 base fuel transient, and the natural circulation takes slightly longer to be established and drops to lower flow rates more quickly. This is due to the elevated temperatures of both the hot and cold pools fairly early in the transient.

Considering the performance of the oxide fuel configuration during a station blackout transient, it is doubtful that oxide fuel will perform adequately in unprotected events as a fast reactor fuel. However, the bottle-shaped comparison will still be investigated in the following section to determine if the improvements seen in the metal designs hold for the oxide designs.

6.3.2. Bottle-Shaped Fuel Configurations (CR = 0.71)

The metal CR = 0.71 bottle-shaped fuel model station blackout transient was run using the exact same parameters as the metal CR = 0.71 base fuel. Figs. 6.19 – 6.23 plot the long and short term results of the metal bottle-shaped fuel station blackout transient. The performance of the oxide CR = 0.71 bottle-shaped fuel is nearly the same as the oxide CR = 0.71 base fuel configuration in shape and magnitude, though a clear comparison of the two configurations will be made in Section 6.4.

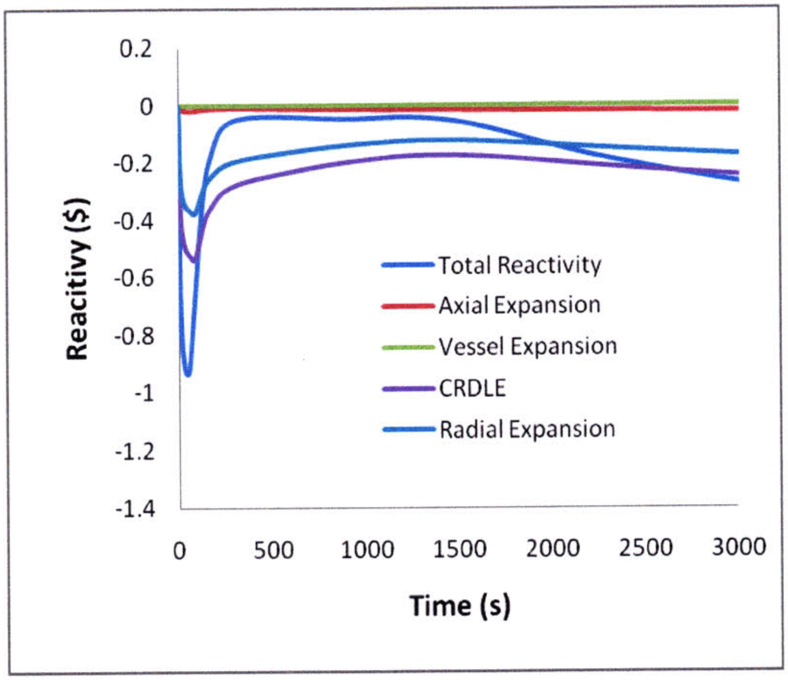

Figure 6.19: Selected reactivity feedbacks for metal CR = 0.71 bottle-shaped fuel configuration during the station blackout

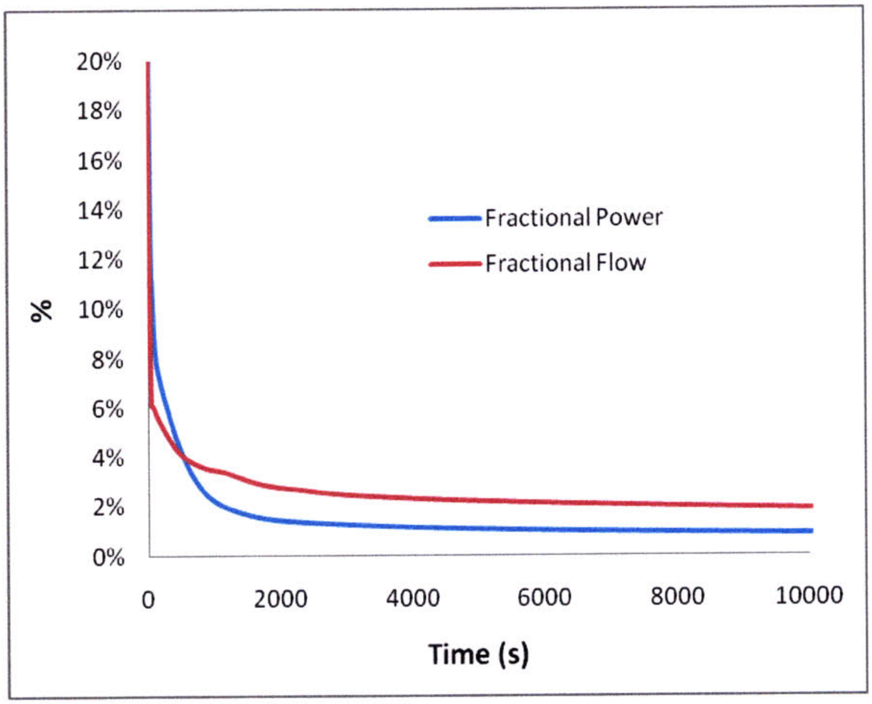

Figure 6.20: Fractional core power and coolant flow rate for the metal CR = 0.71 bottle-shaped fuel configuration during the station blackout

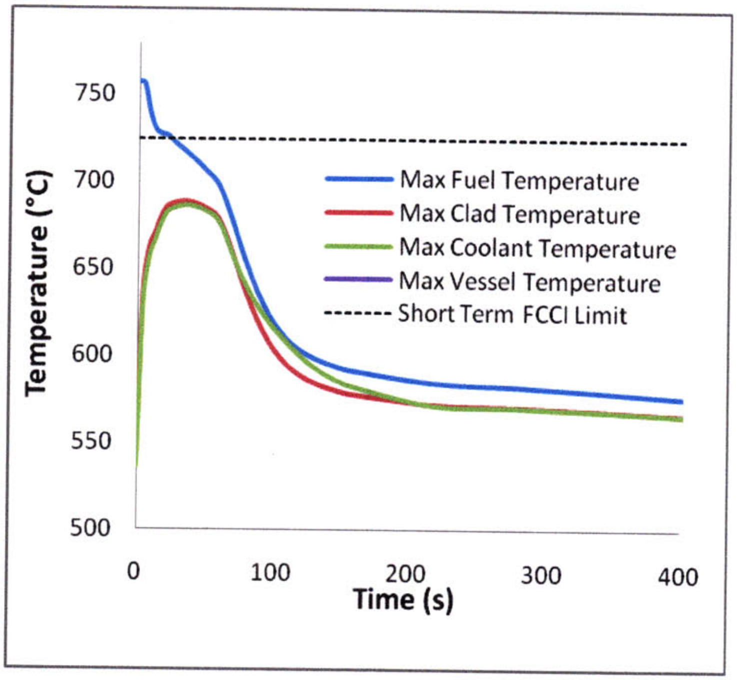

Figure 6.21: Short term key temperatures for the metal CR = 0.71 bottle-shaped fuel configuration during the station blackout

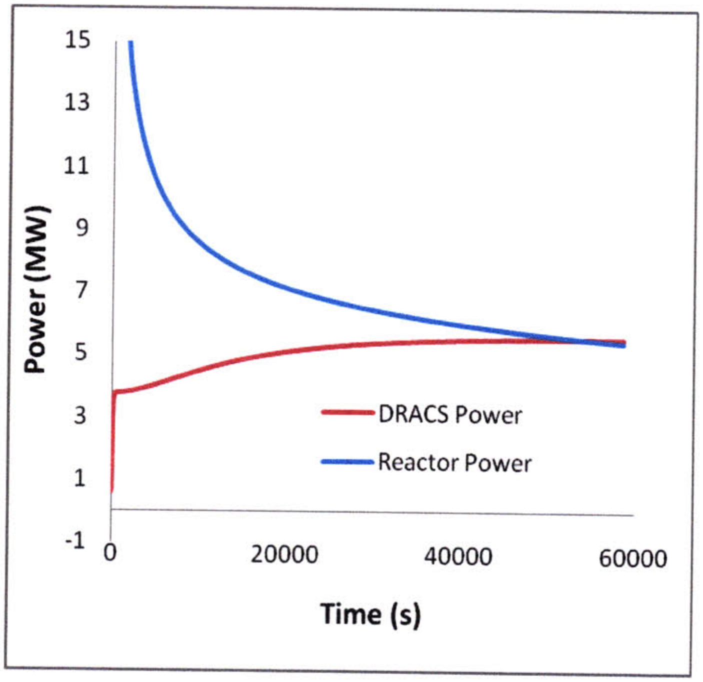

Figure 6.22: Long term DRACS and core power withdrawn for the metal CR = 0.71 bottle-shaped fuel configuration during the station blackout

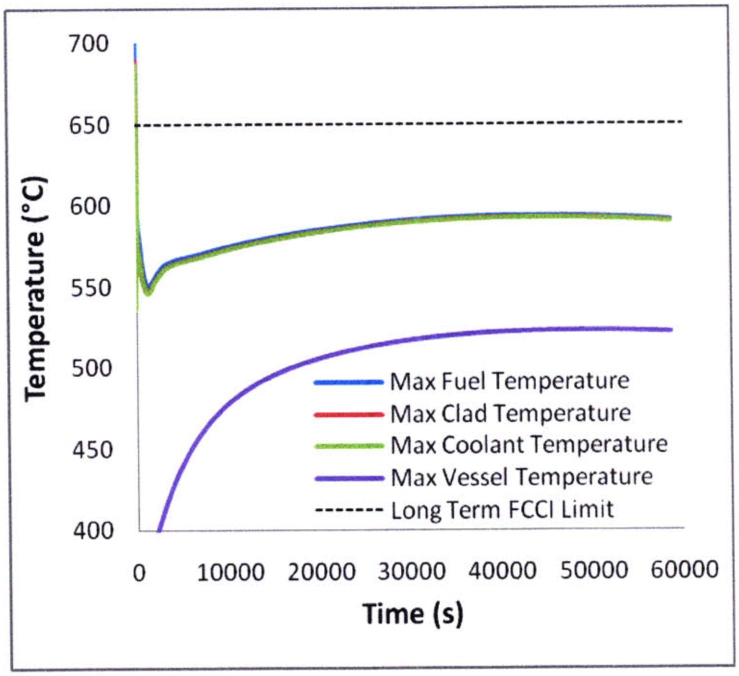

Figure 6.23: Long Term key temperatures for the metal CR = 0.71 bottle-shaped fuel configuration during the station blackout

The metal bottle-shaped fuel performs similarly to the metal base fuel in terms of both peaks and the maximum temperatures. The max clad temperature is 689 °C and occurs after ~39.6 seconds. As with the metal base fuel, natural circulation begins at ~54 seconds with a fractional flow rate of ~6%. This flow decays more slowly than the initial pump coast-down, being driven primarily by the temperature difference between the cold and hot pools. The second clad temperature peak occurs at ~44000 seconds, but is significantly smaller than the clad temperature limits at 593 °C.

The oxide CR = 0.71 bottle-shaped fuel model station blackout transient was run using the exact same parameters as the oxide CR = 0.71 base fuel. Figs. 6.24 – 6.28 plot the long and short term results of the oxide CR = 0.71 bottle-shaped fuel. The bottle-shaped fuel performance shows considerable improvement over the base fuel configuration. However, as with the oxide CR = 0.71 base fuel configuration, the clad temperature exceeds the clad temperature limit of 630 °C from the beginning of the transient, resulting in potential PCMI induced clad-creep failure. This again indicates that the performance of the oxide CR = 0.71 bottle-shaped fuel is still unacceptable. The station blackout transient does not run to completion for the oxide fuel cores, as the onset of core-wide boiling produces code instabilities which cause the code to fail.

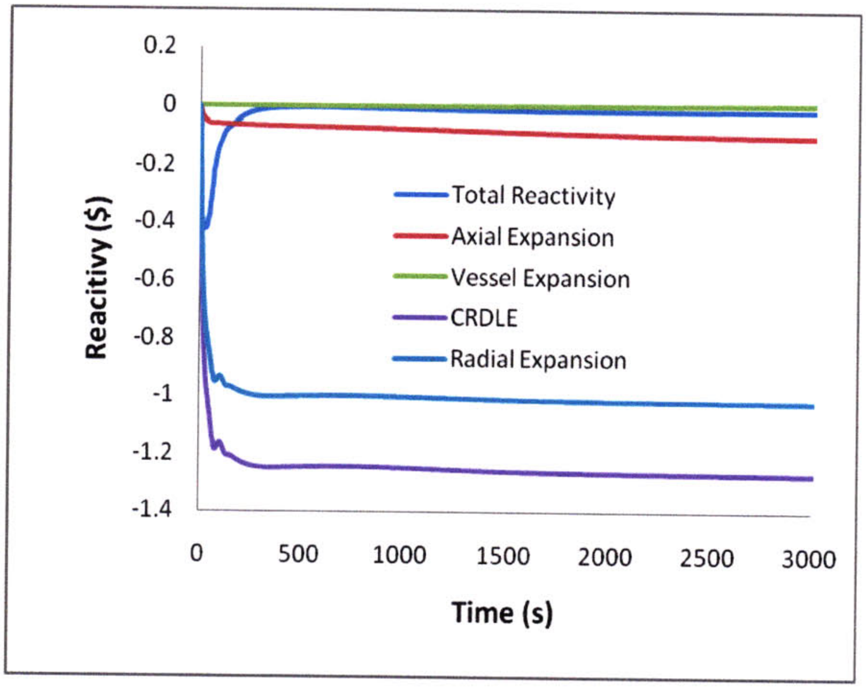

Figure 6.24: Selected reactivity feedbacks for oxide CR = 0.71 bottle-shaped fuel configuration during the station blackout

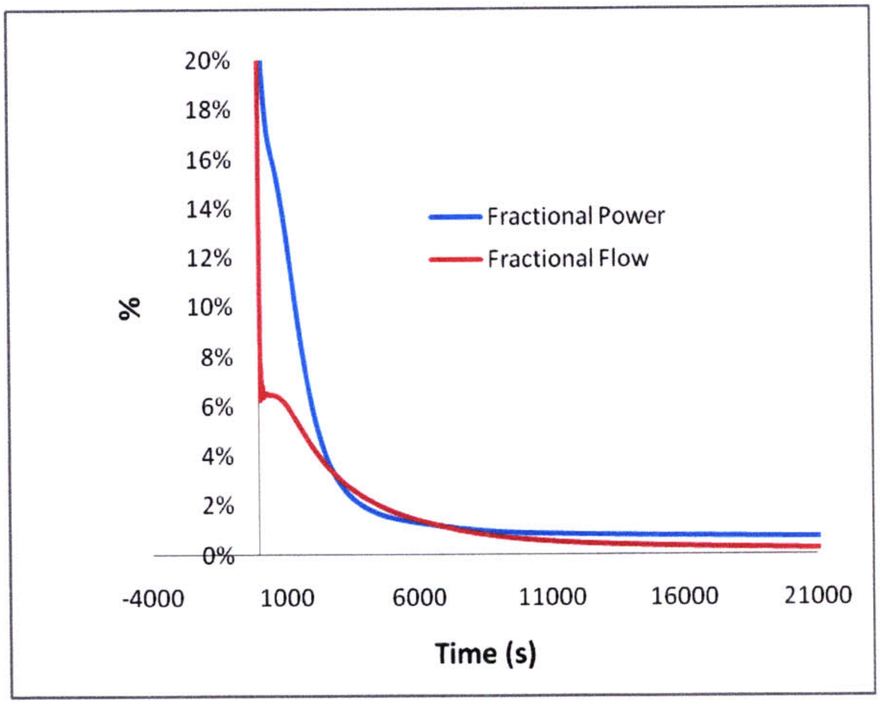

Figure 6.25: Fractional core power and coolant flow rate for the oxide CR = 0.71 bottle-shaped fuel configuration during the station blackout

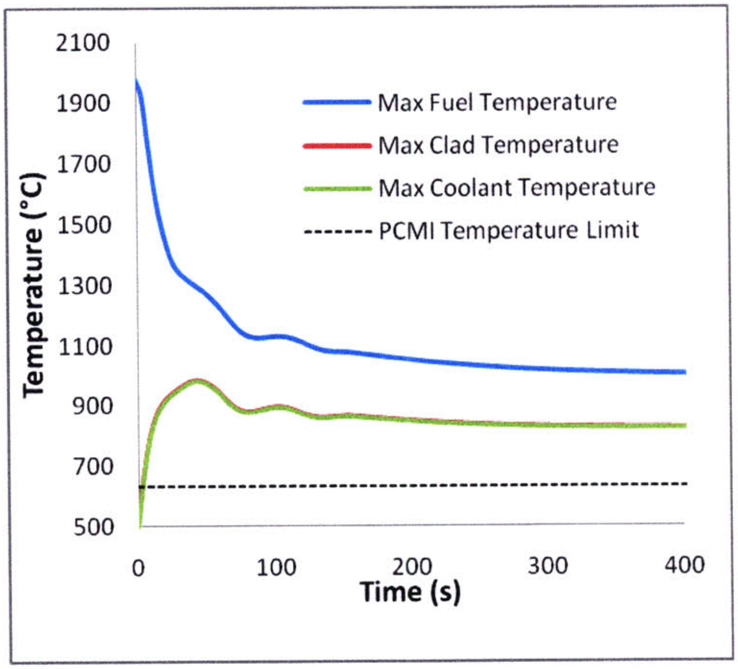

Figure 6.26: Short term key temperatures for the oxide CR = 0.71 bottle-shaped fuel configuration during the station blackout

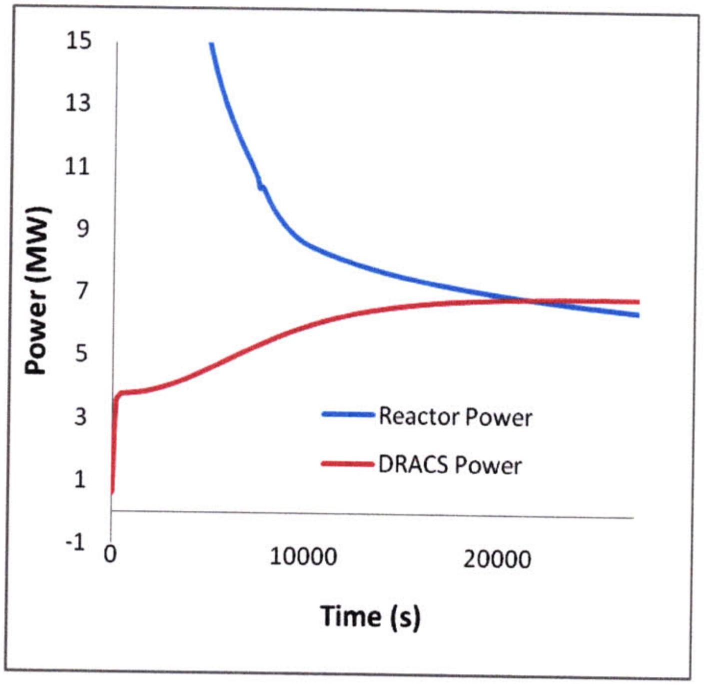

Figure 6.27: Long term DRACS and core power withdrawn for the oxide CR = 0.71 bottle-shaped fuel configuration during the station blackout

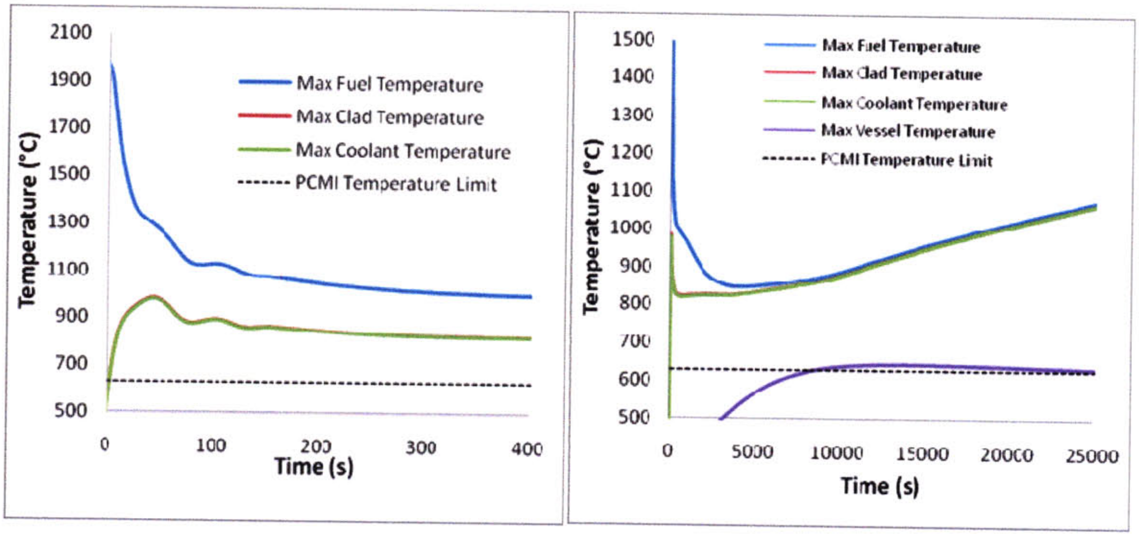

Figure 6.28: Long term key temperatures for the oxide CR = 0.71 bottle-shaped fuel configuration during the station blackout

In order to determine if a longer pump coast-down would ameliorate the oxide base and bottle-shaped fuel transient performances, a station blackout transient was repeated for each of these fuels configurations, but with a pump coast-down relating to a

20 second halving time instead of a 5 second halving time. The short term results are plotted together in Fig. 6.29. The peak temperatures are still too high, and the sodium would still boil. Note that the effect of decreasing the rate of pump coast-down is smaller for bottle-shaped fuel, since the flow rates are naturally higher in the bottle-shaped fuel configuration. A possible solution to this problem is to increase control rod worth, thus effectively increasing the CRDLE feedbacks. However, as discussed in Section 6.1.3, this instigates potential problems with reactor re-criticality and temperature/flow oscillations. For this reason, this method was not investigated, and oxide fuel is deemed unacceptable for use in a SFR due to its performance during an unprotected station blackout transient.

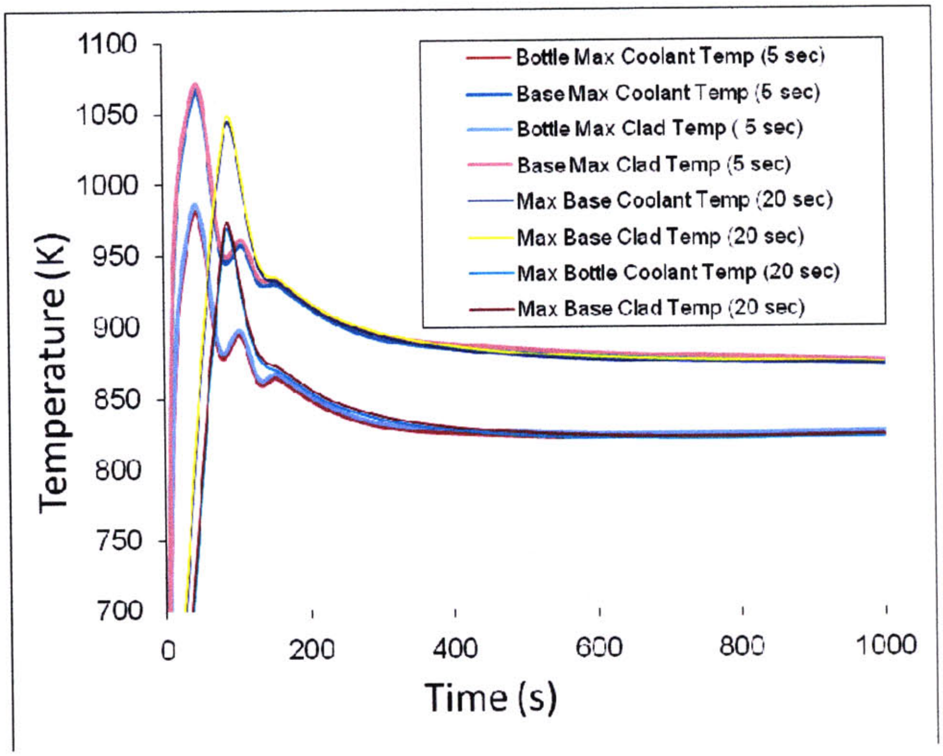

Figure 6.29: Short term key temperatures for the metal CR = 0.71 base fuel configuration during the station blackout

6.3.3 Metal CR = 0.25 Fuel Configurations

A CR = 0.25 model station blackout transient with the exact same parameters as the CR = 0.71 fuel configurations was run for both the solid and annular fuel configurations. The short term performance is noticeably worse for low conversion ratio cores, primarily due to the different reactivity feedbacks. The power level, and thus the size of the peak for both clad and fuel temperatures in the earliest stage of the station blackout transient (~70 seconds), is driven primarily by three reactivity feedbacks: the Doppler coefficient, the fuel density coefficient, and the sodium density coefficient. The sodium density coefficient is nearly 64% higher in the CR = 0.25 cores, while the Doppler coefficient is 50% lower in magnitude, and the fuel density coefficient is 31% higher in magnitude. These changes result in a decrease in the net negative reactivity inserted, which result in a slower decrease in reactor power, and thus a higher temperature peak for the CR = 0.25 fuel configurations. The metal CR = 0.25 base case fuel station blackout transient results for the long and short term are found in Figs. 6.30 – 6.34. During the earlier time-frames of the transient, the short term FCCI clad temperature limit is exceeded. With the pump coast-down curve corresponding to an exponential decay with a 5 second halving time, the initial peak is too high for this core configuration to be acceptable with a peak clad temperature of 764 °C.

During the later time-frames of the transient, the peak fuel temperature is only slightly higher than the peak clad temperatures, as can be seen in Fig. 6.34. The long term peak clad temperature for the CR = 0.25 metal fuel cores is also significantly lower than the short term peak clad temperature (and well below the long term FCCI clad temperature limit). Similarly to the CR = 0.71 metal fuel cores, this indicates again that the second temperature peak is insignificant relative to the first temperature peak.

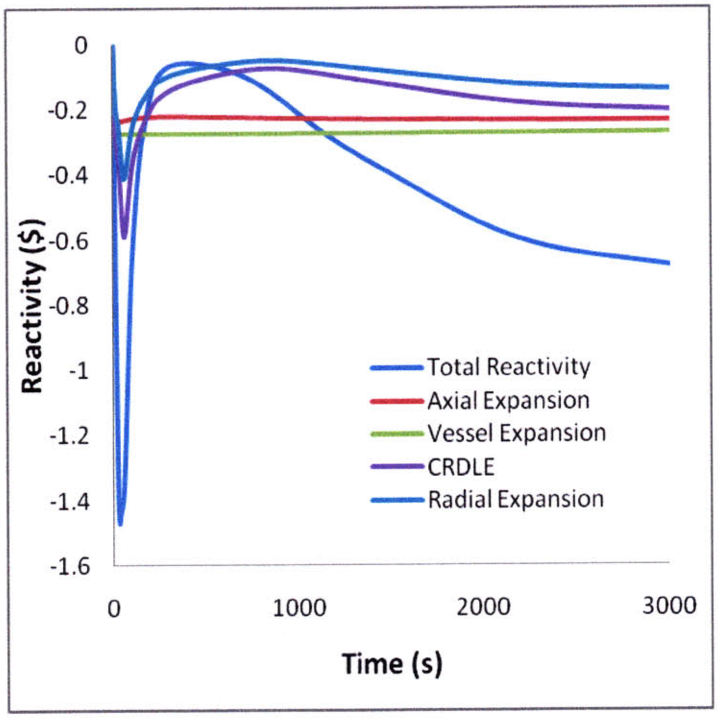

Figure 6.30: Selected reactivity feedbacks for metal CR = 0.25 base fuel configuration during the station blackout

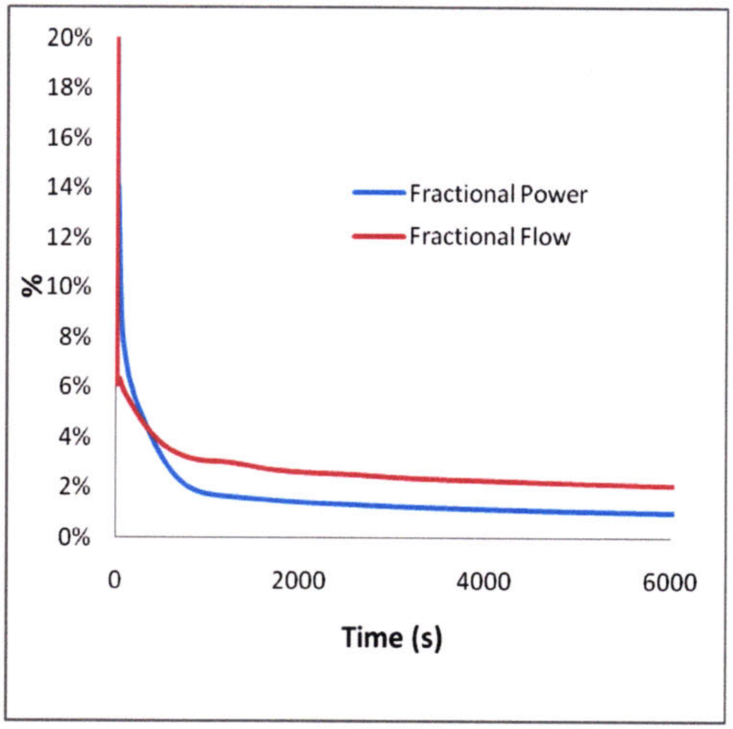

Figure 6.31: Fractional core power and coolant flow rate for the metal CR = 0.25 base fuel configuration during the station blackout

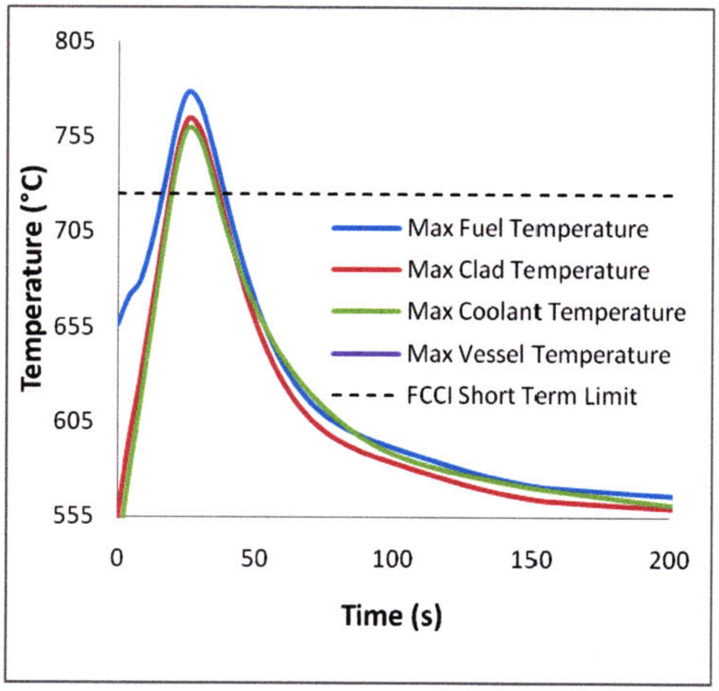

Figure 6.32: Short term key temperatures for the metal CR = 0.25 base fuel configuration during the station blackout

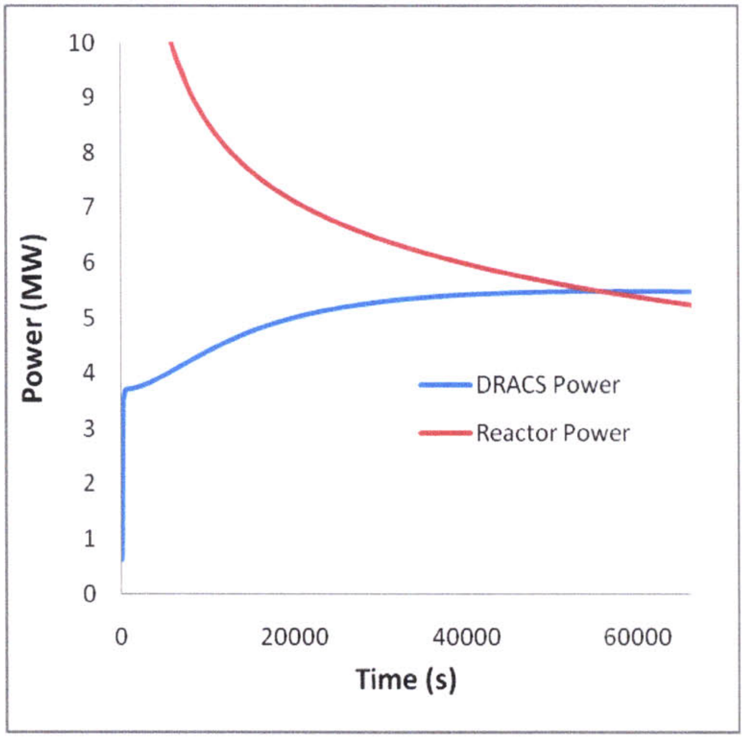

Figure 6.33: Long term DRACS and core power withdrawn for the metal CR = 0.25 base fuel configuration during the station blackout

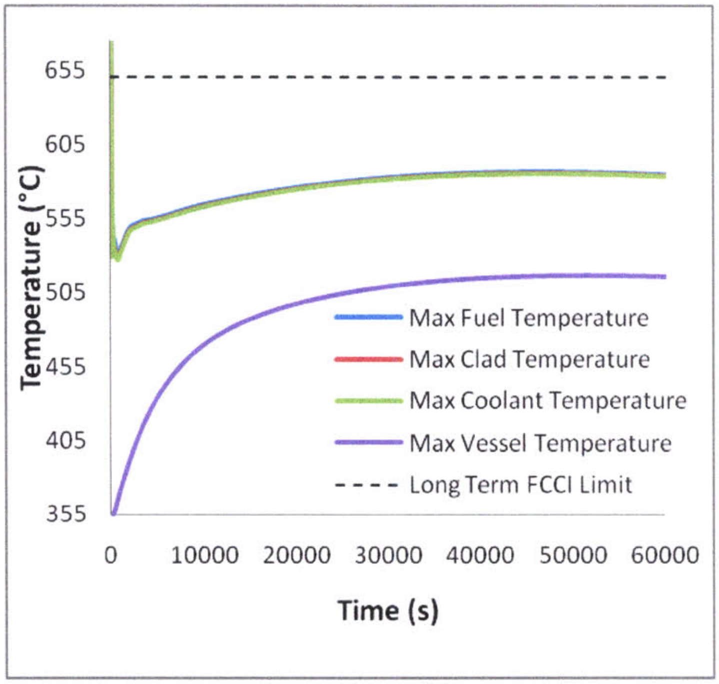

Figure 6.34: Long term key temperatures for the metal CR = 0.25 base fuel configuration during the station blackout

The metal CR = 0.25 annular fuel core model station blackout transient results are found in Figs. 6.35-6.39. Again, the trends for the metal CR = 0.25 annular fuel are very similar to the metal CR = 0.25 base fuel, with slight differences in magnitude and peak location. As with the metal CR = 0.25 base fuel configuration, the initial peak clad temperature for metal CR = 0.25 annular fuel exceeds the FCCI short term limit with a peak clad temperature of ~768.3 °C. The second temperature peak, at 608.9 °C, is well below the long term FCCI limit. Thus, as with the solid fuel configuration, it is the initial peak that is of most concern for the station blackout transient. A comparison of the performance of annular and solid CR = 0.25 core configurations is located in next section.

It is significant to note that in the annular fuel configuration, the max fuel temperature is very close to the max clad temperature (~3 °C higher than the max clad temperature). This makes the max fuel temperature very difficult to discern from the max clad temperature in Fig. 6.37. As with the metal CR = 0.25 base fuel, in the secondary peak, the fuel, coolant, and clad temperatures are all very close and difficult to differentiate on the plot in Fig. 6.39.

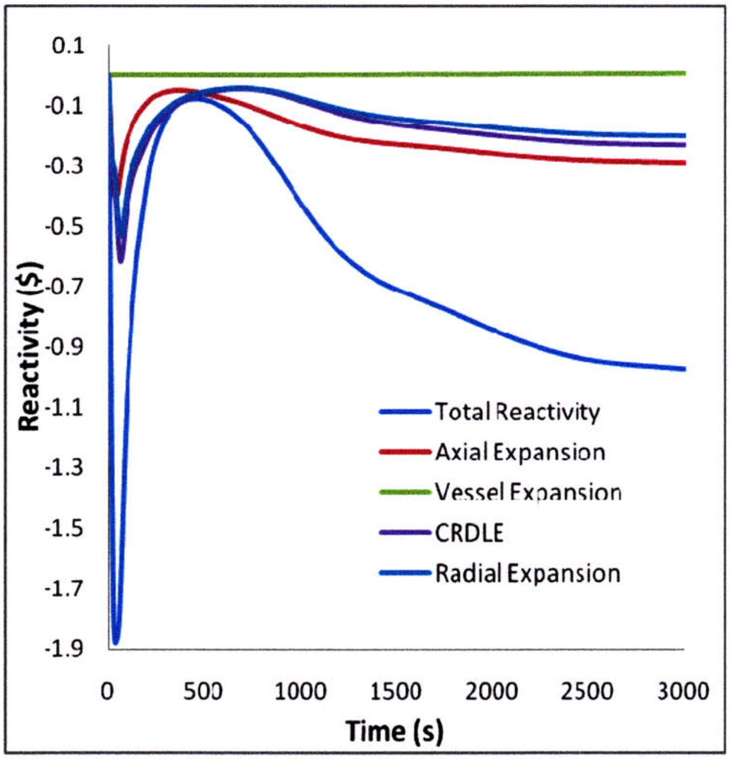

Figure 6.35: Selected reactivity feedbacks for metal CR = 0.25 annular fuel configuration during the station blackout

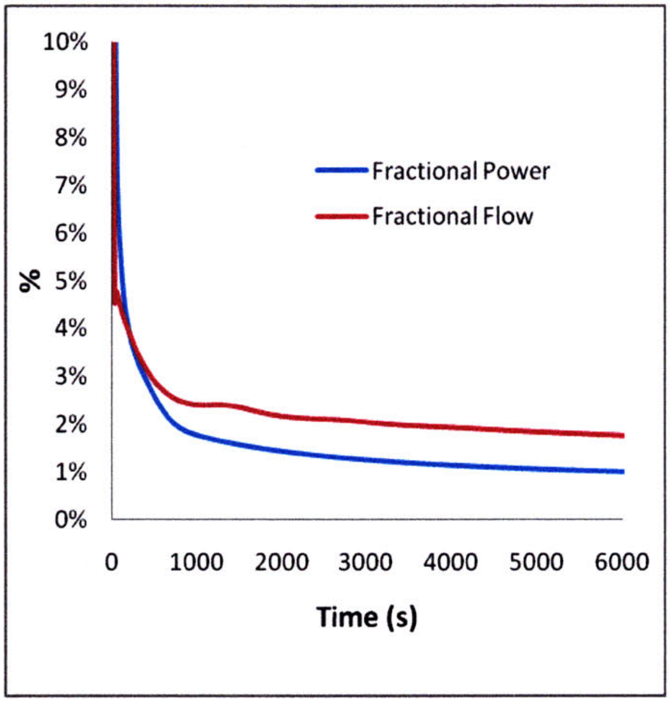

Figure 6.36: Fractional core power and coolant flow rate for the metal CR = 0.25 annular fuel configuration during the station blackout

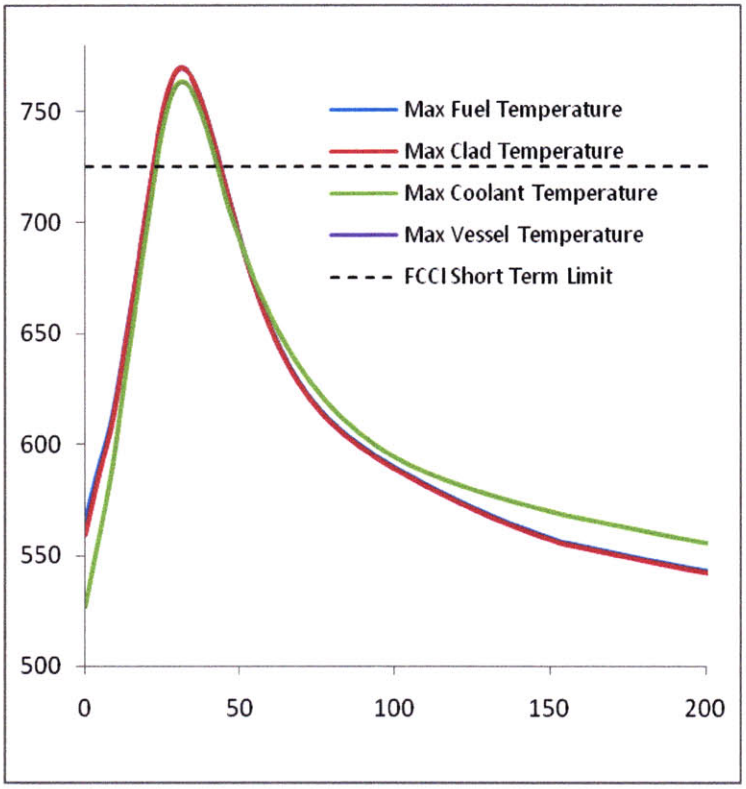

Figure 6.37: Short term key temperatures for the metal CR = 0.25 annular fuel configuration during the station blackout

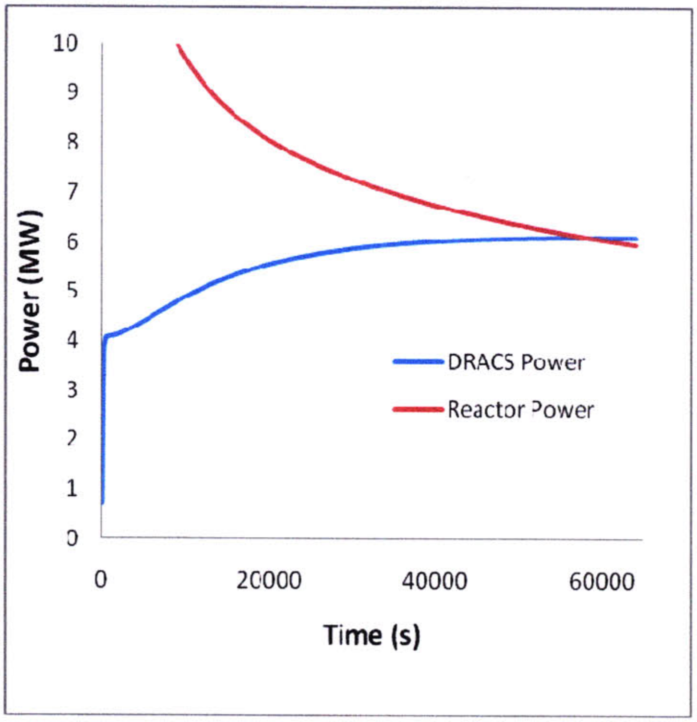

Figure 6.38: Long term DRACS and core power withdrawn for the metal CR = 0.25 annular fuel configuration during the station blackout

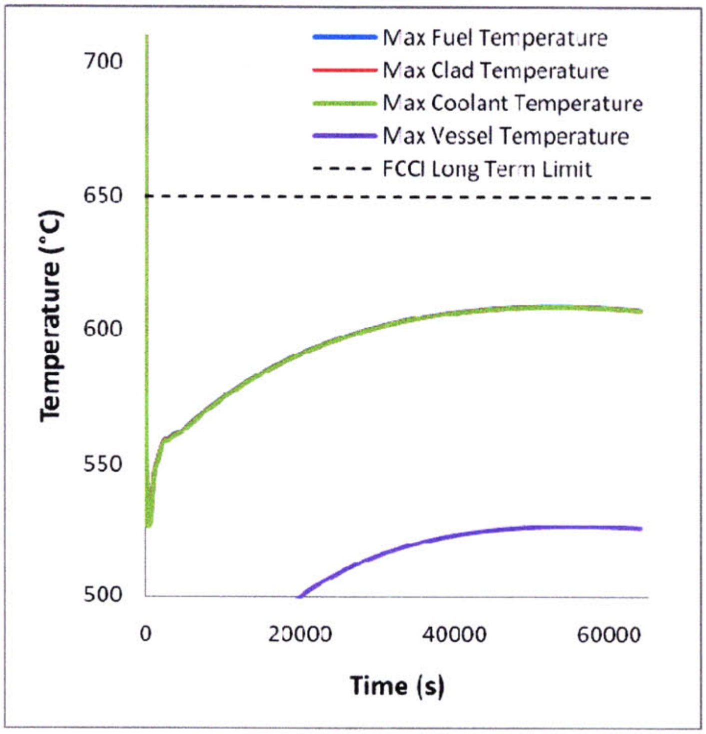

Figure 6.39: Long term key temperatures for the metal CR = 0.25 annular fuel configuration during the station blackout

6.4 Innovative Fuel Configuration Performance (Station Blackout)

The figures of merit for the innovative fuel configurations during the station blackout transient are the maximum cladding temperature and the maximum fuel temperature. If these temperatures are close to or less than the base fuel configurations, then the innovative fuel configurations can be considered acceptable for use in the SFR in terms of safety. The maximum cladding and fuel temperatures for the metal CR = 0.71 fuel configurations are found in Figs. 6.40-6.41 while the fractional flow for each configuration is plotted in Fig. 6.42. The maximum cladding and fuel temperatures for the oxide CR = 0.71 fuel configurations are found in Figs. 6.43-6.44 while the fractional flow for each configuration is plotted in Fig. 6.45.

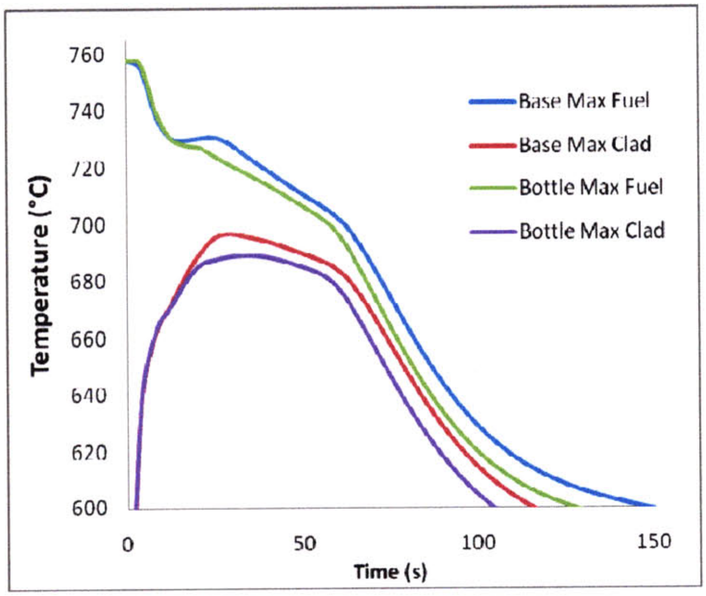

Figure 6.40: Maximum clad and fuel temperatures for the metal CR = 0.71 fuel configurations during a station blackout transient (short term)

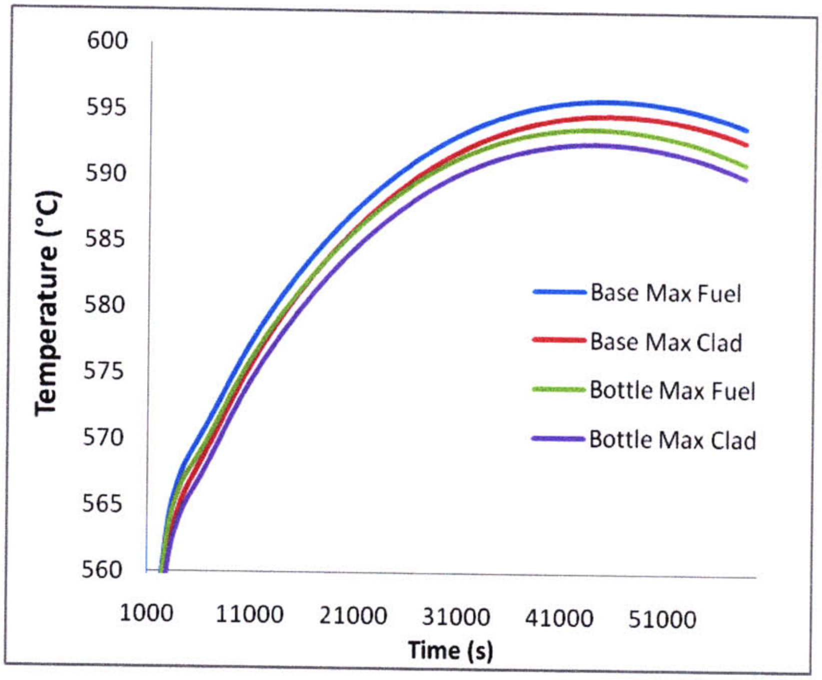

Figure 6.41: Maximum clad and fuel temperatures for the metal CR = 0.71 fuel configurations during a station blackout transient (long term)

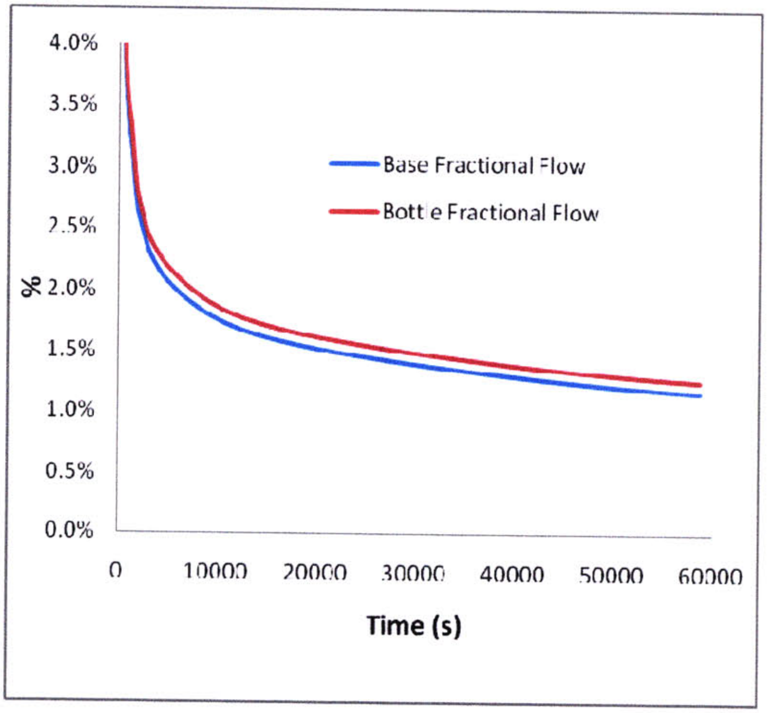

Figure 6.42: Fractional flow rates for the metal CR = 0.71 fuel configurations during a station blackout transient

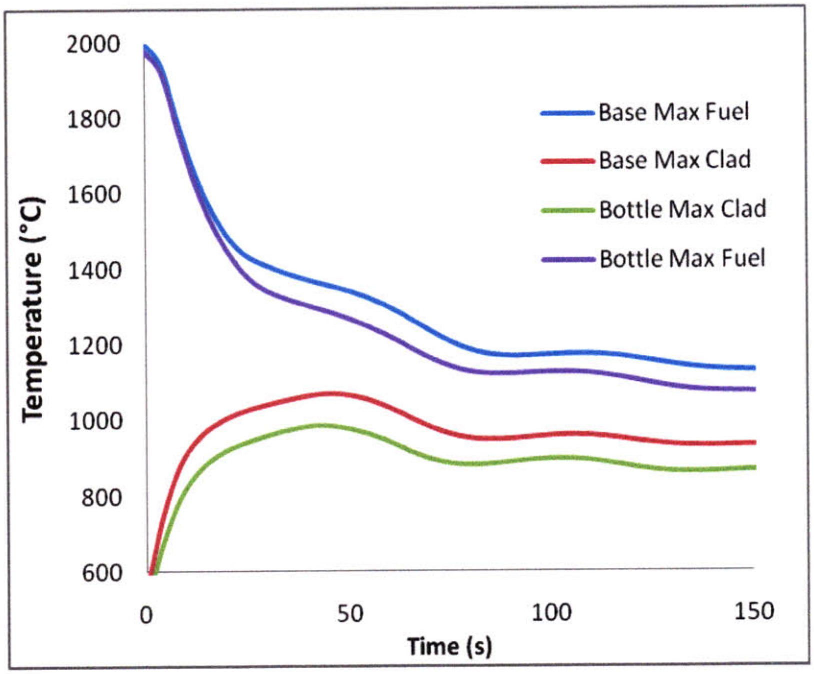

Figure 6.43: Maximum clad and fuel temperatures for the oxide CR = 0.71 fuel configurations during a station blackout transient (short term)

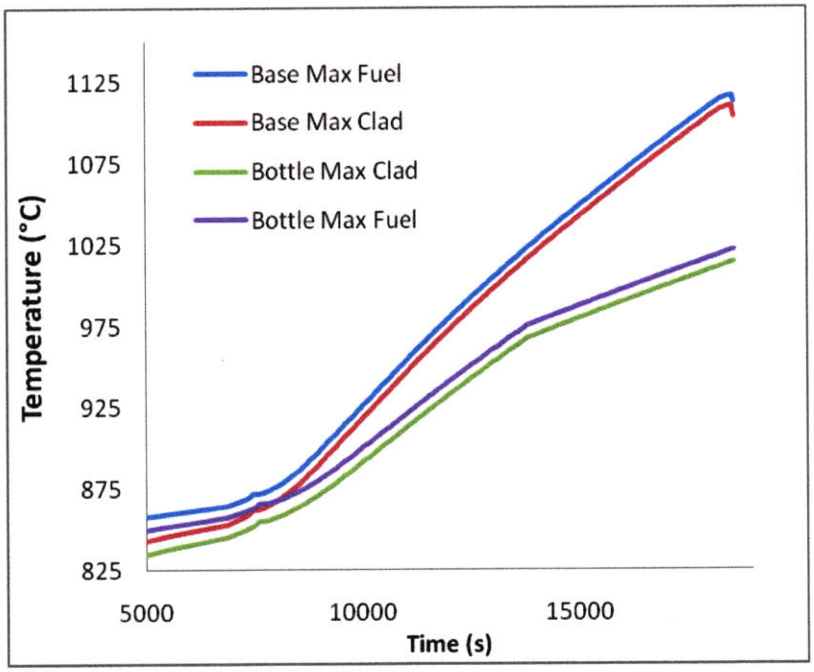

Figure 6.44: Maximum clad and fuel temperatures for the oxide CR = 0.71 fuel configurations during a station blackout transient (long term)

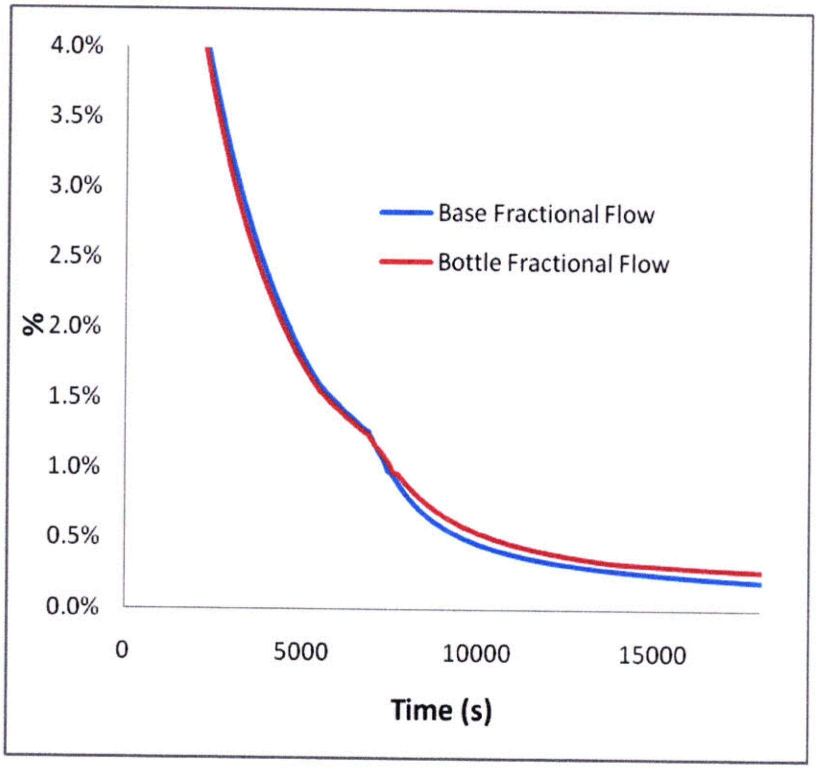

Figure 6.45: Fractional flow rates for the oxide CR = 0.71 fuel configurations during a station blackout transient

The bottle-shaped fuel max temperatures for both metal and oxide have exactly the same short term trends as the base fuel configurations, but shifted down by ~10 °C for the metal fuel and ~90 °C in the oxide fuel due to a lower hydraulic flow resistance and thus a higher natural circulation flow rate. In the long term, the second peak is lower and occurs sooner for the bottle-shaped fuels, again due to the increased natural circulation mass flow rates through the core. This is not explicitly seen in the oxide fuel transients due to the code failure at the onset of boiling in the hot channel. The trend is identical to the metal fuel configuration, however, and an extrapolation indicates that the similarity in these trends will continue. For both configurations, the lower hydraulic resistance across the core results in a significantly lower short term temperature peak due to the higher flow rate as the pump is coasting down.

The annular fuel (uprated case) comparison with solid fuel for the CR = 0.25 fuel configurations are found in Figs. 6.46-6.48. The annular fuel max temperatures in the annular fuel are ~4 °C higher (in the first peak) than for the metal base fuel. Note that initially, (during steady-state operation) the annular peak fuel temperature is lower than the base fuel temperature. However, with the loss of flow in the hottest assembly, the heat transfer coefficient deteriorates. This results in an increasing temperature of the clad and fuel. The fuel temperature in the annular fuel is nearly the same as the clad temperature because of the very low thermal resistance across the fuel. The heat transfer coefficient deteriorates faster for the annular fuel due to thigh higher hydraulic resistance, and thus the fuel/clad temperatures exceed those of the base configuration in the initial clad/fuel temperature peak. Although it is undesirable to have a higher temperature in the annular fuel configurations, the magnitude of the increase is rather small, and thus the performance of the annular fuel is considered acceptable relative to the solid fuel for the purposes of this study. The long term temperature trends indicate that less fractional heat is withdrawn from the annular fuel configuration than for the solid fuel configuration; this is manifested in a higher and later temperature peak in the annular fuel configuration. The long term temperature trends correspond to the increased hydraulic resistance for the annular fuel core and a higher power rating for the annular fuel (this core is uprated by 11.4%), and it is verified by a decreased fractional flow rate through the core in the annular fuel configuration, as seen in Fig. 6.48. Although the peak temperatures are slightly higher in the annular fuel peaks, this difference is very small, and both of the second peak temperatures are significantly less than the FCCI long term limit. Thus, the most limiting constraint of CR = 0.25 fuel configuration performance is the peak clad temperature of the initial higher peak. The annular fuel peak clad temperature is slightly higher than the solid fuel peak clad temperature, but this amount is not enough to consider the annular fuel configuration performance unacceptable.

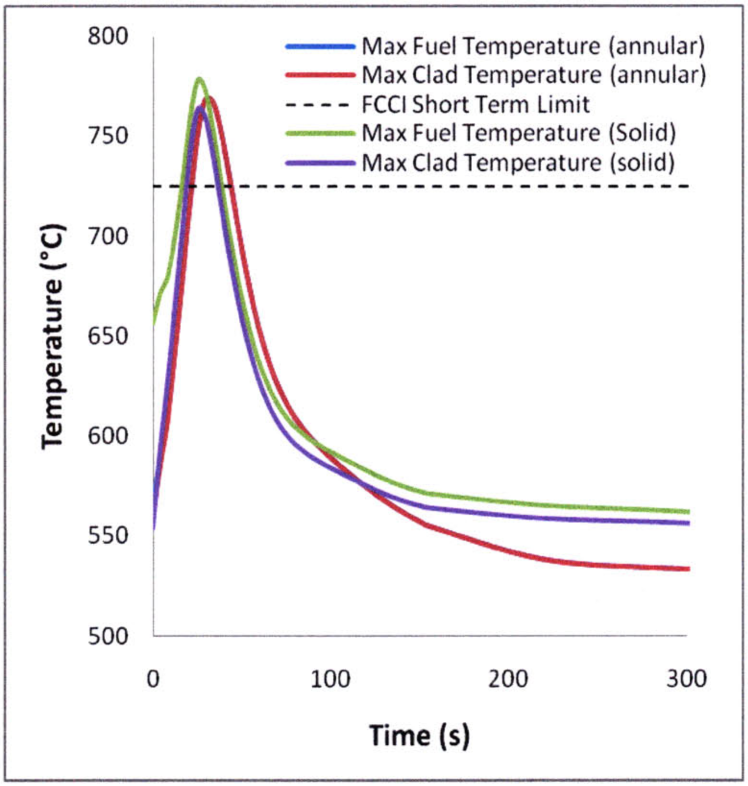

Figure 6.46: Short term maximum clad temperatures for the metal CR = 0.25 fuel configurations during a station blackout transient

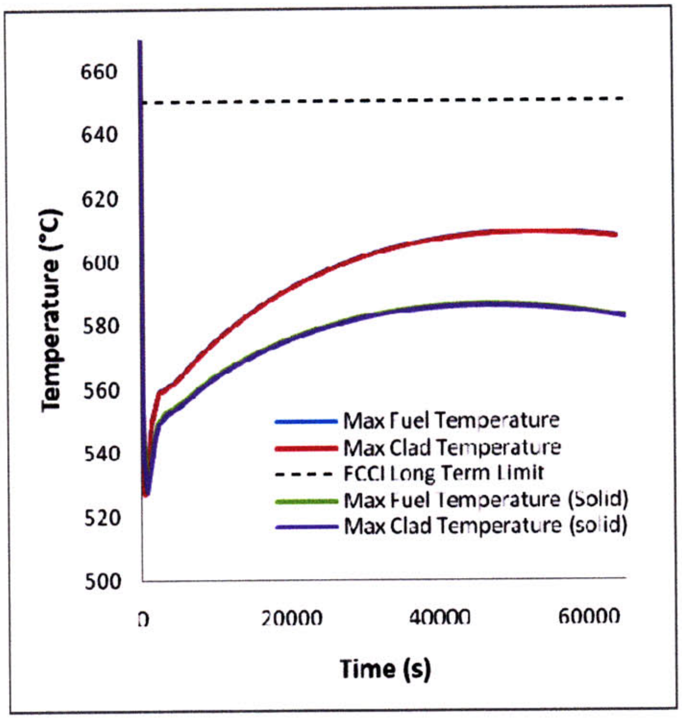

Figure 6.47: Long term maximum clad temperatures for the metal CR = 0.25 fuel configurations during a station blackout transient

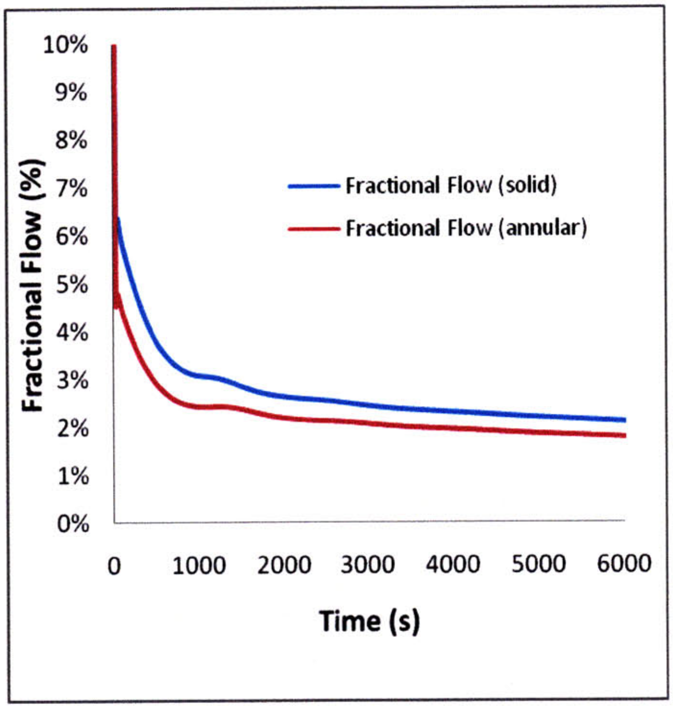

Figure 6.48: Fractional flow rates for the metal CR = 0.25 fuel configurations during a station blackout transient

Because both metal CR = 0.25 fuel configurations have unacceptable performances in the short term temperature peak, it is of interest to note the influence of having a longer pump coast-down, as was investigated with the oxide CR = 0.71 fuel in Section 6.3.2. Fig. 6.49 plots the max fuel and clad temperatures for both solid and annular metal CR = 0.25 fuel configurations for a pump coast-down halving time of 20 seconds, which represents the upper bound of the pump coast-down. As can be seen in this plot, the slower pump coast-down greatly decreases the max fuel temperature so that a max clad temperature for the uprated annular fuel is 651.3 °C, while the max clad temperature for the solid fuel is 647.3 °C. Thus, the low conversion ratio fuel configurations can still be utilized, but at the cost of slightly larger capacitors or flywheels and thus slightly longer pump coast-downs.

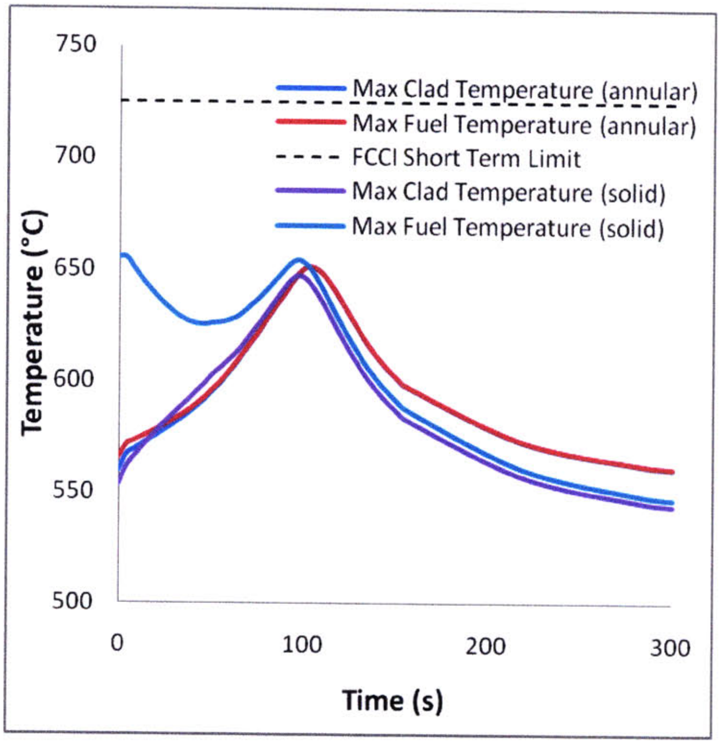

Figure 6.49: Short term maximum clad temperatures for the metal CR = 0.25 fuel configurations during a station blackout transient with a pump coast-down halving time of 20 seconds

6.5 UTOP Accident

The unprotected transient overpower accident represents the insertion of reactivity due to the removal of a control rod with the highest worth. This results in an upward ramp of the core power until the negative feedbacks push the core power back down. The core power reaches an equilibrium value that is slightly higher than the fractional core power. The UTOP transient is modeled for two separate scenarios: a moderate rod removal, and a sudden ejection. Under the first accident, the rod is assumed to be withdrawn at the same rate as the maximum rod insertion rate, due to rod drive stop systems. The second case is a worst-case conservative estimate in which the rod is completely rejected within 0.5 seconds[2]. Each of these cases was applied to the CR = 0.71 base fuel configurations as well as the CR = 0.25 fuel configurations. The bottle-shaped fuel configurations were not included in the UTOP analysis, because the bottle-shaped core region is identical to the solid fuel core region. This indicates that the bottle-shaped fuel configurations will thus perform similarly to the solid fuels.

The maximum rod insertion rate for typical fast reactors is ~0.3cm/s. In the metal and oxide CR = 0.71 base fuel configurations, the total worth of the highest worth control rod bundle is \$4.4. In the metal fuel, this bundle is inserted 23.28 cm into the core at BOEC. This relates to a reactivity insertion rate of 0.9021¢/s as the rod is withdrawn. The maximum reactivity insertion from the removal of the rod is \$0.70, and occurs at 77.6 seconds. In the oxide CR = 0.71 fuel configuration, the bundle is inserted 39.68 cm

---

[2] It may be argued that rod ejection is a physically impossible event in a system operating at near-atmospheric pressure. However, it is analyzed here as a bounding event.

at BOEC. This relates to a reactivity insertion rate of 0.5292¢/s to a maximum value of \$0.70 at 132.3 seconds. In both fuel configurations, the rod ejection accident is simulated by adding all \$0.70 of control rod worth in the course of 0.5 seconds. The reactivity feedbacks for each fuel configuration are the same as for the station blackout transients. The pumps do no stop, but continue to operate at rated conditions, and the DRACS valves do not open.

For the CR = 0.25 cores, previous studies have placed a desirable rod ejection reactivity insertion at below \$1.0 [2.2]. Therefore, the withdrawal rate, maximum worth insertion, and time to complete withdrawal of the highest worth rod bundle for the metal CR = 0.71 base configuration was used for the CR = 0.25 configurations as well.

6.6 UTOP Results

The primary figures of merit for the UTOP transient are the maximum clad and fuel temperatures. It is also of interest to note the contributions to reactivity and the fractional core power for each event. A discussion of these parameters for each fuel configuration is found in each of the following sections.

6.6.1 Base Fuel Configurations (CR = 0.71)

The metal CR = 0.71 base fuel configuration UTOP results are plotted in Figs. 6.50 – 6.53. These include both the moderate rod withdrawal and the sudden rod ejection accidents. The oxide CR = 0.71 base fuel configuration UTOP results are plotted in Figs. 6.54 – 6.57. Again, these plots include both the moderate rod withdrawal and the sudden rod ejection accidents. For metal fuel, the FCCI long term clad temperature limit of 650 °C is also plotted in each of the temperature plots in order to demonstrate the margin to failure for each accident. For oxide fuel, the PCMI temperature limit is plotted as the limiting temperature.

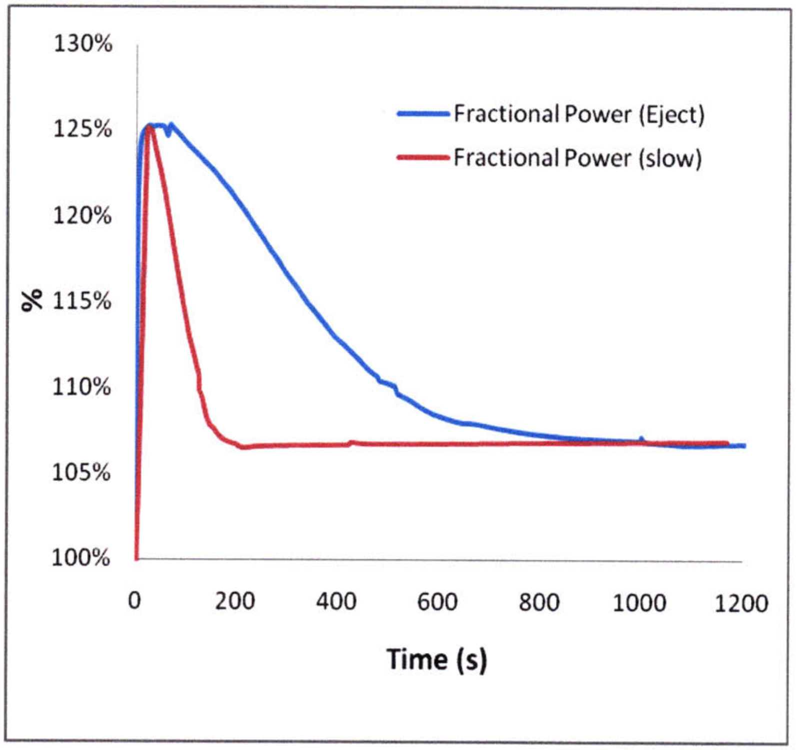

Figure 6.50: Fractional core power for the metal CR = 0.71 base fuel configuration during both slow withdrawal and rod ejection UTOP accidents

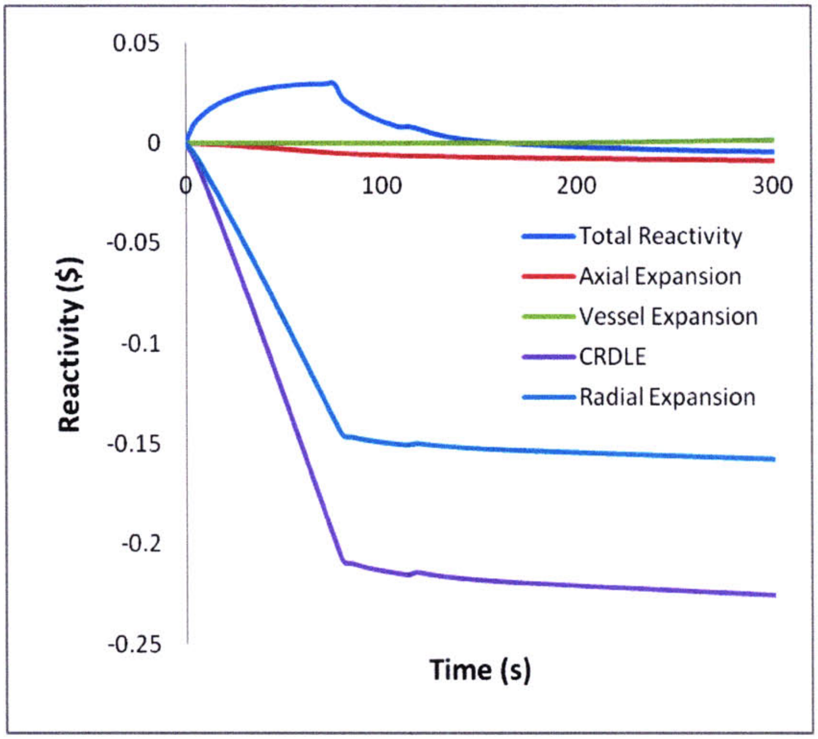

Figure 6.51: Selected reactivity feedbacks for the metal CR = 0.71 base fuel configuration during a slow rod withdrawal UTOP accident

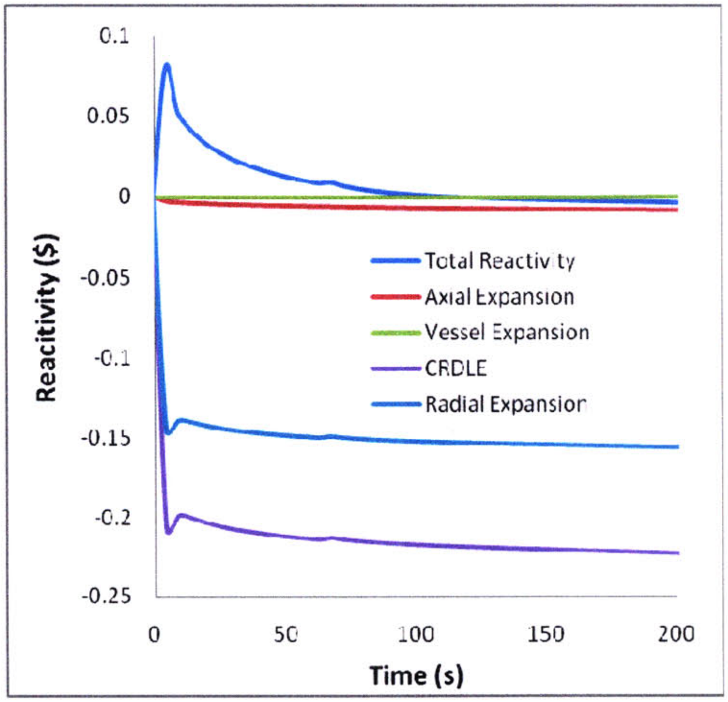

Figure 6.52: Selected reactivity feedbacks for the metal CR = 0.71 base fuel configuration during a rod ejection UTOP accident

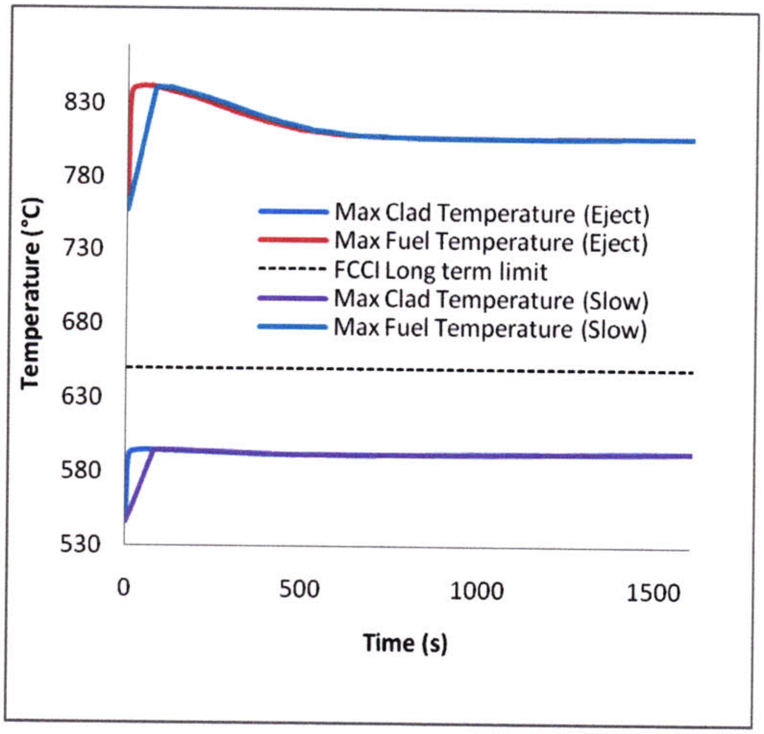

Figure 6.53: Maximum cladding and fuel temperatures for the metal CR = 0.71 base fuel configuration during both slow withdrawal and rod ejection UTOP accidents

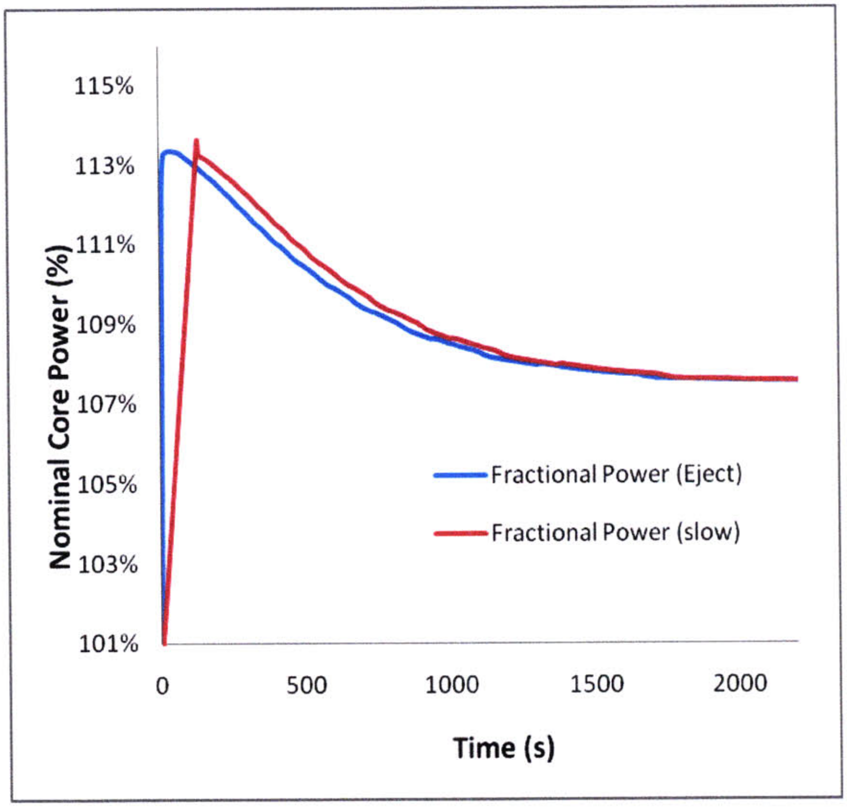

Figure 6.54: Fractional core power for the oxide CR = 0.71 base fuel configuration during both slow withdrawal and rod ejection UTOP accidents

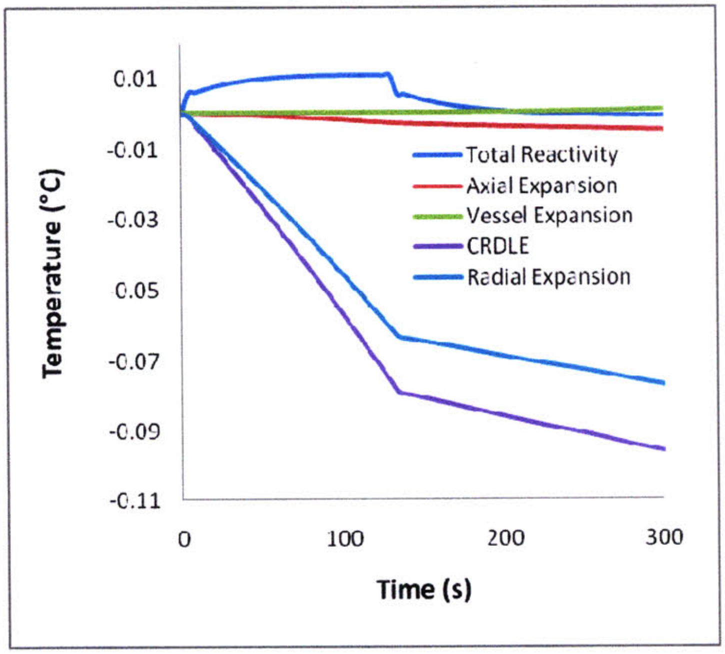

Figure 6.55: Selected reactivity feedbacks for the oxide CR = 0.71 base fuel configuration during a slow rod withdrawal UTOP accident

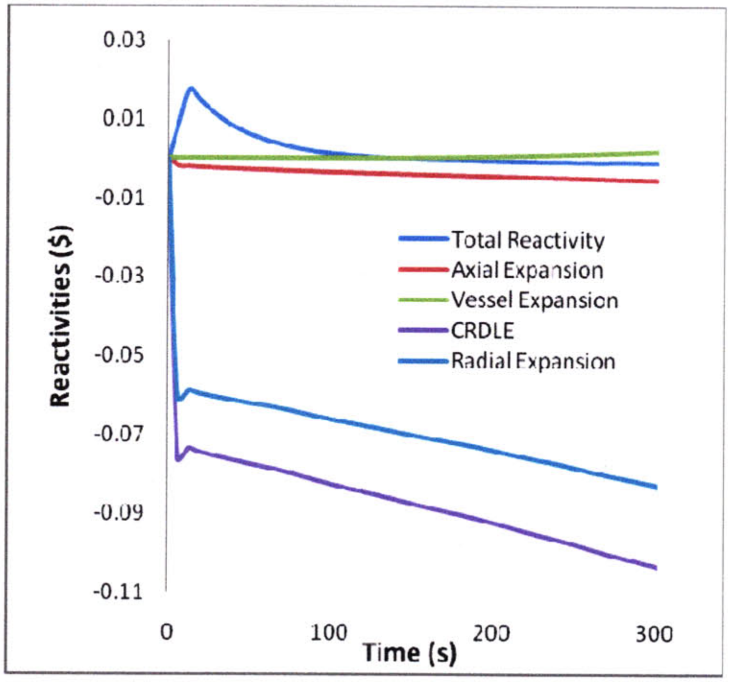

Figure 6.56: Selected reactivity feedbacks for the oxide CR = 0.71 base fuel configuration during a rod ejection UTOP accident

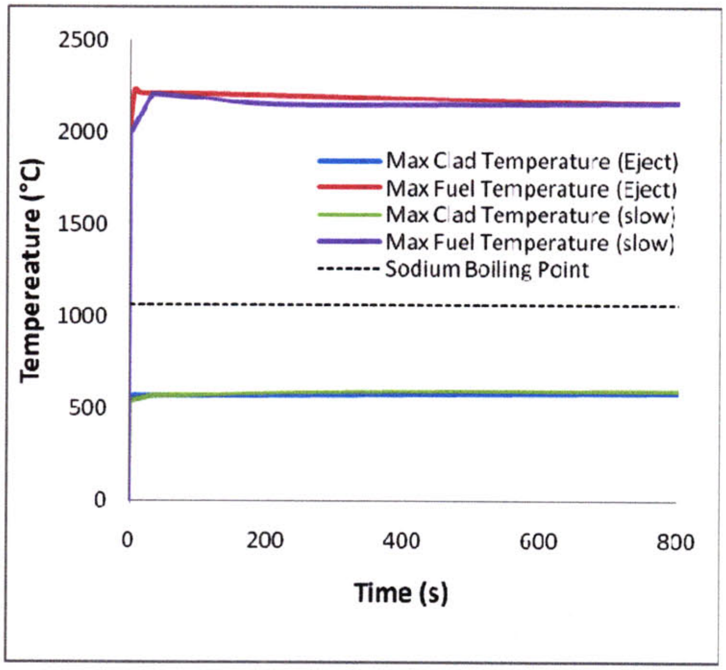

Figure 6.57: Maximum cladding and fuel temperatures for the oxide CR = 0.71 base fuel configuration during both slow withdrawal and rod ejection UTOP accidents

In both the rod ejection and slow rod withdrawal accidents for metal CR = 0.71 base fuel, a maximum cladding temperature of ~600°C was reached. The rod ejection accident resulted in a longer temperature peak; however, the maximum clad temperature is well below the FCCI long term limit, and the amount of time at the higher clad temperature is irrelevant. In both cases, additional reactivity inserted by the withdrawal of the rod results in a power increase of ~25%. The negative reactivity coefficients then reduce the core power until a new steady state level of ~108% of the fractional power is reached. In both cases, the temperature consistently remains well below the long term FCCI limit, indicating that the metal CR = 0.71 base fuel configuration performs adequately during a UTOP transient.

In the oxide CR = 0.71 base fuel configuration, the maximum cladding and fuel temperatures for both slow rod withdrawal and rod ejection accidents peaked at ~607°C. The rod ejection accident produced a wider, longer lasting peak, but this temperature is well below the sodium boiling point, thus verifying the safety of the oxide CR = 0.71 base fuel configuration in a UTOP accident. The peak fractional power was 113%, at which point the negative reactivity feedbacks reduced the core power to a quasi-steady state limit of 107% fractional core power.

Note that for both oxide and metal max clad temperatures, it appears that the temperature remains flat throughout the transient. However, the temperature of the clad follows a similar pattern to the temperature of the fuel, however, this trend is much less exaggerated: the fuel increases initially corresponding to the fuel temperature increase, and then slightly decreases, at which point a very slight and slow increase in temperature is apparent.

6.6.2 Metal CR = 0.25 Base Fuel Configuration

The metal CR = 0.25 base fuel configuration UTOP results are plotted in Figs. 6.58 – 6.61, including both the slow control rod withdrawal and sudden ejection accidents. The FCCI long term maximum cladding temperature limit of 650°C is also plotted Fig. 6.61.

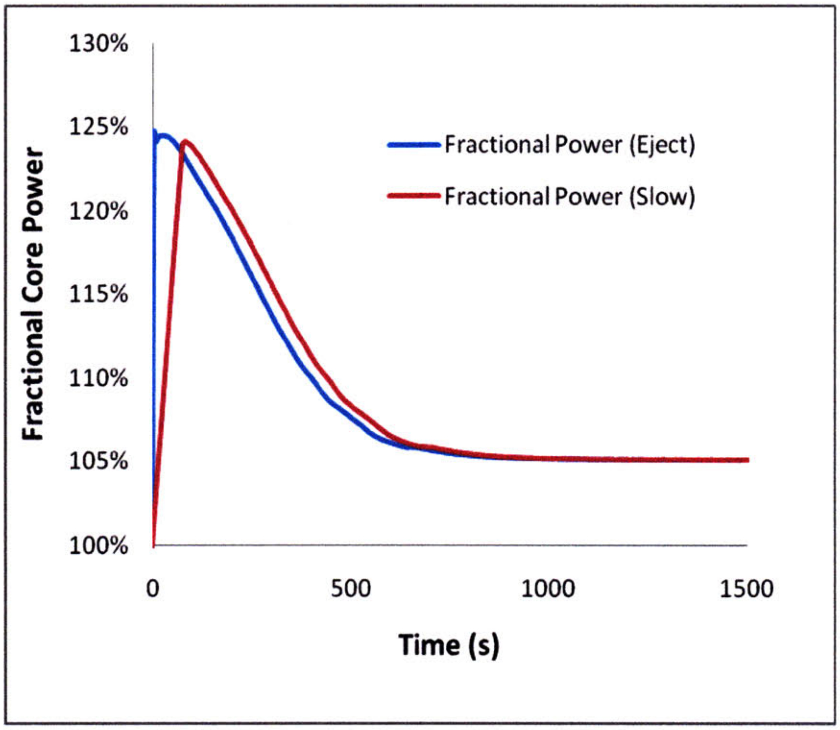

Figure 6.58: Fractional core power for the metal CR = 0.25 base fuel configuration during both slow withdrawal and rod ejection UTOP accidents

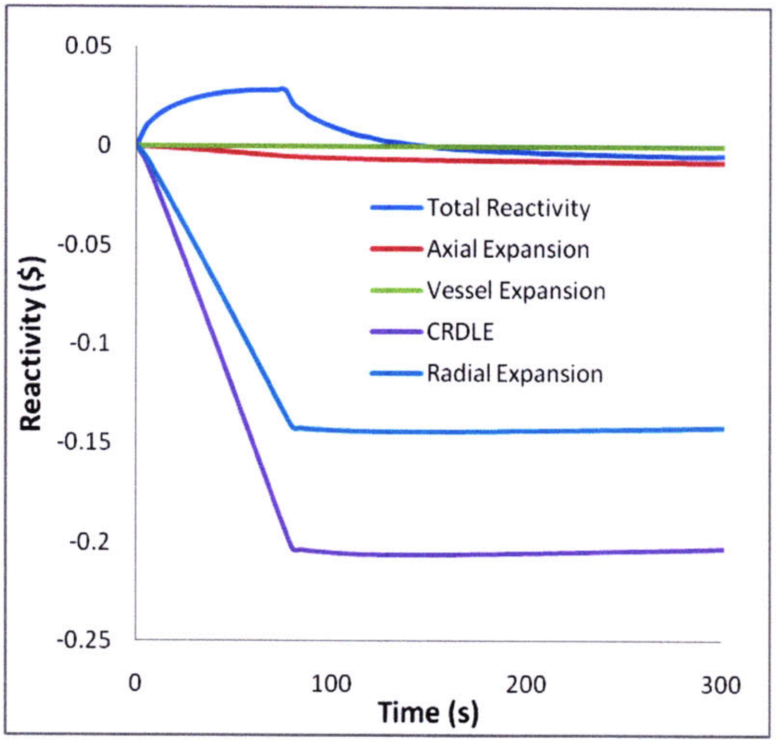

Figure 6.59: Selected reactivity feedbacks for the metal CR = 0.25 base fuel configuration during a slow withdrawal UTOP accident

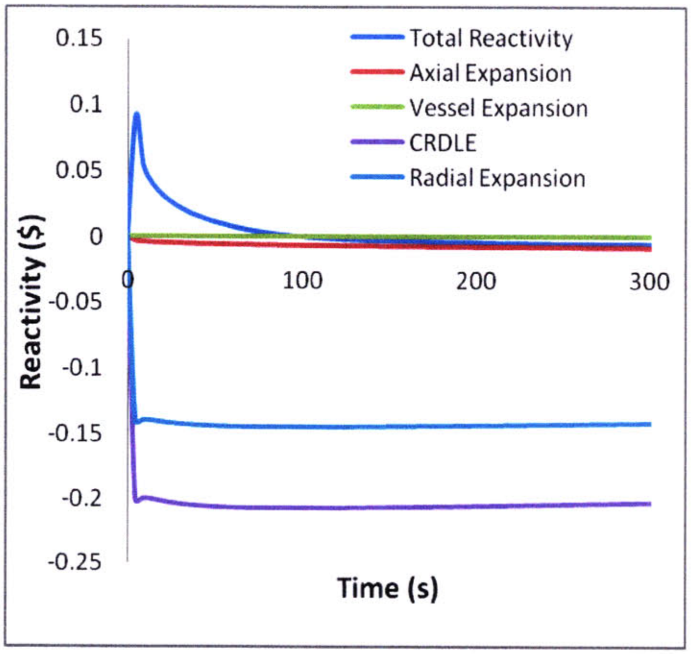

Figure 6.60: Selected reactivity feedbacks for the metal CR = 0.25 base fuel configuration during a rod ejection UTOP accident

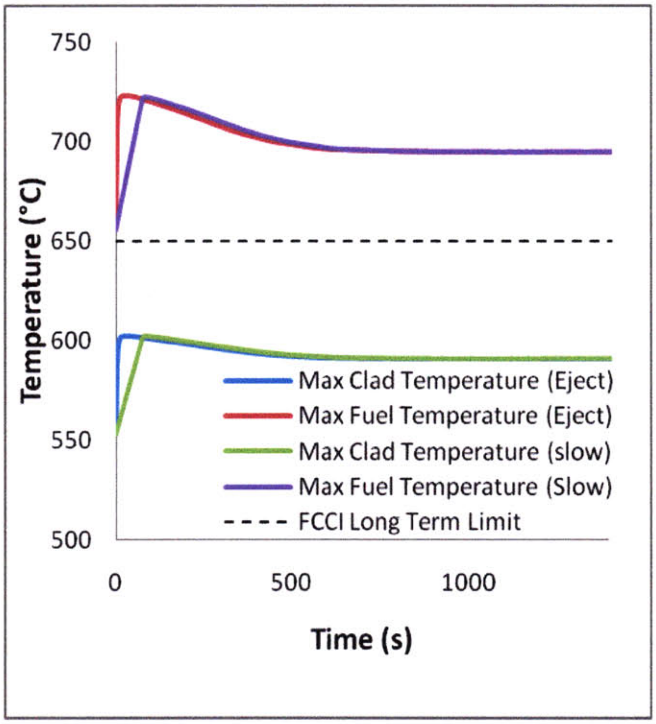

Figure 6.61: Maximum cladding and fuel temperatures for the metal CR = 0.25 base fuel configuration during both slow withdrawal and rod ejection UTOP accidents

For both the rod ejection accident and the slow withdrawal accident, the max clad temperature remains well below long term FCCI limit of 650 °C. In both cases, the reactivity insertion causes an increase in core power, which peaks at 124%, but then the other reactivity feedbacks drive the power back to a level slightly above the fractional power (~105%). In the rod ejection accident, the core fractional power peaks at a slightly larger value than the slow rod ejection, which results in a slightly higher peak clad (602 °C) and fuel temperature for the ejection accident (~722 °C). This difference is small (0.4 °C) and thus is considered negligible. Because the peak clad temperature is slightly higher in the rod ejection accidents, they were used as the point of comparison between solid and annular fuel configurations, as discussed in the next section.

6.6.3 Metal CR = 0.25 Annular Fuel Configuration

The metal CR = 0.25 annular fuel configuration (with a power uprate of 20%) UTOP results are plotted in Figs. 6.62 – 6.65, including both the slow control rod withdrawal and sudden ejection accidents. The FCCI long term maximum cladding temperature limit of 650°C is also plotted Fig. 6.65.

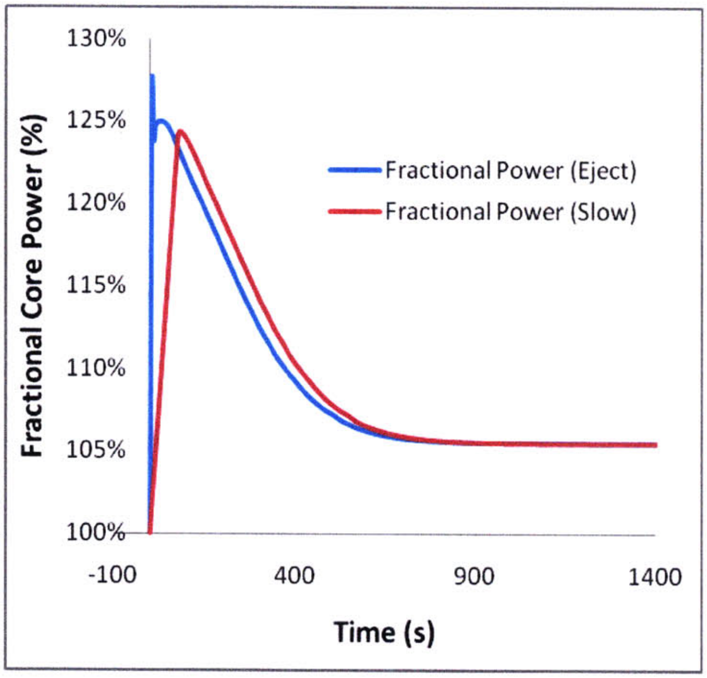

Figure 6.62: Fractional core power for the metal CR = 0.25 annular fuel configuration during both slow withdrawal and rod ejection UTOP accidents

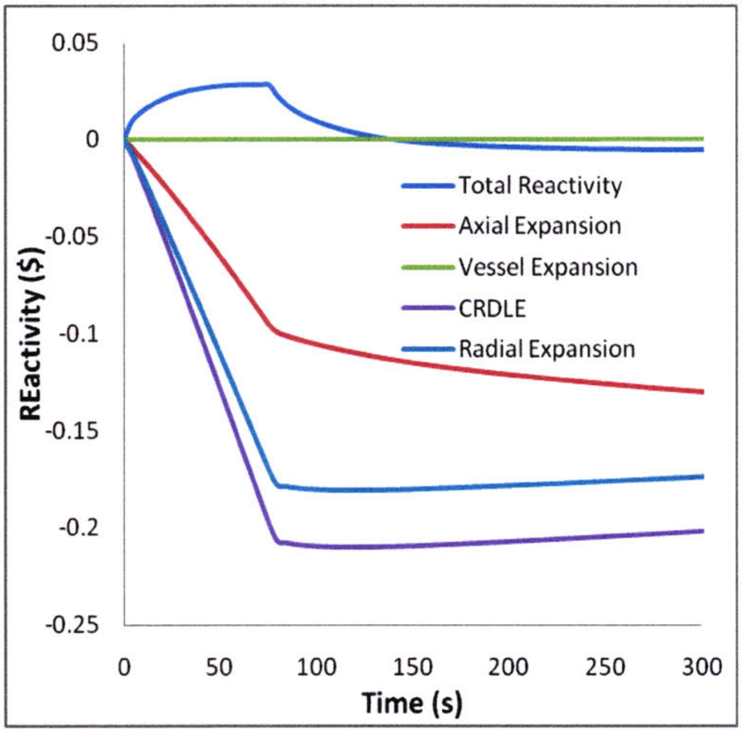

Figure 6.63: Selected reactivity feedbacks for the metal CR = 0.25 annular fuel configuration during a slow withdrawal UTOP accident

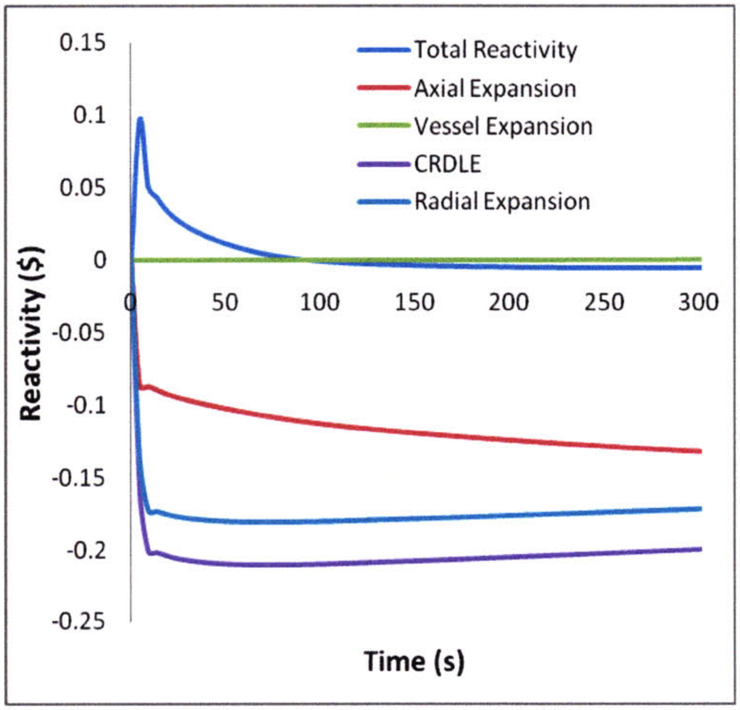

Figure 6.64: Selected reactivity feedbacks for the metal CR = 0.25 annular fuel configuration during a rod ejection UTOP accident

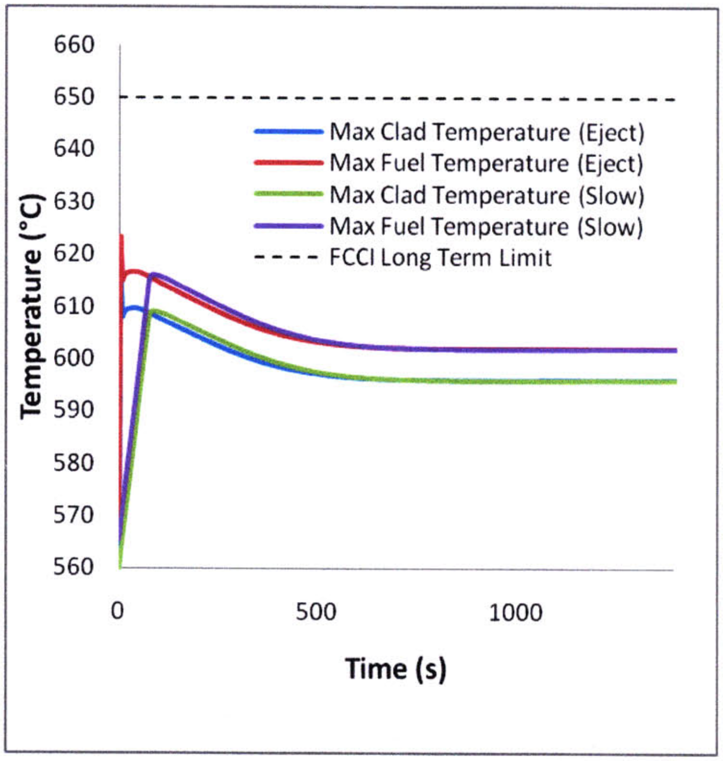

Figure 6.65: Maximum cladding and fuel temperatures for metal CR = 0.25 annular fuel configuration during both slow withdrawal and rod ejection UTOP accidents

Unlike the solid base fuel configuration, the annular fuel configuration rod ejection fractional power initially reaches a higher level of 127%, as compared to the slow ejection fractional power of 124%. This is quickly reduced by the core reactivity feedbacks, until a new steady state power of 105% fractional power is attained. This higher peak in power for the rod ejection accident is reflected in the max clad temperature, which reaches a short term maximum of 622.6 °C instead of the peak clad temperature of 616.2 °C reached in the slow withdrawal accident. Even with a 6.4 °C increase in initial temperature, the max clad temperature is well below the short term FCCI clad temperature limit.

6.7 Annular Fuel Configuration Performance

To be considered a viable fuel option, the annular fuel must perform similarly to or better than the base fuel. A comparison of the annular and base fuel maximum cladding and maximum fuel temperatures are plotted in Fig. 6.66. Also included in this plot is the FCCI long term temperature limit of 650 °C.

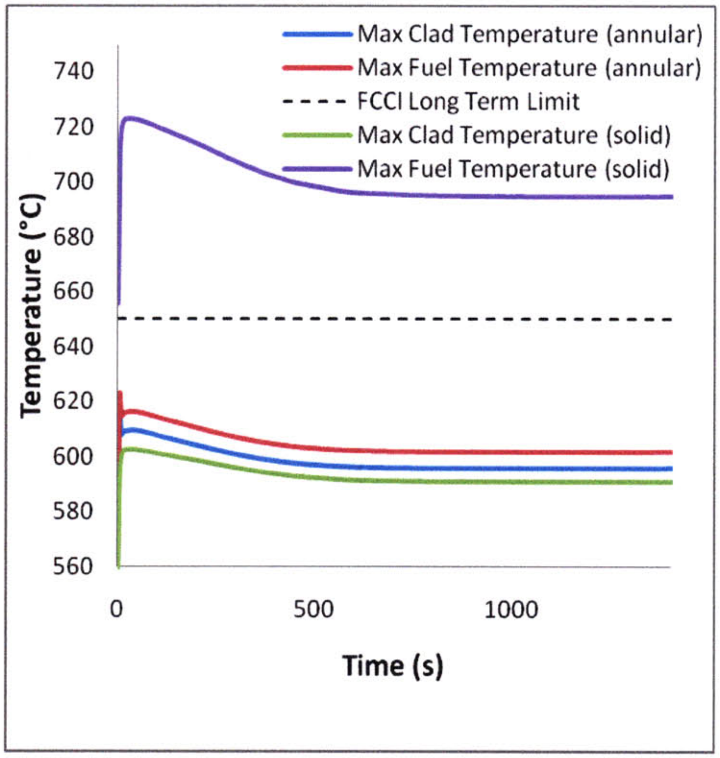

Figure 6.66: Maximum cladding and fuel temperatures for the CR = 0.25 annular and solid metal fuel core configurations a rod ejection UTOP accident

The largest benefit of the annular fuel configuration in a UTOP rod ejection accident is the decrease in max fuel temperature. This parameter is reduced by nearly 100 °C. As with the station blackout accident, however, annular fuel cladding max temperatures are slightly higher than the solid fuel cladding max temperatures. This difference of ~13 °C is relatively small, and not of major concern in the comparison of the fuel performances. Both annular and solid max clad temperatures at the onset of the UTOP rod ejection accident are significantly lower than the short term FCCI limits and are 27.4 °C – 47.4 °C lower than the long term FCCI temperature limits. Thus, both solid and annular fuel configurations maintain adequate safety margins during a UTOP rod ejection accident.

6.8. Conclusions

A summary of the transient analyses performed in this thesis and the key points of the corresponding results can be found in Table 6.2. The metal CR = 0.71 base fuel configuration performs adequately during a station blackout accident, but the oxide CR = 0.71 base fuel configuration fails via sodium coolant boiling. Thus, oxide fuel is not suitable for use in the SFR, if inherent shutdown in unprotected events is required, due to its poor safety performance. The bottle-shaped fuels for both oxide and metal fuel types perform satisfactorily in reducing the maximum clad and fuel temperatures by allowing higher natural circulation flow rates. However, the performance improvement during accidents is marginal, so the main advantage for the bottle-shaped fuel concept remains the substantial reduction of pressure drop and pumping power at steady-state conditions. The metal CR = 0.25 base fuel does not breach clad or fuel temperature limits during a station blackout transient. The metal annular fuel also does not breach clad or fuel temperature limits, although the peak temperatures for both long and short time frames are ~ 4.3 °C higher than those of the metal base fuel. Both innovative fuel configurations for the metal fuel are acceptable in terms of a station blackout accident.

Table 6.2: Transient analyses performed with summary of results

* = base 🟩X = safe - = worse than base 🟨X = safe w/ changes + = better than base 🟥X = unsafe			UTOP		Station blackout
			Slow rod withdrawal	Rod ejection	
Metal	Base	CR = 0.25	*	*	🟨 *
		CR = 0.71	🟩 *	🟩 *	🟩 *
	Bottle-shaped	CR = 0.25			
		CR = 0.71			🟩 +
	Annular	CR = 0.25	🟩 -/+	🟩 -/+	🟨 -/+
		CR = 0.71			
Oxide	Base	CR = 0.25			
		CR = 0.71	🟩 *	🟩 *	🟥 *
	Bottle-shaped	CR = 0.25			
		CR = 0.71			🟥 +
	Annular	CR = 0.25			
		CR = 0.71			

Both metal and oxide CR = 0.71 fuel configurations do not breach safety margins during UTOP transients. The maximum clad temperature is well below the FCCI long term limit for metal fuel and the PCMI limiting temperature for oxide fuel.

The metal CR = 0.25 base and annular configurations were modeled using the same decay power curve, pump coast-down curve, and CRDLE reactivity feedback coefficient as the CR = 0.71 station blackout models. The peak clad temperatures of the metal CR = 0.25 base and annular fuel configurations were 768.3°C and 764 °C, respectively, during a station blackout accident. Both of these temperatures were above the FCCI short term temperature limit of 725 °C. When the pump coast-down halving time was increased to 20 seconds (upper bound), the max clad temperatures for the solid and annular fuels were 647.3°C and 651.3°C, respectively. Thus, the metal CR = 0.25

base and annular fuel configurations could be considered suitably safe during station blackout accidents, but a longer pump coast-down is required.

The clad temperature of the annular fuel configuration is slightly higher than the base fuel clad temperature with a difference of ~4.3 °C. This difference is small, and likely within the uncertainties of the analysis. Thus, the 20% uprated-power annular fuel configuration is performing at approximately the same level during station blackout transients as the base fuel configuration.

During a UTOP transient, both the metal CR = 0.25 base and annular configurations perform adequately. The max clad temperatures of 616 °C and 603 °C are well below the short and long term FCCI clad temperature limits. The annular fuel configuration max clad temperatures are slightly higher than the base fuel configuration max clad temperatures (~13 °C), but this value is small and can be considered within the uncertainties allowed for safety modeling.

Chapter 7: Super-Critical Carbon Dioxide (S-CO_2) PCS

7.1. Introduction

The thermal-hydraulic performance of the innovative fuel configurations has been evaluated as the primary focus of this thesis. The safety analysis of these fuel configurations, as described in Chapter 6, necessitated the creation of a full plant model using RELAP5-3D. This full plant model was coupled with a water/steam PCS boundary rather than a complete PCS. This was done to simplify the model and reduce transient analysis runtime, since a detailed view of the Rankine PCS was not necessary for the standard transients evaluated in this thesis.

Previous SFR concepts have included a Rankine PCS [5.2, 5.3]. However, recent interest has developed in utilizing a super-critical carbon dioxide (S-CO_2) PCS for advanced reactors [7.1, 1.11]. Recent studies have shown that a S-CO_2 PCS can provide some unique benefits during a ULOF transient [6.6]. Thus, a S-CO_2 PCS system was developed and modeled using RELAP5-3D to be coupled with the full plant model described in Chapter 5. A ULOF accident was then simulated for the combined SFR/S-CO_2 PCS model.

The S-CO_2 PCS is a Brayton recompression cycle that utilizes carbon dioxide at high temperatures and pressures as the working fluid. It has been shown that very high efficiencies can be achieved when using this cycle at temperatures above ~500°C [7.2]. The full plant model described in Chapter 5 has a max PCS temperature of ~472°C, however, so the efficiency is lower (~40%) than those achieved in the gas-cooled fast reactor [7.2]. Nevertheless, S-CO_2 cycle is extremely compact offering significant capital cost savings and CO_2 reaction with sodium has slow kinetics and does not generate hydrogen, making this cycle an interesting candidate for SFRs. Of particular interest is the potential for the S-CO_2 PCS to provide a heat sink during a ULOF transient. This would eliminate the need for a safety-grade auxiliary coolant control system, such as the auxiliary feedwater system utilized in typical PWR Rankine cycles. The following chapter describes the S-CO_2 PCS and the S-CO_2 PCS RELAP5-3D model with its steady state results. In addition, the performance of the SFR with a Rankine cycle PCS during a ULOF transient and the performance of the SFR with an S-CO_2 Brayton cycle PCS during a ULOF transient are discussed.

7.2. S-CO_2 Cycle Description

The S-CO_2 PCS used with the SFR is a two loop recompression Brayton cycle with each loop rated at 500MW thermal. Each loop is powered by two 250MW thermal secondary sodium loops. An illustration of the cycle is shown in Fig. 7.1. The CO_2 coolant enters the IHX printed circuit heat exchanger (PCHE) at ~20MPa and is heated to the high cycle temperature. The CO_2 then enters a turbine where it expands and flows into the high temperature recuperator (HTR) PCHE. The HTR effluent enters the hot side of the low temperature recuperator (LTR) where it is cooled further. A portion of the coolant flow is diverted to the recompressing compressor (RC) while the remainder of the coolant flows through the precooler (PC) where it is cooled further by cold water at 32 °C. The cold, post PC CO_2 is then compressed in the main compressor (MC) and subsequently flows through the cold side of the LTR. The LTR effluent then merges with the portion of the fluid that was diverted to the recompressing compressor. The combined fluid then flows through the cold side of the HTR where it is heated by the turbine exhaust, and then flows into the IHX.

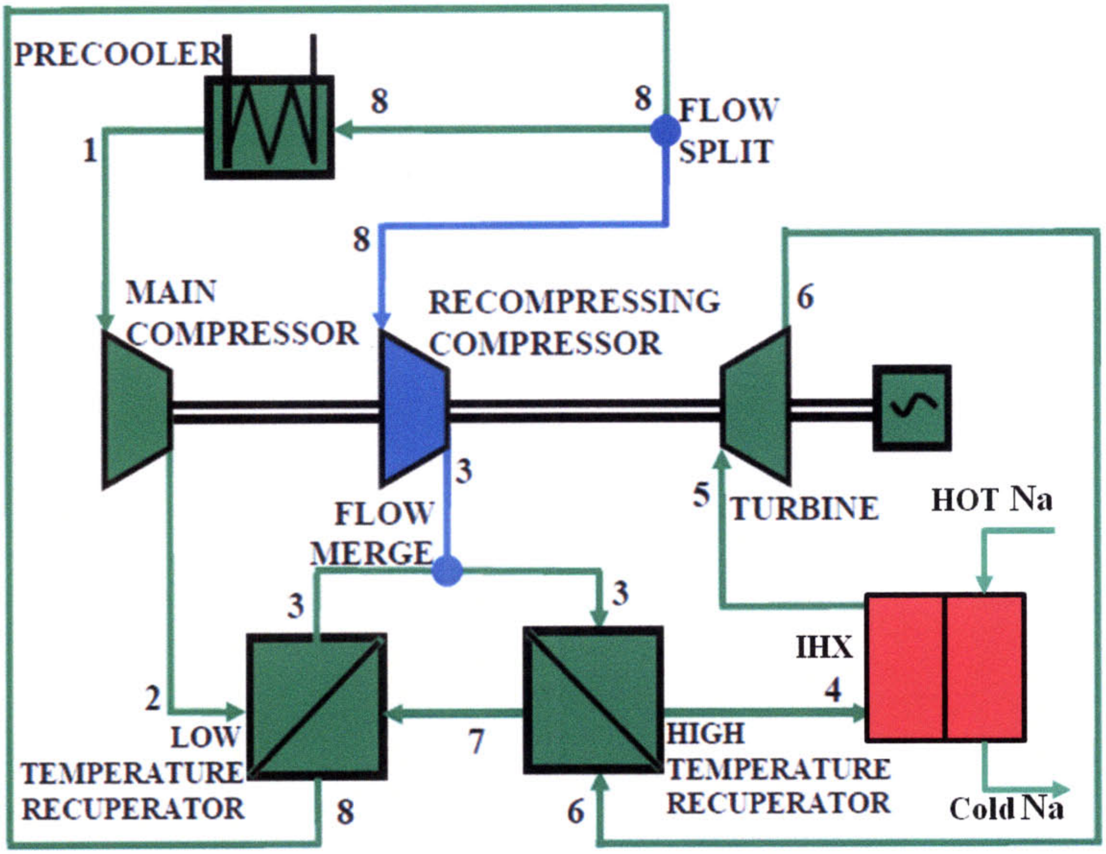

Figure 7.1: Schematic of the S-CO2 recompression cycle [7.1]

The PCHEs are a heat exchanger design developed by HEATRIC, a subsidiary of Meggitt (UK), Ltd [7.3]. These compact heat exchangers are designed to provide highly efficient heat transfer (reaching a thermal effectiveness of 98% [7.3]) at potentially high pressure and temperature conditions). They consist of a number of thin plates, each chemically etched with zig-zag semi-circular channels, as depicted in Fig. 7.2. These plates are then stacked and diffusion bonded, as seen in Fig. 7.3. The coolant flow configuration through the plates is essentially counter-current with hot and cold plates alternating in the stack.

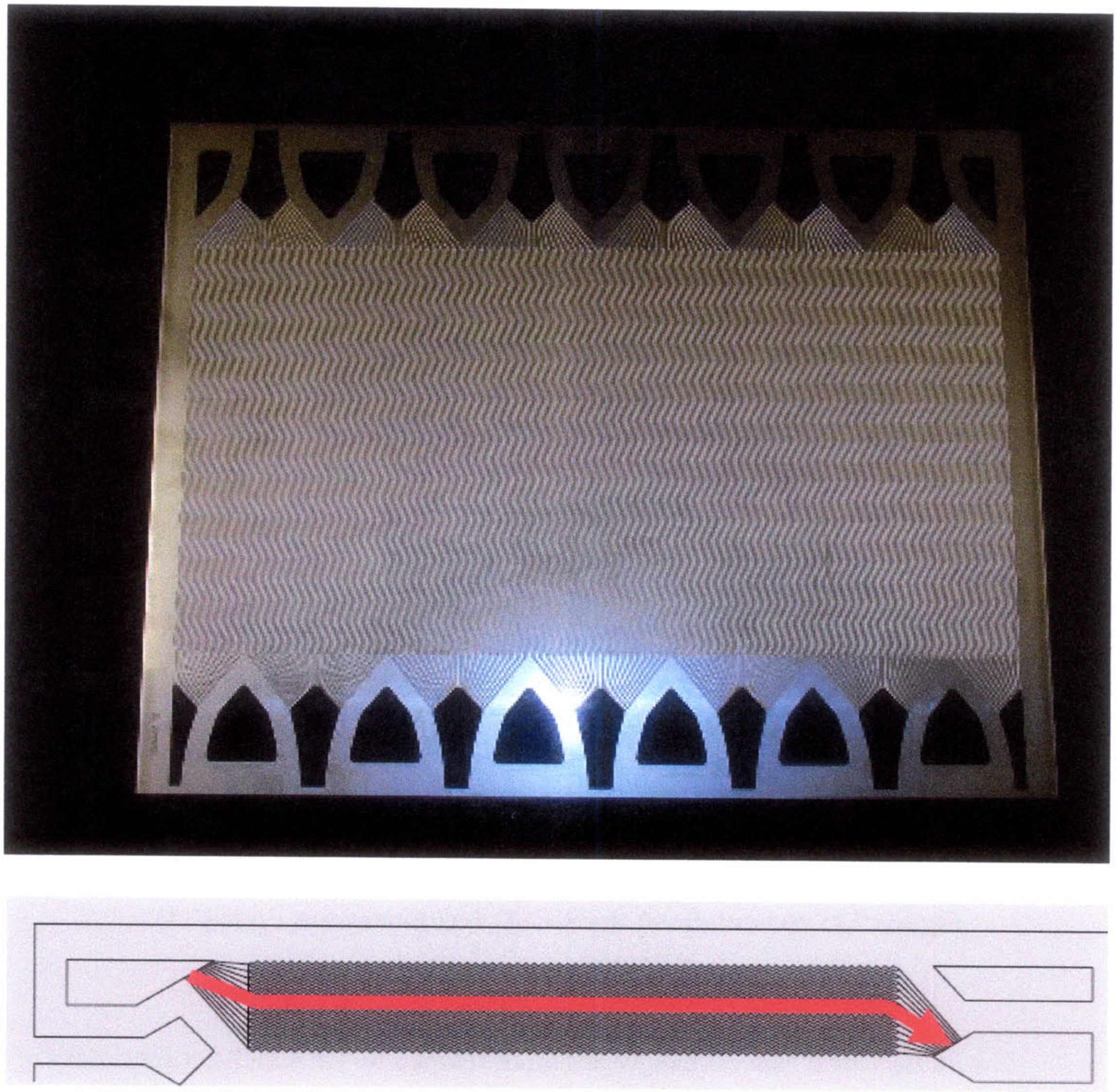

Figure 7.2: Depiction of zig-zag channels etched into PCHE plate – image from HEATRIC

The zig-zag shape of the channels enhances laminar and transitional heat transfer coefficients, but also increases the pressure drop across the channel. The friction factor through each PCHE channel can be approximated if the zig-zag angle is ~127° by the following equation [7.4]:

$$f = 4.8 \cdot \mathrm{Re}^{-0.36} \cdot \left(\frac{2b}{p} \right)^{1.5}, \qquad (7.1)$$

where:

f = the fanning friction factor

b = the channel width (2mm)

p = zig-zag pitch (23mm).

For the heat transfer through the zig-zag channels, there is no publicly available correlation to predict the heat transfer enhancement. However, a "fouling factor" can be applied to approximate the enhanced heat transfer in the zig-zag channels, as described in Section 5.2.1.

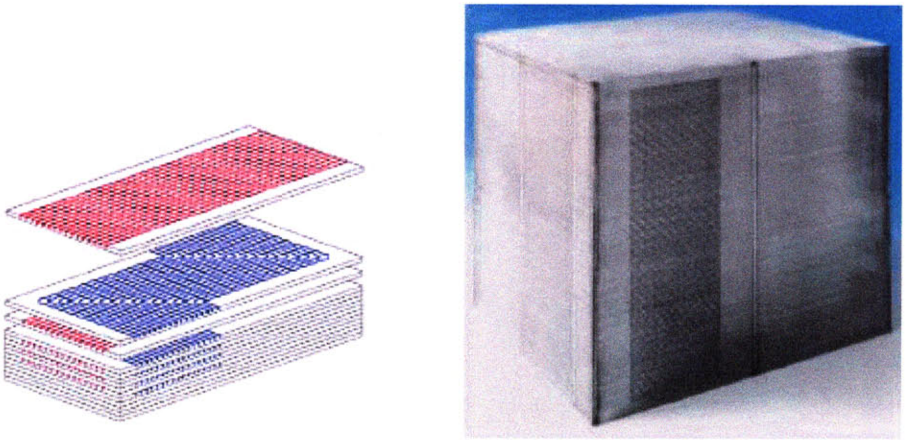

Figure 7.3: Depiction of stacked plates in PCHE core – image from HEATRIC

The compressors are axial compressors and are on the same shaft as the turbine, as depicted in Fig. 7.1. These compressors were designed and sized using Real Gas Radial Compressor (RGRC), an MIT in-house compressor design code [7.5], and the design parameters for 500MWth PCS loop are found in Table 7.1. The code is a mean-line compressor model with losses modeled after Aungier [7.6]. In order to adapt the compressor models to use in RELAP5-3D, the dimensions of the compressor were simplified to determine approximate values for flow path length, average hydraulic diameter, and flow area. The main compressor is a single stage design, but the recompressing compressor is a two-stage design, due to the higher specific volume of the gas.

Table 7.1: Flow geometry of the S-CO_2 compressors [7.7]

	MC	**RC – Stage 1**	**RC2 – Stage 2**
Inlet flow area (m^2)	0.2138	0.2039	0.1444
Flow path length in impeller(m)	0.625	0.839	0.624
Flow path length in diffuser (m)	0.50	0.630	0.603

Average D_h (cm) in impeller	7.12	7.49	4.75
Average D_h (cm) in diffuser	3.21	4.15	3.18
Number of blades	19	21	35
Number of vanes	35	30	20

The hydraulic diameters utilized were a flow path length weighted average of the hydraulic diameters in the impeller and diffuser regions, respectively. The total flow path length was considered to be equal to the sum of the impeller and diffuser flow paths. This assumption under-predicts the volume in the pumps, but this approximation is necessary for inputting these pumps into the RELAP5-3D model, since only a single volume/length combination is allowed for the pump component in RELAP5-3D.

Table 7.2: Performance parameters of the S-SO_2 PCS compressors [7.7]

	MC	RC
Mass flow rate (kg/s)	1580.9	989.6
Static pressure (kPa)	7658.1	7670.9
Temperature (kPa)	304.74	344.4
Density (kg/m^3)	616.68	161.62
Enthalpy (kJ/kg)	302.66	481.65
Entropy (J/kg*K)	1334.8	1904.6
Velocity (m/s)	12	30
Pressure ratio	2.61	2.61
Operating speed (RPM)	3600	3600

The hydraulic diameters listed in Table 7.1 are the averages in each blade passage, based on the inlet and outlet. The inlet flow area is just determined from the hub and tip diameters at the impeller inlet. Due to pretty large density and velocity changes, the total flow area throughout the machine does change, but these changes cannot be modeled in RELAP5-3D, and thus are neglected. This approach is reasonable (especially since this will tend to over-estimate the flow area, thus countering the effects of the flow path length in under-predicting total machine volume) [7.7]. Table 7.2 lists the performance parameters of the main compressor and the recompressing compressor, and Fig. 7.4 – 7.7 show the performance curves for the MC and RC, respectively (static-to-static pressure ratio is simply the compressor inlet-outlet pressure ratio, while the total-to-static efficiency is the performance efficiency of the compressor at the given pressure ratio. An extrapolation of the surge and choke conditions flow and head is plotted on Figs. 7.4 and 7.6 via the red dotted line (note that extrapolations to high pressure ratios are required for these components to initialize correctly in RELAP5-3D). These extrapolations were used in the creation of homologous pump curves, so that pump performance was correctly modeled by RELAP5-3D in the case of these conditions occurring.

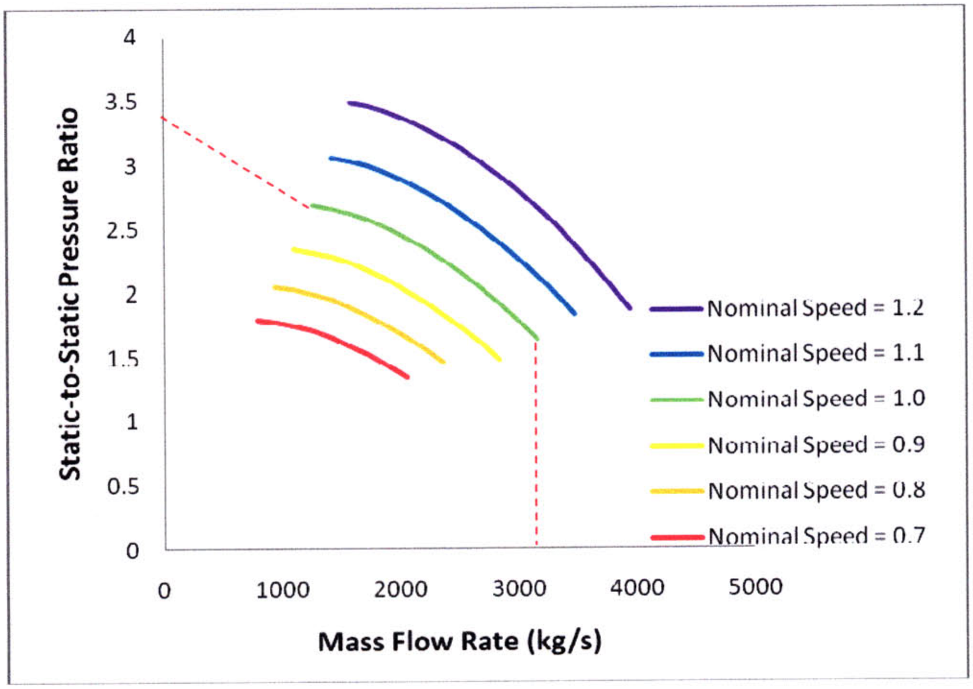

Figure 7.4: Pressure ratio performance curve for main compressor at nominal operating speeds of 0.7 to 1.2 [7.8] (with choke and surge extrapolations for the 100% speed case included)

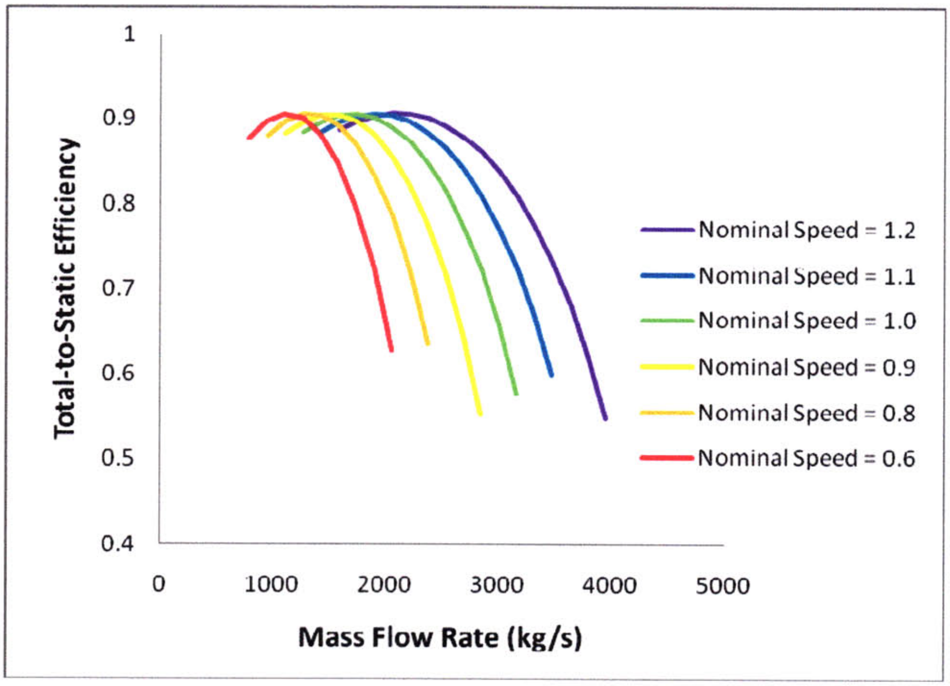

Figure 7.5: Efficiency performance curve for main compressor at nominal operating speeds of 0.7 to 1.2 [7.8]

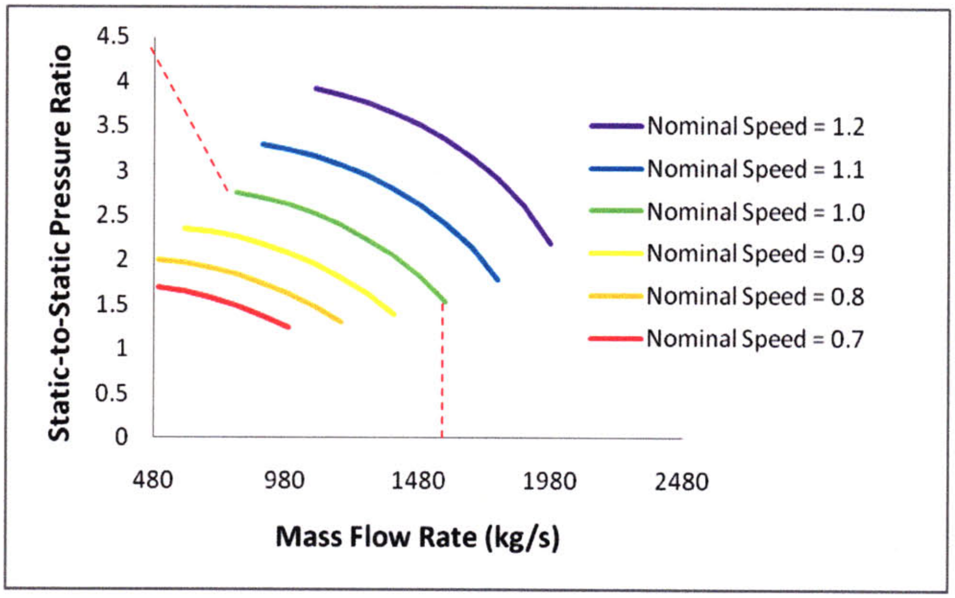

Figure 7.6: Pressure ratio performance curve for recompressing compressor at nominal operating speeds of 0.7 to 1.2 [7.8] (with choke and surge extrapolations for the 100% speed case included)

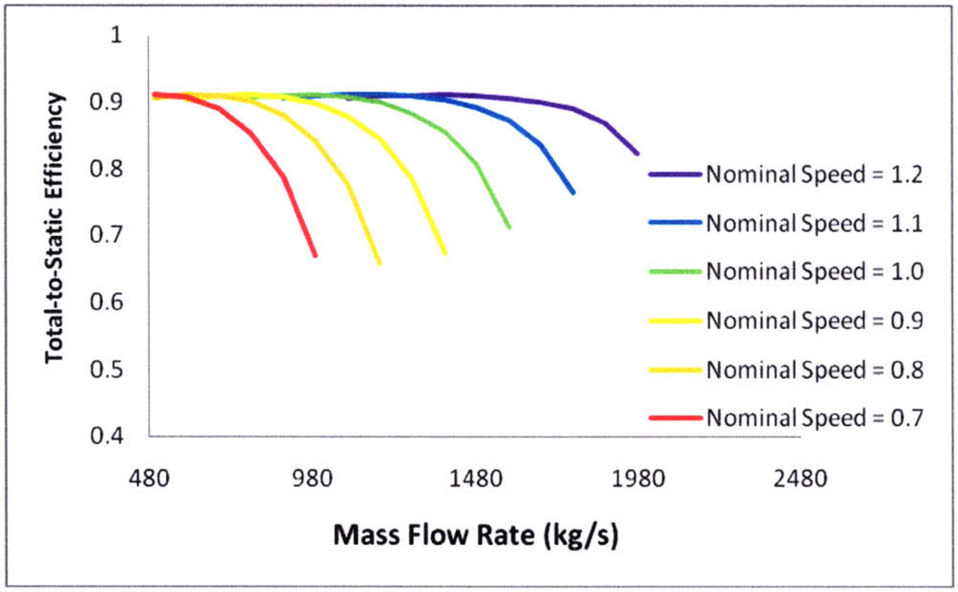

Figure 7.7: Efficiency performance curve for recompressing compressor at nominal operating speeds of 0.7 to 1.2 [7.8]

There was no design code readily available for developing a turbine model (CYCLES III does not include turbine parameters), and thus a detailed turbine model specific to the SFR model was not created. However, the simplistic representation of a turbine in RELAP5-3D negates the need for specific design data. Thus, the turbine was scaled from a 300MW turbine utilized by Pope in S-CO_2 Brayton cycles [1.11] while using parameters from the S-CO_2 turbine designs developed at MIT [7.9]. The turbine RELAP5-3D input parameters are listed along with the other cycle RELAP5-3D input parameters in Section 7.3.

The details of each of the 500 MWth S-CO_2 PCS loops were developed using the code CYCLES III, (adapted from CYCLES II by Ludington [7.6, 1.12, 1.13]). This code calculates the specific dimensions for the PCHEs in the cycle, as well as the various coolant state-points throughout the cycle. CYCLES III can “optimize” the efficiency of the S-CO_2 PCS by adjusting the sizes of the PCHEs until the highest efficiency is obtained. The input parameters to CYCLES III include, but are not limited to, the hot and cold conditions of the IHX, as well as guess values for PCHE sizes and piping between components. Key CYCLES III inputs for the overall cycle can be found in Table 7.3, while the key parameters for each of the PCHE exchangers can be found in Table 7.4.

Table 7.3: Key parameters for each of the 500 MWth S-CO_2 PCS loops (CYCLES III input)

Main compressor outlet pressure (MPa)	20.0
Cycle thermal power (MWth)	500.0
Net thermal efficiency (%)	39.9
Pressure ratio of the main compressor (maximum cycle pressure ratio)	2.6
IHX outlet temperature (°C) (maximum cycle temperature)	472.0
Precooler outlet temperature (°C)	32.0
Main compressor efficiency in dimensionless form	0.89
Recompressing compressor efficiency in dimensionless form	0.86
Turbine efficiency in dimensionless form	0.94
Mechanical efficiency (couplings)	0.99
Generator efficiency	0.98
Frequency converter efficiency (including switchyard losses)	1.0
Cooling water inlet temperature (°C)	20.0
IHX pressure drop (kPa)	60.0

Table 7.4: Key parameters for each PCHE in the 500MW loop S-CO_2 PCS

HX type	HTR	LTR	pre	IHX
Channel type	zig-zag	zig-zag	zig-zag	zig-zag
Hot-to-cold plate frequency (h:c) (h:c:he [IHX])	1:1	1:1	1:1	1:1:1
Channel diameter (mm)	2.0	2.0	2.0	2.5
Total number of channels (hot and cold)	6963664	5299898	2340657	1505904
Plate thickness (mm)	1.5	1.5	1.5	1.5
Module height (m)	1	1	1	11
Module width (m)	1.666667	1.190476	1.538462	0.60000

Module length (m)	0.6	0.75	0.65	1.97915
Heat exchanger volume (m3)	30	28	11	52.2496
Number of axial nodes	40	40	40	40
Precision	0.005	0.005	0.0005	0.0005
Hot side pressure drop (kPa)	43.612	62.917	7.216	2.432
Cold side pressure drop (kPa)	31.954	12.080	-	137.5

The state points and results of the CYCLES III calculation will be listed in Section 7.3. A comparison of these results along with the RELAP5-3D model results will be given as well. It is of interest to note that for the secondary IHX, there is a helium plate for CO_2 leak detection between the hot and cold plates by design, which is the purpose for the additional number in the plate ratio row in Table 4.7. The height of this module was adjusted to match the height of the steam generator in the SFR model for easy insertion of the new PCS boundary.

7.3 RELAP5-3D S-CO_2 PCS Model

The RELAP5-3D model for the S-CO_2 PCS loops is constructed similarly to model of the SFR secondary loops. Fig. 7.8 is a nodalization diagram of the S-CO_2 PCS loops, including the turbine trip valves. This model consists of a series of pipes representing each PCHE, with branch components connecting each pipe. A turbine and two pump components were included to represent the turbo-machinery of the loop. The turbine flow control was incorporated by including a servo and a motor valve component representing the turbine trip valves. Finally, pipe components were used to simulate the zig-zag channel flow with heat structures representing the PCHE core. This heat structure was used to model the transfer of heat between cold and hot streams in each PCHE.

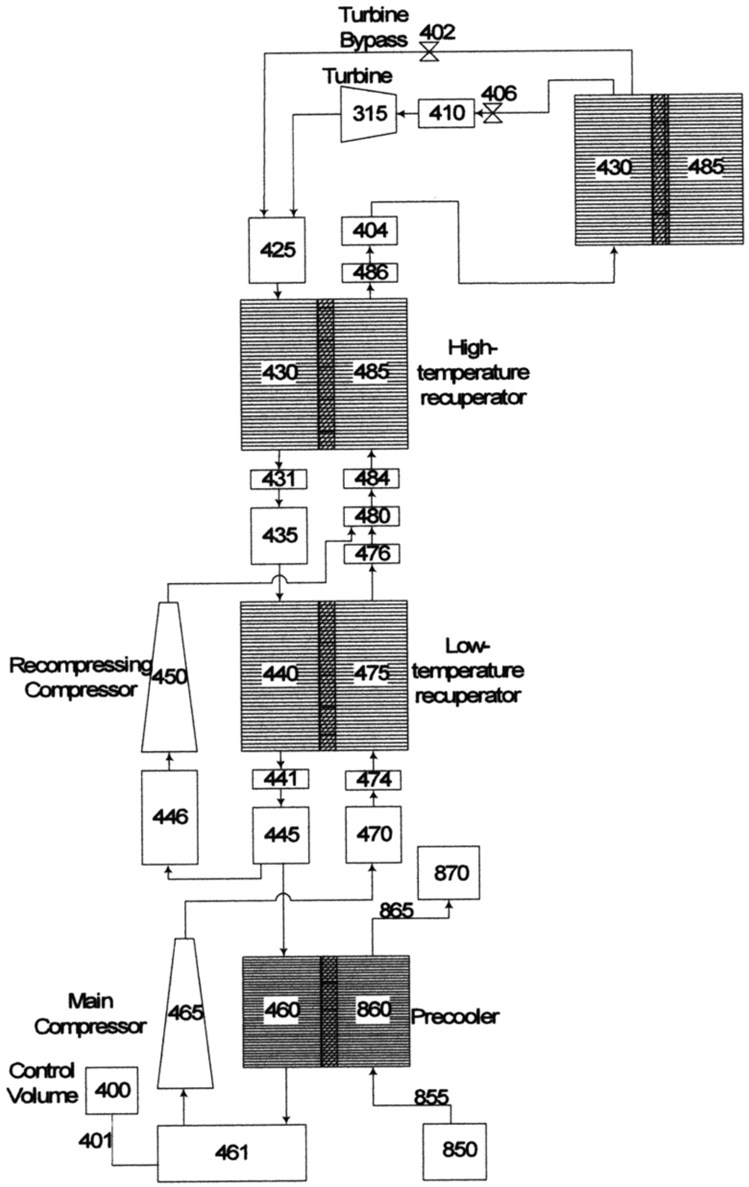

Figure 7.8: Nodalization diagram of RELAP5-3D S-CO$_2$ PCS loops model

The PCHE model pipe components represent the lumping of all the semi-circular channels into a single flow area. The number of channels is multiplied by the area of each channel, providing the total flow area. The length of each PCHE node is slightly different from the node length of the IHX exchangers. Because the PCHE consists of zig-zag channels with a zig-zag angle (defined as the angle of deflection for the channel at the top and bottom of each zig-zag) of $2\cdot\theta$, each node length is equal to:

$$L_n = \frac{L_{PCHE}}{N_n} \cdot \frac{1}{\sin(2\theta)}, \tag{7.2}$$

where:

L_n = flow length per node

L_{PCHE} = length of the PCHE unit

N_n = number of nodes.

The PCHE design used in this model, $\theta = 63.4°$, means that the node length is increased by a factor of 1.25. The hydraulic diameter of the channels is used as the pipe hydraulic diameter and is unaffected by the zig-zag pattern of the channels. The friction factor is calculated in-situ by RELAP5-3D via Eq. (7.1). The branch components connecting the pipe and compressor components utilize minor friction coefficients to provide sufficient piping hydraulic resistance. Determining the minor loss coefficients for each branch was an iterative process that involved adjusting the coefficient until the pressure losses predicted by CYCLES III were achieved. Key parameters of the pipe and compressor components are found in Table 7.5.

Table 7.5: Key parameters of RELAP5-3D S-CO2-PCS components

Number	Description	Type	Volumes	Flow Area (m^2)	Length (m)	Hydraulic Diameter

						(m)
400	Control volume	Time dependent volume	1	1000	1	1.07047
402	Turbine bypass	Valve	-	0.6	-	-
404	IHX inlet	Branch	1	19.74	0.4	0.001833
406	Turbine shutoff	Valve	1	0.6	-	-
405	IHX	Pipe	40	19.74	0.412	0.001833
410	Turbine inlet	Branch	1	19.74	0.1	1.07047
415	Turbine	Turbine	1	1.8	0.6	1.07047
425	Turbine outlet (pipe)	Branch	1	21.877	1.8	-
430	HTR hot side	Pipe	40	21.877	0.0188	0.001222
431	HTR hot out	Branch	1	21.877	0.4	0.001222
435	LTR hot inlet	Branch	1	16.65	2.05	-
440	LTR hot side	Pipe	40	16.65	0.0234	0.001222
441	LTR hot outlet	Branch	1	16.65	0.4	0.001222
445	Precooler entrance	Branch	1	16.65	1.2	-
446	Recompressing compressor entrance	Branch	1	17.22	1.498	2.28976
450	Recompressing compressor	Pump	1	0.3834	1.3143	-
455	Recompressing compressor Outlet	Branch	1	17.22	0.1	2.28976
460	Precooler	Pipe	40	7.353	0.01625	0.001222
461	Precooler exit	Branch	1	7.353	0.4	-
465	Main compressor	Pump	1	0.4276	1.125	-
470	Main compressor outlet	Branch	1	13.333	1.2	2.91849
474	LTR cold inlet	Branch	1	16.65	0.4	-
475	LTR cold side	Pipe	40	16.65	0.234	0.001222
476	LTR outlet	Branch	1	16.65	0.4	-
480	Point 3	Branch	1	13.333	1.65	0
484	HTR cold inlet	Branch	1	21.877	0.4	0.001222
485	HTR cold side	Pipe	40	21.877	0.0188	0.001222
486	HTR cold outlet	Branch	1	21.877	0.4	0.001222
850	Cooling water source	Time dependent volume	1	400	1	11.28
860	Precooler cold side	Pipe	40	7.353	0.01625	0.001222
870	Cooling water sink	Time	1	400	1	11.28

		dependent volume				

The PCHE heat structures were modeled as flat plates with an effective heat conduction thickness of ~60% of the actual plate thickness, which is supported by FLUENT calculations of the PCHE channels [7.10]. In reality, the heat transfer through the PCHE channels is multi-dimensional, but this heat transfer is approximated using the single flat plate exchangers. The recuperators in the RELAP5-3D model were composed of stainless steel 316, while the precooler was composed of titanium.

The PCHE heat structure could be considered a solid rectangular block with thousands of hollow channels within this block. Thus, a simple way to derive a reasonable volumetric heat capacity coefficient is to start with the volumetric heat transfer coefficient for the solid PCHE block, and then multiply this value by a factor representing the hollow spaces representing the channels. For the PCHEs, the channels take up roughly 14% of the PCHE block. Thus, in order to compensate for the abnormal shape of the plate and channel design, the volume properties were modified by dividing the volumetric heat capacity by 1.14 [1.11]. Table 7.6 tabulates the material properties (volumetric heat capacity and thermal conductivity) used for the PCHEs, while Table 7.7 lists the key parameters of the heat structures for these volumes. The zig-zag channels in the PCHE modules facilitate a higher heat transfer coefficient than straight channels. There is currently no correlation that predicts this enhancement, but previous work has found that a multiplication factor of 2.4 will accurately account for the enhanced heat transfer [6.6].

Table 7.6: Material properties (adjusted for volume distortion) of ss-316 and titanium as utilized in the HTR, LTR, and PC [1.11]

SS-316			Titanium		
Temperature (°C)	Volumetric Heat Capacity	Thermal Conductivity (W/m·K)	Temperature (°C)	Volumetric Heat Capacity	Thermal Conductivity (W/m·K)
10	3.12E+06	13.7	-73.15	1.64E+06	20.0
37.78	3.24E+06	14.14	21.85	1.64E+06	20.0
260	3.73E+06	17.63	26.85	1.67E+06	20.0
426.67	3.87E+06	20.24	126.85	2.26E+06	20.0
537.78	3.96E+06	21.99	226.85	2.53E+06	20.0
815.56	4.31E+06	26.35	326.85	2.68E+06	20.0
			526.85	2.84E+06	20.0
			826.85	2.92E+06	20.0

Table 7.7: Key parameters of RELAP5-3D S-CO2-PCS heat structures

Heat Structure	**Description**	**Segments**	**Thickness (mm)**	**Heated Length (m)**
14301	HTR	40	1.2	1342.6
14302	LTR	40	1.2	1342.6
14303	PC	40	0.9	195.6
14304	IHX	40	1.5	407.0

The compressor component model utilized in RELAP5-3D is dependent upon performance curves that indicate the pressure ratio and efficiencies at given shaft speeds. However, the work previously performed at MIT revealed that compressor over-speed and under-speed performances are significant. For example, in the ULOF transient described in Section 7.5, the turbine and generator are decoupled from the grid, thus experiencing a sudden loss of load in the generator. This loss of resistance causes a ramp-up of turbine shaft speed. In order to model accurately the wide range of over-speed and under-speed performances (since the current compressor curves only reach to an over-speed of 20%) the compressors are modeled as pumps, as was done by Pope and Nikiforova [1.11, 6.6]. Utilizing RELAP5-3D pump components requires the conversion of the compressor properties and performance curves to pump homologous curves and rated parameters. This conversion introduces a small error, but this is acceptable considering the preliminary stages of investigation for such conversions.

The homologous pump curves for the main compressor and recompressing compressor were created using the same method as described in Section 5.1.2.2, with a couple of key differences. First, the head curve and efficiency curves were taken from the compressor performance curves described in Figs. 7.4 – 7.7. The pressure ratio for each compressor was converted to pump head according to the equation:

$$H = P_s \cdot (r - 1), \tag{7.3}$$

where:

P_s = compressor static pressure

r = pressure ratio.

Because the RELAP5-3D model consists of two lumped 500MW S-CO_2 PCS loops, the rated flow through each compressor (pump component) is double the flow listed in Table 7.2. Using this method for converting the compressors to pump components, the resulting homologous curves can be found in Figs. 7.9 – 7.10. Note that the extrapolation beyond choke and surge points of the compressors in the RELAP5-3D pump homologous curves is required for initiation in RELAP5-3D and these extrapolations are indicated by the red lines on the homologous curves. Note that a large positive extrapolation was needed in the recompressing compressor for a stable flow to be established by RELAP5-3D. Thus, compressor performance was monitored to determine if either of these conditions were instigated within the compressors during the transient, as described in section 7.5.3.

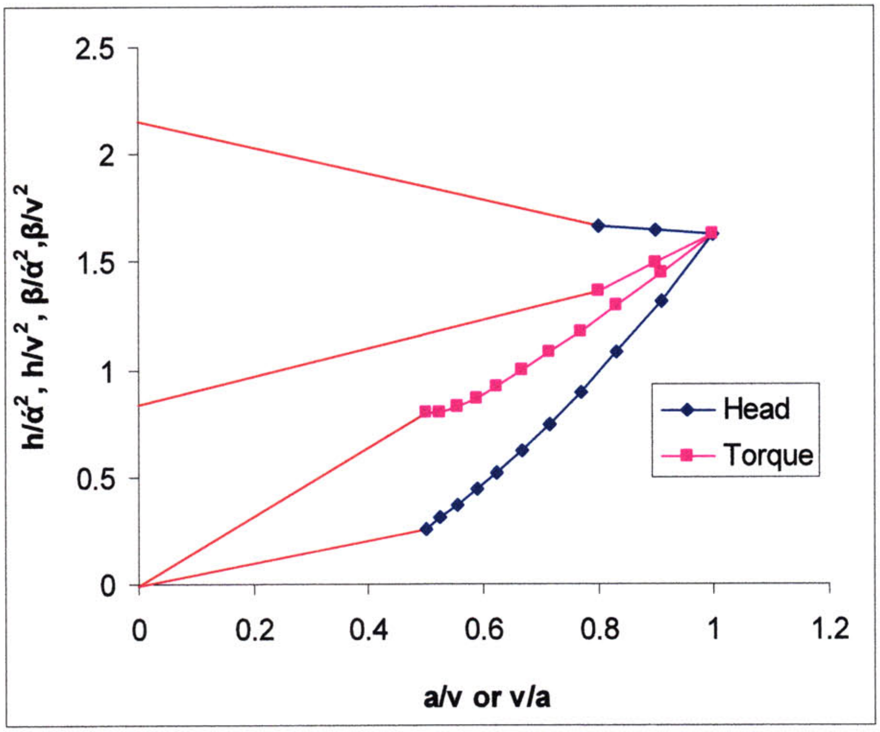

Figure 7.9: Homologous pump curves for the main compressor (radial)

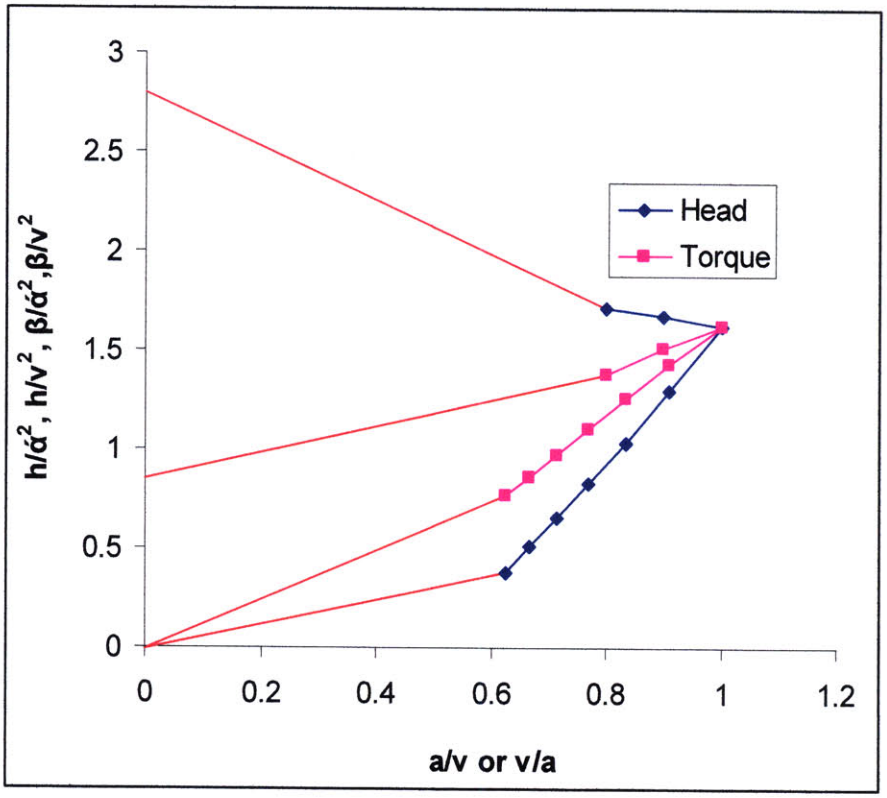

Figure 7.10: Homologous pump curves for the recompressing compressor (radial)

The turbine model in RELAP5-3D requires input of the efficiency, pressure ratio, and flow parameters, as well as the inlet flow area. The efficiency for the 500 MW loop turbine design is 94%, and the pressure ratio is 0.397147. The flow parameters are listed in Table 7.5, while the inlet and outlet flow areas were adjusted, due to lack of a specific design parameter, in order to better match the RELAP5-3D and CYCLES III state points. The final inlet flow area, which provides the closest match to the state-points, is 0.675 m^2.

7.4 RELAP5-3D S-CO_2 PCS Model Results

The performance of the RELAP5-3D model is best rated by comparing key state-points and parameters with the CYCLES III model. The RELAP5-3D model consists of two lumped 500MW loops, and thus the flow rates in the CYCLES III model are doubled to account for the two lumped loops. The most important points to match are the high and low temperatures and the mass flow rates as these parameters are considered the key figures of merit for the RELAP5-3D steady state S-CO_2 PCS model. These important parameters have a strong influence on the cycle efficiency, and thus must match in order for the RELAP5-3D model to be considered sufficient. Other key state-points include the inlet and outlet temperatures and pressures for each component in the S-CO_2 PCS. A comparison of the various state-points of the S-CO_2 PCS cycle can be found in Table 7.8, while the significant parameters of interest are highlighted in yellow.

Table 7.8: Key state-point properties of the CYLES III and RELAP5-3D S-CO2 PCS model (figures of merit highlighted)

	CYCLES III Temperature (°C)	RELAP Temps (°C)	CYCLES III Pressure Drop (kPa)	RELAP Pressure Drop (kPa)	CYCLES III Flow (kg/s)	RELAP Flow (kg/s)
Control volume	-	350.824			-	
IHX in	331.68	317.376	414	872.8	5803.4	5815.1
IHX out	472	471.504			5803.4	5815.1
Turbine in	471.92	465.589	11531.1	10734.8	5803.4	5815.1
Turbine out	367.16	367.256			5803.4	5815.1
HTR hot in	367.07	367.256	43.6	4.56	5803.4	5815.1
HTR hot out	165.36	123.079			5803.4	5815.1
LTR hot in	164.97	123	62.9	5.47	5803.4	5815.1
LTR hot out	70.11	67.223			5803.4	5815.1
Recomp in	68.42	67.21	-12486.4	-11631.7	2504.6	2519
Recomp out	159.73	122.259			2504.6	2519
Precool in	69.94	67.207	7.2	11633.67	3298.8	3296.1
Precool out	32	33.713			3298.8	3296.1

Precool H2O in	20	20	-		15612.2	15612
Precool H2O out	28.73	27.22			15612.2	15612
Mcomp in	31.61	33.713	-12373.6	-11634.3	3298.8	3296.1
Mcomp out	60.16	60.541			3298.8	3296.1
LTR cold in	60.12	60.541	12.1	0.6	3298.8	3296.1
LTR cold out	159.11	116.334			3298.8	3296.1
HTR cold in	159.38	118.9	32	2.9	5803.4	5815.1
HTR cold out	331.99	316.736			5803.4	5815.1
RELAP efficiency	**39.1%**	CYCLES III efficiency	**39.9%**			

As can be seen in Table 7.8, the key figures of merit match closely between the CYCLES III and RELAP5-3D PCS models. The other state-points vary by up to ~35°C. This is primarily due to uncertainties in the turbine design and enthalpy-to-temperature conversions in the codes. In addition, the pressure drops across each of the PCHE's (except for the IHX) are underpredicted by nearly an order of magnitude in the RELAP5-3D model. This indicates that the friction correlation given in Eq. 7.1 underpredicts the pressure drop through the PCHE's. However, the key parameters match very well, and so does the cycle efficiency thus the RELAP5-3D model of the S-CO_2 PCS is considered acceptable for use in the ULOF transients.

7.5 ULOF Transients

It has been shown that utilizing an S-CO_2 PCS can provide for a self-powering heat removal system [7.2], although no actual credit can be claimed for this as a safety system since the cost of making the entire PCS safety-grade is prohibitive [6.6]. It is of interest to investigate the performance of the S-CO_2 PCS as a heat sink during a ULOF transient in the SFR, because of the potential for this system to remove decay heat without the use of a dedicated auxiliary CO_2 injection system. The performance of the S-CO_2 PCS coupled to the SFR during ULOF transient is compared to the performance of a Rankine PCS boundary coupled to the SFR. The constraints and results of these analyses are discussed below.

7.5.1 ULOF Constraints

The primary difference between the ULOF and the station blackout transients is that during a ULOF the heat sink (PCS) remains operable. The constraints for the ULOF transients are similar to those selected for the station blackout. The primary pump coast-down is an exponential decay with a halving time of 5 seconds. The CRDLE feedback is based upon a 6m long CRDL shaft, and the rod worth is 49 $/cm. The DRACS does not initiate throughout this transient, and all cooling is accomplished via natural circulation, with the PCS (not the DRACS) being the heat sink. The first ULOF transient run is the ULOF for a metal CR = 0.71 base fuel configuration with a Rankine PCS boundary. The second ULOF transient run is the ULOF for the metal CR = 0.71 base fuel configuration with a completed S-CO_2 PCS. As with the station blackout and UTOP transients, the max cladding temperature must remain below the short term FCCI limit of 725 °C during the initial peak and below the FCCI long term limit of 650 °C after the initial peak.

7.5.2 Rankine Cycle PCS Boundary ULOF Results

Typically, feedwater regulation in the steam generator is accomplished using the auxiliary feedwater system. This is typically a safety-grade system. Rather than explicitly modeling the steam generator and auxiliary feedwater system, the SG inlet flow is regulated at the PCS boundary; in other words, the water flow into the steam generator is controlled by a time dependant junction. When the primary pumps are tripped, the water flow to the SG is linearly decreased by 0.6% per second to a final flow rate of 10% of the nominal flow. The results of the steam PCS ULOF transient are plotted in Figs. 7.11 to 7.13.

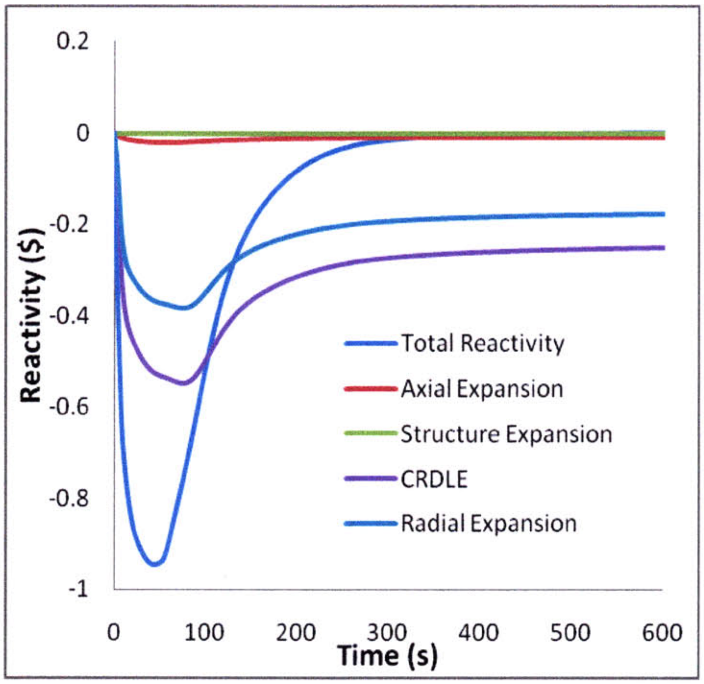

Figure 7.11: Reactivity feedbacks for a ULOF transient with a Rankine PCS boundary (fuel and moderator coefficients not shown)

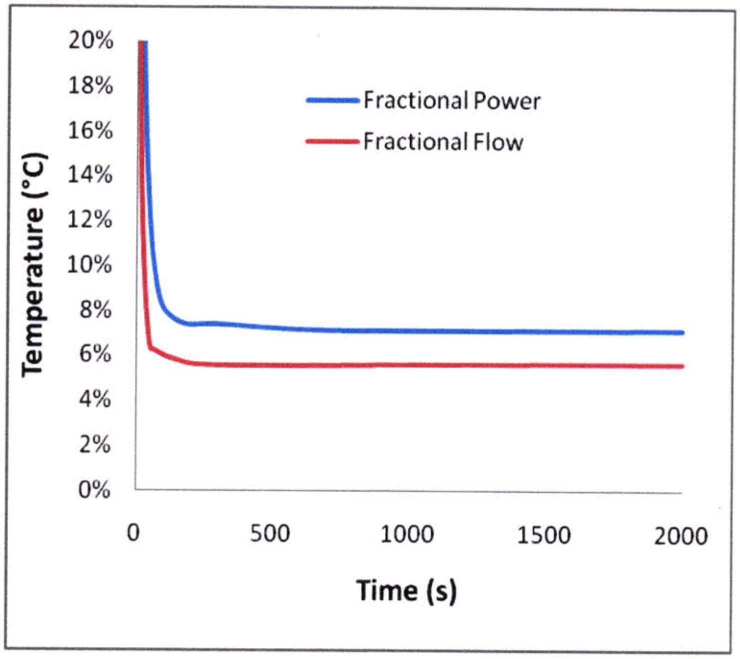

Figure 7.12: Nominal core power and coolant flow rate for a ULOF transient with a Rankine PCS boundary

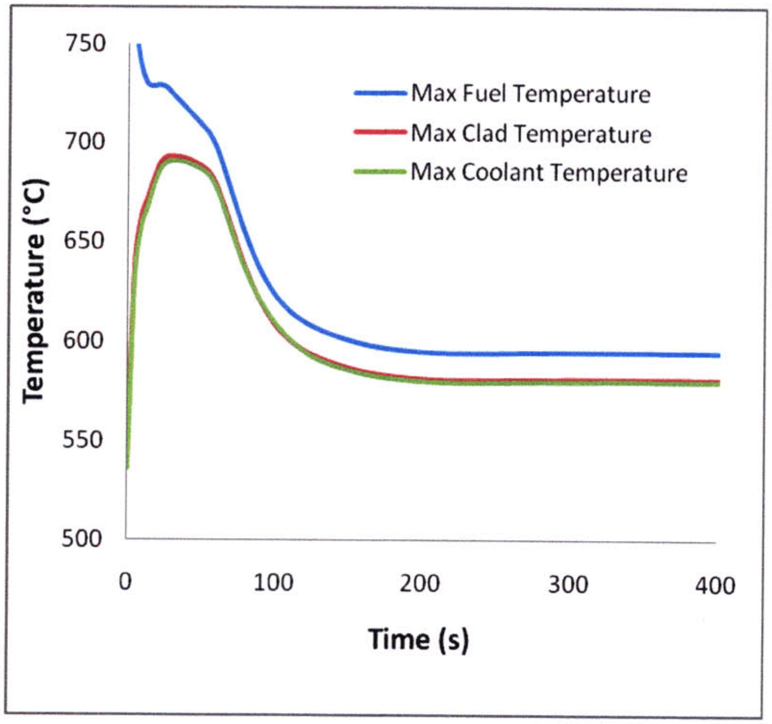

Figure 7.13: Key temperatures for a ULOF transient with a Rankine PCS boundary

It can be seen from Fig. 7.11 that at 10% PCS flow, the overall core reactivity is positive, and the core power increases. However, the natural circulation flow is sufficient to cool the core and prevent major temperature increases. The clad temperature during the initial temperature peak is below the short term FCCI temperature limit at 693.3 °C. Note in Fig. 7.12 the high fractional flow through the core during a ULOF transient. This is noticeably higher than the fractional flow through the core during a station blackout transient (as plotted in Fig. 6.10).

7.5.3 S-CO2 PCS ULOF Results

Upon initiation of the ULOF, the compressors and turbine trip, and the generator decouples from the grid. Because the compressors and turbine are on the same shaft, the energy generated by the turbine turns the shaft and drives the compressors, thus allowing for prolonged operation of the PCS. This prolonged heat withdrawal (assuming cooling water is available to the precooler) allows for decay heat removal without activation of the DRACS units.

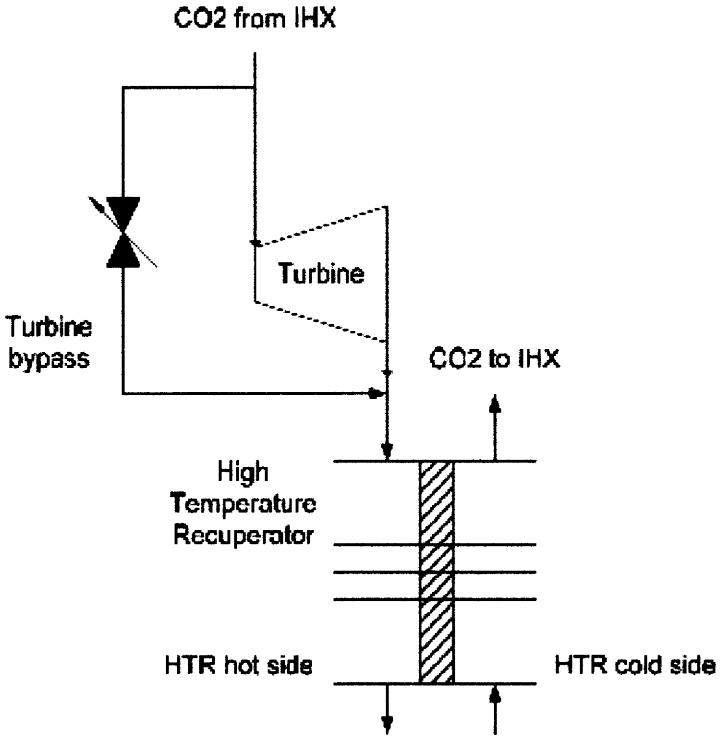

Figure 7.14: Schematic of turbine bypass valve [6.6]

It is critical, however, that a control scheme be implemented to prevent both core overcooling and turbine over-speed accidents. A control scheme based upon actuation of turbine shutoff and turbine bypass trips was developed for the flexible conversion lead-bismuth reactor [6.6]. For this control scheme, a turbine bypass valve, as pictured in Fig. 7.14, opens when the generator is disconnected from the grid. This prevents turbine over-speed, since the imbalance in shaft torque upon loss of electrical load would lead to a rapid increase in shaft speed. The acceleration of the turbine is dependent upon the inertia of the shaft and its components, and these values were scaled directly from the shafts used in the gas-cooled fast reactor [1.11]. Table 7.9 lists the inertia values used in the current S-CO_2 PCS model.

Table 7.9: Inertia of S-CO_2 shaft and components

	Moment of Inertia (kg/m^2)	
PCS rating	500MWth	600MWth*
Recompressing compressor	254.7	305.6
main Compressor	94.3	113.1
turbine	708.3	850.0
generator	1666.7	2000.0
shaft	310.0	372.0

***This is the inertia used for the GFR S-CO_2 PCS components**

Once the turbine speed decreases below the nominal value, the flow to the turbine can be controlled by the turbine bypass valve. This is accomplished by using a shaft speed signal proportional-integral (PI) controller, which acts on the turbine bypass valve. The PI controller measures the "error," or the difference between the shaft speed and a shaft speed set-point. A diagram of the PI controller is shown in Fig. 7.15.

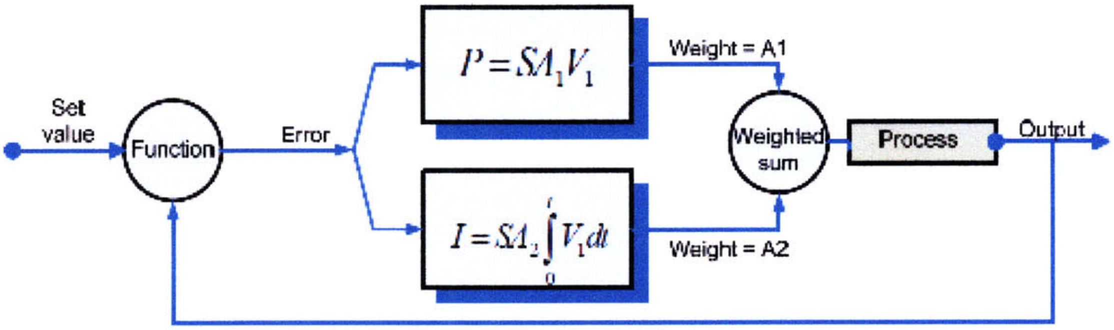

Figure 7.15: PI controller diagram [6.6]

The initial response of the control is due to the proportional component, while the remaining responses are driven primarily by the integral component. It is crucial that appropriate estimated factors (S) and weights (A1 and A2) be selected to ensure smooth performance of the PI controller. If the proportional weight is too high, significant overshoot can occur, resulting in instabilities in the PCS flow, where if it is too long, it may take a long time for the control to converge upon the desired set-point. The integral component relates to the speed and duration of adjustments. If the integral weight is too high, oscillations may hamper the performance of the controller, while if it is too low, the controller may under-respond to changes in shaft speed. Because of the slow changes in reactor power during a ULOF, a low integral weight was selected. The weights and set-point used in the S-CO_2 PCS shaft speed controller are given in Table 7.10. For a more detailed discussion of using a PI controller for turbine shaft speed control in a S-CO_2 PCS, see the flexible conversion ratio lead-bismuth reactor report [6.6].

Table 7.10: PI controller weights and set-point for turbine shaft speed control

Setpoint (Rad/s)	36.7
A_1	2.9
A_2	0.06
S	0.01

The results of the S-CO_2 PCS ULOF are plotted in Figs. 7.16 – 7.19. As with the Rankine PCS boundary ULOF, the clad temperatures are well below the FCCI limits, with a peak temperature of 693.4 °C. The initial peak ends at a slightly higher value than in the Rankine PCS ULOF, but the max clad temperature then steadily decreases in the S-CO2 cooled ULOF, where in the Rankine PCS transient, this post-peak temperature is a quasi-steady state value that remains constant without noticeable decay for up to at least 2000 seconds.

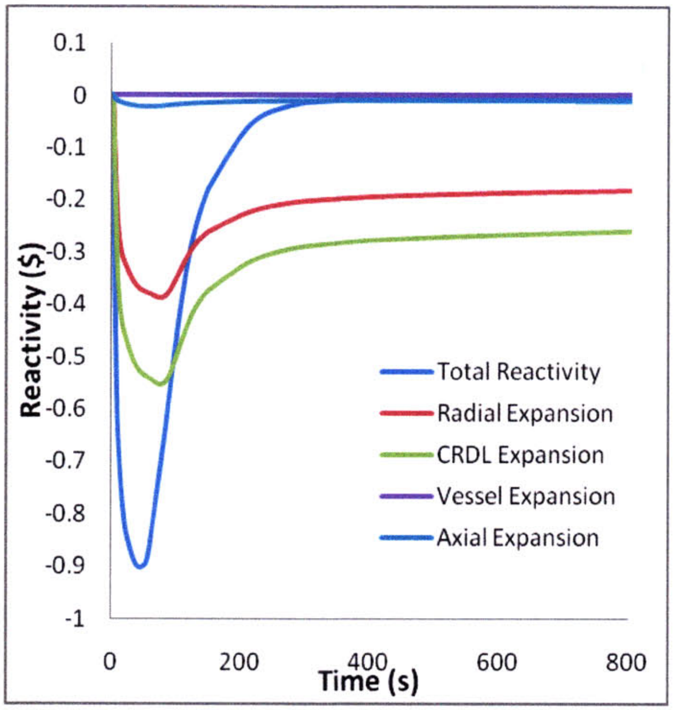

Figure 7.16: Reactivity feedbacks for a ULOF transient with a full S-CO_2 PCS and turbine shaft speed controller (fuel and coolant coefficients not shown)

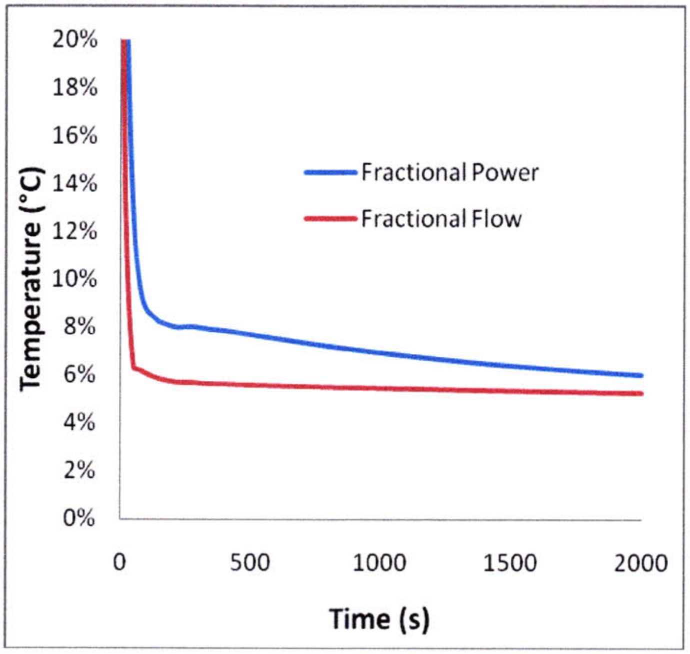

Figure 7.17: Nominal core power and coolant flow rate for a ULOF transient with a full S-CO_2 PCS and turbine shaft speed controller

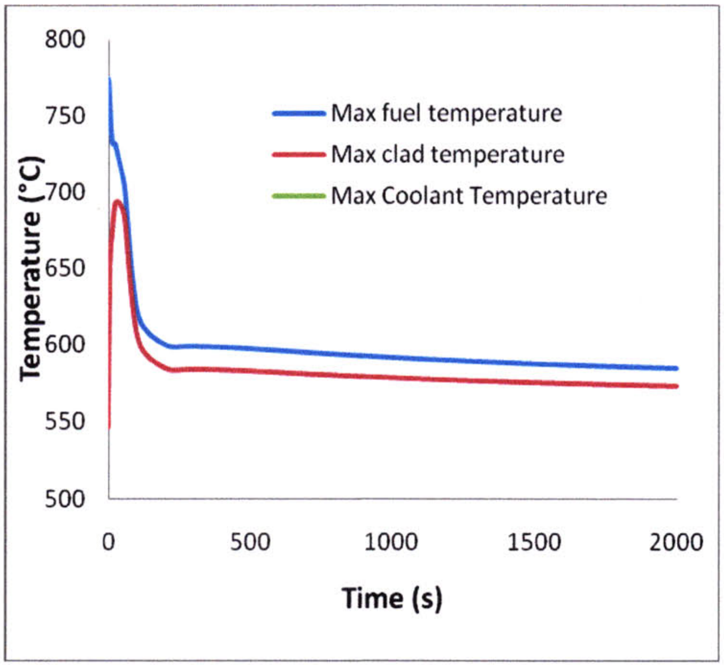

Figure 7.18: Key temperatures for a ULOF transient with a full S-CO_2 PCS and turbine shaft speed controller

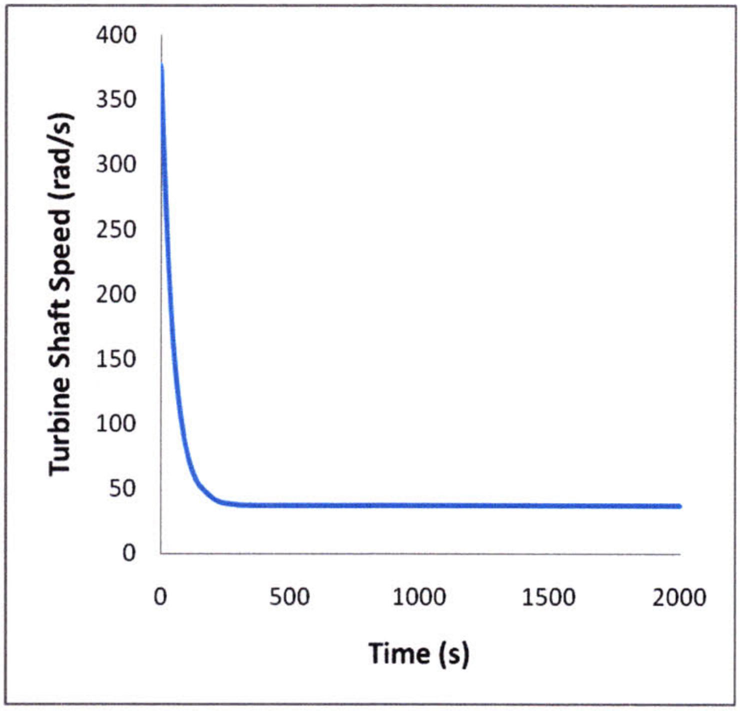

Figure 7.19: Turbine shaft-speed for a ULOF transient with a full S-CO_2 PCS and turbine shaft speed controller

A direct comparison of the peak clad temperature for both Rankine PCS and S-CO_2 PCS is plotted in Fig. 7.20. It can be seen that the S-CO_2 system can effectively remove decay heat from the primary system without the use of a dedicated CO_2 safety injection system. It is only necessary that cooling water be provided to the precooler to maintain the PCS cooling. The performance of the S-CO_2 PCS is dependent upon the use of a turbine shutoff valve control system, and can be fine-tuned through adjustment of the PI controller parameters.

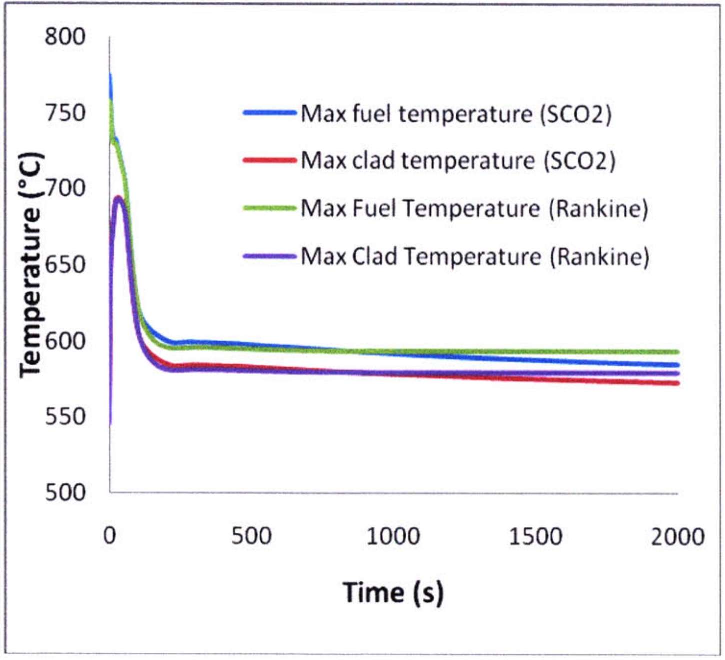

Figure 7.20: Comparison of the maximum clad temperature during a ULOF for a full plant model coupled with a PCS boundary and a full S-CO_2 PCS

However, it is important to investigate the performance of the radial compressors through this transient. These compressors cannot reliably operate if they surge. In addition, if they reach the choke point, then no higher flow rate can be attained regardless of the head. Thus, the compressor speed was plotted against the mass flow rate for the main compressor and the recompressing compressor in Figs. 7.21 and 7.22, respectively. The approximate surge and choke points as a function of compressor mass flow rates are also plotted in these figures.

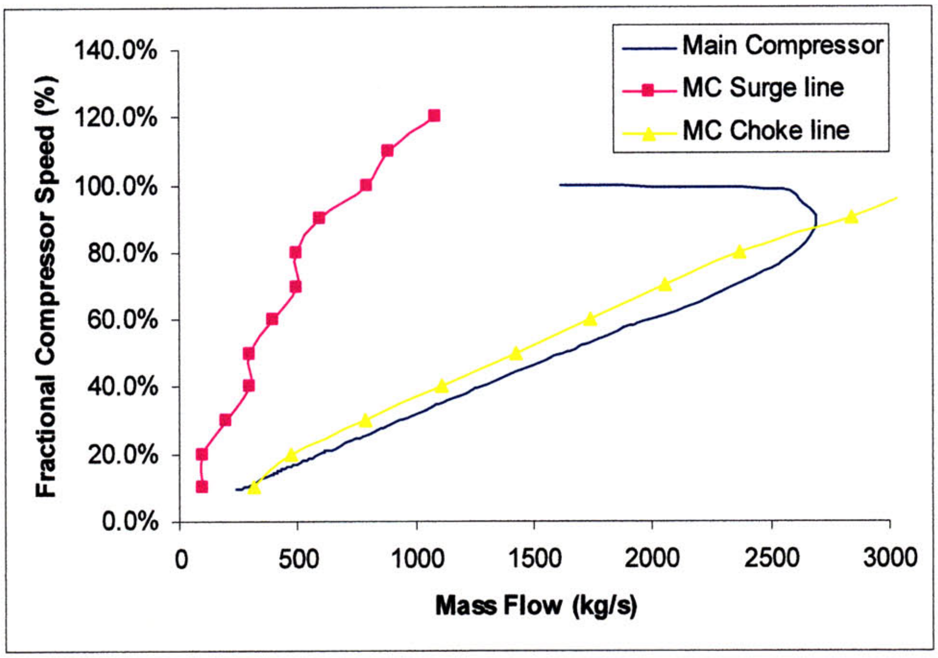

Figure 7.21: Performance of the main compressor through the ULOF transient with surge and choke points

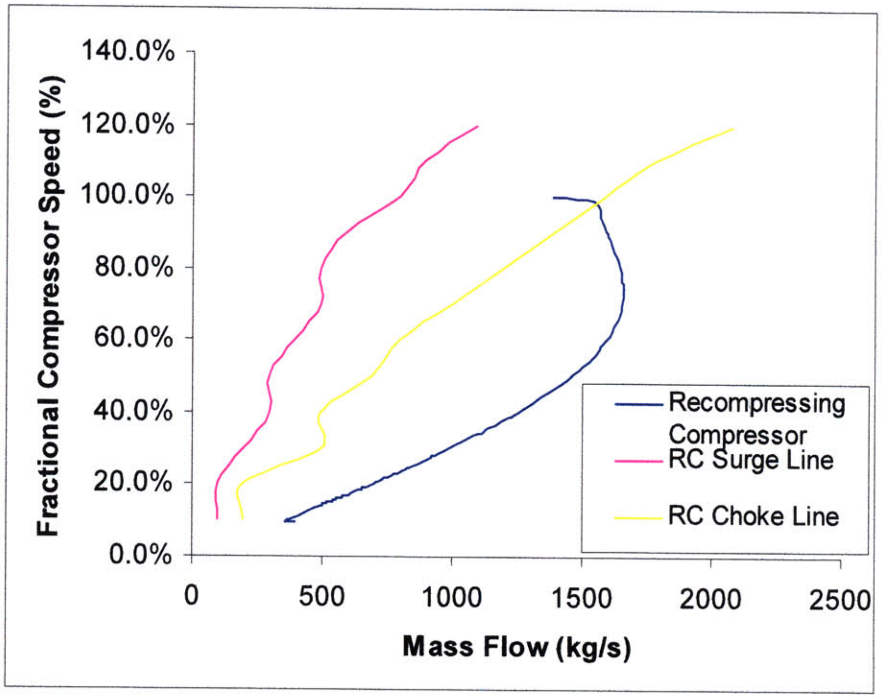

Figure 7.22: Performance of the recompressing compressor through the ULOF transient with surge and choke points

As can be seen, the main compressor operates without crossing the surge line initially, but it comes very close to the choke line and eventually crosses at low compressor speeds, but only slightly. The recompressing compressor, however, crosses the choke line very early in the transient, and remains in the choked region throughout. Thus, S-CO2 PCS is capable of cooling the SFR during a ULOF transient, since the surge point is never crossed for these compressors (since operating over the choke point only indicates that no further flow can be pushed through the compressor). These compressors do not even approach the surge line. This is surprising since flow decay is expected as the transient progresses. The primary reason for this lack of compressor surge is the initial increase in flow rate seen at the beginning of the transient. As the generator and turbomachinery trips, the decrease in resistance results in a sudden but brief increase in mass flow rate. As the turbine bypass valve closes, the loop flow rate begins the expected decay. However, because this flow decay begins after the initial surge in mass flow rate (and thus at a mass flow higher than the nominal mass flow through each compressor), the surge point in the compressors is never reached. As can be seen in Figure 7.22, however, the flow rate exceeds the choke point despite the manual insertion of this point via the homologous pump curves. Future work should investigate the reason for this anomalous compressor behavior, so as to guarantee that the choke flow is a condition that is accurately modeled by the RELAP5-3D homologous curves. This would then verify that the performance of these compressors is considered acceptable.

7.6 Conclusion

A S-CO_2 PCS model was attached to the full plant model using the metal CR = 0.71 fuel described in Chapter 5. The steady state performance of this cycle was adequate for safety modeling purposes, with very little difference between the CYCLES III and RELAP5-3D values in flow rate, high/low coolant temperatures, and efficiencies. Other state-point values did vary, but are not crucial to match for the current study. A ULOF transient was simulated for a metal CR = 0.71 full plant model with both a Rankine PCS and a S-CO_2 PCS. The purpose of this comparison was to determine if the S-CO_2 PCS could provide necessary cooling without the use of auxiliary feedwater system or steam dump to condenser.

Throughout both ULOF transients, the peak clad temperature is never reached. This indicates that the S-CO_2 PCS can remove the decay heat from the primary system without the use of CO_2 safety injection systems during a ULOF comparably to a Rankine cycle PCS with condensers and auxiliary feedwater systems. The decay heat removal by the S-CO_2 PCS requires only a turbine bypass valve system with a well calibrated PI controller and water pumps to maintain cooling water flows in the precooler. These results demonstrate that there would be no need for condensers or an auxiliary CO_2 injection safety-grade system component for a S-CO_2 PCS. The amount of heat removed by the S-CO_2 PCS can be adjusted by altering the PI controller parameters and the set-point for the turbine flow.

Chapter 8: Summary, Conclusions, and Future Work

8.1 Summary

The sodium fast reactor (SFR) is currently being reconsidered as an instrument for actinide management throughout the world, thanks in part to international programs such as the Generation-IV and especially the Global Nuclear Energy Partnership (GNEP). The success of these programs, in particular the GNEP, currently the Advanced Fuel Cycle Initiative (AFCI) program, is dependent upon the ability of the SFR to manage actinide inventory while remaining economically competitive. In order to achieve these goals, the fuel must be able to operate reliably at high burnup and power densities. The primary candidates for the SFR are oxide and metal fuels, each with unique benefits and challenges. In fast reactor systems, the cladding and fuel must perform adequately while experiencing relatively high temperatures (550°C – 600°C), fast neutron flux ($>10^{15}$ n/cm^2), and mechanical stresses (>100MPa). Therefore, the power density of the fuel is limited by fuel-clad chemical interaction (FCCI), the fuel melting point, fuel clad mechanical interaction, sodium boiling, and to a lesser extent the sodium pressure drop in the fuel channels. The first two limitations relate primarily to metal fuel, while the third and fourth relate primarily to oxide fuel, and the last relates to both fuel types. Therefore, innovative fuel configurations that reduce clad stresses, sodium pressure drops, and fuel/clad temperatures could be applied to the SFR core to directly improve the performance and economics. Two particular designs of interest that could potentially improve the performance of the SFR core are the internally and externally cooled annular fuel and the bottle-shaped fuel.

The general objective of this thesis is to investigate the benefit that can be provided by utilizing these fuel configurations from a thermal-hydraulic standpoint. This includes the development of a detailed assembly design for these fuel configurations, the optimization of the geometric and hydraulic parameters of the fuel configurations through subchannel analyses, and the quantification of the thermal hydraulic benefit derived. Additionally, a safety analysis of the innovate fuel configurations is accomplished in which the performance of these fuels during a station blackout and unprotected transient overpower accidents is compared to the performance of the respective standard "base" solid fuel configurations. Finally, utilizing a RELAP5-3D model of the SFR, the performance of a supercritical carbon dioxide (S-CO_2) power conversion system (PCS) coupled to the secondary loops during an unprotected loss of flow accident (ULOF) is compared to the performance of a Rankine cycle PCS coupled to the secondary loops.

8.1.1 Innovative Fuel Configurations

Chapter 2 of this thesis focuses on the development of the assembly design for the bottle-shaped and internally/externally cooled annular fuel. The results of this chapter are summarized in the following sections.

8.1.1.1 Base Fuel Configurations for SFR

The reference fuel configurations were taken from a fuel design study by Hoffman et al. [2.2]. In this study, core and assembly designs were developed for a wide range of conversion ratios (CR), though not for breeding conversion ratios (CR>1), since breeder reactors are not part of the GNEP/AFCI program. Because there is a large degree of uncertainty as to what conversion ratio will be utilized in future SFRs, both high (CR = 1.0) and low (CR = 0.25) conversion ratio designs are included for the base core configurations in this section and are considered bounding conditions for future core configurations.

Both CR = 1.0 and CR = 0.25 configurations consist of hexagonal fuel assemblies (FA) with wire-wrap spacers in the CR = 1.0 configurations and grid spacers in the CR = 0.25 configurations. Both core layouts consist of three enrichment (defined as TRU/HM) zones within the fuel. For the CR = 1.0 configurations, the inner, middle, and outer driver enrichments are 10.7%, 13.3%, and 16.0%, respectively, with an average charge enrichment of 14% for the metal fuel. In the oxide fuel, these enrichments are 13.0%, 16.3%, and 19.5%, respectively, with an average charge enrichment of 17%. For the CR = 0.25 configurations, the inner, middle, and outer driver enrichments are 46.2%, 57.8%, and 69.3%, respectively, with an average charge enrichment of 56% for the metal fuel. For the oxide fuel, these same enrichments are and 50.7%, 63.4%, and 76.1%, respectively, with an average charge enrichment of 60%. The geometric and thermal parameters of each of these fuel configurations are listed in Table 8.1.

8.1.1.2 Annular Fuel Configurations for SFR

Annular fuel is not a new concept. It has been suggested for use previously in a range of reactors, including both PWRs and BWRs [2.8, 2.9]. Annular UO_2 fuel with internal and external cooling has been studied at MIT for over 6 years and has been shown to enable power density increases of up to 50% in PWR cores [2.9]. The large heat transfer surface attainable with simultaneous internal and external cooling reduces the fuel operating temperature and the surface heat flux dramatically. Annular fuel for the sodium fast reactor is made feasible by increasing the overall fuel rod diameter and includes an inner channel in the center of the fuel rod, which is separated from the fuel by an additional clad and bond layer. A scale depiction of the annular fuel rod design compared to the traditional solid fuel pin design is seen in Fig. 8.1. In order to maintain a nearly constant assembly size, the number of fuel rods per assembly must be decreased.

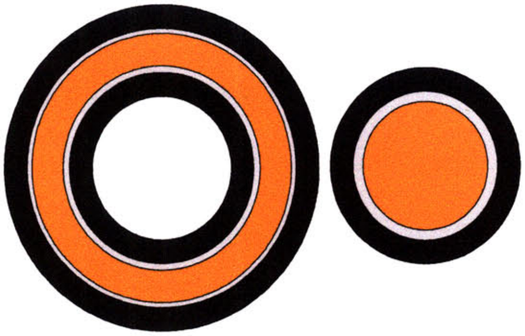

Figure 8.1: Annular fuel rod cross section (left) vs traditional solid fuel rod (right)

In order to maintain clarity of comparison, the following parameters were maintained from the solid to annular fuel configurations:

- The fuel-to-coolant volume ratio and core height: this approximately preserves the overall neutronic characteristics of the core, e.g., spectrum, reactivity coefficients, reactivity letdown, etc.
- Smeared density: this allows for adequate accommodation of fuel swelling under irradiation.
- Inter-assembly gap and FA duct thickness: these parameters provide adequate FA clearance and mechanical robustness, respectively.
- Core power density. This ensures the fairness of the comparison between solid and annular FAs when the assembly size changes.

In comparing the annular FA designs to the ANL designs, the average heat flux at the clad surface and the radial temperature increase in the fuel serve as the primary figures of merit. It is clear that FAs with lower q″ and ΔT than the ANL designs will also have lower clad and fuel temperatures, all else being equal. Therefore, it would be possible to uprate the core power density and/or increase the discharge burnup. The design parameters for each annular fuel configuration can be found in Table 8.1. Note the very high pressure drop across the CR = 1.0 oxide base fuel core due to the tight pitch (the wire wrap is only 0.1 mm thick) and thus high hydraulic resistance.

Table 8.1: Design parameters for base and annular fuel configurations

	Metal CR = 0.25		Metal CR = 1.0		Oxide CR = 0.25		Oxide CR = 1.0	
	Base	**Annular**	**Base**	**Annular**	**Base**	**Annular**	**Base**	**Annular**
Rings	13	11	9	8	10	9	9	7
Pins	540	397	271	217	324	271	271	169
Flat to flat (cm)	15.71	21.32	15.71	21.76	15.71	17.66	15.71	29.56
Pin outer diameter (mm)	4.64	9.29	8.08	13.57	5.56	9.23	8.68	21.16
Pin inner	-	5	-	5	-	5	-	5

diameter (mm)								
P/D_o	1.357	1.087	1.0996	1.062	1.45	1.09	1.023	1.009
Dwire (mm)	-	0.805	0.805	0.805	-	0.805	0.198	0.198
Clad thickness (mm)	0.559	0.559	0.559	0.559	0.635	0.635	0.635	0.653
Fuel volume fraction (%)	17.44	16.79	34.26	35.2	19.73	17.13	49.29	57.44
Bond volume fraction (%)	5.81	5.6	11.42	11.73	1.02	0.89	2.55	2.97
Structure volume fraction (%)	29.15	31.78	25.73	23.68	26.22	35.95	28.58	16.76
Coolant volume fraction (%)	47.6	45.83	28.59	29.38	53.02	46.04	19.58	22.82
Fuel/coolant volume ratio	0.366	0.366	1.198	1.198	0.372	0.372	2.517	2.517
Power density (kW/L)	258.09	258.09	267.59	267.59	191.18	198.22	198.22	198.22
Linear heat rate (kW/m)	12.66	31.27	24.05	56.79	15.63	23.46	17.82	98.62
q" (kW/m^2)	868.33	696.31	947.54	973.71	894.62	524.93	653.37	1199.9
ΔT (°C)	91.57	12.12	174.00	50.16	310.88	28.34	354.45	174.83
q''' (W/cm^3)	1732	1803.9	842.44	820.51	1137	1309.74	434.53	372.48
Inner channel flow (%)	-	55.4	-	51.68	-	55.56	-	25.49
Inner channel power (%)	-	46.43	-	41.88	-	46.25	-	33.84
Core ΔP (kPa)	141.54	188.85	797.73	403.23	99.1	201.32	2885.9	656.56

The annular fuel approach seems very promising for the low-conversion cores, as their initially high P/D_o value allows for easy accommodation of the annular fuel pins. The heat flux at the clad surface for annular fuel is decreased by 19.8% in the metal fuel core and 15.19% in the oxide core, while the radial temperature profile across the fuel pellets is decreased by 86.76% in the metal fuel and 90.9% in the oxide fuel. On the other hand, use of annular fuel pins in the high conversion cores would be problematic due to the tightness of the fuel pin array. The radial temperature profile across the fuel pellets is decreased by 71.17% in the metal fuel and 50.68% in the oxide fuel, but the heat flux at the clad surface is actually *increased* by 2.67% in the metal fuel and 83.65%

in the oxide fuel. Thus, high CR core configurations are best suited to bottle-shaped fuel, while low CR core configurations are best suited to annular fuel.

8.1.1.3 Bottle Shaped Fuel Configurations for SFR

Bottle-shaped fuel refers to a fuel pin whose diameter is smaller in the plenum region than in the active region, which results in a significant decrease in the overall core pressure drop. To compensate for the decrease in radial area of the gas plenum region of the fuel rod, the length of the gas plenum region is increased, thus maintaining a constant gas plenum volume. The gas plenum region has a larger P/D, so grid spacers are used rather than the wire-wrap spacers used in the active core region. In order to utilize this type of innovative fuel, there must be sufficient space in the hot pool above the core to increase the length of the fuel rods by moderate amounts (~10% to 20%). A representation of such bottle-shaped fuel can be seen in Fig. 8.2.

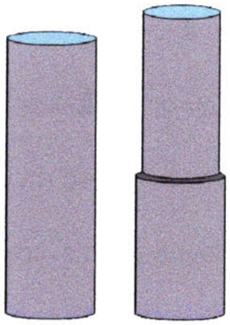

Figure 8.2: Segments of the base (left) and bottle-shaped fuel pins (right) (drawing to scale)

In the bottle-shaped fuel configuration, the active core geometry was maintained from the base fuel configuration, and the pitch of the active region was kept the same in the plenum portion of the fuel rods. The figures of merit for this fuel were the pressure drop across the core and the total length of the fuel rods. In the high CR fuel, the ratio of bottle-shaped to base fuel pin heights is 1.156 for the metal fuel, and 1.183 for oxide fuel. The ratio of bottle-shaped to base core pressure drops is 0.589 for metal fuel and 0.493 for oxide fuel. In the low CR fuel, the ratio of bottle-shaped to base fuel pin heights is 1.162 for the metal fuel, and 1.096 for oxide fuel. The ratio of bottle-shaped to base core pressure drops is 0.814 for metal fuel and 0.894 for oxide fuel. The bottle-shaped fuel configuration is most promising for the high conversion ratios (with pressure drop reductions of up to 60%), since the base fuel has a very tight pitch, while the low conversion ratio cores already have a large P/D, and thus do not benefit from using bottle-shaped fuel rods as much as the CR = 1.0 cores.

8.1.2 RELAP5-3D Subchannel Analysis Model

Chapter 3 describes the creation of the subchannel analysis model and is summarized in this section. Current subchannel codes are not suitable for modeling sodium-cooled assemblies with annular or bottle-shaped fuel. A subchannel model was therefore created using RELAP5-3D to evaluated the performance of innovative fuels. Control variables were used to calculate the transverse heat transfer due to cross flow (pressure induced) and turbulent mixing (wire-wrap induced), using the models by Cheng and Todreas [2.6].

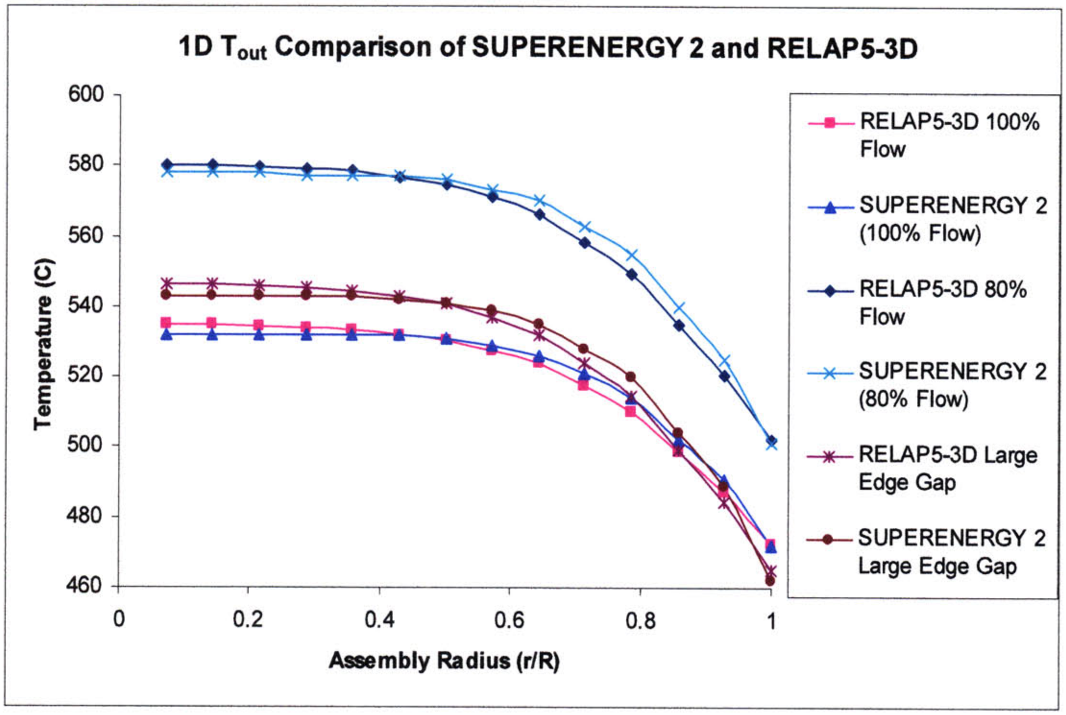

Figure 8.3: 1-D Radial temperature distribution comparison for SE2 and RELAP5-3D

The mass transfer due to these effects cannot be simulated in RELAP5-3D, so a 1-3% error (depending on configuration) is introduced in the edge boundary mass flow values. In the interior channels, the net transverse mass flow is zero due to fluid incompressibility and symmetry. Heat transfer due to axial and radial conduction was simulated, but this effect is negligible during full power, steady-state operation. This model was verified against SUPERENERGY II (SE2) by modeling an 8 ring assembly in both RELAP5-3D and SE2. The resulting 1-D comparison of core outlet temperature can be seen in Fig. 8.3.

As a more robust benchmark, the RELAP5-3D subchannel model was compared to experimental data from the Oak Ridge National Lab (ORNL) 19 pin test [3.23]. The normalized core outlet temperatures, defined as $(T - T_{in})/(T_{out}-T_{in})$, where T_{out} is the outlet bulk temperature measured by the thermocouples. The core outlet temperatures predicted by the RELAP5-3D subchannel model are plotted with the data from the 19-pin test in Fig. 8.4. It can be seen that there is good agreement between the 19-pin test data and the RELAP5-3D subchannel model.

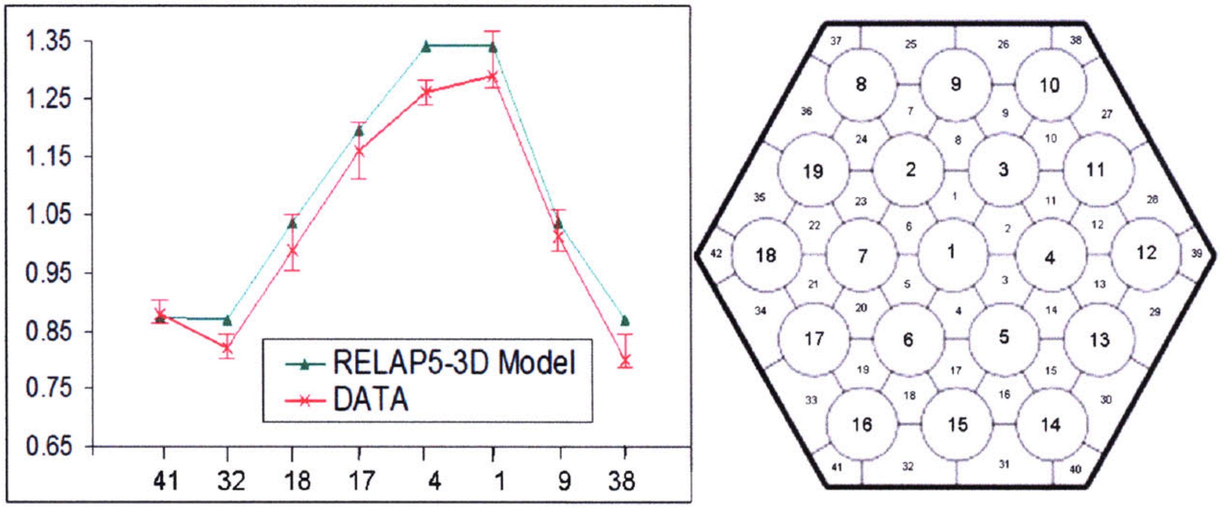

Figure 8.4: Normalized outlet temperatures for ORNL 19-pin test [5.24] and RELAP5-3D subchannel model (left) with subchannel numbering diagram (right)

Though RELAP5-3D is not typically used for subchannel analysis, the subchannel model clearly produces reasonable results. The primary benefits of using the RELAP5-3D subchannel model include flexibility in modeling pin, assembly, and spacer geometries, steady-state and transient modeling capabilities, an analysis of the fuel rods in addition to the coolant, and the inclusion of temperature dependent coolant/clad/fuel properties. The disadvantages include a long runtime (1-24 hours) and a large input deck construction time (~1-3 weeks).

The core outlet temperature distributions across a single assembly in an SFR core are quite large (~30°C at hot conditions). In attempt to flatten this profile, the concept of duct ribs (semi-circular protrusions on the inner walls of the assemblies) was investigated using the RELAP5-3D subchannel analysis model. These duct ribs were successful in reducing the peak outlet temperature within the assembly by ~5-10°C. It is significant to note, however, that the six corner subchannels within the assembly were unaffected by the duct ribs, and thus have a cooler core outlet temperature (~30°C). Future work could investigate a flow area inhibitor in the corner channels to ameliorate this problem. The flattened coolant outlet temperature distribution enables an increase of core-average outlet temperatures while keeping the same margins to the hot spot limit, making possible higher plant efficiency.

8.1.3 RELAP5-3D Subchannel Analysis Model Results

Chapter 4 presents the results of the subchannel analyses for the innovative fuel assembly configurations and is summarized in this section. The core outlet temperature distributions of the annular fuel assemblies for both oxide and metal fuels (with duct ribs included) are shown in Figs. 5 and 6, respectively. The power uprate that can be achieved using annular fuel is 40% for oxide fuel and 45% for metal fuel. This uprate is determined by increasing the power and flow to maintain a constant average core outlet temperature. The limiting parameter of these uprates was the core pressure drop; it was assumed that the pressure drop could not exceed two times the non-uprated value.

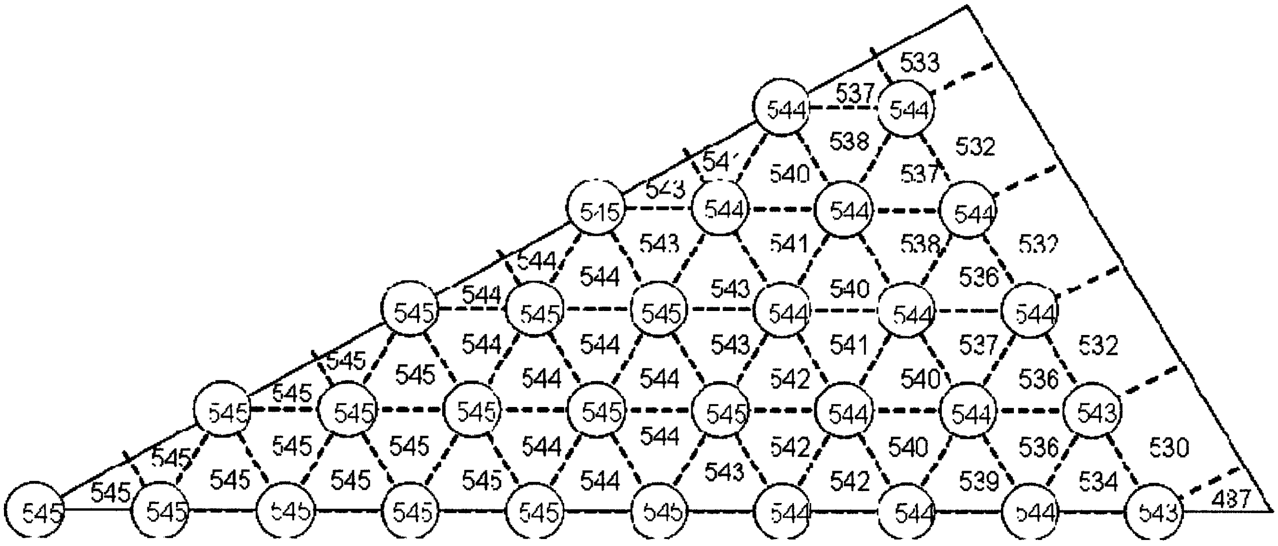

Figure 8.5: Core outlet temperatures for annular oxide fuel assembly model with duct ribs included (the #s within each circle represent the outlet coolant temperature of the corresponding annular fuel rod inner channels)

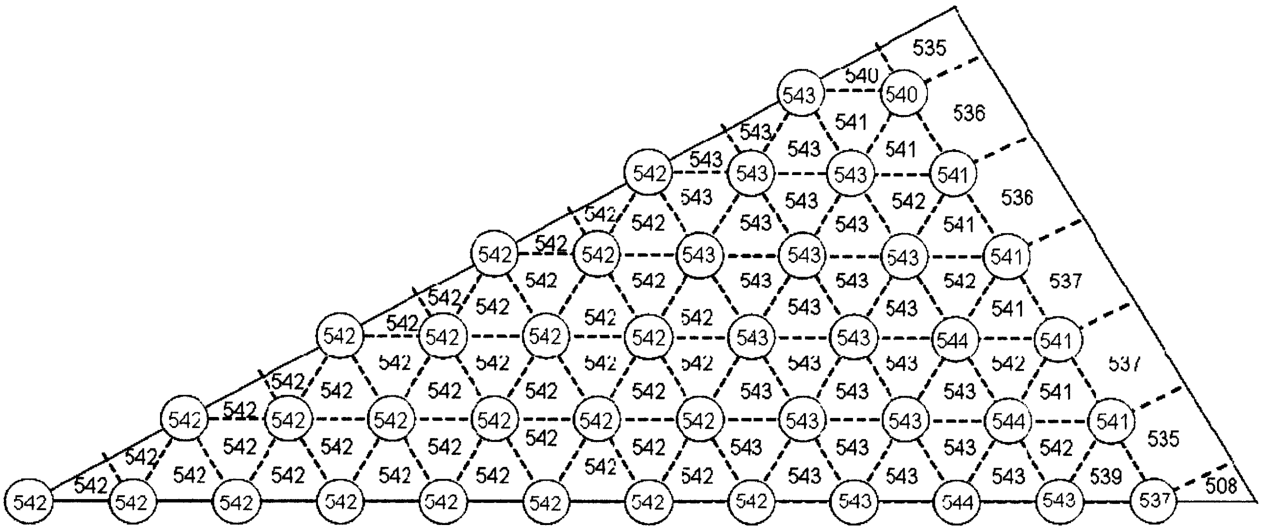

Figure 8.6: Core outlet temperatures for metal annular fuel assembly model with duct ribs included (the #s within each circle represent the outlet coolant temperature of the corresponding annular fuel rod inner channels)

The small inner diameter of the annular fuel configurations (3.6 mm) leaves the assembly susceptible to an inner-annular channel flow blockage accident. The hot channel is assumed to be completely blocked. During this accident, the clad temperature cannot exceed the fuel clad chemical interaction (FCCI) limit of 650°C in the metal fuel, while the sodium must not boil in the oxide fuel. In the oxide annular fuel configurations, the sodium boiled during a blockage accident, thus making the oxide annular fuel configuration unfeasible. In the metal annular fuel configurations, a power uprate of 20% results in a blocked channel max clad temperature of 639°C, which is below the FCCI limit with an ~11°C margin. Thus, a power uprate of 20% is possible for metal annular fuel.

A simplified structural analysis of the annular fuel reveals that during a blockage accident, the inner clad thermally expands about 0.45 mm more than the outer clad. This results in a compressive axial stress on the inner cladding of ~8.78MPa, well above the buckling stress limit, due to the long, thin nature of the inner clad. This means that buckling is a concern during a blockage accident and future work should focus on finding a solution to this problem. On the other hand, shear stresses in the end-cap due to this differential cladding expansion are very low. Therefore, the main structural concern during the complete blockage accident is buckling of the inner clad.

The subchannel analysis of the bottle-shape fuel was performed for the ABR1000 base fuel configuration, which is a CR = 0.71 core configuration. The subchannel analyses of the bottle-shaped fuel configurations revealed that core performance is similar to the base fuel, as expected. The increase in core height is 15.6% in the metal fuel and 18.3% in the oxide fuel, which corresponds to a reduction in core pressure drop of 31.5% for oxide fuel and 36.3% in metal fuel. The maximum primary membrane local shear stress on the core/plenum interface (in the limiting scenario of an abrupt transition from the core to the plenum regions) is 7.602 MPa for metal fuel, and 2.298 MPa for oxide fuel, which is well below the limit of 315MPa for both.

8.1.4 Full Plant Model

Chapter 5 describes the creation of the RELAP5-3D full plant model. The following sections summarize the full plant reference design and the RELAP5-3D model created to simulate the full plant performance during station blackout and UTOP transients.

8.1.4.1 Reference SFR Design

The ABR1000 is a scaled up version of the ABTR, and is the reference design for the safety analyses of the various fuel types [5.3]. This is a pool-type reactor with four 25% secondary loops, four 25% Rankine PCSs, and three 2.5MW direct reactor auxiliary cooling systems (DRACS). A schematic of the pool and sodium flow is found in Fig. 8.7, while a layout of the core is depicted in Fig. 8.8. The radial power peaking within the core is 1.2, while the axial peaking is 1.19 for the oxide fuel core and 1.13 for the metal fuel core. The total power generated in the core is 1000MW.

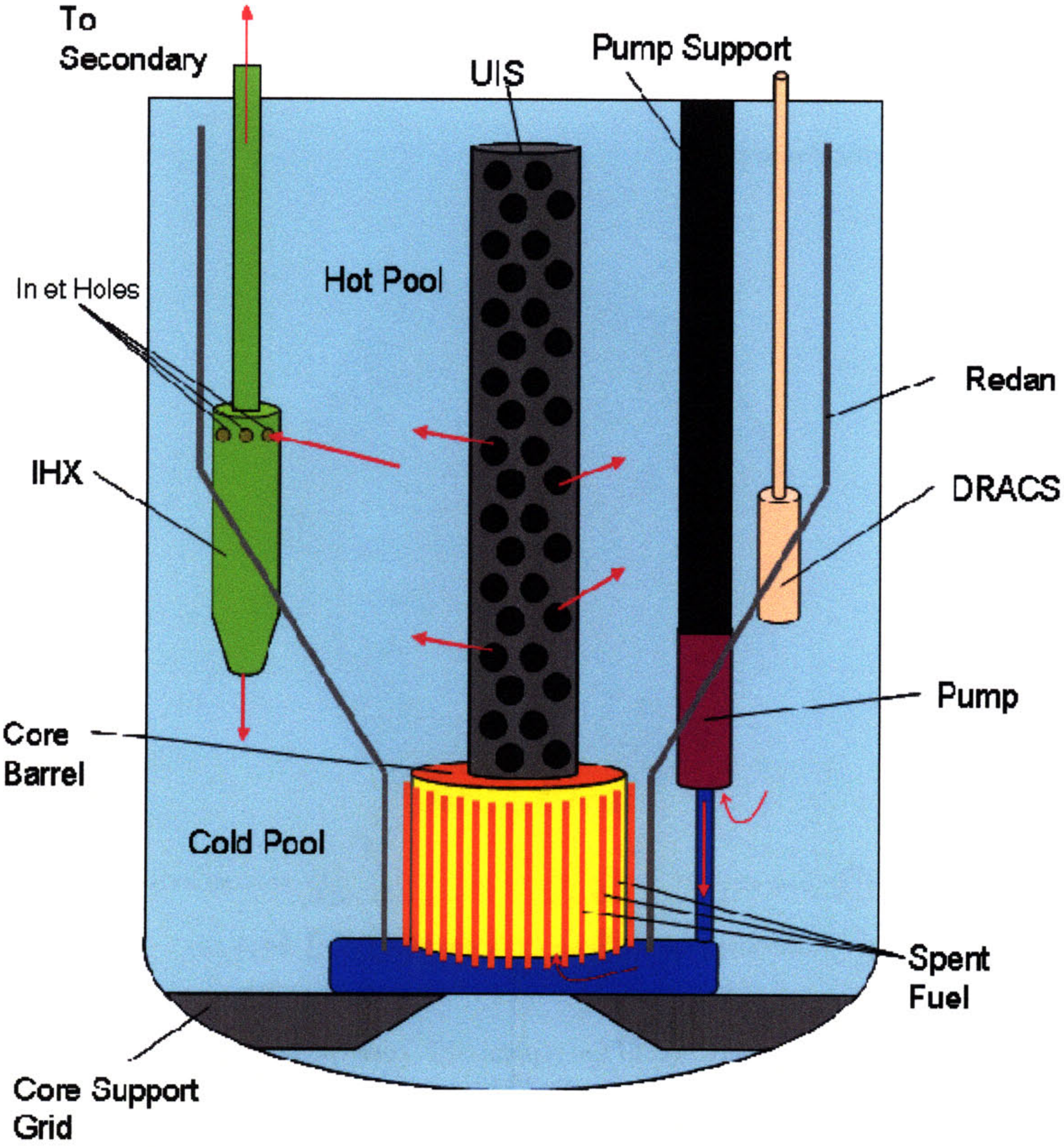

Figure 8.7: Schematic of the key components of the SFR pool-type primary system, including DRACS emergency systems

The intermediate heat exchangers (IHX) are single pass, counter-flow, vertical shell and tube heat exchangers with cold secondary sodium flowing on the tube side. The primary (and secondary) pumps are electromagnetic (EM) double stator annular linear induction pumps (ALIP). The DRACS exchangers are vertical, shell and tube heat exchangers, with a sodium-potassium (NaK) salt flowing through the tubes. This NaK is cooled by outside air flow, which is initiated by the opening of the DRACS valves upon the loss of electrical power.

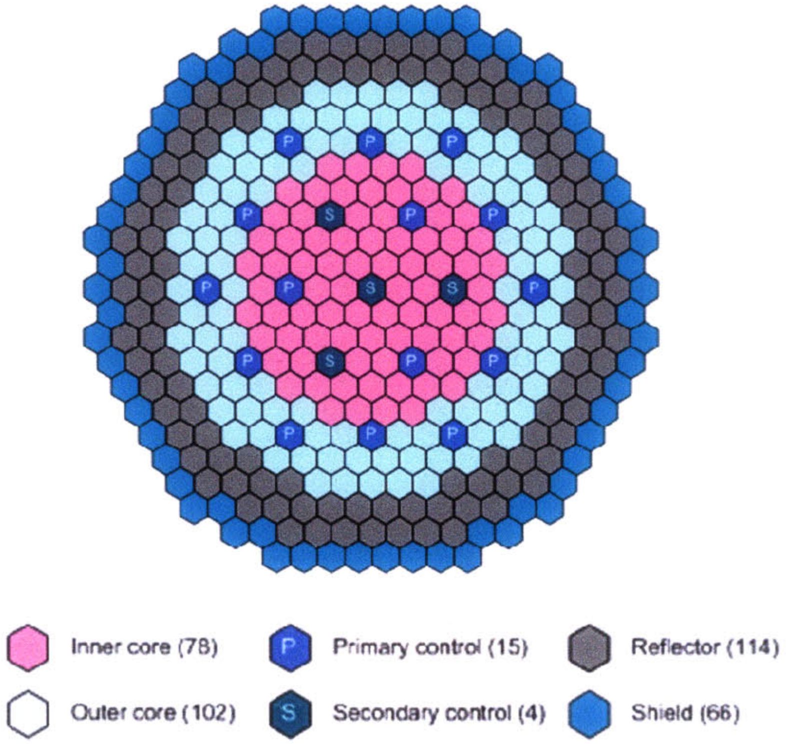

Figure 8.8: Core assembly layout for typical SFR core (metal or oxide) as described in [5.12]

Two of the three DRACS have pumps and compressors to provide optional forced convection for the NaK and air, but this forced convection option was not investigated in this thesis. The secondary loops consist of secondary sodium piping with secondary pumps, purification systems, IHXs, and stream generators.

8.1.4.2 RELAP5-3D Model of Reference SFR Design

A RELAP5-3D model of the full plant was created, with nodalization diagrams found in Figs. 9-11. For simplicity, the four secondary and PCS trains were lumped into a single representative loop. Each of the pumps in the model are modeled using homologous pump curves and the RELAP5-3D centrifugal pump component as if the pumps were mechanical pumps. The heat transfer in the IHXs is enhanced to due baffles and cross flow through the shell, and this is reflected in RELAP5-3D through the use of a multiplication factor of ~3.45.

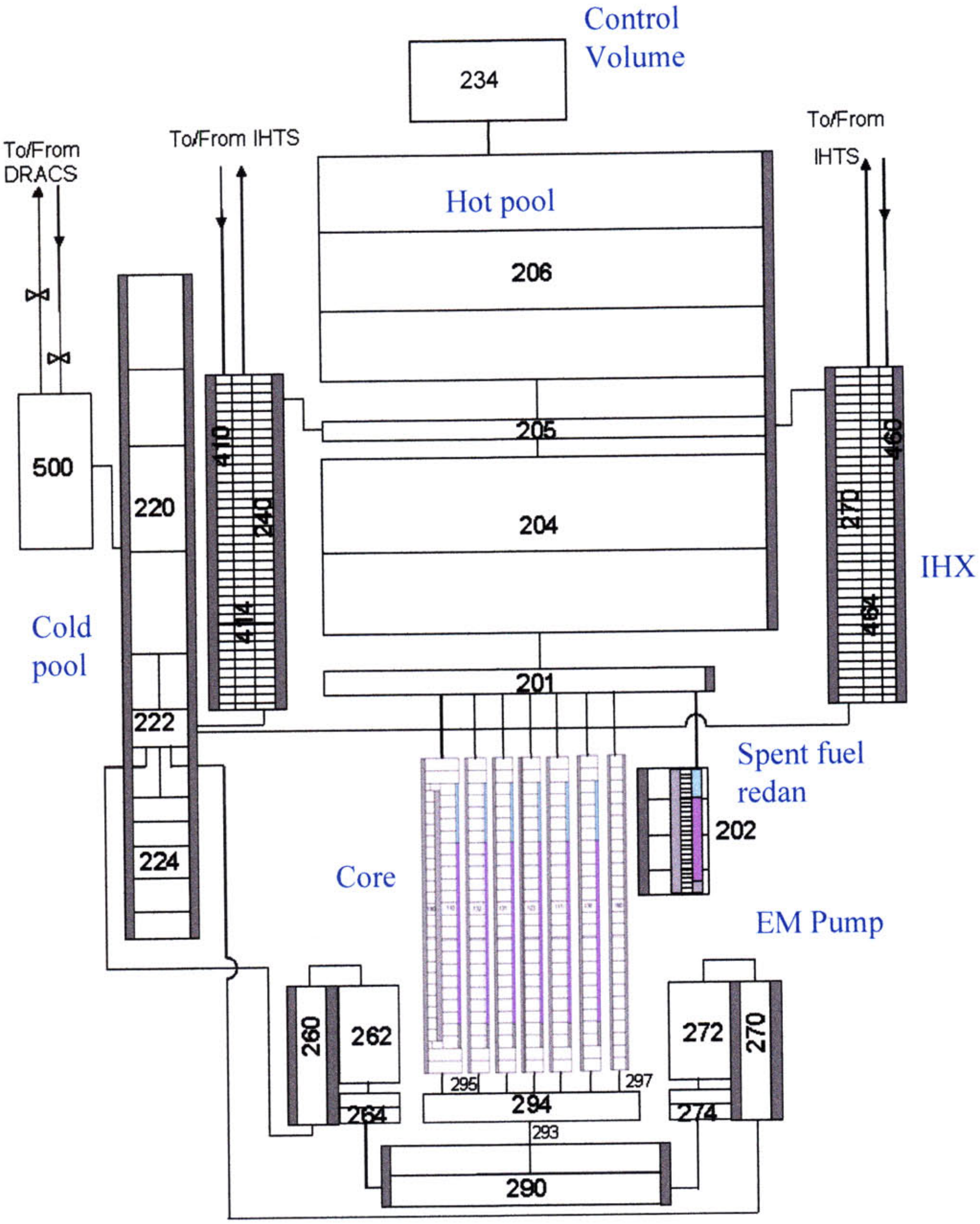

Figure 8.9: Nodalization diagram of primary system (cold and hot pools) RELAP5-3D model

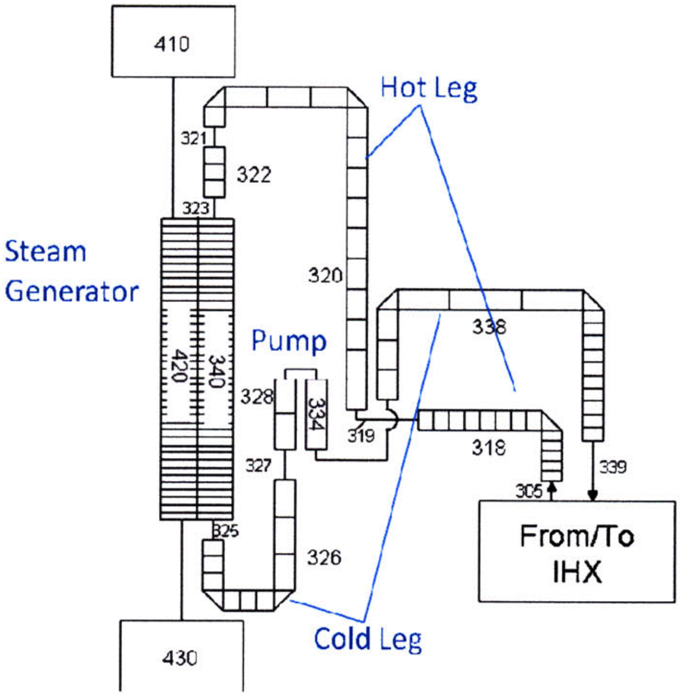

Figure 8.10: Nodalization diagram of secondary loop system

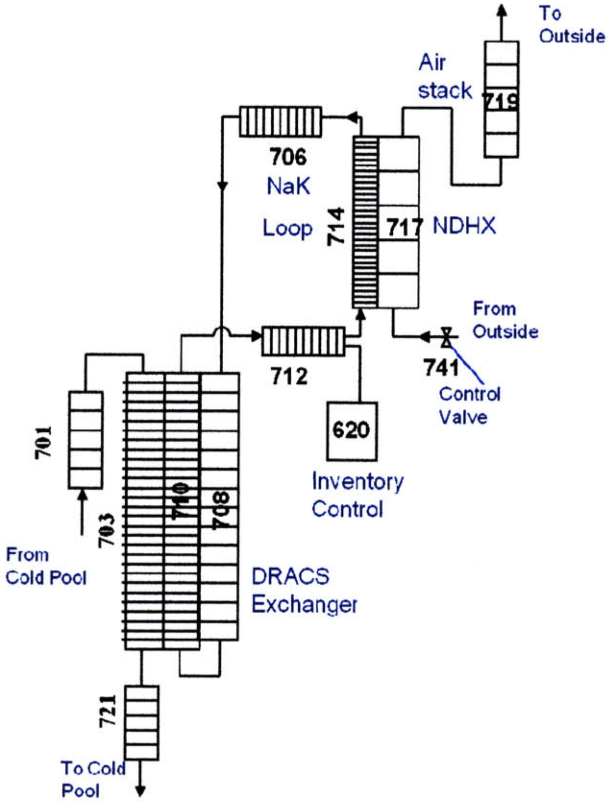

Figure 8.11: Nodalization diagram of the DRACS loop used in the SFR

The core model is created by modeling six flow pipes: the inner driver assemblies, the outer driver assemblies, the hottest assembly, the control assemblies, the shield assemblies, and the reflector assemblies. The flow areas and the heat structures for each of these flow paths were lumped to simplify the core model. The four secondary loops and PCSs were lumped to reduce model runtime so that none of the transients investigated in this thesis involved the secondary loops or PCS system.

In lieu of a full Rankine PCS system, a simple time dependent flow boundary was modeled in which the inlet flow and temperature could be adjusted as a function of time. This allowed for the approximation of accident conditions during either a ULOF or station blackout transient.

Six total core models were created in RELAP5-3D to represent the six fuel configurations to be investigated via transient analyses: the metal CR = 0.71 base fuel, the oxide CR = 0.71 base fuel, the metal CR = 0.71 bottle-shaped fuel, the oxide CR = 0.71 bottle-shaped fuel, the metal CR = 0.25 base fuel, and the metal CR = 0.25 annular fuel. These core models can each be incorporated into the full plant model. In the annular CR = 0.25 core, the assemblies are larger, and thus a new core layout was designed in which the power generation was only 950 MW. Thus a 20 % power uprate results in a power of 1140 MW, or 11.4% over the base core configuration. The reactivity feedbacks for each of the core models (except the bottle-shaped cores, which have the same reactivity feedbacks as the solid CR = 0.71 cores) are listed in Table 8.2. The steady-state performance of the full plant model with each core matches the performance of the reference plant with <1% error in the total mass flow rates and temperatures.

Table 8.2: BOEC core reactivity feedback coefficients for each core model

	Metal CR = 0.71 core	Oxide CR = 0.71 core	Metal CR = 0.25 base core	Metal CR = 0.25 annular core
Effective delayed neutron fraction	0.00335	0.00316	0.0027	0.0027
Prompt neutron lifetime (μs)	0.36	0.48	0.44	0.44
Radial expansion coefficient (¢/°C)	-0.39	-0.32	-0.48	-0.48
Axial expansion coefficient (¢/°C)	-0.05	-0.05	-0.63	-0.63
Fuel density coefficient (¢/°C)	-0.71	-0.46	-0.93	-0.93
Vessel expansion coefficient (¢/°C)	0.06	0.07	0.1	0.1
Sodium temperature coefficient (¢/°C)	0.11	0.1	0.18	0.18
Doppler coefficient (¢/°C)	-0.13	-0.16	-0.06	-0.12

8.1.5 Safety Analysis Results

Chapter 6 describes the results of the station blackout and UTOP transient analyses for both base and innovative fuel configurations. The following sections summarize the results of these analyses. The limiting parameter for each transient is the FCCI limit in metal fuel, and the sodium saturation temperature in the oxide fuel. The FCCI limit is 650°C if the time at the peak temperature is large (hours +), but 725 °C if the time at the peak temperature is small (minutes). The control rod drive line expansion (CRDLE) worth is 49¢/cm for the metal fuel and 35¢/cm for the oxide fuel, and the DRACS are sized to remove 0.25% of the rated core power per loop (two of three loops operating total). The decay power curve is assumed to be 100% Pu-239, similar to reference ABR1000 safety analyses [5.12].

In the station blackout accident, the pump coast-down curve was an exponential decay with a 5 second halving time for each case, while in the UTOP accident, the reactivity insertion simulated a rod ejection, and was 0.70$ in 0.5 seconds.

8.1.5.1 Station Blackout Transient Results

The station blackout long and short term max clad and max fuel temperatures for the metal CR = 0.71 fuel configurations are plotted in Fig. 8.12. Both fuel configurations have clad temperatures well below the FCCI limits, and the bottle-shaped fuel has a slightly lower temperature than the base fuel due to increased natural circulation flow rates.

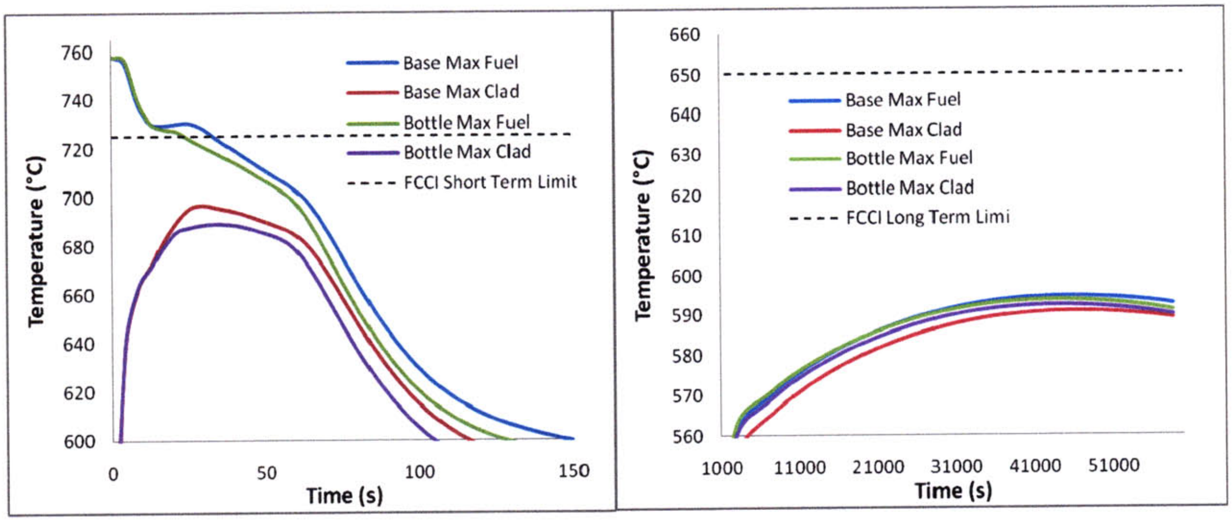

Figure 8.12: Short (left) and long (right) term maximum clad and fuel temperatures for the metal CR = 0.71 fuel configurations during a station blackout transient

The station blackout long and short term max clad and max fuel temperatures for the oxide CR = 0.71 fuel configurations are plotted in Fig. 8.13. Both configurations have coolant temperatures that exceed the sodium saturation temperature, and thus are unacceptable for use in a SFR. However, the bottle-shaped fuel has a significantly lower temperature than the base fuel due to increased natural circulation flow rates.

The station blackout long and short term max clad and max fuel temperatures for the metal CR = 0.25 fuel configurations are plotted in Fig. 8.14. The annular fuel configuration investigated in this analysis has an uprated power and flow rate (11.4%.) and thus the DRACS was uprated by 11.4% as well. Both configurations (base and annular) have max cladding temperatures that do not exceed the FCCI short term limit, but this required the use of a 20 second halving time exponential pump coast-down curve. The annular fuel has a slightly higher temperature than the base fuel (~4°C) due to decreased natural circulation flow rates, and has a higher second peak, though this peak is still well below the clad temperature limit

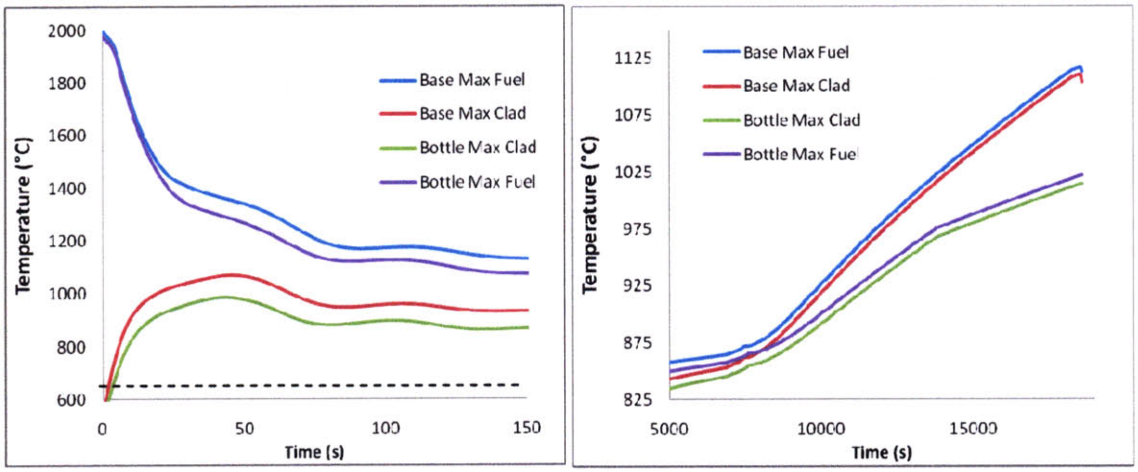

Figure 8.13: Short (left) and long (right) term maximum clad and fuel temperatures for the oxide CR = 0.71 fuel configurations along with the PCMI clad temperature limit (black dotted line) during a station blackout transient

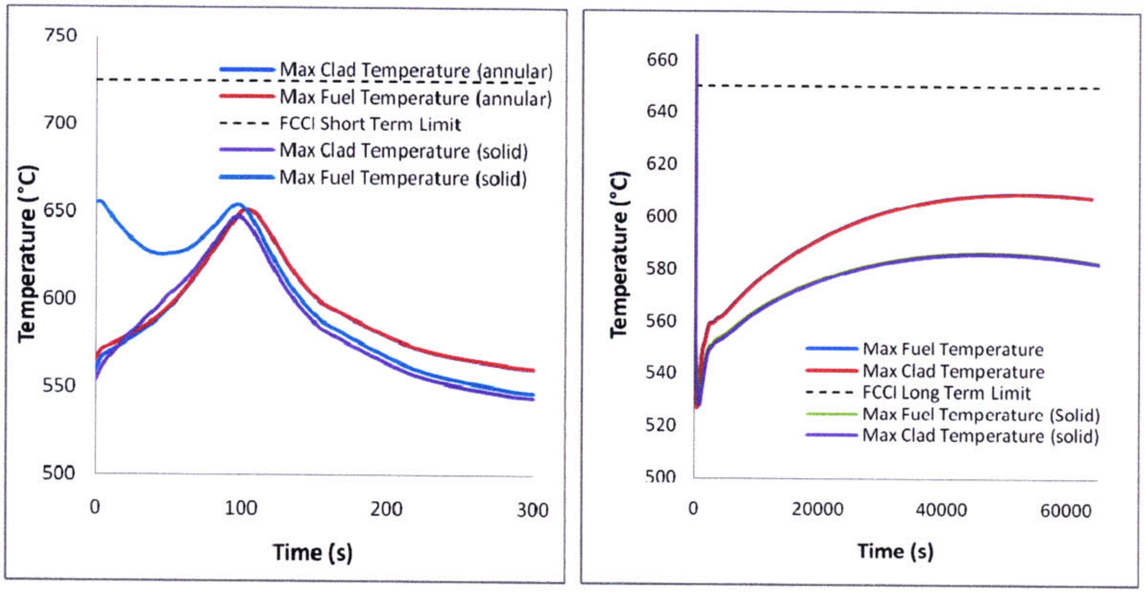

Figure 8.14: Short (left) and long (right) term maximum clad and fuel temperatures for the metal CR = 0.25 fuel configurations during a station blackout transient with a 20 second pump coast-down halving time

8.1.5.2 UTOP Results

The UTOP transients for all the fuel configurations are below the safety limits described above. The annular max clad and max fuel temperatures are plotted in Fig. 8.15. The fuel temperature is greatly reduced in the annular fuel, while the clad temperature is slightly higher, as with the station blackout transients; but this increase is small enough to fall within the acceptable uncertainty range of the transient modeling.

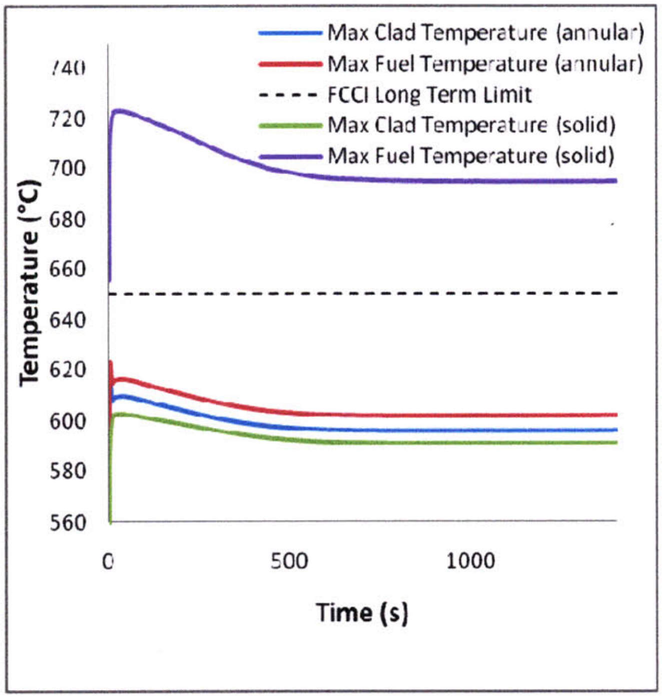

Figure 8.15: Maximum clad and fuel temperatures for the metal CR = 0.25 fuel configurations during a UTOP accident

8.1.5.3 Supercritical Carbon Dioxide Power Conversion System

Chapter 7 of this thesis focuses on the development of a S-CO_2 PCS RELAP5-3D model and of the ULOF results for plants coupled to either a Rankine PCS boundary (as in Chapter 6) or a full S-CO_2 PCS to the full plant model. A similar performance of the SFR using both boundary conditions would verify that an S-CO_2 PCS can be used to withdraw decay heat during a ULOF without resorting to "safety-grade" auxiliary cooling systems [6.6].

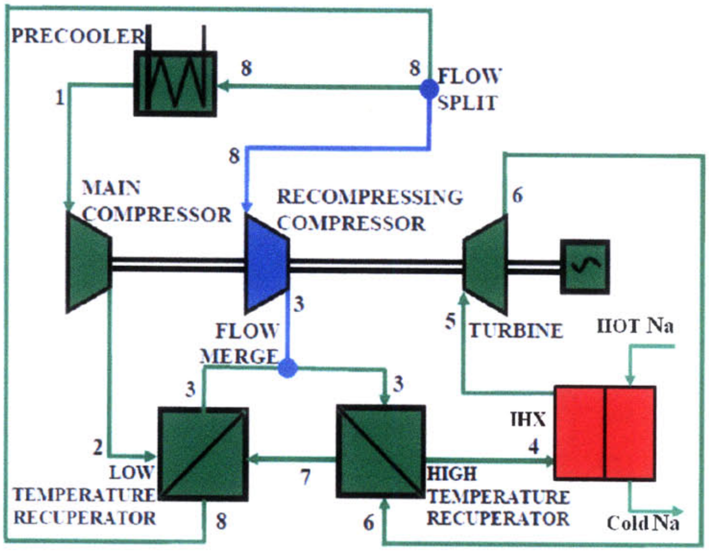

Figure 8.16: Schematic of the S-CO2 recompression cycle [7.1]

The S-CO2 system is nearly identical to the one created for the lead-bismuth flexible conversion reactor [7.2], except that it is sized for 500MW rather than 600 MW. Thus, two S-CO2 PCS are used for our 1000 MWth reactor. The compressors are all modeled as pumps, and the printed circuit heat exchangers (PCHE), turbines, and compressors were all sized using CYCLES III [7.5]. A schematic of the S-CO_2 PCS and the nodalization diagram of the RELAP5-3D model are found in Figs. 8.16 and 8.17, respectively.

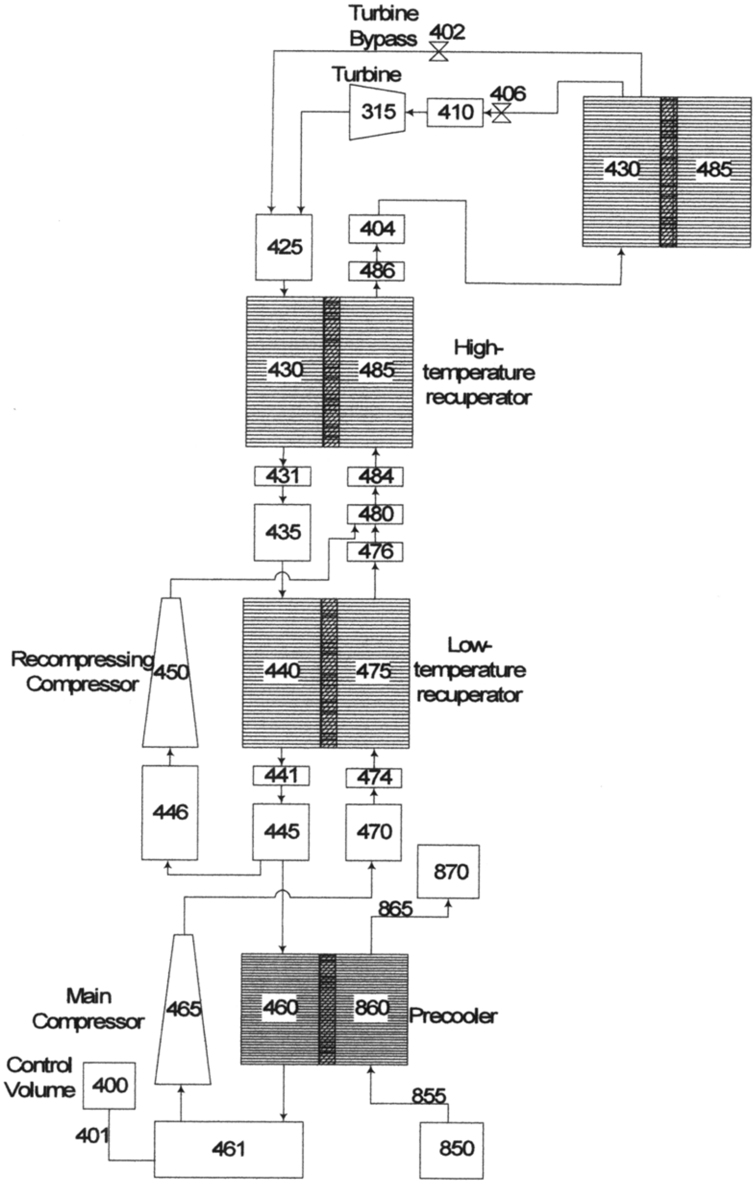

Figure 8.17: Nodalization diagram of RELAP5-3D S-CO_2 PCS loops model

A PI controller and turbine bypass valve were used to moderate the fluid flow through the turbine during the ULOF to prevent turbine overspeed. The setpoint for the PI controller was 36.7 rad/s, or 10% of the nominal speed. In the Rankine PCS boundary, the fluid flow was linearly decreased upon initiation of the ULOF transient to a value of 10% of the nominal flow at 150 seconds. The resulting maximum clad temperatures for both cycles during a ULOF are potted in Fig. 8.18. These runs demonstrate that the S-CO_2 PCS can safely remove the decay heat from the core of the SFR during a ULOF accident without the need for safety-grade auxiliary cooling components.

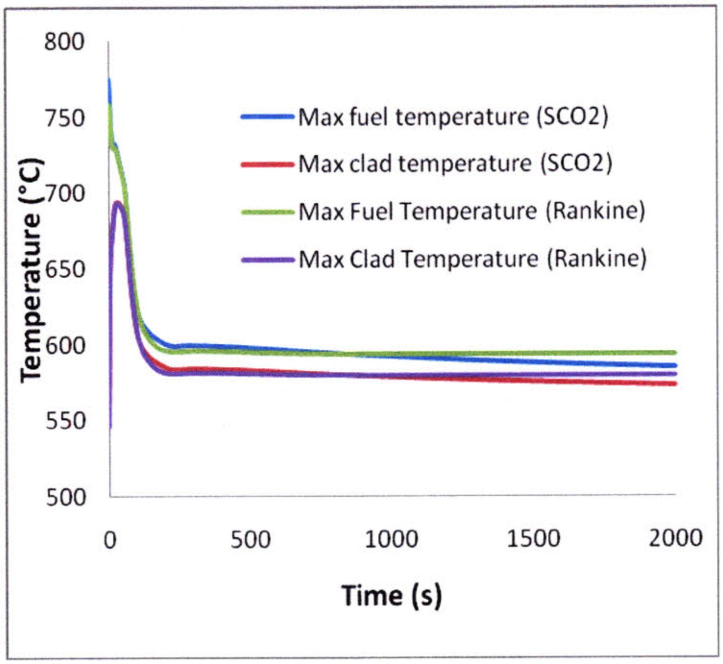

Figure 8.18: Comparison of the maximum clad temperature during a ULOF for a full plant model coupled with a PCS boundary and a full S-CO_2 PCS

8.2 Conclusions

The concepts of annular and bottle-shaped fuel were explored for the SFR fuel assemblies, and optimal parameters for these innovative fuel configurations were described in this thesis. In order to determine the thermal-hydraulic performance of these innovative fuel configurations, a RELAP5-3D subchannel model was created. This model shows great promise in being able to perform subchannel analyses on a wide variety of assembly configurations. The accuracy of the RELAP5-3D subchannel analysis model was verified against other codes and ORNL 19-pin test data.

The annular fuel configurations are best suited for low conversion ratio cores. The magnitude of the power uprate enabled by metal annular fuel in the CR = 0.25 cores is 20%, and is limited by the FCCI constraint during a hypothetical flow blockage of the inner-annular channel blockage due to the small diameters in of the inner-annular flow channel (3.6 mm). On the other hand, a complete blockage of the hottest inner-annular flow channel in the oxide fuel case results in sodium boiling, which renders the annular oxide fuel concept unacceptable for use in a SFR.

The bottle shaped fuel configurations are best suited for high conversion ratio cores. In the CR = 0.71 cores, the bottle-shaped fuel configuration reduced the overall core pressure drop in the fuel channels by ~36.3% in the metal fuel and by ~31.5% in the oxide fuel. The corresponding increase in core height with bottle-shaped fuel is ~15.6% for the metal fuel and ~18.3% for the oxide fuel.

A full plant RELAP5-3D model was created to evaluate the transient performance of the base and innovative fuel configurations during station blackout and UTOP transients. The transient analysis confirmed the good thermal-hydraulic performance of the annular and bottle-shaped fuel designs with respect to their respective solid fuel pin cases, but also revealed the unacceptably high clad temperatures reached during an unprotected station blackout for the oxide fuelled core, in both its solid-fuel-pin and annular-fuel-pin versions.

Finally, an S-CO_2 PCS RELAP5-3D model was created to verify if an S-CO_2 PCS could remove decay heat from a SFR without the use of safety-grade auxiliary cooling systems during a ULOF transient. The max clad temperatures of the SFR fuel when an $S\text{-}CO_2$ PCS is used are nearly the same as those in the SFR cooled by a Rankine PCS. This verifies that the $S\text{-}CO_2$ PCS can remove decay heat from the SFR core during a ULOF accident without the use of safety-grade systems.

8.3 Recommendations for Future Work

The application of internally and externally cooled annular fuel was introduced in this thesis. Some simplifying assumptions were made to allow the modeling of the full CR = 0.25 metal annular fuel core. In order to determine a more optimal configuration, however, a complete neutronic investigation should be undertaken. This should include a more detailed investigation of the ideal assembly layout, an investigation of the appropriate number of control assemblies, and an appropriate rod worth for these control assemblies.

The DRACS used in these analyses were based upon the DRACS designed for the ABR1000. This report assumed a decay heat curve based on 100% Pu-239 fuel, but in reality other TRU nuclides and their fission products contribute to the decay heat curve. The CR = 1.0 decay curve developed under another MIT project [6.6] should be used, which requires an increase in the DRACS heat withdrawal capacity. A more detailed investigation of the DRACS design would be important for this uprate. This investigation should focus particularly on design limits for the DRACS, such as parasitic losses in the steady-state primary pool and size limits of the NaK and air loops.

The structural integrity of the annular fuel configuration is acceptable during steady-state performance. However, should a complete blockage of the hottest subchannel occur, the differential thermal expansion between the inner and outer cladding will result in a compressive force on the inner cladding. This compressive force is larger than the buckling limit, thus indicating that buckling could pose a problem for annular fuel configurations in a SFR. Future work should focus on improving the design of the annular fuel inner cladding or end-cap to prevent buckling. This could include changes to the end-cap design or material or adding supports for the inner cladding or pre-pressurizing the pin to create tensile stresses that compensate for the compressive stresses.

A cover gas system should be incorporated into the system in which the sodium liquid levels of both the cold and hot pools in the primary system are modeled and tracked. The same volume should be used to represent the cover gas for both the hot and cold pools. This will allow for a more accurate modeling of natural circulation and potential spillover of the different pools.

A more accurate property table for CR = 0.25 metal fuel should be used to evaluate the blockage of the IA channel of the annular fuel configuration. This may potentially lead to an increased margin to the FCCI clad limit than the current properties do.

The bottle-shaped fuel configurations resulted in large pressure drop reductions across the core. However, when these fuel configurations were used in the full plant model, the reduction in pressure drop was countered by the increasing height of the control, shield, and reflector assemblies. A better core design should be established that would allow for the core outlet height to be uniform without decreasing the benefit of the bottle-shaped fuel through extension of the non-fuel assemblies. In addition, there are other considerations that were only qualitatively mention in this thesis that must be included to evaluate the feasibility of utilizing bottle-shaped fuel in a SFR. These include the evaluation of the impact of new design on core flowering, the alterations to the reference plant design required for installation, and the increased complexity of both the fuel pins and the assembly design. These considerations should be investigated in detail in order to provide a clear picture of the benefit afforded bottle-shaped fuel and the costs associated with its implementation.

References

[1.1] "The Future of Nuclear Power – An Interdisciplinary MIT Study" July 2003, http://web.mit.edu/nuclearpower/, retrieved May 11, 2009.

[1.2] U.S. DOE, "A Technology Roadmap for Generation IV Nuclear Energy Systems: Ten Nations Preparing Today for Tomorrow's Energy Needs," U.S. DOE Nuclear Research Advisory Committee (NERAC) and the Generation IV International Forum, GIF-002-00, December (2002).

[1.3] H. Zhao, H. Zhang, V. Mousseau, P. F. Peterson, "Improving SFR Economics through Innovations from Thermal Design and Analysis Aspects" Proceedings of the 2008 Internation Congress on Advances in Nuclear Power Plants (ICAPP '08), June, 2008.

[1.4] "Department of Energy Announces New Nuclear Initiative" US Department of Energy Website, http://www.energy.gov/news/3161.htm, Extracted May 11, 2009.

[1.5] E. P. Loewen, et al., "Commercialization of the Global Nuclear Energy Partnership (GNEP)" , Proceedings of the 15th International Conference on Nuclear Engineering (ICONE15), Nagoya, Japan, April, 2007.

[1.6] A. E. Dubberley, Y. Yoshida, C.E. Boardman, and T. Wu, "Superprism Oxide and Metal Fuel Core Designs", Proceedings of ICONE 8, 8th International Conference on Nuclear Engineering, Baltimore, MD, April 2000.

[1.7] J. A. Michelbacher et at., "Experimental Breeder Reactor-II Complex, Post Sodium Draining", INL/CON-05-00647, September, 2005.

[1.8] Y.I. Chang, P.J. Finck, C. Grandy, et al., "Advanced Burner Test Reactor Preconceptual Design Report", ANL-ABR-1 (ANL-AFCI-173), September, 2006.

[1.9] A. E. Dubberley et al., "S-PRISM Fuel Cycle Study For Session 3: Future Deployment Programs and Issues", Proceedings of ICAPP '03, Cordoba Spain, May 2003.

[1.10] A.E. Dubberley et al., "Superprism Oxide and Metal Fuel Core Designs", Proceedings of ICONE 8, Baltimore MD, April, 2000.

[1.11] Pope, M.A., "Thermal-hydraulic Design of a 2400 MWth Direct Supercritical CO2-Cooled Fast Reactor" Report MIT-ANP-TR-104, September, 2006

[1.12] V. Dostal, "Cycles New: FORTRAN 90 CODE description", 2005.

[1.13] D. M. Legault, "Development and Application of a Steady State Code for Supercritical Carbon Dioxide Cycles", Thesis submitted for B.S. Degre, MIT, June 2006.

[1.14] Personal Communication: Matthew Denman (MIT) via email to Matthew Memmott (MIT) May 5, 2009.

[1.15] Personal Communication: Matthew Denman (MIT) via email to Matthew Memmott (MIT) April 27, 2009.

[1.16] K. L. Basehore, N.E. Todreas, "SUPERENERGY-2: A Multiassembly, steady-state computer code for LMFBR core thermal-hydraulic analysis", Pacific Northwest Laboratory, Richland, WA, August 1980.

[2.1] MathCAD® 2001i Professional, Mathsoft Engineering and Education, Inc., Cambridge, MA, USA.

[2.2] E. Hoffman et al., "Preliminary Core Design Studies for the Advanced Burner Reactor over a Wide Range of Conversion Ratios", ANL Report ANL-AFCI-177, September, 2006

[2.3] A.E. Dubberley, Y. Yoshida, C.E. Boardman, and T. Wu, "Superprism Oxide and Metal Fuel Core Designs", Proceedings of ICONE 8, 8th International Conference on Nuclear Engineering, Baltimore, MD, April 2000

[2.4] R. G. Pahl, D. L. Porter, D. C. Crawford, and L. C. Walters, "Irradiation behavior of metallic fast reactor fuels", Fuels and Engineering Division Report ANL/CP—73323, Argonne National Laboratory, November, 1991.

[2.5] N. E. Todreas, M. S. Kazimi, *Nuclear Systems I. Thermal Hydraulic Fundamentals*, pg. 15 – 17, 386 - 391, 684, Taylor and Francis, 1993

[2.6] S. K. Cheng and N. E. Todreas, "Hydrodynamic Models and Correlations for Bare and Wire-Wrapped Hexagonal Rod Bundles – Bundle Friction Factors, Subchannel Friction factors and Mixing Parameters" Nuclear Engineering and Design, 92, 227-251, (1986).

[2.7] J. K. Fink and L. Leibowitz, "Thermodynamic and Transport Properties of Sodium Liquid and Vapor", ANL/RE-95/2, January 1995

[2.8] M. S. Kazimi, J. Buongiorno, T. Conboy, T. Ellis, P. Ferroni, P. Hejzlar, S-P. Kao, A. Karahan, K. Kobayashi, E. Pilat, N.E. Todreas, "Core Design Options for High Power Density BWRs",), MIT Report NFC-PR-089, December 2006.

[2.9] P. Hejzlar P. and M.S. Kazimi, “Annular Fuel for High Power Density PWRs: Motivation and Overview“, Nuclear Technology, 160, 2-15, (2007).

[2.10] I. E. Idelchik, “Handbook of Hydraulic Resistance Second Edition”, pg. 233-235, Hemisphere Publishing Corporation, New York, USA, 1986.

[3.1] “LMFR core thermohydraulics: Status and prospects”, IAEA TecDoc-1157, IAEA, June, 2000, Vienna, Austria.

[3.2] W. Kim et al. “A Subchannel Analysis Code MATRA-LMR for wire-wrapped LMR subassembly”, Annals of Nuclear Energy 29, pg 303-321, April, 2002.

[3.3] F. Dunn, “Integrated Intra-Subassembly”, ANL/CP-74685, presented at 5th Nuclear Reactor Thermal Hydraulics (NUREH-5), Salt Lake City, UT, 1992.

[3.4] T. Takata et. al. “Development of the Cooling Technology on TRU Fuel Pin Bundle During Fuel Fabrication Process (3) Development of Analytical Tool”, Proceedings of the International Congress on Advances in Nuclear Power Plants (ICAPP), 2008, Anaheim, CA, USA, June 2008

[3.5] N. Takemitsue et al., “Thermal-Hydraulic of Partially Blocked Fuel Subassembly with Porous Media” Nenryo Shugotai Porasugu Shuhen Ryuro Heisoku Shiekn Kaiseki. Kenkyu Hokokusho. Heisei 12nen(2000), N20011545, pg. 97, 2000.

[3.6] J. M., Cuta et al. "VIPRE-01 A Thermal-Hydraulic Code for Reactor Cores." *EPRI* 1-3 (1985): NP-2511-CCM.

[3.7] H. Kamide et al., “Study on Mixing due to Transversal Flow in a Subassembly of Fast Reactor (Sodium Experiment using a 37-Pin Subassembly Model”, Proceedings of the 12th International Conference on Nuclear Engineering (ICONE12), Arlington, VA, USA, April 2004.

[3.8] H. Ohshima et al., “Thermal-Hydraulic Analysis of Fast Reactor Fuel Subassembly with Porous Blockages”, Fourth International Seminar on Subchannel Analysis (ISSCA-4), Tokyo, 1997.

[3.9] H. Ohshima, Y. Imai, “Validation Study of Thermal-Hydraulic Program “SPIRAL” for Fuel Pin Bundle of Sodium Cooled Fast Reactor”, 11th International Topical Meeting on Nuclear Reactor Thermal-Hydraulics (NURETH-11), Avignon, France, October, 2005.

[3.10] C. W. Stewart, C. L. Wheeler, R. J. Cena, C. A. McMonagle, J. M. Cuta, D. S. Trent, “COBRA-IV: the Model and the Method,” BNWL- 2214, Batelle Pacific Northwest Laboratories (1979).

[3.11] W.S. Yang, “A LMR Core Thermal-Hydraulics code Based on the ENERGY Model” Journal of the Korean Nuclear Society, Vol. 29, Number 5, pgs 406-416, October 1997.

[3.12] J.D. Macdougall, J.N. Lillington, “The SABRE code for fuel rod cluster thermalhydraulics, Nuclear Engineering and Design, 82, 171-190 1984.

[3.13] U. Bieder, “Qualification of the CFD Code Trio_U for Full Scale Reactor Applications”, Estelle Graffard Nuclear Engineering and Design, Volume 238, Issue 3, March 2008, Pages 671-679.

[3.14] W. Yang, “Analysis of EBR-II Subassembly Outlet Temperature using SE2-ANL” Intra-Laboratory Memo, Argonne National Laboratory, March, 1994.

[3.15] N. E. Todreas, M. S. Kazimi, *Nuclear Systems II. Elements of Thermal Hydraulic Design*, pg.209-212, Taylor and Francis, 2001.

[3.16] N. E. Todreas, M. S. Kazimi, *Nuclear Systems I. Thermal Hydraulic Fundamentals*, pg.684, Taylor and Francis, 1993

[3.17] S. K. Cheng and N. E. Todreas, "Hydrodynamic Models and Correlations for Bare and Wire-Wrapped Hexagonal Rod Bundles – Bundle Friction Factors, Subchannel Friction factors and Mixing Parameters" Nuclear Engineering and Design, 92, 227-251, (1986).

[3.18] I. E. Idelchik, "Handbook of Hydraulic Resistance Second Edition", pg. 608, Hemisphere Publishing Corporation, New York, USA, 1986.

[3.19] C. B. Davis, Evaluation of the Use of Existing RELAP5-3D Models to Represent the Actinide Burner Test Reactor", INL/EXT-07-12228, Idaho National Laboratory, February 2007

[3.20] Y. J. Yoo et al., "Effects of Fluid Axial Conduction on Liquid Metal Natural Circulation and Linear Stability," 2003 ANS/ENS International Winter Meeting, pp.1523-1530, (Global 2003), New Orleans, LA, November, 2003.

[3.21] Personal Communication: Cliff B. Davis (Idaho National Laboratory) by email to Matthew J Memmott (MIT), March 17, 2008.

[3.22] Personal Communication: Jim Cahalan (Argonne National Laboratory) by email to Matthew J Memmott (MIT) March 3, 2008.

[3.23] M. Fontana et al., "Temperature Distribution in the duct wall and at the exit of a 19-Rod Simulated LMFBR Fuel Assembly (FFM Bundle 2A)", Nuclear Technology, Vol. 24, 176-200, November, 1974.

[3.24] A. V. Zhukov, A. P. Sorokin, and N. M. Matjukhin, "Inter-channel exchange in fast reactor subassembly", M., Energoatomizdat, 1991.

[3.25] A. V. Zhukov, A. P. Sorokin, and P. L. Kirillov et al., "The methodical instructions and guidelines on thermohydraulic calculations of fast reactors core", RTM 1604.008-88 GKIAE-IPPE ONTI IPPE, 1989.

[3.26] A. P. Sorokin, A. V. Zhukov, G. P. Bogoslovskaia, G. A. Sorokin, "Thermal Hydraulic Aspects of the Problem of High Burn-out in Fast Reactors", 10th international Meeting of the IAHR working Group on Advanced Nuclear Reactors Thermal Hydraulics, Obninsk, Russia, July 2001.

[4.1] M. J Memmott, J. Buongiorno, P. Hejzlar, "An assessment of Annular Fuel for Sodium-Cooled Fast Reactors" Proceedings of the International Congress on Advances in Nuclear Power Plants (ICAPP), 2008, Anaheim, CA, USA, June 2008.

[4.2] M. J Memmott, J. Buongiorno, P. Hejzlar, "Innovative Fuel Configurations to Improve the Economics of the GNEP Sodium-Cooled Fast Reactor" Progress Report to Idaho National Lab, Battelle Energy Alliance, LLC (BEA), Release No. 00024 under Blanket Master Contract No. 00000063, August, 2008.

[4.3] M. C. Billone et al., "Status of Fuel Element Modeling Codes for Metallic Fuels", Proceedings American Nuclear Society International Conference on Relaible Fuels for Liquid Metal Rectors, Tuscon Arizona, September 7-11, 1986.

[4.4] L.-W. Hu, K. Nagasawa, P. Hejzlar, and M.S. Kazimi, "Thermal Striping in LWR Piping Systems" MIT Report MIT-NSP-TR-007, Cambridge, MA, USA (2003).

[4.5] Personal communication from Matt Denman (MIT) to Matthew Memmott (MIT) via email on August 1, 2008.

[4.6] A. B. Cohen, H. Tsai, and L. A. Neimark, "Fuel/cladding compatibility in U-19Pu-10Zr/HT9-clad fuel at elevated temperatures", Journal of Nuclear Materials, Vol. 204, pg 244-251, 1993.

[4.7] R. J. Roark, "Formulas for stress and strain (fourth edition)", McGraw-Hill, pg 75, 340, 1965.

[4.8] Young, W.C.; Budynas, R.G. (2002). Roark's Formulas for Stress and Strain (7th Edition). McGraw-Hill, pg 427-524.

[4.9] J. Zhao, H. C. No, M. S. Kazimi, "Mechanical Analysis of High Power Internally Cooled Annular Fuel", Nuclear Technology, Vol. 146, Pgs. 164-180, May, 2004.

[4.10] R. J. Amodeo, N. M. Ghoniem, "Development of Design Equations for Ferritic Alloys in Fusion Reactors", Nuclear Engineering and Design/Fusion 2 (1985) Pg. 97-110, North-Holland, Amsterdam.

[5.1] Y. Chikazawa, C. Grandy, "Thermal Analysis of a Fuel-Handling System for Sodium-Cooled Reactor with Minor Actinide-Bearing Metal Fuel" Nuclear Technology, Vol. 165, No. 3, pg 321-332, March, 2009.

[5.2] Personal Communication: Dustin Langewisch (MIT) via email to Matthew Memmott (MIT) June 5, 2008.

[5.3] Y.I. Chang, P.J.Finck, C. Grandy, et al., "Advanced Burner Test Reactor Preconceptual Design Report", ANL-ABR-1 (ANL-AFCI-173), September, 2006.

[5.4] E. E. Feldman, "The Influence of Cyclic Fluid Temperatures on Thermal Stresses Induced in Adjacent Structures," Intra-laboratory Memo, Argonne National Laboratory, March 10, 1975.

[5.5] RELAP5-3D© Code Manual Appendix A: RELAP%-3D© Input Data Requirements, INEEL-EXT-98-00834, Revision 2.3, pgs. A10-1, April 2005.

[5.6] M. C. Billone et al.,"Status of Fuel Element Modeling Codes for Metallic Fuels", Proceedings American Nuclear Society Internation Conference on Relaible Fuels for Liquid Metal Rectors, September 7-11, 1986, Tuscon Arizona; unirradiated values multiplied by 0.7 to account for long-term effects of irradiation

[5.7] "*American National Standard Decay Heat Power in Light Water Reactors*", ANSI/ANS-5.1-2005, American Nuclear Society, 2005.

[5.8] C. B. Davis, "Applicability of RELAP5-3D for Thermal-Hydraulic Analyses of a Sodium-Cooled Actinide Burner Test Reactor", INL/EXT-06-11518, Idaho National Laboratory, July 2006

[5.9] C. B. Davis, "Evaluating the Use of Existing RELAP5-3D Models to Represent the Actinide Burner Test Reactor", INL/EXT-07-12228, Idaho National Laboratory, February, 2007.

[5.10] RELAP5-3D© Code Manual Volume II: User's Guide and Input Requirements, INEEL-EXT-98-00834, Revision 2.3, pgs. 43-53, April 2005.

[5.11] Personal Communication: Rich Denning (ANL) to Matthew Memmott (MIT) August, 2008.

[5.12] C. Grandy, T.K. Kim, T. Fanning and J. Cahalan, "ABR-1000 Design Description and Safety Analysis" Presentation at MIT by Y. Chang, February 15, 2008.

[5.13] W. L. Weaver, E. T. Tomlinson, D. L. Aumiller, "A Generic Semi-Implicity Coupling Methodology for Use in RELAP5-3D", INEEL/JOU-00-01356, Idaho National Lab, 2002.

[5.14] D. L. Aumiller, E. T. Tomlinson, R. C. Bauer, "A coupled RELAP5-3D/CFD methodology with a proof-of-principle calculation" Nuclear Engineering and Design, vol. 205, pg 83-90, 2001.

[6.1] R. B. Baker et al., "Performance of Fast Flux Test Facility Driver and Prototype Driver Fuels", WHC-SA-0974, (1990).

[6.2] Personal Communication: Aydin Karahan (MIT) to Matthew Memmott (MIT) via email, May 15th, 2009.

[6.3] RELAP5-3D© Code Manual Appendix A: RELAP%-3D© Input Data Requirements, INEEL-EXT-98-00834, Revision 2.3, pgs. 83-96, April 2005.

[6.4] Inagaki, et. al "Improving the Safety of Cores for Commercial FBRs," International Conference on Advanced Reactor Safety 1994.

[6.5] American National Standard Decay Heat Power in Light Water Reactors, ANSI/ANS-5.1-2005, American Nuclear Society, 2005.

[6.6] N. E. Todreas, P. Hejzlar, et al., "Flexible Conversion Ratio Fast Reactor Systems Evaluation Final Report", MIT-NFC-PR-101, June, 2008.

[7.1] V. Dostal, M. J. Driscoll, P. Hejzlar, and N. E. Todreas, "CO2 Brayton Cycle Design and Optimization," MIT-ANP-TR-090, November, 2002.

Supercritical CO2-Cooled Fast Reactor" Report MIT-ANP-TR-104, September, 2006

[7.2] A. Nikiforova, P. Hejzlar, N. Todreas, C.J. Fong, "A 2400 MWth Liquid Lead-Cooled Flexible Conversion Ratio (FCR) Reactor" Proceedings of ICAPP '08, Anaheim, CA USA, June 8-12, 2008.

[7.3] http://www.heatric.com, Retrieved May 11th, 2009.

[7.4] F. Pra et al., "Promising Designs of Compact Heat Exchangers for Modular HTRs using the Brayton Cycle", Nuclear Engineering and Design, 238, pg 3160 – 3173, 2008.

[7.5] A.R. Ludington, "Tools for Supercritical Carbon Dioxide Cycle Analysis and the Cycle's Applicability to Sodium Fast Reactors", Thesis for M.S. Degree, MIT, June, 2009.

[7.6] Aungier, R.H., *Centrifugal Compressors*, ASME Press, New York, 2000.

[7.7] Personal Communication: Alexander Rockwell Ludington (MIT) via email to Matthew Memmott (MIT) May 3, 2008.

[7.8] Personal Communication: Alexander Rockwell Ludington (MIT) via email to Matthew Memmott (MIT) March 3, 2008.

[7.9] Y. Wang, G.R. Guenette, P. Hejzlar, M.J. Driscoll, "Aerodynamic Design of Turbomachinery for 300 MWe Supercritical Carbon Dioxide Brayton Power Conversion System", CANES report MIT-GFR-022, March 2005.

[7.10] V. Dostal, , M. J. Driscoll, and P. Hejzlar, "A Supercritical Carbon Dioxide Cycle for Next Generation Nuclear Reactors," MIT-ANP-TR-100, March 10, 2004.

[B.1] Personal Communications: Aydin Karahan (MIT) to Matthew Memmott (MIT), May, 2009

[B.2] Y. S. Touloukian, "Thermal Conductivity: Nonmetalic Solids", IFI/Plenum, New York City, 1970.

[B.3] MATPRO NUREG/CR-6150, Vol. 4, Rev. 1, p. 13-3

Appendix A

The results of annular fuel scoping analysis were benchmarked against two other sources. The basic thermal-hydraulic properties of the most promising cores were compared generally to the properties of the SUPERPRISM core [2.3]. The basic geometric parameters of the most promising annular fuel designs were also input into an annular fuel code developed by Pavel Hejzlar, and similar properties were calculated. This code, designated TAFIX, was originally developed for PWR annular fuel and was modified for sodium coolant by Pavel Hejzlar. It will be hereafter referred to as TAFIX-NA, and is a single fuel pin cell analysis for annular fuel. This code includes gap and clad, however, the thermal analyses described in 2.3.3 do not. This contributes to the differences between the two analyses. Key parameters for both of these benchmarks can be found in Table A.1.

It can readily be seen that the pressure drop in the SUPERPRISM core is substantially larger than in the annular designs. This could be due to the inclusion of form losses (primarily orifices), which were not included in this scoping analysis for simplicity. Additionally, support grids and entrance/exit nozzles could account for some of the increased pressure drop, since none of these were accommodated in the current study. The pressure drop according to TAFIX-NA, which also does not include pressure drops outside the active core, is on the same order of magnitude as this preliminary MathCAD analysis.

Table A.1: Comparison of key parameters from SUPERPRISM design and the same parameters calculated using MathCAD and TAFIX-NA

	MathCAD	TAFIX-NA	Superprism

	Metal	**Oxide**	**Metal**	**Oxide**	**Metal**
D_{o} (mm)	9.29	9.23	9.29	9.23	7.44
Average Linear Heat Rate (kW/m)	28.76	22.37	28.76	22.37	18.90
Assembly Length (cm)	407.14	422.28	407.14	422.28	477.52
Core Power (MW)	1752	1256	1752	1256	1000
Pressure Drop (kPa)	184.60	178.60	172.79	184.76	410.00
Flow Split (%)	51.58	47.43	55.40	55.55	-

Appendix B

This appendix lists the material properties used in the RELAP5-3D subchannel models. Each different material is found in a separate table, and is recorded exactly as input into RELAP5-3D. The oxide fuel and helium gap properties are not included in this appendix, as they are computed within the code. The tables for the metal fuel properties are for irradiated fuel values; the thermal conductivity in these metal fuels is multiplied by 70% in order to account for the loss in thermal conductivity due to porosity. This 30% reduction is commonly accepted, and was used in previous metal fuel models [5.3, B.1]

It should be noted that the thermal conductivity for the CR = 0.25 fuel was taken from [2.2], and is a function of zirconium enrichment, as seen in Fig. B.1. Rather than utilizing the porosity multiplication of 0.5 that is listed in this report, a porosity factor of 0.7 was deemed to be more appropriate [B.1]. In addition, the volumetric heat capacity was not supplied in this reference, and thus the volumetric heat capacity of the 10% Zr fuel was used. In future work, a more accurate correlation for the CR = 0.25 fuel should be used to determine blockage temperatures.

Table B.1: Material properties table for U-16.5Pu-10Zr (inner zone) fuel of the metal CR = 0.71 core [4.3]

Temperature (K)	Thermal Conductivity (W/m·K)	Temperature (K)	Volumetric Heat Capacity (J/m^3·K)
293.15	6.42	300	2.23E+06
373.15	7.49	500	2.49E+06
473.15	8.9	800	3.03E+06
573.15	10.37	1000	3.09E+06
673.15	11.92	1300	3.14E+06
773.15	13.54	1600	3.19E+06
873.15	15.23	1873.15	3.23E+06
973.15	17		

1073.15	18.84
1173.15	20.75
1273.15	22.74
1873.15	36.17

Table B.2: Material properties table for U-20.7Pu-10Zr (outer zone) fuel of the metal CR = 0.71 core [4.3]

Temperature (K)	Thermal Conductivity (W/m·K)	Temperature (K)	Volumetric Heat Capacity (J/m^3·K)
293.15	5.13	300	2.25E+06
373.15	6.19	500	2.50E+06
473.15	7.57	800	3.02E+06
573.15	9.01	1000	3.08E+06
673.15	10.51	1300	3.12E+06
773.15	12.06	1600	3.17E+06
873.15	13.67	1873.15	3.21E+06
973.15	15.34		
1073.15	17.07		
1173.15	18.86		
1273.15	20.7		
1873.15	32.98		

Table B.3: Material properties table for liquid sodium (bond) [2.7]

Temperature (K)	Thermal Conductivity (W/m·K)	Temperature (K)	Volumetric Heat Capacity (J/m^3·K)
371	89.44	371	1.28E+06
400	87.22	400	1.26E+06
500	80.09	500	1.20E+06
600	73.7	600	1.14E+06
700	68	700	1.09E+06
800	62.9	800	1.04E+06
900	58.34	900	1.01E+06
1000	54.24	1000	9.78E+05
1100	50.24	1100	9.54E+05
1200	47.16	1200	9.36E+05
1300	44.03	1300	9.22E+05
1400	41.08	1400	9.11E+05
1500	38.25	1500	9.04E+05
1600	35.45	1600	8.99E+05
1800	29.68	1800	8.93E+05
2000	23.22	2000	8.89E+05

Table B.4: Material properties table for SS-316 (surrogate for HT9)

Temperature (K)	Thermal Conductivity	Volumetric Heat

	(W/m·K)	Capacity Conductivity (J/m^3·K)
310.93	14.143	3.69E+06
533.15	17.632	4.26E+06
699.82	20.249	4.41E+06
810.93	21.994	4.51E+06
1088.71	26.355	4.91E+06

Table B.5: Material properties table for B4C [B.2]

Temperature (K)	Thermal Conductivity (W/m·K)	Temperature (K)	Volumetric Heat Capacity Conductivity (J/m^3·K)
300	30.45	294.3	2.34E+06
400	26.44	481.48	2.95E+06
500	23.36	624.82	3.43E+06
600	20.93	800.37	3.97E+06
700	18.95	915.93	4.30E+06
800	17.32	1049.26	4.66E+06
900	15.94	1092.04	4.76E+06
1000	14.77	4092.04	4.76E+06
1100	13.76		
1200	12.88		
1300	12.1		
1400	11.41		
1500	10.8		
1600	10.25		
1700	9.75		
4000	9.75		

Table B.6: Material properties table for helium gas in reflector [B.3]

Temperature (K)	Thermal Conductivity (W/m·K)	Volumetric Heat Capacity Conductivity (J/m^3·K)
300	0.15	0.1787
400	0.184	0.2198
500	0.216	0.2709
600	0.245	0.3326
700	0.274	0.4128
800	0.301	0.5144
900	0.327	0.6431
1000	0.352	0.8039
1100	0.377	1.0025
1200	0.401	1.2428
1300	0.424	1.5296
1400	0.447	1.8687

1500	0.47	2.265
1600	0.492	2.7222
1700	0.513	3.2453
1800	0.534	3.8401
1900	0.555	4.5114
2000	0.576	5.2639

Table B.7: Material properties table for SS-304 [1.11]

Temperature (K)	Thermal Conductivity (W/m·K)	Volumetric Heat Capacity Conductivity ($J/m^3 \cdot K$)
283.15	13.7	3.12E+06
310.93	14.14	3.24E+06
533.15	17.63	3.73E+06
699.82	20.24	3.87E+06
810.93	21.99	3.96E+06
1088.71	26.35	4.31E+06

Table B.8: Material properties table for Titanium [1.11]

Temperature (K)	Thermal Conductivity (W/m·K)	Volumetric Heat Capacity Conductivity ($J/m^3 \cdot K$)
200	1.64E+06	20
295	1.64E+06	20
300	1.67E+06	20
400	2.26E+06	20
500	2.53E+06	20
600	2.68E+06	20
800	2.84E+06	20
1100	2.92E+06	20

Table B.8: Material properties table for CR = 0.25 metal fuel [2.2, B.1, 4.3]

Temperature (K)	Thermal Conductivity (W/m·K)	Volumetric Heat Capacity Conductivity ($J/m^3 \cdot K$)
300	2.23E+06	9.1
500	2.49E+06	9.1
800	3.03E+06	9.1
1000	3.09E+06	9.1
1300	3.14E+06	9.1
1600	3.19E+06	9.1
1873.15	3.23E+06	9.1

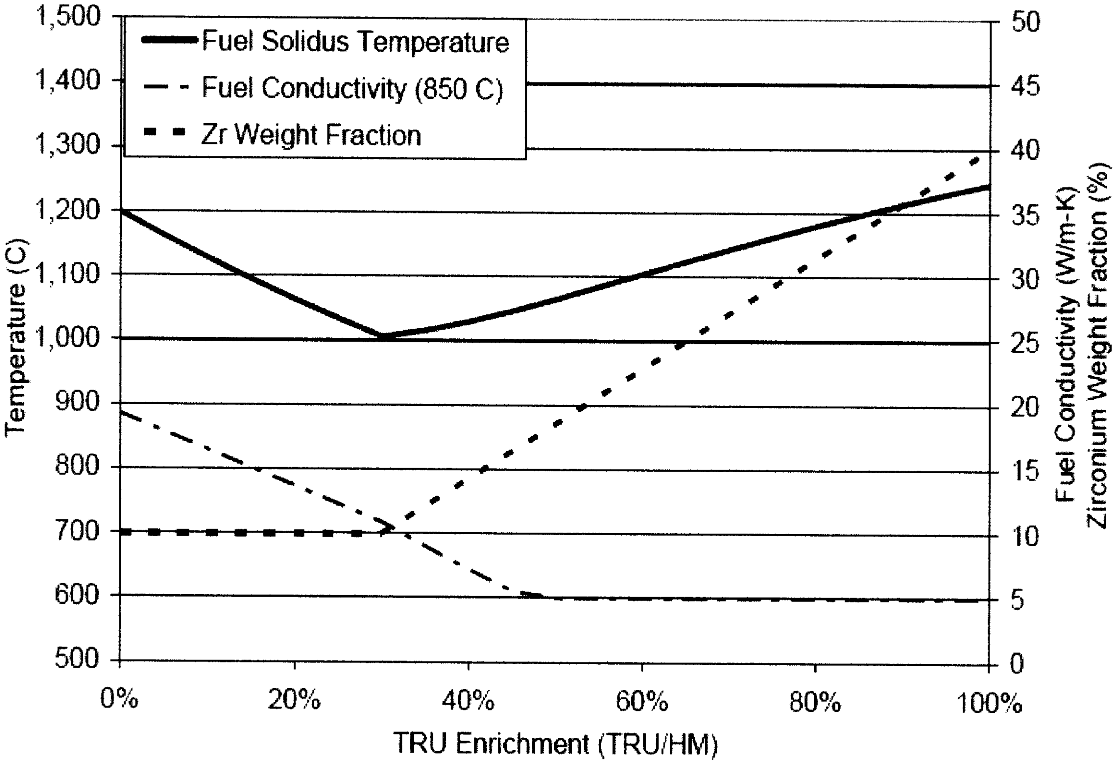

Figure B.1: Material Thermal Conductivity of CR = 0.25 metal fuel as a function of zirconium fraction [2.2]

APPENDIX C

This appendix includes a small sample of the RELAP5-3D code, intended to assist in creating the turbulent mixing heat transfer control variables. In this sample, three internal (triangular) subchannels are modeled (volumes 204, 220, and 222.). Figure A1 indicates the placement of these volumes. The appropriate heat structures are also included, as are the junctions between these volumes. Finally, the control variables which instigate mixing and the "pseudo" heat structures which incorporate this heat exchange are also included. Note that these control variables utilize the junction properties between the two subchannels, and a separate variable is needed to add up the junction effects. For more details concerning the input of pipes, junctions, heat structures, and control variables, see the RELAP5-3D User's manual, Appendix A.

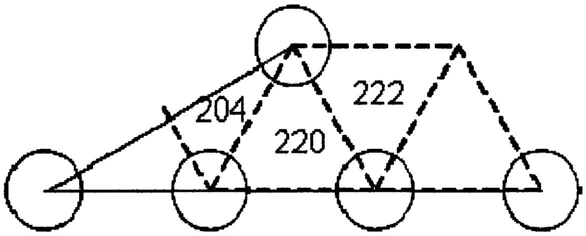

Figure C.1: Top-down view of volumes and heat structures included in Appendix A

Interior or Triangular Subchannels

```
2040000 scedge   pipe
2040001 22
2040102 4.1455e-6  22  * shield, core, gas plenum
2040202 0.0       21
2040301 0.286      1  * shield
2040302 0.06773   16  * core
2040303 0.38223   21  * gas plenum
2040304 0.286     22  * shield
2040601 90. 22
2040802 0.0   0.00261   22  * shield, core, gas plenum
2040902 0.0   0.0      21
2041001 0000000 22
```

```
2041103 00000000 21
2041201 003 5.e5 628.150 0.0 0.0 0.0 22
2041300 1
2041301 0.0 0.0 0.0 21
2042501 0.8571  0.0   1.0  0.0   1.0  0.0  22       * laminar shape factor
2042601 0.0 0.15233   0.18  0.0 0.0 0.0 0.0 0.0 0.0 22  * Chen & Todreas
** y direction **
2041801 7.69e-3  22
2042301 0.0 8.05e-3 22
2042701 0000010 22
** z direction **
2041901 3.85e-3  22
2042401 0.0 1.61e-3 22
2042801 0000010 22
*
2200000 scedge   pipe
2200001 22
2200102 8.291e-6  22  * shield, core, gas plenum
2200202 0.0       21
2200301 0.286      1  * shield
2200302 0.06773   16  * core
2200303 0.38223   21  * gas plenum
2200304 0.286     22  * shield
2200601 90. 22
2200802 0.0   0.00261   22  * shield, core, gas plenum
2200902 0.0   0.0       21
2201001 0000000 22
2201103 00000000 21
2201201 003 5.e5 628.150 0.0 0.0 0.0 22
2201300 1
2201301 0.0 0.0 0.0 21
2202501 0.8571  0.0   1.0  0.0   1.0  0.0  22       * laminar shape factor
2202601 0.0 0.15233   0.18  0.0 0.0 0.0 0.0 0.0 0.0 22  * Chen & Todreas
** y direction **
2201801 7.69e-3  22
2202301 0.0 1.61e-3 22
2202701 0000010 22
** z direction **
2201901 7.69e-3  22
2202401 0.0 1.61e-3 22
2202801 0000010 22
*
2220000 scedge   pipe
2220001 22
2220102 8.291e-6  22  * shield, core, gas plenum
2220202 0.0       21
2220301 0.286      1  * shield
2220302 0.06773   16  * core
2220303 0.38223   21  * gas plenum
2220304 0.286     22  * shield
2220601 90. 22
2220802 0.0   0.00261   22  * shield, core, gas plenum
2220902 0.0   0.0       21
2221001 0000000 22
2221103 00000000 21
2221201 003 5.e5 628.150 0.0 0.0 0.0 22
```

```
2221300 1
2221301 0.0 0.0 0.0 21
2222501 0.8571  0.0   1.0  0.0   1.0  0.0  22       * laminar shape factor
2222601 0.0 0.15233   0.18  0.0 0.0 0.0 0.0 0.0 0.0 22  * Chen & Todreas
** y direction **
2221801 7.69e-3  22
2222301 0.0 1.61e-3 22
2222701 0000010 22
** z direction **
2221901 7.69e-3  22
2222401 0.0 1.61e-3 22
2222801 0000010 22
```

Transverse Junctions

```
*
3010000 jz1   mtpljun
3010001 22  0
3010011 204010006 220010005 2.302e-4 0.57 0.57 00000003  1.0  1.0  1.0
3010012 000010000 000010000 0  1
3010021 204020006 220020005 5.453e-5 0.57 0.57 00000003  1.0  1.0  1.0
3010022 000010000 000010000 0  16
3010031 204170006 220170005 3.077e-4 0.57 0.57 00000003  1.0  1.0  1.0
3010032 000010000 000010000 0  21
3010041 204220006 220220005 2.302e-4 0.57 0.57 00000003  1.0  1.0  1.0
3010042 000000000 000000000 0  22
3011011 0.0   0.0   22
*
3200000 jy9   mtpljun
3200001 22  0
3200011 220010004 222010003 2.302e-4 0.57 0.57 00000003  1.0  1.0  1.0
3200012 000010000 000010000 0  1
3200021 220020004 222020003 5.453e-5 0.57 0.57 00000003  1.0  1.0  1.0
3200022 000010000 000010000 0  16
3200031 220170004 222170003 3.077e-4 0.57 0.57 00000003  1.0  1.0  1.0
3200032 000010000 000010000 0  21
3200041 220220004 222220003 2.302e-4 0.57 0.57 00000003  1.0  1.0  1.0
3200042 000000000 000000000 0  22
3201011 0.0   0.0   22
```

Fuel Rod Heat Structures

```
* ROD2
14011000 1  5 2 1 0.0
14011100 0 1
14011101 4 0.004040
14011201 003 4
14011301 0. 4
14011400 0
14011401 375.15  5
14011501 0        0    0   1 0.02383  1
14011601 204010000 00000 111 1 0.02383  1
14011701 0 0.0       0. 0.  1
14011900 1
14011901 0.0 100. 100. 0.  0. 0. 0. 1.0 3.4994  1.1   1.  1
```

```
14012000 15 9 2 1 0.
14012100 0 1
14012101 5 0.003015
14012102 1 0.003481
14012103 2 0.004040
14012201 001 5
14012202 002 6
14012203 003 8
14012301 1. 5
14012302 0. 8
14012400 0
14012401 375.15  9
14012501 0        0    0   1 0.00564 15
14012601 204020000 10000 111 1 0.00564 15
14012701 111 0.00556 0. 0.  15
14012900 1
14012901 0.0 100. 100. 0.  0. 0. 0. 1.0 3.4994  1.1   1. 15
14013000 5  3 2 1 0.003481
14013100 0 1
14013101 2 0.004040
14013201 003 2
14013301 0. 2
14013400 0
14013401 375.15  3
14013501 0        0    0   1 0.03186  5
14013601 204170000 10000 111 1 0.03186  5
14013701 0 0.0      0. 0.  5
14013900 1
14013901 0.0 100. 100. 0.  0. 0. 0. 1.0 3.4994  1.1   1.  5
14014000 1  5 2 1 0.0
14014100 0 1
14014101 4 0.004040
14014201 003 4
14014301 0. 4
14014400 0
14014401 375.15  5
14014501 0        0    0   1 0.02383  1
14014601 204220000 00000 111 1 0.02383  1
14014701 0 0.0      0. 0.  1
14014900 1
14014901 0.0 100. 100. 0.  0. 0. 0. 1.0 3.4994  1.1   1.  1
*
* ROD2
14021000 1  5 2 1 0.0
14021100 0 1
14021101 4 0.004040
14021201 003 4
14021301 0. 4
14021400 0
14021401 375.15  5
14021501 0        0    0   1 0.04767  1
14021601 220010000 00000 111 1 0.04767  1
14021701 0 0.0      0. 0.  1
14021900 1
14021901 0.0 100. 100. 0.  0. 0. 0. 1.0 3.4994  1.1   1.  1
14022000 15 9 2 1 0.
```

```
14022100 0 1
14022101 5 0.003015
14022102 1 0.003481
14022103 2 0.004040
14022201 001 5
14022202 002 6
14022203 003 8
14022301 1. 5
14022302 0. 8
14022400 0
14022401 375.15  9
14022501 0       0     0   1 0.01129 15
14022601 220020000 10000 111 1 0.01129 15
14022701 111 0.01111 0. 0.  15
14022900 1
14022901 0.0 100. 100. 0.  0. 0. 0. 1.0 3.4994  1.1   1. 15
14023000 5  3 2 1 0.003481
14023100 0 1
14023101 2 0.004040
14023201 003 2
14023301 0. 2
14023400 0
14023401 375.15  3
14023501 0       0     0   1 0.06371  5
14023601 220170000 10000 111 1 0.06371  5
14023701 0 0.0      0. 0.  5
14023900 1
14023901 0.0 100. 100. 0.  0. 0. 0. 1.0 3.4994  1.1   1.  5
14024000 1  5 2 1 0.0
14024100 0 1
14024101 4 0.004040
14024201 003 4
14024301 0. 4
14024400 0
14024401 375.15  5
14024501 0       0     0   1 0.04767  1
14024601 220220000 00000 111 1 0.04767  1
14024701 0 0.0      0. 0.  1
14024900 1
14024901 0.0 100. 100. 0.  0. 0. 0. 1.0 3.4994  1.1   1.  1
*
* ROD2
14031000 1  5 2 1 0.0
14031100 0 1
14031101 4 0.004040
14031201 003 4
14031301 0. 4
14031400 0
14031401 375.15  5
14031501 0       0     0   1 0.04767  1
14031601 222010000 00000 111 1 0.04767  1
14031701 0 0.0      0. 0.  1
14031900 1
14031901 0.0 100. 100. 0.  0. 0. 0. 1.0 3.4994  1.1   1.  1
14032000 15 9 2 1 0.
14032100 0 1
```

```
14032101 5 0.003015
14032102 1 0.003481
14032103 2 0.004040
14032201 001 5
14032202 002 6
14032203 003 8
14032301 1. 5
14032302 0. 8
14032400 0
14032401 375.15  9
14032501 0       0    0   1 0.01129 15
14032601 222020000 10000 111 1 0.01129 15
14032701 111 0.01111 0. 0.  15
14032900 1
14032901 0.0 100. 100. 0.  0. 0. 0. 1.0 3.4994  1.1   1. 15
14033000 5  3 2 1 0.003481
14033100 0 1
14033101 2 0.004040
14033201 003 2
14033301 0. 2
14033400 0
14033401 375.15  3
14033501 0       0    0   1 0.06371  5
14033601 222170000 10000 111 1 0.06371  5
14033701 0 0.0     0. 0.  5
14033900 1
14033901 0.0 100. 100. 0.  0. 0. 0. 1.0 3.4994  1.1   1.  5
14034000 1  5 2 1 0.0
14034100 0 1
14034101 4 0.004040
14034201 003 4
14034301 0. 4
14034400 0
14034401 375.15  5
14034501 0       0    0   1 0.04767  1
14034601 222220000 00000 111 1 0.04767  1
14034701 0 0.0     0. 0.  1
14034900 1
14034901 0.0 100. 100. 0.  0. 0. 0. 1.0 3.4994  1.1   1.  1
*
* ROD6
14181000 1  5 2 1 0.0
14181100 0 1
14181101 4 0.004040
14181201 003 4
14181301 0. 4
14181400 0
14181401 375.15  5
14181501 0       0    0   1 0.04767  1
14181601 204010000 00000 111 1 0.04767  1
14181701 0 0.0     0. 0.  1
14181900 1
14181901 0.0 100. 100. 0.  0. 0. 0. 1.0 3.4994  1.1   1.  1
14182000 15 9 2 1 0.
14182100 0 1
14182101 5 0.003015
```

```
14182102 1 0.003481
14182103 2 0.004040
14182201 001 5
14182202 002 6
14182203 003 8
14182301 1. 5
14182302 0. 8
14182400 0
14182401 375.15  9
14182501 0       0    0    1 0.01129 15
14182601 204020000 10000 111 1 0.01129 15
14182701 111 0.01111 0. 0.  15
14182900 1
14182901 0.0 100. 100. 0.  0. 0. 0. 1.0 3.4994  1.1   1. 15
14183000 5  3 2 1 0.003481
14183100 0 1
14183101 2 0.004040
14183201 003 2
14183301 0. 2
14183400 0
14183401 375.15  3
14183501 0       0    0    1 0.06371  5
14183601 204170000 10000 111 1 0.06371  5
14183701 0 0.0      0. 0.  5
14183900 1
14183901 0.0 100. 100. 0.  0. 0. 0. 1.0 3.4994  1.1   1.  5
14184000 1  5 2 1 0.0
14184100 0 1
14184101 4 0.004040
14184201 003 4
14184301 0. 4
14184400 0
14184401 375.15  5
14184501 0       0    0    1 0.04767  1
14184601 204220000 00000 111 1 0.04767  1
14184701 0 0.0      0. 0.  1
14184900 1
14184901 0.0 100. 100. 0.  0. 0. 0. 1.0 3.4994  1.1   1.  1
*
* ROD6
14191000 1  5 2 1 0.0
14191100 0 1
14191101 4 0.004040
14191201 003 4
14191301 0. 4
14191400 0
14191401 375.15  5
14191501 0       0    0    1 0.04767  1
14191601 220010000 00000 111 1 0.04767  1
14191701 0 0.0      0. 0.  1
14191900 1
14191901 0.0 100. 100. 0.  0. 0. 0. 1.0 3.4994  1.1   1.  1
14192000 15 9 2 1 0.
14192100 0 1
14192101 5 0.003015
14192102 1 0.003481
```

```
14192103 2 0.004040
14192201 001 5
14192202 002 6
14192203 003 8
14192301 1. 5
14192302 0. 8
14192400 0
14192401 375.15  9
14192501 0        0    0   1 0.01129 15
14192601 220020000 10000 111 1 0.01129 15
14192701 111 0.01111 0. 0.  15
14192900 1
14192901 0.0 100. 100. 0.  0. 0. 0. 1.0 3.4994  1.1   1. 15
14193000 5  3 2 1 0.003481
14193100 0 1
14193101 2 0.004040
14193201 003 2
14193301 0. 2
14193400 0
14193401 375.15  3
14193501 0        0    0   1 0.06371  5
14193601 220170000 10000 111 1 0.06371  5
14193701 0 0.0      0. 0.  5
14193900 1
14193901 0.0 100. 100. 0.  0. 0. 0. 1.0 3.4994  1.1   1.  5
14194000 1  5 2 1 0.0
14194100 0 1
14194101 4 0.004040
14194201 003 4
14194301 0. 4
14194400 0
14194401 375.15  5
14194501 0        0    0   1 0.04767  1
14194601 220220000 00000 111 1 0.04767  1
14194701 0 0.0      0. 0.  1
14194900 1
14194901 0.0 100. 100. 0.  0. 0. 0. 1.0 3.4994  1.1   1.  1
*
* ROD11
14201000 1  5 2 1 0.0
14201100 0 1
14201101 4 0.004040
14201201 003 4
14201301 0. 4
14201400 0
14201401 375.15  5
14201501 0        0    0   1 0.04767  1
14201601 220010000 00000 111 1 0.04767  1
14201701 0 0.0      0. 0.  1
14201900 1
14201901 0.0 100. 100. 0.  0. 0. 0. 1.0 3.4994  1.1   1.  1
14202000 15 9 2 1 0.
14202100 0 1
14202101 5 0.003015
14202102 1 0.003481
14202103 2 0.004040
```

```
14202201 001 5
14202202 002 6
14202203 003 8
14202301 1. 5
14202302 0. 8
14202400 0
14202401 375.15  9
14202501 0        0    0   1 0.01129 15
14202601 220020000 10000 111 1 0.01129 15
14202701 111 0.01111 0. 0.  15
14202900 1
14202901 0.0 100. 100. 0.  0. 0. 0. 1.0 3.4994  1.1   1. 15
14203000 5  3 2 1 0.003481
14203100 0 1
14203101 2 0.004040
14203201 003 2
14203301 0. 2
14203400 0
14203401 375.15  3
14203501 0        0    0   1 0.06371  5
14203601 220170000 10000 111 1 0.06371  5
14203701 0 0.0      0. 0.  5
14203900 1
14203901 0.0 100. 100. 0.  0. 0. 0. 1.0 3.4994  1.1   1.  5
14204000 1  5 2 1 0.0
14204100 0 1
14204101 4 0.004040
14204201 003 4
14204301 0. 4
14204400 0
14204401 375.15  5
14204501 0        0    0   1 0.04767  1
14204601 220220000 00000 111 1 0.04767  1
14204701 0 0.0      0. 0.  1
14204900 1
14204901 0.0 100. 100. 0.  0. 0. 0. 1.0 3.4994  1.1   1.  1
*
* ROD11
14211000 1  5 2 1 0.0
14211100 0 1
14211101 4 0.004040
14211201 003 4
14211301 0. 4
14211400 0
14211401 375.15  5
14211501 0        0    0   1 0.04767  1
14211601 222010000 00000 111 1 0.04767  1
14211701 0 0.0      0. 0.  1
14211900 1
14211901 0.0 100. 100. 0.  0. 0. 0. 1.0 3.4994  1.1   1.  1
14212000 15 9 2 1 0.
14212100 0 1
14212101 5 0.003015
14212102 1 0.003481
14212103 2 0.004040
14212201 001 5
```

```
14212202 002 6
14212203 003 8
14212301 1. 5
14212302 0. 8
14212400 0
14212401 375.15  9
14212501 0        0    0   1 0.01129 15
14212601 222020000 10000 111 1 0.01129 15
14212701 111 0.01111 0. 0.  15
14212900 1
14212901 0.0 100. 100. 0.  0. 0. 0. 1.0 3.4994  1.1   1. 15
14213000 5  3 2 1 0.003481
14213100 0 1
14213101 2 0.004040
14213201 003 2
14213301 0. 2
14213400 0
14213401 375.15  3
14213501 0        0    0   1 0.06371  5
14213601 222170000 10000 111 1 0.06371  5
14213701 0 0.0      0. 0.  5
14213900 1
14213901 0.0 100. 100. 0.  0. 0. 0. 1.0 3.4994  1.1   1.  5
14214000 1  5 2 1 0.0
14214100 0 1
14214101 4 0.004040
14214201 003 4
14214301 0. 4
14214400 0
14214401 375.15  5
14214501 0        0    0   1 0.04767  1
14214601 222220000 00000 111 1 0.04767  1
14214701 0 0.0      0. 0.  1
14214900 1
14214901 0.0 100. 100. 0.  0. 0. 0. 1.0 3.4994  1.1   1.  1
```

Mixing Control Variables

This first group of control variables determines the axial mass flux of the coolant in each volume of the subchannel pipe. The multiplier represents $1/A_{cs}$, where A_{cs} is the cross sectional flow area of the respective subchannel.

```
20500230  G20401    sum       0.5    0.0   1
20500231  0.0 2.41422E+05 mflowj 201020100  2.41422E+05 mflowj 204010000
20500240  G20402    sum       0.5    0.0   1
20500241  0.0 2.41422E+05 mflowj 204010000  2.41422E+05 mflowj 204020000
```

```
20500250  G20403   sum      0.5   0.0   1
20500251  0.0 2.41422E+05 mflowj 204020000  2.41422E+05 mflowj 204030000
20500260  G20404   sum      0.5   0.0   1
20500261  0.0 2.41422E+05 mflowj 204030000  2.41422E+05 mflowj 204040000
20500270  G20405   sum      0.5   0.0   1
20500271  0.0 2.41422E+05 mflowj 204040000  2.41422E+05 mflowj 204050000
20500280  G20406   sum      0.5   0.0   1
20500281  0.0 2.41422E+05 mflowj 204050000  2.41422E+05 mflowj 204060000
20500290  G20407   sum      0.5   0.0   1
20500291  0.0 2.41422E+05 mflowj 204060000  2.41422E+05 mflowj 204070000
20500300  G20408   sum      0.5   0.0   1
20500301  0.0 2.41422E+05 mflowj 204070000  2.41422E+05 mflowj 204080000
20500310  G20409   sum      0.5   0.0   1
20500311  0.0 2.41422E+05 mflowj 204080000  2.41422E+05 mflowj 204090000
20500320  G20410   sum      0.5   0.0   1
20500321  0.0 2.41422E+05 mflowj 204090000  2.41422E+05 mflowj 204100000
20500330  G20411   sum      0.5   0.0   1
20500331  0.0 2.41422E+05 mflowj 204100000  2.41422E+05 mflowj 204110000
20500340  G20412   sum      0.5   0.0   1
20500341  0.0 2.41422E+05 mflowj 204110000  2.41422E+05 mflowj 204120000
20500350  G20413   sum      0.5   0.0   1
20500351  0.0 2.41422E+05 mflowj 204120000  2.41422E+05 mflowj 204130000
20500360  G20414   sum      0.5   0.0   1
20500361  0.0 2.41422E+05 mflowj 204130000  2.41422E+05 mflowj 204140000
20500370  G20415   sum      0.5   0.0   1
20500371  0.0 2.41422E+05 mflowj 204140000  2.41422E+05 mflowj 204150000
20500380  G20416   sum      0.5   0.0   1
20500381  0.0 2.41422E+05 mflowj 204150000  2.41422E+05 mflowj 204160000
20500390  G20417   sum      0.5   0.0   1
20500391  0.0 2.41422E+05 mflowj 204160000  2.41422E+05 mflowj 204170000
20500400  G20418   sum      0.5   0.0   1
20500401  0.0 2.41422E+05 mflowj 204170000  2.41422E+05 mflowj 204180000
20500410  G20419   sum      0.5   0.0   1
20500411  0.0 2.41422E+05 mflowj 204180000  2.41422E+05 mflowj 204190000
20500420  G20420   sum      0.5   0.0   1
20500421  0.0 2.41422E+05 mflowj 204190000  2.41422E+05 mflowj 204200000
20500430  G20421   sum      0.5   0.0   1
20500431  0.0 2.41422E+05 mflowj 204200000  2.41422E+05 mflowj 204210000
20500440  G20422   sum      0.5   0.0   1
20500441  0.0 2.41422E+05 mflowj 204210000  2.41422E+05 mflowj 293020100
20501990  G22001   sum      0.5   0.0   1
20501991  0.0 1.20612E+05 mflowj 203010100  1.20612E+05 mflowj 220010000
20502000  G22002   sum      0.5   0.0   1
20502001  0.0 1.20612E+05 mflowj 220010000  1.20612E+05 mflowj 220020000
20502010  G22003   sum      0.5   0.0   1
20502011  0.0 1.20612E+05 mflowj 220020000  1.20612E+05 mflowj 220030000
20502020  G22004   sum      0.5   0.0   1
20502021  0.0 1.20612E+05 mflowj 220030000  1.20612E+05 mflowj 220040000
20502030  G22005   sum      0.5   0.0   1
20502031  0.0 1.20612E+05 mflowj 220040000  1.20612E+05 mflowj 220050000
20502040  G22006   sum      0.5   0.0   1
20502041  0.0 1.20612E+05 mflowj 220050000  1.20612E+05 mflowj 220060000
20502050  G22007   sum      0.5   0.0   1
20502051  0.0 1.20612E+05 mflowj 220060000  1.20612E+05 mflowj 220070000
20502060  G22008   sum      0.5   0.0   1
20502061  0.0 1.20612E+05 mflowj 220070000  1.20612E+05 mflowj 220080000
```

```
20502070 G22009   sum       0.5   0.0   1
20502071  0.0 1.20612E+05 mflowj 220080000  1.20612E+05 mflowj 220090000
20502080  G22010   sum       0.5   0.0   1
20502081  0.0 1.20612E+05 mflowj 220090000  1.20612E+05 mflowj 220100000
20502090  G22011   sum       0.5   0.0   1
20502091  0.0 1.20612E+05 mflowj 220100000  1.20612E+05 mflowj 220110000
20502100  G22012   sum       0.5   0.0   1
20502101  0.0 1.20612E+05 mflowj 220110000  1.20612E+05 mflowj 220120000
20502110  G22013   sum       0.5   0.0   1
20502111  0.0 1.20612E+05 mflowj 220120000  1.20612E+05 mflowj 220130000
20502120  G22014   sum       0.5   0.0   1
20502121  0.0 1.20612E+05 mflowj 220130000  1.20612E+05 mflowj 220140000
20502130  G22015   sum       0.5   0.0   1
20502131  0.0 1.20612E+05 mflowj 220140000  1.20612E+05 mflowj 220150000
20502140  G22016   sum       0.5   0.0   1
20502141  0.0 1.20612E+05 mflowj 220150000  1.20612E+05 mflowj 220160000
20502150  G22017   sum       0.5   0.0   1
20502151  0.0 1.20612E+05 mflowj 220160000  1.20612E+05 mflowj 220170000
20502160  G22018   sum       0.5   0.0   1
20502161  0.0 1.20612E+05 mflowj 220170000  1.20612E+05 mflowj 220180000
20502170  G22019   sum       0.5   0.0   1
20502171  0.0 1.20612E+05 mflowj 220180000  1.20612E+05 mflowj 220190000
20502180  G22020   sum       0.5   0.0   1
20502181  0.0 1.20612E+05 mflowj 220190000  1.20612E+05 mflowj 220200000
20502190  G22021   sum       0.5   0.0   1
20502191  0.0 1.20612E+05 mflowj 220200000  1.20612E+05 mflowj 220210000
20502200  G22022   sum       0.5   0.0   1
20502201  0.0 1.20612E+05 mflowj 220210000  1.20612E+05 mflowj 295010100
20502210  G22201   sum       0.5   0.0   1
20502211  0.0 1.20612E+05 mflowj 203020100  1.20612E+05 mflowj 222010000
20502220  G22202   sum       0.5   0.0   1
20502221  0.0 1.20612E+05 mflowj 222010000  1.20612E+05 mflowj 222020000
20502230  G22203   sum       0.5   0.0   1
20502231  0.0 1.20612E+05 mflowj 222020000  1.20612E+05 mflowj 222030000
20502240  G22204   sum       0.5   0.0   1
20502241  0.0 1.20612E+05 mflowj 222030000  1.20612E+05 mflowj 222040000
20502250  G22205   sum       0.5   0.0   1
20502251  0.0 1.20612E+05 mflowj 222040000  1.20612E+05 mflowj 222050000
20502260  G22206   sum       0.5   0.0   1
20502261  0.0 1.20612E+05 mflowj 222050000  1.20612E+05 mflowj 222060000
20502270  G22207   sum       0.5   0.0   1
20502271  0.0 1.20612E+05 mflowj 222060000  1.20612E+05 mflowj 222070000
20502280  G22208   sum       0.5   0.0   1
20502281  0.0 1.20612E+05 mflowj 222070000  1.20612E+05 mflowj 222080000
20502290  G22209   sum       0.5   0.0   1
20502291  0.0 1.20612E+05 mflowj 222080000  1.20612E+05 mflowj 222090000
20502300  G22210   sum       0.5   0.0   1
20502301  0.0 1.20612E+05 mflowj 222090000  1.20612E+05 mflowj 222100000
20502310  G22211   sum       0.5   0.0   1
20502311  0.0 1.20612E+05 mflowj 222100000  1.20612E+05 mflowj 222110000
20502320  G22212   sum       0.5   0.0   1
20502321  0.0 1.20612E+05 mflowj 222110000  1.20612E+05 mflowj 222120000
20502330  G22213   sum       0.5   0.0   1
20502331  0.0 1.20612E+05 mflowj 222120000  1.20612E+05 mflowj 222130000
20502340  G22214   sum       0.5   0.0   1
20502341  0.0 1.20612E+05 mflowj 222130000  1.20612E+05 mflowj 222140000
```

```
20502350 G22215   sum     0.5   0.0  1
20502351 0.0 1.20612E+05 mflowj 222140000 1.20612E+05 mflowj 222150000
20502360 G22216   sum     0.5   0.0  1
20502361 0.0 1.20612E+05 mflowj 222150000 1.20612E+05 mflowj 222160000
20502370 G22217   sum     0.5   0.0  1
20502371 0.0 1.20612E+05 mflowj 222160000 1.20612E+05 mflowj 222170000
20502380 G22218   sum     0.5   0.0  1
20502381 0.0 1.20612E+05 mflowj 222170000 1.20612E+05 mflowj 222180000
20502390 G22219   sum     0.5   0.0  1
20502391 0.0 1.20612E+05 mflowj 222180000 1.20612E+05 mflowj 222190000
20502400 G22220   sum     0.5   0.0  1
20502401 0.0 1.20612E+05 mflowj 222190000 1.20612E+05 mflowj 222200000
20502410 G22221   sum     0.5   0.0  1
20502411 0.0 1.20612E+05 mflowj 222200000 1.20612E+05 mflowj 222210000
20502420 G22222   sum     0.5   0.0  1
20502421 0.0 1.20612E+05 mflowj 222210000 1.20612E+05 mflowj 295020100
```

Heat Flow Calculation Control Variables

There are 4 such control variables per volume in the subchannel pipe (each pipe contains 22 volumes). The first volume determines the heat capacity in the transverse junction as the arithmetic average the heat capacity in the two adjacent volumes. The second control variable determines the mass flow based upon the transverse area, ε^*, and the axial mass flux calculated in the previous control variables. The multiplier represents the product of the transverse area and ε^*. The third variable determines the temperature difference between the two adjacent volumes. The fourth and final variable per volume determines the heat transfer between variables by multiplying the previous 3.

```
* Junction 301
*
20555010 Cp30101  sum    0.5       0.0  1
20555011 0.0  1.0  csubpf 204010000   1.0  csubpf 220010000
20555020 mT30101  sum   9.28610E-6  0.0  1
20555021 0.0  1.0 cntrlvar  0023     1.0 cntrlvar  0199
20555030 dT30101  sum    1.0       0.0  1
20555031 0.0  1.0  tempf 204010000  -1.0  tempf 220010000
20555040 QJ30101  mult   1.0       0.0  1
20555041 cntrlvar 5501  cntrlvar 5502  cntrlvar 5503
20555050 Cp30102  sum    0.5       0.0  1
```

```
20555051  0.0  1.0  csubpf 204020000   1.0  csubpf 220020000
20555060  mT30102   sum    2.19923E-6  0.0   1
20555061  0.0  1.0 cntrlvar  0024      1.0 cntrlvar  0200
20555070  dT30102   sum    1.0     0.0   1
20555071  0.0  1.0  tempf  204020000  -1.0  tempf  220020000
20555080  QJ30102   mult    1.0     0.0   1
20555081  cntrlvar  5505  cntrlvar  5506  cntrlvar  5507
20555090  Cp30103   sum    0.5     0.0   1
20555091  0.0  1.0  csubpf 204030000   1.0  csubpf 220030000
20555100  mT30103   sum    2.19923E-6  0.0   1
20555101  0.0  1.0 cntrlvar  0025      1.0 cntrlvar  0201
20555110  dT30103   sum    1.0     0.0   1
20555111  0.0  1.0  tempf  204030000  -1.0  tempf  220030000
20555120  QJ30103   mult    1.0     0.0   1
20555121  cntrlvar  5509  cntrlvar  5510  cntrlvar  5511
20555130  Cp30104   sum    0.5     0.0   1
20555131  0.0  1.0  csubpf 204040000   1.0  csubpf 220040000
20555140  mT30104   sum    2.19923E-6  0.0   1
20555141  0.0  1.0 cntrlvar  0026      1.0 cntrlvar  0202
20555150  dT30104   sum    1.0     0.0   1
20555151  0.0  1.0  tempf  204040000  -1.0  tempf  220040000
20555160  QJ30104   mult    1.0     0.0   1
20555161  cntrlvar  5513  cntrlvar  5514  cntrlvar  5515
20555170  Cp30105   sum    0.5     0.0   1
20555171  0.0  1.0  csubpf 204050000   1.0  csubpf 220050000
20555180  mT30105   sum    2.19923E-6  0.0   1
20555181  0.0  1.0 cntrlvar  0027      1.0 cntrlvar  0203
20555190  dT30105   sum    1.0     0.0   1
20555191  0.0  1.0  tempf  204050000  -1.0  tempf  220050000
20555200  QJ30105   mult    1.0     0.0   1
20555201  cntrlvar  5517  cntrlvar  5518  cntrlvar  5519
20555210  Cp30106   sum    0.5     0.0   1
20555211  0.0  1.0  csubpf 204060000   1.0  csubpf 220060000
20555220  mT30106   sum    2.19923E-6  0.0   1
20555221  0.0  1.0 cntrlvar  0028      1.0 cntrlvar  0204
20555230  dT30106   sum    1.0     0.0   1
20555231  0.0  1.0  tempf  204060000  -1.0  tempf  220060000
20555240  QJ30106   mult    1.0     0.0   1
20555241  cntrlvar  5521  cntrlvar  5522  cntrlvar  5523
20555250  Cp30107   sum    0.5     0.0   1
20555251  0.0  1.0  csubpf 204070000   1.0  csubpf 220070000
20555260  mT30107   sum    2.19923E-6  0.0   1
20555261  0.0  1.0 cntrlvar  0029      1.0 cntrlvar  0205
20555270  dT30107   sum    1.0     0.0   1
20555271  0.0  1.0  tempf  204070000  -1.0  tempf  220070000
20555280  QJ30107   mult    1.0     0.0   1
20555281  cntrlvar  5525  cntrlvar  5526  cntrlvar  5527
20555290  Cp30108   sum    0.5     0.0   1
20555291  0.0  1.0  csubpf 204080000   1.0  csubpf 220080000
20555300  mT30108   sum    2.19923E-6  0.0   1
20555301  0.0  1.0 cntrlvar  0030      1.0 cntrlvar  0206
20555310  dT30108   sum    1.0     0.0   1
20555311  0.0  1.0  tempf  204080000  -1.0  tempf  220080000
20555320  QJ30108   mult    1.0     0.0   1
20555321  cntrlvar  5529  cntrlvar  5530  cntrlvar  5531
20555330  Cp30109   sum    0.5     0.0   1
```

```
20555331 0.0 1.0 csubpf 204090000  1.0 csubpf 220090000
20555340 mT30109  sum   2.19923E-6 0.0  1
20555341 0.0 1.0 cntrlvar 0031   1.0 cntrlvar 0207
20555350 dT30109  sum    1.0      0.0  1
20555351 0.0 1.0 tempf 204090000 -1.0 tempf 220090000
20555360 QJ30109  mult   1.0      0.0  1
20555361 cntrlvar 5533  cntrlvar 5534  cntrlvar 5535
20555370 Cp30110  sum    0.5      0.0  1
20555371 0.0 1.0 csubpf 204100000  1.0 csubpf 220100000
20555380 mT30110  sum   2.19923E-6 0.0  1
20555381 0.0 1.0 cntrlvar 0032   1.0 cntrlvar 0208
20555390 dT30110  sum    1.0      0.0  1
20555391 0.0 1.0 tempf 204100000 -1.0 tempf 220100000
20555400 QJ30110  mult   1.0      0.0  1
20555401 cntrlvar 5537  cntrlvar 5538  cntrlvar 5539
20555410 Cp30111  sum    0.5      0.0  1
20555411 0.0 1.0 csubpf 204110000  1.0 csubpf 220110000
20555420 mT30111  sum   2.19923E-6 0.0  1
20555421 0.0 1.0 cntrlvar 0033   1.0 cntrlvar 0209
20555430 dT30111  sum    1.0      0.0  1
20555431 0.0 1.0 tempf 204110000 -1.0 tempf 220110000
20555440 QJ30111  mult   1.0      0.0  1
20555441 cntrlvar 5541  cntrlvar 5542  cntrlvar 5543
20555450 Cp30112  sum    0.5      0.0  1
20555451 0.0 1.0 csubpf 204120000  1.0 csubpf 220120000
20555460 mT30112  sum   2.19923E-6 0.0  1
20555461 0.0 1.0 cntrlvar 0034   1.0 cntrlvar 0210
20555470 dT30112  sum    1.0      0.0  1
20555471 0.0 1.0 tempf 204120000 -1.0 tempf 220120000
20555480 QJ30112  mult   1.0      0.0  1
20555481 cntrlvar 5545  cntrlvar 5546  cntrlvar 5547
20555490 Cp30113  sum    0.5      0.0  1
20555491 0.0 1.0 csubpf 204130000  1.0 csubpf 220130000
20555500 mT30113  sum   2.19923E-6 0.0  1
20555501 0.0 1.0 cntrlvar 0035   1.0 cntrlvar 0211
20555510 dT30113  sum    1.0      0.0  1
20555511 0.0 1.0 tempf 204130000 -1.0 tempf 220130000
20555520 QJ30113  mult   1.0      0.0  1
20555521 cntrlvar 5549  cntrlvar 5550  cntrlvar 5551
20555530 Cp30114  sum    0.5      0.0  1
20555531 0.0 1.0 csubpf 204140000  1.0 csubpf 220140000
20555540 mT30114  sum   2.19923E-6 0.0  1
20555541 0.0 1.0 cntrlvar 0036   1.0 cntrlvar 0212
20555550 dT30114  sum    1.0      0.0  1
20555551 0.0 1.0 tempf 204140000 -1.0 tempf 220140000
20555560 QJ30114  mult   1.0      0.0  1
20555561 cntrlvar 5553  cntrlvar 5554  cntrlvar 5555
20555570 Cp30115  sum    0.5      0.0  1
20555571 0.0 1.0 csubpf 204150000  1.0 csubpf 220150000
20555580 mT30115  sum   2.19923E-6 0.0  1
20555581 0.0 1.0 cntrlvar 0037   1.0 cntrlvar 0213
20555590 dT30115  sum    1.0      0.0  1
20555591 0.0 1.0 tempf 204150000 -1.0 tempf 220150000
20555600 QJ30115  mult   1.0      0.0  1
20555601 cntrlvar 5557  cntrlvar 5558  cntrlvar 5559
20555610 Cp30116  sum    0.5      0.0  1
```

```
20555611  0.0  1.0  csubpf 204160000   1.0  csubpf 220160000
20555620  mT30116   sum    2.19923E-6  0.0   1
20555621  0.0  1.0 cntrlvar  0038     1.0 cntrlvar  0214
20555630  dT30116   sum     1.0       0.0   1
20555631  0.0  1.0  tempf  204160000  -1.0  tempf  220160000
20555640  QJ30116   mult    1.0       0.0   1
20555641  cntrlvar  5561  cntrlvar  5562  cntrlvar  5563
20555650  Cp30117   sum     0.5       0.0   1
20555651  0.0  1.0  csubpf 204170000   1.0  csubpf 220170000
20555660  mT30117   sum    1.24122E-5  0.0   1
20555661  0.0  1.0 cntrlvar  0039     1.0 cntrlvar  0215
20555670  dT30117   sum     1.0       0.0   1
20555671  0.0  1.0  tempf  204170000  -1.0  tempf  220170000
20555680  QJ30117   mult    1.0       0.0   1
20555681  cntrlvar  5565  cntrlvar  5566  cntrlvar  5567
20555690  Cp30118   sum     0.5       0.0   1
20555691  0.0  1.0  csubpf 204180000   1.0  csubpf 220180000
20555700  mT30118   sum    1.24122E-5  0.0   1
20555701  0.0  1.0 cntrlvar  0040     1.0 cntrlvar  0216
20555710  dT30118   sum     1.0       0.0   1
20555711  0.0  1.0  tempf  204180000  -1.0  tempf  220180000
20555720  QJ30118   mult    1.0       0.0   1
20555721  cntrlvar  5569  cntrlvar  5570  cntrlvar  5571
20555730  Cp30119   sum     0.5       0.0   1
20555731  0.0  1.0  csubpf 204190000   1.0  csubpf 220190000
20555740  mT30119   sum    1.24122E-5  0.0   1
20555741  0.0  1.0 cntrlvar  0041     1.0 cntrlvar  0217
20555750  dT30119   sum     1.0       0.0   1
20555751  0.0  1.0  tempf  204190000  -1.0  tempf  220190000
20555760  QJ30119   mult    1.0       0.0   1
20555761  cntrlvar  5573  cntrlvar  5574  cntrlvar  5575
20555770  Cp30120   sum     0.5       0.0   1
20555771  0.0  1.0  csubpf 204200000   1.0  csubpf 220200000
20555780  mT30120   sum    1.24122E-5  0.0   1
20555781  0.0  1.0 cntrlvar  0042     1.0 cntrlvar  0218
20555790  dT30120   sum     1.0       0.0   1
20555791  0.0  1.0  tempf  204200000  -1.0  tempf  220200000
20555800  QJ30120   mult    1.0       0.0   1
20555801  cntrlvar  5577  cntrlvar  5578  cntrlvar  5579
20555810  Cp30121   sum     0.5       0.0   1
20555811  0.0  1.0  csubpf 204210000   1.0  csubpf 220210000
20555820  mT30121   sum    1.24122E-5  0.0   1
20555821  0.0  1.0 cntrlvar  0043     1.0 cntrlvar  0219
20555830  dT30121   sum     1.0       0.0   1
20555831  0.0  1.0  tempf  204210000  -1.0  tempf  220210000
20555840  QJ30121   mult    1.0       0.0   1
20555841  cntrlvar  5581  cntrlvar  5582  cntrlvar  5583
20555850  Cp30122   sum     0.5       0.0   1
20555851  0.0  1.0  csubpf 204220000   1.0  csubpf 220220000
20555860  mT30122   sum    9.28610E-6  0.0   1
20555861  0.0  1.0 cntrlvar  0044     1.0 cntrlvar  0220
20555870  dT30122   sum     1.0       0.0   1
20555871  0.0  1.0  tempf  204220000  -1.0  tempf  220220000
20555880  QJ30122   mult    1.0       0.0   1
20555881  cntrlvar  5585  cntrlvar  5586  cntrlvar  5587
*
```

```
* Junction 320
*
20518010  Cp32001  sum     0.5       0.0  1
20518011  0.0  1.0  csubpf 220010000   1.0  csubpf 222010000
20518020  mT32001  sum    9.28610E-6  0.0  1
20518021  0.0  1.0 cntrlvar  0199     1.0 cntrlvar  0221
20518030  dT32001  sum     1.0       0.0  1
20518031  0.0  1.0  tempf  220010000  -1.0  tempf  222010000
20518040  QJ32001  mult    1.0       0.0  1
20518041  cntrlvar  1801  cntrlvar  1802  cntrlvar  1803
20518050  Cp32002  sum     0.5       0.0  1
20518051  0.0  1.0  csubpf 220020000   1.0  csubpf 222020000
20518060  mT32002  sum    2.19923E-6  0.0  1
20518061  0.0  1.0 cntrlvar  0200     1.0 cntrlvar  0222
20518070  dT32002  sum     1.0       0.0  1
20518071  0.0  1.0  tempf  220020000  -1.0  tempf  222020000
20518080  QJ32002  mult    1.0       0.0  1
20518081  cntrlvar  1805  cntrlvar  1806  cntrlvar  1807
20518090  Cp32003  sum     0.5       0.0  1
20518091  0.0  1.0  csubpf 220030000   1.0  csubpf 222030000
20518100  mT32003  sum    2.19923E-6  0.0  1
20518101  0.0  1.0 cntrlvar  0201     1.0 cntrlvar  0223
20518110  dT32003  sum     1.0       0.0  1
20518111  0.0  1.0  tempf  220030000  -1.0  tempf  222030000
20518120  QJ32003  mult    1.0       0.0  1
20518121  cntrlvar  1809  cntrlvar  1810  cntrlvar  1811
20518130  Cp32004  sum     0.5       0.0  1
20518131  0.0  1.0  csubpf 220040000   1.0  csubpf 222040000
20518140  mT32004  sum    2.19923E-6  0.0  1
20518141  0.0  1.0 cntrlvar  0202     1.0 cntrlvar  0224
20518150  dT32004  sum     1.0       0.0  1
20518151  0.0  1.0  tempf  220040000  -1.0  tempf  222040000
20518160  QJ32004  mult    1.0       0.0  1
20518161  cntrlvar  1813  cntrlvar  1814  cntrlvar  1815
20518170  Cp32005  sum     0.5       0.0  1
20518171  0.0  1.0  csubpf 220050000   1.0  csubpf 222050000
20518180  mT32005  sum    2.19923E-6  0.0  1
20518181  0.0  1.0 cntrlvar  0203     1.0 cntrlvar  0225
20518190  dT32005  sum     1.0       0.0  1
20518191  0.0  1.0  tempf  220050000  -1.0  tempf  222050000
20518200  QJ32005  mult    1.0       0.0  1
20518201  cntrlvar  1817  cntrlvar  1818  cntrlvar  1819
20518210  Cp32006  sum     0.5       0.0  1
20518211  0.0  1.0  csubpf 220060000   1.0  csubpf 222060000
20518220  mT32006  sum    2.19923E-6  0.0  1
20518221  0.0  1.0 cntrlvar  0204     1.0 cntrlvar  0226
20518230  dT32006  sum     1.0       0.0  1
20518231  0.0  1.0  tempf  220060000  -1.0  tempf  222060000
20518240  QJ32006  mult    1.0       0.0  1
20518241  cntrlvar  1821  cntrlvar  1822  cntrlvar  1823
20518250  Cp32007  sum     0.5       0.0  1
20518251  0.0  1.0  csubpf 220070000   1.0  csubpf 222070000
20518260  mT32007  sum    2.19923E-6  0.0  1
20518261  0.0  1.0 cntrlvar  0205     1.0 cntrlvar  0227
20518270  dT32007  sum     1.0       0.0  1
20518271  0.0  1.0  tempf  220070000  -1.0  tempf  222070000
```

```
20518280 QJ32007  mult   1.0      0.0  1
20518281 cntrlvar 1825  cntrlvar 1826  cntrlvar 1827
20518290 Cp32008  sum    0.5      0.0  1
20518291 0.0 1.0 csubpf 220080000  1.0 csubpf 222080000
20518300 mT32008  sum    2.19923E-6 0.0  1
20518301 0.0 1.0 cntrlvar 0206    1.0 cntrlvar 0228
20518310 dT32008  sum    1.0      0.0  1
20518311 0.0 1.0 tempf 220080000 -1.0 tempf 222080000
20518320 QJ32008  mult   1.0      0.0  1
20518321 cntrlvar 1829  cntrlvar 1830  cntrlvar 1831
20518330 Cp32009  sum    0.5      0.0  1
20518331 0.0 1.0 csubpf 220090000  1.0 csubpf 222090000
20518340 mT32009  sum    2.19923E-6 0.0  1
20518341 0.0 1.0 cntrlvar 0207    1.0 cntrlvar 0229
20518350 dT32009  sum    1.0      0.0  1
20518351 0.0 1.0 tempf 220090000 -1.0 tempf 222090000
20518360 QJ32009  mult   1.0      0.0  1
20518361 cntrlvar 1833  cntrlvar 1834  cntrlvar 1835
20518370 Cp32010  sum    0.5      0.0  1
20518371 0.0 1.0 csubpf 220100000  1.0 csubpf 222100000
20518380 mT32010  sum    2.19923E-6 0.0  1
20518381 0.0 1.0 cntrlvar 0208    1.0 cntrlvar 0230
20518390 dT32010  sum    1.0      0.0  1
20518391 0.0 1.0 tempf 220100000 -1.0 tempf 222100000
20518400 QJ32010  mult   1.0      0.0  1
20518401 cntrlvar 1837  cntrlvar 1838  cntrlvar 1839
20518410 Cp32011  sum    0.5      0.0  1
20518411 0.0 1.0 csubpf 220110000  1.0 csubpf 222110000
20518420 mT32011  sum    2.19923E-6 0.0  1
20518421 0.0 1.0 cntrlvar 0209    1.0 cntrlvar 0231
20518430 dT32011  sum    1.0      0.0  1
20518431 0.0 1.0 tempf 220110000 -1.0 tempf 222110000
20518440 QJ32011  mult   1.0      0.0  1
20518441 cntrlvar 1841  cntrlvar 1842  cntrlvar 1843
20518450 Cp32012  sum    0.5      0.0  1
20518451 0.0 1.0 csubpf 220120000  1.0 csubpf 222120000
20518460 mT32012  sum    2.19923E-6 0.0  1
20518461 0.0 1.0 cntrlvar 0210    1.0 cntrlvar 0232
20518470 dT32012  sum    1.0      0.0  1
20518471 0.0 1.0 tempf 220120000 -1.0 tempf 222120000
20518480 QJ32012  mult   1.0      0.0  1
20518481 cntrlvar 1845  cntrlvar 1846  cntrlvar 1847
20518490 Cp32013  sum    0.5      0.0  1
20518491 0.0 1.0 csubpf 220130000  1.0 csubpf 222130000
20518500 mT32013  sum    2.19923E-6 0.0  1
20518501 0.0 1.0 cntrlvar 0211    1.0 cntrlvar 0233
20518510 dT32013  sum    1.0      0.0  1
20518511 0.0 1.0 tempf 220130000 -1.0 tempf 222130000
20518520 QJ32013  mult   1.0      0.0  1
20518521 cntrlvar 1849  cntrlvar 1850  cntrlvar 1851
20518530 Cp32014  sum    0.5      0.0  1
20518531 0.0 1.0 csubpf 220140000  1.0 csubpf 222140000
20518540 mT32014  sum    2.19923E-6 0.0  1
20518541 0.0 1.0 cntrlvar 0212    1.0 cntrlvar 0234
20518550 dT32014  sum    1.0      0.0  1
20518551 0.0 1.0 tempf 220140000 -1.0 tempf 222140000
```

```
20518560 QJ32014  mult    1.0       0.0  1
20518561 cntrlvar 1853  cntrlvar 1854  cntrlvar 1855
20518570 Cp32015  sum     0.5       0.0  1
20518571 0.0 1.0 csubpf 220150000  1.0 csubpf 222150000
20518580 mT32015  sum   2.19923E-6  0.0  1
20518581 0.0 1.0 cntrlvar 0213    1.0 cntrlvar 0235
20518590 dT32015  sum     1.0       0.0  1
20518591 0.0 1.0 tempf 220150000  -1.0 tempf 222150000
20518600 QJ32015  mult    1.0       0.0  1
20518601 cntrlvar 1857  cntrlvar 1858  cntrlvar 1859
20518610 Cp32016  sum     0.5       0.0  1
20518611 0.0 1.0 csubpf 220160000  1.0 csubpf 222160000
20518620 mT32016  sum   2.19923E-6  0.0  1
20518621 0.0 1.0 cntrlvar 0214    1.0 cntrlvar 0236
20518630 dT32016  sum     1.0       0.0  1
20518631 0.0 1.0 tempf 220160000  -1.0 tempf 222160000
20518640 QJ32016  mult    1.0       0.0  1
20518641 cntrlvar 1861  cntrlvar 1862  cntrlvar 1863
20518650 Cp32017  sum     0.5       0.0  1
20518651 0.0 1.0 csubpf 220170000  1.0 csubpf 222170000
20518660 mT32017  sum   1.24122E-5  0.0  1
20518661 0.0 1.0 cntrlvar 0215    1.0 cntrlvar 0237
20518670 dT32017  sum     1.0       0.0  1
20518671 0.0 1.0 tempf 220170000  -1.0 tempf 222170000
20518680 QJ32017  mult    1.0       0.0  1
20518681 cntrlvar 1865  cntrlvar 1866  cntrlvar 1867
20518690 Cp32018  sum     0.5       0.0  1
20518691 0.0 1.0 csubpf 220180000  1.0 csubpf 222180000
20518700 mT32018  sum   1.24122E-5  0.0  1
20518701 0.0 1.0 cntrlvar 0216    1.0 cntrlvar 0238
20518710 dT32018  sum     1.0       0.0  1
20518711 0.0 1.0 tempf 220180000  -1.0 tempf 222180000
20518720 QJ32018  mult    1.0       0.0  1
20518721 cntrlvar 1869  cntrlvar 1870  cntrlvar 1871
20518730 Cp32019  sum     0.5       0.0  1
20518731 0.0 1.0 csubpf 220190000  1.0 csubpf 222190000
20518740 mT32019  sum   1.24122E-5  0.0  1
20518741 0.0 1.0 cntrlvar 0217    1.0 cntrlvar 0239
20518750 dT32019  sum     1.0       0.0  1
20518751 0.0 1.0 tempf 220190000  -1.0 tempf 222190000
20518760 QJ32019  mult    1.0       0.0  1
20518761 cntrlvar 1873  cntrlvar 1874  cntrlvar 1875
20518770 Cp32020  sum     0.5       0.0  1
20518771 0.0 1.0 csubpf 220200000  1.0 csubpf 222200000
20518780 mT32020  sum   1.24122E-5  0.0  1
20518781 0.0 1.0 cntrlvar 0218    1.0 cntrlvar 0240
20518790 dT32020  sum     1.0       0.0  1
20518791 0.0 1.0 tempf 220200000  -1.0 tempf 222200000
20518800 QJ32020  mult    1.0       0.0  1
20518801 cntrlvar 1877  cntrlvar 1878  cntrlvar 1879
20518810 Cp32021  sum     0.5       0.0  1
20518811 0.0 1.0 csubpf 220210000  1.0 csubpf 222210000
20518820 mT32021  sum   1.24122E-5  0.0  1
20518821 0.0 1.0 cntrlvar 0219    1.0 cntrlvar 0241
20518830 dT32021  sum     1.0       0.0  1
20518831 0.0 1.0 tempf 220210000  -1.0 tempf 222210000
```

```
20518840 QJ32021  mult    1.0      0.0  1
20518841 cntrlvar 1881  cntrlvar 1882  cntrlvar 1883
20518850 Cp32022  sum     0.5      0.0  1
20518851 0.0 1.0 csubpf 220220000   1.0 csubpf 222220000
20518860 mT32022  sum     9.28610E-6 0.0  1
20518861 0.0 1.0 cntrlvar 0220     1.0 cntrlvar 0242
20518870 dT32022  sum     1.0      0.0  1
20518871 0.0 1.0 tempf 220220000  -1.0 tempf 222220000
20518880 QJ32022  mult    1.0      0.0  1
20518881 cntrlvar 1885  cntrlvar 1886  cntrlvar 1887
```

Volume heat addition/subtraction Control Variables

These control variables evaluate the net heat added to/subtracted from each segment within the subchannel pipe. It is the sum of the heat transfer via the inlet transverse junctions less the sum of the heat transfer via the outlet transverse junctions. In the current example there are only 2 junctions, 1 inlet and 1 outlet. However, depending on the location in the assembly other volumes may have 1, 2, or 3 junctions, with no more than 2 inlet or outlet junctions in the same volume.

```
* Volume 220
*
20583230 QJ22001  sum      1.0   0.0  1
20583231 0.0 1.0 cntrlvar 5504  -1.0 cntrlvar 1804
20583240 QJ22002  sum      1.0   0.0  1
20583241 0.0 1.0 cntrlvar 5508  -1.0 cntrlvar 1808
20583250 QJ22003  sum      1.0   0.0  1
20583251 0.0 1.0 cntrlvar 5512  -1.0 cntrlvar 1812
20583260 QJ22004  sum      1.0   0.0  1
20583261 0.0 1.0 cntrlvar 5516  -1.0 cntrlvar 1816
20583270 QJ22005  sum      1.0   0.0  1
20583271 0.0 1.0 cntrlvar 5520  -1.0 cntrlvar 1820
20583280 QJ22006  sum      1.0   0.0  1
20583281 0.0 1.0 cntrlvar 5524  -1.0 cntrlvar 1824
20583290 QJ22007  sum      1.0   0.0  1
20583291 0.0 1.0 cntrlvar 5528  -1.0 cntrlvar 1828
20583300 QJ22008  sum      1.0   0.0  1
20583301 0.0 1.0 cntrlvar 5532  -1.0 cntrlvar 1832
20583310 QJ22009  sum      1.0   0.0  1
20583311 0.0 1.0 cntrlvar 5536  -1.0 cntrlvar 1836
20583320 QJ22010  sum      1.0   0.0  1
20583321 0.0 1.0 cntrlvar 5540  -1.0 cntrlvar 1840
20583330 QJ22011  sum      1.0   0.0  1
```

```
20583331  0.0  1.0  cntrlvar 5544   -1.0  cntrlvar 1844
20583340  QJ22012   sum      1.0   0.0   1
20583341  0.0  1.0  cntrlvar 5548   -1.0  cntrlvar 1848
20583350  QJ22013   sum      1.0   0.0   1
20583351  0.0  1.0  cntrlvar 5552   -1.0  cntrlvar 1852
20583360  QJ22014   sum      1.0   0.0   1
20583361  0.0  1.0  cntrlvar 5556   -1.0  cntrlvar 1856
20583370  QJ22015   sum      1.0   0.0   1
20583371  0.0  1.0  cntrlvar 5560   -1.0  cntrlvar 1860
20583380  QJ22016   sum      1.0   0.0   1
20583381  0.0  1.0  cntrlvar 5564   -1.0  cntrlvar 1864
20583390  QJ22017   sum      1.0   0.0   1
20583391  0.0  1.0  cntrlvar 5568   -1.0  cntrlvar 1868
20583400  QJ22018   sum      1.0   0.0   1
20583401  0.0  1.0  cntrlvar 5572   -1.0  cntrlvar 1872
20583410  QJ22019   sum      1.0   0.0   1
20583411  0.0  1.0  cntrlvar 5576   -1.0  cntrlvar 1876
20583420  QJ22020   sum      1.0   0.0   1
20583421  0.0  1.0  cntrlvar 5580   -1.0  cntrlvar 1880
20583430  QJ22021   sum      1.0   0.0   1
20583431  0.0  1.0  cntrlvar 5584   -1.0  cntrlvar 1884
20583440  QJ22022   sum      1.0   0.0   1
20583441  0.0  1.0  cntrlvar 5588   -1.0  cntrlvar 1888
```

Pseudo Heat Structures

These heat structures are used to add the heat transfer due to mixing to each volume. By referencing a control variable instead of a heating table, the code will input this amount of heating calculated by the given control variable into the fluid each time step. Additionally, the heat for these structures is deposited directly into the fluid, so that no heat is absorbed into the structure itself.

```
*
10021000 22  2 2 1 0.001905
10021100 0 1
10021101 1 0.001908
10021201 003 1
10021301 0. 1
10021400 0
10021401 628.15  2
10021501 0        0    0     1 0.01129   22
10021601 220020000  00000  111 1 0.01129   22
10021701 18323 0.0 0.0 1. 1
10021702 18324 0.0 0.0 1. 2
10021703 18325 0.0 0.0 1. 3
```

```
10021704 18326 0.0 0.0 1. 4
10021705 18327 0.0 0.0 1. 5
10021706 18328 0.0 0.0 1. 6
10021707 18329 0.0 0.0 1. 7
10021708 18330 0.0 0.0 1. 8
10021709 18331 0.0 0.0 1. 9
10021710 18332 0.0 0.0 1. 10
10021711 18333 0.0 0.0 1. 11
10021712 18134 0.0 0.0 1. 12
10021713 18135 0.0 0.0 1. 13
10021714 18136 0.0 0.0 1. 14
10021715 18137 0.0 0.0 1. 15
10021716 18338 0.0 0.0 1. 16
10021717 18339 0.0 0.0 1. 17
10021718 18340 0.0 0.0 1. 18
10021719 18141 0.0 0.0 1. 19
10021720 18142 0.0 0.0 1. 20
10021721 18143 0.0 0.0 1. 21
10021722 18144 0.0 0.0 1. 22

10021900 1
10021901 0.0 100. 100. 0.  0. 0. 0. 1.0 3.4994  1.1   1.  22
```